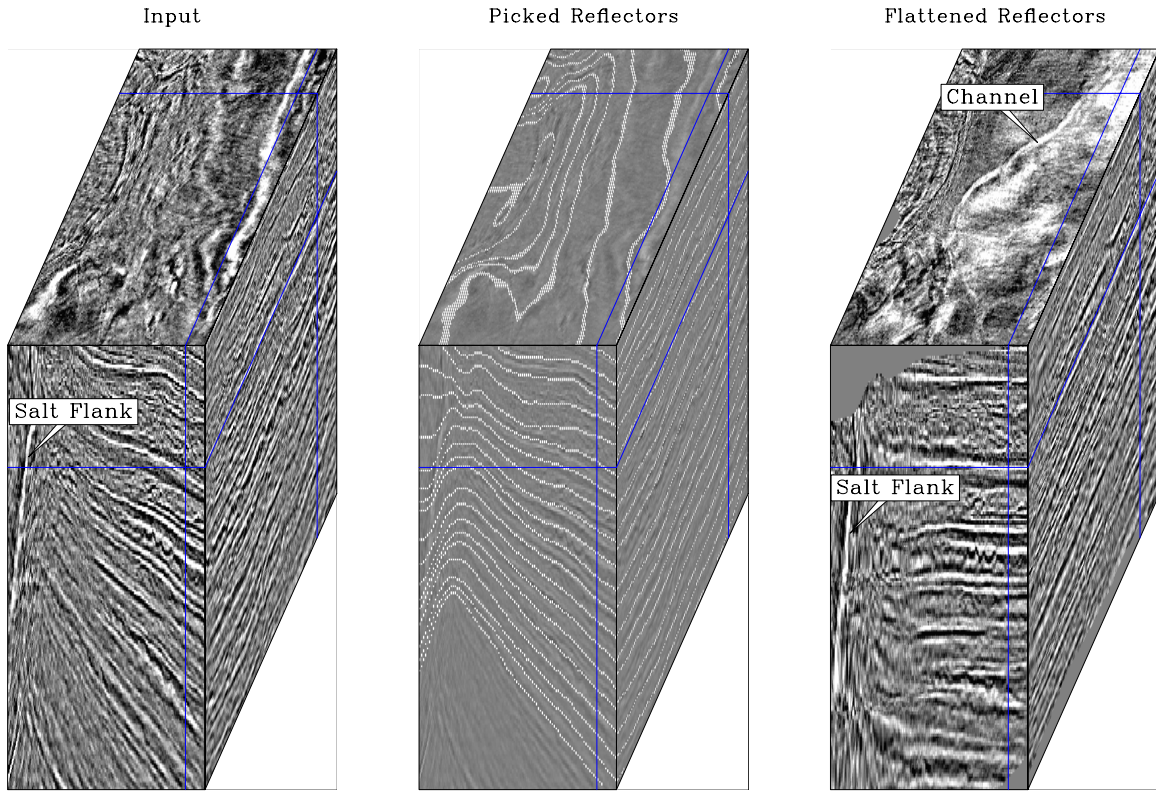


STANFORD EXPLORATION PROJECT

*Gabriel Alvarez, Brad Artman, James Berryman, Biondo Biondi, Jon Claerbout,
Robert Clapp, Marie Clapp, William Curry, Sergey Fomel, Antoine Guitton, Jesse Lomask,
Daniel Rosales, Satyakee Sen, Guojian Shan, Jeff Shragge, Alejandro Valenciano, Ioan Vlad,
Huazhong Wang, and Charles Wilson*

Report Number 120, April 2005



Copyright © 2005

by the Board of Trustees of the Leland Stanford Junior University

Stanford, California 94305

*Copying permitted for all internal purposes of the Sponsors of
Stanford Exploration Project*

Preface

The electronic version of this report¹ makes the included programs and applications available to the reader. The markings [ER], [CR], and [NR] are promises by the author about the reproducibility of each figure result. Reproducibility is a way of organizing computational research that allows both the author and the reader of a publication to verify the reported results. Reproducibility facilitates the transfer of knowledge within SEP and between SEP and its sponsors.

ER denotes Easily Reproducible and are the results of processing described in the paper. The author claims that you can reproduce such a figure from the programs, parameters, and makefiles included in the electronic document. The data must either be included in the electronic distribution, be easily available to all researchers (e.g., SEG-EAGE data sets), or be available in the SEP data library². We assume you have a UNIX workstation with Fortran, Fortran90, C, X-Windows system and the software downloadable from our website (SEP makerules, SEPlib, and the SEP latex package), or other free software such as SU. Before the publication of the electronic document, someone other than the author tests the author's claim by destroying and rebuilding all ER figures. Some ER figures may not be reproducible by outsiders because they depend on data sets that are too large to distribute, or data that we do not have permission to redistribute but are in the SEP data library.

CR denotes Conditional Reproducibility. The author certifies that the commands are in place to reproduce the figure if certain resources are available. SEP staff have only attempted to make sure that the makefile rules exist and the source codes referenced are provided. The primary reasons for the CR designation is that the processing requires 20 minutes or more, or commercial packages such as Matlab or Mathematica.

M denotes a figure that may be viewed as a movie in the web version of the report. A movie may be either ER or CR.

NR denotes Non-Reproducible figures. SEP discourages authors from flagging their figures as NR except for figures that are used solely for motivation, comparison, or illustration of the theory, such as: artist drawings, scannings, or figures taken from SEP reports not by the authors or from non-SEP publications.

Our testing is currently limited to LINUX 2.4 (using the Portland Group Fortran90 compiler), but the code should be portable to other architectures. Reader's suggestions are welcome. For more information on reproducing SEP's electronic documents, please visit <http://sepwww.stanford.edu/research/redoc/>.

¹<http://sepwww.stanford.edu/private/docs/sep120>

²http://sepwww.stanford.edu/public/docs/sepdata/lib/toc_html/

SEP-120 — TABLE OF CONTENTS

Inversion

<i>Clapp M. L. and Clapp R. G.</i> , 3-D subsalt imaging via regularized inversion with model preconditioning	1
<i>Valenciano A. A., Biondi B., and Guitton A.</i> , Target-oriented wave-equation inversion	23
<i>Clapp R. G.</i> , Inversion and fault tolerant parallelization using Python.....	41

Anisotropy

<i>Shan G. and Biondi B.</i> , Imaging steeply dipping reflectors in TI media by wavefield extrapolation.....	63
<i>Biondi B.</i> , Angle-domain common image gathers for anisotropic migration	77
<i>Shan G. and Biondi B.</i> , 3D wavefield extrapolation in laterally-varying tilted	105
<i>Sen S. and Biondi B.</i> , Common azimuth migration for elliptical and VTI media.....	125

Automated interpretation

<i>Lomask J., Guitton A., Fomel S., and Claerbout J.</i> , Update on flattening without picking ..	137
<i>Lomask J., Guitton A., and Valenciano A.</i> , Flattening without picking faults	159
<i>Guitton A., Lomask J., and Fomel S.</i> , Non-linear estimation of vertical delays with a quasi-	167
<i>Lomask J. and Biondi B.</i> , Image segmentation with bounds	179

Interpolation and amplitudes regularization

<i>Clapp R. G.</i> , Data regularization: inversion with azimuth move-out	187
<i>Wilson C. K. and Guitton A.</i> , Interpolation and signal extraction of teleseismic wavefields with the linear radon transform.....	197
<i>Vlad I.</i> , Focusing-effect AVO/AVA: overview of results and assessment of problems	217
<i>Curry W.</i> , Interpolating with data-space prediction-error filters.....	237
<i>Curry W.</i> , Non-stationary PEFs and large gaps	247

Imaging

<i>Shragge J., Artman B., and Biondi B.</i> , ADCIGs for forward-scattered wavefields	257
<i>Artman B.</i> , Time windowing passive seismic data in the frequency domain	273
<i>Rosales D. A. and Biondi B.</i> , Converted-wave common-azimuth migration	279
<i>Rosales D. A. and Biondi B.</i> , Converted-mode angle-domain common-image gathers for migration velocity analysis	285
<i>Shragge J.</i> , Orthogonal mesh generation for Riemannian wavefield extrapolation	299
<i>Alvarez G. and Artman B.</i> , Wavefield extrapolation in frequency-wavenumber domain for spatially-varying velocity models	311
<i>Vlad I.</i> , Migration and modeling of seismic data affected by focusing-effect AVO/AVA....	319
<i>Artman B. and Fomel S.</i> , Fourier-domain imaging condition for shot-profile migration	325
<i>Wang H. and Shan G.</i> , A self-adaptive algorithm for choosing reference velocities in the presence of lateral velocity variations	333
<i>Wang H. and Shan G.</i> , Unified seismic-wave imaging - from data space to model space ...	347

Multiples and noise attenuation

<i>Alvarez G.</i> , Water-bottom and diffracted 2D multiple reflections in data space and image space	365
<i>Rosales D. A. and Guitton A.</i> , Multiple attenuation: data space vs. image space - A real data example	377
<i>Guitton A.</i> , Sparse radon transforms with a bound-constrained approach	389
<i>Artman B. and Guitton A.</i> , Removal of linear events with combined radon transforms	395

Rock Physics

<i>Berryman J. G.</i> , Using knowledge of microstructure to improve estimates and bounds on elastic constants and transport coefficients in heterogeneous media	407
<i>Berryman J. G.</i> , Geomechanical constants of heterogeneous reservoirs: pore fluid effects on shear modulus	437

SEP article published or in press, 2004-05	469
--	-----

SEP phone directory	473
Research personnel	475
SEP sponsors for 2004-05	483

3-D subsalt imaging via regularized inversion with model preconditioning

Marie L. Clapp and Robert G. Clapp¹

ABSTRACT

Subsalt imaging is a difficult but increasingly important problem. The poor illumination that occurs when seismic energy is affected by the complex subsurface at and around salt bodies causes significant shadow zones in migration results. These shadow zones may contain real signal, but it is weak compared to the artifacts caused by multipathing and poor illumination. To reduce artifacts and recover this energy, thereby improving the image, we use an imaging (migration) operator in a regularized least-squares inversion. The regularization operator acts on the offset ray parameter (reflection angle) axis of the model space. Performing several iterations of regularized inversion that penalize large changes along the offset ray parameter axis results in an image with recognizable events in the shadow zones and fewer artifacts. We perform regularized inversion with model preconditioning on real 2-D and 3-D data to obtain seismic images that are better in poorly illuminated areas than migration results.

INTRODUCTION

Our ongoing quest for hydrocarbons requires that we improve our ability to image the earth's subsurface. This is particularly true in areas around salt bodies, which can be good hydrocarbon traps but cause poor seismic illumination in the surrounding subsurface. Conventional imaging techniques such as migration cannot provide an adequate picture of these poorly illuminated areas (Muerdter et al., 1996; Prucha et al., 1998). In such areas, random noise and processing artifacts can easily obscure the small amount of signal that exists. A common type of artifact seen in these areas is caused by multipathing. Many authors have reduced these artifacts by generating images through Kirchhoff-type migration that create angle domain common image gathers (Xu et al., 2001). The artifacts are even better handled by downward-continuation migration (Prucha et al., 1999a; Stolk and Symes, 2004). However, reducing multipathing artifacts does not significantly improve the image where illumination is poor. To create improvements, we will have to deal with both these artifacts and the poor illumination which means we must move beyond migration.

Although migration is not sufficient to image the subsurface in areas with poor illumination, we can use migration as an imaging operator in a least-squares inversion scheme (Nemeth

¹email: marie@sep.stanford.edu, bob@sep.stanford.edu

et al., 1999; Duquet and Marfurt, 1999; Ronen and Liner, 2000). In areas with poor illumination, the inversion problem is ill-conditioned, therefore it is wise to regularize the inversion scheme (Tikhonov and Arsenin, 1977). The regularization operator can be designed to exploit knowledge we have about the expected amplitude behavior and dip orientation of events in the image (Prucha and Biondi, 2002).

When using regularized inversion for imaging, the choice of regularization operator is critical. If it were possible for the subsurface to be perfectly illuminated, we would expect the amplitudes of the seismic events to vary smoothly with reflection angle. Therefore, an intelligent and fairly safe choice of regularization is to penalize large amplitude changes as the reflection angle varies for a given point in the subsurface (Kuehl and Sacchi, 2001; Prucha and Biondi, 2002). We refer to this as “geophysical” regularization. This process will help to reduce artifacts and improve the image.

In this paper, we examine the effects of geophysically regularized inversion on a real 3-D dataset. We will begin by explaining the basic theory of regularized inversion with model preconditioning (RIP). We will then demonstrate its use on a real 2-D line and the real 3-D volume that the 2-D line is taken from.

BASIC THEORY

Our inversion scheme is based on the downward-continuation migration explained by Prucha et al. (1999a). To summarize, this migration is carried out by downward continuing the wavefield in frequency space, slant stacking at each depth, and extracting the image at zero time. The result is an image in depth (z), space (x and y), and offset ray parameter (p_h). Offset ray parameter is related to the reflection angle (θ) and the dip angle of the reflector (ϕ) in 2-D as:

$$\frac{\partial t}{\partial h} = p_h = \frac{2 \sin \theta \cos \phi}{V(z, x)}. \quad (1)$$

In complex areas, the image produced by downward-continuation migration will suffer from poor illumination. To compensate for this, we use the migration as an operator in a least-squares inversion. The inversion procedure used in this paper can be expressed as fitting goals as follows:

$$\begin{aligned} \mathbf{0} &\approx \mathbf{Lm} - \mathbf{d} \\ \mathbf{0} &\approx \epsilon \mathbf{Am}. \end{aligned} \quad (2)$$

The first equation is the “data fitting goal,” meaning that it is responsible for making a model that is consistent with the data. The second equation is the “model styling goal,” meaning that it allows us to impose some idea of what the model should look like using the regularization operator \mathbf{A} . The model styling goal also helps to prevent a divergent result.

In the data fitting goal, \mathbf{d} is the input data and \mathbf{m} is the image obtained through inversion. \mathbf{L} is a linear operator, in this case it is the adjoint of the downward-continuation migration scheme summarized above and explained by Prucha et al. (1999b). In the model styling goal, \mathbf{A} is a regularization operator and ϵ controls the strength of the regularization.

Unfortunately, the inversion process described by fitting goals (2) can take many iterations to produce a satisfactory result. We can reduce the necessary number of iterations by making the problem a preconditioned one. We use the preconditioning transformation $\mathbf{m} = \mathbf{A}^{-1}\mathbf{p}$ (Fomel et al., 1997; Fomel and Claerbout, 2003) to give us the following fitting goals:

$$\begin{aligned}\mathbf{0} &\approx \mathbf{L}\mathbf{A}^{-1}\mathbf{p} - \mathbf{d} \\ \mathbf{0} &\approx \epsilon\mathbf{p}.\end{aligned}\tag{3}$$

\mathbf{A}^{-1} is obtained by mapping the multi-dimensional regularization operator \mathbf{A} to helical space and applying polynomial division (Claerbout, 1998). We call this least-squares minimization scheme Regularized Inversion with model Preconditioning (RIP).

The question now is what the regularization operator \mathbf{A} is. In this paper, we will use geophysical regularization, which acts horizontally along the offset ray parameter axis (Clapp, 2003). It is designed to penalize sudden large changes in amplitudes, such as those caused by poor illumination.

THE DATASET

The dataset upon which we have chosen to demonstrate RIP is a subset of the real 3-D Gulf of Mexico dataset provided to SEP by BP and ExxonMobil. The portion of the 3-D velocity model for the subset we are using can be seen in Figure 1. This subset contains 600 inline positions and 72 crossline positions. The salt body on the right side causes significant shadow zones that may mask potential hydrocarbon reservoirs. There are known 3-D faults in the sediments away from the salt and it is likely that more faults exist beneath salt in the shadow zones. The velocity model is believed to be accurate, which is important given the nature of our geophysical regularization operator.

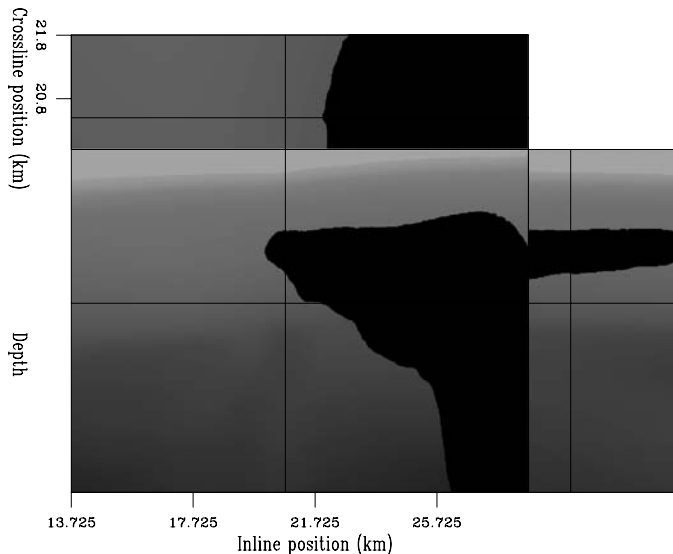
2-D RESULTS

To test RIP on a real 2-D example, we extracted a single line from the subset of the deep water Gulf of Mexico dataset. This line is located at the crossline position of 20 km, chosen in an attempt to minimize the 3-D effects of the salt structure. However, this line will still be affected by the 3-D faults known to run through this volume.

Recall that the regularization operator used for geophysical RIP acts along the offset ray parameter axis. The strength of regularization (see the fitting goals (3)) for this real data example, $\epsilon = .001$, was chosen by trial and error. We have chosen to display the results after

Figure 1: Subset of the BP Gulf of Mexico velocity model.

`marie1-bpvel` [CR]



6 iterations which was selected based on data space residuals, as will be explained later. The result can be seen in Figure 2. The migration result is displayed above the geophysical RIP result. Both show a common ray parameter section on the left and a common image gather (CIG) on the right. The vertical lines indicate which common reflection point (CRP) location and offset ray parameter value the panels are taken from. The effect of the regularization is clearest in the CIG. The common ray parameter section also shows the effects. The result shows a crisper image after RIP, with fewer artifacts. To see the improvements more clearly, we have zoomed in on the area beneath the salt in Figure 3.

In Figure 3, the same ovals are shown on the migration result (top) and the geophysical RIP result (bottom). It is particularly clear that the holes in the common image gather are being filled by RIP. The whole common ray parameter section is cleaner than the one from the migration result. The subsalt reflectors are extending into the shadow zones everywhere, particularly in the areas indicated by the ovals. Geophysical RIP produces a cleaner result with better illumination than migration.

It is also interesting to stack the results (Figure 4). Once again, the stack of the migration result is shown on top and the stack of the result after 6 iterations of geophysical RIP is on the bottom. The ovals indicate where the reflectors extend farther into the shadow zones. In the RIP result, some reflectors can be seen almost all the way through the poorly illuminated areas. Also, the artifacts seen in the stack of the migration result are reduced in the RIP result.

As mentioned earlier, we chose to display the RIP results after 6 iterations based on an examination of the data space residuals as the least-squares inversion was performed. The data space residuals for each iteration can be seen in Figure 5. Each row is a collection of CMP gathers taken from locations across the whole survey. We have taken the envelope of the energy and clipped the high values, which appear as solid black regions. The first row is the original data, the second row shows the same CMP gathers after 2 iterations, the third row is after 4 iterations, fourth row after 6 iterations, fifth row after 8 iterations and sixth after 10

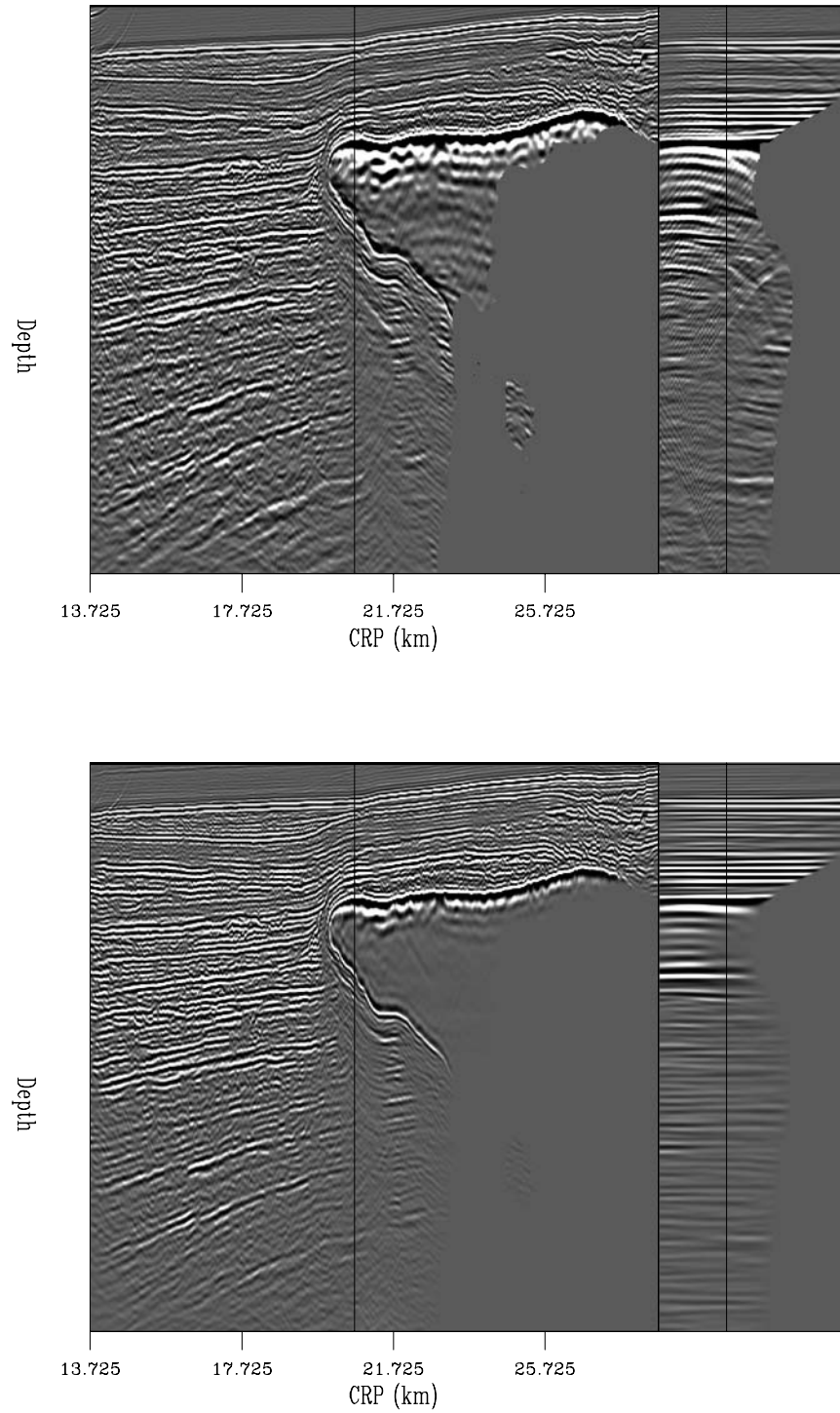


Figure 2: Top: result of downward-continuation migration of 2-D line. Left part is a common offset ray parameter section at $p_h = .265$, right part is a common image gather from $CRP = 20.675$. Bottom: result of 6 iterations of geophysical RIP. marie1-bp2d.1 [CR,M]

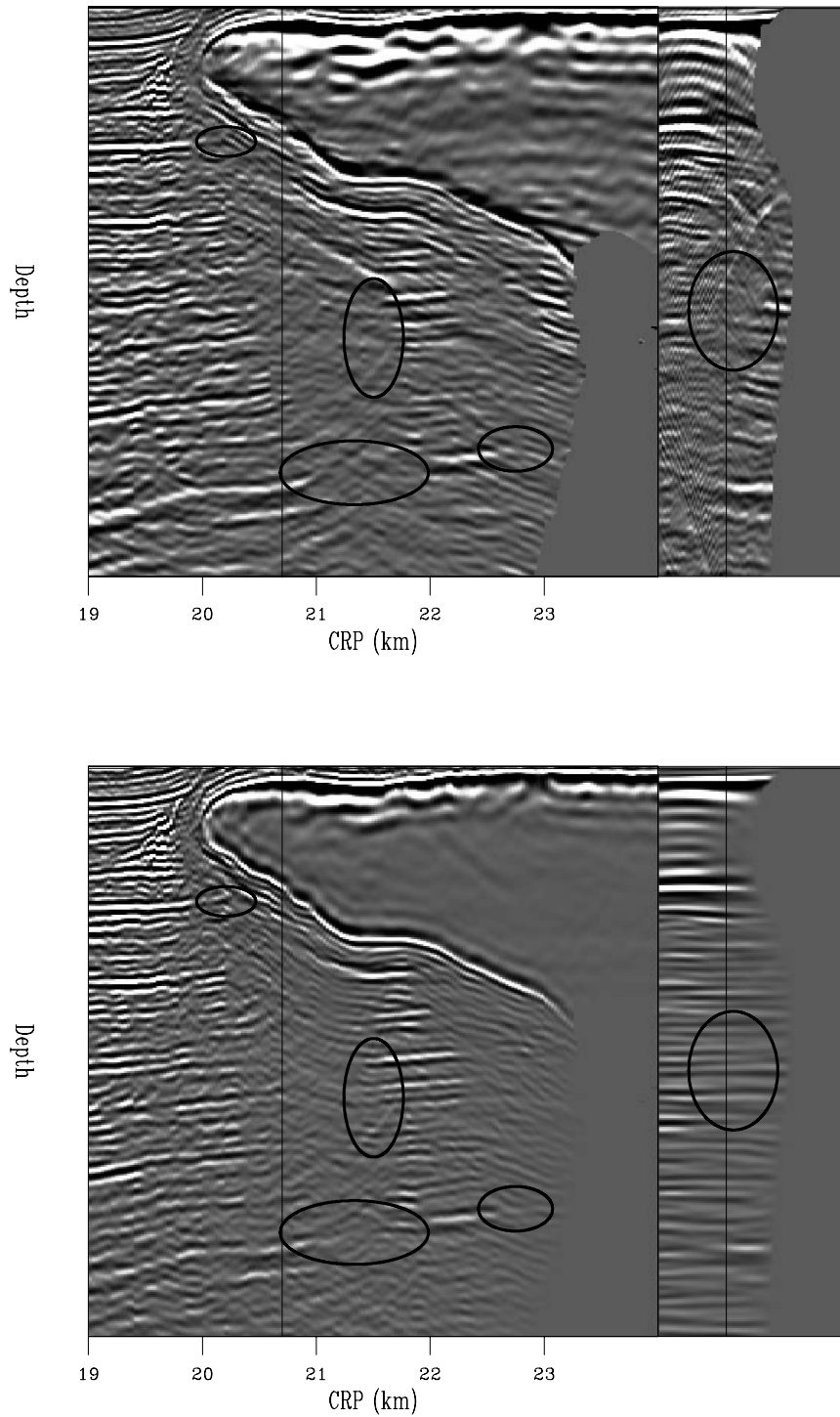


Figure 3: Zoomed portion of Figure 2. Top: result of downward-continuation migration of 2-D line. Left part is a common offset ray parameter section at $p_h = .265$, right part is a common image gather from $CRP = 20.675$. Bottom: result of 6 iterations of geophysical RIP. Ovals indicate areas where poor illumination exists in the migration result and is improved in the RIP result. `marie1-zbp2d.1` [CR,M]

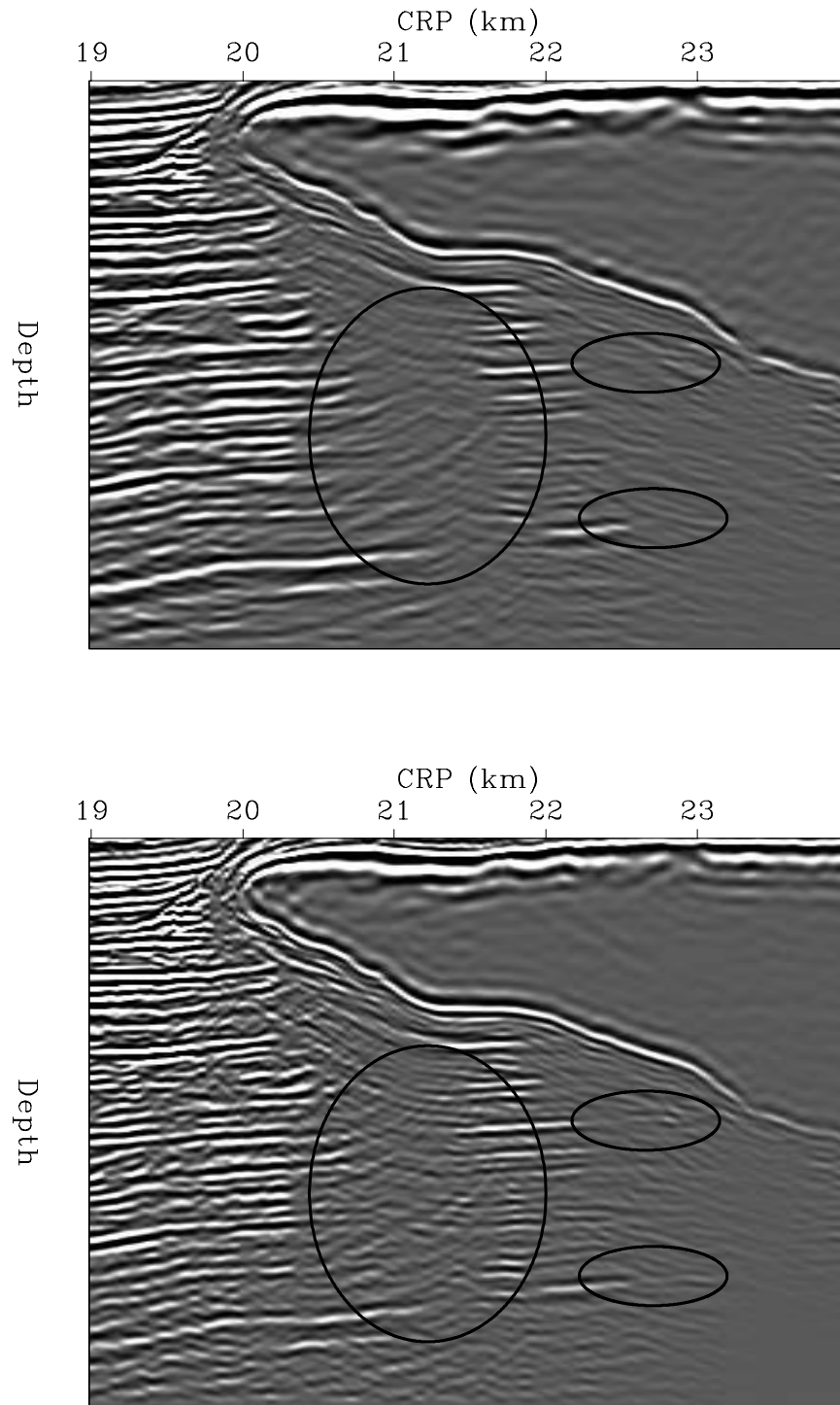


Figure 4: Top: stack of the result of downward-continuation migration of 2-D line. Bottom: stack of the result of 6 iterations of geophysical RIP. Ovals indicate areas where poor illumination exists in the migration result and is improved in the RIP result. marie1-zstackbp2d
[CR,M]

iterations. The salt body begins at a CMP location between the fifth and sixth gathers shown in each row.

The biggest change in the residual energy occurs within the first two iterations, as would be expected. We see that the residual energy away from the salt decreases quickly (the black areas decrease). The residual energy associated with the salt also decreases, with the exception of energy that is caused by converted waves that our acoustic code cannot properly handle. The small change in residual energy between the sixth and tenth iterations indicates that the inversion is nearing convergence. Therefore, we expect very little change in the image after 6 iterations.

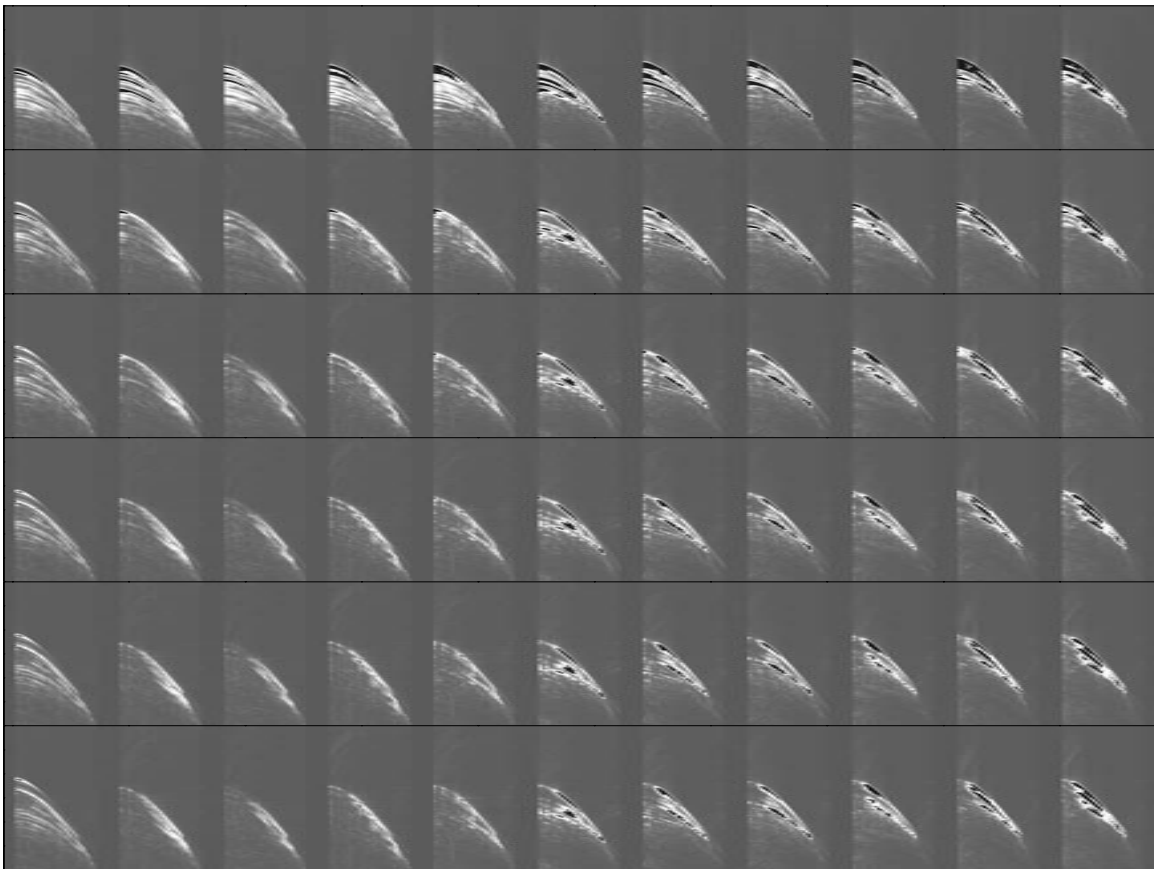


Figure 5: Comparison of the data space residuals from RIP with geophysical regularization. The vertical axis is time, the horizontal axis is offset. Each row is a collection of CMP gathers taken from locations across the whole survey, taking the envelope of the energy and clipping the high values (indicated by black). The first row is the original data, the second row shows the same CMP gathers after 2 iterations, the third row is after 4 iterations, fourth row after 6 iterations, fifth row after 8 iterations and sixth after 10 iterations. `marie1-comp.resid` [CR,M]

3-D RESULTS

To apply RIP to 3-D data, we chose to change our migration operator from downward-continuation migration to common azimuth migration (Biondi and Palacharla, 1996). This helps to keep our computational needs relatively low for a 3-D imaging problem. It also means that we will only be handling the inline offsets, so geophysical RIP will only be acting along the inline offset ray parameter.

Comparison of 3-D stacked results

The stack of the common azimuth migration (CAM) result (upper panels of Figures 6 and 7) of this 3-D cube is good, indicating that the velocity model is fairly accurate. There are 3-D faults visible away from the salt. Under the salt, the shadow zones caused by poor illumination are easy to identify, although they are full of noise and artifacts.

We performed 7 iterations of 3-D geophysical RIP. The result of the stack can be seen in the lower panels of Figure 6 and Figure 7. The two figures display different inline, crossline, and depth slices, but the types of improvements are the same. In both figures, ovals on the stacked migration result and the stacked geophysical RIP result indicate particular areas where RIP has improved the image. In Fig. 6, oval “A” indicates reflectors that can be followed under the salt nose after imaging with RIP. Ovals “B”, “C”, and “D” show areas on the inline section where the reflectors can be traced almost entirely through the shadow zones after RIP. In the crossline section, many more reflectors are seen after RIP, particularly in oval “E”. In Fig. 7, ovals “A”, “B”, and “C” show areas on the inline section where the reflectors can be traced almost entirely through the shadow zones after RIP and oval “D” shows reflectors and a possible fault in the crossline section.

It is not surprising that the comparison of the migration stack and the RIP stack show less impressive improvements than seen in the 2-D example. Performing only 7 iterations of geophysical RIP, which is regularizing only the inline p_h axis, will not change the image enough to show very significant effects in the stacked volumes. Although there were more substantial improvements in the stacks after 6 iterations of RIP on a 2-D line taken from this dataset (Fig. 4), inverting a 3-D problem means that it can take many more iterations to get similar improvements. However, 3-D RIP does result in clear improvements over the migration results.

Comparison of unstacked inline results

Using CAM as the imaging operator in our least-squares inversion means that our geophysical regularization operator will only be acting along the inline p_h axis. Therefore, the most significant changes between the CAM result and the geophysical RIP result will be seen in unstacked results. To study these, we have selected several unstacked inline volumes from crossline=20.9 km. These volumes can be seen in Figures 8 through 15, where (if you rotate the pages 90° counter-clockwise) we are displaying the depth slice on the top of the figure,

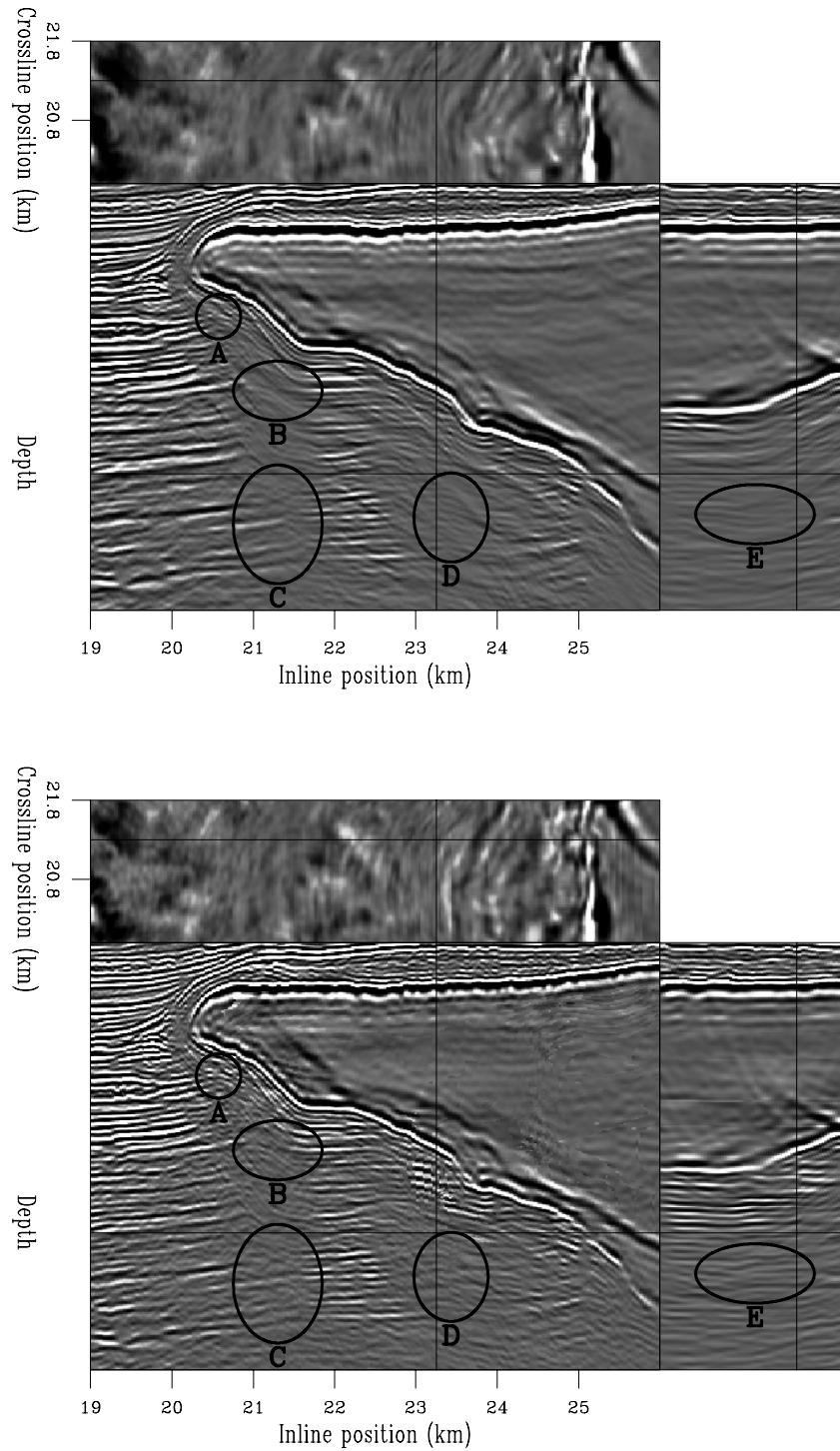


Figure 6: Zoomed 3-D image displayed with depth slice, inline section from crossline=21.3 km and crossline section from inline=23.25 km. Top: stack after common azimuth migration. Bottom: stack after 7 iterations of geophysical RIP. Ovals indicate areas of particular improvement in the RIP result. `marie1-zstack3d.1` [CR,M]

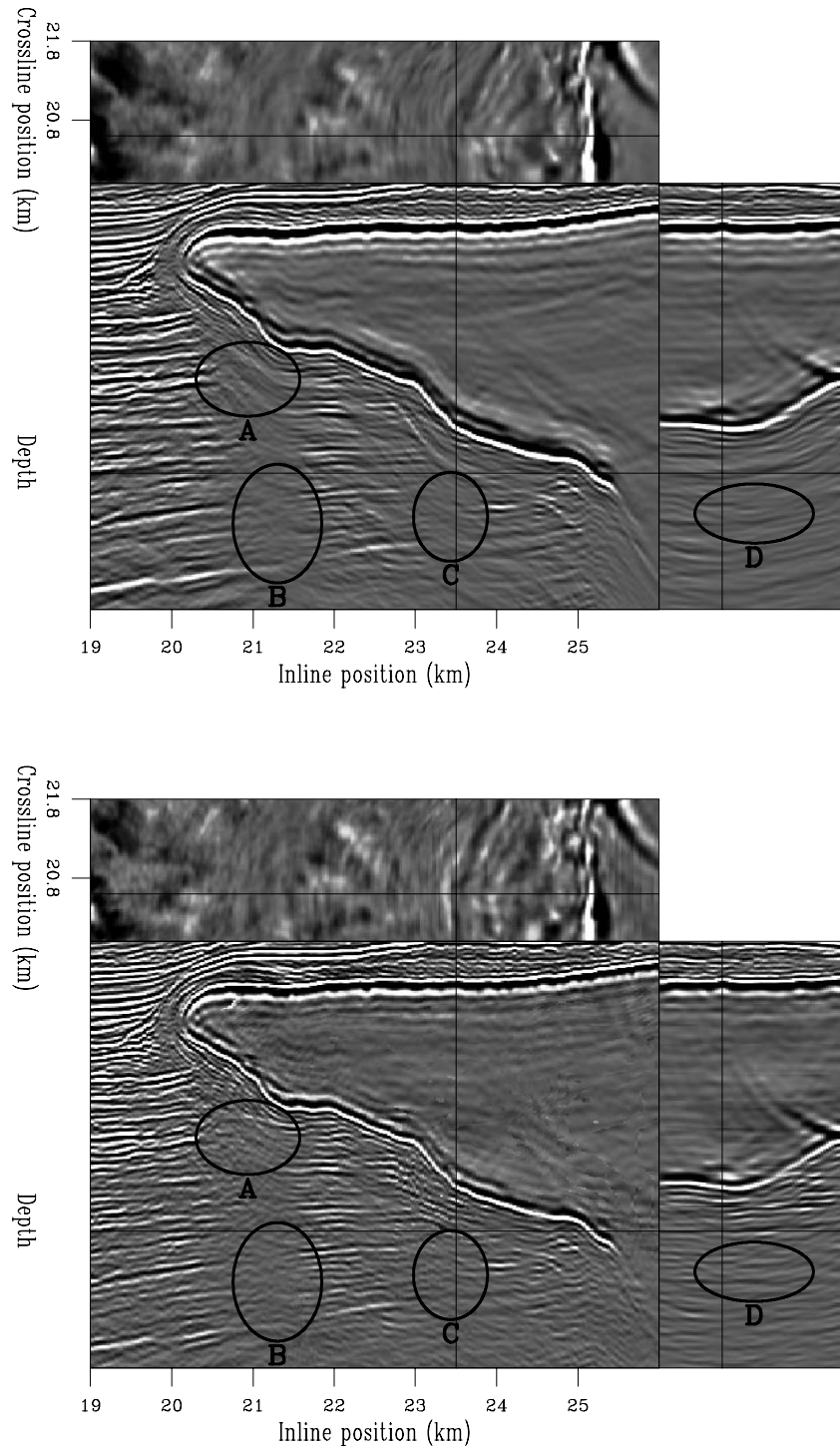


Figure 7: Zoomed 3-D image displayed with depth slice, inline section from crossline=20.6 km and crossline section from inline=23.5 km. Top: stack after common azimuth migration. Bottom: stack after 7 iterations of geophysical RIP. Ovals indicate areas of particular improvement in the RIP result. `marie1-zstack3d.2` [CR,M]

the common inline p_h section on the left, and the common image gather to the right of the common inline p_h section. The migration result is shown first, then the geophysical RIP result for each (common inline p_h section - common image gather) pair.

Figures 8 and 9 show a common inline p_h section from $p_h = .1875$ and a common image gather from inline position 20.375 km. Comparing Figure 8 and Figure 9, the RIP result is considerably cleaner. The effects of the regularization are clear in the common image gather (right part of the figures), where the unlabeled oval indicates gaps in the events that are filled by RIP. In the common inline p_h section, the ovals indicate particular areas of the shadow zones that are being filled in. Oval "A" highlights a reflector that, in the migration result, is discontinuous and has inconsistent amplitudes where it does exist. In the RIP result, this reflector is continuous with strong amplitudes along its full extent. Oval "B" extends across one of the shadow zones. The shadow zone is considerably cleaner in the RIP result, with almost none of the up-sweeping artifacts seen in the migration result. Also, the reflectors themselves extend farther into the shadow zone, particularly on the right side of the oval. The events also extend farther into the shadow zone indicated by oval "C".

Moving further under the salt and to a larger offset ray parameter, Figures 10 and 11 show a common inline p_h section from $p_h = .2325$ and a common image gather from inline position 21.65 km. The unlabeled oval in the common image gather shows events that have been strengthened and are more horizontal in the RIP result (Fig. 11) than the migration result (Fig. 10). The ovals marked "A", "B", and "C" on the common p_h sections show the same type of improvement seen in the previous comparison (Figs. 8 and 9). The reflectors at the right side of oval "B" in Figure 11 extend much farther into the shadow zone than those from the migration result.

Another interesting comparison can be made at common inline p_h section from $p_h = .15$ and a common image gather from inline position 20.9 km (Figures 12 and 13). In this migration result (Fig. 12), the common image gather once again has events with gaps caused by poor illumination, indicated by the unlabeled oval. These gaps are largely filled by 7 iterations of RIP, as seen in Figure 13. We see the same improvements in ovals "A", "B", and "C" as discussed for the previous two comparisons. In this comparison, there is an additional oval "D" that indicated reflectors under the salt that are less affected by artifacts and more likely to be accurate in the RIP result than in the migration result.

Finally, looking at the same common image gather from inline position 20.9 km but moving the common inline p_h section to $p_h = .2925$, we compare Figures 14 and 15. In this common p_h section, the effect of a critical angle mute applied during the inversion process can be seen in and below the salt body. The oval in the common image gather shows the same events with gaps in the migration result (Fig. 14) that are filled by RIP (Fig. 15) that was seen in the previous comparison. It is interesting to see that the improvements seen in the "A", "B", and "C" ovals in the previous examples are also seen in this example, at a much larger p_h . Obviously, RIP has a positive effect for a large range of p_h .

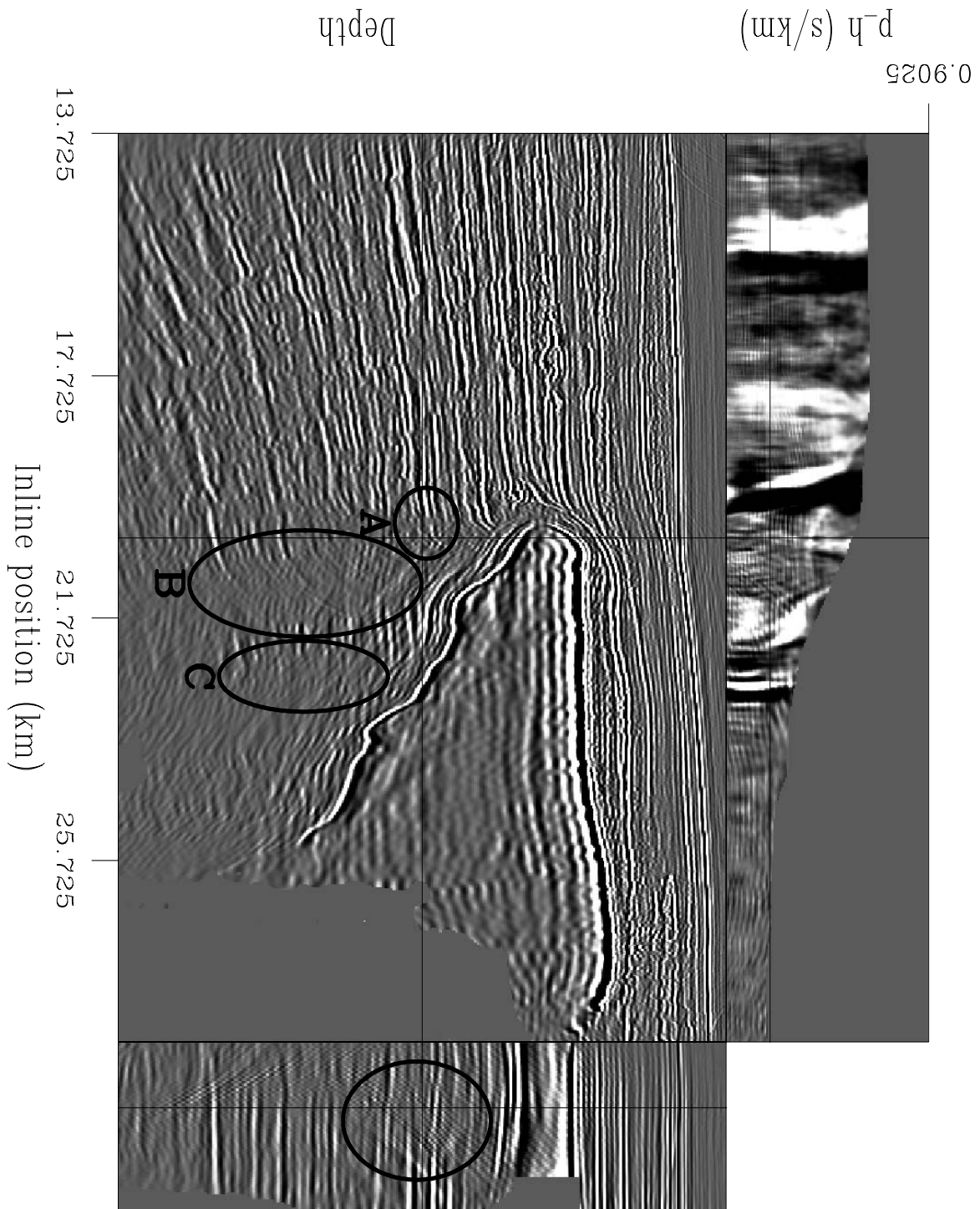
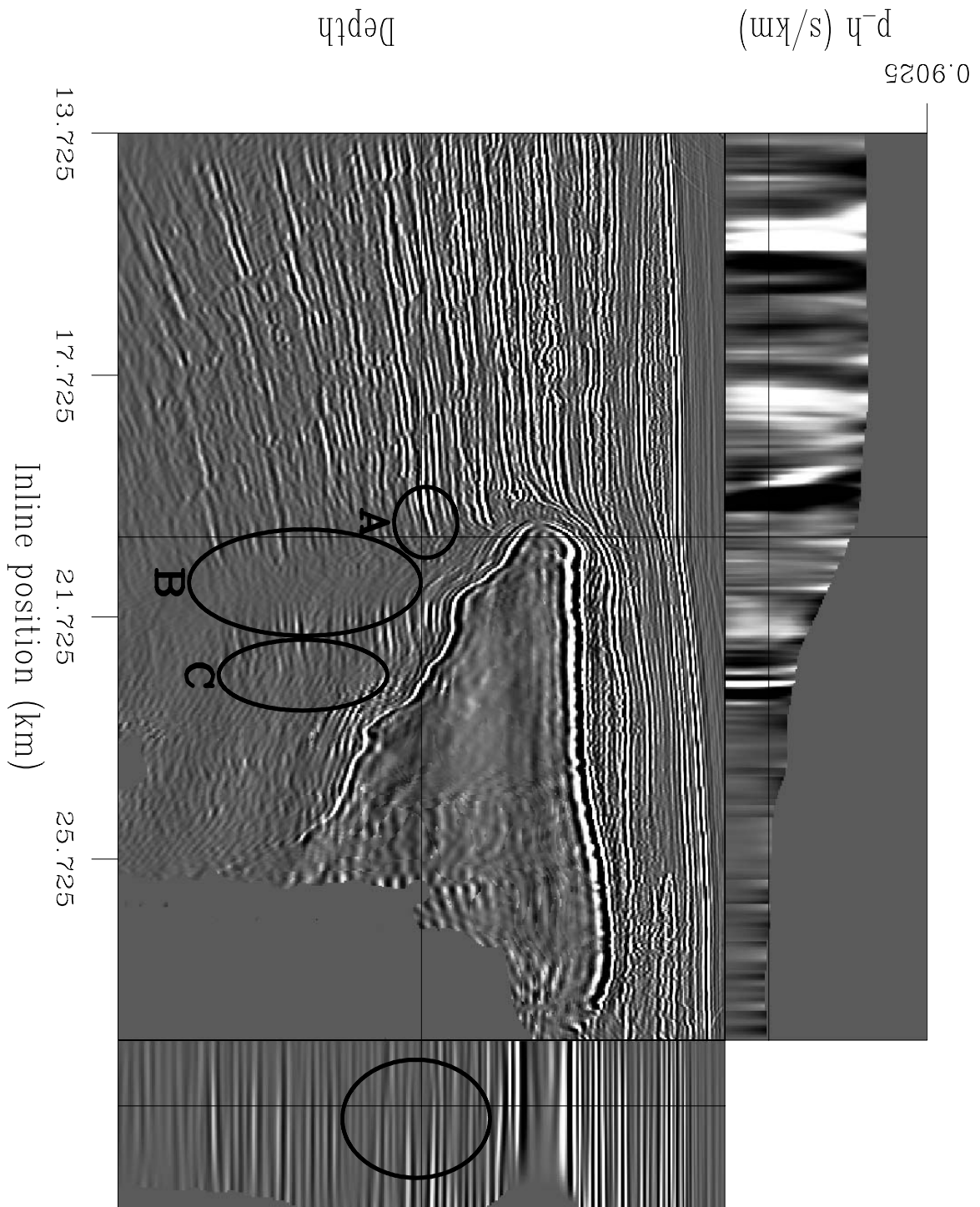


Figure 8: Migration result. Crossline=20.9 km, common inline p_h section from $p_h = .1875$, and common image gather from inline=20.375 km. Compare with Figure 9. marie1-bp3d.mig.1 [CR]



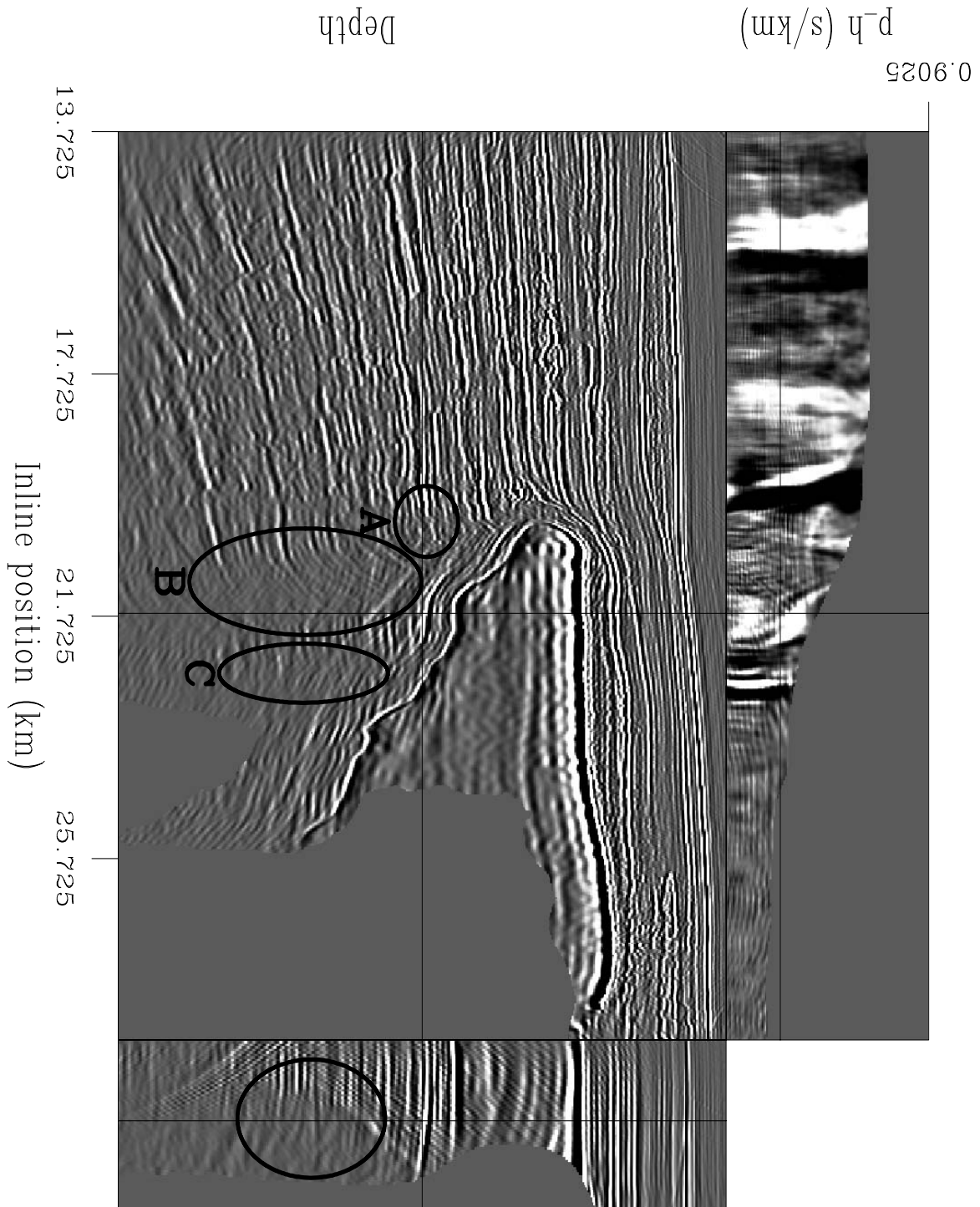


Figure 10: Migration result. Crossline=20.9 km, common inline p_h section from $p_h = .2325$, and common image gather from inline=21.65 km. Compare with Figure 11. marie1-bp3d.mig.2 [CR]

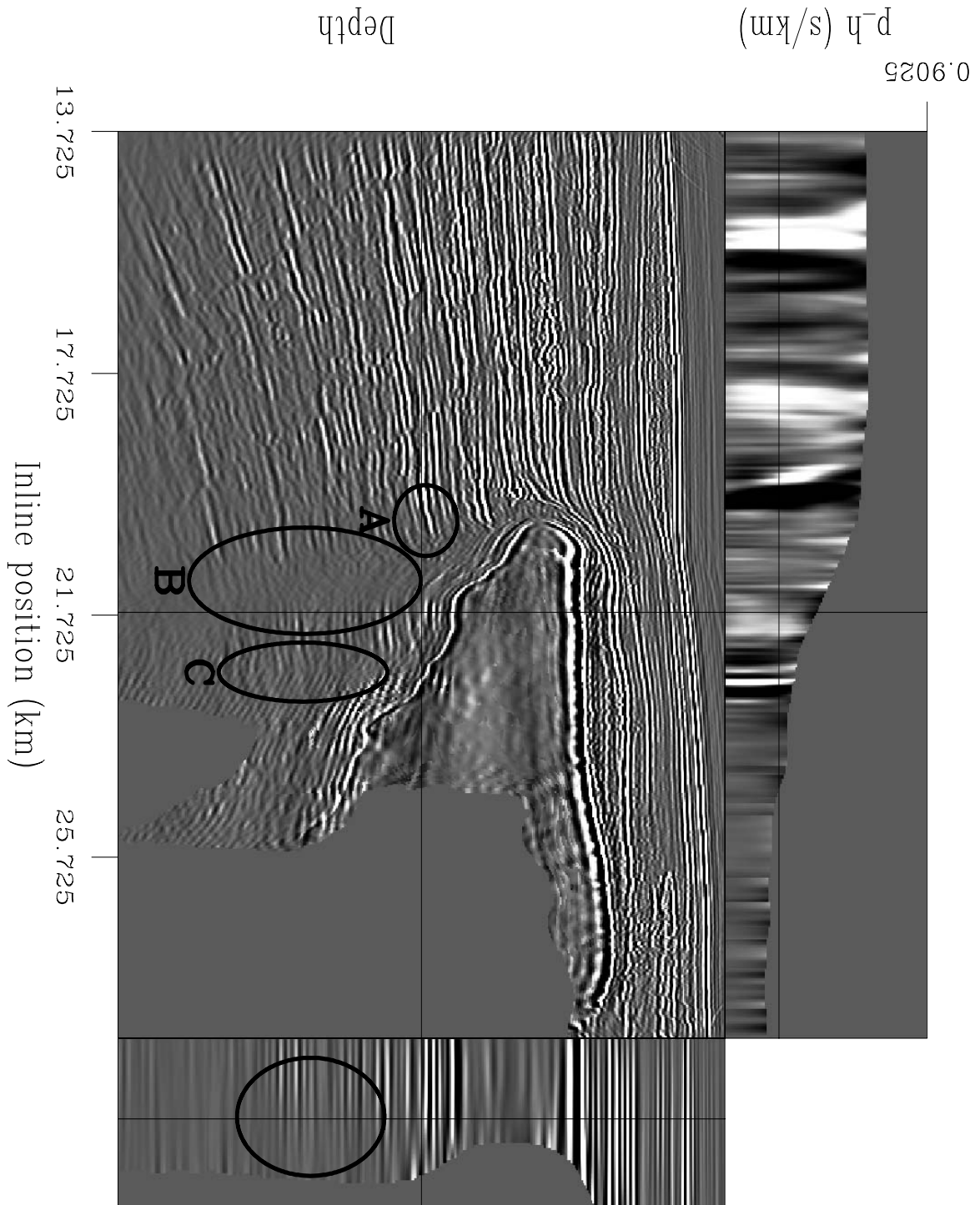


Figure 11: Geophysical RIP result. Crossline=20.9 km, common inline p_h section from $p_h = .2325$, and common image gather from inline=21.65 km. Compare with Figure 10. marie1-bp3d.geop.2 [CR]

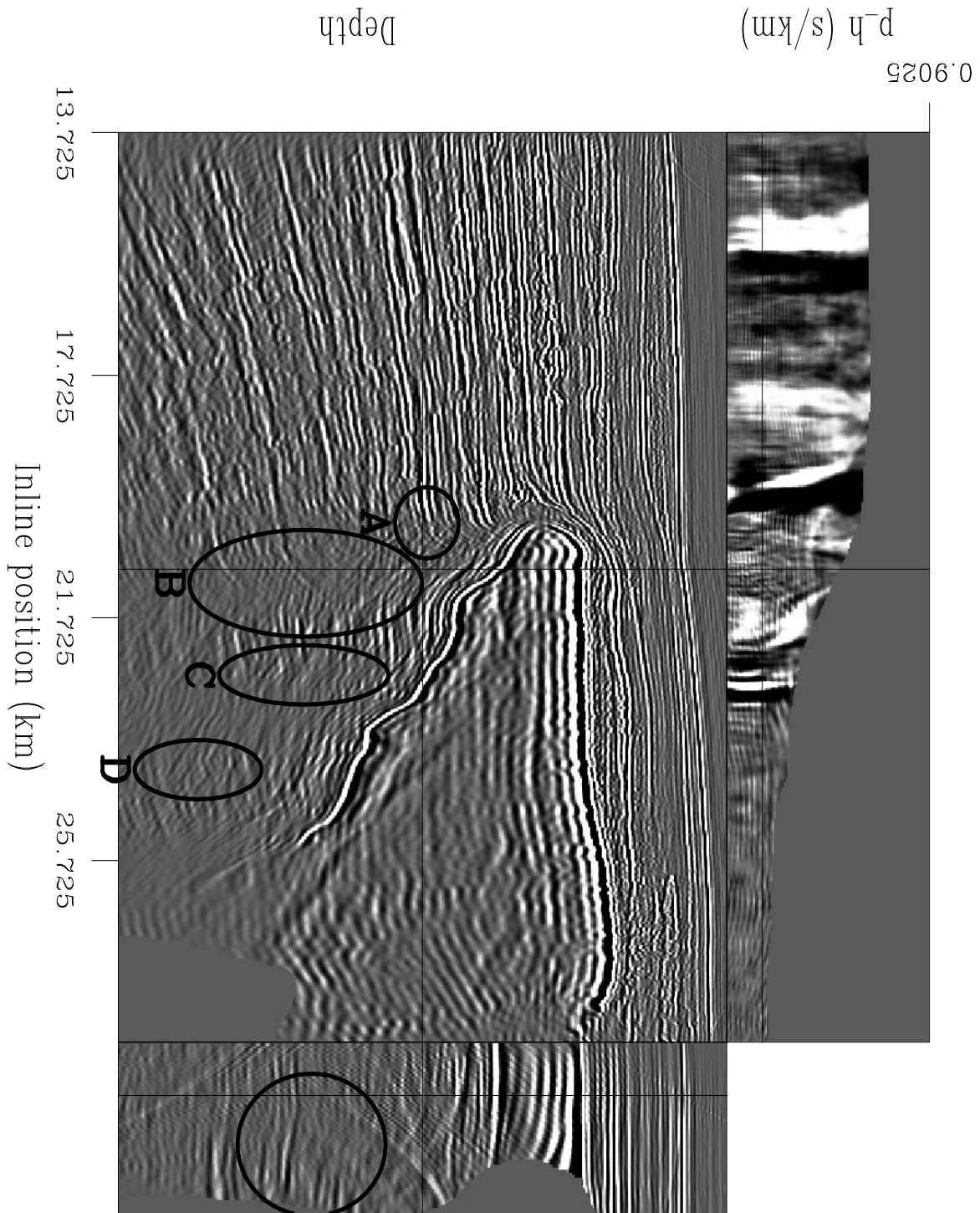


Figure 12: Migration result. Crossline=20.9 km, common inline p_h section from $p_h = .15$, and common image gather from inline=20.9 km. Compare with Figure 13. marie1-bp3d.mig.3
 [CR]

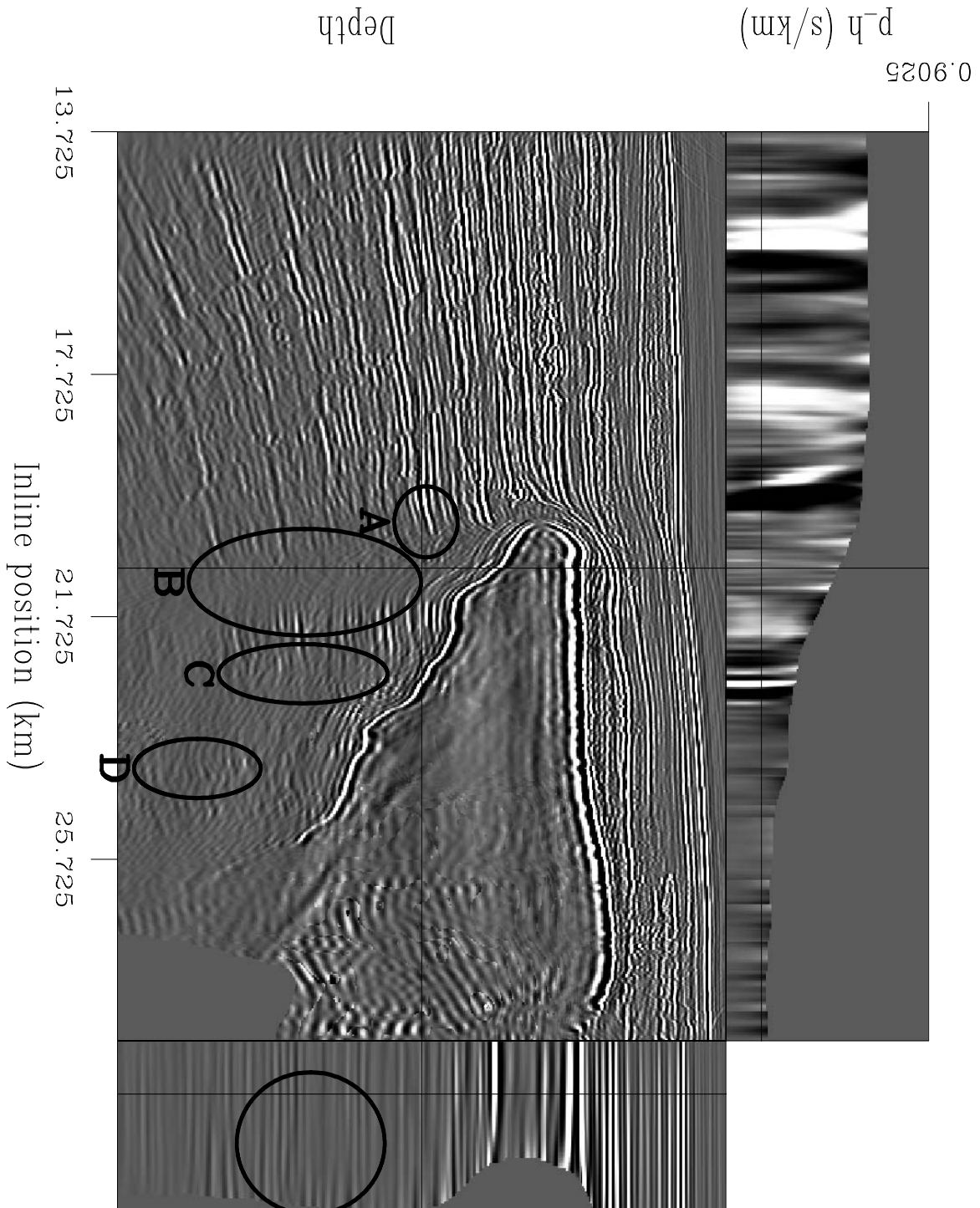


Figure 13: Geophysical RIP result. Crossline=20.9 km, common inline p_h section from $p_h = .15$, and common image gather from inline= 20.9 km. Compare with Figure 12. marie1-bp3d.geop.3 [CR]

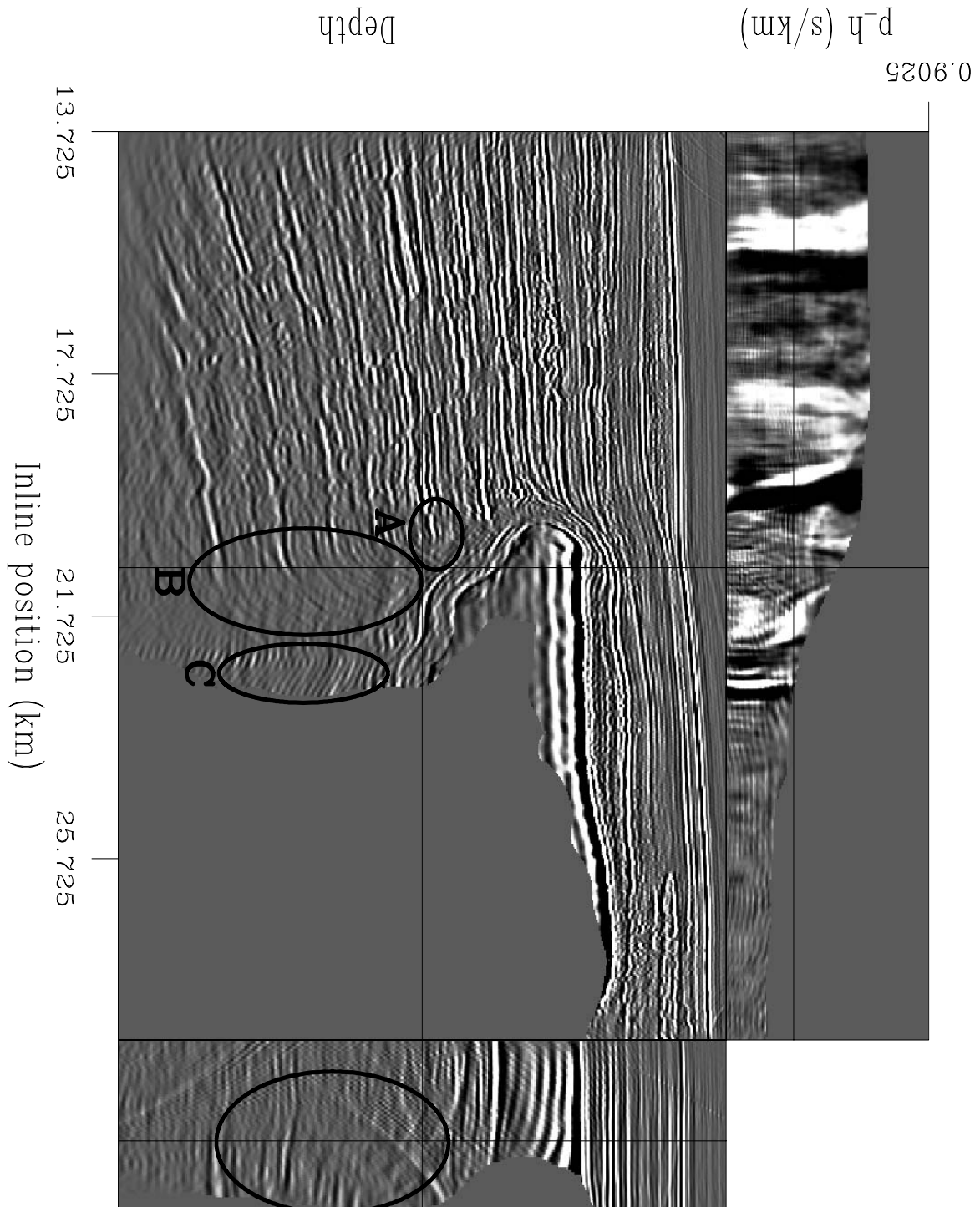


Figure 14: Migration result. Crossline=20.9 km, common inline p_h section from $p_h = .2925$, and common image gather from inline=20.9 km. Compare with Figure 15. marie1-bp3d.mig.4 [CR]

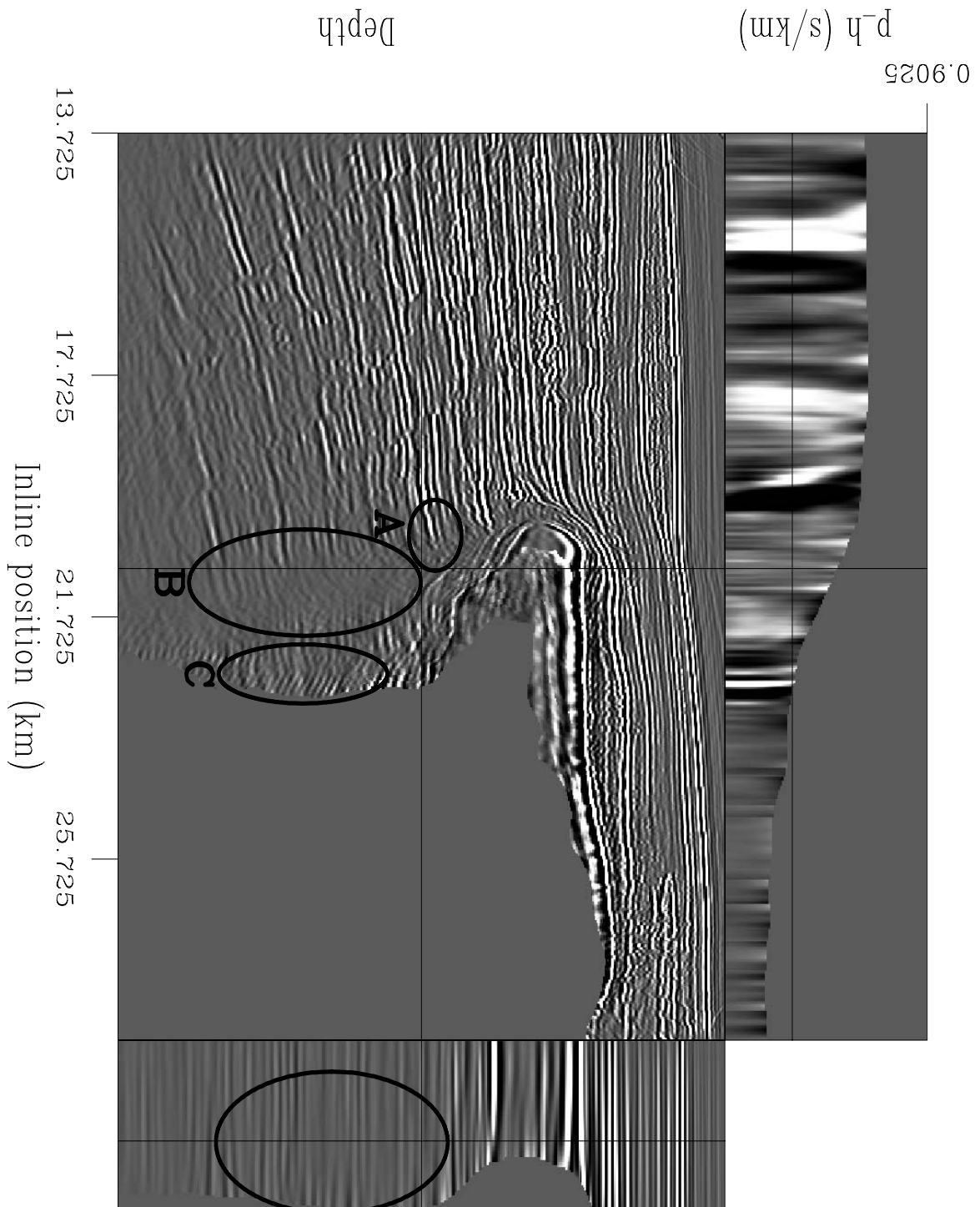


Figure 15: Geophysical RIP result. Crossline=20.9 km, common inline p_h section from $p_h = .2925$, and common image gather from inline=20.9 km. Compare with Figure 14. marie1-bp3d.geop.4 [CR]

SUMMARY

We have demonstrated the use of regularized inversion with model preconditioning (RIP) with two different imaging operators (downward-continuation migration and common azimuth migration) and a geophysical regularization operator (regularization along the offset ray parameter axis). RIP was applied to a real 2-D line and the 3-D volume that the 2-D line was taken from. In both the 2-D and 3-D cases, RIP was able to improve the resulting image, cleaning up artifacts and increasing the continuity of reflectors through shadow zones caused by poor illumination.

ACKNOWLEDGMENTS

We would like to thank BP and ExxonMobil, particularly Frederic Billette and John Etgen, for providing us with the Gulf of Mexico dataset.

REFERENCES

- Biondi, B., and Palacharla, G., 1996, 3-d prestack migration of common-azimuth data: *Geophysics*, **61**, no. 06, 1822–1832.
- Claerbout, J., 1998, Multidimensional recursive filters via a helix: *Geophysics*, **63**, no. 05, 1532–1541.
- Clapp, M. L., 2003, Velocity sensitivity of subsalt imaging through regularized inversion: *SEP-114*, 57–66.
- Duquet, B., and Marfurt, K. J., 1999, Filtering coherent noise during prestack depth migration: *Geophysics*, **64**, no. 4, 1054–1066.
- Fomel, S., and Claerbout, J., 2003, Multidimensional recursive filter preconditioning in geophysical estimation problems: *Geophysics*, **68**, no. 2, 577–588.
- Fomel, S., Clapp, R., and Claerbout, J., 1997, Missing data interpolation by recursive filter preconditioning: *SEP-95*, 15–25.
- Kuehl, H., and Sacchi, M., 2001, Generalized least-squares dsr migration using a common angle imaging condition: 71st Ann. Internat. Meeting, Soc. Expl. Geophysics, Expanded Abstracts, 1025–1028.
- Muerdter, D. R., Lindsay, R. O., and Ratcliff, D. W., 1996, Imaging under the edges of salt sheets: a raytracing study: Soc. Expl. Geophys., 66th Annual Internat. Mtg., Soc. Expl. Geophys., Expanded Abstracts, 578–580.
- Nemeth, T., Wu, C., and Schuster, G. T., 1999, Least-squares migration of incomplete reflection data: *Geophysics*, **64**, no. 1, 208–221.

- Prucha, M., and Biondi, B., 2002, Subsalt event regularization with steering filters: 72th Ann. Internat. Meeting, Soc. Expl. Geophysics, Expanded Abstracts, 824–827.
- Prucha, M. L., Clapp, R. G., and Biondi, B. L., 1998, Imaging under the edges of salt bodies: Analysis of an Elf North Sea dataset: SEP-97, 35–44.
- Prucha, M., Biondi, B., and Symes, W., 1999a, Angle-domain common image gathers by wave-equation migration: 69th Ann. Internat. Meeting, Soc. Expl. Geophysics, Expanded Abstracts, 824–827.
- Prucha, M. L., Biondi, B. L., and Symes, W. W., 1999b, Angle-domain common image gathers by wave-equation migration: SEP-100, 101–112.
- Ronen, S., and Liner, C. L., 2000, Least-squares DMO and migration: *Geophysics*, **65**, no. 5, 1364–1371.
- Stolk, C., and Symes, W., 2004, Kinematic artifacts in prestack depth migration: *Geophysics*, **69**, no. 2, 562–575.
- Tikhonov, A. N., and Arsenin, V. Y., 1977, *Solution of ill-posed problems*: John Wiley and Sons.
- Xu, S., Chauris, H., Lambare, G., and Noble, M., 2001, Common angle image gather - A strategy for imaging complex media: *Geophysics*, **66**, no. 6, 1877–1894.

Target-oriented wave-equation inversion

Alejandro A. Valenciano, Biondo Biondi, and Antoine Guitton¹

ABSTRACT

A target-oriented strategy can be applied to estimate the wave-equation least-squares inverse image ($\hat{\mathbf{m}}$) by explicitly computing the Hessian (\mathbf{H}). The least-squares inverse image is obtained as the solution, using a conjugate gradient algorithm, of a non-stationary least-squares filtering problem $\mathbf{H}\hat{\mathbf{m}} = \mathbf{m}_{mig}$ (where \mathbf{m}_{mig} is the migration image, and the rows of the Hessian are non-stationary filters). This approach allows us to perform the number of iterations necessary to achieve the convergence, by exploiting the sparsity and structure of the Hessian matrix. The results on a constant velocity model and a model with a velocity Gaussian anomaly show the validity of the method.

INTRODUCTION

Seismic imaging (migration) operators are non-unitary (Claerbout, 1992) because they depend on: (1) the seismic experiment acquisition geometry (Nemeth et al., 1999; Duquet and Marfurt, 1999; Ronen and Liner, 2000), (2) the complex subsurface geometry (Prucha et al., 2000; Kuehl and Sacchi, 2001), and (3) the bandlimited characteristics of the seismic data (Chavent and Plessix, 1999). Often, they produce images with reflectors correctly positioned but with biased amplitudes.

Attempts to solve this problem have used the power of geophysical inverse theory (Tarantola, 1987), which compensates for the experimental deficiencies (e.g., acquisition geometry, obstacles) by weighting the migration result with the inverse of the Hessian. However, the main difficulty with this approach is the explicit calculation of the Hessian and its inverse.

Since accurate imaging of reflectors is more important at the reservoir level, we propose to compute the Hessian in a target-oriented fashion (Valenciano and Biondi, 2004). This allows us to reduce the Hessian matrix dimensions. We also exploit the sparsity and structure of the Hessian matrix to dramatically reduce the amount of computation while constructing it. After, we compute the least-squares inverse image as the solution of a non-stationary least-squares filtering problem, by means of a conjugate gradient algorithm.

In this paper, we first discuss the structure and sparsity of the target-oriented Hessian. After that, we show how to compute the least-squares inverse image by solving a non-stationary least-squares filtering problem. We illustrate the methodology with two numerical examples,

¹email: valencia@sep.stanford.edu, biondo@sep.stanford.edu, antoine@sep.stanford.edu

the first in a constant velocity model, and the second in a velocity model with a low velocity Gaussian anomaly.

LINEAR LEAST-SQUARES INVERSION

Tarantola (1987) formalizes the geophysical inverse problem by giving a theoretical approach to compensate for the experiment's deficiencies (e.g., acquisition geometry, obstacles), while being consistent with the acquired data. His approach can be summarized as follows: given a linear modeling operator \mathbf{L} to compute synthetic data \mathbf{d} ,

$$\mathbf{d} = \mathbf{L}\mathbf{m}, \quad (1)$$

where \mathbf{m} is a reflectivity model, and given the recorded data \mathbf{d}_{obs} , a quadratic cost function,

$$S(\mathbf{m}) = \|\mathbf{d} - \mathbf{d}_{obs}\|^2 = \|\mathbf{L}\mathbf{m} - \mathbf{d}_{obs}\|^2, \quad (2)$$

is formed. The model of the earth $\hat{\mathbf{m}}$ that minimize $S(\mathbf{m})$ is given by

$$\hat{\mathbf{m}} = (\mathbf{L}'\mathbf{L})^{-1}\mathbf{L}'\mathbf{d}_{obs} \quad (3)$$

$$\hat{\mathbf{m}} = \mathbf{H}^{-1}\mathbf{m}_{mig}, \quad (4)$$

where \mathbf{L}' (migration operator) is the adjoint of the linear modeling operator \mathbf{L} , \mathbf{m}_{mig} is the migration image, and $\mathbf{H} = \mathbf{L}'\mathbf{L}$ is the Hessian of $S(\mathbf{m})$.

The main difficulty with this approach is the explicit calculation of the Hessian inverse. In practice, it is more feasible to compute the least-squares inverse image as the solution of the linear system of equations

$$\mathbf{H}\hat{\mathbf{m}} = \mathbf{m}_{mig}, \quad (5)$$

by using an iterative conjugate gradient algorithm.

Another difficulty with this approach is that the explicit calculation of the Hessian for the entire model space is unfeasible in practice. In the next section we discuss a way to overcome this problem.

TARGET-ORIENTED HESSIAN: DIMENSIONS AND STRUCTURE

Since accurate imaging of reflectors is more important in the neighborhood of the reservoir, it makes sense to restrain the model space to the target area. A way to achieve this objective is to write the modeling operator \mathbf{L} in a target-oriented fashion and explicitly compute the Hessian.

Target-oriented Hessian

In general, the synthetic data for one frequency, a shot positioned at $\mathbf{x}_s = (0, x_s, y_s)$ and a receiver positioned at $\mathbf{x}_r = (0, x_r, y_r)$ can be given by a linear operator \mathbf{L} acting on the full model space $\mathbf{m}(\mathbf{x})$ with $\mathbf{x} = (z, x, y)$ ($\mathbf{x} = (z, x)$ in $2D$) as

$$\mathbf{d}(\mathbf{x}_s, \mathbf{x}_r; \omega) = \mathbf{L}\mathbf{m}(\mathbf{x}) = \sum_{\mathbf{x}} \mathbf{G}(\mathbf{x}, \mathbf{x}_s; \omega) \mathbf{G}(\mathbf{x}, \mathbf{x}_r; \omega) \mathbf{m}(\mathbf{x}), \quad (6)$$

where $\mathbf{G}(\mathbf{x}, \mathbf{x}_s; \omega)$ and $\mathbf{G}(\mathbf{x}, \mathbf{x}_r; \omega)$ are the Green functions from the shot position \mathbf{x}_s and the receiver position \mathbf{x}_r to a point in the model space \mathbf{x} , respectively.

In equation (6), we use two important properties (Ehinger et al., 1996): first, the Green functions are computed by means of the one-way wave equation, and second, the extrapolation is performed by using the adequate paraxial wave equations (flux conservation) (Bamberger et al., 1988).

The quadratic cost function is

$$S(\mathbf{m}) = \sum_{\omega} \sum_{\mathbf{x}_s} \sum_{\mathbf{x}_r} \|\mathbf{d} - \mathbf{d}_{obs}\|^2, \quad (7)$$

and its second derivative with respect to the model parameters $\mathbf{m}(\mathbf{x})$ and $\mathbf{m}(\mathbf{y})$ is the Hessian

$$\begin{aligned} \mathbf{H}(\mathbf{x}, \mathbf{y}) &= \frac{\partial^2 S(\mathbf{m})}{\partial \mathbf{m}(\mathbf{x}) \partial \mathbf{m}(\mathbf{y})} \\ \mathbf{H}(\mathbf{x}, \mathbf{y}) &= \sum_{\omega} \sum_{\mathbf{x}_s} \mathbf{G}'(\mathbf{x}, \mathbf{x}_s; \omega) \mathbf{G}(\mathbf{y}, \mathbf{x}_s; \omega) \sum_{\mathbf{x}_r} \mathbf{G}'(\mathbf{x}, \mathbf{x}_r; \omega) \mathbf{G}(\mathbf{y}, \mathbf{x}_r; \omega), \end{aligned} \quad (8)$$

where $\mathbf{G}'(\mathbf{x}, \mathbf{x}_r; \omega)$ is the adjoint of $\mathbf{G}(\mathbf{x}, \mathbf{x}_r; \omega)$.

Notice that computing $\mathbf{H}(\mathbf{x}, \mathbf{y})$ in equation (8) needs only the precomputed Green functions at model points \mathbf{x} and \mathbf{y} . Thus, the size of the problem can be considerably reduced by computing the Green functions only at the target location \mathbf{x}_T , reducing equation (8) to

$$\mathbf{H}(\mathbf{x}_T, \mathbf{y}_T) = \sum_{\omega} \sum_{\mathbf{x}_s} \mathbf{G}'(\mathbf{x}_T, \mathbf{x}_s; \omega) \mathbf{G}(\mathbf{y}_T, \mathbf{x}_s; \omega) \sum_{\mathbf{x}_r} \mathbf{G}'(\mathbf{x}_T, \mathbf{x}_r; \omega) \mathbf{G}(\mathbf{y}_T, \mathbf{x}_r; \omega). \quad (9)$$

Hessian sparsity and structure

Since the main contributions of the Hessian occurs around the diagonal (Chavent and Plessix, 1999; Valenciano and Biondi, 2004), additional computational savings can be obtain by limiting the computation of equation (9) to \mathbf{y}_T points close to \mathbf{x}_T . This reduces equation (9) to

$$\mathbf{H}(\mathbf{x}_T, \mathbf{x}_T + \mathbf{a}_x) = \sum_{\omega} \sum_{\mathbf{x}_s} \mathbf{G}'(\mathbf{x}_T, \mathbf{x}_s; \omega) \mathbf{G}(\mathbf{x}_T + \mathbf{a}_x, \mathbf{x}_s; \omega) \sum_{\mathbf{x}_r} \mathbf{G}'(\mathbf{x}_T, \mathbf{x}_r; \omega) \mathbf{G}(\mathbf{x}_T + \mathbf{a}_x, \mathbf{x}_r; \omega), \quad (10)$$

where $\mathbf{a}_x = (a_z, a_x, a_y)$ is the “offset” from the point \mathbf{x}_T . Thus only a few elements of the Hessian matrix are computed (non-stationary filter coefficients).

To be able to perform the multidimensional convolution operation in equation (5), the computed Hessian elements in equation (10) have to be placed on a helix (Claerbout, 1998). After that, each row of the Hessian matrix is a multidimensional filter applied to the whole model space.

Chavent and Plessix (1999) qualitatively discuss the amount of the spreading away from the diagonal of the Hessian matrix. Future research will address the optimal number of filter coefficients needed to account for the spreading, since this number has a direct impact on the cost of the method.

NON-STATIONARY LEAST-SQUARES FILTERING

Even though the target-oriented Hessian has a smaller number of rows and columns in equation (9), its condition number could be high, making the solution of the non-stationary least-squares filtering problem in equation (5) unstable. One solution is adding a smoothing regularization operator to equation (5):

$$\begin{aligned} \mathbf{H}\hat{\mathbf{m}} - \mathbf{m}_{mig} &\approx 0, \\ \epsilon \mathbf{I}\hat{\mathbf{m}} &\approx 0, \end{aligned} \tag{11}$$

where the choice of the identity operator (\mathbf{I}) as regularization operator is arbitrary. Changing the ϵ parameter for such a simple regularization operator is equivalent to stopping the conjugate gradient solver after a different number of iterations.

A more sophisticated regularization scheme could involve applying an smoothing operator in the angle (or ray parameter) dimension (Prucha et al., 2000; Kuehl and Sacchi, 2001). More research need to be done regarding that subject, which is of extreme importance to obtain stable and meaningful results in real case scenarios.

NUMERICAL EXAMPLES

In this section we show two numerical examples of target-oriented Hessians and the corresponding least-squares inverse images. The first example is a constant velocity model and the second is a model with a velocity Gaussian anomaly. The second one was designed to study the effects of uneven illumination due to overburden structure.

Constant-velocity model

Explicitly computing the Hessian is possible when following a target-oriented strategy that exploits the Hessian sparsity and structure. We created a synthetic dataset, using equation

6, with a constant-reflectivity flat reflector (at $z = 0.8 \text{ km}$) in a constant-velocity medium ($v = 2.0 \text{ km s}^{-1}$). Assuming a land acquisition geometry, where the shots and receivers were positioned every 20 m on the interval $\mathbf{x} = [-0.8, 0.8] \text{ km}$. Valenciano and Biondi (2004) discuss in detail the banded nature and sparsity of the Hessian matrix for the constant-velocity model.

Figure 1 shows a 15×15 coefficient filter at constant depth as the x coordinate moves from the corner to the center of the acquisition. Figure 1a shows point 1, with coordinates $\mathbf{x} = (0.8, -0.6)$ (corner of the acquisition). Figure 1b shows point 2, with coordinates $\mathbf{x} = (0.8, -0.4)$. Figure 1c shows point 3, with coordinates $\mathbf{x} = (0.8, -0.2)$. Figure 1d shows point 4, with coordinates $\mathbf{x} = (0.2, 0)$ (at the center of the acquisition).

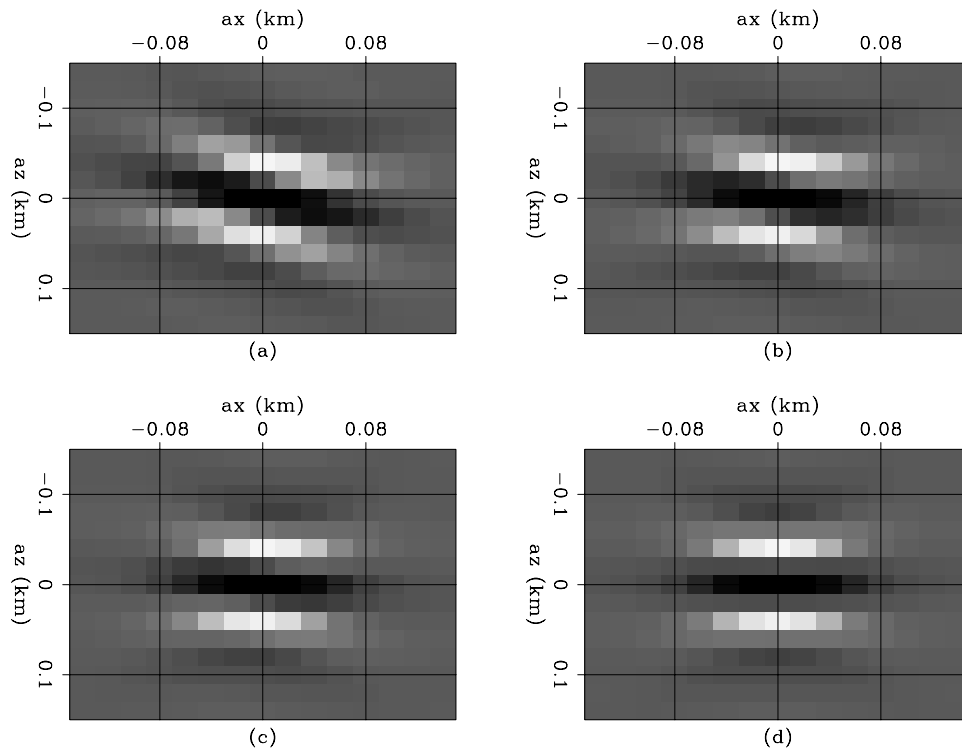


Figure 1: Hessian of the constant-velocity model, (a) point 1 $\mathbf{x} = (0.8, -0.6)$, (b) point 2 $\mathbf{x} = (0.8, -0.4)$, (c) point 3 $\mathbf{x} = (0.8, -0.2)$, and (d) point 4 $\mathbf{x} = (0.2, 0)$. [alejandrol-hessian_phase_const](#) [CR]

Figure 2 shows the envelope of the 15×15 coefficient filter shown in Figure 1. The energy of the ellipses become dimmer away from the center, indicating that these points have lower illumination due to the acquisition geometry. To correct this effect we computed the least-squares inverse image, by the method described in the above section.

Two different numbers of filter coefficients were used. Figures 3 and 4 show the inversion results for a filter of 11×11 coefficients, whereas Figures 5 and 6 show the inversion results for a filter of 15×15 coefficients. Figure 7 shows a comparison of the best results of both filter sizes.

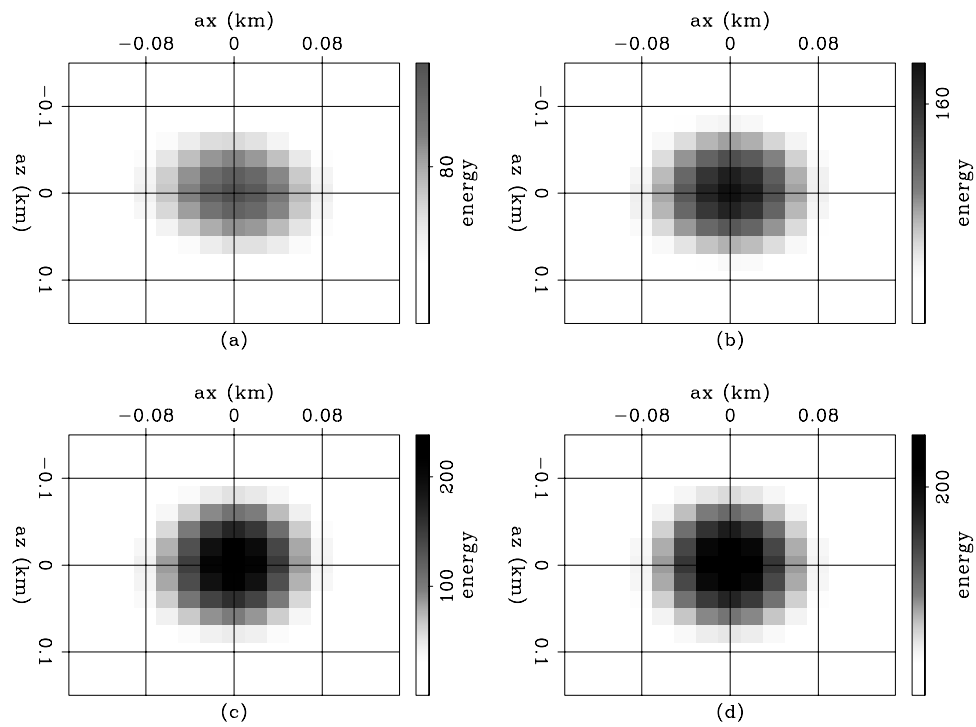


Figure 2: Envelope of the Hessian of the constant-velocity model, (a) point 1 $\mathbf{x} = (0.8, -0.6)$, (b) point 2 $\mathbf{x} = (0.8, -0.4)$, (c) point 3 $\mathbf{x} = (0.8, -0.2)$, and (d) point 4 $\mathbf{x} = (0.2, 0)$.
 alejandro1-hessian_const [CR]

The panels in Figure 3 show the least-squares inverse image for different numbers of iterations for a filter of 11×11 coefficients: 3a for 10 iterations, 3b for 20 iterations, 3c for 100 iterations, and 3d for migration. Notice how the image amplitudes become more even. Figure 4 shows the comparison of the same least-squares inverse image results at the reflector depth. The image amplitude after 100 iterations is the best result. The conjugate gradient algorithm further balances the image amplitudes, which reduces the effects of the acquisition geometry and the bandlimited characteristic of the seismic data.

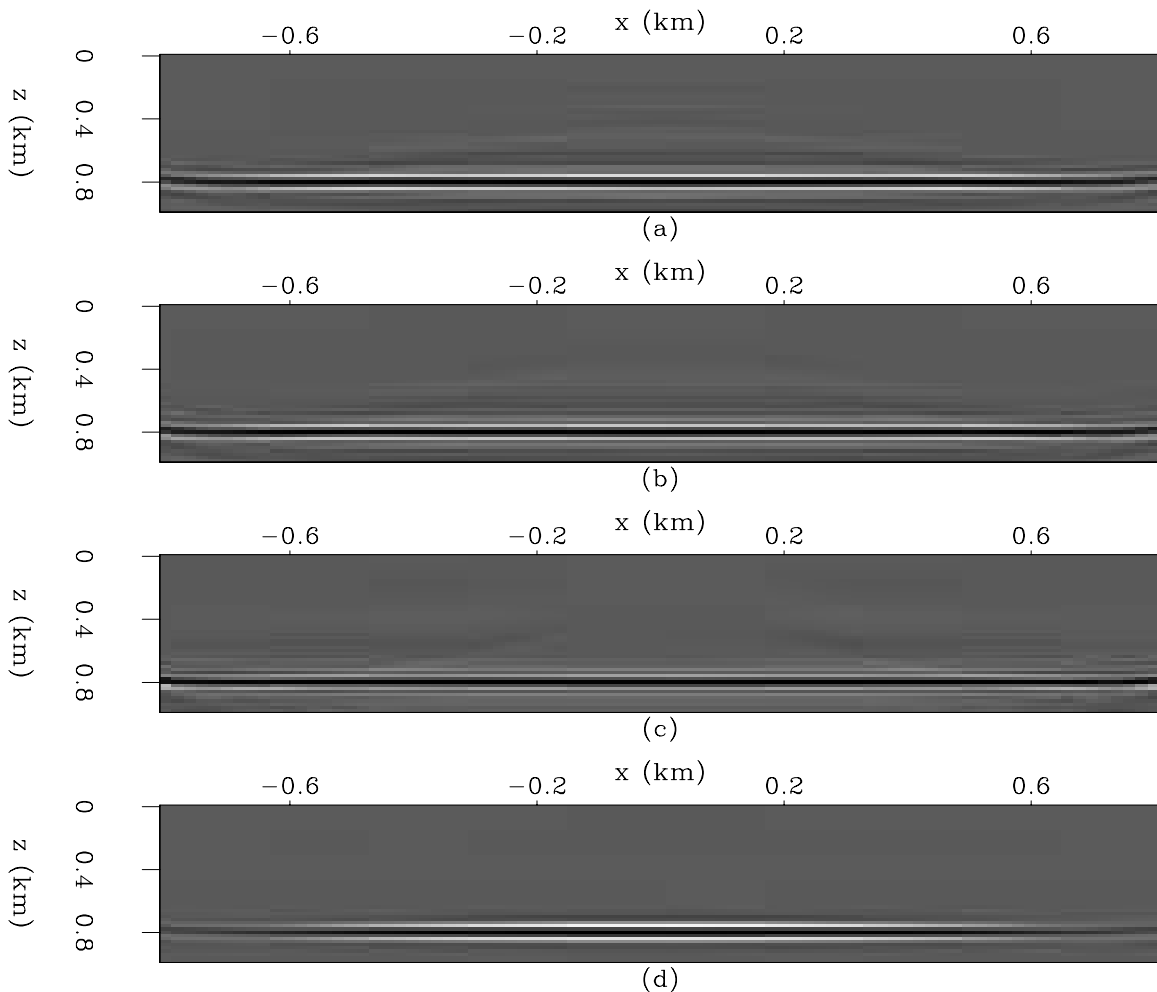


Figure 3: Constant-velocity inversion using a filter size of 11×11 coefficients: (a) 10 iterations, (b) 20 iterations, (c) 100 iterations, and (d) migration. [alejandro1-inv_const_11](#) [CR]

The panels in Figure 5 show the least-squares inverse image for different number of iterations for a filter of 15×15 coefficients: 5a for 10 iterations, 5b for 20 iterations, 5c for 100 iterations, and 5d for migration. Notice again, how the image amplitudes become more even. Figure 6 shows the comparison of the same least-squares inverse image results at the reflector depth. The image amplitude after 100 iterations is the best result. The conjugate gradient algorithm once again further balances the image amplitudes.

Figure 7 compares the migration result to the best inversion results for filter sizes 11×11

Figure 4: Amplitudes extracted at reflector depth from Figure 3, filter size of 11×11 coefficients. `alejandrol-inv_const_pp_11` [CR]

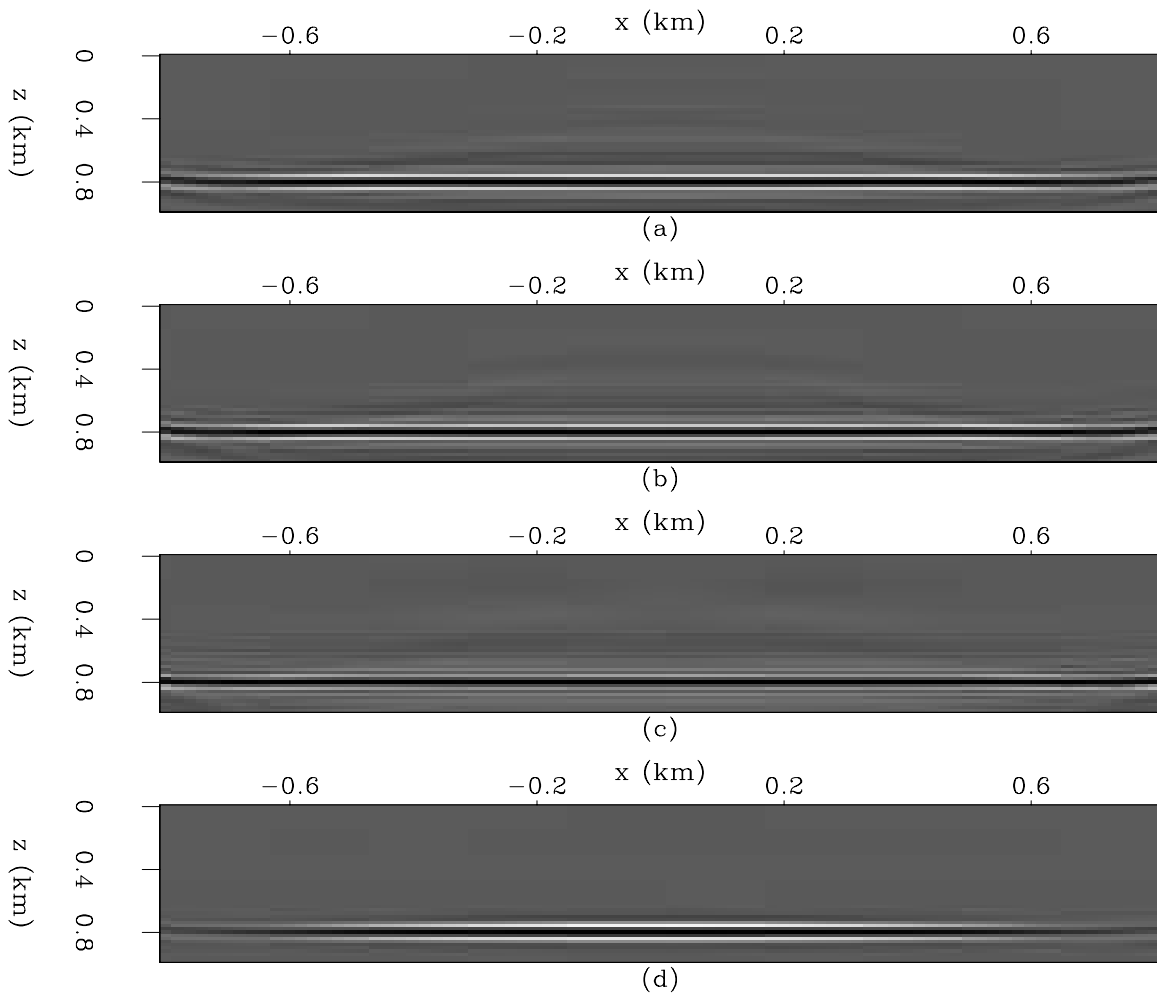
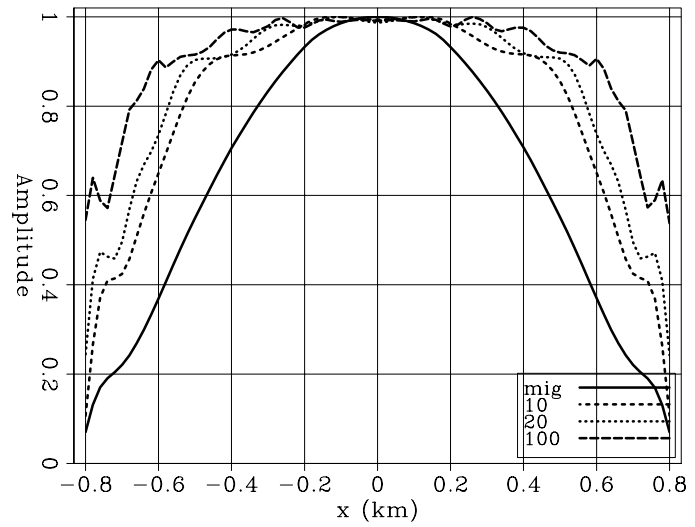
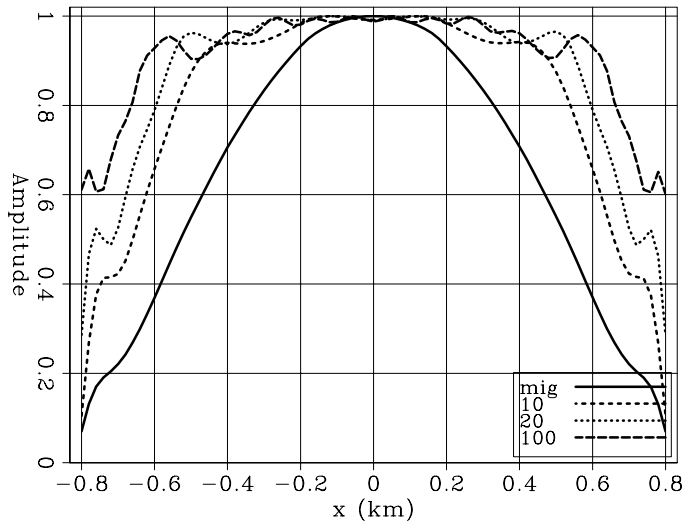


Figure 5: Constant-velocity inversion using a filter size of 15×15 coefficients: (a) 10 iterations, (b) 20 iterations, (c) 100 iterations, and (d) migration. `alejandrol-inv_const_15` [CR]

Figure 6: Amplitudes extracted at reflector depth from Figure 5, filter size of 15×15 coefficients.

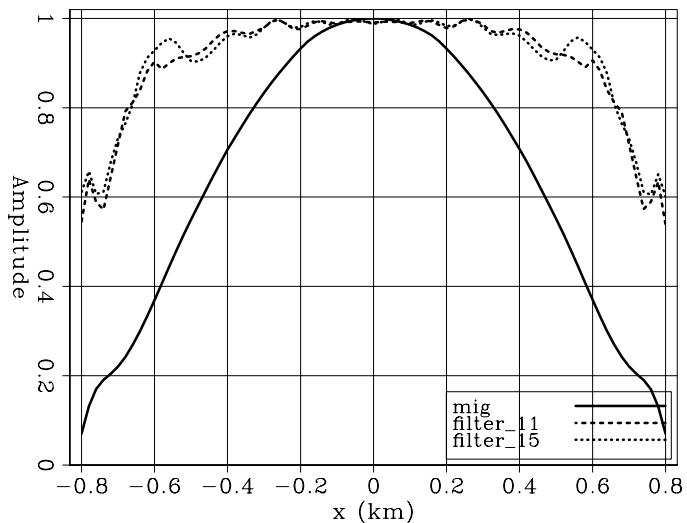
`alejandrol-inv_const_pp_15` [CR]



coefficients, 15×15 coefficients. There is not much difference in the recovered amplitudes, thus a filter size of 11×11 should be sufficient.

Figure 7: Comparison the migration result to the best inversion results for filter sizes 11×11 coefficients and 15×15 coefficients.

`alejandrol-inv_const_filter` [CR]



Gaussian anomaly velocity model

We created a synthetic dataset, using equation 6, from a model with a constant-reflectivity flat reflector lying beneath a Gaussian low velocity anomaly (Figure 8). Again, we assumed a land acquisition geometry, where the shots and receivers were positioned every 10 m on the interval $\mathbf{x} = [-3.0, 3.0] \text{ km}$.

Figure 9 shows a 15×15 coefficient filter at constant depth as the x coordinate moves from the corner to the center of the acquisition. Figure 9a shows point 1, with coordinates $\mathbf{x} = (2.0, -2.5)$ (corner of the acquisition). Figure 9b shows point 2, with coordinates $\mathbf{x} = (2.0, -1.5)$. Figure 9c shows point 3, with coordinates $\mathbf{x} = (2.0, -0.8)$. Figure 9d shows

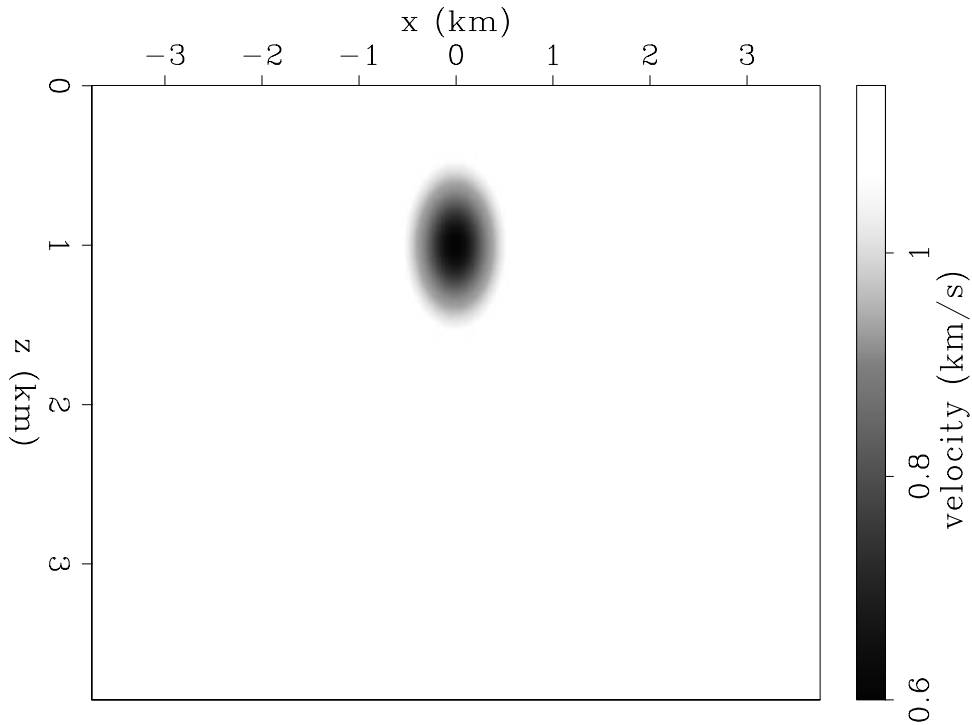


Figure 8: Gaussian anomaly velocity model. alejandro1-bill [ER]

point 4, with coordinates $\mathbf{x} = (2.0, 0.0)$ (at the center of the acquisition). Figure 10 shows the envelope of the 15×15 coefficient filter shown in Figure 9. Differently to the constant velocity case, the higher energy is at point 3 ($\mathbf{x} = (2.0, -0.8)$) (away from the center). This is due to a focusing effect created by the Gaussian velocity anomaly. To correct this effect we computed the least-squares inverse image, by the method described in the above section.

As with the previous example, two different numbers of filter coefficients were used. Figures 11 and 12 show the inversion results for a filter of 11×11 coefficients, whereas Figures 13 and 14 show the inversion results for a filter of 15×15 coefficients. Figure 15 shows a comparison of the best results of both filter sizes.

The panels in Figure 11 show the least-squares inverse image for different number of iterations for a filter of 11×11 coefficients: 11a for 10 iterations, 11b for 20 iterations, 11c for 100 iterations, and 11d for migration. Notice how the image amplitudes become more even, but as the number of iterations increase the result becomes unstable. Figure 12 compares the same least-squares inverse image results at the reflector depth. The image amplitude after 10 iterations is the best result. The conjugate gradient algorithm further balances the image amplitudes, which reduces the effects of acquisition geometry and the bandlimited characteristic of the seismic data. But is not as good reducing the focusing effect (amplitude anomaly at $\mathbf{x} = (2.0, -0.8)$).

The panels in Figure 13 show the least-squares inverse image for different number of iterations for a filter of 15×15 coefficients: 13a for 10 iterations, 13b for 20 iterations, 13c for

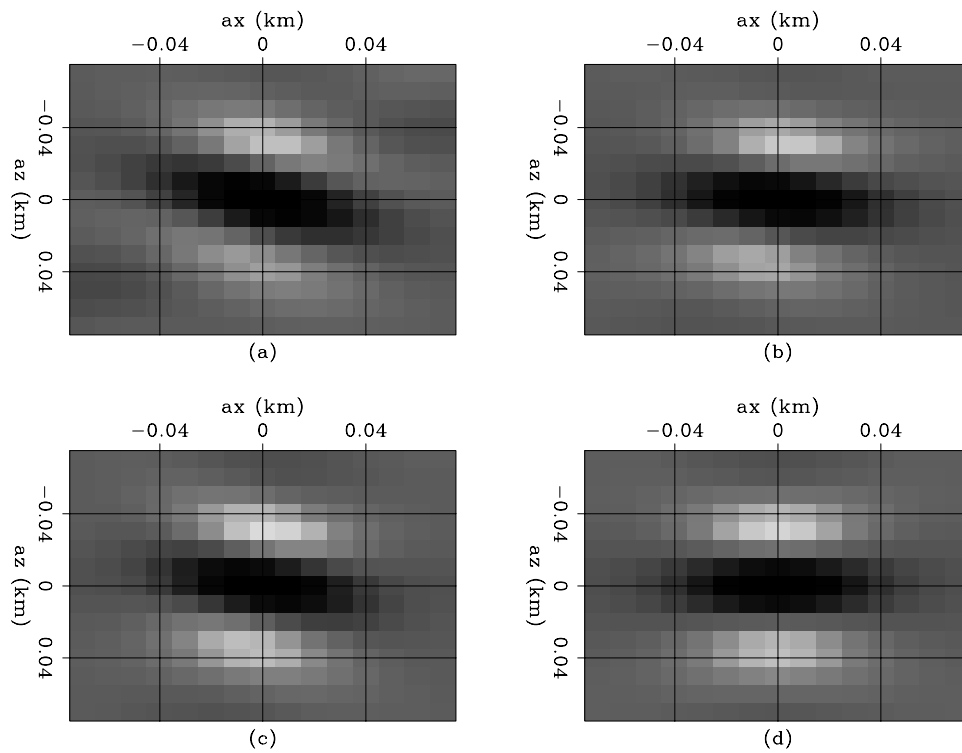


Figure 9: Hessian of the Gaussian anomaly velocity model, (a) point 1 $\mathbf{x} = (2.0, -2.5)$, (b) point 2 $\mathbf{x} = (2.0, -1.5)$, (c) point 3 $\mathbf{x} = (2.0, -0.8)$, and (d) point 4 $\mathbf{x} = (2.0, 0.0)$.
`alejandrol-hessian_phase_bill_filter` [CR]

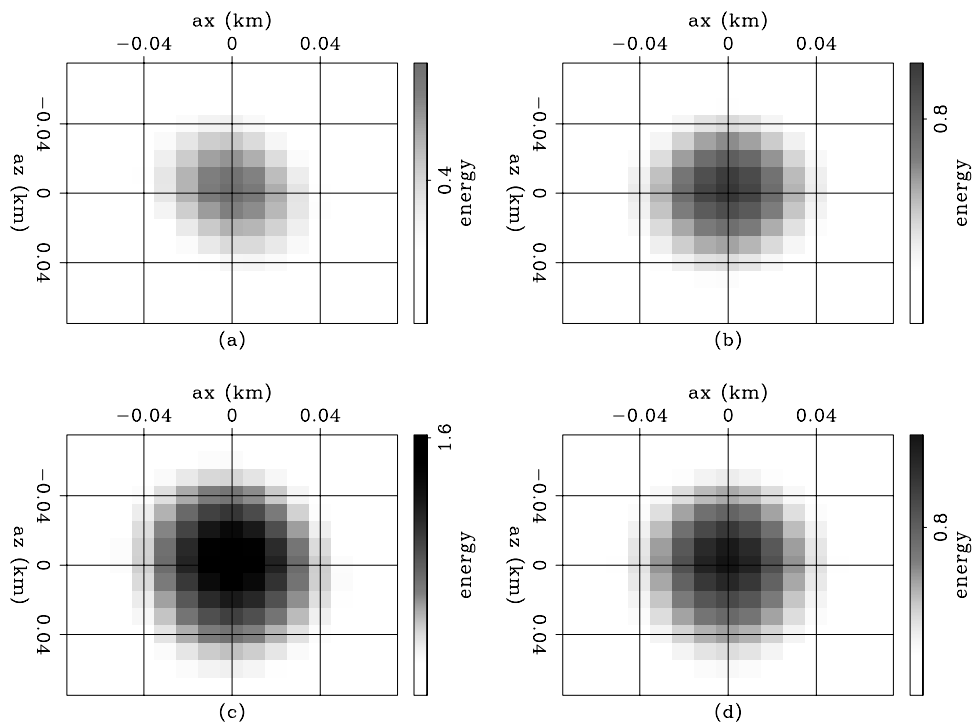


Figure 10: Envelope of the Hessian of the Gaussian anomaly velocity model, (a) point 1 $\mathbf{x} = (2.0, -2.5)$, (b) point 2 $\mathbf{x} = (2.0, -1.5)$, (c) point 3 $\mathbf{x} = (2.0, -0.8)$, and (d) point 4 $\mathbf{x} = (2.0, 0.0)$. `alejandrol-hessian_bill_filter` [CR]

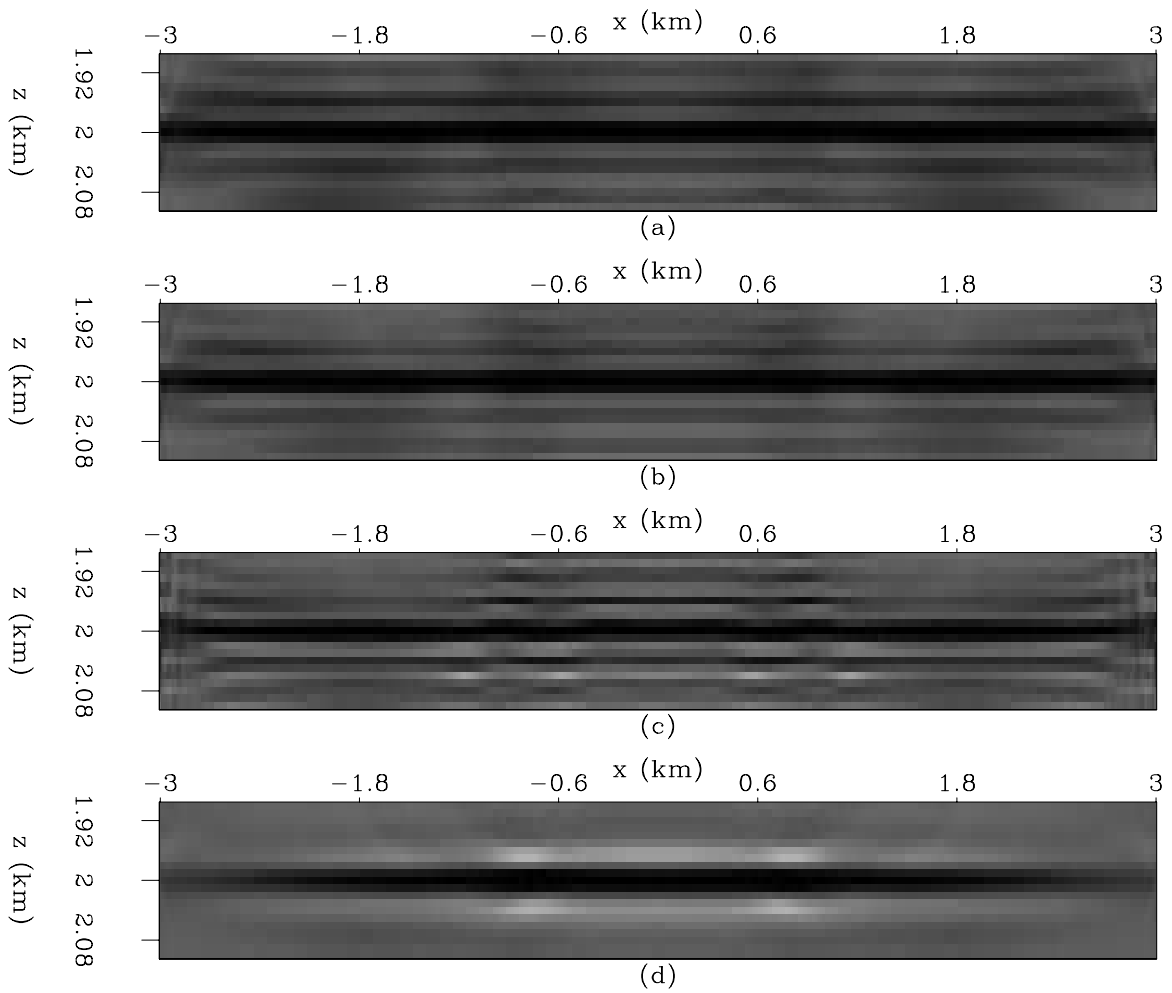
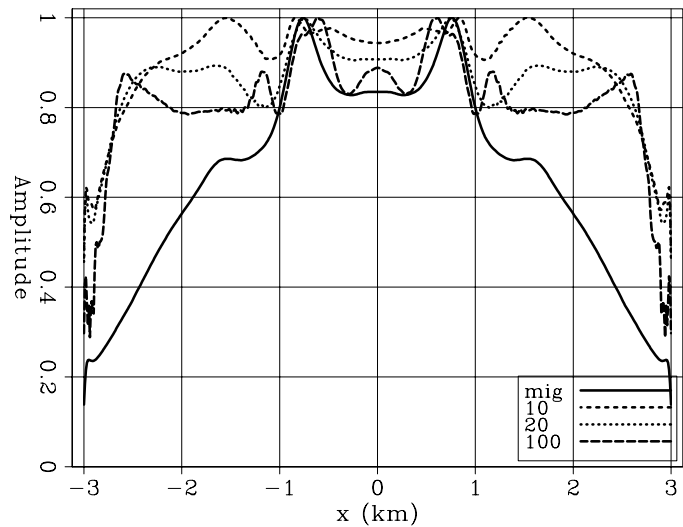


Figure 11: Gaussian anomaly velocity inversion using a filter size of 11×11 coefficients: (a) 10 iterations, (b) 20 iterations, (c) 100 iterations, and (d) migration. `alejandrol-inv_bill_11` [CR]

Figure 12: Amplitudes extracted at reflector depth from Figure 11, filter size of 11×11 coefficients. `alejandrol-inv_pp_11` [CR]



100 iterations, and 13d for migration. Notice how the image amplitudes become more even, as the number of iterations increase. Figure 14 shows the comparison of the same least-squares inverse image results at the reflector depth. The image amplitude after 100 iterations is the best result. The conjugate gradient algorithm further balances the image amplitudes, reducing the focusing effect as well as the effects of the acquisition geometry and the bandlimited characteristic of the seismic data.

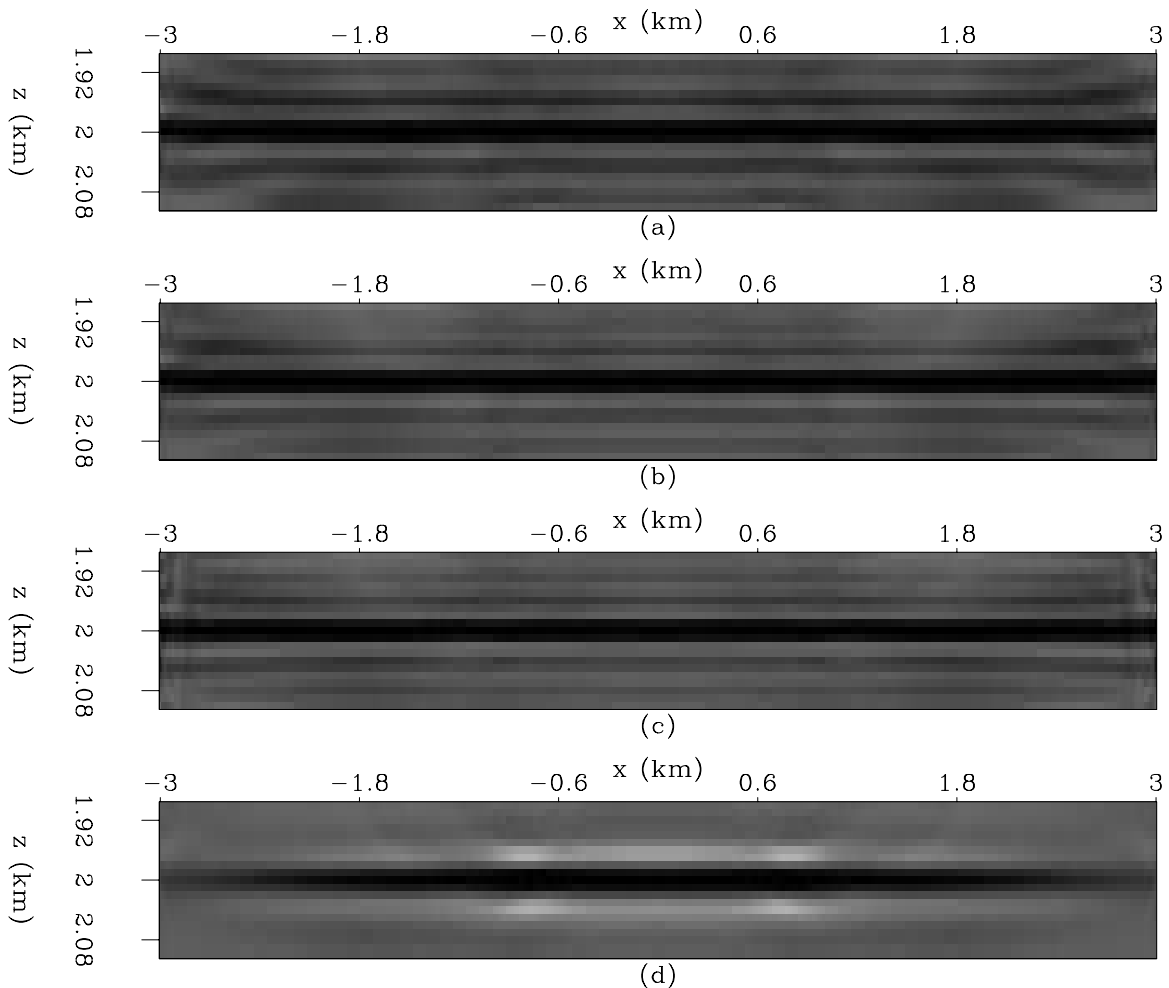


Figure 13: Gaussian anomaly velocity inversion using a filter size of 15×15 coefficients: (a) 10 iterations, (b) 20 iterations, (c) 100 iterations, and (d) migration. [alejandro1-inv_bill_15](#) [CR]

Figure 15 the migration result to the 100 iterations inversion results for filter sizes 11×11 coefficients, 15×15 coefficients. There is a big difference in the recover amplitudes for the different filter sizes being the 15×15 coefficient filter the one that better reduces the effect of the focusing effect on the amplitudes. More research needs to be done to find a way to *a priori* predict the proper filter size.

Figure 14: Amplitudes extracted at reflector depth from Figure 13, filter size of 15×15 coefficients. `alejandro1-inv_pp_15` [CR]

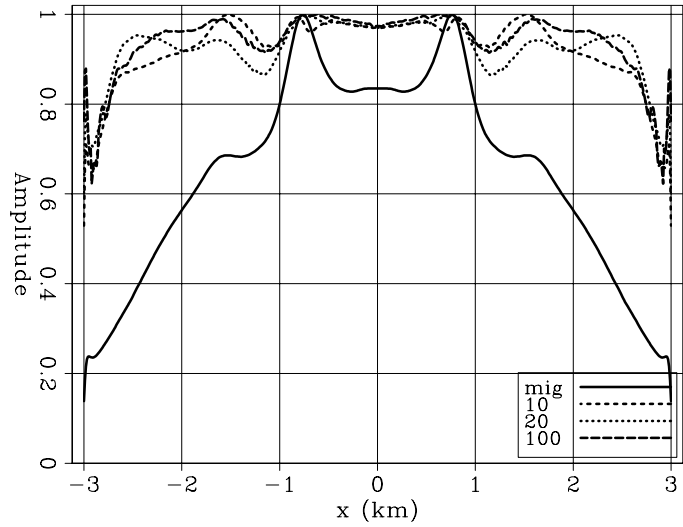
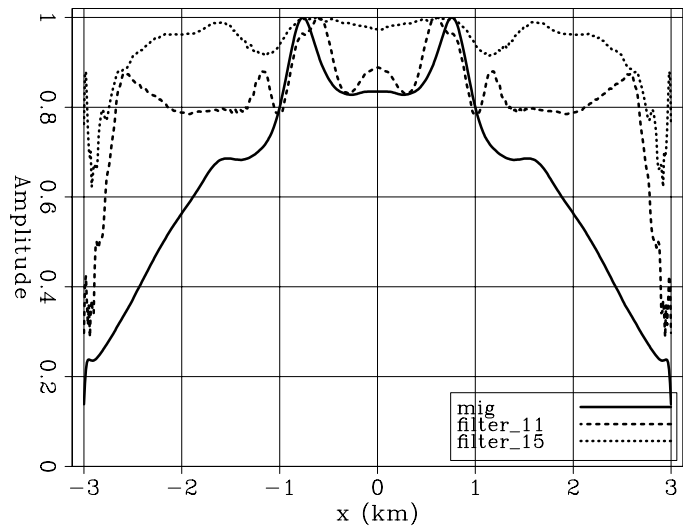


Figure 15: Comparison the migration result to the 100 iterations inversion results for filter sizes 11×11 coefficients and 15×15 coefficients. `alejandro1-inv_filter` [CR]



CONCLUSIONS

Since accurate imaging of reflections is more important in the neighborhood of the reservoir, a target-oriented strategy can be applied to estimate the wave-equation least-squares inverse image by explicitly computing the Hessian. The main contributions of the Hessian occurs around the diagonal, that is why additional computational savings can be obtain by limiting the its computation to only few elements around it. The least-squares inverse image is then computed as the solution, using a conjugate gradient algorithm, of a non-stationary least-squares filtering problem. This approach allows to perform the number of iterations necessary to achieve the convergence.

Results on the constant velocity model show that the inversion recovers the correct image amplitudes. In this case a filter size of 11×11 is enough to obtain a good result. However, something different happens in the Gaussian anomaly velocity model case, where the inversion gives noisy results if a filter size of 11×11 is used. After adding more coefficients to the filter (filter size of 15×15) a more stable result was obtained.

ACKNOWLEDGMENTS

I would like to thank Bill Symes and TRIP for the Gaussian anomaly velocity model used in this paper.

REFERENCES

- Bamberger, A., Engquist, B., Halpern, L., and Joly, P., 1988, Paraxial approximation in heterogeneous media: *SIAM J. Appl. Math.*, **48**, 98–128.
- Chavent, G., and Plessix, R. E., 1999, An optimal true-amplitude least-squares prestack depth-migration operator: *Geophysics*, **64**, no. 2, 508–515.
- Claerbout, J. F., 1992, *Earth soundings analysis, processing versus inversion*: Blackwell Scientific Publications.
- Claerbout, J. F., 1998, Multidimensional recursive filters via a helix: *Geophysics*, **63**, no. 5, 1532–1541.
- Duquet, B., and Marfurt, K. J., 1999, Filtering coherent noise during prestack depth migration: *Geophysics*, **64**, no. 4, 1054–1066.
- Ehinger, A., Lailly, P., and Marfurt, K. J., 1996, Green's function implementation of common-offset wave-equation migration: *Geophysics*, **61**, no. 06, 1813–1821.
- Kuehl, H., and Sacchi, M., 2001, Generalized least-squares DSR migration using a common angle imaging condtion: *Soc. of Expl. Geophys.*, 71st Ann. Internat. Mtg, 1025–1028.

- Nemeth, T., Wu, C., and Schuster, G. T., 1999, Least-squares migration of incomplete reflection data: *Geophysics*, **64**, no. 1, 208–221.
- Prucha, M. L., Clapp, R. G., and Biondi, B., 2000, Seismic image regularization in the reflection angle domain: *SEP-103*, 109–119.
- Ronen, S., and Liner, C. L., 2000, Least-squares DMO and migration: *Geophysics*, **65**, no. 5, 1364–1371.
- Tarantola, A., 1987, *Inverse problem theory*: Elsevier.
- Valenciano, A. A., and Biondi, B., 2004, Target-oriented computation of the wave-equation imaging Hessian: *SEP-117*, 63–76.



Inversion and fault tolerant parallelization using Python

Robert G. Clapp¹

ABSTRACT

Many current areas of research at SEP involve large-scale inversion problems that must be parallelized in order to be tractable. Writing fault-tolerant, parallel code requires significant programming expertise and overhead. In this paper, a library, written in Python, is described that effectively simulates a fault-tolerant parallel code, using simple serial programs. In addition, the library provides the ability to use these parallel objects in out-of-core inversion problems in a fault-tolerant manner.

INTRODUCTION

The large size of today's oil industry problems necessitates harnessing the power of clusters. The problem is that as we add nodes, we increase our odds of node failure. Inversion on large-scale problems is even more problematic. Operators can take days to weeks to run (Sava and Biondi, 2003; Clapp and Clapp, 2005) and can involve multiple instances of complex operations (Clapp, 2003). Running these problems on Beowulf clusters poses a problem as the odds of a multi-week job running without a node failing are low.

In Clapp (2004a), I described a library, written in Python, that allows auto-parallelization with a high-level of fault tolerance for almost any SEPlib program. Instead of handling parallelization within a compiled code at the library level, the parallelization is done at the script level which sits on top of the executables. The Python library distributes and collects the datasets, keeps track of what portions of the parallel job are done, and monitors the state of the nodes. The distribution and collection are done through MPI but individual jobs are all serial codes. The code is written using Python's object-oriented capabilities so it is easily expandable. A parallel job is described by a series of files and a series of tasks.

For inversion problems, Clapp (2004b) describes a Python inversion library which uses abstract vector and operator descriptions. From these abstract classes I derive specific classes to handle out-of-core problems. Operators become wrappers around SEPlib programs and vectors wrappers around SEPlib files.

In this paper I introduce an improved version of the library described in Clapp (2004a) and Clapp (2004b). The new version provides significant additional flexibility. Multiple programs can be combined into single executables. Parallel files can now be SEP3D files, and/or involve

¹email: bob@sep.stanford.edu

overlapping patches. Inversion can be done on parallel files (instead of collected on some master node), saving disk space and transfer time.

In the first portion of the paper I will cover the basic Python parallel and inversion objects. In the second portion I will show several examples on how to use these objects to accomplish tasks that are both memory and computationally intensive.

BASIC BUILDING BLOCKS

Before delving into parallel and inversion objects, it is useful to go over some core objects that are used extensively by the more advanced parallel and inversion objects. These objects provide interaction with the command line, SEP files, and keep track of what the program has accomplished and what needs to be done.

Parameter

The `SEP.parameter.parameter` is a holding class for information about a parameter that can be described by an ASCII string. It can store documentation about the parameter, its current value, and/or some default value for the parameter. In addition to providing a simple mechanism for accessing arbitrary objects, it is also useful for documenting programs/objects and checking to make sure all parameters required for a given routine have been set.

Parameters

The `SEP.args.basic` object can be thought of as a collection of parameters accessible using SEP programming conventions. You can request a parameter using `par.par("tag")`, optionally with a default value, and an error if it doesn't exist. You can also add a parameter `par.add_param("tag", value)` to the collection. The `SEP.args.basic` can be initialized from a file, another collection of parameters, or an empty set can be created. It has the ability to output its contents in various manners. For example, it can return a simple dictionary linking parameters to their values or can return the parameters in a sep-style convention (`par=val`) in either a list or string form. It can also write its contents into a file.

Sepfile

A SEPlib file object `SEP.sepfile.sep_file` is built from one to three `SEP.args.basic` objects (history file, header format file, and grid format file). You can access the collection of parameters directly through the history, headers, and grid objects (e.g. `sep.history.par("n1")`). In addition it has the concept of axes and keys (if the data is SEP3D and possesses headers). You can get the number of dimensions, retrieve and set axes (`n,o,d,label,unit`) and keys (`name,format,type`), and return the size of the dataset.

Status

The status object `SEP.stat_sep.status` keeps track of the progress of a job. It is a dictionary linking a job descriptor to a list of properties of that job descriptor. For example, when doing a parallel job, the list will include the status of the job *todo*, *sent*, *running*, *finished*, *collected*, the machine the job is run on, the progress of the job, where the `stderr` and `stdout` of the job is stored, and how many times the job has failed to run correctly. The status information is written to an ASCII file that enables a job to be restarted automatically. The class also has the ability to store parameter information in the status file which can be automatically read at startup.

Options, Flows, and Programs

Programs generally follow a fairly standard flow. First you read in parameters from the command line, then process these parameters, potentially creating new parameters, and finally you run the algorithm. You can think of a flow as series of programs, where you run through these basic steps for each program. An example is wave-equation migration. To perform wave-equation migration a typical flow would be to choose the reference velocities, convert the data to the frequency domain, migrate the data, transpose the data, and create angle gathers. All of these steps could be independent programs, combined into a single program, or a multitude of other possible variations. The advantage of combining these steps into a single program is that many times they share parameters, so you are simplifying the user's jobs. The disadvantage is the code becomes more difficult to manage.

The options, flow, and program objects attempt to allow the simplicity of simple programs that perform a single operation, with the advantage of a shared parameter space. A `SEP.opt_base.options` is an extension of the `SEP.args.basic` class. It has several additional abilities:

- It can output self-documentation based on its set of parameters.
- It introduces five additional functions:
 - The `read_params(args, prefix)` extracts from the `SEP.args.basic` object all of the parameters that the options group has been initialized with. If the parameter is required and doesn't exist it returns an error with the self-doc for the parameter. The prefix argument will limit the search of `args` to parameters that begin with `prefix`, everything after the prefix will be assumed to be the name of the parameter for the object.
 - `build_check_params()` which builds additional parameters and checks parameter validity based on command line arguments.
 - The function `prep_run(restart)` runs the task associated with the parameter group. Examples might be running a serial code or a parallel job.

- Finally `clean_files()` is meant to remove any unneeded files after the execution of the job.

The `SEP.opt_base.options` is currently inherited by four classes. The `SEP.opt_none.options` is for a group of options that aren't associated with a job. The `prep_run` and `clean_files` routines are by default empty. The `SEP.opt_prog.options` is for a set of options associated with a serial code. The `prep_run` function executes the code with the parameters associated with the object. The final two children, `SEP.par_job.par_job` and `SEP.solv_base.solver`, are discussed later.

The `SEP.flow.flow` object is a collection of parameter groups and flows. In the migration example we might have the velocity selection and migration as independent programs, where each has a parameter group associated with them. The angle gathers might be a flow composed of transposing the data and then creating the angle gathers. The `SEP.opt_flow.flow` object is initialized with a set of flows, a set of parameter groups, the order in which to run them, and potentially prefixes associated with the individual flows and parameter groups. The *prefixes* argument is a dictionary linking a given parameter group or flow to the prefix that all of its parameters will be initialized with.

The flow object has two basic functions: `add_options` and `prep_run`. The first function takes in a set of parameters *args* and runs `read_params(args,prefix)`. It then runs `build_check_params` on each parameter group and flow.

The `prep_run` call in a flow `prep_run` and `clean_files` parameter groups and flows. It is also regulated by a `SEP.stat_sep.status` object that allows that job to be restarted.

The final object, `SEP.prog.prog` inherits from the flow object. In addition, it has the concept of description and usage blocks for documentation, and by default uses the command line arguments when parsing parameters.

PARALLEL OBJECTS

The library is currently designed for coarse-grain parallel jobs that fit on a single processor (no inter-process communication necessary). The user writes a serial code that works on a portion or all of the dataset. Each parallel job is broken up into a series of *tasks*. These *tasks* can have the same, or different parameters, and the various input and output files can be distributed in several different manners. There are three basic classes of parallel objects: core objects that handle communication, parallel file objects that describe how a given file is distributed and parallel job objects that handle distributing the various tasks.

Parallel building blocks

There are several basic objects that are needed to do any remote processing. You need to know how to execute remote commands, what machines to run on, how to execute commands that

run on multiple machines at once, and how to send messages between the master process and remote processes.

The `SEP.rc` is the simplest of these build blocks. It defines two variables, `SEP.rc.shell` and `SEP.rc.cp`, which is the shell for a remote process and the copy command. It defaults to using `rsh` and `rcp` for these variables but can be set to using the secure alternatives. It also provides the functions `cp_to(mach,file_in,file_out)` and `cp_from(mach,file_in,file_out)` which return the command strings needed for transferring a file.

The `SEP.mach_base.mach` provides the framework for keeping track of what machines are available. It inherits from the `SEP.stat_sep.status` object to store its current state. It provides a mechanism for testing whether a node is functional. It requires that its children provide a mechanism to create an initial list of machines to run on. It identifies each processor on a machine through a *machine label*, which takes the form `mach-x`, where `mach` is the machine name and `x` is a processor number associated with that machine. The child classes `SEP.mach_file.mach` and `SEP.mach_list.mach` are the simplest two examples, which read their list of available machines from a file or from a supplied list. A future module might interact with a master server allowing a job to shrink or grow based on current computer usage.

In an environment where a master node isn't exporting a disk, or when you don't want to rely on that master node being up, it is necessary to copy a program to all the slave nodes. The class `SEP.distribute_prog.distribute` provides a mechanism to distribute a given program to these nodes. It copies an executable to the `/tmp` directory with a unique name, and returns that name to the calling program. It also has a cleaning method to remove the program from the nodes.

The class `SEP.pc_base.communicator` provides framework for running a job on multiple machines simultaneously. It is initialized with the speed of the network. It expects its children to override the function `prep_run` which defines how to run a parallel job given the list of nodes, the command line arguments, and how many bytes are going to be processed. The last argument is used as a mechanism to calculate how long a job should take, therefore a mechanism to test whether a job is hung and should be killed. The class `SEP.pc_mpich.communicator` is the only current example. It uses MPICH as its communication model.

Communicating with a series of remote processes can be a tricky proposition. The standard Unix approach, a socket, has an important limitation in that it can not have more than `X`, where `X` is a small number, of processes waiting to establish a connection. This limitation can be reached either by having too many processes talking on a given socket or by the actions brought on by the socket communication taking too long. The library accounts for both these limitations. The basic concept is that a parallel job might spawn several sockets simultaneously. Each socket will communicate with a maximum number of processes (60 by default). The actions taken after receiving a message will be limited writing to a text file. The class `SEP.par_msg.msg_object` has the ability to read and write a message. Its child, `SEP.par_msg.server_msg_obj`, receives the message over a socket using `SEP.sep_socket.sep_server` class.

Parallel files

As mentioned at the beginning of this section we are going to be running a series of remote processes with local versions of SEPlib files. The parallel file objects control these local versions. They store not only the names of the files but also handle distributing and collecting the files.

The base parallel class `SEP.pf_base.parfile` inherits from both the `SEP.sepfile.sep_file` and the `SEP.stat_sep.status` classes. It is initialized with *at least* an ASCII description, *name*, the usage of the file *usage* ("INPUT" or "OUTPUT"), and the *tag* that the program uses to access it (e.g. `<`, `data=`, `>`). In addition, it must be either initialized with the list of *tasks*, mentioned above, or have its status loaded from disk using the *load* argument. In addition the user can specify

add Whether we are adding the results contained in the parallel file to a preexisting file.

remove Whether (default) or not the local versions of the parallel file should be removed once the jobs is finished.

collect_it Whether (default) or not an output file should be collected when the parallel job is finished.

The two most important functions are the ability to `collect` all of the portions of the parallel file onto the master node, and `tags` which returns the tag that should be used when accessing a local version of the file. The `tags` function is passed in a dictionary linking *task* with the machine it will be run on. A local name for the section of the data is found or created and, if needed, a local version of the file is distributed to the node. The inheritance chart for the parallel file objects can be seen in Figure 1.

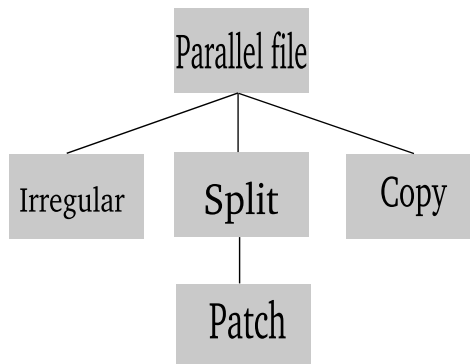


Figure 1: The inheritance chart for the parallel file objects. `bob1-parfile`
[NR]

The class `SEP.pf_copy.parfile` is the simplest of the parallel files. It only works with a regular SEPlib cube. If the named file is an input file, `SEP.pf_copy.parfile` copies the entire file to each node. If the named file is an output file, a collection all of the local version will be summed to produce the final output. This class has the additional initialization argument *reuse_par*, which tells how to signify to the program that the file already exists. This argument

is added to the returned parameters in `tags` when dealing with an output file that already exists. An example of a `SEP.pf_copy.parfile` is the velocity and image files in migration. The `reuse_par` argument would be needed when the image file is already created on the node, to signify that we need to add to rather than replace, the image. Transferring the data is done in megabyte-sized chunks from one node to the next to build up the image using `Copy_join` or to distribute using `Copy_split`.

The class `SEP.pf_split.parfile` allows a parallel file to be split along one or more axes. It is initialized with the additional parameter `dff_axis`, the axis or axes we are splitting along, and `nblock`, the number of portion that axis will be split into. An example of a `SEP.pf_split.parfile` file would be the frequencies in downward-continuation migration. The same principal is used to transfer the data. Megabyte-sized chunks are passed from one node to the next using `Patch_split` and `Patch_join`. When a node contains a given chunk, it is read from or written to disk, otherwise it just passes what it received.

The class `SEP.pf_patch.parfile` inherits from `SEP.pf_split.parfile`. It is used when overlapping patches of a dataset are needed. It adds the additional initialization argument `noverlap`, which tells how much overlap between the patches along each axis. An example would be the image space in shot-profile migration. When collecting, it applies a triangle in the overlapped region.

The last type of parallel file is the class `SEP.pf_irreg.parfile`. It currently can only be used as input. It is defined for irregular datasets (aka SEP3D). It has the ability to be split along multiple axes and have overlapping patches. It use `sep3d_split` for distribution. The distribution is fairly smart. It does not attempt to sort the dataset but instead makes sure that each local version of the data contains an updated `data_record_number`. As a result, it can be a very effective method to handle large-sized sorts.

PARALLEL JOBS

The controlling process for running a parallel job comes from the `SEP.pj_base.par_job` class or its children. It is derived from the `SEP.opt_base.options` class for parameter handling. There are also numerous optional parameters that can tune the performance on a cluster. There are two required parameters to initialize a parallel job. The first is a dictionary `files` whose values are the parallel files needed for the job. A second is a dictionary `sect_pars` linking tasks to parameters. In addition, most parallel jobs will have `program`, the executable that will be run on each node, and `global_pars`, a list of parameters that each job will need in addition to those described in `sect_pars`. There is a number of other options such as `device` (which tells what Ethernet device the cluster is connected to) that can be useful to tune performance on a given cluster.

At the start of a parallel job, several communication threads are forked. Each of these threads' purpose will be to handle communication between a set of slave processes (the jobs on remote machines) and the master machine. The master thread then requests a list of all of the machines that are available. It checks to make sure each of these machines is functional.

It then begins a loop that runs until each job has run to completion.

The loop begins by requesting from the machine object a list of available *machine labels*. It has to parse this list if any of the parallel files are of type `SEP.pf_copy.parfile` and are being used as output. Only a single process can be started on a given node until the file has been created. It then matches available jobs to the remaining *machine labels*, and requests from each parallel file object a local version of that file. It takes the parameters in *global_pars*, the task parameters in *sect_pars*, and adds in parameters telling the jobs how to communicate with the socket it has been assigned to. Then the command line for a given job is constructed by the *command_func* routine. By default this routine builds the command line based on *program* defined in the initialization. This function can be overwritten for more complex tasks. It forks a new thread for each job, and records that a job has been sent. These forked threads will exit when the job has been completed. If the exit status of the job is not 0, the job will be listed as failing.

Once a series of jobs has been started, the master thread reads the series of files written to by the `SEP.par_msg.server_msg_obj` objects, and updates the status of each job. The status messages come in several forms:

running A task has successfully started. Notification that a job has started successfully is important in the case of an output `SEP.pf_copy.parfile`. The signal is sent when the output file has been successfully created and notifies the server that it is safe to start other jobs on the node.

finished The task has completed successfully. When a job has finished, the machine is marked available. If all jobs are finished the loop is exited.

progress The task has completed a certain portion of its job. If a job is restarted this information is included in the command line options for the job.

failed The task failed. The machine status is checked. If it is no longer working, all jobs that have completed on that node are marked as needing to be rerun.² If the node is working, the task is guaranteed to be assigned to another node. If it fails more than twice (also configurable) the job is exited.

The process then sleeps and restarts the loops. Every few minutes it checks to see if any nodes have failed or if any previously failed nodes now work. If the job loop exits successfully, the sockets are shut down and the parallel files are collected as necessary.

There are two extensions to the `SEP.pj_base.par_job` object. The `SEP.pj_simple.par_job` class is all that is needed for most parallel jobs. It takes the additional command line arguments:

command The name of the program to run.

²It is possible to tell the parallel job to not rerun these jobs with the assumption that the problems with the node will be fixed.

files The list of files the jobs needs.

tags The list of tags associated with the `files` described above.

usage The usage for each of the files.

nblock The number of parts to break the files into.

axis The axis in which each file is split along.

file_type The file type for each distributed file (*DISTRIBUTE* or *COPY*).

The object then builds all of the appropriate parallel file objects.

The final parallel job class, `SEP.pj_split.par_job`, is useful for many inversion problems. It is initialized with a dictionary `assign_map` linking the job with the machine, or more precisely a machine label, specifying where the jobs should be run. By always running a specific portion of the dataset on a given node, you can avoid collecting the dataset at each step in the inversion process. It can also be useful in things like wave-equation migration velocity analysis where a large file, in the velocity analysis case the wave-field, is needed for calculations. The downside of this approach is, if a node goes down, the job can not run to completion but must terminate when it has accomplished the work on all the remaining nodes.

INVERSION OBJECTS

There are three class trees in the inversion library. The vector class tree defines how to do mathematical functions on a stream of numbers. An operator knows its domain (model space) and range (data space) and how to map a vector from one to the other. Finally, the solver class defines how to estimate a model vector given an operator.

Vector objects

Vectors are simply a stream of numbers that exist in some space. The base vector class is `SEP.vec_base.vector`. The base class defines a series of functions that must be overridden by its children.

clone() Return a copy of the vector.

clone_space() Return a copy of the space the vector exists in.

zero() Zero the vector.

random() Put random numbers into the vector.

scale(val) Scale the vector by the number *val*.

add(vec) Add *vec* to the vector.

scale_add_scale(scale1,vec,scale2) Scale the vector by *scale1* and then add *vec* scaled by *scale2*.

multiply(vec) Multiply the vector by the vector *vec*.

dot(vec) Return the dot product of the vector with the vector *vec*.

load(name) Load the vector *name*.

size() Return the size of the vector.

clean() Clean the vector, remove it from memory and/or disk.

The `SEP.vec_super.vector` class is derived from the `SEP.vec_base.vector` class. It is simply a collection of more than one vector. It applies all mathematical operations on each vector independently.

The `SEP.vec_oc.vector` class is an out-of-core vector that exists in a file. The `SEP.vec_sep.vector` class is inherited from the `SEP.vec_oc.vector` class and the `SEP.sepfile.sep_file` class. It is vectors that are stored in SEPlib files. It uses the SEPlib program `solver_ops` to perform mathematical operations. The `SEP.vec_oc.vector` should not be used by a programmer because the data type (complex or float) has not been defined. The `SEP.vec_sfloat.vector` and `SEP.vec_scmplx.vector` classes define the float and complex version of the a SEP out-of-core dataset.

There are six additional vector classes for use with parallel jobs. The current inheritance tree for the vector is shown in Figure 2. The `SEP.pv_copy.cmplx_vector` and `SEP.pv_copy.float_vector` classes are for files that are shared among the nodes (derived from the `SEP.pf_copy.parfile`) class and are distributed and collected, before and after each parallel operation. The `SEP.pv_spli.cmplx_vector` and `SEP.pv_spli.float_vector` vectors are also distributed and collected, but are split among the nodes and inherited from `SEP.pf_split.parfile`. The final two vectors, `SEP.pv_always_split.cmplx_vector` and `SEP.pv_always_split.float_vector`, also inherit from the `SEP.pf_split.parfile` class. These two classes are never collected or distributed and exist solely on the nodes. Parallel operators using these vector need to be derived from the `SEP.pj_split.par_job` class. Mathematical operations are done in parallel using the `solver_ops_split` program.

Operator

The base operator class is `SEP.op_base.operator`. It is initialized with a name (an ASCII string) and by a domain and range vector that are derived from the `SEP.vec_base.vector` class. It can also be initialized with a verbosity flag, *verb*, on whether to print out a message message, *msg* (which defaults to the program name), when applying the forward or adjoint. The forward and adjoint functions require model and data space vectors, which are tested to make sure that they correspond to the domain and range vectors for the operator.

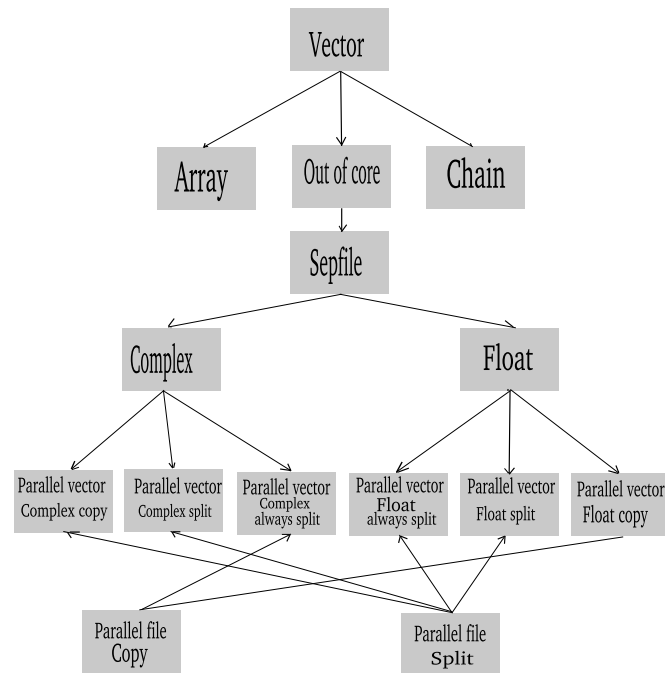


Figure 2: Vector inheritance tree.

`bob1-vector` [NR]

In addition, the forward and adjoint functions have several optional arguments. The *add* is used in to signify that the output of the operation should be added to an existing vector. The *restart* can be used to signify that we are restarting the operator. When the operator is being used an inversion problem, two additional arguments will be passed. The *iter* argument corresponds to the current iteration. The *status* argument is a `SEP.status_sep.status` object used to keep track of the progress of the inversion. If passed in, the starting and finishing of the operation will be recorded in the status file. The forward and adjoint functions only deal with keeping track of the progress of the inversion. The real work is done by the `adjoint_op` and `forward_op` functions. These two functions must be overridden by its children. The `SEP.oc_base.operator` defines a function `dot_test` which tests to make sure the operator passes the dot product test. The `init_op(restart)` function is defined to perform operations needed before the operator is initialized for the first time. The *restart* argument is used to signify whether the job is being restarted.

The simplest operator that is derived from the `SEP.op_base.operator` class is the `SEP.op_scale.operator` operator. This operator is simply a diagonal operator where elements along the diagonal are constant. It uses the `SEP.vec_base.vector` vector operations to run the forward and adjoint. It is used by the solver to apply ϵ when doing regularized or preconditioned inversion.

Two classes for combining operator are also derived. The first `SEP.op_combo.chain` class chains two or more operators together (eg. \mathbf{AB}), where \mathbf{A} and \mathbf{B} are both operators. When initialized, it checks to make sure that the domain of \mathbf{A} and the range of \mathbf{B} are the same space. The `init_op` function is overridden to create the temporary vector of the shared space. The `SEP.op_combo.array` class is used to define an array of operators. The number of columns and rows, along with the operators, are passed in during initialization. It can be useful for

regularized problems and building complex inversion operators. The range and domain vectors are constructed from the `SEP.op_super.vector` vector class.

The current operator tree can be seen in Figure 3. An out-of-core operator class, `SEP.op_oc.operator`, is also derived from the `SEP.op_base.operator` class. This class expects its inputs and outputs will be stored on disk. The `SEP.op_oc_serial.operator` is used for operators that are applied by a serial code. The class is derived from both the `SEP.op_oc.-operator` and `SEP.opt_par_group.par_group`. It is initialized by the location of the serial code *prog* and optionally the *name*, a description of the operator (defaulting to the program name), a verbosity flag (*verb*), and the message to print when applying the operator (*msg*). Other operator's parameters are set using the `SEP.opt_par_group.par_group` parameter methodology.

domain and range The domain and range vectors. These are expected to be derived from the `SEP.op_oc.vector` class.

domain_tag and range_tag The tags the program uses for the domain and range vectors, defaults to `model=` and `data=`.

restart_com The command line argument to specify a restart, defaults to none.

adj_com The command line argument when running the adjoint, defaults to `adj=y`.

add_com The command line argument when adding to the output, defaults to `add=y`.

The `forward_op` and `adjoint_op` become calls to the serial code.

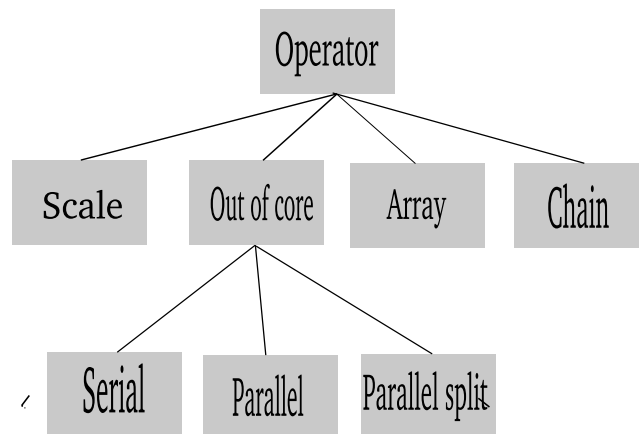


Figure 3: The inheritance class for operators `bob1-operator` [NR]

The final two operator classes, `SEP.op_oc_par.operator` and `SEP.op_oc_par_split.operator`, are for parallel jobs. They are derived from the `SEP.pj_base.par_job` and `SEP.pj_split.par_job` class along with the `SEP.op_oc.operator` class. The `SEP.op_oc_par.operator` class is designed for jobs where the domain and range vectors will be distributed and collected before and after the parallel job. The `SEP.op_oc_par_split.operator` class is useful

for problems where distributing and collecting the files after every operation is not practical. All of the initialization and parameters are generally handled the same as for the `SEP.op_oc_serial.operator`. The domain and range vectors are either `SEP.pv_copy.vector` or `SEP.pv_split.vector` in the case of `SEP.op_oc_par.operator` operator. In the case of the `SEP.op_oc_par_split.operator` object, the vectors must be of the `SEP.pv_always_split.vector` type. To run the operator, a parallel job is executed rather than running a serial code.

Solvers

The base solver class, `SEP.solv_base.solver`, is inherited from `SEP.opt_base.options`. The solver keeps track of its progress using the `SEP.stat_sep.status` module. It expects that the parameters *niter*, the number of iterations, and *stepper*, the class that calculates the step to be set by the time `prep_run` is called. The function `iter` iterates *niter* times. To make expanding the solver easier, it includes a dummy function `end_iter(iter)` that is run at the end of each iteration. This function can be overwritten to do things like write out the model at each iteration.

There are three classes derived from the `SEP.solv_base.solver` class. The `SEP.solv_smp.solver` class is designed for solving problems of the form

$$Q(\mathbf{m}) = \|\mathbf{d} - \mathbf{Lm}\|^2 \quad (1)$$

where \mathbf{d} is the data, \mathbf{L} is the operator, and \mathbf{m} is the model. It expects that its children set the operator *op*, the data *data*, the model *model* before its `prep_run` function is invoked. It will also look for a weighting operator *wop*, a model vector *v*, an initial model *m0*, and an initial residual vector *resd*. From this information, an initial residual model vector are calculated and `SEP.solv_base.solver`'s `prep_run` is invoked.

The `SEP.solv_reg.solver` class is also derived from `SEP.solv_base.solver` class. It is used for regularized inversion problems of the form,

$$Q(\mathbf{m}) = \|\mathbf{d} - \mathbf{Lm}\|^2 + \epsilon^2 \|\mathbf{Am}\|^2, \quad (2)$$

where \mathbf{A} is the regularization operator. It expects all of the arguments of `SEP.solv_smp.solver` with the addition of regularization operator *reg* and the relative weighting parameter ϵ *eps*. In addition accepts the optional residual model space vector *resm*.

The final solver derived from `SEP.solv_base.solver` is `SEP.solve_prec.solver`. It is used from regularized problems with model preconditioning of the form,

$$Q(\mathbf{p}) = \|\mathbf{d} - \mathbf{LBm}\|^2 + \epsilon^2 \|\mathbf{p}\|^2, \quad (3)$$

where \mathbf{B} is the preconditioning operator and \mathbf{p} is the preconditioned variable, where $\mathbf{m} = \mathbf{Bp}$. It expects all of the same parameters of `SEP.solv_reg.solver`, with *reg* removed and *prec*, the preconditioning operator, added.

All of the solvers are currently linear solvers. Adding non-linear solvers would be fairly easy. They all require a step function. Currently only a conjugate gradient step function is available in `SEP.cgstep.cgstep`.

PROGRAM FUNCTIONS

There are two required and three optional functions available to the programmer. The required functions go near the beginning and ending of the program. The first, `sep_begin_prog`, tells the server that the program has started successfully. It should be used when it is safe to start another instance of the program on the same node. This latter requirement is important when sharing an output space (`COPY`) on a node. If you are adding to the output space you need insure that the output file has been created by the first instance of the program. The other required function is `sep_end_prog`. This should be used after all of the output files have been completely written to. The server interprets it as a sign of completion for the job.

The `sep_progress` function enables effective job restarting. The programmer can use this function to signify a checkpoint in the code. When restarting a job, both the restart flag and the last progress message will be passed as arguments for the restarting job. In the case when you are sharing an output space, you should use this function whenever you write to the shared file. The final two functions are when you are sharing an output space. The `sep_open_lock(tag)` locks (if already locked waits for the file to become available) a SEPlib tag. The `sep_close_lock(tag)` function frees a tag so another process can safely read or write to it. All of these commands perform no function when they are not a portion of a parallel job.

EXAMPLES

Examples are the most effective way to learn how to use a piece of software. In this section, I will go over several examples. I will begin by showing how to build a flow of multiple programs. I then will give an example of how to run a simple parallel job. The third example will show how to an out-of-core inversion using serial codes, and the final example will show how to do an inversion using parallel objects.

Creating a flow

Creating a wrapper to a serial code involves creating two objects. The first object is a class that knows the parameters for the program and how to execute it. An example is `scale.py` which tells how to run a simple scaling program.

```
import SEP.opt_prog          #handle the parameters for the program
class scale(SEP.opt_prog.options): #inherit from both
    def __init__(self,name="scale"): #initialization method
        SEP.opt_prog.options.__init__(self,name) #initialize parameters
        self.set_prog("Scale.x")
    def add_doc_params(self):
        """Add the parameters for scaling a dataset"""
        self.add_doc_param("stdout",doc="Output file")
```

```
self.add_doc_param("scale",doc="Scale the dataset by a given value")
```

The second object will use the above class as in input to a program (SEP.prog.prog) object. The script `scale.py` is an example of using the above `scale` object.

```
#!/usr/bin/env python
import scale          #the scale object code
import SEP.prog      #the program object code

scale=scale.scale("Scale")      #initialize the scale object
program=SEP.prog.prog("Scale.py ", #the name of the program for self-doc
    "Scale.py pars ", #Usage for self-doc
    [scale], #the components of the program
    ["Scale using the SEP python library"]) #description doc
program.get_options()          #read the command line arguments
program.prep_run()            #run the program
```

The script functions the same way as normal SEPlib program. If no arguments are given, self-doc is returned. If an argument that is needed isn't present an error is given (in this case including the self-doc for the parameter).

Things get more interesting when we add a second program. In this case, we will add a simple program that will create a 2-D array with a plane of ones at some location. The script `line.py` provides the wrapper for the program.

```
import SEP.opt_prog #parameters
class line(SEP.opt_prog.options):
    def __init__(self,name="scale"):
        SEP.opt_prog.options.__init__(self,name)
        self.add_prog("Line.x")
    def add_doc_params(self):
        """Add the parameters for scaling a dataset"""
        #add parameters with default values
        self.add_doc_param("stdout",doc="Output file")
        self.add_doc_param("n1",10,doc="The number of sample first axis ")
        self.add_doc_param("o1",0.,doc="Origin of the first axis")
        self.add_doc_param("d1",1.,doc="Sampling of the first axis")
        self.add_doc_param("n2",10,doc="The number of sample second axis ")
        self.add_doc_param("o2",0.,doc="Origin of the second axis")
        self.add_doc_param("d2",1.,doc="Sampling of the second axis")
        self.add_doc_param("sample",5,doc="Sample number at which to create line")
```

We can write a script that combines these two programs. The new program `Line_scale.py` will first create the array with the program `line`, then use that output as input to the scaling

program. Combining the programs involves three additional steps. First, we will need to create a parameter object, `SEP.opt_prog.options`, that will be responsible for storing the input and output file information. Second, we will need to inherit from both the `line` and `scale` objects. We will change the initialization of these object is to include the new parameter object. We will remove from the documentation the input and output file requests. We will set the input and output file names based on the new parameter object. The final changes involve how to recognize the parameters for the various programs. We will introduce a new dictionary *prefixes* which maps a prefix to the parameter objects. In the example below, you will now use *line_n1* to set the number of samples in the output space.

```
#!/usr/bin/env python
import scale,line      #import both objects
import SEP.opt_prog
import SEP.prog

class main_args(SEP.prog): #the main parameters
    def __init__(self):
        SEP.opt_prog.options.__init__(self,"MAIN")
        self.add_doc_param("stdout",doc="Output file")

class my_line(line.line): #inherit from the line object
    def __init__(self,main_pars,name):
        line.line.__init__(self,name) #initialize the line.line structure
        self.main=main_pars #store the main programs parameter class
    def add_doc_params(self):
        line.line.add_doc_params(self) #add the parameters described in line
        self.del_par("stdout")a #delete the line parameter
    def prep_run(self,restart):
        #set the stdout a temp file based on the stdout of the main program
        self.add_param("stdout","%s.temp"%self.main.param("stdout"))
        line.line.prep_run(self,restart)

class my_scale(scale.scale): #inherit the scale calss
    def __init__(self,main_pars,name):
        scale.scale.__init__(self,name) #initialize the scale class
        self.main=main_pars
    def add_doc_params(self):
        scale.scale.add_doc_params(self)
        self.del_par("stdin") ;self.del_par("stdout") #delete in and out
    def prep_run(self,restart):
        #add in out (in is temp file from line)
        self.add_param("stdin","%s.inter"%self.main.param("stdout"))
        self.add_param("stdout",self.main.param("stdout"))
        scale.scale.prep_run(self)
```

```

main=main_args() #create the main arguments
line=my_line(main,"Line") #create the line arguments
scale=my_scale(main,"Scale") #create the scale arguments
prefixes={} #prefix dictionary
prefixes["Line"]="line_" #prefix for all line parameters
prefixes["Scale"]="scale_" #prefix for all scale parameters
program=SEP.prog.prog("Scale_line ",
    "Scale_line.py pars outtag= ",
    [line,scale], #now we have two objects in the flow
    ["Create a line and then scale it using the SEP python library"],
    prefixes=prefixes #the prefixes associated with the objects
)

program.get_options() #get the options
program.prep_run() #run the flow

```

Simple parallel jobs

For many parallel jobs, the program `Parallel` is all that is needed. `Parallel` is meant for parallel jobs where the input and output are either distributed, `SEP.pf_splist.parfile`, or share input, `SEP.pf_copy.parfile`, and the data is partitioned along a single axis for each file. It also requires that you are running a single program on each node (rather than some more complex operation) and you aren't wanting to add the output to another file. The required arguments to `Parallel` are composed of the program name, *command*, the number of blocks to break the program into *nblock*, and a series of lists (comma separated).

files The name of the parallel file(s).

tags The tags associated with each file.

axis The axis that each file is split along. If the file is shared, the axis is ignored for this file.

usage The usage for each file "INPUT" or "OUTPUT".

file_type The parallel file type for each file ("DISTRIBUTE" or "COPY").

All arguments that aren't part of the `Parallel` program are passed as command line arguments to parallelized serial code.

The program is effective for parallelizing code where the computational cost is significantly more than the cost of transferring the data (migration and modeling for example). It is also effective when handling problems that benefit from being held in memory (operations such as transposes). For example, a multi-gigabyte 2-D file could be transposed at marginally more than the cost of distributing and collecting the dataset through

```
Parallel files="in.H,out.H" tags="stdin,stdout" axis="2,1" usage="INPUT,OUTPUT"\
file_type="DISTRIBUTE,DISTRIBUTE"
```

Complex parallel job

The script `fdmod.py` in the report directory parallelizes 2-D finite difference modeling using the SEPlib program `Fdmod`. The general form is the same as seen in the scripts in the flow example. The `fdmod_par` object extends the `SEP.pj_base.par_job` class. The user describes a regular spaced set of shot locations using the parameters `oxs,dxs,nxs,ozs` and the number different blocks to break the problem into using `nblock`. Each job process a different set of shot locations and needs its own set of parameters. The function `build_sect_pars` calculates the parameters that vary as a function of job and stores the contents in the dictionary `sect_pars`.

```
def build_sect_params(self):
    """Build parameters for parallel job"""
    sect_pars={}
    nxs=int(self.param("nxs"))
    oxs=float(self.param("oxs"))
    dxs=float(self.param("dxs"))
    ozs=float(self.param("ozs"))
    nblock=self.param("nblock")
    if not nblock: nblock=nxs
    nblock=int(nblock)
    imin=int(n/nblock)
    nextra=n-nblock*imin
    itot=0
    for i in range(nblock):
        sect_pars[str(i)]=SEP.args.basic(name=str(i))
        ol=o+d*itot
        dl=d
        nl=imin
        if i < nextra: nl=nl+1
        itot=itot+nl
        sect_pars[str(i)].add_string("nzs=1 ozs=%f dzs=1."%(ozs))
        sect_pars[str(i)].add_string("nxs=%d oxs=%f dxs=%f"%(nl,ol,dl))
    return sect_pars
```

The `prep_run` function creates the list of parameters and defines a dictionary of parallel files. The velocity space is copied to all of the nodes using the `SEP.pf_copy.parfile` class, the output shot gather files are spread across the cluster using the `SEP.pf_split.parfile` object.

```
par_files={}
```

```

par_files["vel"]=SEP.pf_copy.parfile(name=self.param("intag"),
    tag="intag=",usage="INPUT",njobs=len(sect_pars.keys()),restart=restart)

par_files["hsfile"]=SEP.pf_split.parfile(name=self.param("hsfile"),
    dff_axis=3,tag="hsfile=",usage="OUTPUT",njobs=len(sect_pars.keys()),
    restart=restart,nblock=len(sect_pars.keys()))

```

The section parameters, the parallel files, and the modeling program are then added to the objects parameters and the parallel job is initialized.

```

self.add_param("files",par_files)
self.add_param("sect_pars",sect_pars)
self.add_param("program","%s/Fdmod"%SEP.paths.sepbindir)
SEP.pj_base.par_job.prep_run(self)

```

Inversion example

The script `Interp.py` does out-of-core interpolation. The program `Interp.x` interpolates from an irregular to a regular mesh. The program `reg.x` convolves with a three point filter. We then can turn these program into operators.

```

interp_op=SEP.op_oc_serial.operator("Interp.x")
reg      =SEP.op_oc_serial.operator("reg.x")

```

We then extend the solver object. We require the operator *op* and regularization operator *reg*. (*n1,ol,d1*).

```

class solver(SEP.solv_reg.solver):
    def __init__(self,op,reg):
        SEP.solv_reg.solver.__init__("SOLVER")
        self.add_param("op",op)
        self.add_param("reg",reg)

```

We require the user to specify the model *model*, the data *data*, ϵ *eps*, and the number of iterations *niter*, and the dimensions of the output space

```

def add_doc_params(self):
    self.add_doc_param("eps",1.,"Epsilon")
    self.add_doc_param("niter",1,"Number of iterations")
    self.add_doc_param("model",doc="Model (output)")
    self.add_doc_param("data",doc="Data (input)")
    self.add_doc_param("n1",doc="number of samples (axis 1)")
    self.add_doc_param("ol",doc="First sample (axis 1)")
    self.add_doc_param("d1",doc="Sampling (axis 1)")

```

We create the data vector from a file and create the model vector.

```
def prep_run(self, restart=None):
    self.add_param("data", SEP.vec_sfloat.vector(tag="data"))
    self.add_param("model", SEP.vec_sfloat.vector(name="model"))
    self.param("model").set_axis(1, self.param("n1").
        self.param("o1", self.param("d1")))
    self.param("model").zero()
```

We add the domain and range vectors for the operator and the regularization operator.

```
self.param("op").add_param("domain", self.main.param("model"))
self.param("op").add_param("range", self.main.param("data"))
self.param("reg").add_param("domain", self.main.param("model"))
self.param("reg").add_param("range", self.main.param("model"))
```

Finally we create the step operator and run the `prep_run` function for the operators and the regularization solver.

```
self.add_param("cgstep", SEP.cgstep.cgstep("cgstep"))
self.param("op").prep_run(restart)
self.param("reg").prep_run(restart)
SEP.solv_reg.solver.prep_run(self, restart)
```

We create the solver object, the program object, read the parameters, and run the job.

```
solv=solver(interp_op, reg_op)

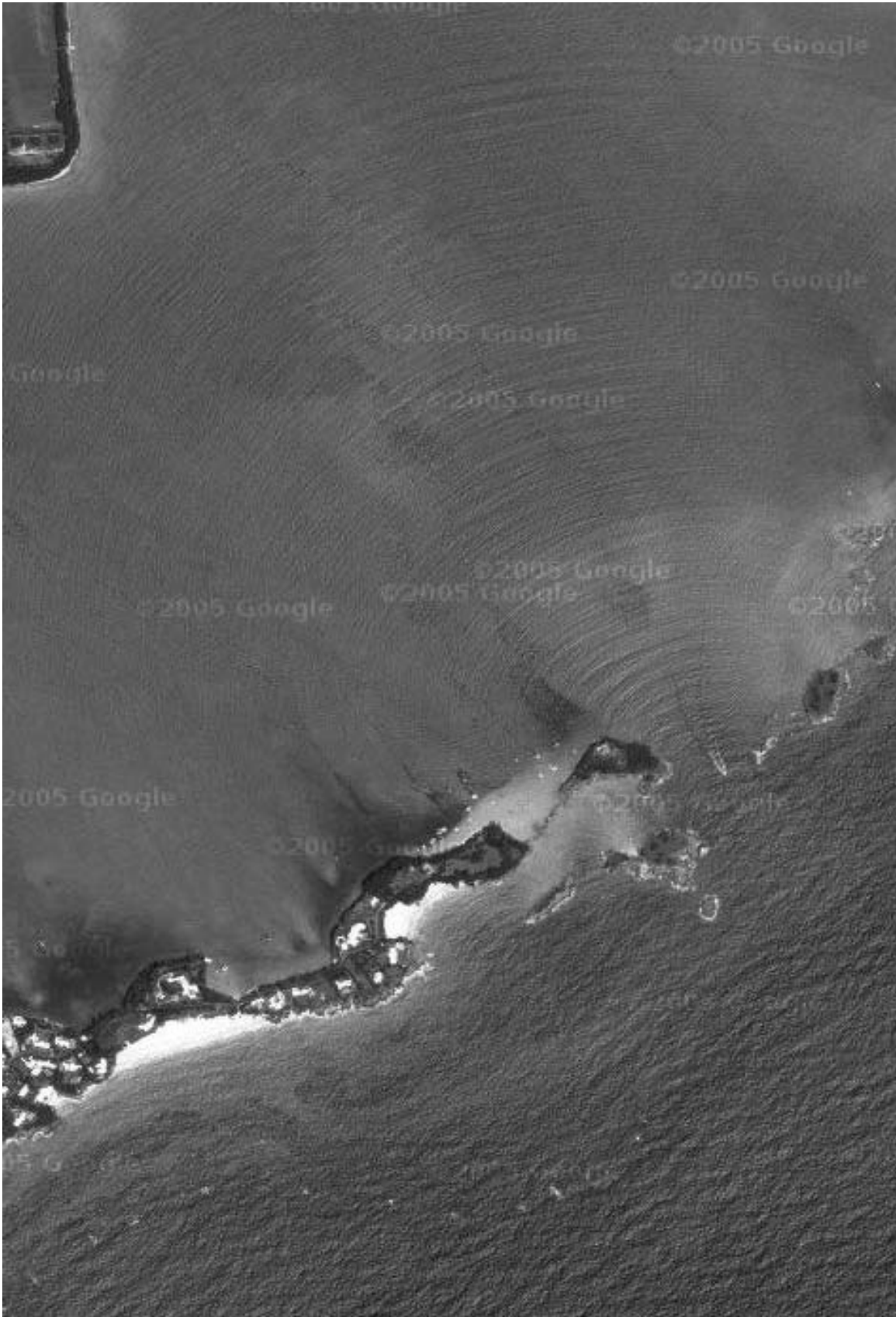
program=SEP.opt_prog.prog("Interpolate ",
    "Interp.py model= data= ",
    [interp_op, reg_op, solv],
    ["Interpolation using the SEP python library"])
program.get_options()
program.prep_run()
```

CONCLUSIONS

In this paper I present simple serial codes that can be used to create much more complex objects with minimal additional coding overhead. These objects can take the form of complex program chains. In addition the serial codes can be used to create coarse-grained parallel programs. A further option is to use simple serial codes in a parallel out-of-core inversion, using both serial and parallel operators. Examples demonstrate how to accomplish each of these goals.

REFERENCES

- Clapp, M. L., and Clapp, R. G., 2005, 3-d subsalt imaging via regularized inversion with model preconditioning: SEP-**120**, 1–22.
- Clapp, M. L., 2003, Directions in 3-D imaging - Strike, dip, both?: SEP-**113**, 363–368.
- Clapp, R. G., 2004a, Fault tolerant parallel SEPlib: SEP-**117**, 175–182.
- Clapp, R. G., 2004b, A python solver for out of core, fault tolerant inversion: SEP-**117**, 183–190.
- Sava, P., and Biondi, B., 2003, Wave-equation MVA: Born Rytov and beyond: SEP-**114**, 83–94.



Imaging steeply dipping reflectors in TI media by wavefield extrapolation

Guojian Shan and Biondo Biondi¹

ABSTRACT

We develop an anisotropic plane-wave migration method based on wavefield extrapolation. In this new scheme, we decompose both source and receiver wavefields into plane waves by delaying shots. For each plane wave, we design a tilted coordinate system whose tilting angle depends on the propagation direction of the plane wave. The wavefield extrapolation is done by an implicit isotropic operator plus an explicit anisotropic correction operator. We apply this method on a synthetic dataset. The results show that our scheme can accurately handle overturned waves and image steeply dipping reflectors in transversely isotropic media with a vertical axis of symmetry (VTI).

INTRODUCTION

VTI media is one of the simplest and most practically important types of anisotropic media. Steeply dipping structures, such as faults and salt flanks, are important for the interpretation of seismic data. The waves relating to steeply dipping reflectors usually propagate in a direction far from vertical. If we do not account for the anisotropy in the migration, steeply dipping reflectors will be imaged with large positional errors or will vanish from the image. To image steeply dipping reflectors in anisotropic media, we need an anisotropic wavefield-extrapolation operator that can handle waves propagating in a direction far from the vertical direction.

Many methods have been proposed to extrapolate wavefields and image reflectors in VTI or tilted TI media (Ristow and Ruhl, 1997; Rousseau, 1997; Ferguson and Margrave, 1998; Uzcategui, 1995; Zhang et al., 2001a,b). Baumstein and Anderson (2003) extrapolate wavefields in VTI media with a reference anisotropic phase-shift operator plus an explicit correction filter. Shan and Biondi (2004b) extrapolate wavefields in tilted TI media with an isotropic operator followed by an explicit anisotropic correction filter.

The waves related to steeply dipping reflectors usually propagate far from the vertical direction. Kirchhoff methods can propagate these waves correctly, but they are less reliable for imaging complex structure because of the high-frequency approximation. Reverse-time migration (Whitmore, 1983; Baysal et al., 1983; Biondi and Shan, 2002), which is based on the two-way wave equation, can propagate these waves accurately; however anisotropic

¹email: shan@sep.stanford.edu, biondo@sep.stanford.edu

reverse-time migration is still prohibitively expensive. Algorithms such as beam migration (Brandsberg-Dahl and Etgen, 2003; Hill, 2001; Gray et al., 2002; Albertin et al., 2001) and coordinate-transformation-based migration (Higginbotham et al., 1985; Etgen, 2002; Sava and Fomel, 2004; Shan and Biondi, 2004a), extrapolate wavefields in a direction close to the propagation direction, and can handle these waves at a wide angle.

In this paper, we apply plane-wave migration in tilted coordinates for VTI media. VTI media in Cartesian coordinates become to tilted TI media in tilted coordinates. We extrapolate the wavefields with an isotropic operator followed by an explicit anisotropic correction. We first discuss VTI media in tilted coordinates, then review plane-wave migration in tilted coordinates, and finally show the migration results for a synthetic dataset.

VTI MEDIA IN TILTED COORDINATES

A VTI medium is a medium that is transversely isotropic and has a vertical axis of symmetry. The phase-velocity $V(\theta)$ of P-waves in VTI media can be expressed in Thomsen notation as follows (Tsvankin, 1996):

$$\frac{V^2(\theta)}{V_{P0}^2} = 1 + \varepsilon \sin^2(\theta) - \frac{f}{2} \pm \frac{f}{2} \sqrt{\left(1 + \frac{2\varepsilon \sin^2(\theta)}{f}\right)^2 - \frac{2(\varepsilon - \delta) \sin^2(2\theta)}{f}}, \quad (1)$$

where θ is the phase angle of the propagating wave, and $f = 1 - (V_{S0}/V_{P0})^2$. V_{P0} and V_{S0} are the P- and SV-wave velocities in the vertical direction, respectively, and ε and δ are anisotropy parameters defined by Thomsen (1986):

$$\varepsilon = \frac{C_{11} - C_{33}}{2C_{33}}, \delta = \frac{(C_{11} + C_{44})^2 - (C_{33} - C_{44})^2}{2C_{33}(C_{33} - C_{44})},$$

where C_{ij} are elastic moduli. In equation (1), $V(\theta)$ is the P-wave phase-velocity when the sign in front of the square root is positive, and the SV-wave phase velocity for a negative sign.

For plane-wave propagation, the phase angle θ is related to the wavenumbers k_x and k_z by the following relations:

$$\sin \theta = \frac{V(\theta)k_x}{\omega}, \quad \cos \theta = \frac{V(\theta)k_z}{\omega}, \quad (2)$$

where ω is the temporal frequency. From Cartesian coordinates to tilted coordinates, we do a transformation as follows:

$$\begin{pmatrix} x' \\ z' \end{pmatrix} = \begin{pmatrix} \cos \varphi & \sin \varphi \\ -\sin \varphi & \cos \varphi \end{pmatrix} \begin{pmatrix} x \\ z \end{pmatrix}. \quad (3)$$

where φ is the rotation angle.

Figure 1 illustrates this change of symmetry axis during the coordinate transformation. The layered structure has a symmetry axis in the vertical direction in Cartesian coordinates

(x, z) in the left panel. When we rotate the coordinates from (x, z) to (x', z') , the symmetry axis in the new coordinates (x', z') deviates from the z' direction.

In tilted coordinates (x', z') , we have the following relation between wavenumber $k_{x'}, k_{z'}$ and phase angle θ' :

$$\sin \theta' = \frac{V(\theta')k_{x'}}{\omega}, \quad \cos \theta' = \frac{V(\theta')k_{z'}}{\omega}. \quad (4)$$

The symmetry axis is not vertical in tilted coordinates, so the angle between the direction of wave propagation and the symmetry axis is not the phase angle θ' , but $\theta' - \varphi$, where φ is the tilting angle of the tilted coordinates. Therefore, VTI media in Cartesian coordinates become tilted TI media. The P-wave phase velocity in tilted coordinates can be expressed as

$$\frac{V^2(\theta', \varphi)}{V_{P0}^2} = 1 + \varepsilon \sin^2(\theta' - \varphi) - \frac{f}{2} \pm \frac{f}{2} \sqrt{\left(1 + \frac{2\varepsilon \sin^2(\theta' - \varphi)}{f}\right)^2 - \frac{2(\varepsilon - \delta) \sin^2(2(\theta' - \varphi))}{f}}. \quad (5)$$

Thus for a VTI medium in tilted coordinates we need a wave-extrapolation operator that can

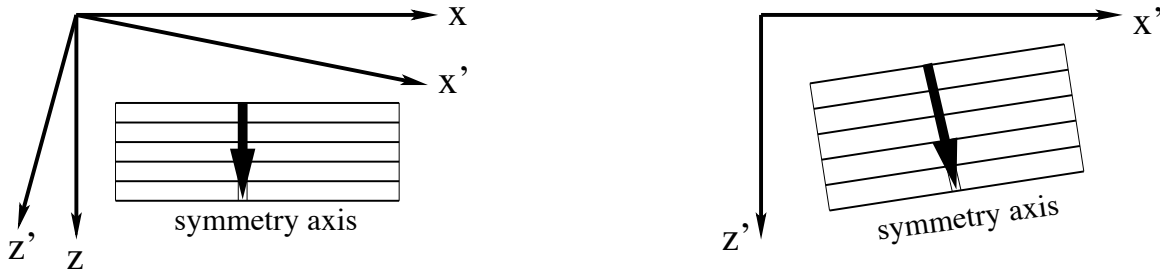


Figure 1: VTI media in tilted coordinates. Left panel is a layer structure in Cartesian coordinates. Right panel is the layer structure in tilted coordinates. `guojian1-vtilt` [NR]

downward extrapolate the wavefield in tilted TI media. From equations (4) and (5), we can solve $k_{z'}$ as a function of $\varphi, \varepsilon, \delta$, and ω/V_{P0} . The wavefield can be extrapolated in two steps. First, the wavefield is extrapolated by an isotropic operator as follows:

$$\bar{P}(z + \Delta z) = P(z) e^{ik_z^{iso} \Delta z}, \quad (6)$$

where $k_z^{iso} = \sqrt{(\omega/V_{P0})^2 - (k_x')^2}$ is the isotropic vertical spatial wavenumber. This isotropic operator can be implemented by the split-step method (Stoffa et al., 1990), the general screen propagator (Huang and Wu, 1996), or Fourier finite difference (FFD) (Ristow and Ruhl, 1994). Next, the wavefield is corrected by an explicit correction operator. This correction operator is designed in the Fourier domain, and is implemented in the space domain. The correction operator in the Fourier domain is a phase-shift operator:

$$P(z + \Delta z) = \bar{P}(z + \Delta z) e^{i(k_z' - k_z^{iso}) \Delta z}. \quad (7)$$

In the space domain, this correction operator is a convolution filter. The coefficients of the convolution filter depend on $\varphi, \varepsilon, \delta$, and ω/V_{P0} , and they can be estimated by the weighted least-squares method (Shan and Biondi, 2004b).

ANISOTROPIC PLANE-WAVE MIGRATION IN TILTED COORDINATES

In plane-wave migration (Rietveld, 1995; Duquet et al., 2001; Liu et al., 2002; Zhang et al., 2003) source wavefields are decomposed into plane waves, and the receiver wavefields are re-arranged corresponding to their respective plane-wave source. Shan and Biondi (2004a) apply plane-wave migration in tilted coordinates for an isotropic medium. For each plane wave, proper tilted coordinates are designed, whose tilting angle is selected according to the direction in which the plane wave propagates. Source and receiver wavefields are downward continued in these tilted coordinates. Images and dip-dependent angle-domain common-image gathers (CIGs) are generated by cross-correlation.

Anisotropic plane-wave migration is the same as isotropic plane-wave migration, except that an anisotropic correction operator is applied after the isotropic wavefield extrapolation at each depth step. Since the correction operator is explicit, we build a table of convolution coefficients before we run the wavefield extrapolation. If the medium at a point in space is isotropic ($\varepsilon = \delta = 0$), only the isotropic extrapolation will occur. Otherwise, the anisotropic correction operator will be applied to the wavefield. For anisotropic correction, we search for the filter coefficients corresponding to the tilting angle φ , anisotropy parameters ε and δ and the value of ω/V_{P0} in the table and convolve the wavefield at that spatial position with these coefficients. As in the isotropic case, images and dip-dependent angle-domain CIGs can be created by cross-correlating the source and receiver wavefields.

NUMERICAL EXAMPLE

We test our method on a synthetic dataset and compare the results of isotropic and anisotropic migration. Figure 2 shows the model of the synthetic data we use to test our method. Figure 2(a) is the density model, Figure 2(b) is the vertical P-wave velocity model, and Figure 2(c) is the map of the anisotropy parameter ε . The anisotropy parameter δ is 0 for this dataset. The salt flank is very steep, and its top part over hangs. In the sediments, the vertical P-velocity increases gradually with the depth. One sediment layer (between 2000 m and 3000 m) is strongly anisotropic. Our aim is to image the flank of the salt dome and the sediment reflector below the anisotropic layer and near the salt dome accurately. Figure 3 shows a near-offset section of the synthetic data. Notice the strong energy reflected from the salt flank in the near offset data.

Figure 4 shows the results of the isotropic migration for this dataset. Figure 4(a) is the result of the isotropic plane-wave migration in Cartesian coordinates, and Figure 4(b) is the result of the isotropic plane-wave migration in tilted coordinates. In Figure 4(a), the salt flank is totally lost. This is because waves related to the salt flank are overturned, and the one-way wave-equation downward continuation method can not extrapolate them correctly. In Figure 4(b), although a weak steeply dipping reflector can be seen, it is not at the correct position, because the anisotropy in the sediment layer was neglected.

Figure 5 shows the results of the anisotropic migration for this dataset. Figure 5(a) is the anisotropic plane-wave migration in Cartesian coordinates, and Figure 5(b) is the anisotropic

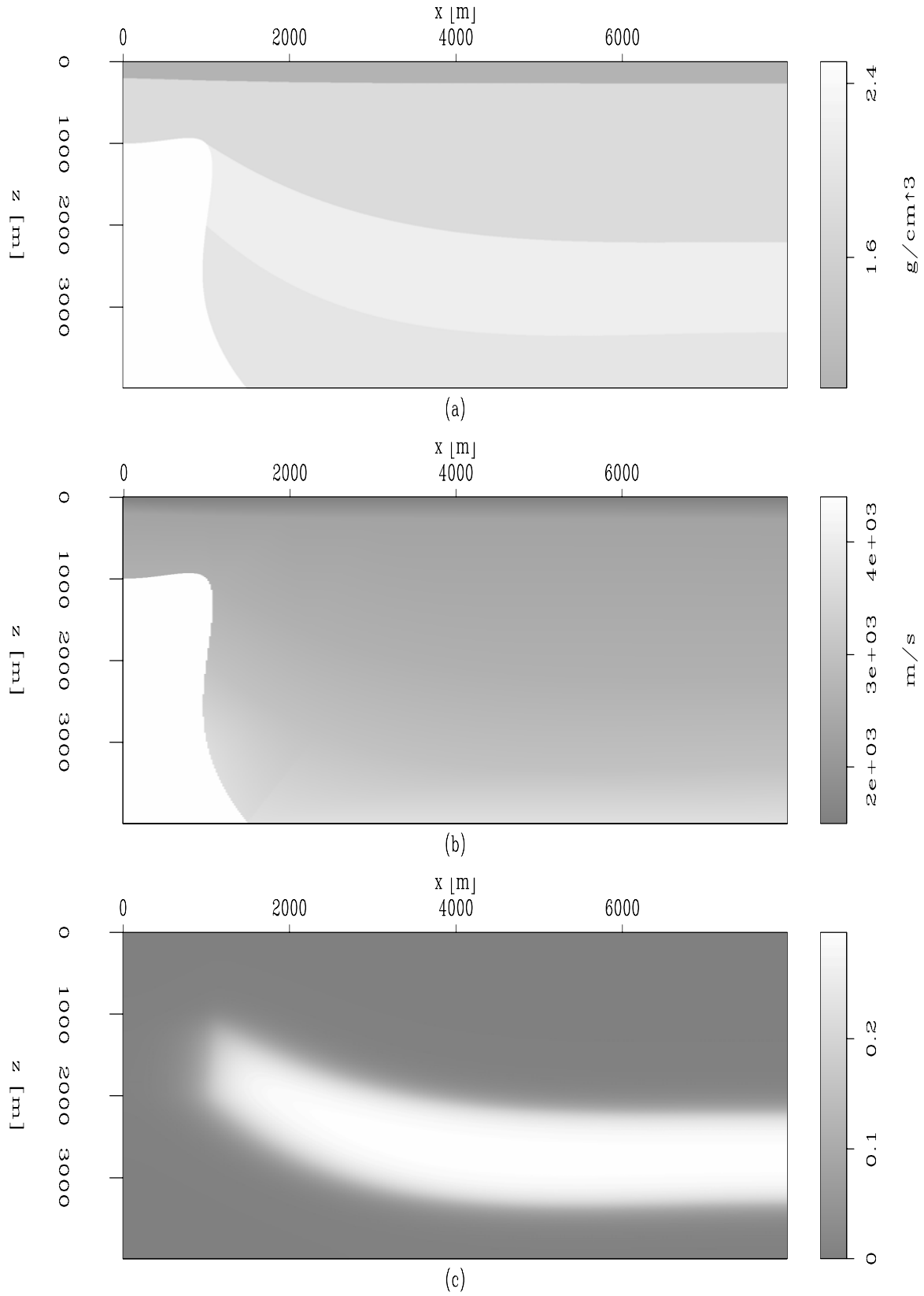


Figure 2: Model of the synthetic dataset. (a) Density model; (b) Velocity model; (c) Anisotropy parameter ε . `guojian1-model` [ER]

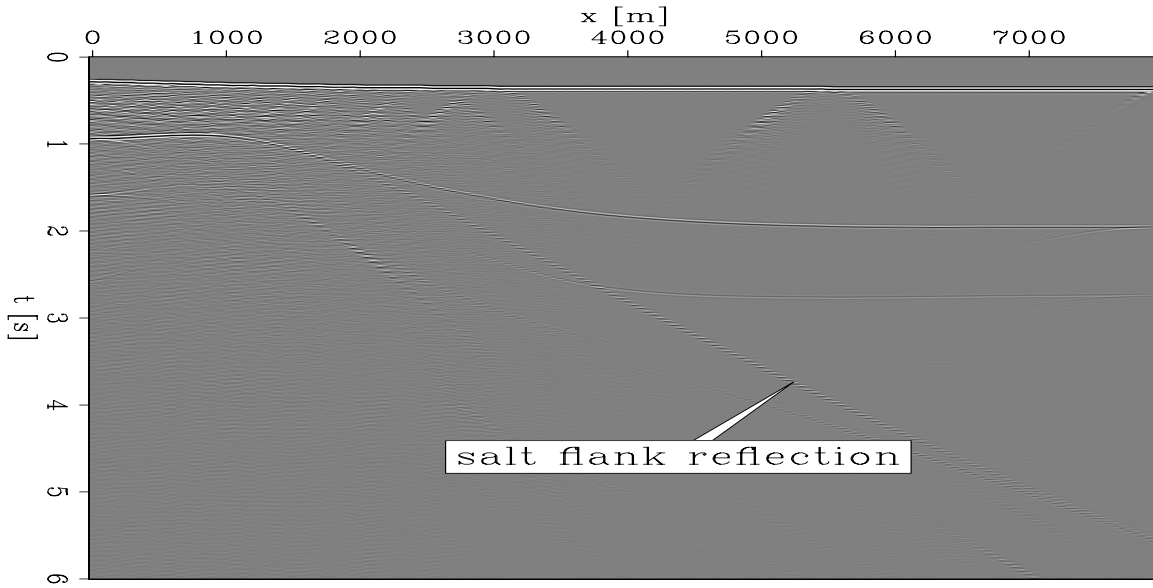
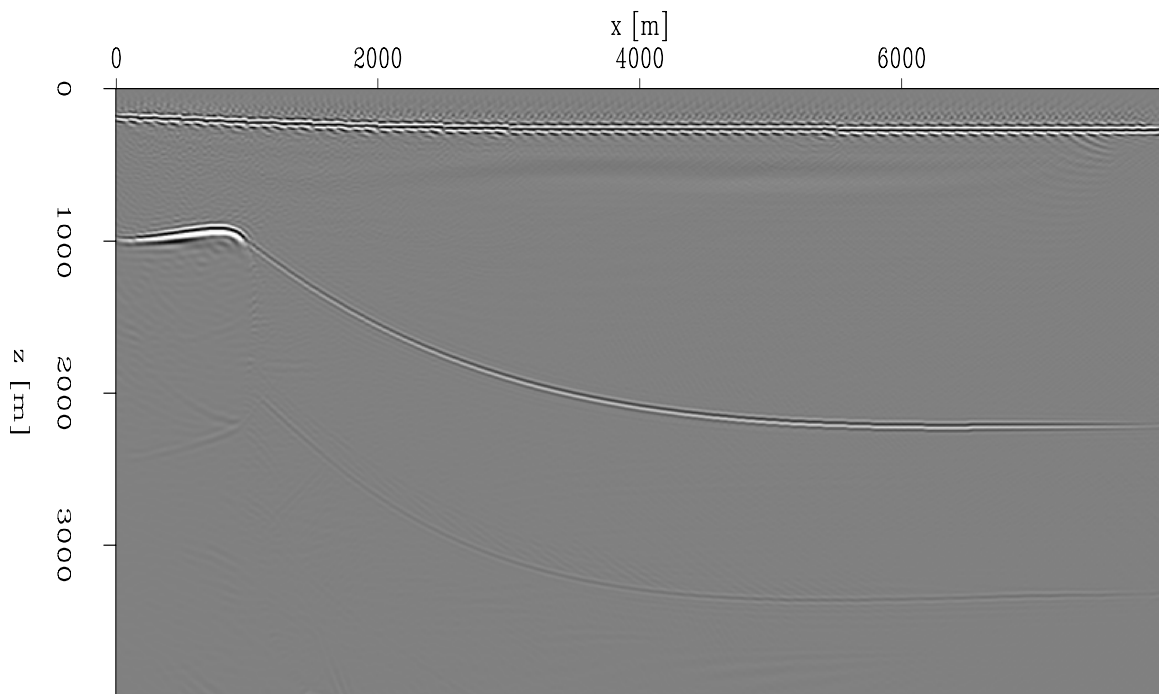


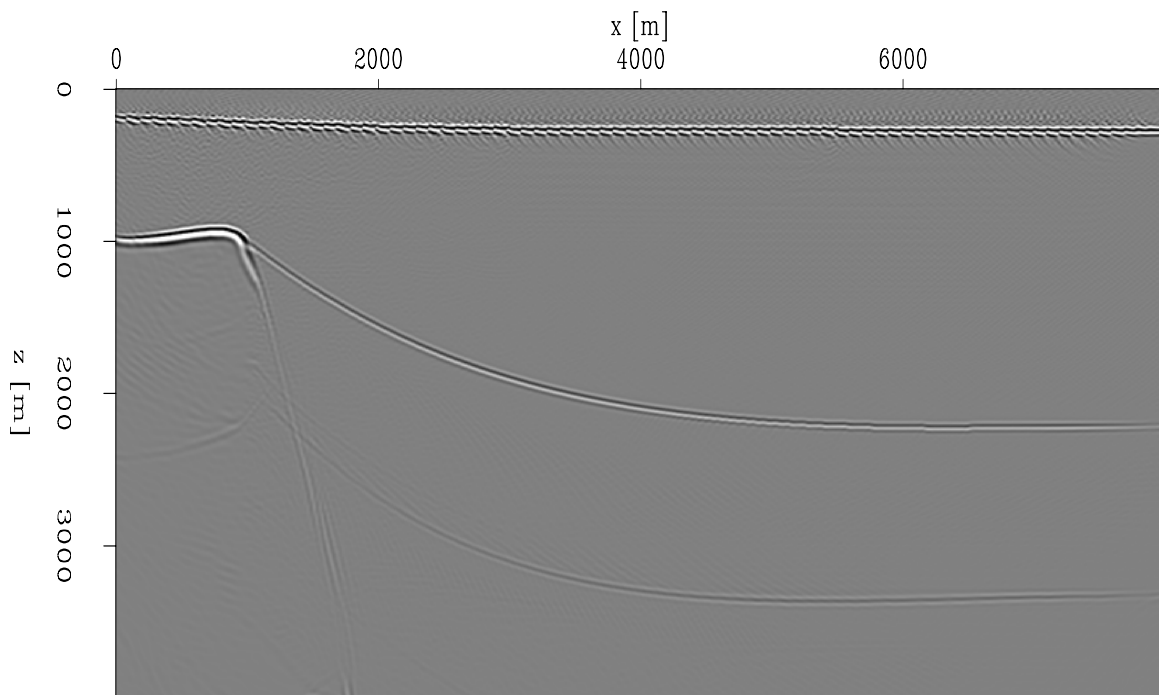
Figure 3: A near-offset section of the synthetic data. `guojian1-nearoffset` [ER]

plane-wave migration in tilted coordinates. In Figure 5(a), the top part of the salt flank is lost due to overturned waves, but the bottom part of the salt flank is correctly imaged, but is not focused by the isotropic migration (Figures 4(a) and 4 (b)). In Figure 5(b), the image is greatly improved compared to the previous three images. Both the top and bottom parts of the salt flank are well imaged. In Figure 5(b), the reflector below the anisotropic layer is stronger and more continuous near the salt flank compared to that in the isotropic migration result. To check if the reflectors are imaged at the correct positions, we overlay the images with the density model in Figure 6. Figure 6(a) is the isotropic migration result overlaid with the density model. Figure 6(b) is the anisotropic migration result overlaid with the density model. The salt flank matches the density model very well in the image obtained by the anisotropic migration, while it deviates from the model in the isotropic one. The flat part of the reflector below the anisotropic layer is not affected much by the anisotropy. Both the isotropic and anisotropic migration image it at the correction position.

Figure 7 shows the horizontal angle-domain CIGs at the horizontal location $x = 4000\text{m}$. Figure 7(a) is obtained by the isotropic migration, and Figure 7(b) is obtained by the anisotropic migration. Figure 8 shows the vertical angle-domain CIGs at the vertical location $z = 1500\text{m}$. Figure 8(a) is obtained by the isotropic migration, and Figure 8(b) is obtained by the anisotropic migration. Although we use the true, vertical P-wave velocity in the isotropic migration, we find a small curvature in the horizontal angle gathers at the reflector below the anisotropic layer (at $z = 3300\text{ m}$ in Figure 7), and a big curvature in the vertical angle gathers at the salt flank (x between 1000 m and 1500 m in Figure 8). In the anisotropic migration, the angle gathers are flat at these locations. The big curvature of the angle gathers at the steeply dipping reflectors can be used as a tool to estimate the error in the anisotropy parameters used in the migrations.

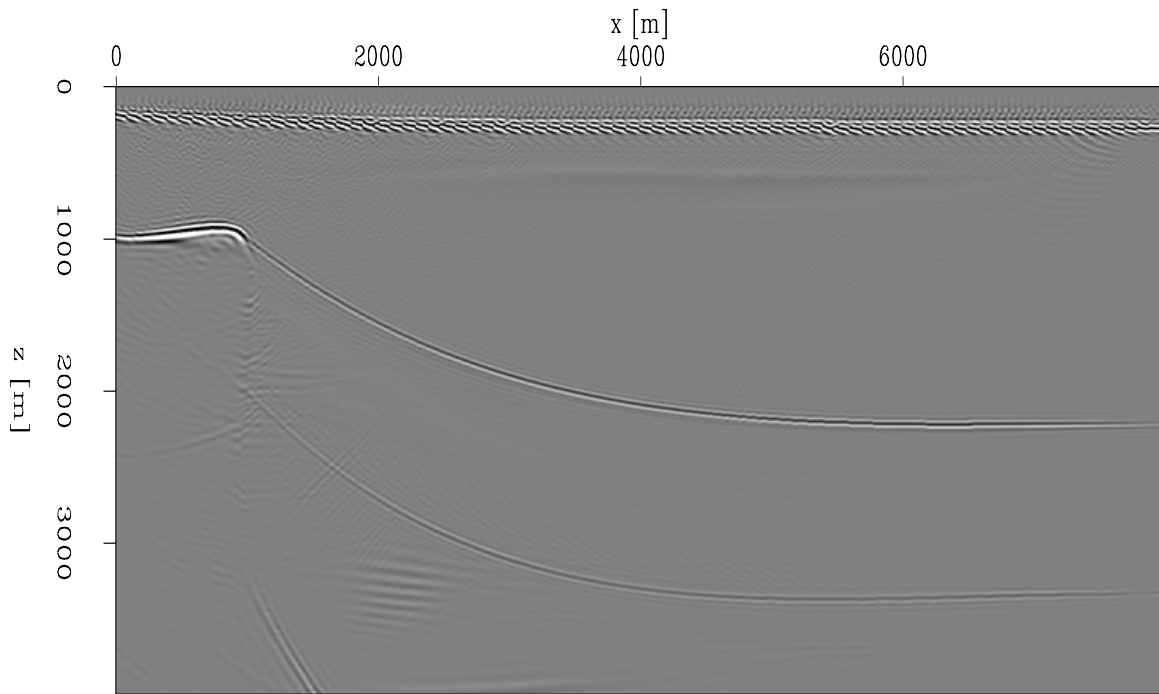


(a)

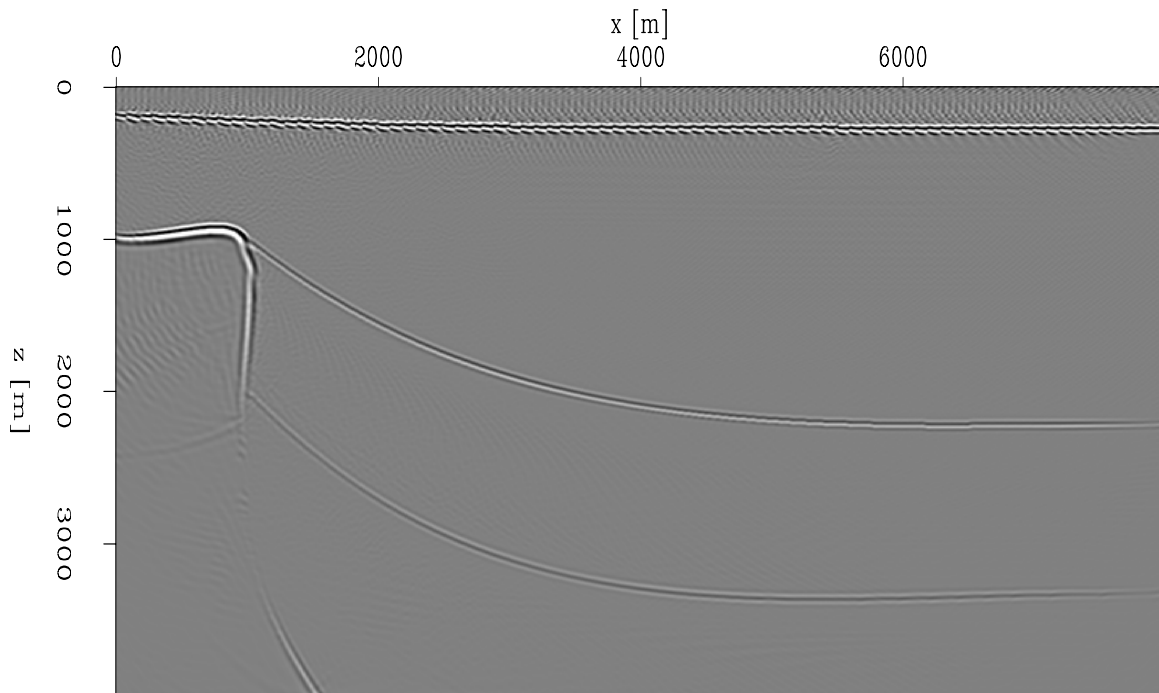


(b)

Figure 4: Isotropic plane-wave migration results: (a) in Cartesian coordinates; (b) in tilted coordinates. `guojian1-iso` [CR]

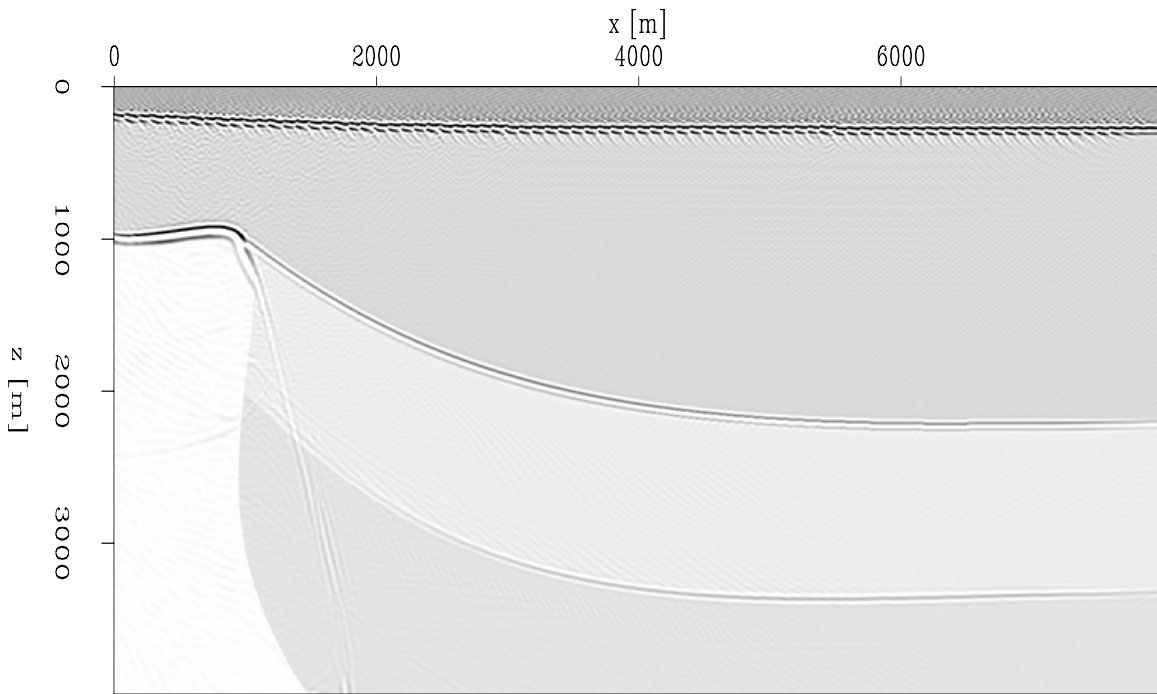


(a)

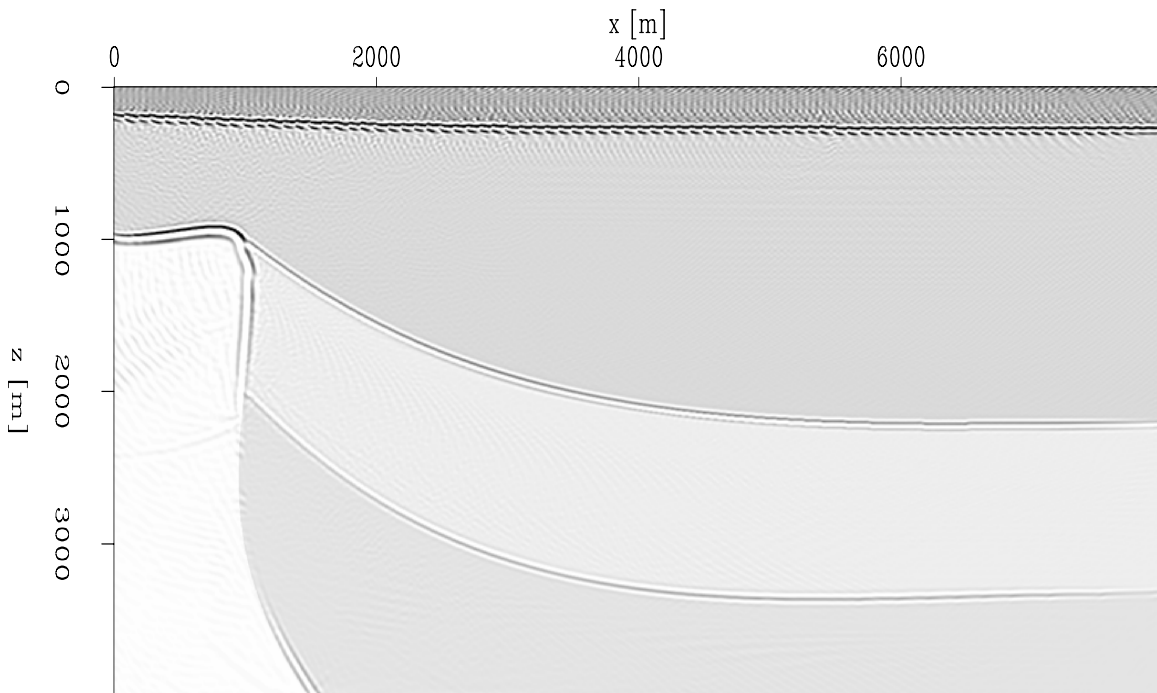


(b)

Figure 5: Anisotropic plane-wave migration results: (a) in Cartesian coordinates; (b) in tilted coordinates. `guojian1-ani` [CR]



(a)



(b)

Figure 6: Migration results overlaid with density model: (a) isotropic migration; (b) anisotropic migration. `guojian1-isoanidn` [CR]

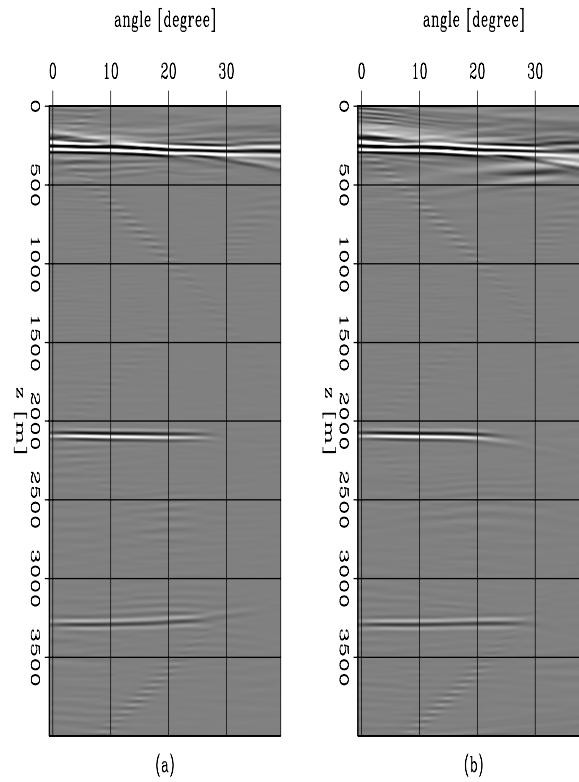


Figure 7: Horizontal angle-domain CIGs at $x = 4000\text{m}$: (a) isotropic migration; (b) anisotropic migration. `guojian1-ang4000` [CR]

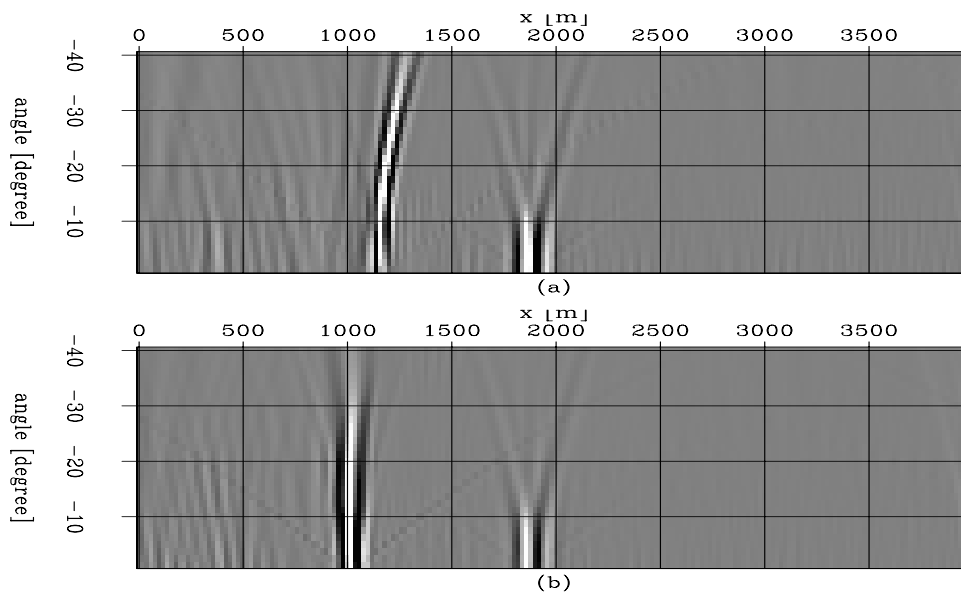


Figure 8: Vertical angle-domain CIGs at $z = 1500\text{m}$: (a) isotropic migration; (b) anisotropic migration. `guojian1-ang1500` [CR]

CONCLUSION

We image steeply dipping reflectors in VTI media by anisotropic plane-wave migration in tilted coordinates. We decompose source and receiver wavefields into plane waves and extrapolate the wavefields with an implicit isotropic operator followed by an explicit anisotropic correction in tilted coordinates. We apply our method to a synthetic dataset. The results show that our method can handle overturned waves and accurately image steeply dipping reflectors in VTI media. We generate angle-domain CIGs by cross-correlation.

ACKNOWLEDGMENTS

We would like to thank ExxonMobil for making the synthetic data available.

REFERENCES

- Albertin, U., Yingst, D., and Jaramillo, H., 2001, Comparing common-offset Maslov, Gaussian beam, and coherent state migrations *in* 71st Ann. Internat. Mtg. Soc. of Expl. Geophys., 913–916.
- Baumstein, A., and Anderson, J., 2003, Wavefield extrapolation in laterally varying VTI media *in* 73rd Ann. Internat. Mtg. Soc. of Expl. Geophys., 945–948.
- Baysal, E., Kosloff, D. D., and Sherwood, J. W. C., 1983, Reverse time migration: Geophysics, **48**, 1514–1524.
- Biondi, B., and Shan, G., 2002, Prestack imaging of overturned reflections by reverse time migration *in* 72nd Ann. Internat. Mtg. Soc. of Expl. Geophys., 1284–1287.
- Brandsberg-Dahl, S., and Etgen, J., 2003, Beam-wave imaging *in* Expanded Abstracts. Soc. of Expl. Geophys., 977–980.
- Duquet, B., Lailly, P., and Ehinger, A., 2001, 3-D plane wave migration of streamer data *in* 71st Ann. Internat. Mtg. Soc. of Expl. Geophys., 1033–1036.
- Etgen, J., 2002, Waves, beams and dimensions: an illuminating if incoherent view of the future of migration: 72nd Ann. Internat. Mtg. Soc. of Expl. Geophys., invited presentation.
- Ferguson, R. J., and Margrave, G. F., 1998, Depth migration in TI media by nonstationary phase shift *in* 68th Ann. Internat. Mtg. Soc. of Expl. Geophys., 1831–1834.
- Gray, S., Nottfors, C., and Bleistein, N., 2002, Imaging using multi-arrivals: Gaussian beams or multi-arrival Kirchhoff? *in* 72nd Ann. Internat. Mtg. Soc. of Expl. Geophys., 1117–1120.

- Higginbotham, J. H., Shin, Y., and Sukup, D. V., 1985, Directional depth migration (short note): *Geophysics*, **50**, 1784–1796.
- Hill, N. R., 2001, Prestack Gaussian-beam depth migration: *Geophysics*, **66**, 1240–1250.
- Huang, L. Y., and Wu, R. S., 1996, Prestack depth migration with acoustic screen propagators *in* 66th Ann. Internat. Mtg. Soc. of Expl. Geophys., 415–418.
- Liu, F., Stolt, R., Hanson, D., and Day, R., 2002, Plane wave source composition: An accurate phase encoding scheme for prestack migration *in* 72nd Ann. Internat. Mtg. Soc. of Expl. Geophys., 1156–1159.
- Rietveld, W. E. A., 1995, Controlled illumination of prestack seismic migration *in* Ph.D. thesis. Delft University of Technology.
- Ristow, D., and Ruhl, T., 1994, Fourier finite-difference migration: *Geophysics*, **59**, 1882–1893.
- , 1997, Migration in transversely isotropic media using implicit operators *in* 67th Ann. Internat. Mtg. Soc. of Expl. Geophys., 1699–1702.
- Rousseau, J. H. L., 1997, Depth migration in heterogeneous, transversely isotropic media with the phase-shift-plus-interpolation method *in* 67th Ann. Internat. Mtg. Soc. of Expl. Geophys., 1703–1706.
- Sava, P., and Fomel, S., 2004, Wavefield extrapolation in Riemannian coordinates *in* Expanded Abstracts. Soc. of Expl. Geophys.
- Shan, G., and Biondi, B., 2004a, Imaging overturned waves by plane-wave migration in tilted coordinates: 74th Ann. Internat. Mtg., Soc. of Expl. Geophys., Expanded Abstracts, 969–972.
- , 2004b, Wavefield extrapolation in laterally-varying tilted TI media: SEP- **117**, 1–10.
- Stoffa, P. L., Fokkema, J. T., de Luna Freire, R. M., and Kessinger, W. P., 1990, Split-step Fourier migration: *Geophysics*, **55**, 410–421.
- Thomsen, L., 1986, Weak elastic anisotropy: *Geophysics*, **51**, 1954–1966.
- Tsvankin, I., 1996, P-wave signatures and notation for transversely isotropic media: An overview: *Geophysics*, **61**, 467–483.
- Uzcategui, O., 1995, 2-D depth migration in transversely isotropic media using explicit operators: *Geophysics*, **60**, 1819–1829.
- Whitmore, N. D., 1983, Iterative depth migration by backward time propagation *in* 53rd Ann. Internat. Mtg. Soc. of Expl. Geophys., Session:S10.1.
- Zhang, J., Verschuur, D. J., and Wapenaar, C. P. A., 2001a, Depth migration of shot records in heterogeneous, transversely isotropic media using optimum explicit operators: *Geophys. Prosp.*, **49**, 287–299.

Zhang, J., Wapenaar, C., and Verschuur, D., 2001b, 3-D depth migration in VTI media with explicit extrapolation operators *in* 71st Ann. Internat. Mtg. Soc. of Expl. Geophys., 1085–1088.

Zhang, Y., Sun, J., Notfors, C., and Gray, S., 2003, Delayed-shot 3-D prestack depth migration *in* Expanded Abstracts. Soc. of Expl. Geophys., 1027–1030.



Angle-domain common image gathers for anisotropic migration

*Biondo Biondi*¹

ABSTRACT

I present a general methodology for computing and analyzing Angle Domain Common Image Gathers (ADCIGs) in conjunction with anisotropic wavefield-continuation migration. I demonstrate that the aperture angles estimated by transforming prestack images using slant stacks along the subsurface-offset axis are a good approximation of the phase aperture angles, and that they are exactly equal to the phase aperture angles for flat events in VTI media.

I introduce a generalization of the concept of migration impulse response for the computation of prestack images function of the subsurface offset that enables a straightforward analytical analysis of the reflector movements caused by perturbations in anisotropic parameters. This analysis shows that the Residual Moveout (RMO) in migrated ADCIGs is function of both the phase aperture angle and the group aperture angle. The dependency of the RMO function on the group angles adds some complexity to the RMO analysis because the computation of group angles from phase angles, which are measured from the ADCIGs, depends on the local background anisotropic velocity at the reflector point. Several numerical examples demonstrate the accuracy of the RMO function predicted by my kinematic analysis, and in contrast, that the approximation of the group angles by the phase angles may lead to substantial errors for events reflected at wide aperture angles.

INTRODUCTION

Angle Domain Common Image Gathers (ADCIGs) are a useful tool for updating migration velocity after wavefield-continuation migration (Biondi and Sava, 1999; Clapp and Biondi, 2000). When the migration velocity is not accurate, the inconsistency of the migrated events along the aperture-angle axis is proportional to the migration velocity errors and provides the quantitative information necessary to update the velocity function.

All the methods for computing ADCIGs currently available in the literature are limited to isotropic migration; this is true for both the methods applied during downward continuation before imaging (Prucha et al., 1999), and the methods applied on the prestack migrated image as a post-processing operator (Sava and Fomel, 2003; Rickett and Sava, 2002; Biondi and Tisserant, 2004). Similarly, the quantitative analysis of the residual moveout measured in ADCIGs caused by migration-velocity errors is also limited to the isotropic case (Biondi and Symes, 2003; Biondi and Tisserant, 2004).

¹**email:** not available

In this paper I generalize the methodologies for computing and analyzing ADCIGs to prestack images obtained by wavefield-continuation anisotropic migration. This work is practically motivated by two current trends in the seismic exploration industry: 1) data are recorded with increasingly long offsets, improving the resolution and reliability of the estimation of anisotropic parameters from surface data, 2) anisotropic prestack depth migration is increasingly being used in areas, like near or under salt bodies, where the image quality, and consequently the velocity estimation process, could benefit from the use of wavefield-continuation migration (Bear et al., 2003; Sarkar and Tsvankin, 2004a). In this perspective, other papers in this report present complementary work that is aimed at developing methods for cost-efficient anisotropic 3-D prestack migration (Sen and Biondi, 2005), and overturned-events anisotropic 3-D prestack migration (Shan and Biondi, 2005b,a).

Sarkar and Tsvankin (2003, 2004b) analyze the effect of velocity errors on offset-domain CIGs produced by Kirchhoff migration. They demonstrate the effectiveness of their method by successfully applying it to a West Africa data set (Sarkar and Tsvankin, 2004a). In this paper, I provide the basic analytical tools necessary to perform anisotropic migration velocity analysis for data sets that benefit from imaging with wavefield-continuation migration instead of Kirchhoff migration.

The main conceptual differences between isotropic ADCIGs and anisotropic ADCIGs are related to the fact that in anisotropic wave-propagation the phase angles and velocities are different from the group angles and velocities (Tsvankin, 2001). Therefore, the first question that I will address is: which aperture angles are we measuring in the ADCIGs? I demonstrate that the transformation to angle domain maps the reflection into the phase-angle domain. Strictly speaking this mapping is exact only for events normal to the isotropic axis of symmetry (e.g. flat events for Vertical Transverse Isotropic (VTI) media), because the presence of dips skews the estimates in ways similar to when geological-dips bias the estimation of aperture angles while computing ADCIGs for converted events (Rosales and Rickett, 2001; Rosales and Biondi, 2005). Fortunately, in the anisotropic case, the biases caused by geological dips are less likely to create problems in practical applications than in the converted waves case. The simple numerical examples shown in this paper seem to indicate that, for realistic values of anisotropy, the errors caused by the geological dips is small and can be neglected. This approximation greatly simplifies the computation of ADCIGs and thus makes their application more attractive.

The second question I address is: is the residual moveout caused by velocity errors only function of the phase angles, or does it also depend on the group angles? In the second part of this paper I demonstrate that the residual moveout is function of both the angles and that neglecting its dependency on the group angles leads to substantial inaccuracy in the predicted RMO function.

PHASE AND GROUP ANGLES AND VELOCITIES

In anisotropic media the group angles and velocities do not coincide with the phase angles and velocities. The transformation from phase velocity \tilde{V} to group velocity V is conventionally

defined as the following (Tsvankin, 2001):

$$V = \sqrt{\tilde{V}^2 + \left(\frac{d\tilde{V}}{d\tilde{\theta}}\right)^2}, \quad (1)$$

where $\tilde{\theta}$ is the phase propagation angle. The associated transformation from phase angles to group angles θ is defined as:

$$\tan\theta = \frac{\tan\tilde{\theta} + \frac{1}{V} \frac{d\tilde{V}}{d\tilde{\theta}}}{1 - \frac{1}{V} \frac{d\tilde{V}}{d\tilde{\theta}} \tan\tilde{\theta}}. \quad (2)$$

Notice that throughout this paper I use the tilde symbol to distinguish between phase quantities (with a tilde) and group quantities (without a tilde).

Dellinger and Muir (1985) propose, and heuristically motivate, the following symmetric relations for the inverse transforms:

$$\tilde{S} = \sqrt{S^2 + \left(\frac{dS}{d\theta}\right)^2}, \quad (3)$$

where \tilde{S} and S are respectively the phase slowness and the group slowness, and

$$\tan\tilde{\theta} = \frac{\tan\theta + \frac{1}{S} \frac{dS}{d\theta}}{1 - \frac{1}{S} \frac{dS}{d\theta} \tan\theta}. \quad (4)$$

I use the heuristic relation in equation 4 to derive some of the analytical results presented in this paper. Furthermore, I use all the above relationships to compute the kinematic numerical results presented in this paper.

The numerical results, though not the analytical results, are also dependent on the choice of a specific approximation of the anisotropic phase-velocity function. I used the following VTI approximation for the phase velocity:

$$\tilde{V}_{\text{VTI}}^2(\theta) = \frac{V_V^2 \cos^2\theta + V_H^2 \sin^2\theta + \sqrt{(V_V^2 \cos^2\theta + V_H^2 \sin^2\theta)^4 + V_V^2 (V_N^2 - V_H^2) \sin^2 2\theta}}{2}, \quad (5)$$

where V_V , V_H , V_N , are respectively the vertical velocity, the horizontal velocity and the NMO velocity. Following Fowler (2003), the corresponding approximation for the group velocity is the following:

$$S_{\text{VTI}}^2(\theta) = \frac{S_V^2 \cos^2\theta + S_H^2 \sin^2\theta + \sqrt{(S_V^2 \cos^2\theta + S_H^2 \sin^2\theta)^4 + S_V^2 (S_N^2 - S_H^2) \sin^2 2\theta}}{2}, \quad (6)$$

where S_V , S_H , S_N , are respectively the vertical slowness, the horizontal slowness and the NMO slowness.

The numerical results obtained by modeling and migrating synthetic seismic data were obtained by source-receiver depth continuation (upward for modeling and downward for migration) using the following dispersion relation:

$$k_z = \frac{\omega}{V_V} \sqrt{\frac{\omega^2 - V_H^2 k_x^2}{\omega^2 + (V_N^2 - V_H^2) k_x^2}}, \quad (7)$$

where ω is the temporal frequency, and k_x and k_z are respectively the horizontal and vertical wavenumbers. The dispersion relation shown in equation 7 corresponds to the velocity and slowness functions in equations 5 and 6 (Fowler, 2003).

Anisotropic parameters used for numerical tests

To verify the accuracy of the results under realistic but different anisotropic conditions, in the numerical examples I used three set of anisotropic Thomsen parameters representing three different rocks described by Tsvankin (2001):

- Taylor Sand : $\epsilon = 0.110$ $\delta = -0.035$, $\rightarrow \eta = .155$,
- Mesa Clay Shale : $\epsilon = 0.189$, $\delta = 0.204 \rightarrow \eta = -.010$,
- GreenLight River Shale : $\epsilon = 0.0975$, $\delta = -0.11$, $\rightarrow \eta = .266$.

Notice that the GreenLight River Shale is derived from the Green River Shale described by Tsvankin (2001) by halving the anisotropic parameters (ϵ and δ), because the strong unelliptical nature of the original one ($\eta = .74$) caused the group-slowness approximation in equation 6 to break down, and made the kinematic computations based on ray tracing, and thus on group velocity and angles, inconsistent with wavefield migrations based on the dispersion relation in equation 7. Notice that the GreenLight River Shale is still the most unelliptical among the set of rocks I am using.

ANGLE GATHERS BY ANISOTROPIC DOWNWARD-CONTINUATION MIGRATION

In anisotropic media, when the reflector is dipping with respect to the normal to the isotropic axis of symmetry (horizontal direction for VTI) the incident and reflected aperture angle differ. This difference is caused by the fact that, although the phase slowness is function of the propagation angle, Snell law requires that the components parallel to the reflector of the incident and reflected slowness vectors must match at the interface. However, we can still define an “average” aperture angle $\tilde{\gamma}$ and “average” dip angle $\tilde{\alpha}_x$ using the following relationships:

$$\tilde{\gamma} = \frac{\tilde{\beta}_r - \tilde{\beta}_s}{2}, \quad \text{and} \quad \tilde{\alpha}_x = \frac{\tilde{\beta}_s + \tilde{\beta}_r}{2}, \quad (8)$$

where the $\tilde{\beta}_s$ and $\tilde{\beta}_r$ are the phase angles of the downgoing and upgoing plane waves, respectively.

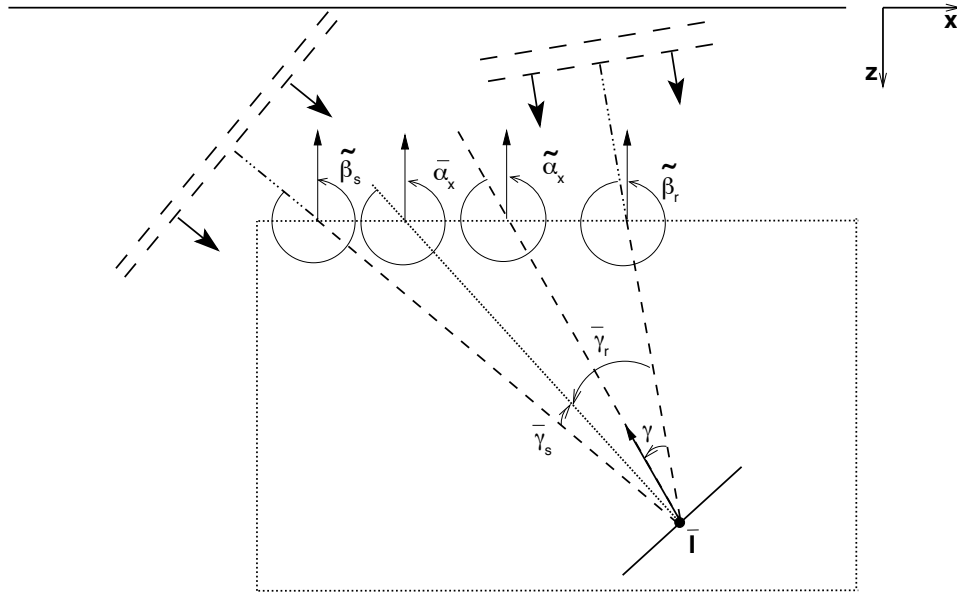


Figure 1: Sketch representing the reflection of a plane wave in an anisotropic medium.
biondo1-cig-aniso-v2 [NR]

Figure 1 shows the geometric interpretation of these angles. Notice that the average dip angle $\tilde{\alpha}_x$ is different from the true geological dip angle $\bar{\alpha}_x$, and that the average aperture angle $\tilde{\gamma}$ is obviously different from the true aperture angles $\tilde{\gamma}_s$ and $\tilde{\gamma}_r$. However, the five angles are related and, if needed, the true angles can be derived from the average angles (Rosales and Biondi, 2005).

The transformation to the angle domain transforms the prestack image from the migrated subsurface offset domain h_ξ , to the angle domain by a slant stack transform. The transformation axis is thus the physical dip of the image along the subsurface offset; that is, $\partial z_\xi / \partial h_\xi$. The dip angles can be similarly related to the midpoint dips in the image; that is, $\partial z_\xi / \partial m_\xi$. Following the derivation of acoustic isotropic ADCIGs by Sava and Fomel (2003) and of converted-waves ADCIGs by Rosales and Rickett (2001), we can write the following relationships between the propagation angles and the derivative measured from the wavefield:

$$\left. \frac{\partial t}{\partial z_\xi} \right|_{(m_\xi = \bar{m}_\xi, h_\xi = \bar{h}_\xi)} = \tilde{S}_s \cos(\tilde{\alpha}_x - \tilde{\gamma}) - \tilde{S}_r \cos(\tilde{\alpha}_x + \tilde{\gamma}), \quad (9)$$

$$\left. \frac{\partial t}{\partial m_\xi} \right|_{(z_\xi = \bar{z}_\xi, h_\xi = \bar{h}_\xi)} = \tilde{S}_s \sin(\tilde{\alpha}_x - \tilde{\gamma}) + \tilde{S}_r \sin(\tilde{\alpha}_x + \tilde{\gamma}), \quad (10)$$

$$\left. \frac{\partial t}{\partial h_\xi} \right|_{(z_\xi = \bar{z}_\xi, m_\xi = \bar{m}_\xi)} = \tilde{S}_s \sin(\tilde{\alpha}_x - \tilde{\gamma}) - \tilde{S}_r \sin(\tilde{\alpha}_x + \tilde{\gamma}), \quad (11)$$

where \tilde{S}_s and \tilde{S}_r are the phase slownesses for the source and receiver wavefields, respectively. We obtain the expression for the offset dip by taking the ratio of equation 11 with equation 9, and similarly for the midpoint dips by taking the ratio of equation 10 with equation 9, and

after some algebraic manipulations, we obtain the following expressions:

$$\left. \frac{\partial z_\xi}{\partial h_\xi} \right|_{(m_\xi = \bar{m}_\xi)} = \frac{\tan \tilde{\gamma} + \frac{\tilde{S}_r - \tilde{S}_s}{\tilde{S}_r + \tilde{S}_s} \tan \tilde{\alpha}_x}{1 - \frac{\tilde{S}_r - \tilde{S}_s}{\tilde{S}_r + \tilde{S}_s} \tan \tilde{\alpha}_x \tan \tilde{\gamma}}, \quad (12)$$

$$\left. \frac{\partial z_\xi}{\partial m_\xi} \right|_{(h_\xi = \bar{h}_\xi)} = \frac{\tan \tilde{\alpha}_x + \frac{\tilde{S}_r - \tilde{S}_s}{\tilde{S}_r + \tilde{S}_s} \tan \tilde{\gamma}}{1 - \frac{\tilde{S}_r - \tilde{S}_s}{\tilde{S}_r + \tilde{S}_s} \tan \tilde{\gamma} \tan \tilde{\alpha}_x}. \quad (13)$$

In contrast with the equivalent relationships valid for isotropic media, these relationships depend on both the aperture angle $\tilde{\gamma}$ and the dip angle $\tilde{\alpha}_x$. The expression for the offset dip (equation 9) simplifies into the known relationship valid in isotropic media when either the difference between the phase slownesses is zero, or the dip angle $\tilde{\alpha}_x$ is zero. In VTI media this happens for flat geological dips. In a general TI medium this condition is fulfilled when the geological dip is normal to the axis of symmetry.

Solving for $\tan \tilde{\gamma}$ and $\tan \tilde{\alpha}_x$ we obtain the following:

$$\tan \tilde{\gamma} = \frac{\frac{\partial z_\xi}{\partial h_\xi} - \Delta_{\tilde{\gamma}} \tan \tilde{\alpha}_x}{1 + \frac{\partial z_\xi}{\partial h_\xi} \Delta_{\tilde{\gamma}} \tan \tilde{\alpha}_x}, \quad (14)$$

$$\tan \tilde{\alpha}_x = \frac{\frac{\partial z_\xi}{\partial m_\xi} - \Delta_{\tilde{\gamma}} \tan \tilde{\gamma}}{1 + \frac{\partial z_\xi}{\partial m_\xi} \Delta_{\tilde{\gamma}} \tan \tilde{\gamma}}, \quad (15)$$

where for convenience I substituted the symbol $\Delta_{\tilde{\gamma}}$ for the “normalized slowness difference” $(\tilde{S}_r - \tilde{S}_s)/(\tilde{S}_r + \tilde{S}_s)$.

Substituting equation 15 in equation 14, and equation 14 into equation 15, we get the following two quadratic expressions that can be solved to estimate the angles as a function of the dips measured from the image:

$$\left[\frac{\partial z_\xi}{\partial m_\xi} \Delta_{\tilde{\gamma}} - \frac{\partial z_\xi}{\partial h_\xi} \Delta_{\tilde{\gamma}}^2 \right] \tan^2 \tilde{\gamma} + [1 - \Delta_{\tilde{\gamma}}^2] \tan \tilde{\gamma} + \frac{\partial z_\xi}{\partial m_\xi} \Delta_{\tilde{\gamma}} - \frac{\partial z_\xi}{\partial h_\xi} = 0 \quad (16)$$

$$\left[\frac{\partial z_\xi}{\partial h_\xi} \Delta_{\tilde{\gamma}} - \frac{\partial z_\xi}{\partial m_\xi} \Delta_{\tilde{\gamma}}^2 \right] \tan^2 \tilde{\alpha}_x + [1 - \Delta_{\tilde{\gamma}}^2] \tan \tilde{\alpha}_x + \frac{\partial z_\xi}{\partial h_\xi} \Delta_{\tilde{\gamma}} - \frac{\partial z_\xi}{\partial m_\xi} = 0 \quad (17)$$

These are two independent quadratic equations in $\tan \tilde{\gamma}$ and $\tan \tilde{\alpha}_x$ that can be solved independently. If the “normalized slowness difference” $\Delta_{\tilde{\gamma}}$ between the slowness along the propagation directions of the source and receiver wavefields are known, we can directly compute $\tilde{\gamma}$ and $\tilde{\alpha}_x$, and then the true $\tilde{\beta}_s$ and $\tilde{\beta}_r$. One important case in this category is when we image converted waves.

For anisotropic velocities, the slownesses depend on the propagation angles, and thus the normalized difference depends on the unknown $\tilde{\gamma}$ and $\tilde{\alpha}_x$. In practice, these equations can be solved by a simple iterative process that starts by assuming the “normalized difference” to be equal to zero. In all numerical test I conducted this iterative process converges to the correct solution in only a few iterations, and thus is not computationally demanding.

The dependency of equations 16 and 17 from the slowness function is also an impediment to the use of efficient Fourier-domain methods to perform the transformation to angle domain, because the slowness function cannot be assumed to be constant. Fortunately, the numerical examples shown below indicate that for practical values of the anisotropy parameters the dependency of the estimate from the dip angles can be safely ignored for small dips, and it is unlikely to constitute a problem for steep dips.

KINEMATIC ANALYSIS OF ADCIGS BY INTEGRAL MIGRATION

The analysis shown in the previous section provides the fundamental equations to relate the offset and midpoint dips measured from prestack images to the phase angles at the reflection point. However, the previous analysis is not directly applicable to the analysis of residual moveout in the ADCIGs caused by velocity errors because it is based on plane waves and not rays. We are interested in relating traveltimes errors accumulated during the propagation in the overburden to movements of the migrated events in the ADCIG; the traveltimes errors are naturally evaluated along rays, which are related to group velocity and angles. To overcome this difficulty, in this section I introduce an integral formulation of the methodology to compute angle gathers that enables a simple link between ADCIGs and kinematics.

My analysis is based on the conceptual generalization of integral (Kirchhoff) migration to the computation of sub-surface offset gathers. Integral migration is defined by the summation surfaces over which the data are integrated to compute the image at every point in the image space. The shapes of these summation surfaces are usually computed as the sum of the time delays from the image point (z_ξ, m_ξ) in the subsurface to the source and receiver locations at the surface. The basic idea underlying the generalization I introduce in this paper, is that we can compute the summation surfaces by evaluating the time delays starting not from the same point in the subsurface for both the source and receiver rays, but starting from two points horizontally shifted by $\pm h_\xi$ with respect to the image point. The summation of data along these surfaces produces a prestack image as a function of the subsurface offset that is kinematically equivalent to the image created by wavefield-continuation migrations such as source-receiver downward continuation, or shot-profile migration in conjunction to the generalized imaging condition discussed by Rickett and Sava (2002). Therefore, the kinematic analysis that follows, and its conclusions, are independent from the migration method applied to compute the prestack images. An interesting observation is that the ADCIGs computed using this generalization of integral migration should be immune from the artifacts that affect angle gathers computed by conventional integral migration and discussed by Stolk and Symes (2003).

Generalized migration impulse response in parametric form

Integral migration can be conceptually performed by spreading the data along spreading surfaces as well as by summing data along the summation surfaces discussed above. The spreading surfaces are duals of the summation surfaces and represent the impulse response of the migration operator. In homogeneous anisotropic medium the shape of the impulse responses

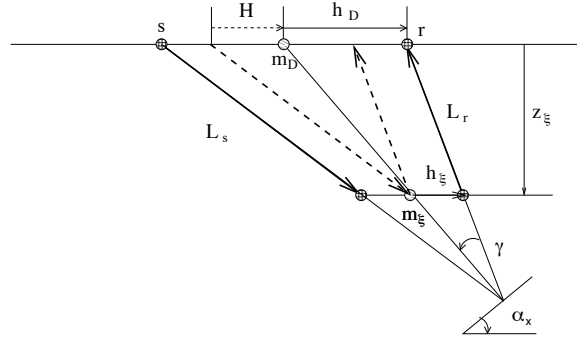


Figure 2: Geometry used for evaluating the impulse response of the generalized integral migration.

`biondo1-imp-resp` [NR]

of the generalized integral migration can be easily evaluated analytically as a function of the subsurface offset h_ξ , in addition to the usual image depth z_ξ and midpoint m_ξ . Figure 2 illustrates the geometry used to evaluate this impulse response. Notice that the angles in this figure (α_x and γ) are missing a tilde because they are group angles, and not phase angles as in the previous section. In an isotropic medium these angles are the dip and aperture angles, but in an anisotropic medium these angles are not easily related to the geological dip and the reflection aperture angles. They can be thought of as convenient parameters to evaluate the impulse response.

Simple trigonometry applied to Figure 2 allows us to express the impulse response in parametric form, as a function of α_x and γ . If we migrate an impulse recorded at time t_D , midpoint m_D and surface offset h_D , the migration impulse response can be expressed as follows:

$$z_\xi = L(\alpha_x, \gamma) \frac{\cos^2 \alpha_x - \sin^2 \gamma}{\cos \alpha_x \cos \gamma}, \quad (18)$$

$$m_\xi = m_D - L(\alpha_x, \gamma) \frac{\sin \alpha_x}{\cos \gamma}, \quad (19)$$

$$h_\xi = h_D - H = h_D - L(\alpha_x, \gamma) \frac{\sin \gamma}{\cos \alpha_x}, \quad (20)$$

with

$$L(\alpha_x, \gamma) = \frac{L_s + L_r}{2}. \quad (21)$$

In a isotropic medium the half path-length L would be simply given by $t_D/2S$, but in an anisotropic medium it is function of the angles. Its two components L_s and L_r can be calculated by solving the following system of linear equations:

$$t_D = S_s L_s + S_r L_r, \quad (22)$$

$$z_s - z_r = L_s \cos(\alpha_x - \gamma) - L_r \cos(\alpha_x + \gamma) = 0. \quad (23)$$

Equation 22 constraints the total travelttime to be equal to the impulse time, and equations 23 constraints the depth of the end point of the two rays (z_s and z_r) to be equal, since the subsurface offset is assumed to be horizontal. The solution of this system of equation yields the following for the half path-length:

$$L(\alpha_x, \gamma) = \frac{L_s + L_r}{2} = \frac{t_D}{(S_r + S_s) + (S_r - S_s) \tan \alpha_x \tan \gamma}. \quad (24)$$

The combination of equation 24 and equations 18–20 enables the evaluation of the generalized migration impulse response in a arbitrary homogeneous anisotropic medium.

Figure 3 shows a 3-D rendering of the impulse response computed using the previous equations for an impulse with $t_D = .9$ seconds, $m_D = 0$ kilometers, and $h_D = .4$ kilometers, and vertical slowness $S_V = 1$ s/km; the anisotropy parameters correspond to the Taylor Sand as listed in the table on page 80. The gray line (green in color) superimposed onto the impulse response is the result of cutting the surface at zero subsurface offset, and thus corresponds to the conventional impulse response of prestack migration. The black line superimposed onto the impulse response is the result of cutting the surface at zero midpoint. In Figure 4 these two lines are superimposed onto the corresponding vertical sections cut from the images computed by an anisotropic wavefield source-receiver migration applied with the same parameters described above. Figure 4b shows the conventional migration impulse response, whereas Figure 4a shows the zero-midpoint section. The lines computed by applying the kinematic equations perfectly match the impulse responses computed using wavefield migration, confirming the accuracy of the kinematic equations.

Analytical evaluation of the tangent plane to the impulse response

The expression for the generalized impulse response of prestack anisotropic migration leads to the analytical evaluation of the offset dip and midpoint dip along the planes tangent to the impulse response, as a function of the group angles and velocity. In this section I demonstrate that in the simple case of flat reflectors this analysis leads to exactly the same results as the phase-space analysis presented in the previous section. The derivation of the general relationships expressed in equations 13 and 12, which are valid for an arbitrary reflector's dip, is left to the reader.

By applying elementary analytical geometry, I demonstrate in Appendix A that the derivative of the depth with respect to the subsurface offset, at constant midpoint, is given by:

$$\left. \frac{\partial z_\xi}{\partial h_\xi} \right|_{m_\xi = \bar{m}_\xi} = - \frac{\frac{\partial z_\xi}{\partial \alpha_x} \frac{\partial m_\xi}{\partial \gamma} - \frac{\partial z_\xi}{\partial \gamma} \frac{\partial m_\xi}{\partial \alpha_x}}{\frac{\partial m_\xi}{\partial \alpha_x} \frac{\partial h_\xi}{\partial \gamma} - \frac{\partial m_\xi}{\partial \gamma} \frac{\partial h_\xi}{\partial \alpha_x}}, \quad (25)$$

and the derivative of the depth with respect to the midpoint, at constant subsurface offset, is given by:

$$\left. \frac{\partial z_\xi}{\partial m_\xi} \right|_{h_\xi = \bar{h}_\xi} = - \frac{\frac{\partial z_\xi}{\partial \alpha_x} \frac{\partial h_\xi}{\partial \gamma} - \frac{\partial z_\xi}{\partial \gamma} \frac{\partial h_\xi}{\partial \alpha_x}}{\frac{\partial m_\xi}{\partial \alpha_x} \frac{\partial h_\xi}{\partial \gamma} - \frac{\partial m_\xi}{\partial \gamma} \frac{\partial h_\xi}{\partial \alpha_x}}. \quad (26)$$

In the special case of flat reflectors the $\partial z_\xi / \partial \alpha_x$ and $\partial h_\xi / \partial \gamma$ vanish, and thus equation 25

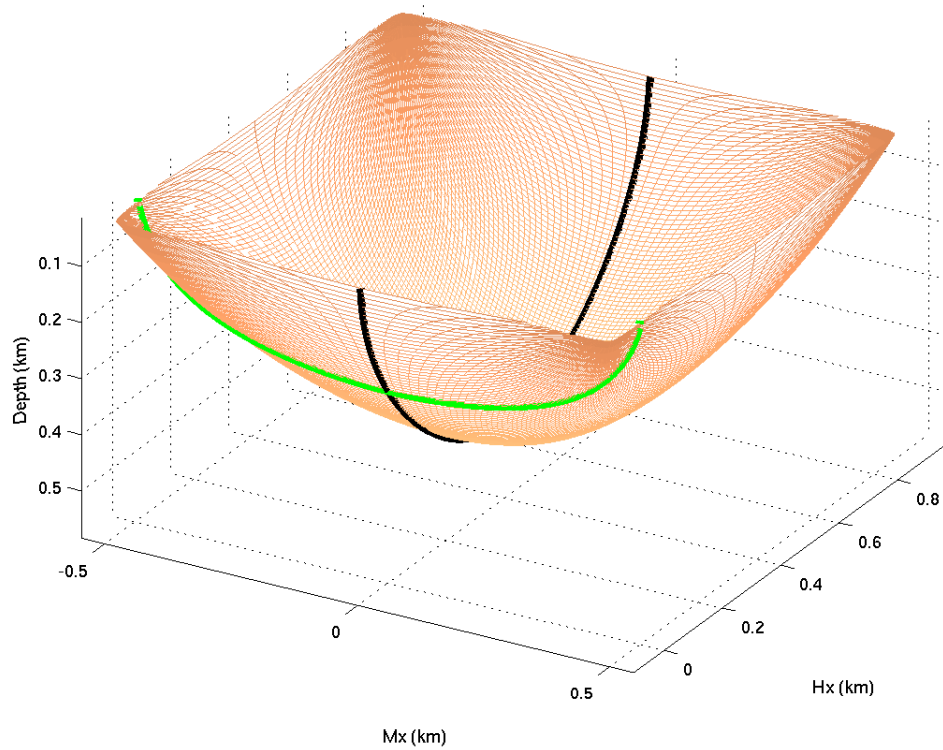
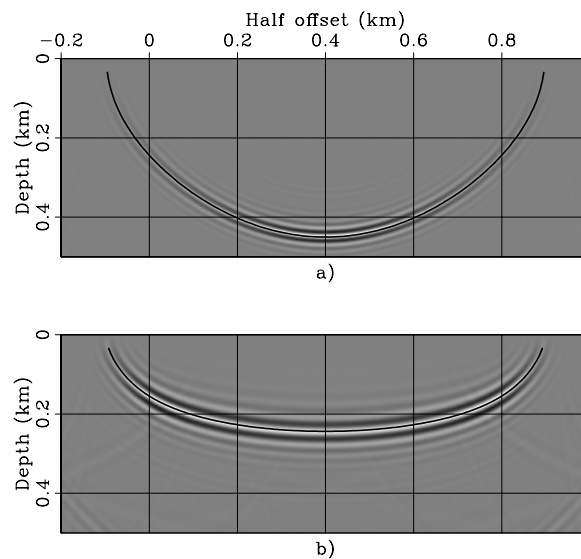


Figure 3: Impulse response of generalized anisotropic prestack migration. The gray line (green in color) superimposed onto the impulse response corresponds to the conventional impulse response of prestack migration. `biondo1-surf_taylor_hxd_dot_4` [CR]

Figure 4: Vertical sections cut from the impulse response computed by an anisotropic wavefield source-receiver migration. The lines superimposed onto the images correspond to the lines superimposed onto the surface shown in Figure 3 and are computed by applying the kinematic expressions presented in equations 18–24. `biondo1-Surf-taylor_hxd_4-overn` [CR]



simplifies into the following expression:

$$\begin{aligned} \left. \frac{\partial z_\xi}{\partial h_\xi} \right|_{(m_\xi=\bar{m}_\xi, \alpha_x=0)} &= \frac{\left(\left. \frac{\partial z_\xi}{\partial \gamma} \right|_{L=\bar{L}} + \frac{\partial L}{\partial \gamma} \cos \gamma \right) \frac{\partial m_\xi}{\partial \alpha_x}}{\left(\left. \frac{\partial h_\xi}{\partial \gamma} \right|_{L=\bar{L}} - \frac{\partial L}{\partial \gamma} \sin \gamma \right) \frac{\partial m_\xi}{\partial \alpha_x}} \\ &= \frac{\left. \frac{\partial z_\xi}{\partial \gamma} \right|_{L=\bar{L}} + \frac{\partial L}{\partial \gamma} \cos \gamma}{\left. \frac{\partial h_\xi}{\partial \gamma} \right|_{L=\bar{L}} - \frac{\partial L}{\partial \gamma} \sin \gamma}. \end{aligned} \quad (27)$$

$$(28)$$

By substituting into equation 27 the appropriate derivative of the image coordinates and of the half path-length with respect to the angles, all provided in Appendix A, I further simplify the expression into the following:

$$\left. \frac{\partial z_\xi}{\partial h_\xi} \right|_{(m_\xi=\bar{m}_\xi, \alpha_x=0)} = \frac{\tan \gamma + \frac{1}{S} \frac{\partial S}{\partial \gamma}}{1 - \frac{1}{S} \frac{\partial S}{\partial \gamma} \tan \gamma}. \quad (29)$$

Finally, by applying the transformation from group angles into phase angles expressed in equation 4, I obtain the final result that for flat reflectors the subsurface-offset dip is exactly equal to the tangent of the phase aperture angle $\tilde{\gamma}$; that is:

$$\left. \frac{\partial z_\xi}{\partial h_\xi} \right|_{(m_\xi=\bar{m}_\xi, \alpha_x=0)} = \tan \tilde{\gamma}. \quad (30)$$

Numerical examples of aperture angle along impulse responses

The analytical kinematic results can be verified by numerical computations of impulse responses by wavefield migration and transformation of the resulting prestack image cubes into the angle domain. Figure 5 shows four zero subsurface-offset sections cut through the impulse responses computed by wavefield-continuation anisotropic migration for the three anisotropic rocks described in the table on page 80 and for an isotropic rock. The parameters defining the impulse responses are the same as for Figure 3; that is, $t_D = .9$ seconds, $m_D = 0$ kilometers, and $h_D = .4$ kilometers, and vertical slowness $S_V = 1$ s/km. Figure 5a shows the isotropic case, Figure 5b shows the Taylor Sand case, Figure 5c shows the Mesa Clay Shale case, and Figure 5d shows the GreenLight River Shale case. As in Figure 4, the line superimposed onto the images represent the impulse response computed using the kinematic expressions in equations 18–24. The kinematic curves perfectly predicts the shape of the images even for very steep dips.

Figure 6 shows two-dimensional slices cut through the cube obtained by the transformation to the angle domain of the impulse responses shown in Figure 5. The slices are cut at the midpoint and depth corresponding to the expected location of the impulse responses; that is, at the location tracked by the lines shown in Figure 5. There are three lines superimposed onto the angle-domain images. The solid lines display the numerical computation of $\arctan(\partial z_\xi / \partial h_\xi)$ by applying equation 25. They perfectly track, as expected, the results of the transformation

of the prestack images to angle domain. The dotted lines display the phase aperture angle $\tilde{\gamma}$. As expected, they overlap with the solid line around the zero midpoint (i.e. flat reflector), and depart from them at larger midpoints, which correspond to steeper reflections. However, the error introduced by ignoring the difference between $\arctan(\partial z_\xi / \partial h_\xi)$ and $\tilde{\gamma}$ is small, and likely to be negligible in most practical situations. Finally, the dashed lines display the group aperture angle γ . The differences between γ and $\tilde{\gamma}$ are substantial, up to 20% in some cases. Ignoring them might be detrimental to the application of ADCIGs. Notice that in the isotropic case the three lines perfectly overlap and all of them match the image.

ANISOTROPIC RESIDUAL MOVEOUT FOR FLAT REFLECTORS

The kinematic formulation of the generalized impulse response presented in the previous section enables a simple analysis of the residual moveout (RMO) in ADCIGs caused by errors in anisotropic velocity parameters. For the sake of simplicity, at the present, I limit my analysis to reflections from flat interfaces. However, a generalization of the flat-events analysis to dipping events should be conceptually straightforward, though not necessarily simple from the analytical point of view.

A VTI velocity function, either group or phase, is described by the following vector of three velocities $\mathbf{V} = (V_V, V_H, V_N)$, as for example used in equations 5, or by the corresponding vector of three slownesses $\mathbf{S} = (S_V, S_H, S_N)$ used in equation 6. I define the perturbations as one multiplicative factors for each of the velocities and one multiplicative factor for all velocities; that is, the perturbed velocity ${}_\rho \mathbf{V}$ is defined as:

$${}_\rho \mathbf{V} = ({}_\rho V_V, {}_\rho V_H, {}_\rho V_N) = \rho_V (\rho_{V_V} V_V, \rho_{V_H} V_H, \rho_{V_N} V_N). \quad (31)$$

The velocity-parameter perturbations is thus defined by the following four-components vector $\rho = (\rho_V, \rho_{V_V}, \rho_{V_H}, \rho_{V_N})$.

For flat reflectors, the transformation to angle domain maps an image point at coordinates (z_ξ, h_ξ) into an image point with coordinates $(z_\gamma, \tilde{\gamma})$ according to the following mapping:

$$\tilde{\gamma} = \arctan \left. \frac{\partial z_\xi}{\partial h_\xi} \right|_{m_\xi = \bar{m}_\xi}, \quad (32)$$

$$z_\gamma = z_\xi - h_\xi \left. \frac{\partial z_\xi}{\partial h_\xi} \right|_{m_\xi = \bar{m}_\xi} = z_\xi - h_\xi \tan \tilde{\gamma}. \quad (33)$$

The partial derivative of the angle-domain depth z_γ with respect to the i -th component in the perturbation vector can be expressed as follows:

$$\begin{aligned} \frac{\partial z_\gamma}{\partial \rho_i} &= \frac{\partial z_\gamma}{\partial L} \frac{\partial L}{\partial \rho_i} + \frac{\partial z_\gamma}{\partial \gamma} \frac{\partial \gamma}{\partial \rho_i} + \frac{\partial z_\gamma}{\partial \tilde{\gamma}} \frac{\partial \tilde{\gamma}}{\partial \rho_i} \\ &= \frac{\partial z_\gamma}{\partial L} \frac{\partial L}{\partial S} \left(\frac{\partial S}{\partial \rho_i} + \frac{\partial S}{\partial \gamma} \frac{\partial \gamma}{\partial \rho_i} \right) + \frac{\partial z_\gamma}{\partial \gamma} \frac{\partial \gamma}{\partial \rho_i} + \frac{\partial z_\gamma}{\partial \tilde{\gamma}} \frac{\partial \tilde{\gamma}}{\partial \rho_i} \\ &= \frac{\partial z_\gamma}{\partial L} \frac{\partial L}{\partial S} \frac{\partial S}{\partial \rho_i} + \left(\frac{\partial z_\gamma}{\partial L} \frac{\partial L}{\partial S} \frac{\partial S}{\partial \gamma} + \frac{\partial z_\gamma}{\partial \gamma} \right) \frac{\partial \gamma}{\partial \rho_i} + \frac{\partial z_\gamma}{\partial \tilde{\gamma}} \frac{\partial \tilde{\gamma}}{\partial \rho_i}. \end{aligned} \quad (34)$$

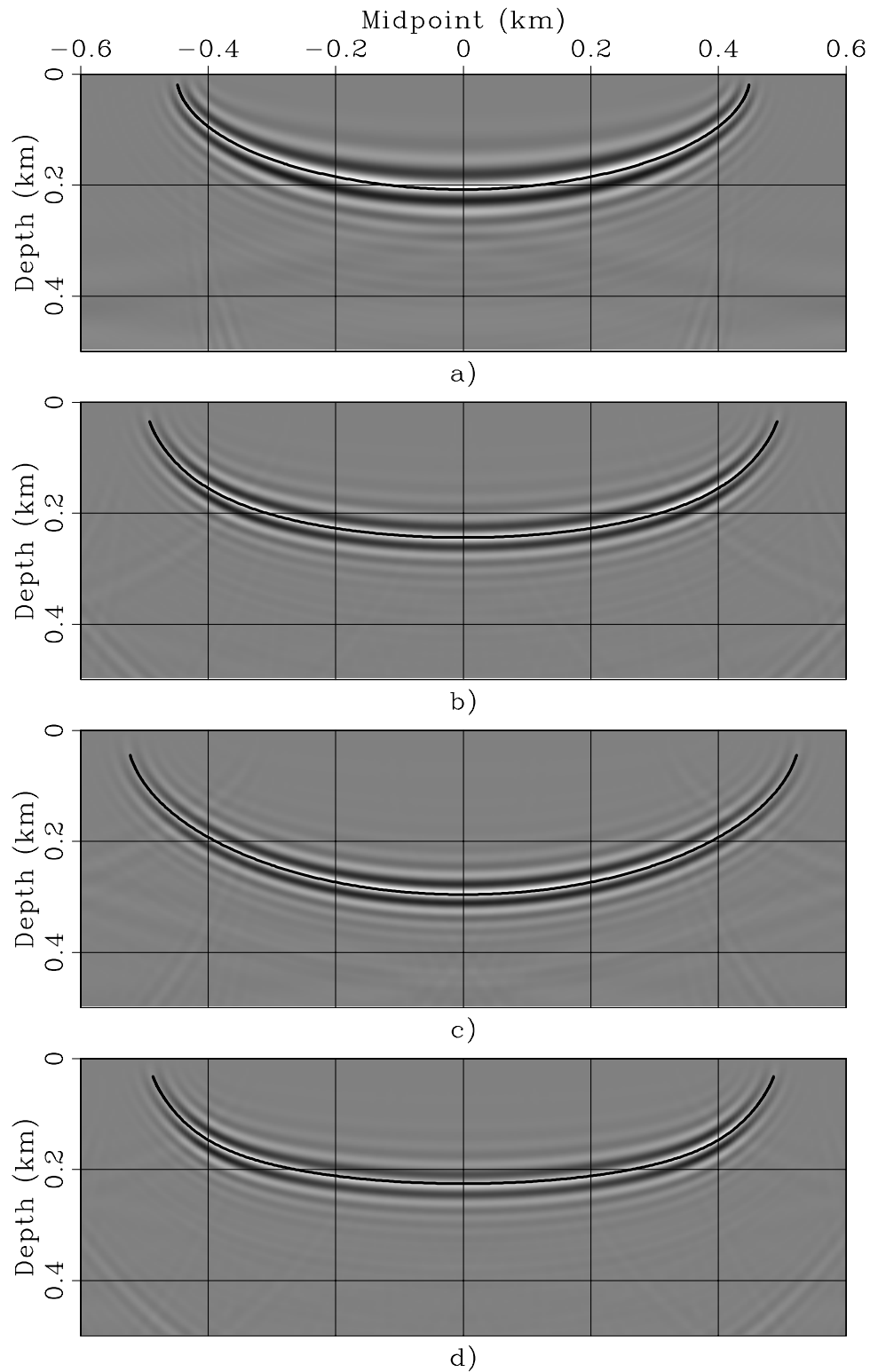


Figure 5: Impulse responses evaluated at zero subsurface offset for four rock types: a) Isotropic, b) Taylor Sand, c) Mesa Clay Shale, and d) GreenLight River Shale. Superimposed onto the images are the impulse responses computed by the kinematic expressions presented in equations 18–24. `biondo1-Quad_hxd_4-overn` [CR]

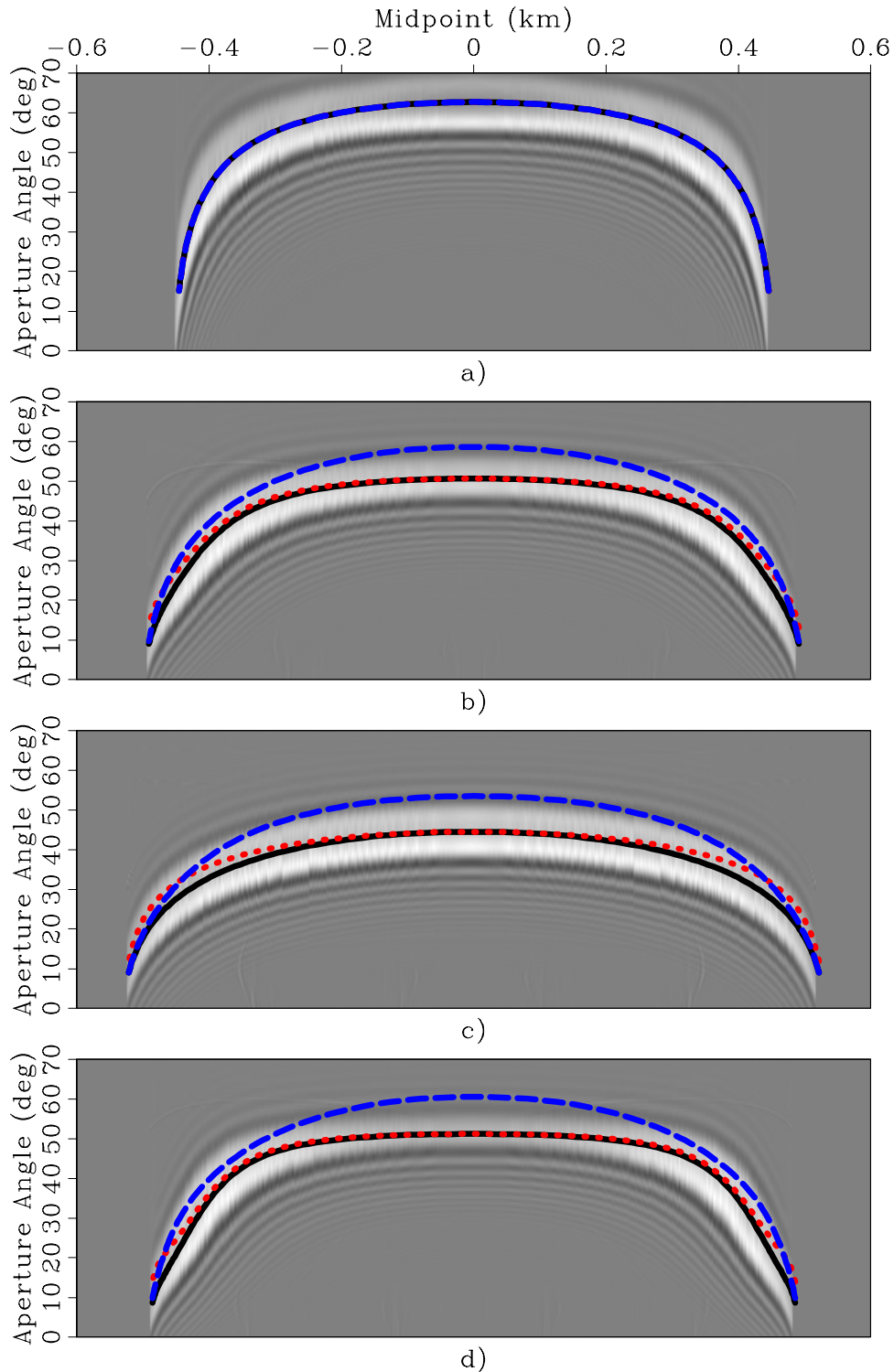


Figure 6: Slices of the impulse responses transformed into the angle-domain for four rock types: a) Isotropic, b) Taylor Sand, c) Mesa Clay Shale, and d) GreenLight River Shale. Superimposed onto the images there are the curves computed by applying the kinematic analysis: γ (dashed line), $\tilde{\gamma}$ (dotted line), and $\arctan(\partial z_{\xi}/\partial h_{\xi})$ (solid line).

`biondo1-Quad_Mx-Ang_hxd_4-overn` [CR]

In Appendix B I demonstrate that the terms multiplying the partial derivatives with respect to the angles are zero, and equation 34 simplifies into:

$$\frac{\partial z_\gamma}{\partial \rho_i} = \frac{\partial z_\gamma}{\partial L} \frac{\partial L}{\partial S} \frac{\partial S}{\partial \rho_i}, \quad (35)$$

where

$$\frac{\partial z_\gamma}{\partial L} = \frac{\partial z_\xi}{\partial L} - \frac{\partial h_\xi}{\partial L} \tan \tilde{\gamma} = \cos \gamma + \sin \gamma \tan \tilde{\gamma}, \quad (36)$$

and

$$\frac{\partial L}{\partial S(\gamma)} = -\frac{z_\xi}{S(\gamma) \cos \gamma}, \quad (37)$$

Uniform scaling of velocity

The derivative with respect to the perturbation component ρ_V has the following particularly simple form:

$$\frac{\partial z_\gamma}{\partial \rho_V} = z_\xi (1 + \tan \gamma \tan \tilde{\gamma}), \quad (38)$$

because the derivative of the slowness with respect to a uniform scaling of the velocity has the following simple form:

$$\frac{\partial S(\gamma)}{\partial \rho_V} = -S(\gamma), \quad (39)$$

that leads to the derivative $\partial L / \partial \rho_V$ to be independent from the “local” shape of the anisotropic slowness function. Intuitively, this simplification is related to the fact that the “shape” of the wavefronts is not affected by a uniform scaling of the velocity.

The residual moveout Δz_{RMO} is defined as the difference between the reflector movement at finite aperture angle $\tilde{\gamma}$ and the reflector movement at normal incidence. From equation 38 the partial derivative of Δz_{RMO} with respect to ρ_V is equal to the following expression:

$$\frac{\partial \Delta z_{\text{RMO}}}{\partial \rho_V} = z_\xi \tan \gamma \tan \tilde{\gamma}. \quad (40)$$

When the medium is isotropic, and the phase angles are equal to the group angles, the RMO expression in equation 40 becomes the RMO expression introduced by Biondi and Symes (2003). The dependency of equation 40 from the group angles makes its use in RMO analysis somewhat less convenient, because it requires the transformation of phase angles (measured directly from the image) into group angles by applying equation 1. The computational cost of evaluating equation 1 is negligible, but its use makes the computations dependent on the local values of the background anisotropic velocity function. On the other hand, the following numerical examples show that substantial errors are introduced when the distinction between

the group and phase angles is neglected, and the phase angle is used instead of the group angle in equation 40.

Figure 7 shows ADCIGs when an anisotropic velocity was perturbed by $\rho_V = .99$. The four panels correspond to four rock types: a) Isotropic, b) Taylor Sand, c) Mesa Clay Shale, and d) GreenLight River Shale. Superimposed onto the images are the RMO functions computed using equation 40. The solid line was computed by computing $\tan \gamma$ from $\tan \tilde{\gamma}$ by applying equation 1, whereas the dashed line was computed by approximating $\tan \gamma$ as equal to $\tan \tilde{\gamma}$. The RMO curves computed using the correct group angle perfectly match the residual moveout of the images. On the contrary, when the phase angles are used instead of the group angles, significant errors are introduced even for such a small perturbation in the parameters ($\rho_V = .99$). It is interesting to notice that the errors are larger for the rock types exhibiting strong unelliptical anisotropy (Taylors Sand and GreenLight River Shale) than for the strongly anisotropic but quasi-elliptical rock (Mesa Clay Shale).

The expression for the RMO function derived in equation 40 is based on a linearization, and thus when the the perturbations in velocity parameters are large it is not as accurate as it is when the perturbations are small (e.g. $\rho_V = .99$). Figure 8 illustrates this fact by showing a similar experiment as the one shown in Figure 7, but with a perturbation 10 times larger; that is, with $\rho_V = .9$. As in Figure 7, the four panels correspond to four rock types: a) Isotropic, b) Taylor Sand, c) Mesa Clay Shale, and d) GreenLight River Shale, and the lines superimposed onto the images are the RMO functions computed by using the correct values for $\tan \gamma$ (solid lines), and by using $\tan \tilde{\gamma}$ in place of $\tan \gamma$ (dashed lines). With large perturbations, the predicted RMO functions differ from the actual RMO functions at wide aperture angles even when the correct values of the group angles are used in equation 40. However, even with such large perturbations the predicted RMO functions are still useful approximations of the actual RMO functions. In particular, it can be observed that the predicted RMO function correctly approximates the differences in shape of the actual RMO function among the rock types. These shape variations are related to the variations in shape of the wavefronts, which are reflected in the predicted RMO function through the variations in the mapping from phase angles to group angles.

Arbitrary scaling of velocity

The expressions of the derivative of z_γ with respect to arbitrary perturbations of individual velocity components (i.e. V_V , V_H , and V_N) are slightly more complex than with respect to ρ_V because the wavefronts are deformed when the velocity components are unevenly perturbed. These derivatives can be expressed as:

$$\frac{\partial z_\gamma}{\partial \rho_{V_V}} = -\frac{z_\xi}{S(\gamma)} \frac{\partial S(\gamma)}{\partial \rho_{V_V}} (1 + \tan \gamma \tan \tilde{\gamma}), \quad (41)$$

$$\frac{\partial z_\gamma}{\partial \rho_{V_H}} = -\frac{z_\xi}{S(\gamma)} \frac{\partial S(\gamma)}{\partial \rho_{V_H}} (1 + \tan \gamma \tan \tilde{\gamma}), \quad (42)$$

$$\frac{\partial z_\gamma}{\partial \rho_{V_N}}, = -\frac{z_\xi}{S(\gamma)} \frac{\partial S(\gamma)}{\partial \rho_{V_N}} (1 + \tan \gamma \tan \tilde{\gamma}). \quad (43)$$

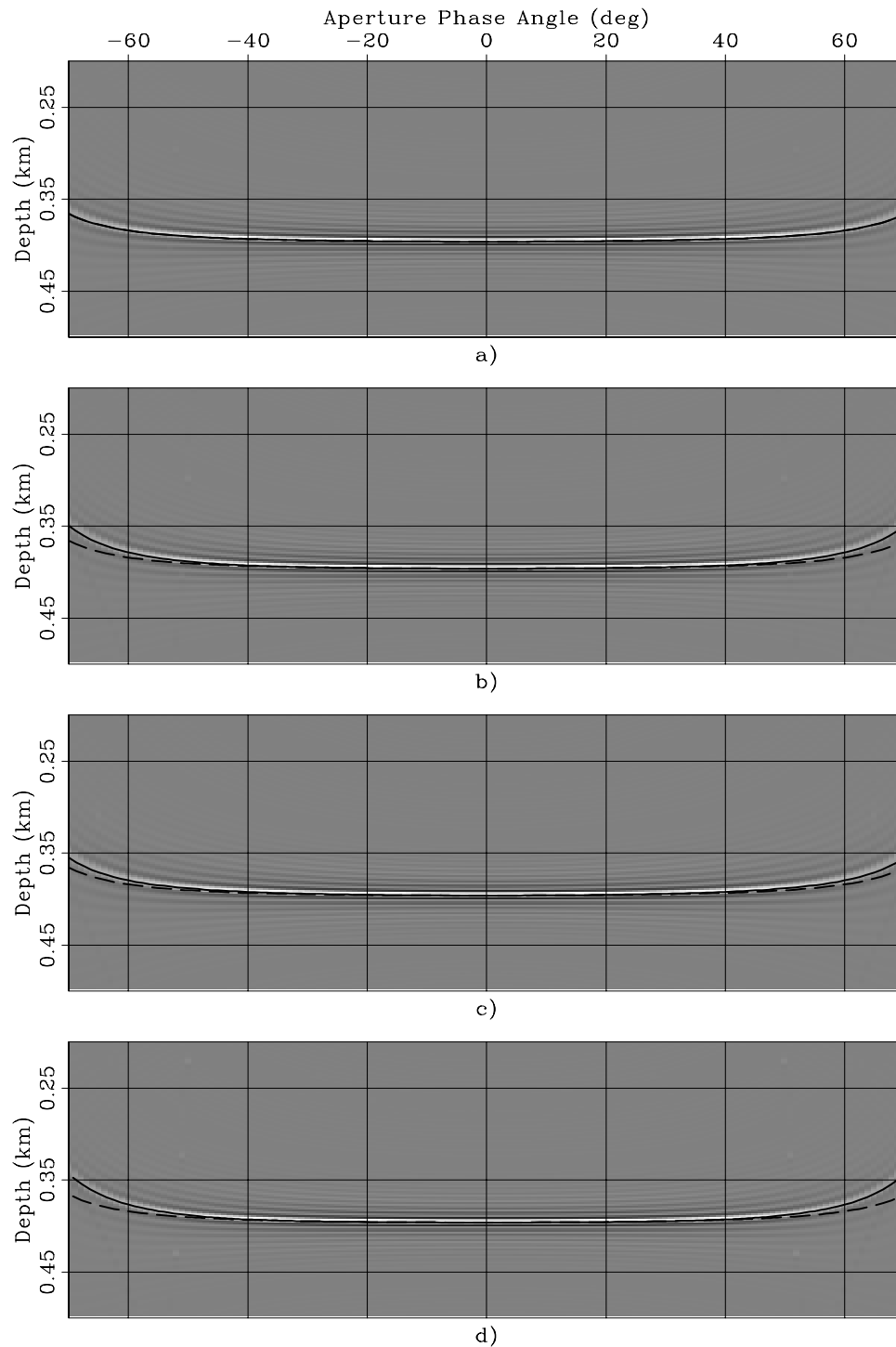


Figure 7: ADCIGs obtained when a constant anisotropic velocity was perturbed by $\rho_V = .99$ for four rock types: a) Isotropic, b) Taylor Sand, c) Mesa Clay Shale, and d) GreenLight River Shale. Superimposed onto the images are the RMO functions computed using equation 40. The solid line was computed when $\tan \gamma$ was derived from $\tan \tilde{\gamma}$ by applying equation 1, whereas the dashed line was computed by approximating $\tan \gamma$ as equal to $\tan \tilde{\gamma}$.

biondo1-Quad_Aniso-rho.99_overn [CR]

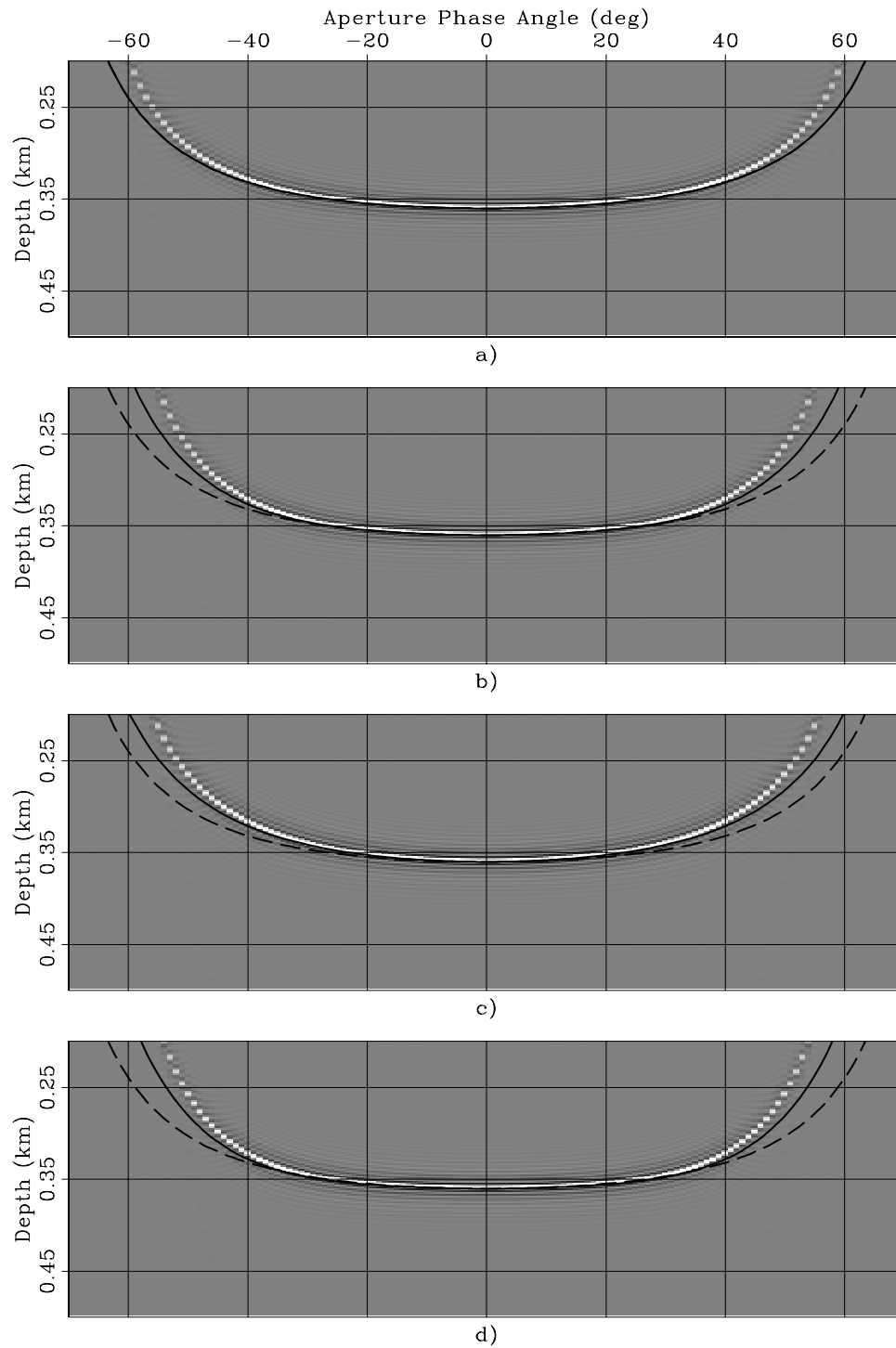


Figure 8: ADCIGs obtained when a constant anisotropic velocity was perturbed by $\rho_V = .9$ for four rock types: a) Isotropic, b) Taylor Sand, c) Mesa Clay Shale, and d) GreenLight River Shale. Superimposed onto the images are the RMO functions computed using equation 40. The solid line was computed when $\tan \gamma$ was derived from $\tan \tilde{\gamma}$ by applying equation 1, whereas the dashed line was computed by approximating $\tan \gamma$ as equal to $\tan \tilde{\gamma}$. `biondo1-Quad_Aniso-rho.9_overn` [CR]

The expressions for the derivatives of the slowness function with respect to the perturbation parameters depend on the particular form chosen to approximate the slowness function. Appendix C derives these derivative for the VTI group slowness function approximation expressed in equation 6, which I used for the numerical experiments shown in this paper.

The partial derivatives of the RMO function Δz_{RMO} are directly derived from the partial derivatives of z_γ , taking into account that for flat reflectors only the vertical velocity component V_V influences the image depth of normal incidence. The derivatives of Δz_{RMO} can thus be written as follows:

$$\frac{\partial \Delta z_{\text{RMO}}}{\partial \rho_{V_V}} = -\frac{z_\xi}{S(\gamma)} \frac{\partial S(\gamma)}{\partial \rho_{V_V}} (1 + \tan \gamma \tan \tilde{\gamma}) - z_\xi, \quad (44)$$

$$\frac{\partial \Delta z_{\text{RMO}}}{\partial \rho_{V_H}} = -\frac{z_\xi}{S(\gamma)} \frac{\partial S(\gamma)}{\partial \rho_{V_H}} (1 + \tan \gamma \tan \tilde{\gamma}), \quad (45)$$

$$\frac{\partial \Delta z_{\text{RMO}}}{\partial \rho_{V_N}} = -\frac{z_\xi}{S(\gamma)} \frac{\partial S(\gamma)}{\partial \rho_{V_N}} (1 + \tan \gamma \tan \tilde{\gamma}). \quad (46)$$

Figures 9 and 10 show examples of the application of the generalized RMO functions expressed in equations 44–46. As in Figures 7– 8, I show the ADCIGs for three different anisotropic rock types, but, differently from the previous figures, not for the isotropic case. The order of the rock types is the same as in Figures 7– 8; that is: panels a) correspond to Taylor Sand, panels b) to Mesa Clay Shale, and panels c) to GreenLight River Shale. Furthermore, as in Figures 7– 8, one figure (Figure 10) shows the ADCIG obtained with a smaller perturbation than the ADCIGs shown in the other figure (Figure 9). The ADCIGs shown in Figure 9 were obtained by performing *isotropic* migration on the synthetic data modeled assuming *anisotropic* velocity. The ADCIGs shown in Figure 10 were computed by scaling by .25 the parameter perturbations used to compute Figure 9. The lines superimposed onto the images are the RMO functions computed by using the correct values for $\tan \gamma$ (solid lines), and by using $\tan \tilde{\gamma}$ in place of $\tan \gamma$ (dashed lines).

The predicted RMO functions accurately track the actual RMO functions when the parameter perturbations are sufficiently small to be within the range of accuracy of the linearization at the basis of the derivation of equation 40 (Figure 10). But even when the perturbations are large (Figure 9) and cause a substantial RMO (up to 30% of the reflector depth) the predicted RMO functions are excellent approximations of the actual RMO functions.

The RMO functions associated with the two strongly unelliptical rocks (Taylor Sand and GreenLight River Shale) exhibit a characteristic oscillatory behavior; the events at narrow-aperture angles are imaged deeper than the normal incidence event, whereas the events at wide-aperture angles are imaged shallower. This oscillatory behavior is well predicted by the analytical RMO function introduced in equations 44–46.

In contrast, the approximation of the group angles with the phase angles (dashed lines in the figures) seriously deteriorates the accuracy of the predicted RMO functions. Notice that, in contrast with the uniform perturbation case illustrated in Figures 7– 8, the dashed lines are different among the panels, because the derivatives of the slowness function with respect to the perturbation parameters depend on the anisotropic parameters of the background medium.

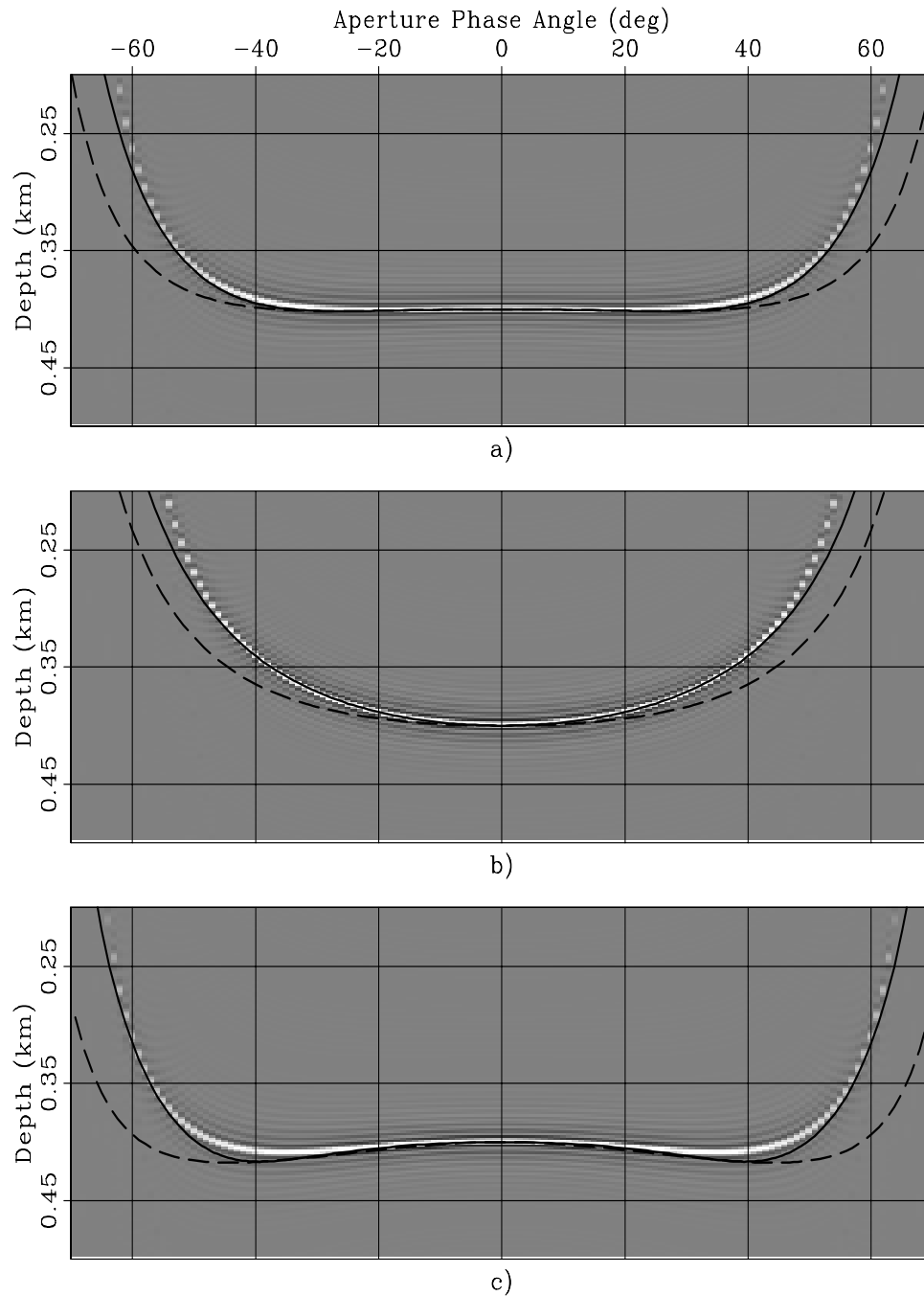


Figure 9: ADCIGs obtained when data modeled with an *anisotropic* velocity have been migrated using an *isotropic* velocity. The anisotropic data were modeled assuming three rock types: a) Taylor Sand, b) Mesa Clay Shale, and c) GreenLight River Shale. Superimposed onto the images are the RMO functions computed using equation 40. The solid line was computed when $\tan \gamma$ was derived from $\tan \tilde{\gamma}$ by applying equation 1, whereas the dashed line was computed by approximating $\tan \gamma$ as equal to $\tan \tilde{\gamma}$. biondo1-Trio_Aniso-iso_overn [CR]

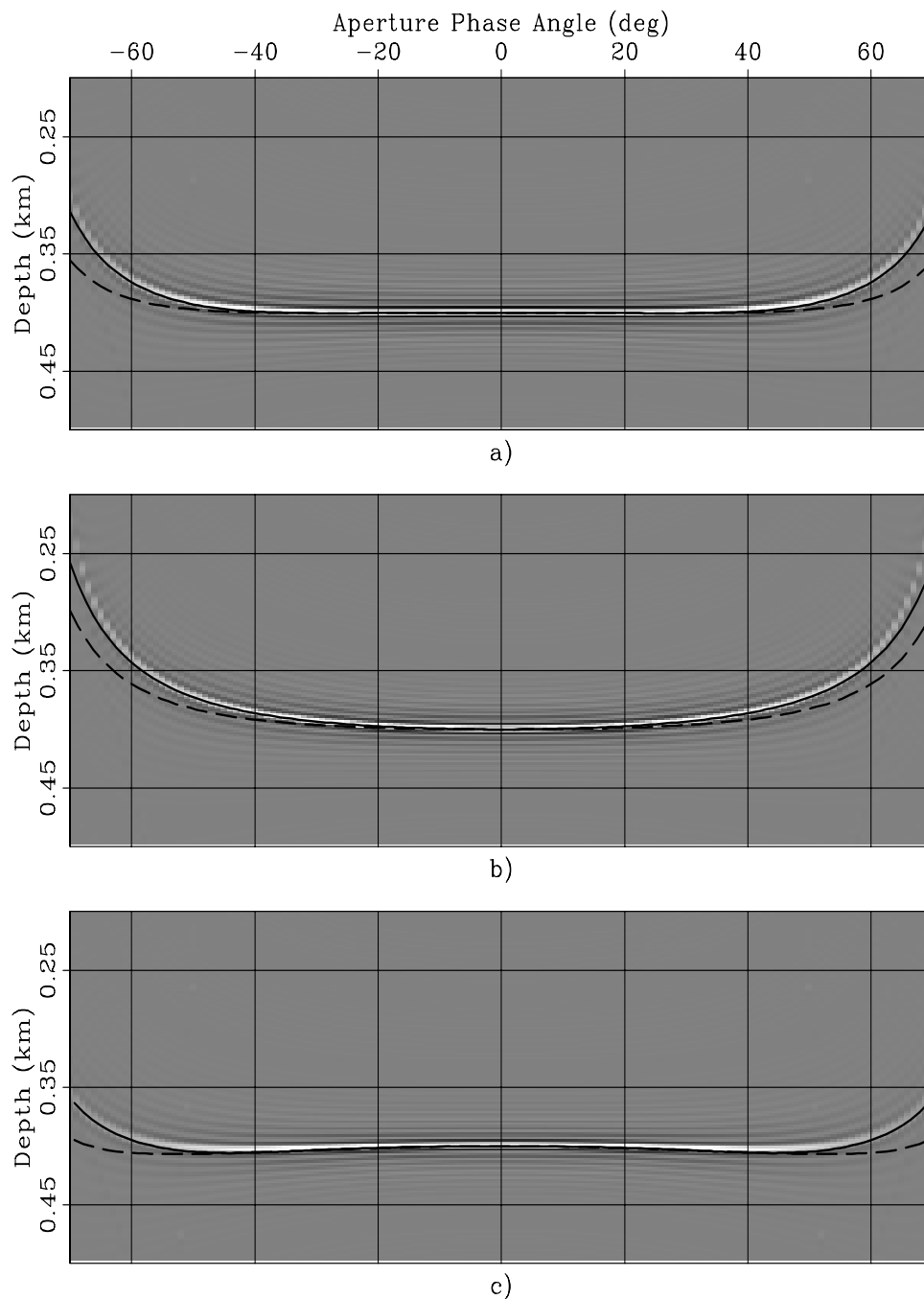


Figure 10: ADCIGs obtained when data modeled with an *anisotropic* velocity have been migrated using a *less anisotropic* velocity; that is, with anisotropic parameters obtained by scaling by .25 the parameter perturbations used to compute Figure 9. The anisotropic data were modeled assuming three rock types: a) Taylor Sand, b) Mesa Clay Shale, and c) Green-Light River Shale. Superimposed onto the images are the RMO functions computed using equation 40. The solid line was computed when $\tan \gamma$ was derived from $\tan \tilde{\gamma}$ by applying equation 1, whereas the dashed line was computed by approximating $\tan \gamma$ as equal to $\tan \tilde{\gamma}$.

biondo1-Trio_Aniso-scaled_overn [CR]

Conversion of depth errors into traveltimes errors

The RMO functions derived above can be directly used in a layered-based vertical updating of the velocity function after migration. However, in complex media it is often desirable to invert the depth errors measured from ADCIGs into velocity-parameters perturbations through a tomographic procedure. To be able to apply a tomographic method, we must perform an additional step to convert the depth errors measured from ADCIGs into traveltimes errors. This depth-to-time conversion can be easily accomplished by slightly rewriting the chain of partial derivatives in equation 35, and obtain the following relationship:

$$\frac{\partial z_\gamma}{\partial t} = \frac{\partial z_\gamma}{\partial L} \frac{\partial L}{\partial t} = \frac{\cos \gamma + \sin \gamma \tan \tilde{\gamma}}{S(\gamma)}, \quad (47)$$

which can be directly applied to convert depth errors into traveltimes perturbations to be used in tomography.

CONCLUSIONS

The methodology for computing and analyzing ADCIGs that has been recently developed for isotropic media can be generalized to prestack images computed using anisotropic prestack migration. The transformation to angle domain performed by slant-stacking the subsurface-offset axis generates angle gathers that are approximately function of the phase aperture angle. In VTI media the approximation is exact for flat reflectors, and even for dipping reflectors it seems to be sufficiently accurate for practical applications with realistic anisotropic parameters.

The linearized analysis of ADCIGs obtained by anisotropic migration shows that the RMO function observed when the migration velocity is inaccurate is function of both the phase aperture angle and the group aperture angle. The numerical examples show that the linearized expression of the RMO function accurately predicts the actual RMO function measured after wavefield migration.

A simple modification of the analysis that yields the expression of the RMO function leads also to a linearized relationship between depth errors measured in ADCIGs and traveltimes errors accumulated along the wavepaths. This relationship should enable the development of migration velocity analysis methods based on tomographic velocity-updating procedures.

REFERENCES

- Bear, L., Dickens, T., and Traynin, P. Incorporating nonseismic information for improved imaging with anisotropic PSDM, 2003.
- Biondi, B., and Sava, P., 1999, Wave-equation migration velocity analysis: 69th Ann. Internat. Meeting, Soc. of Expl. Geophys., Expanded Abstracts, 1723–1726.

- Biondi, B., and Symes, W. W., 2003, Angle-domain common-image gathers for migration velocity analysis by wavefield-continuation imaging: *Geophysics*, **69**, 1283–1298.
- Biondi, B., and Tisserant, T., 2004, 3-D angle-domain common-image gathers for migration velocity analysis: *Geophysical Prospecting*, **52**, 575–591.
- Clapp, R., and Biondi, B., 2000, Tau domain migration velocity analysis using angle CRP gathers and geologic constrains: 70th Ann. Internat. Meeting, Soc. of Expl. Geophys., 926–929.
- Dellinger, J., and Muir, F., 1985, Two domains of anisotropy: SEP-**44**, 59–62.
- Fowler, P., 2003, Practical VTI approximations: a systematic anatomy: *Journal of Applied Geophysics*, **69**, 347–367.
- Prucha, M., Biondi, B., and Symes, W. W., 1999, Angle-domain common-image gathers by wave-equation migration: 69th Ann. Internat. Meeting, Soc. Expl. Geophys., Expanded Abstracts, 824–827.
- Rickett, J., and Sava, P., 2002, Offset and angle-domain common image-point gathers for shot-profile migration: *Geophysics*, **67**, 883–889.
- Rosales, D. A., and Biondi, B., 2005, Converted-mode angle-domain common-image gathers for migration velocity analysis: SEP-**120**, 283–296.
- Rosales, D., and Rickett, J., 2001, *ps*-wave polarity reversal in angle domain common-image gathers: SEP-**108**, 35–44.
- Sarkar, D., and Tsvankin, I., 2003, Analysis of image gathers in factorized vti media: *Geophysics*, **68**, 2016–2025.
- Sarkar, D., and Tsvankin, I. Anisotropic migration velocity analysis: Application to a data set from West Africa., 2004.
- Sarkar, D., and Tsvankin, I., 2004b, Migration velocity analysis in factorized vti media: *Geophysics*, **69**, 708–718.
- Sava, P., and Fomel, S., 2003, Angle-domain common-image gathers by wavefield continuation methods: *Geophysics*, **68**, 1065–1074.
- Sen, S., and Biondi, B., 2005, Common azimuth migration for elliptical and VTI media: SEP-**120**, 125–136.
- Shan, G., and Biondi, B., 2005a, 3D wavefield extrapolation in laterally-varying tilted TI media: SEP-**120**, 105–124.
- Shan, G., and Biondi, B., 2005b, Imaging steeply dipping reflectors in TI media by wavefield extrapolation: SEP-**120**, 63–76.

Stolk, C. C., and Symes, W. W., 2003, Kinematic artifacts in prestack depth migration: Geophysics: accepted for publication, **69**, 562–575.

Tsvankin, I., 2001, Seismic signatures and analysis of reflection data in anisotropic media: Elsevier Science.

APPENDIX A - ANALYTICAL EVALUATION OF THE TANGENT PLANE TO THE IMPULSE RESPONSE

In this appendix I derive the expressions for evaluating the derivatives of image depth z_ξ with respect to the subsurface offset h_ξ and the midpoint m_ξ ; these derivatives are computed along the tangent plane to the impulse response of the generalized migration operator, which is defined in equations 18–24.

I start by deriving the equation for the vector normal to the impulse-response surface, \vec{n} :

$$\begin{aligned} \vec{n} &= \begin{vmatrix} \vec{z}_\xi & \vec{m}_\xi & \vec{h}_\xi \\ \frac{\partial z_\xi}{\partial \alpha_x} & \frac{\partial m_\xi}{\partial \alpha_x} & \frac{\partial h_\xi}{\partial \alpha_x} \\ \frac{\partial z_\xi}{\partial \gamma} & \frac{\partial m_\xi}{\partial \gamma} & \frac{\partial h_\xi}{\partial \gamma} \end{vmatrix} \\ &= \left(\frac{\partial m_\xi}{\partial \alpha_x} \frac{\partial h_\xi}{\partial \gamma} - \frac{\partial m_\xi}{\partial \gamma} \frac{\partial h_\xi}{\partial \alpha_x} \right) \vec{z}_\xi + \left(-\frac{\partial z_\xi}{\partial \alpha_x} \frac{\partial h_\xi}{\partial \gamma} + \frac{\partial z_\xi}{\partial \gamma} \frac{\partial h_\xi}{\partial \alpha_x} \right) \vec{m}_\xi + \left(\frac{\partial z_\xi}{\partial \alpha_x} \frac{\partial m_\xi}{\partial \gamma} - \frac{\partial z_\xi}{\partial \gamma} \frac{\partial m_\xi}{\partial \alpha_x} \right) \vec{h}_\xi, \end{aligned} \quad (48)$$

where \vec{z}_ξ , \vec{m}_ξ , and \vec{h}_ξ are respectively the unit vectors along the three dimensions z_ξ , m_ξ , and h_ξ .

The equation of the tangent plane at the image point with coordinates $(\bar{z}_\xi, \bar{m}_\xi, \bar{h}_\xi)$ is given by:

$$\begin{aligned} T(z_\xi, m_\xi, h_\xi) &= \left(\frac{\partial m_\xi}{\partial \alpha_x} \frac{\partial h_\xi}{\partial \gamma} - \frac{\partial m_\xi}{\partial \gamma} \frac{\partial h_\xi}{\partial \alpha_x} \right) (z_\xi - \bar{z}_\xi) \\ &+ \left(-\frac{\partial z_\xi}{\partial \alpha_x} \frac{\partial h_\xi}{\partial \gamma} + \frac{\partial z_\xi}{\partial \gamma} \frac{\partial h_\xi}{\partial \alpha_x} \right) (m_\xi - \bar{m}_\xi) \\ &+ \left(\frac{\partial z_\xi}{\partial \alpha_x} \frac{\partial m_\xi}{\partial \gamma} - \frac{\partial z_\xi}{\partial \gamma} \frac{\partial m_\xi}{\partial \alpha_x} \right) (h_\xi - \bar{h}_\xi) = 0. \end{aligned} \quad (49)$$

The derivative of the depth with respect to the subsurface offset, at constant midpoint, is given by:

$$\left. \frac{\partial z_\xi}{\partial h_\xi} \right|_{m_\xi = \bar{m}_\xi} = - \frac{\left. \frac{\partial T}{\partial h_\xi} \right|_{m_\xi = \bar{m}_\xi}}{\left. \frac{\partial T}{\partial z_\xi} \right|_{m_\xi = \bar{m}_\xi}} = - \frac{\frac{\partial z_\xi}{\partial \alpha_x} \frac{\partial m_\xi}{\partial \gamma} - \frac{\partial z_\xi}{\partial \gamma} \frac{\partial m_\xi}{\partial \alpha_x}}{\frac{\partial m_\xi}{\partial \alpha_x} \frac{\partial h_\xi}{\partial \gamma} - \frac{\partial m_\xi}{\partial \gamma} \frac{\partial h_\xi}{\partial \alpha_x}}. \quad (50)$$

and similarly the derivative of the depth with respect to the midpoint, at constant subsurface offset, is given by:

$$\left. \frac{\partial z_\xi}{\partial m_\xi} \right|_{h_\xi = \bar{h}_\xi} = - \frac{\left. \frac{\partial T}{\partial m_\xi} \right|_{h_\xi = \bar{h}_\xi}}{\left. \frac{\partial T}{\partial z_\xi} \right|_{h_\xi = \bar{h}_\xi}} = - \frac{\frac{\partial z_\xi}{\partial \alpha_x} \frac{\partial h_\xi}{\partial \gamma} - \frac{\partial z_\xi}{\partial \gamma} \frac{\partial h_\xi}{\partial \alpha_x}}{\frac{\partial m_\xi}{\partial \alpha_x} \frac{\partial h_\xi}{\partial \gamma} - \frac{\partial m_\xi}{\partial \gamma} \frac{\partial h_\xi}{\partial \alpha_x}}. \quad (51)$$

To evaluate equations 50–51. we need to evaluate the following partial derivatives, obtained by differentiating the expressions in equations 18–20:

$$\begin{aligned} \frac{\partial z_\xi}{\partial \alpha_x} &= -L(\alpha_x, \gamma) \frac{\tan \alpha_x}{\cos \alpha_x \cos \gamma} (\cos^2 \alpha_x + \sin^2 \gamma) + \frac{\partial L(\alpha_x, \gamma)}{\partial \alpha_x} \frac{\cos^2 \alpha_x - \sin^2 \gamma}{\cos \alpha_x \cos \gamma}, \\ \frac{\partial z_\xi}{\partial \gamma} &= -L(\alpha_x, \gamma) \frac{\tan \gamma}{\cos \alpha_x \cos \gamma} (\cos^2 \gamma + \sin^2 \alpha_x) + \frac{\partial L(\alpha_x, \gamma)}{\partial \gamma} \frac{\cos^2 \alpha_x - \sin^2 \gamma}{\cos \alpha_x \cos \gamma}, \\ \frac{\partial m_\xi}{\partial \alpha_x} &= -L(\alpha_x, \gamma) \frac{\cos \alpha_x}{\cos \gamma} - \frac{\partial L(\alpha_x, \gamma)}{\partial \alpha_x} \frac{\sin \alpha_x}{\cos \gamma}, \\ \frac{\partial m_\xi}{\partial \gamma} &= -L(\alpha_x, \gamma) \frac{\sin \gamma \sin \alpha_x}{\cos^2 \gamma} - \frac{\partial L(\alpha_x, \gamma)}{\partial \gamma} \frac{\sin \alpha_x}{\cos \gamma}, \\ \frac{\partial h_\xi}{\partial \alpha_x} &= -L(\alpha_x, \gamma) \frac{\sin \gamma \sin \alpha_x}{\cos^2 \alpha_x} - \frac{\partial L(\alpha_x, \gamma)}{\partial \alpha_x} \frac{\sin \gamma}{\cos \alpha_x}, \\ \frac{\partial h_\xi}{\partial \gamma} &= -L(\alpha_x, \gamma) \frac{\cos \gamma}{\cos \alpha_x} - \frac{\partial L(\alpha_x, \gamma)}{\partial \gamma} \frac{\sin \gamma}{\cos \alpha_x}. \end{aligned} \quad (52)$$

The derivative of path length are evaluated as following:

$$\begin{aligned} \frac{\partial L}{\partial \alpha_x} &= \frac{-t_D}{[(S_r + S_s) + (S_r - S_s) \tan \alpha_x \tan \gamma]^2} \\ &\left[\left(\frac{\partial S_r}{\partial \alpha_x} + \frac{\partial S_s}{\partial \alpha_x} \right) + \left(\frac{\partial S_r}{\partial \alpha_x} - \frac{\partial S_s}{\partial \alpha_x} \right) \tan \alpha_x \tan \gamma + \frac{(S_r - S_s) \tan \gamma}{\cos^2 \alpha_x} \right], \end{aligned} \quad (53)$$

and

$$\begin{aligned} \frac{\partial L}{\partial \gamma} &= \frac{-t_D}{[(S_r + S_s) + (S_r - S_s) \tan \alpha_x \tan \gamma]^2} \\ &\left[\left(\frac{\partial S_r}{\partial \gamma} + \frac{\partial S_s}{\partial \gamma} \right) + \left(\frac{\partial S_r}{\partial \gamma} - \frac{\partial S_s}{\partial \gamma} \right) \tan \alpha_x \tan \gamma + \frac{(S_r - S_s) \tan \alpha_x}{\cos^2 \gamma} \right]. \end{aligned} \quad (54)$$

Application to the isotropic case

The application to the isotropic case is simpler than the anisotropic case because the derivative of the path length is zero, but it is instructive since it verifies known results through a completely different derivation. Substituting equations 52 into equation 50, I obtain:

$$\begin{aligned} \left. \frac{\partial z_\xi}{\partial h_\xi} \right|_{m_\xi = \bar{m}_\xi} &= - \frac{L^2 \tan \gamma \left[\frac{\tan^2 \alpha_x}{\cos^2 \gamma} (\cos^2 \alpha_x + \sin^2 \gamma) - \frac{1}{\cos^2 \gamma} (\cos^2 \gamma + \sin^2 \alpha_x) \right]}{L^2 [1 - \tan^2 \alpha_x \tan^2 \gamma]} \\ &= - \frac{L^2 \tan \gamma \left[-1 + \sin^2 \alpha_x \left(\frac{1}{\cos^2 \gamma} - \frac{1}{\cos^2 \gamma} \right) + \tan^2 \alpha_x \tan^2 \gamma \right]}{L^2 [1 - \tan^2 \alpha_x \tan^2 \gamma]} \\ &= \tan \gamma, \end{aligned} \quad (55)$$

which shows that $\partial z_\xi / \partial h_\xi$ is independent from the dip angle α_x . This expression is consistent with the 2-D analysis by Sava and Fomel (2003) and the 3-D analysis by Biondi and Tisserant (2004).

APPENDIX B

In this appendix I demonstrate that the terms in equation 34 multiplying the partial derivatives with respect to the angles; that is, $\partial\gamma/\partial\rho_i$ and $\partial\tilde{\gamma}/\partial\rho_i$, are zero when evaluated at the point when the events are correctly migrated at zero subsurface offset. We are interested in estimating the RMO function measured for an incorrect velocity. That RMO function can be seen as a perturbation around the image obtained with the correct velocity.

After simple evaluation of partial derivatives the term multiplying $\partial\gamma/\partial\rho_i$ in equation 34 can be written as the following:

$$\begin{aligned} \left(\frac{\partial z_\gamma}{\partial L} \frac{\partial L}{\partial S(\gamma)} \frac{\partial S(\gamma)}{\partial \gamma} + \frac{\partial z_\gamma}{\partial \gamma} \right) &= -\frac{z_\xi (\cos \gamma + \sin \gamma \tan \tilde{\gamma})}{S(\gamma) \cos \gamma} \frac{\partial S(\gamma)}{\partial \gamma} - L (\sin \gamma - \cos \gamma \tan \tilde{\gamma}) \\ &= -z_\xi \left[(1 + \tan \gamma \tan \tilde{\gamma}) \frac{\partial S(\gamma)}{\partial \gamma} + \tan \gamma - \tan \tilde{\gamma} \right], \end{aligned} \quad (56)$$

that can be easily demonstrated to be equal to zero after substitution of the relationship between phase angles and group angles presented in equation 4.

The term multiplying $\partial\tilde{\gamma}/\partial\rho_i$ is equal to

$$\frac{\partial z}{\partial \tilde{\gamma}} = -h_\xi \frac{1}{\cos^2 \tilde{\gamma}}, \quad (57)$$

which is obviously equal to zero when the subsurface offset is zero, the point around which we are interested in expanding the RMO function.

APPENDIX C - DERIVATIVES OF VTI SLOWNESS FUNCTION WITH RESPECT TO THE PERTURBATION PARAMETERS

In this Appendix I present the analytical expressions for the derivatives of the VTI group slowness function expressed in equation 6 in the main text. These derivatives are necessary for the numerical computation of the RMO functions.

The VTI slowness function can be approximated as (Fowler, 2003):

$$\begin{aligned} S_{\text{VTI}}^2(\theta) &= \frac{S_V^2 \cos^2 \theta + S_H^2 \sin^2 \theta + \sqrt{(S_V^2 \cos^2 \theta + S_H^2 \sin^2 \theta)^4 + S_V^2 (S_N^2 - S_H^2) \sin^2 2\theta}}{2} \\ &= \frac{S_{\text{EII}}^2(\theta) + \sqrt{S_{\text{EII}}^4(\theta) + S_V^2 (S_N^2 - S_H^2) \sin^2 2\theta}}{2}, \end{aligned} \quad (58)$$

where

$$S_{\text{EII}}^2(\theta) = S_V^2 \cos^2 \theta + S_H^2 \sin^2 \theta \quad (59)$$

is the elliptical component.

The derivatives are then written as:

$$\left. \frac{\partial S_{\text{VTI}}(\theta)}{\partial \rho_{V_V}} \right|_{\rho=1} = \frac{S_{\text{EII}}(\theta)}{2S_{\text{VTI}}(\theta)} \frac{\partial S_{\text{EII}}(\theta)}{\partial \rho_{V_V}} + \frac{2 \frac{\partial S_{\text{EII}}(\theta)}{\partial \rho_{V_V}} S_{\text{EII}}^3(\theta) - S_V^2 (S_N^2 - S_H^2) \sin^2 2\theta}{4S_{\text{VTI}}(\theta) \sqrt{S_{\text{EII}}^2(\theta) + S_V^2 (S_N^2 - S_H^2) \sin^2 2\theta}} \quad (60)$$

$$\left. \frac{\partial S_{\text{VTI}}(\theta)}{\partial \rho_{V_H}} \right|_{\rho=1} = \frac{S_{\text{EII}}(\theta)}{2S_{\text{VTI}}(\theta)} \frac{\partial S_{\text{EII}}(\theta)}{\partial \rho_{V_H}} + \frac{2 \frac{\partial S_{\text{EII}}(\theta)}{\partial \rho_{V_H}} S_{\text{EII}}^3(\theta) + S_V^2 S_H^2 \sin^2 2\theta}{4S_{\text{VTI}}(\theta) \sqrt{S_{\text{EII}}^2(\theta) + S_V^2 (S_N^2 - S_H^2) \sin^2 2\theta}} \quad (61)$$

$$\left. \frac{\partial S_{\text{VTI}}(\theta)}{\partial \rho_{V_N}} \right|_{\rho=1} = \frac{-S_V^2 S_N^2 \sin^2 2\theta}{4S_{\text{VTI}}(\theta) \sqrt{S_{\text{EII}}^2(\theta) + S_V^2 (S_N^2 - S_H^2) \sin^2 2\theta}}, \quad (62)$$

where the derivatives of the elliptical component with respect to ρ_{V_V} and ρ_{V_H} are:

$$\left. \frac{\partial S_{\text{EII}}(\theta)}{\partial \rho_{V_V}} \right|_{\rho=1} = \frac{-S_V^2 \cos^2 \theta}{S_{\text{EII}}(\theta)} \quad (63)$$

$$\left. \frac{\partial S_{\text{EII}}(\theta)}{\partial \rho_{V_H}} \right|_{\rho=1} = \frac{-S_H^2 \sin^2 \theta}{S_{\text{EII}}(\theta)}. \quad (64)$$



3D wavefield extrapolation in laterally-varying tilted TI media

Guojian Shan and Biondo Biondi¹

ABSTRACT

We develop a new 3D wavefield-extrapolation method for a transversely isotropic (TI) medium with a symmetry axis. The wavefield extrapolation is done by an implicit isotropic extrapolation operator with an explicit correction operator. The explicit correction is a 2D convolution operator in the space domain, whose coefficients are estimated by a weighted least-squares method in the Fourier domain. The extrapolation operator is stable and suitable for laterally-varying 3D TI media. This new method can be used to extrapolate wavefields in a 3D transversely isotropic medium with a vertical symmetry axis (VTI) in tilted coordinates. We also discuss the effects of the filter length on its accuracy and shorten the filter by changing the least-squares weighting function. We present the impulse response of our algorithm and compare it with the anisotropic phase-shift method.

INTRODUCTION

Many rocks are anisotropic, and most sedimentary rocks can be approximated as TI media. If anisotropy is not taken into account in the migration, reflectors, especially steeply dipping reflectors, will be imaged incorrectly. To image the reflector in a TI medium, it is important to use an anisotropic wavefield-extrapolation method. Implicit methods (Ristow and Ruhl, 1997), phase-shift-plus-interpolation (PSPI) (Rousseau, 1997), non-stationary phase-shift (Ferguson and Margrave, 1998), explicit operators (Uzcatogui, 1995; Zhang et al., 2001a,b), and reference anisotropic phase-shift with an explicit correction filter (Baumstein and Anderson, 2003) have been developed to extrapolate wavefields in 2D VTI, 3D VTI, or 2D tilted TI media.

Explicit extrapolation operators have proved useful in isotropic wavefield extrapolation (Holberg, 1988; Blacquiere et al., 1989; Thorbecke, 1997). The dispersion relation in a tilted TI medium is very complicated, and it is very difficult to design an implicit extrapolation operator for it. However, explicit operators can still handle in the same way as isotropic media. In 3D, the circular symmetry of the isotropic or VTI media allows us to design a 1D algorithm to replace the 2D convolution operator by McClellan transformations (Hale, 1991b,a; Zhang et al., 2001b). For tilted TI media, the deviation of the symmetry axis from the vertical direction breaks that circular symmetry. As a result, a 2D convolution operator has to be designed for the wavefield extrapolation in 3D tilted TI media.

¹email: shan@sep.stanford.edu, biondo@sep.stanford.edu

Tilted coordinates (Shan and Biondi, 2004a) are used to extrapolate wavefields in a direction close to the wave propagation direction. We can use tilted coordinates to get good accuracy for high-angle energy using a less accurate operator. A VTI medium in Cartesian coordinates becomes a tilted TI medium in tilted coordinates. Thus to extrapolate wavefields in tilted coordinates in a VTI medium, we need an extrapolation operator for tilted TI media.

In this paper, we extrapolate the wavefield in 3D tilted TI media using an implicit isotropic operator with an explicit anisotropic correction (Shan and Biondi, 2004b). We begin by first deriving the 3D dispersion relation in tilted TI media. Then we discuss how to design 2D antisymmetric convolution operators in the Fourier domain for tilted TI media. We discuss how the length of the filter affects the accuracy of the operator and propose a way to design short 2D filters. Finally, we present 3D impulse response for a tilted TI medium of our algorithm.

3D DISPERSION RELATION IN TILTED TI MEDIA

In 3D VTI media, the phase velocity of P- and SV-waves in Thomsen's notation can be expressed as follows (Tsvankin, 1996):

$$\frac{V^2(\theta)}{V_{P0}^2} = 1 + \varepsilon \sin^2(\theta) - \frac{f}{2} \pm \frac{f}{2} \sqrt{\left(1 + \frac{2\varepsilon \sin^2(\theta)}{f}\right)^2 - \frac{2(\varepsilon - \delta) \sin^2(2\theta)}{f}}, \quad (1)$$

where θ is the phase angle of the propagating wave, and $f = 1 - (V_{S0}/V_{P0})^2$. V_{P0} and V_{S0} are the P- and SV- wave velocities in the vertical direction, respectively. The anisotropy parameters ε and δ are defined by Thomsen (1986):

$$\varepsilon = \frac{C_{11} - C_{33}}{2C_{33}}, \delta = \frac{(C_{11} + C_{44})^2 - (C_{33} - C_{44})^2}{2C_{33}(C_{33} - C_{44})},$$

where C_{ij} are elastic moduli. In equation (1), $V(\theta)$ is the P-wave phase-velocity when the sign in front of the square root is positive, and the SV-wave phase velocity for a negative sign. Let k'_x , k'_y and k'_z be the wavenumbers for VTI media in Cartesian coordinates. For plane-wave propagation, the phase angle θ is related to the wavenumbers k'_x , k'_y and k'_z by the following relations:

$$\sin \theta = \frac{V(\theta)k'_r}{\omega}, \quad \cos \theta = \frac{V(\theta)k'_z}{\omega}, \quad (2)$$

where ω is the temporal frequency, and $k'_r = \sqrt{(k'_x)^2 + (k'_y)^2}$. From equations (1) and (2), we can derive the dispersion relation for 3D VTI media as follows:

$$b_6(k'_z)^4 + b_5(k'_r)^4 + b_4(k'_z)^2(k'_r)^2 + b_3(k'_z)^2 + b_2(k'_r)^2 + b_1 = 0, \quad (3)$$

where

$$\begin{aligned}
b_6 &= f - 1, \\
b_5 &= (f - 1)(1 + 2\varepsilon), \\
b_4 &= 2[(f - 1)(1 + \varepsilon) - f(\varepsilon - \delta)], \\
b_3 &= \left(\frac{\omega}{v_p}\right)^2 (2 - f), \\
b_2 &= (2 + 2\varepsilon - f)\left(\frac{\omega}{v_p}\right), \\
b_1 &= \left(\frac{\omega}{v_p}\right)^4.
\end{aligned} \tag{4}$$

For tilted TI media, the symmetry axis deviates from the vertical direction. We need two angles to describe the tilting direction, the tilting angle φ and the azimuth of the tilting direction ψ . We first assume $\psi = 0$, that is the symmetry axis is in the plane $y = 0$. Then we generalize the dispersion relation to the case that $\psi \neq 0$ by coordinate rotation.

For a tilted TI medium, if we rotate the coordinates so that the symmetry axis is the axis z' , it becomes a VTI medium in the new coordinates. Let k_x , k_y , and k_z be the wavenumbers for a tilted TI medium in Cartesian coordinates. k'_x , k'_y and k'_z , which are the wavenumbers for VTI media in Cartesian coordinates, can also be considered as the wavenumbers for tilted TI media in the rotated coordinates. For the case that $\psi = 0$, the dispersion relation can be obtained from equation (3) by rotating the coordinates as follows:

$$\begin{pmatrix} k'_x \\ k'_z \end{pmatrix} = \begin{pmatrix} \cos \varphi & -\sin \varphi \\ \sin \varphi & \sin \varphi \end{pmatrix} \begin{pmatrix} k_x \\ k_z \end{pmatrix}. \tag{5}$$

We can re-organize the the dispersion relation and obtain the equation for the wavenumber k_z as follows:

$$a_4 k_z^4 + a_3 k_z^3 + a_2 k_z^2 + a_1 k_z + a_0 = 0, \tag{6}$$

where

$$\begin{aligned}
a_4 &= (f - 1) + 2\varepsilon(f - 1)\sin^2 \varphi - \frac{f}{2}(\varepsilon - \delta)\sin^2 2\varphi, \\
a_3 &= 2(f - 1)\varepsilon \sin 2\varphi - f(\varepsilon - \delta)\sin 4\varphi, \\
a_2 &= [2(f - 1)(1 + \varepsilon) - f(\varepsilon - \delta)(2\cos^2 2\varphi - \sin^2 2\varphi)]k_x^2 \\
&\quad + 2[(f - 1)(1 + \varepsilon) + (f - 1)\varepsilon \sin^2 \varphi - f(\varepsilon - \delta)\cos^2 \varphi]k_y^2 \\
&\quad + \left(\frac{\omega}{v_{p0}}\right)^2 (2\varepsilon \sin^2 \varphi + 2 - f), \\
a_1 &= [2(f - 1)\varepsilon \sin 2\varphi + f(\varepsilon - \delta)\sin 4\varphi]k_x^3 \\
&\quad + 2\sin 2\varphi[(f - 1)\varepsilon + f(\varepsilon - \delta)]k_x k_y^2 \\
&\quad + 2\varepsilon \left(\frac{\omega}{v_{p0}}\right)^2 \sin 2\varphi k_x, \\
a_0 &= [(f - 1)(1 + 2\varepsilon \cos^2 \varphi) - \frac{f}{2}(\varepsilon - \delta)\sin^2 2\varphi]k_x^4 + (f - 1)(1 + 2\varepsilon)k_y^4 \\
&\quad + 2[(f - 1)(1 + \varepsilon + \varepsilon \cos^2 \varphi) - f(\varepsilon - \delta)\sin^2 \varphi]k_x^2 k_y^2 \\
&\quad + \left(\frac{\omega}{v_{p0}}\right)^2 (2 - f + 2\varepsilon \cos^2 \varphi)k_x^2 + 2\left(\frac{\omega}{v_{p0}}\right)^2 (2 + \varepsilon - f)k_y^2.
\end{aligned} \tag{7}$$

Equation (6) is a quartic equation in k_z . Given k_x , k_y , the velocity v_{p0} , the anisotropy parameters ε and δ , and the tilting angle φ , we can calculate all the coefficients of equation (6), and

it can be solved analytically (Abramowitz and Stegun, 1972). Usually there are four solutions for equation (6). Two of them are related to the up- and down-going P-wave, and the other two are related to the up- and down-going SV-wave, respectively.

Let k''_x , k''_y and k''_z be the wavenumbers for tilted TI media with a general ψ in the original coordinate system. For general ψ , after solving equation (6), we can get the wavenumber k''_z by rotating coordinates (k_x, k_y) as follows:

$$\begin{pmatrix} k''_x \\ k''_y \end{pmatrix} = \begin{pmatrix} \cos \psi & -\sin \psi \\ \sin \psi & \cos \psi \end{pmatrix} \begin{pmatrix} k_x \\ k_y \end{pmatrix}. \quad (8)$$

Figure 1 shows k''_z as a function of k_x and k_y in a constant tilted TI medium. In this medium, the velocity is 2000 m/s, ε is 0.4, δ is 0.2, φ is $\frac{\pi}{6}$ and ψ is 0. The frequency used in Figure 1 is 57 Hz.

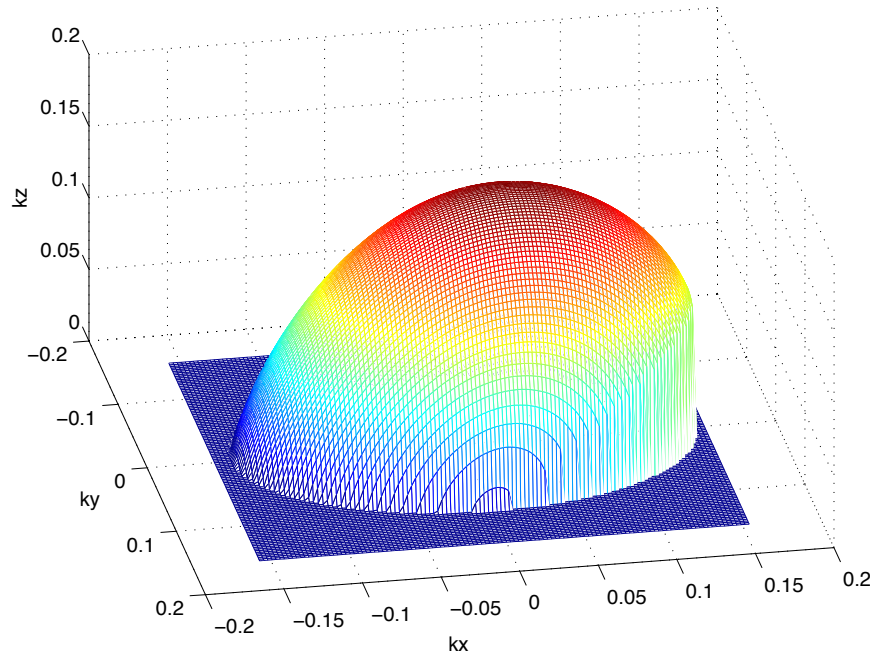


Figure 1: Dispersion relation of 3D tilted TI media. guojian2-dispersion [NR]

WAVEFIELD EXTRAPOLATION OPERATOR

For a homogeneous medium, the wavefield can be extrapolated by an anisotropic phase shift in the Fourier domain as follows:

$$P^{z+1}(k_x, k_y) = P^z(k_x, k_y)e^{k_z \Delta z}. \quad (9)$$

In reality, the velocity and anisotropy parameters change laterally. PSPI, explicit methods, or a combination of PSPI and explicit correction will remedy this problem. We extrapolate the wavefield by an isotropic operator with an explicit correction operator as follows:

$$P^{z+1}(k_x, k_y) = \left[P^z(k_x, k_y) e^{k_z^{iso} \Delta z} \right] e^{(k_z - k_z^{iso}) \Delta z}. \quad (10)$$

where $k_z^{iso} = \sqrt{\frac{\omega^2}{V_{p0}^2} - (k_x^2 + k_y^2)}$. In VTI media, the correction operator $e^{(k_z - k_z^{iso}) \Delta z}$ is circularly symmetric. This allows us to use a 1D algorithm to replace the 2D operator by McClellan transformations (McClellan and Parks, 1972; McClellan and Chan, 1977; Hale, 1991a). However, tilting the symmetry axis in tilted TI media breaks the circular symmetry. As a result, we need to design a 2D convolution operator in the Fourier domain for wavefield extrapolation in 3D tilted TI media.

The correction operator is not symmetric for axes x or y in tilted TI media. This means

$$F(k_x, k_y) = e^{(k_z(k_x, k_y) - k_z^{iso}) \Delta z}$$

is not an even function of k_x and k_y . However, we can decompose the function $F(k_x, k_y)$ into either even or odd functions of k_x and k_y , and approximate the even parts with cosine functions and the odd parts with sine functions.

We can decompose the function $F(k_x, k_y)$ into even and odd parts for the axis k_x by

$$F^e(k_x, k_y) = \frac{1}{2} [F(k_x, k_y) + F(-k_x, k_y)], \quad (11)$$

$$F^o(k_x, k_y) = \frac{1}{2} [F(k_x, k_y) - F(-k_x, k_y)]. \quad (12)$$

We can decompose the operator F^e and F^o into odd or even parts for the axis k_y by

$$F^{ee}(k_x, k_y) = \frac{1}{2} [F^e(k_x, k_y) + F^e(k_x, -k_y)], \quad (13)$$

$$F^{eo}(k_x, k_y) = \frac{1}{2} [F^e(k_x, k_y) - F^e(k_x, -k_y)], \quad (14)$$

$$F^{oe}(k_x, k_y) = \frac{1}{2} [F^o(k_x, k_y) + F^o(k_x, -k_y)], \quad (15)$$

$$F^{oo}(k_x, k_y) = \frac{1}{2} [F^o(k_x, k_y) - F^o(k_x, -k_y)]. \quad (16)$$

The function $F^{ee}(k_x, k_y)$ is an even function of both k_x and k_y , so it can be approximated by

$$F^{ee}(k_x, k_y) = \sum_{n_x, n_y} a_{n_x n_y}^{ee} \cos(n_x \Delta x k_x) \cos(n_y \Delta y k_y), \quad (17)$$

The function $F^{oe}(k_x, k_y)$ is an even function of k_y and an odd function of k_x , so it can be approximated by

$$F^{oe}(k_x, k_y) = \sum_{n_x, n_y} a_{n_x n_y}^{oe} \sin(n_x \Delta x k_x) \cos(n_y \Delta y k_y). \quad (18)$$

The function $F^{eo}(k_x, k_y)$ is an even function of k_x and an odd function of k_y , so it can be approximated by

$$F^{eo}(k_x, k_y) = \sum_{n_x, n_y} a_{n_x n_y}^{eo} \cos(n_x \Delta x k_x) \sin(n_y \Delta y k_y). \quad (19)$$

The function $F^{oo}(k_x, k_y)$ is an odd function of both k_x, k_y , so it can be approximated by

$$F^{oo}(k_x, k_y) = \sum_{n_x, n_y} a_{n_x n_y}^{oo} \sin(n_x \Delta x k_x) \sin(n_y \Delta y k_y). \quad (20)$$

Coefficients $a_{n_x n_y}^{ee}$, $a_{n_x n_y}^{oe}$, $a_{n_x n_y}^{eo}$ and $a_{n_x n_y}^{oo}$ can be estimated by the weighted least-square method (Thorbecke, 1997), which can be solved by QR decomposition (Baumstein and Anderson, 2003; Shan and Biondi, 2004b). Appendix A discusses how to estimate the coefficients $a_{n_x n_y}^{ee}$, $a_{n_x n_y}^{oe}$, $a_{n_x n_y}^{eo}$ and $a_{n_x n_y}^{oo}$ in detail.

The original operator $F(k_x, k_y)$ can be obtained from $F^{ee}(k_x, k_y)$, $F^{eo}(k_x, k_y)$, $F^{oe}(k_x, k_y)$ and $F^{oo}(k_x, k_y)$ by

$$F(k_x, k_y) = F^{ee}(k_x, k_y) + F^{eo}(k_x, k_y) + F^{oe}(k_x, k_y) + F^{oo}(k_x, k_y). \quad (21)$$

Appendix B derives the inverse Fourier transform of the functions $F^{ee}(k_x, k_y)$, $F^{eo}(k_x, k_y)$, $F^{oe}(k_x, k_y)$ and $F^{oo}(k_x, k_y)$, and obtains the inverse Fourier transform of the function $F(k_x, k_y)$ as follows:

$$\mathcal{F}^{-1}\{F(k_x, k_y)\} = \sum_{n_x, n_y} c_{n_x, n_y} \delta(x + n_x \Delta x, y + n_y \Delta y), \quad (22)$$

where

$$n_x = -N_x, -N_x + 1, \dots, -1, 0, 1, \dots, N_x - 1, N_x,$$

$$n_y = -N_y, -N_y + 1, \dots, -1, 0, 1, \dots, N_y - 1, N_y,$$

and c_{n_x, n_y} is as follows:

$$c_{00} = a_{00}^{ee}, \quad (23)$$

$$c_{n_x, n_y} = \frac{1}{4} \left[\left(a_{n_x n_y}^{ee} - a_{n_x n_y}^{oo} \right) + i \left(a_{n_x n_y}^{eo} + a_{n_x n_y}^{oe} \right) \right], \quad \text{if } n_x > 0 \text{ and } n_y > 0 \quad (24)$$

$$c_{n_x, n_y} = \frac{1}{4} \left[\left(a_{n_x n_y}^{ee} + a_{n_x n_y}^{oo} \right) + i \left(a_{n_x n_y}^{eo} - a_{n_x n_y}^{oe} \right) \right], \quad \text{if } n_x < 0 \text{ and } n_y > 0, \quad (25)$$

$$c_{n_x, n_y} = \frac{1}{4} \left[\left(a_{n_x n_y}^{ee} + a_{n_x n_y}^{oo} \right) + i \left(-a_{n_x n_y}^{eo} + a_{n_x n_y}^{oe} \right) \right], \quad \text{if } n_x > 0 \text{ and } n_y < 0 \quad (26)$$

$$c_{n_x, n_y} = \frac{1}{4} \left[\left(a_{n_x n_y}^{ee} - a_{n_x n_y}^{oo} \right) - i \left(a_{n_x n_y}^{eo} + a_{n_x n_y}^{oe} \right) \right]. \quad \text{if } n_x < 0 \text{ and } n_y < 0 \quad (27)$$

Let $P^z(x, y)$ be the inverse Fourier transform of $P^z(k_x, k_y)$. It is well known that

$$\delta(x + n_x \Delta x, y + n_y \Delta y) ** P^z(x, y) = P^z(x + n_x \Delta x, y + n_y \Delta y),$$

where “**” is 2D convolution. From the Fourier transform theory, we have

$$\mathcal{F}^{-1}\{F(k_x, k_y)P^z(k_x, k_y)\} = \mathcal{F}^{-1}\{F(k_x, k_y)\} ** P^z(x, y). \quad (28)$$

Therefore, we can apply the correction operator on the wavefield in the space domain as follows:

$$\mathcal{F}^{-1}\{F(k_x, k_y)\} ** P^z(x, y) = \sum_{n_x, n_y} c_{n_x, n_y} P^z(x + n_x \Delta x, y + n_y \Delta y). \quad (29)$$

From the above derivation, we know that the correction operator is designed in the Fourier domain and is implemented as a convolution in the space domain. For a laterally varying medium, we build a table of the convolution coefficients. When we run wavefield extrapolation, for each space position, we search for the corresponding convolution coefficients from that table and convolve the wavefield with these coefficients at that space position.

FILTER LENGTH, COST, AND ACCURACY

For 3D tilted TI media, the explicit correction operator is a 2D convolution operator. For a medium with lateral variation, a table of the convolution coefficients c_{n_x, n_y} are calculated before the wavefield extrapolation. Long filters can extrapolate high-angle energy accurately. However, it is too expensive to run a 2D convolution filter as long as 19 points in both the x and y directions. Furthermore, it is not practical to store such a big table in the memory. By the weighted least-square method, we can shorten the filter length at the price of losing accuracy for the high-angle energy.

We test a 2D example to check how the length of a filter affects its accuracy. The medium is homogeneous, in which the P-wave velocity in the direction parallel to the symmetry axis is 2000m/s, $\varepsilon = 0.4$, $\delta = 0.2$ and $\varphi = \frac{\pi}{6}$. The frequency is 45.0 Hz.

Let k_x^{max} be the beginning wavenumber for the evanescent energy. We assign a weight of 1 to the wavenumbers smaller than k_x^{max} and a weight of 0.001 to the wavenumbers bigger than k_x^{max} . In Figure 2, the phase for the even part of the 19-point filter example is very close to the true operator. In this model, the beginning wavenumber for the evanescent energy k_x^{max} is 0.15. In Figure 3, the phase curve for the even part of the 5-point filter oscillates around the true operator. The 5-point filter is not accurate even for the low wavenumber energy. If our aim is to guarantee the accuracy of the low-angle (low-wavenumber) energy, we can assign big weights to the low-angle energy but small weights to the high-angle energy. We can also smooth the amplitude and phase of the high angle-energy. Now we assign a weight of 1 to the wavenumbers smaller than $\frac{5}{6}k_x^{max}$ and a weight of 0.001 to the wavenumbers bigger than $\frac{5}{6}k_x^{max}$. In this model, $\frac{5}{6}k_x^{max}$ is 0.125. Figure 4 shows the phase curve of the 5-point filter after we change the weighting policy. The new 5-point filter is very close to the true operator at the low wavenumbers (smaller than 0.12) but has a big error at the high wavenumbers.

Though we lose the accuracy of high-angle energy when shorten the filter when we shorten the filter, we greatly improve the efficiency of our algorithm. If we use the 5-point filter in both

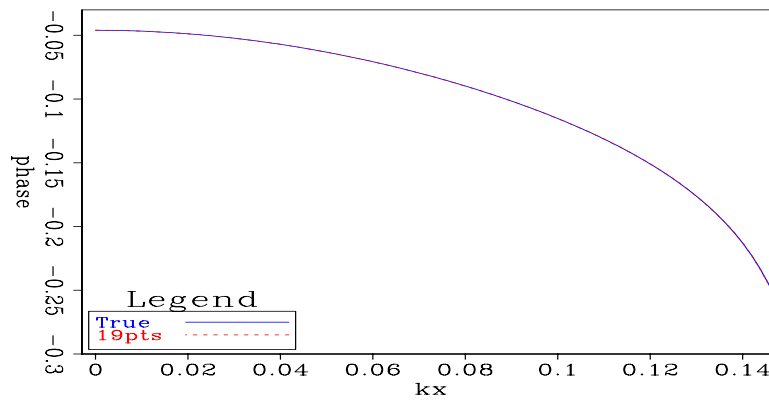


Figure 2: Comparison between the phase curves for the even part of the 19-point filter and the true operator. The continuous curve is the phase of the true operator and the dashed line is the phase of the 19-point filter. `guojian2-approx19` [ER]

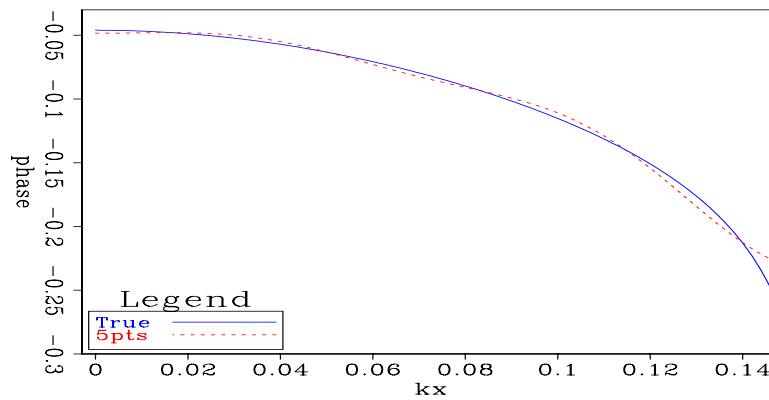


Figure 3: Comparison between the phase curves for the even part of the 5-point filter and the true operator. The continuous curve is the phase of the true operator and the dashed line is the phase of the 5-point filter. `guojian2-approx5` [ER]

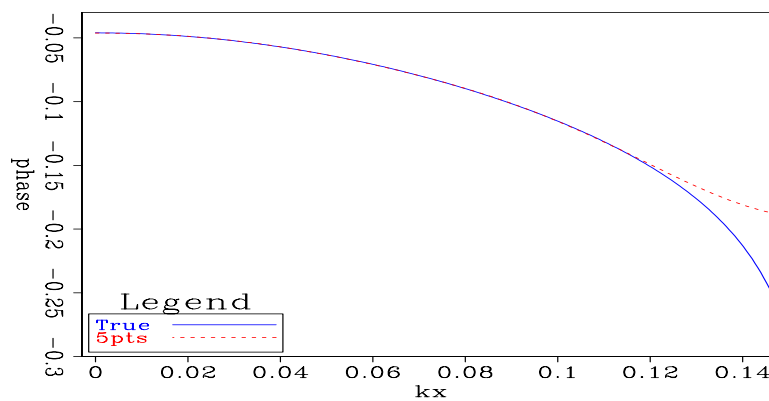


Figure 4: Comparison between the phase curves for the even part of the new 5-point filter and the true operator. The continuous curve is the phase of the true operator and the dashed line is the phase of the new 5-point filter. `guojian2-approxw5` [ER]

inline and crossline directions in 3D wavefield extrapolation, the correction operator is a 9×9 2D filter, while it is a 37×37 2D filter if we use the 19-point filter. Therefore using the 5-pointer filter, computation cost for the convolution in 3D wavefield extrapolation is about $\frac{1}{16}$ the cost using the 19-pointer filter. Furthermore, when the media is not homogeneous, searching for the coefficients of a filter in the coefficient table plays an important role in 3D. The total size of the coefficient table of the 5-point filter is about $\frac{1}{16}$ the size of the 19-point filter in 3D. If we build the table with 100 discrete $\omega/V_{p0}s$, 10 discrete εs and 10 discrete δs , the size of table is about 8 Megabyte for the 5-point filter and is about 128 Megabyte for the 19-point filter. The speed of searching in a 8 Megabyte is much faster than that in a 128 Megabyte table. By shortening the filter, we can greatly reduce the cost for the explicit correction operator in 3D wavefield extrapolation.

We lose the accuracy of high-angle energy when we shorten the length of the filter. But we can apply plane-wave decomposition and tilted coordinates (Shan and Biondi, 2004a) to make the wavefield-extrapolation direction close to the direction of wave propagation. By doing this, we can get good accuracy for the high-angle energy even with a less accurate operator.

NUMERICAL EXAMPLE

We first compare the 19-point filter and the improved 5-point filter using a 2D impulse response and a 2D synthetic dataset example. Then we show the 3D impulse responses for the improved 5-point filter and compare them with the impulse response of the anisotropic phase-shift method.

2D impulse response

Figure 5 compares the impulse response of the 19-point filter with that of the improved 5-point filter. The medium of the impulse response is a homogeneous medium, in which the velocity is 2000 m/s, the anisotropy parameters $\varepsilon = 0.4$ and $\delta = 0.2$, and the tilting angle $\varphi = \frac{\pi}{6}$. The travel time for the three impulse are 0.4 s, 0.6 s and 0.8 s, respectively. From Figure 5, we can see that the impulse response of the improved 5-point filter is very similar to that of the 19-point filter at low-angle energy but is different from the 19-point filter at high-angle energy. The improved 5-point filter is accurate for the energy up to 50° in the impulse response, compared to the 19-point filter.

A synthetic anisotropic dataset

Figure 6 compares the 19-point filter with the new 5-point filter for the migration of an anisotropic synthetic dataset. Shan and Biondi (2005) migrate this dataset with the anisotropic plane-wave migration in tilted coordinates. Figure 6(a) shows the density model of this synthetic dataset. We can see the steeply dipping salt flank in the density model. Figure 6(b) is the anisotropic plane-wave migration in tilted coordinates with the 19-point filter. Figure 6(c)

is the anisotropic plane-wave migration in tilted coordinates with the improved 5-point filter. The migration result of the new 5-point filter is very close to the 19-point filter, though it loses a little resolution at the salt flank. This synthetic data example shows that we can get good accuracy for high-angle energy in tilted coordinates, though we use the improved 5-point filter, which is less accurate than 19-point filter.

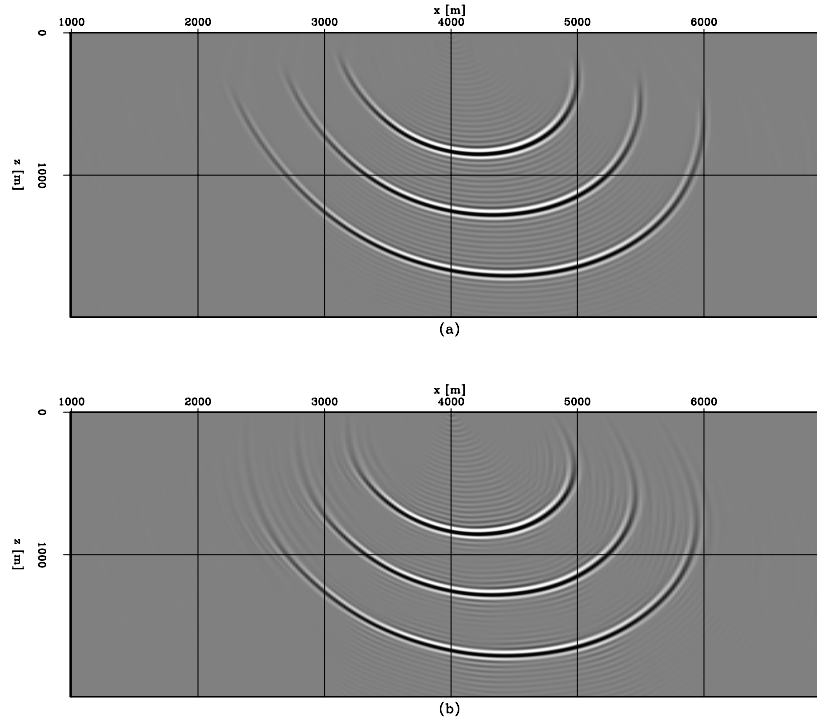


Figure 5: Comparison of the 2D impulse response of the 19-point filter and the improved 5-point filter. (a) The impulse response of the 19-point filter. (b) The impulse response of the improved 5-point filter. guojian2-oldnew [CR]

3D impulse response

Figures 7-9 compare the impulse responses of our algorithm with those of anisotropic phase shift method. The medium is a homogeneous, tilted TI medium. The symmetry axis of the medium is in the (x, z) plane and is tilted 30° from the vertical direction. The P-wave velocity in the direction parallel to the symmetry axis is 2000 m/s. The anisotropy parameters ε and δ are 0.4 and 0.2, respectively. The location of the impulse is at $x = 2000$ m and $y = 2000$ m. The travel time for the three impulses are 0.4 s, 0.6 s and 0.8 s, respectively. Figure 7 shows a depth slice of the impulse responses at $z = 1500$ m. Figure 7(a) is obtained with our algorithm and Figure 7(b) is obtained with the anisotropic phase-shift method. First, Figure 7(a) is very similar to 7(b). Second, the depth slice of the impulse response is not a circle. The wave propagates faster in y than in x direction. Third, the impulse location $x = 2000$ m and $y = 2000$ m is not the center of the impulse response. The impulse response is symmetric along $y = 2000$ m, but it is not symmetric along $x = 2000$ m. Figure 8 shows an in-line slice of

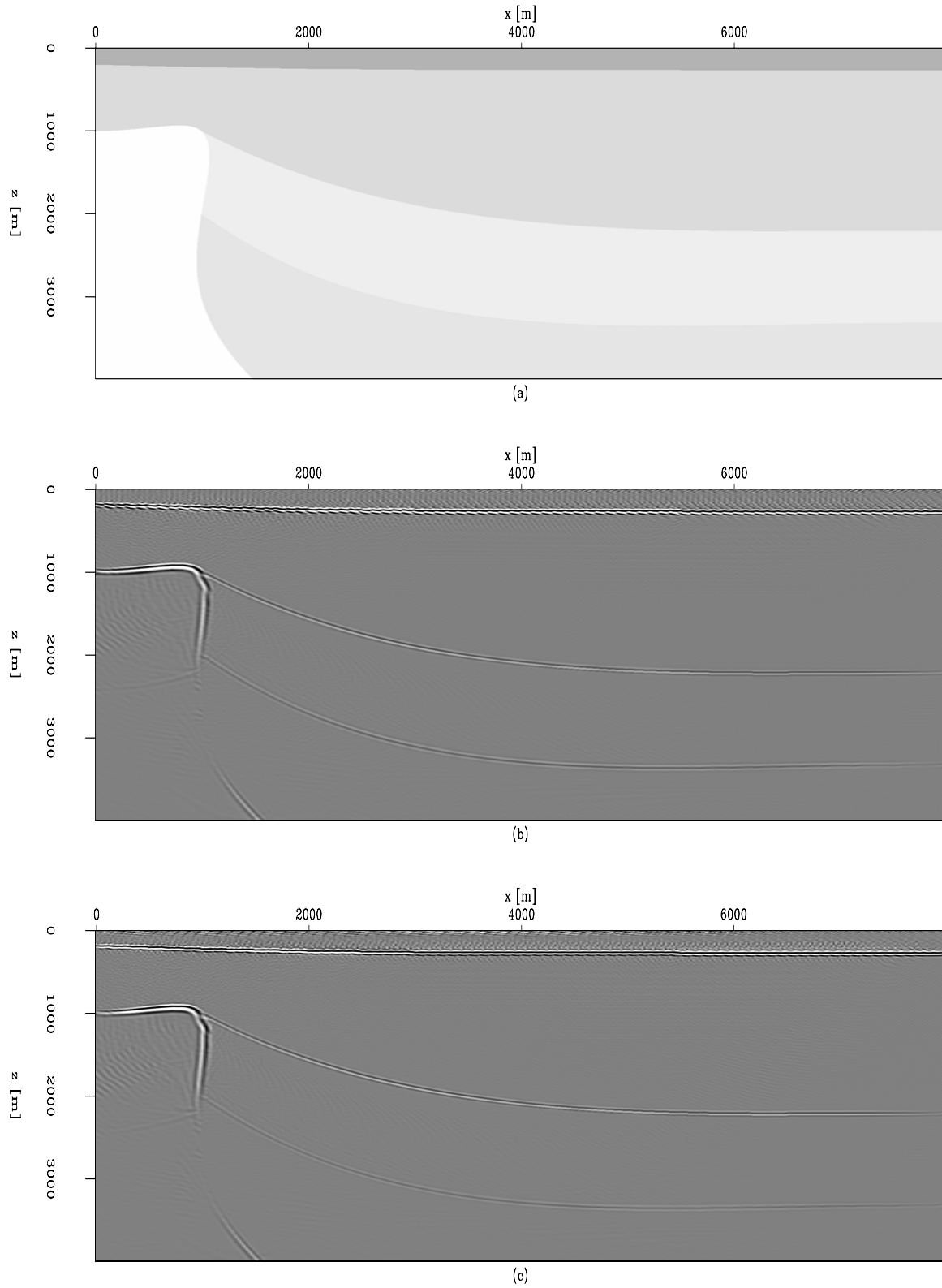


Figure 6: Comparison of the anisotropic plane-wave migration of a synthetic dataset by the 19-point filter and the new 5-point filter. (a) The density model. (b) The migration result of the 19-point filter. (c) The migration result of the new 5-point filter. [guojian2-filtercom](#) [CR]

the impulse responses at $y = 2000$ m. Figure 8(a) is obtained with our algorithm and Figure 8(b) is obtained with the anisotropic phase-shift method. Figure 9 shows a cross-line slice of the impulse responses at $x = 2000$ m. Figure 9(a) is obtained with our algorithm and Figure 9(b) is obtained with the anisotropic phase-shift method. From Figure 8 and 9, we can see that the impulse of our algorithm is very close to that of the anisotropic phase-shift method at low-angle energy and is different from the the anisotropic phase-shift method at high-angle energy. Since the medium is homogeneous, the anisotropic phase-shift method is accurate. So our algorithm is accurate for the energy up to 50° in the impulse response, compared to the anisotropic phase-shift method.

CONCLUSION

We present a 3D wavefield-extrapolation algorithm for tilted TI media. The wavefield is extrapolated by an implicit isotropic operator with an explicit anisotropic correction. Tilted TI media are not circularly symmetric, therefore the explicit anisotropic correction has to be a 2D convolution operator. It is designed by a weighed least-square method. With proper weights, we can shorten the correction operator and reduce the computation cost at the price of losing the accuracy of high-angle energy. A 2D synthetic dataset example shows that we can still have good accuracy for high-angle energy by decomposing the wavefields into plane waves and extrapolating them in tilted coordinates. 3D impulse responses show that our algorithm is accurate up to 50° with the short 2D filter.

ACKNOWLEDGMENTS

We would like to thank ExxonMobil for making the synthetic data available.

REFERENCES

- Abramowitz, M., and Stegun, I., 1972, Solutions of quartic equations *in* Handbook of Mathematical Functions with Formulas, Graphs, and Mathematical Tables. New York: Dover., 17–18.
- Baumstein, A., and Anderson, J., 2003, Wavefield extrapolation in laterally varying VTI media *in* 73rd Ann. Internat. Mtg. Soc. of Expl. Geophys., 945–948.
- Blacquiere, G., Debeye, H. W. J., Wapenaar, C. P. A., and Berkhout, A. J., 1989, 3D table-driven migration: Geophys. Prosp., **37**, 925–958.
- Ferguson, R. J., and Margrave, G. F., 1998, Depth migration in TI media by nonstationary phase shift *in* 68th Ann. Internat. Mtg. Soc. of Expl. Geophys., 1831–1834.
- Hale, D., 1991a, 3-D depth migration via McClellan transformations: Geophysics, **56**, 1778–1785.

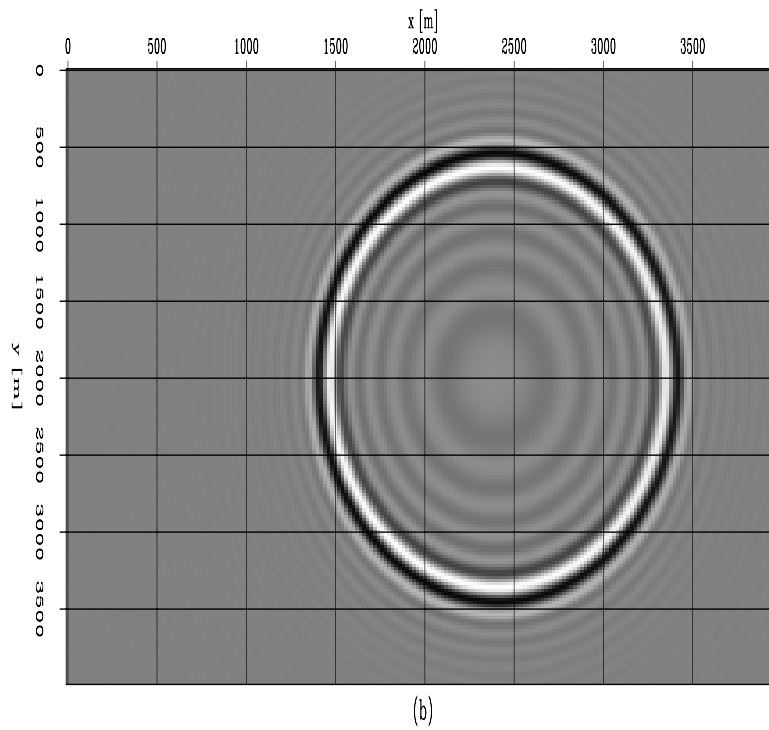
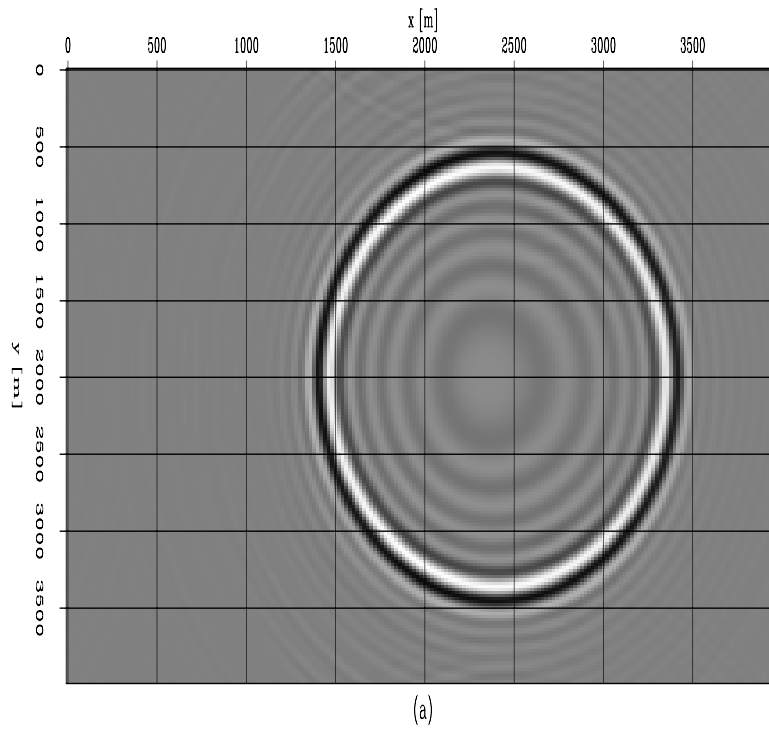


Figure 7: A horizontal slice of the 3D impulse response in a tilted TI medium at a depth of $z = 1000$ m: (a) Our algorithm. (b) The anisotropic phase-shift method. [guojian2-depth](#) [CR]

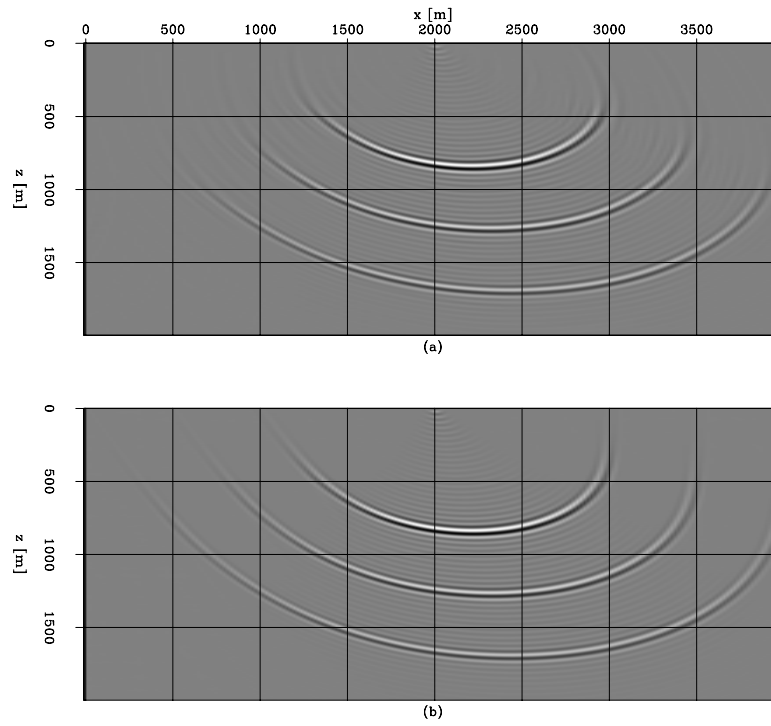


Figure 8: An inline slice of the 3D impulse response in a tilted TI medium at $y = 2000$ m: (a) Our algorithm. (b) The anisotropic phase-shift method. `guojian2-inline` [CR]

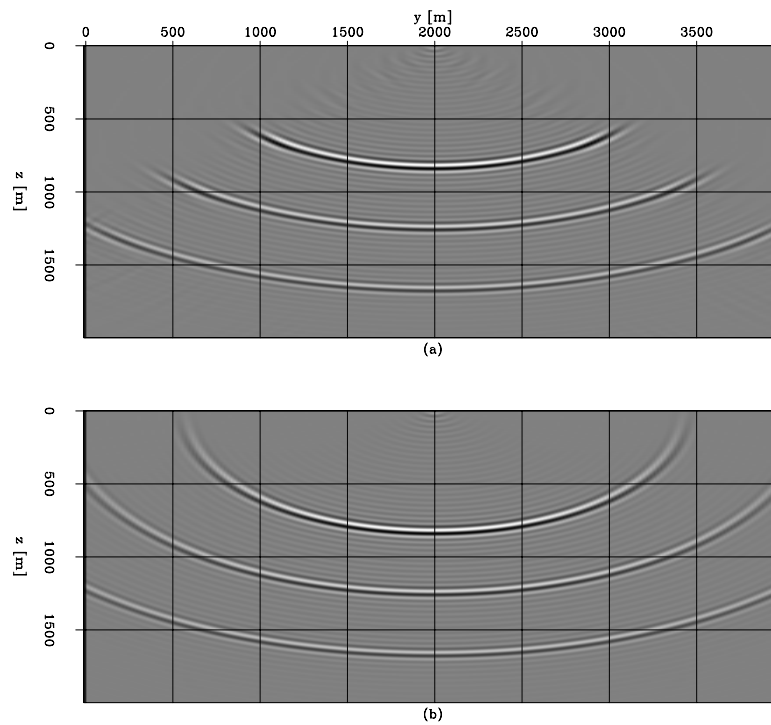


Figure 9: A cross-line slice of the 3D impulse response in a tilted TI medium at $x = 2000$ m: (a) Our algorithm. (b) The anisotropic phase-shift method. `guojian2-cross` [CR]

- , 1991b, Stable explicit depth extrapolation of seismic wavefields: *Geophysics*, **56**, 1770–1777.
- Holberg, O., 1988, Towards optimum one-way wave propagation: *Geophys. Prosp.*, **36**, 99–114.
- McClellan, J., and Chan, D., 1977, A 2-D FIR filter structure derived from the Chebychev recursion: *IEEE Trans. Circuits Syst.*, **CAS-24**, 372–378.
- McClellan, J. H., and Parks, T. W., 1972, Equiripple approximation of fan filters: *Geophysics*, **37**, 573–583.
- Ristow, D., and Ruhl, T., 1997, Migration in transversely isotropic media using implicit operators *in* 67th Ann. Internat. Mtg. Soc. of Expl. Geophys., 1699–1702.
- Rousseau, J. H. L., 1997, Depth migration in heterogeneous, transversely isotropic media with the phase-shift-plus-interpolation method *in* 67th Ann. Internat. Mtg. Soc. of Expl. Geophys., 1703–1706.
- Shan, G., and Biondi, B., 2004a, Imaging overturned waves by plane-wave migration in tilted coordinates: 74th Ann. Internat. Mtg., Soc. of Expl. Geophys., Expanded Abstracts, 969–972.
- , 2004b, Wavefield extrapolation in laterally-varying tilted TI media: SEP- **117**, 1–10.
- , 2005, Imaging steeply dipping reflectors in TI media by wavefield extrapolation: SEP- **120**, 63–76.
- Thomsen, L., 1986, Weak elastic anisotropy: *Geophysics*, **51**, 1954–1966.
- Thorbecke, J., 1997, Common focus point technology *in* Ph.D. thesis. Delft University of Technology.
- Tsvankin, I., 1996, P-wave signatures and notation for transversely isotropic media: An overview: *Geophysics*, **61**, 467–483.
- Uzcategui, O., 1995, 2-D depth migration in transversely isotropic media using explicit operators: *Geophysics*, **60**, 1819–1829.
- Zhang, J., Verschuur, D. J., and Wapenaar, C. P. A., 2001a, Depth migration of shot records in heterogeneous, transversely isotropic media using optimum explicit operators: *Geophys. Prosp.*, **49**, 287–299.
- Zhang, J., Wapenaar, C., and Verschuur, D., 2001b, 3-D depth migration in VTI media with explicit extrapolation operators *in* 71st Ann. Internat. Mtg. Soc. of Expl. Geophys., 1085–1088.

APPENDIX A

This appendix discusses how to estimate the coefficients $a_{n_x n_y}^{ee}$, $a_{n_x n_y}^{oe}$, $a_{n_x n_y}^{eo}$ and $a_{n_x n_y}^{oo}$ in equations (17)-(20).

We begin with equation (17), as the other three equations are silimiar. Let Δk_x and Δk_y be the sampling of the wavenumbers k_x and k_y , respectively. To mimic the behavior of the original operator F^{ee} , we need to estimate $a_{n_x n_y}^{ee}$, so that

$$F^{ee}(k_x, k_y) \approx \sum_{n_x, n_y} a_{n_x n_y}^{ee} \cos(n_x \Delta x k_x) \cos(n_y \Delta y k_y),$$

for $k_x \in [0, k_x^{Nyquist}]$ and $k_y \in [0, k_y^{Nyquist}]$, where $k_x^{Nyquist}$ is the Nyquist wavenumber $\frac{\pi}{\Delta x}$ and $k_y^{Nyquist}$ is the Nyquist wavenumber $\frac{\pi}{\Delta y}$. Let M_x be $k_x^{Nyquist} / \Delta k_x$ and M_y be $k_y^{Nyquist} / \Delta k_y$. The coefficients can be estimated by the following fitting goals:

$$\mathbf{W}(\mathbf{A}^{ee} \mathbf{a}^{ee} - \mathbf{f}^{ee}) \approx \mathbf{0}, \quad (\text{A-1})$$

where

$$\mathbf{a}^{ee} = \left(a_{00}^{ee}, a_{10}^{ee}, \dots, a_{n_x-1, n_y}^{ee}, a_{n_x, n_y}^{ee}, a_{n_x+1, n_y}^{ee}, \dots, a_{N_x, N_y}^{ee} \right)^T.$$

\mathbf{A}^{ee} is a matrix with the elements

$$A_{mn}^{ee} = \cos(m_x n_x \Delta k_x \Delta x) \cos(m_y n_y \Delta k_y \Delta y),$$

where $m = m_y(M_y + 1) + m_x$ and $n = n_y(N_y + 1) + n_x$. \mathbf{f}^{ee} is a vector as follows

$$\mathbf{f}^{ee} = \left(f_{00}^{ee}, f_{10}^{ee}, \dots, f_{m_x-1, m_y}^{ee}, a_{m_x, m_y}^{ee}, f_{m_x+1, m_y}^{ee}, \dots, f_{M_x, M_y}^{ee} \right)^T,$$

where $f_{m_x, m_y}^{ee} = F^{ee}(m_x \Delta k_x, m_y \Delta k_y)$. \mathbf{W} is a diagonal matrix with the weights for the wavenumbers k_x, k_y . High weights are assigned to the wavenumbers of interest. The wavenumbers, such as the evacent energy, are not of interest and are assigned low weights. Given the same weight matrix \mathbf{W} , the matrix $\mathbf{W}\mathbf{A}^{ee}$ are same though f^{ee} changes with the function $F^{ee}(k_x, k_y)$. Therefore, QR decomposition is a good way to solve the fitting goal (A-1). First, we run QR decomposition on matrix $\mathbf{W}\mathbf{A}$: $\mathbf{W}\mathbf{A} = \mathbf{Q}\mathbf{R}$, where \mathbf{Q} is an orthogonal matrix and \mathbf{R} is an upper triangular matrix. We write down the matrixes \mathbf{Q} and \mathbf{R} . Given the function $F^{ee}(k_x, k_y)$, we calculate \mathbf{f}^{ee} . The solution of fitting goal (A-1) \mathbf{a}^{ee} is given by

$$\mathbf{a}^{ee} = \mathbf{R}^{-1} \mathbf{Q}^T \mathbf{W} \mathbf{f}^{ee}. \quad (\text{A-2})$$

For equation (18), we have the following fitting goal:

$$\mathbf{W}(\mathbf{A}^{oe} \mathbf{a}^{oe} - \mathbf{f}^{oe}) \approx \mathbf{0}, \quad (\text{A-3})$$

where

$$\mathbf{a}^{oe} = \left(a_{00}^{oe}, a_{10}^{oe}, \dots, a_{n_x-1, n_y}^{oe}, a_{n_x, n_y}^{oe}, a_{n_x+1, n_y}^{oe}, \dots, a_{N_x, N_y}^{oe} \right)^T,$$

and \mathbf{f}^{oe} in equation (A-3) is

$$\mathbf{f}^{oe} = \left(f_{00}^{oe}, f_{10}^{oe}, \dots, f_{m_x-1, m_y}^{oe}, a_{m_x, m_y}^{oe}, f_{m_x+1, m_y}^{oe}, \dots, f_{M_x, M_y}^{oe} \right)^T,$$

where $f_{m_x, m_y}^{oe} = F^{oe}(m_x \Delta k_x, m_y \Delta k_y)$. \mathbf{A}^{oe} in equation (A-3) is a matrix with the elements

$$A_{mn}^{oe} = \sin(m_x n_x \Delta k_x \Delta x) \cos(m_y n_y \Delta k_y \Delta y),$$

where $m = m_y(M_x + 1) + m_x$ and $n = n_y(N_x + 1) + n_x$. For equation (19), we have the following fitting goal:

$$\mathbf{W}(\mathbf{A}^{eo} \mathbf{a}^{eo} - \mathbf{f}^{eo}) \approx \mathbf{0}, \quad (\text{A-4})$$

where

$$\mathbf{a}^{eo} = \left(a_{00}^{eo}, a_{10}^{eo}, \dots, a_{n_x-1, n_y}^{eo}, a_{n_x, n_y}^{eo}, a_{n_x+1, n_y}^{eo}, \dots, a_{N_x, N_y}^{eo} \right)^T,$$

and \mathbf{f}^{eo} in equation (A-3) is

$$\mathbf{f}^{eo} = \left(f_{00}^{eo}, f_{10}^{eo}, \dots, f_{m_x-1, m_y}^{eo}, a_{m_x, m_y}^{eo}, f_{m_x+1, m_y}^{eo}, \dots, f_{M_x, M_y}^{eo} \right)^T,$$

where $f_{m_x, m_y}^{eo} = F^{eo}(m_x \Delta k_x, m_y \Delta k_y)$. \mathbf{A}^{eo} in equation (A-4) is a matrix with the elements

$$A_{mn}^{eo} = \cos(m_x n_x \Delta k_x \Delta x) \sin(m_y n_y \Delta k_y \Delta y),$$

where $m = m_y(M_x + 1) + m_x$ and $n = n_y(N_x + 1) + n_x$. For equation (20), we have the following fitting goal:

$$\mathbf{W}(\mathbf{A}^{oo} \mathbf{a}^{oo} - \mathbf{f}^{oo}) \approx \mathbf{0}, \quad (\text{A-5})$$

where

$$\mathbf{a}^{oo} = \left(a_{00}^{oo}, a_{10}^{oo}, \dots, a_{n_x-1, n_y}^{oo}, a_{n_x, n_y}^{oo}, a_{n_x+1, n_y}^{oo}, \dots, a_{N_x, N_y}^{oo} \right)^T,$$

and \mathbf{f}^{oo} in equation (A-3) is

$$\mathbf{f}^{oo} = \left(f_{00}^{oo}, f_{10}^{oo}, \dots, f_{m_x-1, m_y}^{oo}, a_{m_x, m_y}^{oo}, f_{m_x+1, m_y}^{oo}, \dots, f_{M_x, M_y}^{oo} \right)^T,$$

where $f_{m_x, m_y}^{oo} = F^{oo}(m_x \Delta k_x, m_y \Delta k_y)$. \mathbf{A}^{oo} in equation (A-5) is a matrix with the elements

$$A_{mn}^{oo} = \sin(m_x n_x \Delta k_x \Delta x) \sin(m_y n_y \Delta k_y \Delta y),$$

where $m = m_y(M_x + 1) + m_x$ and $n = n_y(N_x + 1) + n_x$. Fitting goals (A-3), (A-4), and (A-5) can be solved in the same way as equation (A-1). The solution of fitting goal (A-3), (A-4), (A-5) are given by

$$\mathbf{a}^{oe} = (\mathbf{R}^{oe})^{-1} (\mathbf{Q}^{oe})^T \mathbf{W} \mathbf{f}^{oe}, \quad (\text{A-6})$$

$$\mathbf{a}^{eo} = (\mathbf{R}^{eo})^{-1} (\mathbf{Q}^{eo})^T \mathbf{W} \mathbf{f}^{eo}, \quad (\text{A-7})$$

$$\mathbf{a}^{oo} = (\mathbf{R}^{oo})^{-1} (\mathbf{Q}^{oo})^T \mathbf{W} \mathbf{f}^{oo}, \quad (\text{A-8})$$

where \mathbf{Q}^{oe} , \mathbf{R}^{oe} , \mathbf{Q}^{eo} , \mathbf{R}^{eo} and \mathbf{Q}^{oo} , \mathbf{R}^{oo} are the QR decomposition result of the matrixs $\mathbf{W} \mathbf{A}^{oe}$, $\mathbf{W} \mathbf{A}^{eo}$ and $\mathbf{W} \mathbf{A}^{oo}$, respectively.

APPENDIX B

In this appendix, we derive the inverse Fourier transform of the correction operator $F(k_x, k_y)$.

It is well known that the inverse Fourier transform of the function $\cos n_x \Delta x k_x$, $\sin n_x \Delta x k_x$, $\cos n_y \Delta y k_y$, $\sin n_y \Delta y k_y$ are:

$$\mathcal{F}^{-1}\{\cos(n_x \Delta x k_x)\} = \frac{1}{2}(\delta(x - n_x \Delta x) + \delta(x + n_x \Delta x)), \quad (\text{B-1})$$

$$\mathcal{F}^{-1}\{\sin(n_x \Delta x k_x)\} = \frac{1}{2i}(\delta(x - n_x \Delta x) - \delta(x + n_x \Delta x)), \quad (\text{B-2})$$

$$\mathcal{F}^{-1}\{\cos(n_y \Delta y k_y)\} = \frac{1}{2}(\delta(y - n_y \Delta y) + \delta(y + n_y \Delta y)), \quad (\text{B-3})$$

$$\mathcal{F}^{-1}\{\sin(n_y \Delta y k_y)\} = \frac{1}{2i}(\delta(y - n_y \Delta y) - \delta(y + n_y \Delta y)). \quad (\text{B-4})$$

Let $\delta_{\pm n_x} = \delta(x \pm n_x \Delta x)$, $\delta_{\pm n_y} = \delta(y \pm n_y \Delta y)$ and $\delta_{\pm n_x, \pm n_y} = \delta(x \pm n_x \Delta x, y \pm n_y \Delta y)$. The inverse Fourier transform of the function $\cos(n_x \Delta x k_x) \cos(n_y \Delta y k_y)$ is :

$$\mathcal{F}^{-1}\{\cos(n_x \Delta x k_x) \cos(n_y \Delta y k_y)\} = \frac{1}{4}(\delta_{-n_x} + \delta_{+n_x}) * (\delta_{-n_y} + \delta_{+n_y}) \quad (\text{B-5})$$

$$= \frac{1}{4}(\delta_{-n_x, -n_y} + \delta_{-n_x, +n_y} + \delta_{+n_x, -n_y} + \delta_{+n_x, +n_y}). \quad (\text{B-6})$$

Similarly, the inverse Fourier transform of the functions $\cos(n_x \Delta x k_x) \sin(n_y \Delta y k_y)$, $\sin(n_x \Delta x k_x) \cos(n_y \Delta y k_y)$ and $\sin(n_x \Delta x k_x) \sin(n_y \Delta y k_y)$ are :

$$\mathcal{F}^{-1}\{\cos(n_x \Delta x k_x) \sin(n_y \Delta y k_y)\} = -\frac{i}{4}(\delta_{-n_x, -n_y} - \delta_{-n_x, +n_y} + \delta_{+n_x, -n_y} - \delta_{+n_x, +n_y}), \quad (\text{B-7})$$

$$\mathcal{F}^{-1}\{\sin(n_x \Delta x k_x) \cos(n_y \Delta y k_y)\} = -\frac{i}{4}(\delta_{-n_x, -n_y} + \delta_{-n_x, +n_y} - \delta_{+n_x, -n_y} - \delta_{+n_x, +n_y}), \quad (\text{B-8})$$

$$\mathcal{F}^{-1}\{\sin(n_x \Delta x k_x) \sin(n_y \Delta y k_y)\} = -\frac{1}{4}(\delta_{-n_x, -n_y} - \delta_{-n_x, +n_y} - \delta_{+n_x, -n_y} + \delta_{+n_x, +n_y}). \quad (\text{B-9})$$

Therefore the inverse Fourier transform of the functions $F^{ee}(k_x, k_y)$, $F^{oe}(k_x, k_y)$, $F^{eo}(k_x, k_y)$ and $F^{oo}(k_x, k_y)$ are:

$$\mathcal{F}^{-1}\{F^{ee}(k_x, k_y)\} = \sum_{n_x, n_y} \frac{1}{4} a_{n_x, n_y}^{ee} (\delta_{-n_x, -n_y} + \delta_{-n_x, +n_y} + \delta_{+n_x, -n_y} + \delta_{+n_x, +n_y}), \quad (\text{B-10})$$

$$\mathcal{F}^{-1}\{F^{oe}(k_x, k_y)\} = \sum_{n_x, n_y} -\frac{i}{4} a_{n_x, n_y}^{oe} (\delta_{-n_x, -n_y} + \delta_{-n_x, +n_y} - \delta_{+n_x, -n_y} - \delta_{+n_x, +n_y}), \quad (\text{B-11})$$

$$\mathcal{F}^{-1}\{F^{eo}(k_x, k_y)\} = \sum_{n_x, n_y} -\frac{i}{4} a_{n_x, n_y}^{eo} (\delta_{-n_x, -n_y} - \delta_{-n_x, +n_y} + \delta_{+n_x, -n_y} - \delta_{+n_x, +n_y}), \quad (\text{B-12})$$

$$\mathcal{F}^{-1}\{F^{oo}(k_x, k_y)\} = \sum_{n_x, n_y} -\frac{1}{4} a_{n_x, n_y}^{oo} (\delta_{-n_x, -n_y} - \delta_{-n_x, +n_y} - \delta_{+n_x, -n_y} + \delta_{+n_x, +n_y}). \quad (\text{B-13})$$

The correction operator $F(k_x, k_y)$ is the sum of $F^{ee}(k_x, k_y)$, $F^{oe}(k_x, k_y)$, $F^{eo}(k_x, k_y)$ and $F^{oo}(k_x, k_y)$. Therefore the inverse Fourier transform of the correction operator is:

$$\mathcal{F}^{-1}\{F(k_x, k_y)\} = \mathcal{F}^{-1}\{F^{ee}(k_x, k_y)\} + \mathcal{F}^{-1}\{F^{oe}(k_x, k_y)\} + \mathcal{F}^{-1}\{F^{eo}(k_x, k_y)\} + \mathcal{F}^{-1}\{F^{oo}(k_x, k_y)\} \quad (\text{B-14})$$

$$= \frac{1}{4} \sum_{n_x, n_y} (\delta_{-n_x, -n_y} c_{-n_x, -n_y} + \delta_{-n_x, +n_y} c_{-n_x, +n_y} + \delta_{+n_x, -n_y} c_{+n_x, -n_y} + \delta_{+n_x, +n_y} c_{+n_x, +n_y}) \quad (\text{B-15})$$

where

$$c_{-n_x, -n_y} = [(a_{n_x, n_y}^{ee} - a_{n_x, n_y}^{oo}) - i(a_{n_x, n_y}^{eo} + a_{n_x, n_y}^{oe})], \quad (\text{B-16})$$

$$c_{-n_x, +n_y} = [(a_{n_x, n_y}^{ee} + a_{n_x, n_y}^{oo}) + i(a_{n_x, n_y}^{eo} - a_{n_x, n_y}^{oe})], \quad (\text{B-17})$$

$$c_{+n_x, -n_y} = [(a_{n_x, n_y}^{ee} + a_{n_x, n_y}^{oo}) - i(a_{n_x, n_y}^{eo} - a_{n_x, n_y}^{oe})], \quad (\text{B-18})$$

$$c_{+n_x, +n_y} = [(a_{n_x, n_y}^{ee} - a_{n_x, n_y}^{oo}) + i(a_{n_x, n_y}^{eo} + a_{n_x, n_y}^{oe})]. \quad (\text{B-19})$$



Common azimuth migration for elliptical and VTI media

Satyakee Sen and Biondo Biondi¹

ABSTRACT

We derive the Common Azimuth downward continuation operator for elliptically anisotropic and VTI media. For elliptically anisotropic media, the Common Azimuth downward continuation operator derived by a stationary phase approximation of the full 3-D downward continuation operator is exact and it agrees with the constraint imposed by the Common Azimuth approximation on the propagation direction of the source and receiver rays. For VTI media, the dispersion relationship is much more complicated and results in a quartic equation for the stationary path. We introduce a bounded form of Common Azimuth migration for this kind of media, which allows us to develop closed-form analytical solutions without directly solving the quartic equation. Error analysis indicates that the derived analytical solution has similar accuracy as that obtained by solving the full quartic equation. 3-D impulse responses of the anisotropic Common Azimuth downward continuation operator also show significant differences compared to the isotropic operator even at moderate propagation angles.

INTRODUCTION

Over the past several decades, anisotropy has been recognized as one of the important factors effecting the accuracy of seismic imaging methods. If anisotropy is not taken into account by wavefield extrapolation operators, subsurface reflectors (especially steeply dipping ones) will be mispositioned. Thus, incorporating anisotropy into existing isotropic wavefield continuation operators has gained significant importance over the past several years. Several methods have been developed to handle anisotropy which include both implicit and explicit extrapolation operators. These include anisotropic implicit methods (Ristow and Ruhl, 1997), anisotropic PSPI (Rousseau, 1997), explicit operators (Uzcategui, 1995), (Zhang et al., 2001), reference isotropic with explicit correction filters (Baumstein and Anderson, 2003) and explicit anisotropic correction filters (Shan and Biondi, 2004). However, no such method has been developed to incorporate anisotropy into the Common Azimuth migration operator. Common Azimuth migration (Biondi and Palacharla, 1996) is one of the most computationally effective wavefield continuation method for large 3-D marine surveys. The computational effectiveness of this method can be attributed to the stationary path approximation that this method uses which shrinks the computational volume for full 3-D wavefields from a five-dimensional space to a four-dimensional space. This greatly reduces the computations that are involved

¹email: ssen@sep.stanford.edu, biondo@sep.stanford.edu

at each depth step. Thus, it would be extremely beneficial if anisotropy can be incorporated into the existing isotropic Common Azimuth migration downward continuation operator. In this paper, we develop a method for introducing anisotropy into Common Azimuth migration. In the following sections, we develop the anisotropic Common Azimuth migration operator, firstly for the relatively simple elliptically anisotropy media and then for the more complex VTI media. We then perform error analysis for our derived analytical solution for the VTI media and finally compare the 3-D impulse responses of the elliptically anisotropic Common Azimuth operator with that of the isotropic operator.

ELLIPTICAL ANISOTROPY

In this section, we derive the Common Azimuth downward continuation operator for an elliptically anisotropic media. The 3-D dispersion relation for VTI media given by Alkhalifah (1998) is:

$$k_z = \frac{\omega}{v} \sqrt{\frac{\frac{\omega^2}{v^2} - (k_x^2 + k_y^2)(1 + 2\epsilon)}{\frac{\omega^2}{v^2} - 2(k_x^2 + k_y^2)\eta(1 + 2\delta)}}, \quad (1)$$

where v is the vertical P wave velocity and $\mathbf{k}(k_x, k_y, k_z)$ is the wavenumber vector in Cartesian coordinates and ω is the circular frequency. The anisotropic parameters ϵ and δ are defined as:

$$\epsilon = \frac{C_{11} - C_{33}}{2C_{33}}, \delta = \frac{(C_{11} + C_{44})^2 - (C_{33} - C_{44})^2}{2C_{33}(C_{33} - C_{44})}. \quad (2)$$

In deriving this dispersion relation it is assumed that the shear wave velocity is zero. This assumption holds for the remainder of this paper. Now for an elliptically anisotropic media we have $\eta = 0$ (in other words $\epsilon = \delta$) so that the above equation simplifies to:

$$k_z = \sqrt{\frac{\omega^2}{v^2} - (k_x^2 + k_y^2)(1 + 2\epsilon)}. \quad (3)$$

Thus in 3-D the vertical wavenumber for the full Double Square Root (DSR) form of the elliptically anisotropic migration operator is:

$$k_z = \sqrt{\frac{\omega^2}{v(\mathbf{s}, z)^2} - (k_{sx}^2 + k_{sy}^2)(1 + 2\epsilon)} + \sqrt{\frac{\omega^2}{v(\mathbf{r}, z)^2} - (k_{rx}^2 + k_{ry}^2)(1 + 2\epsilon)}. \quad (4)$$

where $\mathbf{k}_s(k_{sx}, k_{sy})$ is the source wavenumber vector and $\mathbf{k}_r(k_{rx}, k_{ry})$ is receiver wavenumber vector. The equivalent form in midpoint-offset coordinates can be obtained by using the following simple transformations between the wavenumbers:

$$\mathbf{k}_s = \frac{\mathbf{k}_m - \mathbf{k}_h}{2}, \quad (5)$$

$$\mathbf{k}_r = \frac{\mathbf{k}_m + \mathbf{k}_h}{2}. \quad (6)$$

where $\mathbf{k}_m(k_{mx}, k_{my})$ is the midpoint wavenumber vector and $\mathbf{k}_h(k_{hx}, k_{hy})$ is the offset wavenumber vector. Substituting these transformations in equation (4) gives the vertical wavenumber for the elliptically anisotropic migration operator in midpoint-offset coordinates

$$k_z = \sqrt{\frac{\omega^2}{v(\mathbf{s}, z)^2} - \frac{1}{4} \left\{ (k_{mx} - k_{hx})^2 + (k_{my} - k_{hy})^2 \right\} (1 + 2\epsilon) + \frac{\omega^2}{v(\mathbf{r}, z)^2} - \frac{1}{4} \left\{ (k_{mx} + k_{hx})^2 + (k_{my} + k_{hy})^2 \right\} (1 + 2\epsilon)} \quad (7)$$

The Common Azimuth downward continuation operator introduces a reduction in the dimensionality of the dataset by evaluating the new wavefield at a subsequent depth step only along the offset azimuth of the data in the previous depth step. The downward continuation operator (Biondi and Palacharla, 1996) can be expressed as:

$$\begin{aligned} P_{z+\Delta z}(\omega, \mathbf{k}_m, k_{x_h}, y_h = 0) &= \int_{-\infty}^{+\infty} dk_{y_h} P_z(\omega, \mathbf{k}_m, k_{x_h}, y_h = 0) e^{-ik_z \Delta z} \\ &= P_z(\omega, \mathbf{k}_m, k_{x_h}, y_h = 0) \left\{ \int_{-\infty}^{+\infty} dk_{y_h} e^{-ik_z \Delta z} \right\} \\ &\approx P_z(\omega, \mathbf{k}_m, k_{x_h}, y_h = 0) A(\omega, \mathbf{k}_m, k_{x_h}) e^{-i\hat{k}_z \Delta z}. \end{aligned} \quad (8)$$

Since the common azimuth data is independent of k_{hy} , the integral can be pulled inside and analytically approximated by the stationary phase method. The stationary path approximation for the above operator can be found by setting the derivative of the wavenumber k_z with respect to k_{hy} to zero. This gives:

$$\hat{k}_{hy} = k_{my} \frac{\sqrt{\frac{\omega^2}{v(\mathbf{r}, z)^2} - \frac{1}{4}(k_{mx} + k_{hx})^2(1 + 2\epsilon)} \mp \sqrt{\frac{\omega^2}{v(\mathbf{s}, z)^2} - \frac{1}{4}(k_{mx} - k_{hx})^2(1 + 2\epsilon)}}{\sqrt{\frac{\omega^2}{v(\mathbf{r}, z)^2} - \frac{1}{4}(k_{mx} + k_{hx})^2(1 + 2\epsilon)} \pm \sqrt{\frac{\omega^2}{v(\mathbf{s}, z)^2} - \frac{1}{4}(k_{mx} - k_{hx})^2(1 + 2\epsilon)}} \quad (9)$$

As in the case of the isotropic Common Azimuth migration operator, the above equation has two solutions. In choosing between these two solutions, we consider the limiting case of the in-line offset wavenumber (k_{hx}) equal to zero. In this case, one of the solution diverges while the other one, which has a minus sign on the numerator, goes to zero. We accept this solution. This gives the stationary path approximation for an elliptically anisotropic media. Hence, the new vertical wavenumber, \hat{k}_{ze} for elliptically anisotropic media is evaluated along the stationary path given in equation(9) and is equal to:

$$\hat{k}_{ze} = DSR[\omega, \mathbf{k}_m, k_{hx}, \hat{k}_{hy}, z] \quad (10)$$

STATIONARY PATH AND THE CONSTRAINTS ON THE RAY DIRECTIONS

In this section we show that the stationary path approximation derived in the previous section (equation (9)) is equivalent to imposing the constraint that the source and receiver rays must

be coplanar. For this constraint to hold, the following relation must be satisfied among the ray parameters:

$$\frac{p_{ry}}{p_{sy}} = \frac{p_{rz}}{p_{sz}} \quad (11)$$

where (p_{sx}, p_{sy}, p_{sz}) are the rays downward propagating the sources and (p_{rx}, p_{ry}, p_{rz}) are the rays downward propagating the receivers. Applying the transformation from wavenumbers to ray parameter using the relation $\mathbf{p} = \mathbf{k}\omega$ to equation (3) we have:

$$p_z = \sqrt{\frac{\omega^2}{v^2} - \omega^2(p_x^2 + p_y^2)(1 + 2\epsilon)}. \quad (12)$$

Substituting equation (12) in equation (11) and after some algebra we get:

$$\frac{p_{ry} - p_{sy}}{p_{ry} + p_{sy}} = \frac{\sqrt{\frac{1}{v^2} - p_{rx}^2(1 + 2\epsilon)} - \sqrt{\frac{1}{v^2} - p_{sx}^2(1 + 2\epsilon)}}{\sqrt{\frac{1}{v^2} - p_{rx}^2(1 + 2\epsilon)} + \sqrt{\frac{1}{v^2} - p_{sx}^2(1 + 2\epsilon)}}. \quad (13)$$

Substituting the following relations in equation(13) gives the stationary path approximation derived in the previous section given by equation (9):

$$p_{sx} = \frac{k_{mx} - k_{hx}}{2\omega}, \quad (14)$$

$$p_{sy} = \frac{k_{my} - k_{hy}}{2\omega}, \quad (15)$$

$$p_{rx} = \frac{k_{mx} + k_{hx}}{2\omega}, \quad (16)$$

$$p_{ry} = \frac{k_{my} + k_{hy}}{2\omega}. \quad (17)$$

VTI COMMON AZIMUTH WITH BOUNDS

In this section, we derive an analytical form for the Common Azimuth migration operator for VTI media. As before, we start with the dispersion relation given by Alkhalifah (1998), now represented in terms of ray parameters:

$$p_z = \frac{1}{v} \sqrt{\frac{1 - (1 + 2\epsilon)(p_x^2 + p_y^2)v^2}{1 - 2\eta(1 + 2\delta)(p_x^2 + p_y^2)v^2}}. \quad (18)$$

Using the geometrical constraints on the ray path for Common Azimuth migration (equation(11)) and after some simplifications, we get:

$$a_0 p_{sy}^4 + a_1 p_{ry}^4 + a_2 p_{ry}^2 + a_3 p_{sy}^2 = 0. \quad (19)$$

where

$$a_0 = 2\eta(1 + 2\delta)v_s^4, \quad (20)$$

$$a_1 = -2\eta(1 + 2\delta)v_r^4, \quad (21)$$

$$a_2 = v_r^2 \left\{ 1 - 2\eta(1 + 2\delta)v_r^2 p_{rx}^2 - (1 + 2\epsilon)p_{rx}^2 v_s^2 \right\}, \quad (22)$$

$$a_3 = -v_s^2 \left\{ 1 - 2\eta(1 + 2\delta)v_s^2 p_{sx}^2 - (1 + 2\epsilon)p_{sx}^2 v_r^2 \right\}. \quad (23)$$

Note that equation (19) is a quartic equation in both k_{hy} and k_{my} . This equation might be solved numerically for k_{hy} for given k_{my} values. But we want to have a closed form analytical solution. Rewriting equation (19) in a more suitable form, we get:

$$\begin{aligned} & v_r^2 p_{ry}^2 \left\{ 1 - 2\eta(1 + 2\delta)v_r^2 p_{rx}^2 - 2\eta(1 + 2\delta)v_r^2 p_{ry}^2 \right\} - \\ & v_s^2 p_{sy}^2 \left\{ 1 - 2\eta(1 + 2\delta)v_r^2 p_{sx}^2 - 2\eta(1 + 2\delta)v_r^2 p_{sy}^2 \right\} - A_0 + A_1 = 0. \end{aligned} \quad (24)$$

where

$$A_0 = v_r^2 p_{ry}^2 (1 + 2\epsilon) p_{sx}^2 v_s^2, \quad (25)$$

$$A_1 = v_s^2 p_{sy}^2 (1 + 2\epsilon) p_{rx}^2. \quad (26)$$

Considering the first term in the curly bracket on the RHS of equation(24), we observe that in order to drop the fourth order term in p_{ry} , we need:

$$1 - 2\eta(1 + 2\delta)v_r^2 p_{rx}^2 \gg 2\eta(1 + 2\delta)v_r^2 p_{ry}^2. \quad (27)$$

This can be rewritten as:

$$1 - 2\eta(1 + 2\delta)\sin^2\theta_x \gg 2\eta(1 + 2\delta)\sin^2\theta_y. \quad (28)$$

Recognizing that $\sin^2\theta$ is bounded in the interval (0, 1), we can write:

$$1 \gg 4 | \eta(1 + 2\delta) |. \quad (29)$$

Thus, we obtain a bound on η as:

$$| \eta | \ll \frac{1}{4(1 + 2\delta)} \approx \frac{1}{4}. \quad (30)$$

A similar analysis can be carried out for the second term in curly brackets on the RHS of equation (24) for dropping the fourth order term in p_{sy} , which again gives the same bound on η . Thus for VTI media, when the above bound holds, we can drop the fourth order terms in equation (19) giving:

$$\frac{p_{ry}}{p_{sy}} = \frac{\sqrt{\frac{1}{v_r^2} - \left\{ (1+2\epsilon)p_{rx}^2 + 2\eta(1+2\delta)\frac{v_s^2}{v_r^2}p_{sx}^2 \right\}}}{\sqrt{\frac{1}{v_s^2} - \left\{ (1+2\epsilon)p_{sx}^2 + 2\eta(1+2\delta)\frac{v_r^2}{v_s^2}p_{rx}^2 \right\}}} \quad (31)$$

Now using equations (14) to (17), we get:

$$\frac{\hat{k}_{hy}}{k_{my}} = \frac{A-B}{A+B}, \quad (32)$$

where

$$A = \sqrt{\frac{\omega^2}{v_r^2} - \frac{1}{4} \left\{ (1+2\epsilon)(k_{mx} + k_{hx})^2 + 2\eta(1+2\delta)\frac{v_s^2}{v_r^2}(k_{mx} - k_{hx})^2 \right\}}, \quad (33)$$

and

$$B = \sqrt{\frac{\omega^2}{v_s^2} - \frac{1}{4} \left\{ (1+2\epsilon)(k_{mx} - k_{hx})^2 + 2\eta(1+2\delta)\frac{v_r^2}{v_s^2}(k_{mx} + k_{hx})^2 \right\}}. \quad (34)$$

This equation gives an analytical form of the stationary path approximation for VTI media. As before, the vertical wavenumber, \hat{k}_{zvti} , is evaluated along this stationary path as:

$$\hat{k}_{zvti} = DSR[\omega, \mathbf{k}_m, k_{hx}, \hat{k}_{hy}, z] \quad (35)$$

Note that when $\eta = 0$, meaning for elliptically anisotropic media equation (34), reduces to equation (9) derived earlier for elliptically anisotropy media.

ERROR ANALYSIS

In this section, we compare the accuracy of the approximated analytical stationary path approximation for VTI media with the one obtained by numerically solving the full quartic equation for different η values (top panel of Figures 1-3). From the plots, we observe that the approximated analytical equation has similar accuracy as the one obtained by solving the quartic equation. Even when the η value exceeds the bound that was given in the previous section, the relative error is still sufficiently small. This indicates that our approximation should hold for a wide range of η values. The middle panel of Figures 1-3 shows the relative error between the isotropic and the analytically derived anisotropic stationary path. The bottom panels of figures 1-3 show the vertical wavenumbers computed for isotropic and anisotropic media for different η values. It can be seen that there are significant differences between the anisotropic and isotropic k_z values which, if ignored, will lead to significant mispositioning of migrated events.

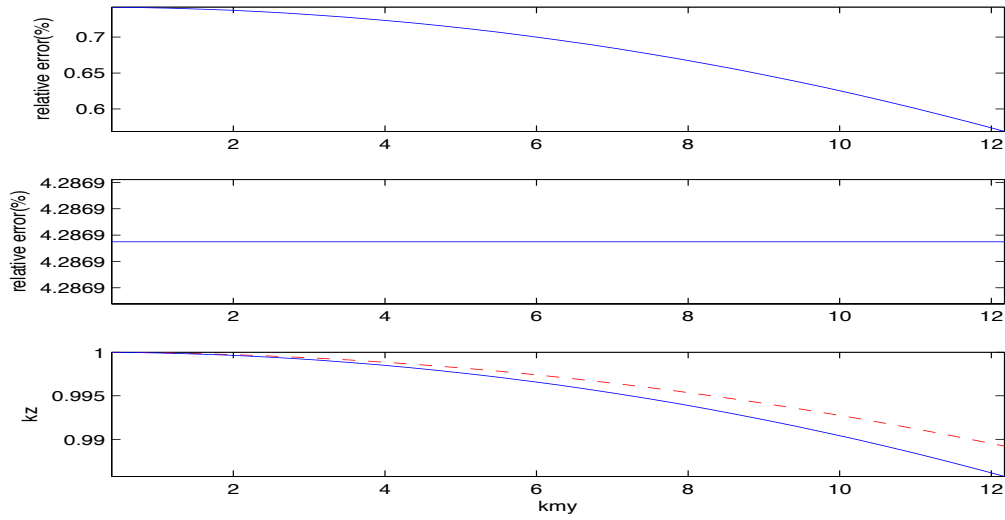


Figure 1: Relative Error plots for $\eta = 0.08$, relative error in k_{hy} between analytical and quartic solutions (top panel), relative error between analytical anisotropic and isotropic k_{hy} (middle panel), relative error between anisotropic (solid) and isotropic (dashed) k_z (bottom panel)
ssen-eta08 [CR]

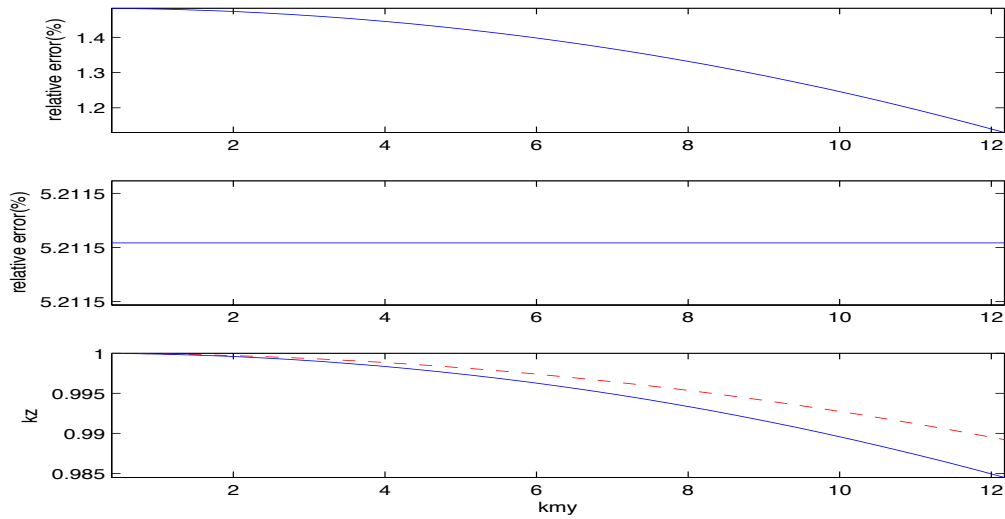


Figure 2: Relative error plots for $\eta = 17$, relative error in k_{hy} between analytical and quartic solutions (top panel), relative error between analytical anisotropic and isotropic k_{hy} (middle panel), relative error between anisotropic (solid) and isotropic (dashed) k_z (bottom panel)
ssen-eta17 [CR]

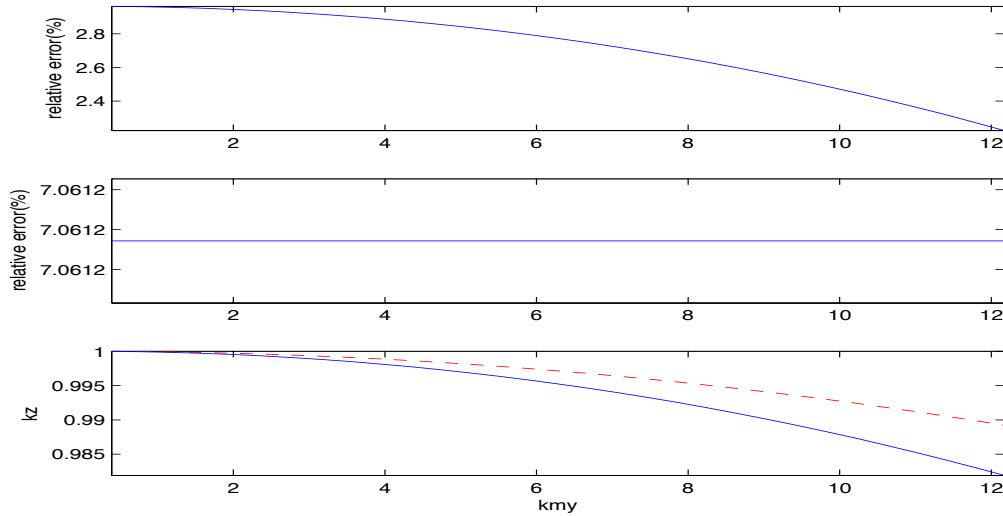


Figure 3: Relative error plots for $\eta = 0.33$, relative error in k_{hy} between analytical and quartic solutions (top panel), relative error between analytical anisotropic and isotropic k_{hy} (middle panel), relative error between anisotropic (solid) and isotropic (dashed) k_z (bottom panel)

`ssen-eta33` [CR]

3-D IMPULSE RESPONSES

In this section, we compare the 3-D impulse responses of the anisotropic Common Azimuth migration operator with the corresponding isotropic one. For this paper, we consider impulse responses for elliptical anisotropy only. The vertical P wave velocity in the medium is 2000 m/s. The anisotropic parameters ϵ and δ are both equal to 0.15. Figures 4 and 5 show in-line sections of the 3-D impulse responses for elliptically anisotropic and isotropic media respectively. These figures clearly show the difference of incorporating anisotropy into the Common Azimuth downward continuation operator, especially for energy propagating at moderate to steep angles. Figures 6 and 7 show cross-line sections of the 3-D impulse responses for elliptically anisotropic and isotropic media respectively. Again it can be seen that there are significant differences for energy propagating at moderate to steep angles once anisotropy is incorporated into the Common Azimuth operator. Finally, Figures 8 and 9 show depth slices of the 3-D impulse responses for elliptically anisotropic and isotropic media respectively. Again, we also observe significant differences between the two depth slices, especially the more elliptical nature of the depth slice for the anisotropic operator.

CONCLUSION

We have derived a Common Azimuth migration operator for elliptically anisotropic and VTI media. The elliptically anisotropic Common Azimuth migration operator is exact for all range

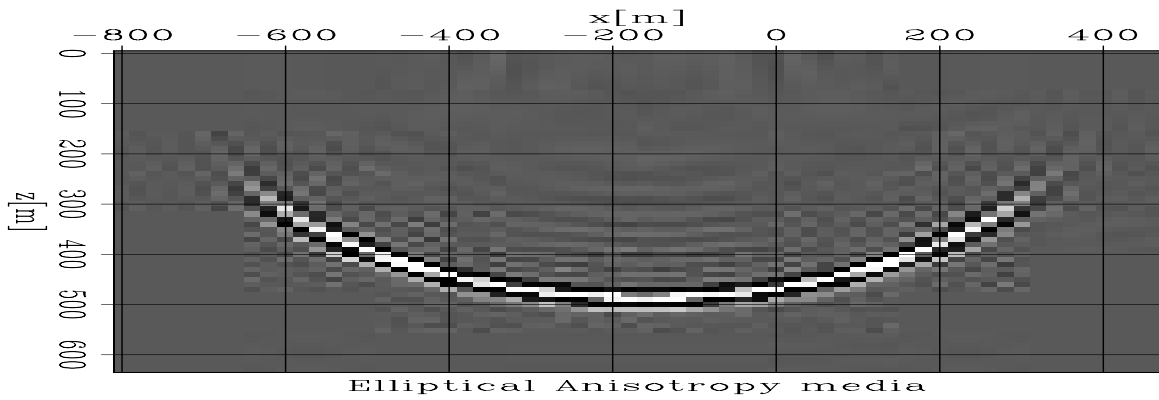


Figure 4: An inline slice of the 3D impulse response in an elliptically anisotropic media at $y = 0$ m. `ssen-aniso15_inline` [CR]

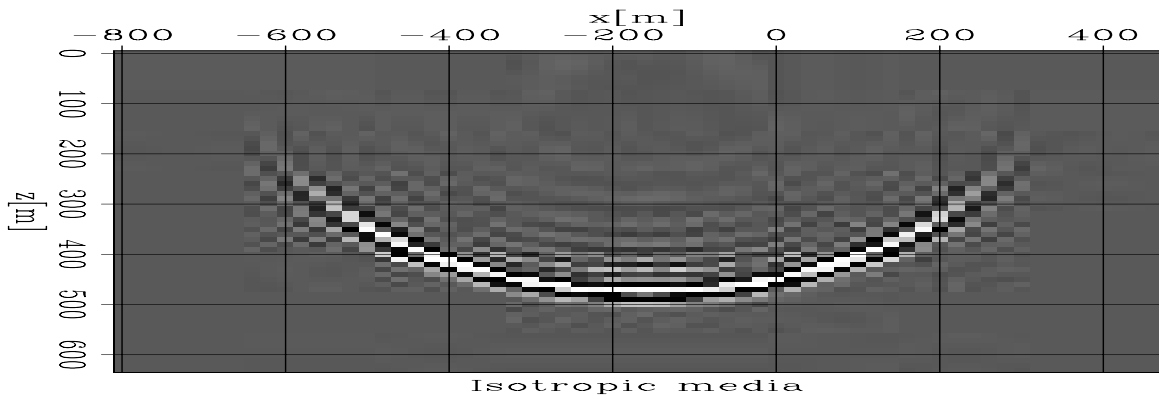


Figure 5: An inline slice of the 3D impulse response in an isotropic media at $y = 0$ m. `ssen-iso_inline` [CR]

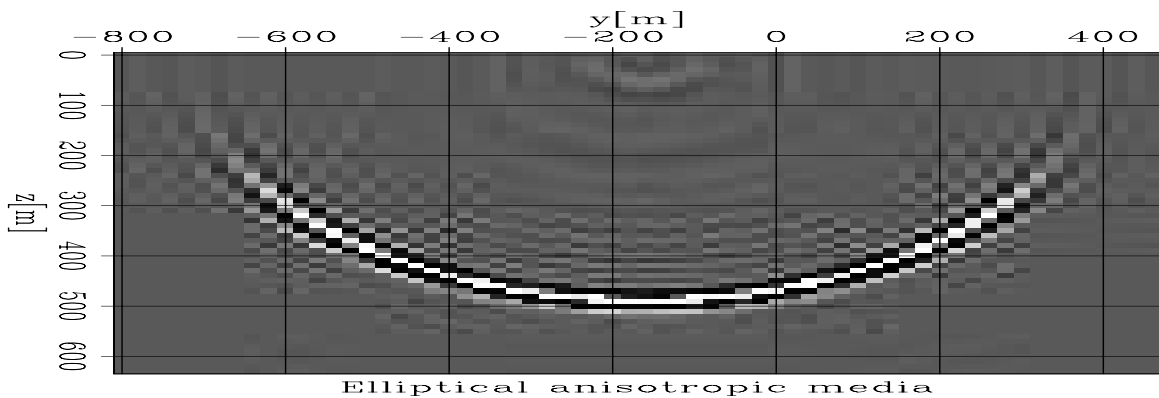


Figure 6: A cross-line slice of the 3D impulse response in an elliptically anisotropic media at $x = 0$ m. `ssen-aniso15_xline` [CR]

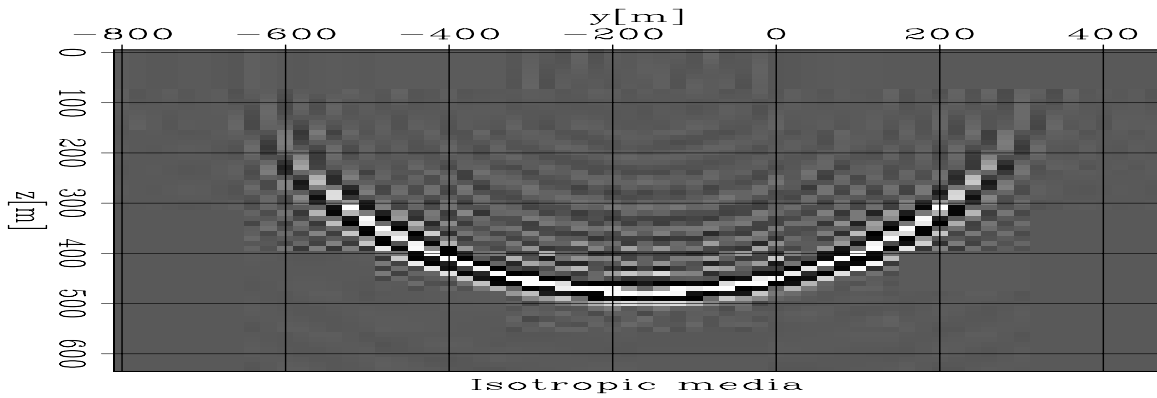


Figure 7: A cross-line slice of the 3D impulse response in an isotropic media at $x = 0$ m
`ssen-iso_xline` [CR]

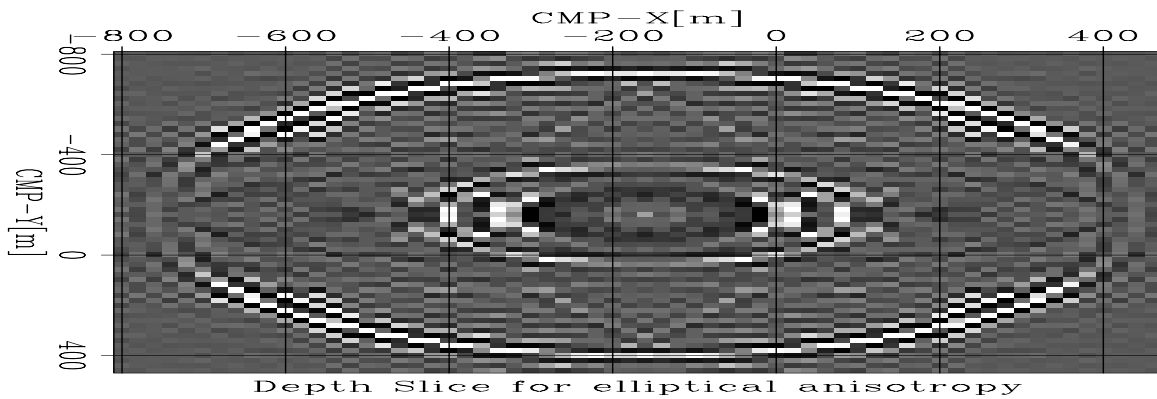


Figure 8: A horizontal slice of the 3D impulse response in an elliptically anisotropic media at a depth of $z = 600$ m.
`ssen-aniso15_depth_slice` [CR]

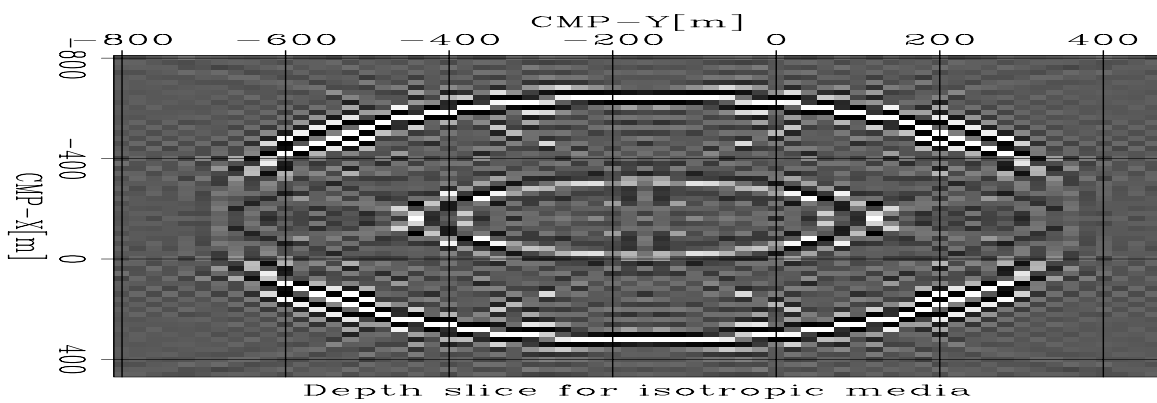


Figure 9: A horizontal slice of the 3D impulse response in an isotropic medium at $z = 600$ m.
`ssen-iso_depth_slice` [CR]

of the governing anisotropic parameters, namely δ and ϵ . The Common Azimuth operator that we have developed for VTI media is a bounded one, meaning that it should be accurate within the certain bounds on the anisotropic parameters. But the error analysis indicates that even when these bounds are exceeded, the approximation is still good and the accuracy is comparable to the one obtained by solving the full quartic equation. 3-D impulse responses show that there are significant differences between the isotropic and anisotropic Common Azimuth downward continuation operator, which needs to be taken into account by the migration algorithm.

REFERENCES

- Alkhalifah, T., 1998, An acoustic wave equation for anisotropic media: *Geophysics*, **65**, no. 4, 1239–1250.
- Baumstein, A., and Anderson, J., 2003, Wavefield extrapolation in laterally varying vti media: 73rd Annual Internat. Mtg., Society Of Exploration Geophysicists, Expanded Abstract, 945–948.
- Biondi, B., and Palacharla, G., 1996, 3-d prestack migration for common-azimuth data: *Geophysics*, **61**, no. 6, 1822–1832.
- Ristow, D., and Ruhl, T., 1997, Migration in transversely isotropic media using implicit operators: 67th Annual Internat. Mtg., Society Of Exploration Geophysicists, Expanded Abstracts, 1699–1702.
- Rousseau, J. H. L., 1997, Depth migration in heterogeneous transversely isotropic media with the phase shift plus interpolation method.: 67th Annual Internat. Mtg., Society Of Exploration Geophysicists, Expanded Abstracts, 1703–1706.
- Shan, G., and Biondi, B., 2004, Wavefield extrapolation in laterally varying tilted ti media: Report 117., Stanford Exploration Project, SEP, 1–9.
- Uzcategui, O., 1995, 2-d depth migration in transversely isotropic media using explicit operators: *Geophysics*, **60**, no. 5, 1819–1829.
- Zhang, J., Verschuur, D. J., and Wapenaar, C. P., 2001, Depth migration of shot records in heterogeneously transversely isotropic media using optimum explicit operators: *Geophysical Prospecting*, **49**, no. 4, 287–289.



Update on flattening without picking

Jesse Lomask, Antoine Guitton, Sergey Fomel, and Jon Claerbout¹

ABSTRACT

We present a method for efficiently flattening 3D seismic data volumes. First local dips are calculated over the entire seismic volume. The dips are then resolved into time shifts using a Gauss-Newton iterative approach that exploits the Fourier domain to maximize efficiency. To handle faults (discontinuous reflections), we apply a weight inversion scheme. This approach successfully flattens a synthetic faulted model, a field salt piercement dataset, a field dataset with an angular unconformity, and a faulted field dataset.

INTRODUCTION

In spite of numerous advances in computational power in recent years, interpretation still requires a lot of manual picking. One of the main goals of interpretation is to extract from the seismic data geological and reservoir features. One commonly used interpretation technique that helps with this effort is to flatten data on horizons [e.g. Lee (2001)]. This procedure removes structure and allows the interpreter to see geological features as they were emplaced. For instance, after flattening seismic data, an interpreter can see in one image an entire flood plain complete with meandering channels. However, in order to flatten seismic data, a horizon needs to be identified and tracked throughout the data volume. If the structure changes often with depth, then many horizons need to be identified and tracked. This picking process can be time consuming and expensive.

Certain interpretation visualization products and auto-pickers seek to make picking and flattening processes as efficient as possible. However, they often suffer from weaknesses that prevent them from being truly practical. For example, 3-D volume interpretation packages allow interpreters to view their data with depth perception using stereo glasses. These products have an opacity ability (James et al., 2002) that allows interpreters to make unwanted data transparent. Unfortunately, unless the zone of interest has a known unique range of attribute values, interpreters resort to picking on 2-D slices. Additionally, traditional amplitude-based auto-pickers can fail if the horizon being tracked has significant amplitude variation, or worse, polarity reversal. Other tracking techniques such as artificial neural networks are less sensitive to amplitude variations but are still prone to error if the seismic wavelet character varies significantly from the training data (Leggett et al., 1996).

¹**email:** lomask@sep.stanford.edu, antoine@sep.stanford.edu, sergey.fomel@beg.utexas.edu, jon@sep.stanford.edu

In this document, we propose a method for automatically flattening entire 3-D seismic cubes without picking that we first presented in Lomask (2003a). This is essentially an algorithm that is efficient enough to perform dense picking on entire 3D cubes at once. Our method involves first calculating dips everywhere in the data using a dip estimation technique (Claerbout, 1992; Fomel, 2002). These dips are resolved into time shifts via a non-linear least-squares problem. The data are subsequently shifted according to the time shifts to output a flattened volume. Bienati et al. (1999a,b); Bienati and Spagnolini (2001, 1998) use a similar approach to resolve numerically the dips into time shifts for the purpose of auto-picking horizons and flattening gathers, yet solving a linear version of the problem and without flattening the full volume at once. Stark (2004) takes a full volume approach to achieve the same end yet is unwrapping instantaneous phase. Blinov and Petrou (2003) use dynamic programming to track horizons by summing local dips. Here, a version of the non-linear problem of summing local dips (Lomask, 2003b; Guitton et al., 2005) is solved iteratively using a Gauss-Newton approach. Each iteration utilizes the Fourier domain to invert efficiently a linearized operator much like the approach of Ghiglia and Romero (1994) for unwrapping two-dimensional phase. For faulted data, weights identifying the faults are applied within the iterative scheme, allowing reconstruction of horizons for certain fault geometries. As with amplitude based auto-pickers, amplitude variation also affects the quality of the dip estimation and will, in turn, impact the quality of this flattening method. However, the effect will be less significant because this method can flatten the entire data cube at once, globally, in a least-squares sense, minimizing the effect of questionable dip information. Additionally, flattening the entire cube at once should make the method more robust in noisy data or complicated structures. Once a seismic volume is flattened, automatic horizon tracking becomes a trivial matter of reversing the flattening process to unflatten flat surfaces. The prestack applications for this method are numerous and can be easily incorporated into an automatic velocity picking scheme (Guitton et al., 2004).

In the following sections, we present an overview of the flattening methodology and a series of real world geological challenges for this method in order of increasing difficulty. The first is a 3D synthetic that is flattened to demonstrate how we can flatten faulted, folded data. Then we present a structurally simple salt piercement 3D field data from the Gulf of Mexico. We consider it structurally simple because the dip does not change much with depth. Increasing complexity, we flatten 3D field data from the North Sea that contains an unconformity and has significant folding. Lastly, we illustrate how this method is used to flatten datasets with faults on a field 3D Gulf of Mexico dataset.

FLATTENING THEORY

The basic idea is similar to phase unwrapping (Claerbout, 1999), but instead of summing phase differences to get total phase, dips are summed to get total time shifts that are then used to flatten the data. To apply the shifts, a reference is held constant and all other traces are shifted vertically to match it.

The first step is to calculate dips everywhere in the 3-D seismic cube. Dip can be efficiently

calculated using a plane-wave destructor as described in Claerbout (1992) or with an improved dip estimator that is described in Fomel (2002). We primarily use the latter. For each point in the data cube, two components of dip, p_x and p_y , are estimated in the x direction and y direction, respectively. These can be represented everywhere on the mesh as vectors \mathbf{p}_x and \mathbf{p}_y .

Our goal is to find a time-shift (or depth-shift) field $\tau(x, y, z)$ such that its gradient approximates the dip $\mathbf{p}(x, y, \tau)$. Our objective function is:

$$J(\tau) = \int \int \left[\left(\mathbf{p}_x(\tau, x, y) - \frac{\partial \tau}{\partial x} \right)^2 + \left(\mathbf{p}_y(\tau, x, y) - \frac{\partial \tau}{\partial y} \right)^2 \right] dx dy \quad (1)$$

The Euler-Lagrange equation is used in calculus of variations (Farlow, 1993) to find a function (τ) that will minimize a functional (J).

We apply the Euler-Lagrange equation to equation (1) to find:

$$\frac{\partial^2 \tau}{\partial x^2} + \frac{\partial^2 \tau}{\partial y^2} = \frac{\partial \mathbf{p}_x}{\partial x} + \frac{\partial \mathbf{p}_y}{\partial y} + \frac{1}{2} \frac{\partial (\mathbf{p}_x^2 + \mathbf{p}_y^2)}{\partial \tau}. \quad (2)$$

In our method, we ignore the last term of equation (2) and iteratively solve:

$$\frac{\partial^2 \tau}{\partial x^2} + \frac{\partial^2 \tau}{\partial y^2} = \frac{\partial \mathbf{p}_x}{\partial x} + \frac{\partial \mathbf{p}_y}{\partial y}. \quad (3)$$

This equation can be rewritten using the gradient ($\nabla = [\frac{\partial}{\partial x} \quad \frac{\partial}{\partial y}]'$) and the estimated dip ($\mathbf{p} = [\mathbf{p}_x \quad \mathbf{p}_y]'$)

$$\nabla' \nabla \tau = \nabla' \mathbf{p}. \quad (4)$$

Ultimately, the regression to be solved is:

$$\nabla \tau = \mathbf{p}. \quad (5)$$

This equation means that we need to find a time-shift field $\tau(x, y, z)$ such that its gradient approximates the dip $\mathbf{p}(x, y, \tau)$. Note that the estimated dip $\mathbf{p}(x, y, \tau)$ field is a function of the unknown $\tau(x, y, t)$ field, making this problem non-linear and, therefore, difficult to solve directly.

We solve this using a Gauss-Newton approach by iterating over equations (6)-(8)

iterate {

$$\mathbf{r} = [\nabla \tau_k - \mathbf{p}] \quad (6)$$

$$\Delta \tau = (\nabla' \nabla)^{-1} \nabla' \mathbf{r} \quad (7)$$

$$\tau_{k+1} = \tau_k + \Delta \tau \quad (8)$$

}

To dramatically improve efficiency, we solve equation (7) in the Fourier domain. We apply the divergence to the estimated dips and divide by the z-transform of the Laplacian in the Fourier domain with:

$$\Delta \boldsymbol{\tau} \approx \text{FFT}_{2\text{D}}^{-1} \left[\frac{\text{FFT}_{2\text{D}}[\nabla' \mathbf{r}]}{-Z_x^{-1} - Z_y^{-1} + 4 - Z_x - Z_y} \right] \quad (9)$$

where $Z_x = e^{iw\Delta x}$ and $Z_y = e^{iw\Delta y}$. This amounts to calling both a forward and inverse FFT in each iteration. The ability to invert the 2D Laplacian in one step is the key to this method's exceptional performance.

Once we have converged the resulting time-shift field, $\boldsymbol{\tau}(x, y, t)$ contains all of the time-shifts required to map the original unflattened data to flattened data. This is implemented by applying the time-shifts relative to a reference trace. In other words, each trace is shifted to match the reference trace.

In general, we operate on a one-time slice at a time. After iterating until convergence, we then select the next time slice and proceed down through the cube. In this way, each time slice is solved independently.

The process of flattening tends to alter the spectrum of the data by stretching and compressing in time. Even worse, it can disrupt its continuity. To insure a monotonic and continuous result, it should be sufficient to first smooth the input dips in time (or depth). In some instances, it may be necessary to enforce smoothness during the integration of the dips. This can easily be accomplished by defining a 3D gradient operator with an adjustable smoothing parameter as:

$$\nabla_{\epsilon} \boldsymbol{\tau} = \begin{bmatrix} \frac{\partial \boldsymbol{\tau}}{\partial x} \\ \frac{\partial \boldsymbol{\tau}}{\partial y} \\ \epsilon \frac{\partial \boldsymbol{\tau}}{\partial z} \end{bmatrix} \approx \begin{bmatrix} \mathbf{p}_x \\ \mathbf{p}_y \\ 0 \end{bmatrix} = \mathbf{p}. \quad (10)$$

Our new operator ∇_{ϵ} has a scalar parameter ϵ used to control the amount of vertical smoothing. This requires integrating the entire 3D volume of dips at once rather than slice by slice. The 2D FFT's in equation (9) are replaced with 3D FFT's. Consequently, each iteration is slowed.

Weighted solution for faults

Local dips estimated at fault discontinuities can be inaccurate. We can, however, sum dips around the faults and ignore the spurious dips across the faults to get a flattened result.

We can add a weight to the residual to ignore fitting equations that are affected by the bad dips estimated at the faults. The regression to be solved is now:

$$\mathbf{W} \nabla \boldsymbol{\tau} = \mathbf{W} \mathbf{p}. \quad (11)$$

We iterate over the same equations as before, except equation (6) is now replaced with:

$$\mathbf{r} = \mathbf{W}[\nabla\tau_{\mathbf{k}} - \mathbf{p}] \quad (12)$$

Because we cannot apply a non-stationary weight in the Fourier domain, we use the same Fourier method as shown in equation (9). This means that the Fourier method is not approximating the inverse as well as before. The cost of this is more iterations, but method is still relatively efficient compared to other iterative methods. This approach is similar to Ghiglia and Romero (1994) for phase unwrapping.

Computational cost

For a data cube with dimensions $n = n_1 \times n_2 \times n_3$, each iteration requires n_1 forward and reverse 2D FFT's. Therefore, number of operations per iteration is about $8n(1 + \log(4n_2 \times n_3))$. The number of iterations is a function of the variability of the structure and the degree of weighting. For instance, if the structure is constant with depth, then it will be flattened in one iteration. On the other hand, if a weight is applied and the structure changes much with depth, it may take as many as 100 iterations.

EXAMPLES OF 3D FLATTENING

Here we demonstrate this flattening method's efficacy on synthetic and field 3D datasets. We start with a synthetic to illustrate how this method can handle faults with folds. Then we use several 3D field datasets to demonstrate how this method handles folds, angular unconformities, and faults.

Synthetic Data

Figure 1 is a 3D synthetic dataset that presents two geological challenges. Firstly, the structure is changing with depth, requiring multiple non-linear iterations. Secondly, a significant fault is present in the middle of the cube. Dips estimated at fault discontinuities are, in general, inaccurate and will compromise the quality of the flattening result. However, knowing the position of the fault, we pass it as a weight to equation (12). In this case, we used a binary weight of 0's at the fault (and a few samples on each side) and 1's everywhere else.

The flattening result is shown in Figure 2. Notice the cube is very flat except in the area of the fault itself. This method is able to flatten this cube because we passed it a weight identifying the fault and the fault is limited laterally. That is, the tip-line of the fault is contained within the data cube, enabling dips to be summed around the fault.

The estimated τ field used to flatten data can also be used to reverse the process. That is, we can use the time-shifts to unflatten data that is already flat. By unflattening flat surfaces and overlaying them on the data, we are essentially picking any or all of the horizons in the data-cube. Figure 3 displays every 20th horizon overlain on the synthetic data shown in Figure 1.

We could just as easily have displayed every horizon but the image would appear too cluttered. Notice that the horizons are well tracked even across a fault.

Chevron Gulf of Mexico Salt Peircement Data

Figure 4 is a field 3D data cube from the Gulf of Mexico provided by Chevron. It consists of structurally simple horizons that have been warped up around a salt peircement. Numerous channels can be seen in time slices. In the time slice at the top of Figure 4, a channel can be seen snaking across the south side. Figure 5 shows the flattened output of the data in Figure 4. The seismic cube has been converted from a stack of time slices to a stack of horizon slices. Notice that the low frequency banding present in the unflattened data is no longer present in the flattened data. This is because horizons are no longer cutting across the image. Several channels are now easily viewed on the horizon slice. Also, notice the salt dome appears to be more localized in Figure 5.

Figure 5 displays three horizons overlain on the original data in Figure 4. The horizons track the reflectors on the flanks of the salt well as expected. Within the salt, the horizons gradually get off their respective reflector events as the estimated dip becomes very inaccurate. The time slice at the top displays the swath of a tracked horizon.

Elf North Sea Unconformity Data

Figure 7 shows a 3D Elf North Sea data set. Marked by considerable folding and a sharp angular unconformity, this data presents a formidable flattening challenge.

The flattening result is shown in Figure 8. In order to preserve the continuity of the data, we used a smoothing parameter ϵ of 1.0 in equation (10). Thus, it is no surprise that the result is not completely flat. Had we used an ϵ of 0.0, the data would be flatter but would lose its continuity. Consequently, the trade-off between continuity and flatness emerges in cases of pinch-outs and unconformities. Notice that at the bottom of the section, there are some discontinuities introduced by the flattening process.

When it comes to overlaying the picks on the data, an ϵ of 0.0 is preferable. The results are shown in Figure 9. The time slice at the top shows the swaths of two different horizons. Overall, the picked horizons track up to and along the unconformity. The only significant errors occur where the data quality is questionable and, as a result, the estimated dip is inaccurate.

Chevron Gulf of Mexico Faulted Data

Figure 10 is an image of faulted Gulf of Mexico data. When a significant discontinuity occurs within a data-set, local dip estimators return incorrect estimates. Faults with significant displacement contaminate the dip estimation at the faults. This, in turn, results in unsatisfactory flattening results.

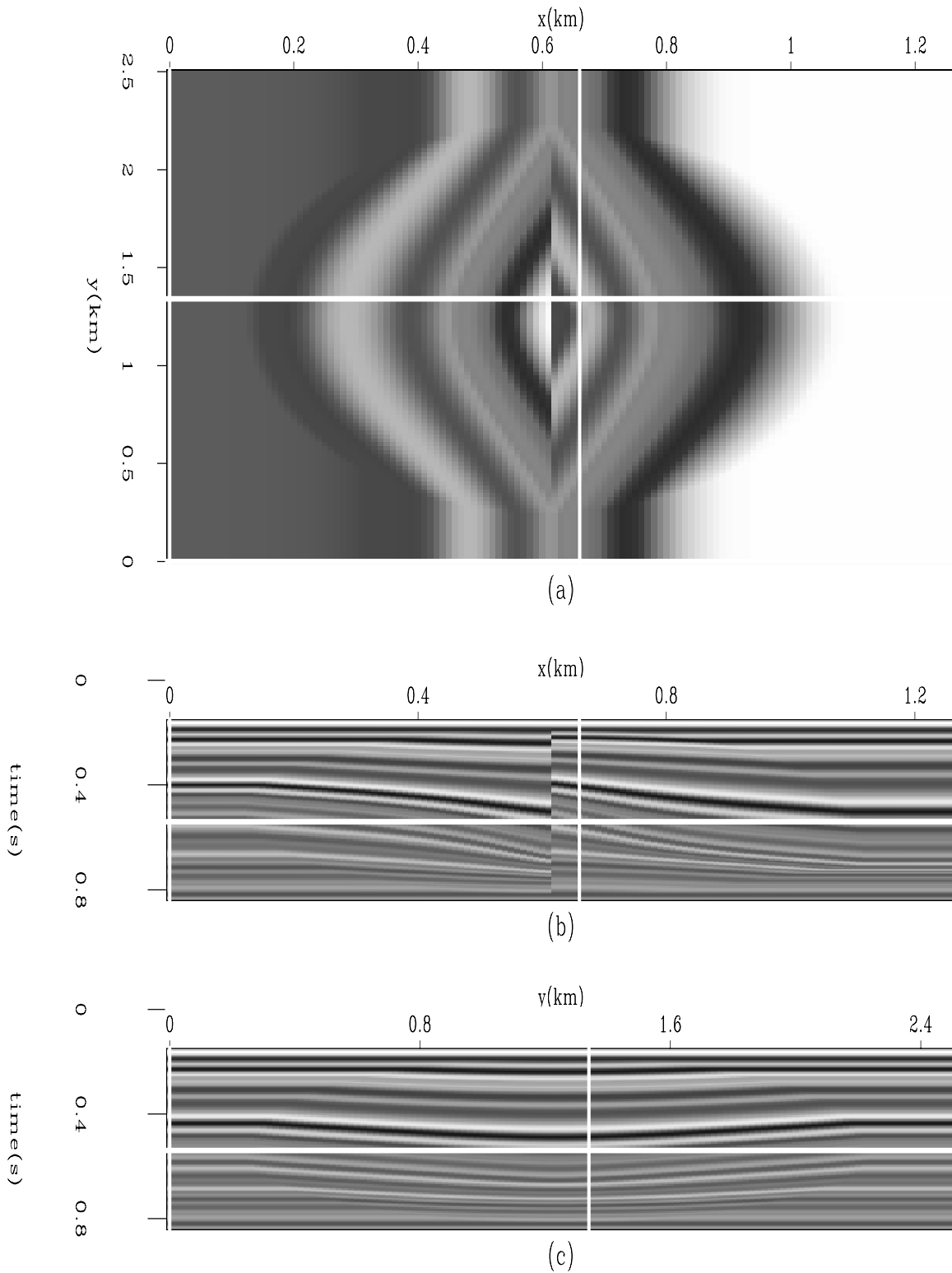


Figure 1: A synthetic model with structure varying with depth that necessitates multiple iterations as well as a vertical discontinuity representing a fault. (a) The time slice at time = .54 s. (b) An in-line section at $y = 1.34$ km. (c) A cross-line section at $x = .66$ km. jesse1-down_lap
[ER]

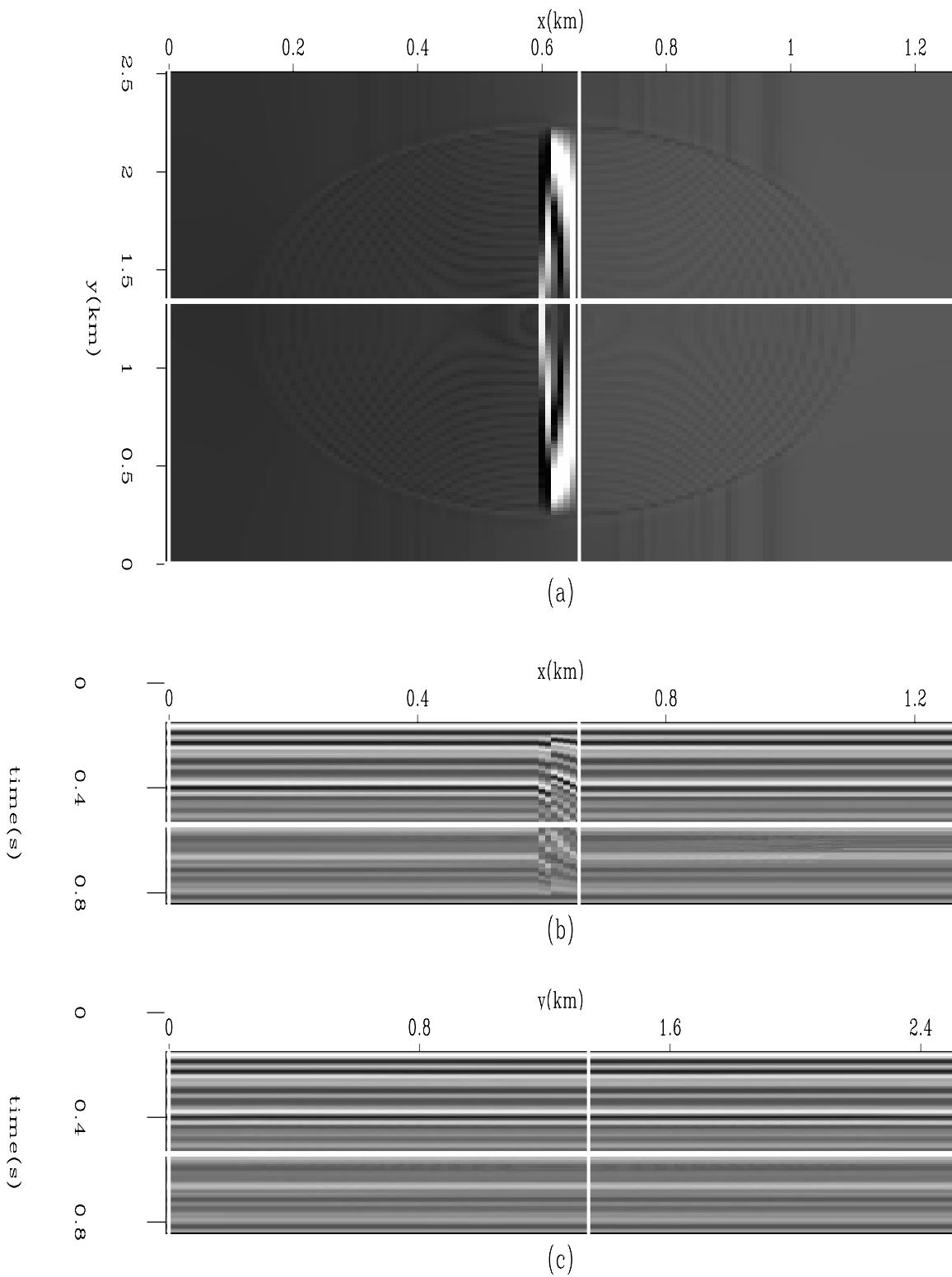


Figure 2: Result of flattening of Figure 1. Notice it is flat on both sides of the fault zone. (a) The horizon slice at time=.54 s. (b) An in-line section at $y=1.34$ km. (c) A cross-line section at $x=.66$ km. `jesse1-down_lap_flat` [ER]

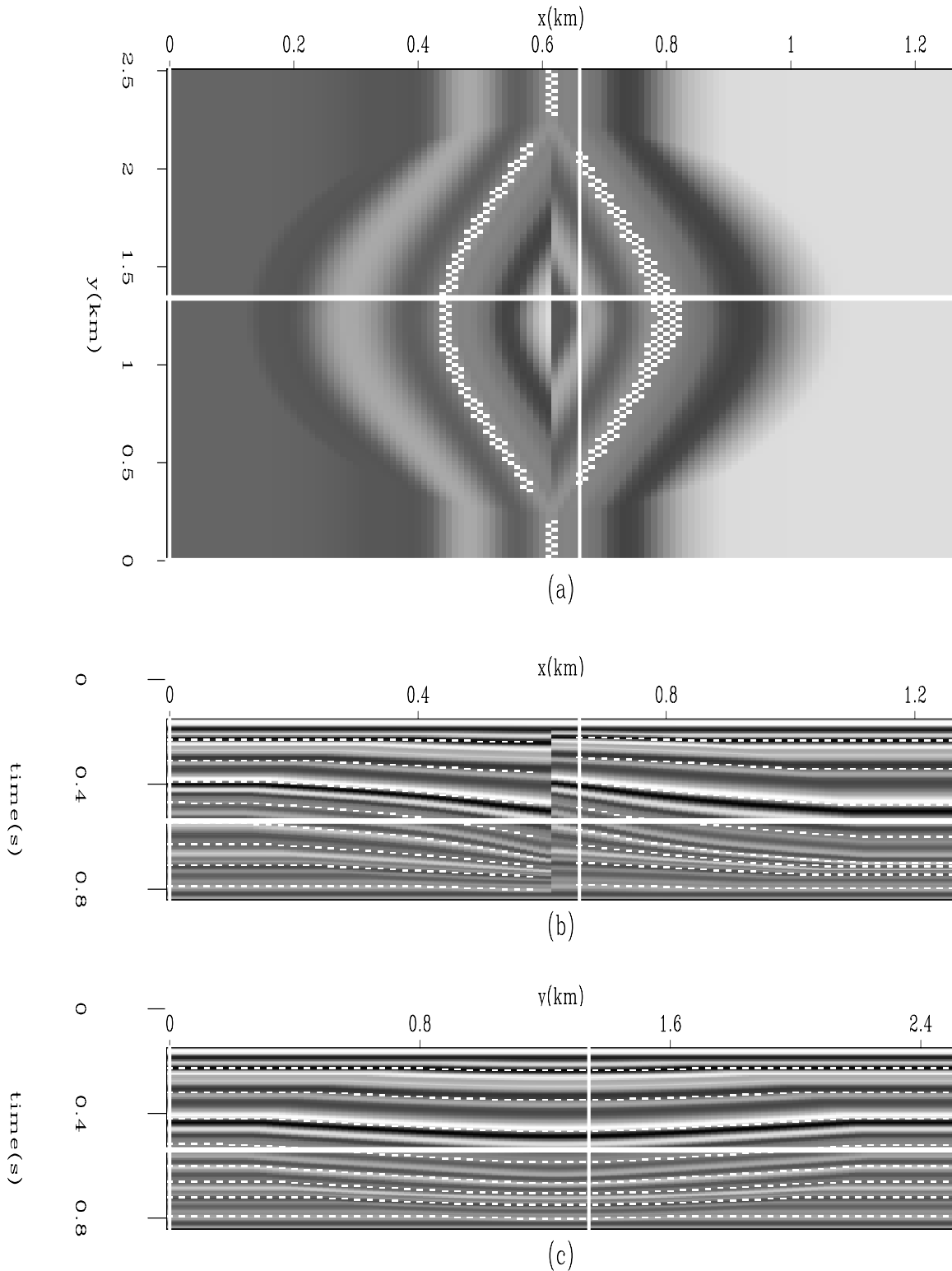


Figure 3: Result of overlaying tracked horizons on the image in Figure 1. The gap between reflections is where the weight was applied. It successfully tracks the horizons. (a) The time slice at time = 0.54 s. (b) An in-line section at $y = 1.34$ km. (c) A cross-line section at $x = 0.66$ km.

`jesse1-down_lap.horizon_overlay` [ER]

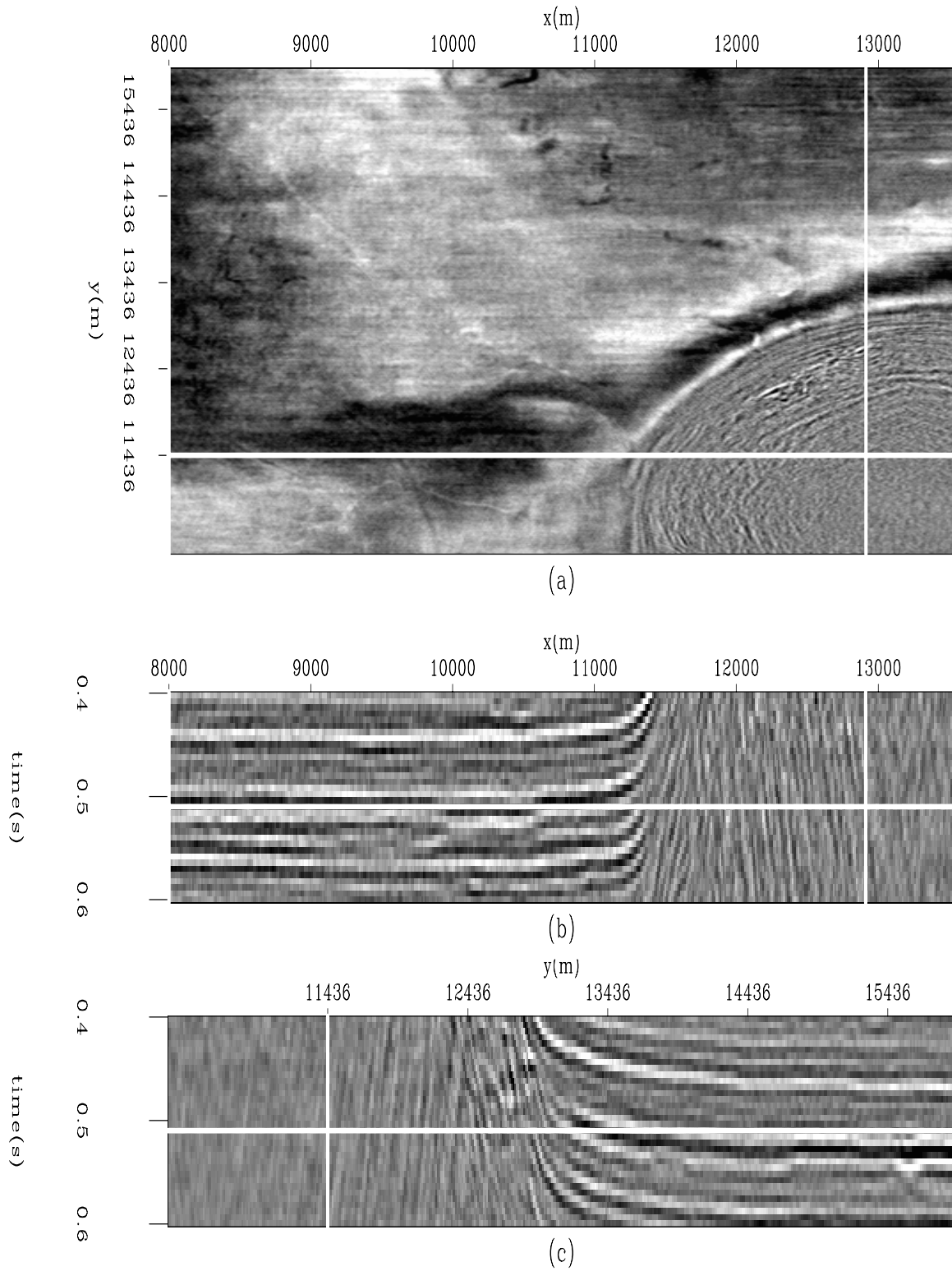


Figure 4: Chevron Gulf of Mexico data. Notice the beds have been forced up to steep angles by the emplacement of a salt piercement. There is some evidence of channels in the time slice. (a) The time slice at $time=.51$ s. (b) An in-line section at $y=11436.1$ m. (c) A cross-line section at $x=12911$ m. jesse1-chev [ER]

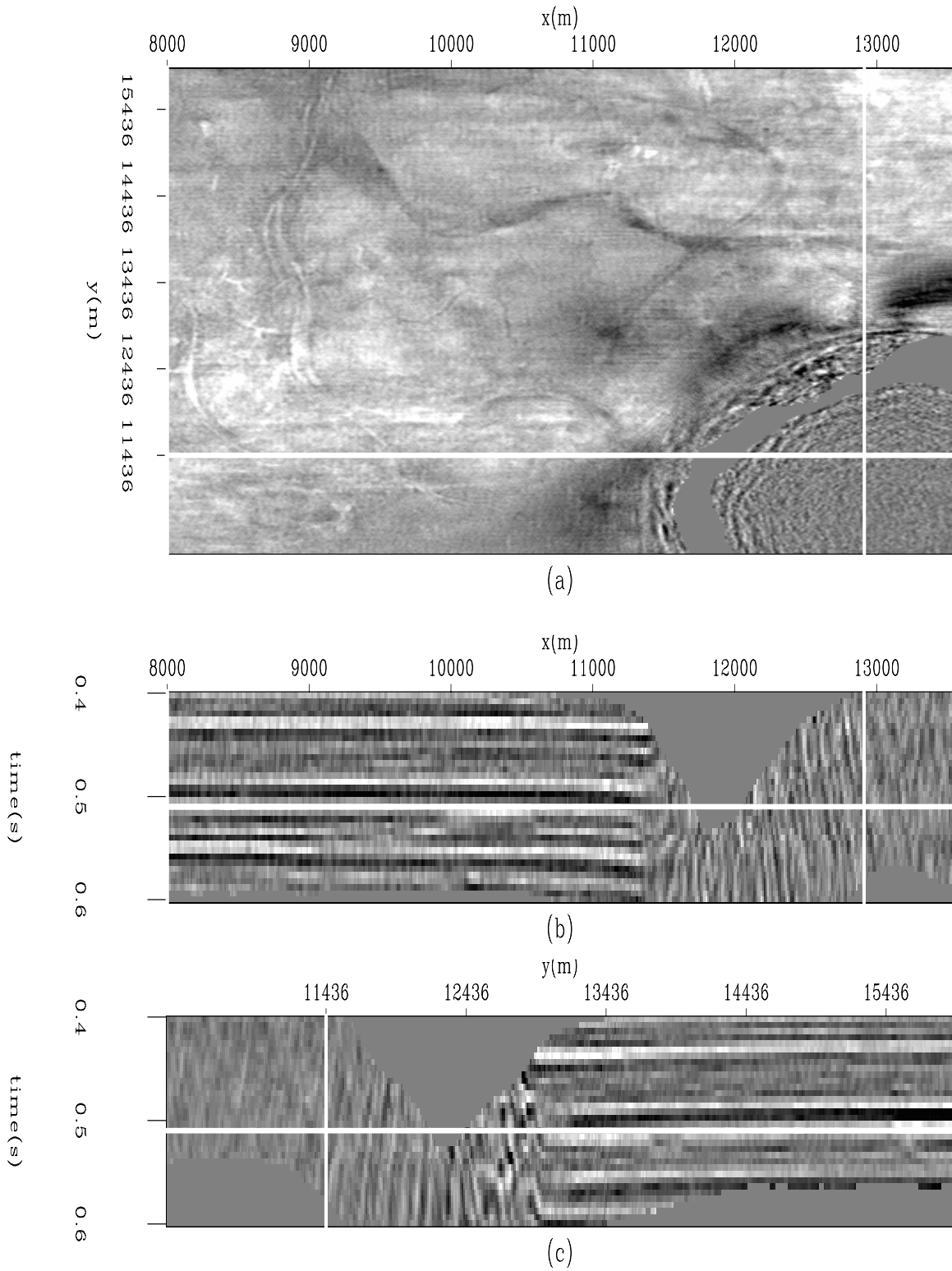


Figure 5: Result of flattening of Figure 4. The top panel is now a horizon slice displaying several channels. The vertical sections illustrate that the cube is flat in both the x and y directions. (a) The horizon slice at time = 0.51 s. (b) An in-line section at $y = 11436.1 m$. (c) A cross-line section at $x = 12911 m$. `jesse1-chev.3Dflat` [ER]

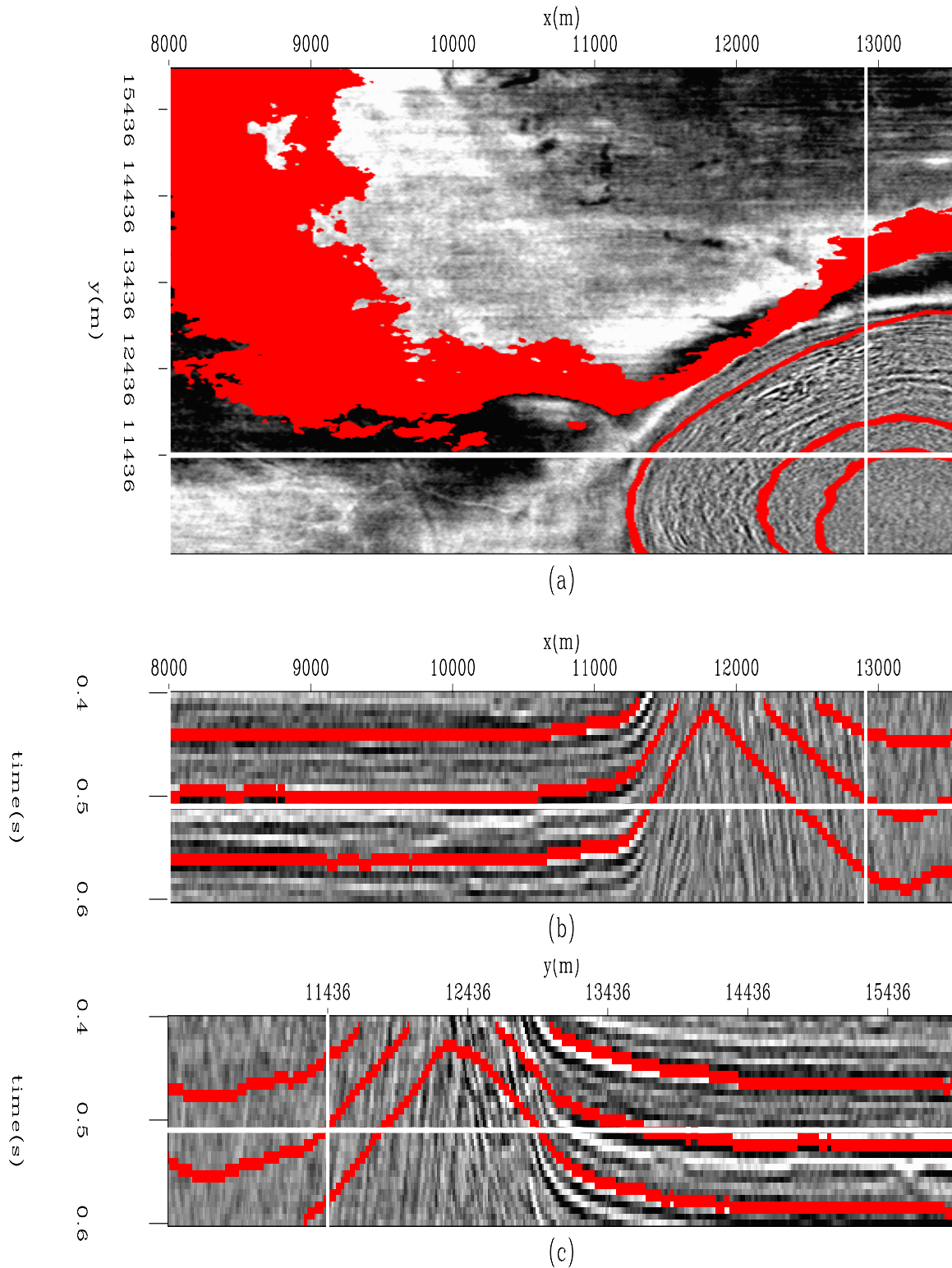


Figure 6: Result of overlaying tracked horizons on the image in Figure 4. It successfully tracks the horizons even to the considerably steep dips leading into the salt piercement. (a) The time slice at $time=.51$ s. (b) An in-line section at $y=11436.1$ m. (c) A cross-line section at $x=12911$ m. `jesse1-chev.horizon_overlay` [ER]

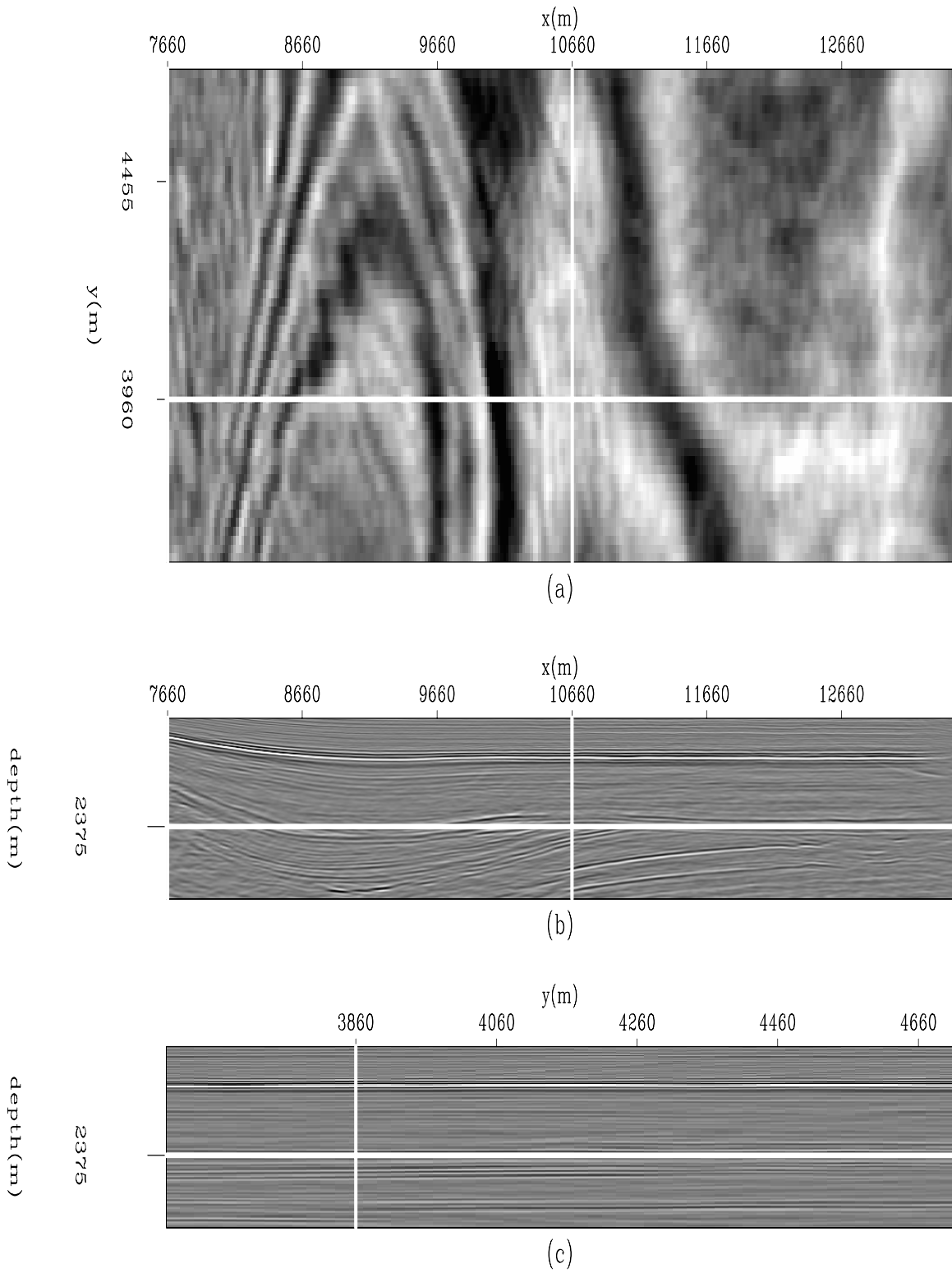


Figure 7: Elf North Sea data. Observe the angular unconformity at 2425 meters. (a) The depth slice at depth=2375 m. (b) An in-line section at y=3960 m. (c) A cross-line section at x=10660 m. jesse1-elf [ER]

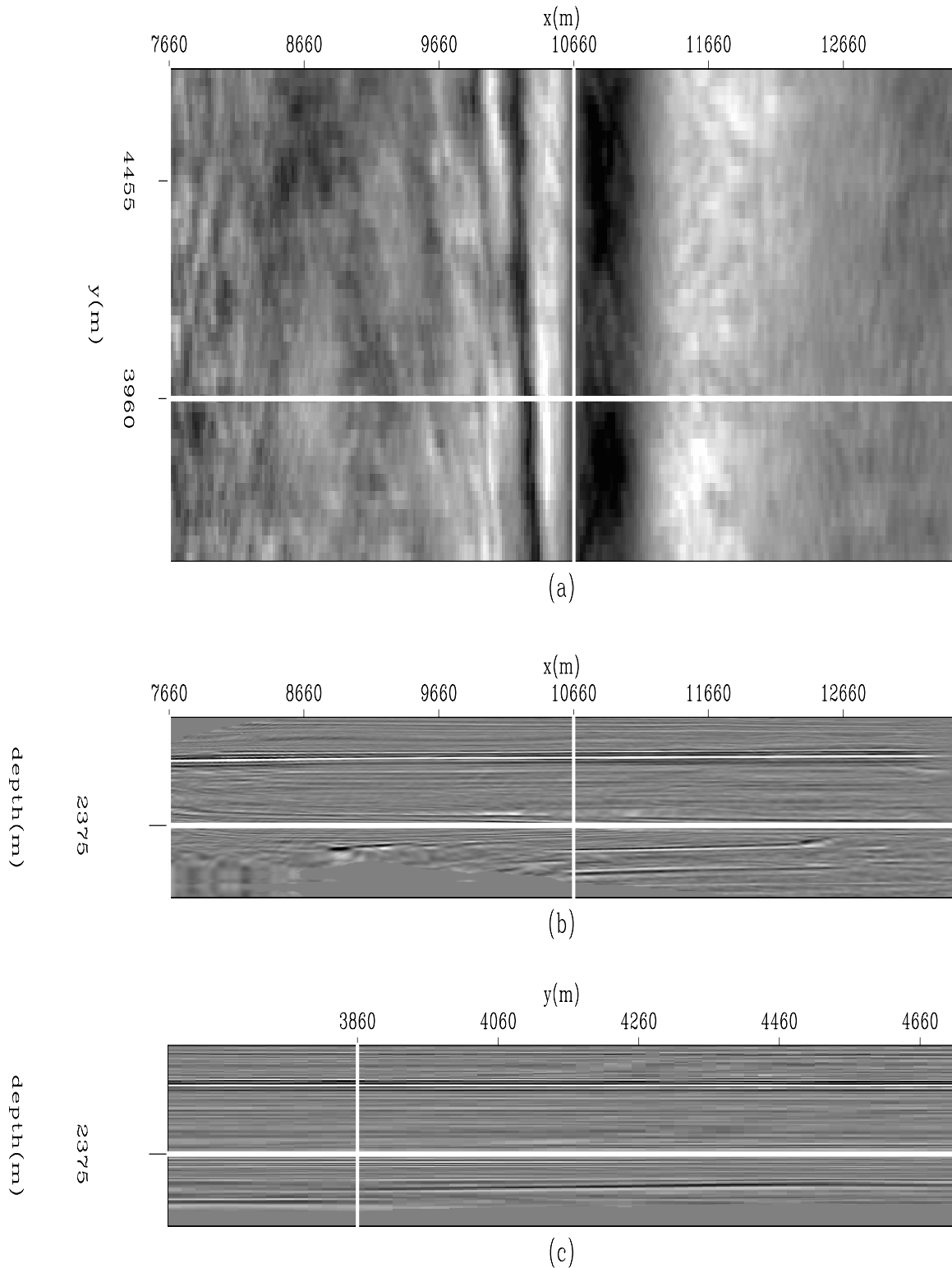


Figure 8: The result of flattening of Figure 7. This image illustrates the trade-off between data continuity preservation and flatness. We used a smoothing parameter ϵ of 1.0 to make this figure. Had we used a smaller ϵ , the output would be flatter but artifacts would be introduced into the data. (a) The horizon slice at depth=2375 m. (b) An in-line section at y=3960 m. (c) A cross-line section at x=10660 m. `jesse1-elf_flat` [ER]

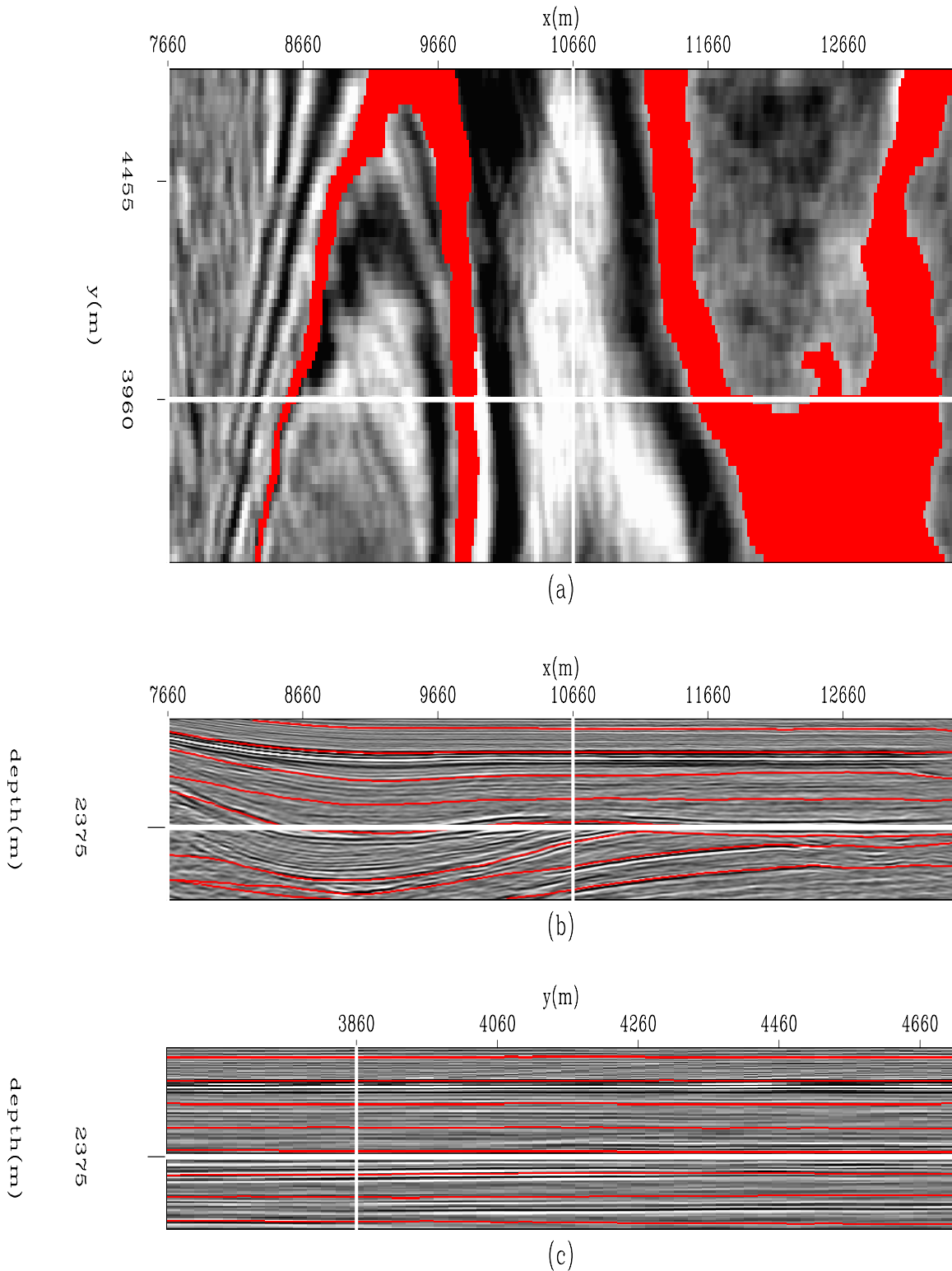


Figure 9: The result of overlaying tracked horizons on the image in Figure 7. Because the smoothing parameter ϵ is 0.0, horizons that lead to the angular unconformity are tracked. (a) The depth slice at $depth=2375$ m. (b) An in-line section at $y=3960$ m. (c) A cross-line section at $x=10660$ m. `jesse1-elf.horizon_overlay` [ER]

We use the crude binary weight cube shown in Figure 11 to identify areas where the inversion should ignore incorrect dips. This weight was created by manual picking. It should be noted that a suitable weight can also, in principle, be made from an automatic fault detector.

The flattening results are shown in Figure 12. Notice that the horizons are flat, even directly across from the fault. Also, notice the presence of a channel in the horizon slice. Figure 13 shows the original data with one unflattened horizon overlying it. It successfully tracks the horizon even across the fault. The time slice at the top of Figure 13 shows a horizon that is being partially cut by the fault at about $x=2600$ m.

DISCUSSION

To be fair, it should be noted that the flattening method only acts in the vertical dimension. This implicitly imposes several limitations. For instance, only vertical faults and beds that are not overturned can be properly restored. Also, the true stratigraphic thickness will be lost and replaced with the true vertical thickness at the reference trace.

The potential prestack applications of this method are numerous, and many of the challenges that must be overcome for poststack data are also present in prestack data.

The integrated time shift data has many potential uses. This method can easily be adapted to flatten data cubes on one or any particular combination of horizons. This would assist geologists in analyzing thicknesses for rates of deposition and timing of structural events.

CONCLUSIONS

We have developed a method to efficiently and robustly flatten 3D seismic cubes. This method uses an efficient implementation of the Fast Fourier transform within a non-linear iterative scheme. We demonstrated its effectiveness on a series of synthetic and field test cases.

Data cubes with vertical, laterally limited faults can be flattened by applying a residual weight. This allows horizons to be tracked across these faults.

We envision a tool that can be quickly and easily implemented by interpreters exploiting its superior computational performance. This method can provide an initial picking that interpreters can then adjust.

ACKNOWLEDGMENT

We would like to thank Chevron and Elf for the data used in this paper.

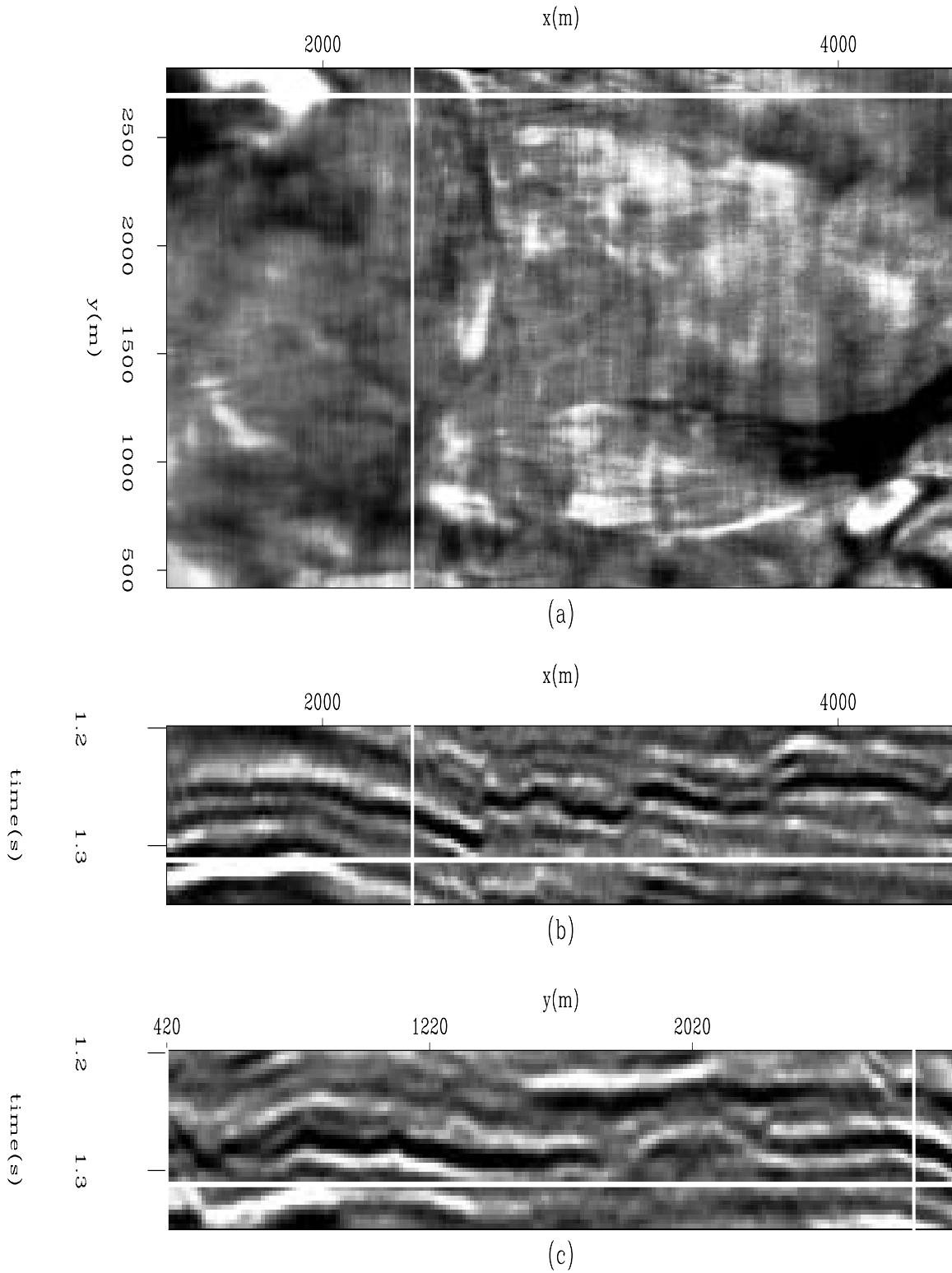


Figure 10: Faulted Chevron Gulf of Mexico data. The 2D vertical section shows fault with significant displacement (enough to cause our dip estimator to return erroneous values). (a) The time slice at $t=1.32$ s. (b) An in-line section at $y=2693$ m. (c) A cross-line section at $x=2348$ m. [jesse1-shoal](#) [ER]

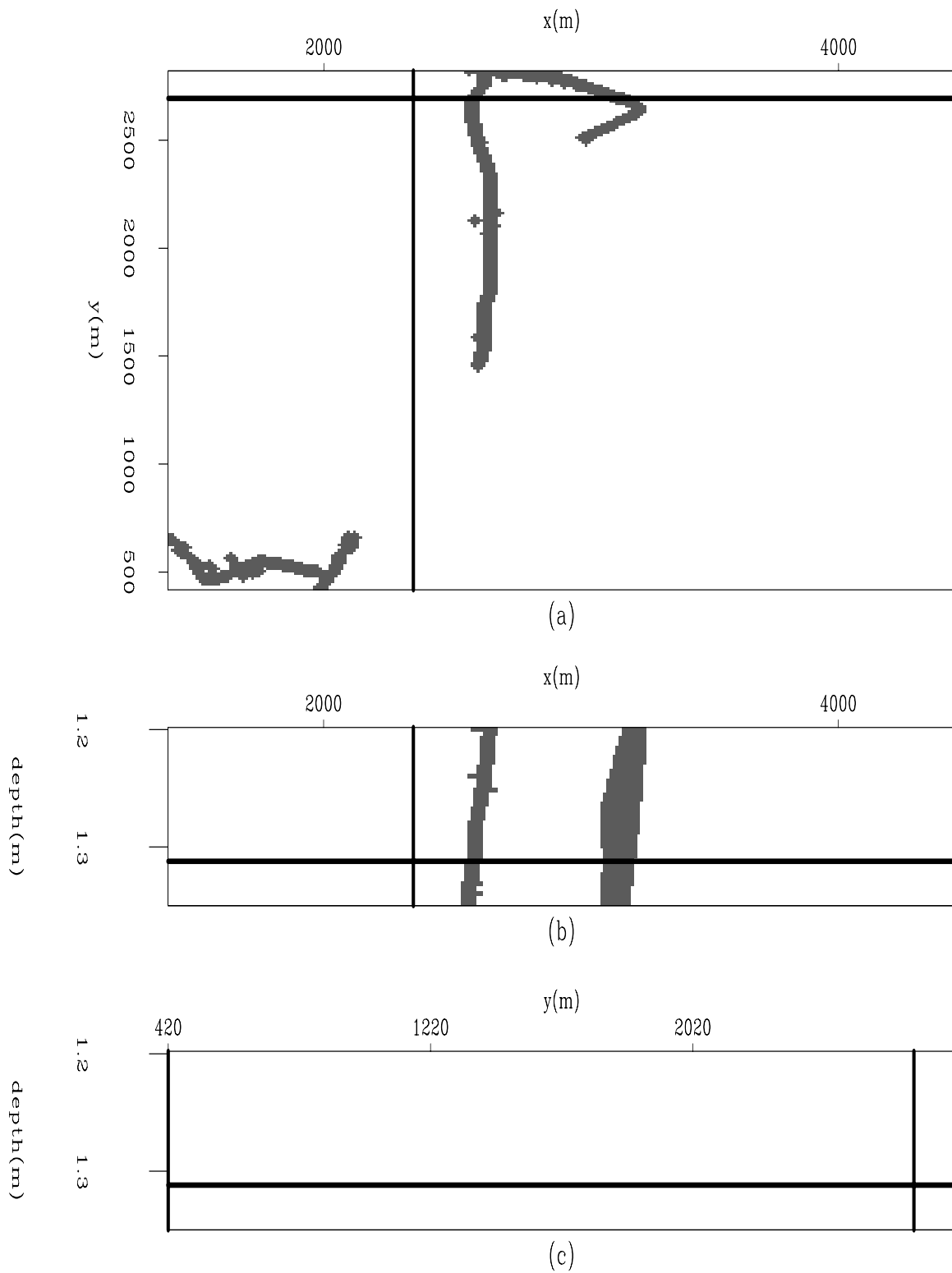


Figure 11: A weight identifying the faults data displayed in 10. (a) The time slice at time=1.32 s. (b) An in-line section at $y=2693$ m. (c) A cross-line section at $x=2348$ m.

`jesse1-shoal.wt` [ER]

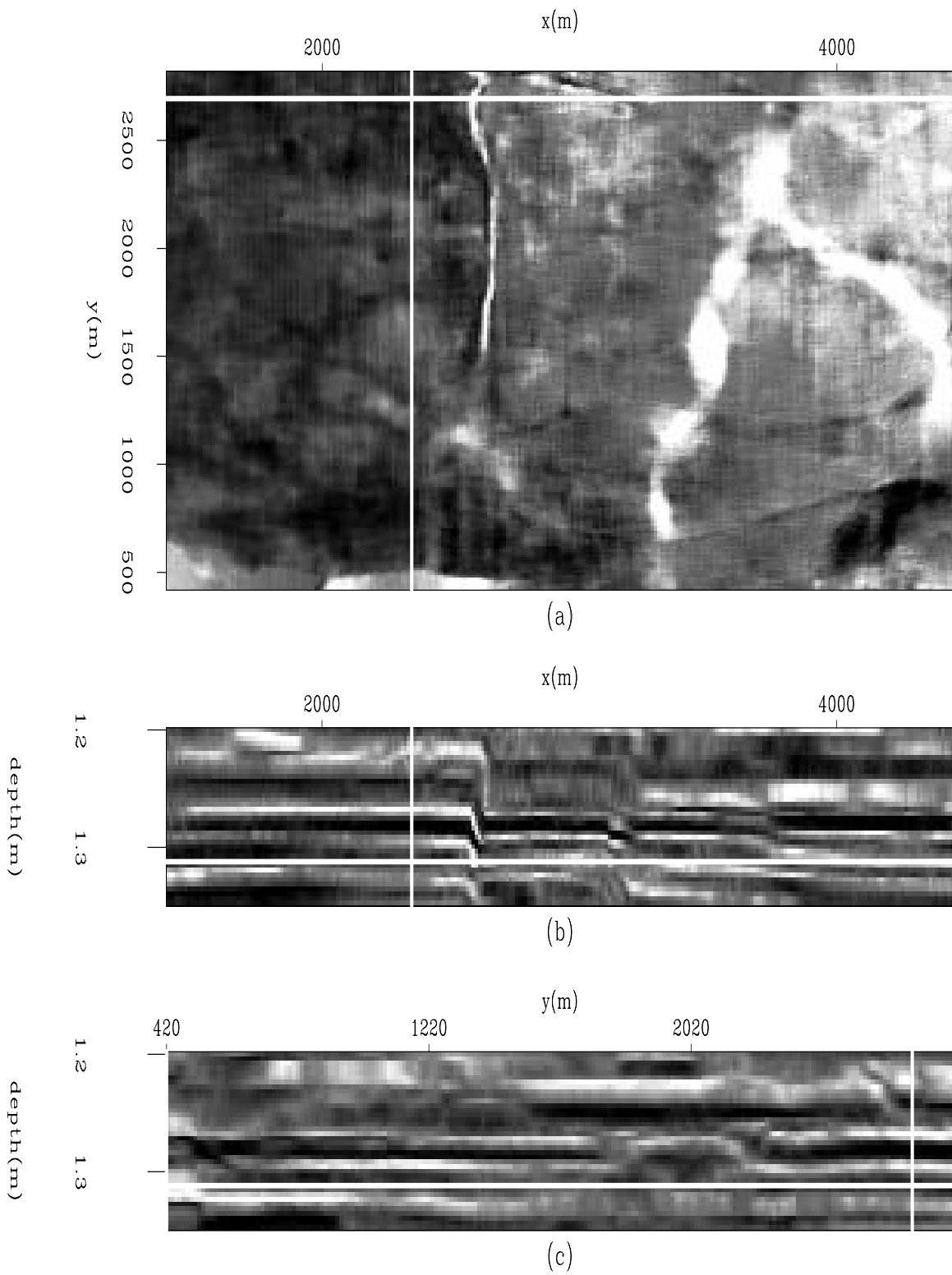


Figure 12: The result of flattening of Figure 10. (a) The horizon slice at time=1.32 s. (b) An in-line section at y=2693 m. (c) A cross-line section at x=2348 m. `jesse1-shoal.flat` [ER]

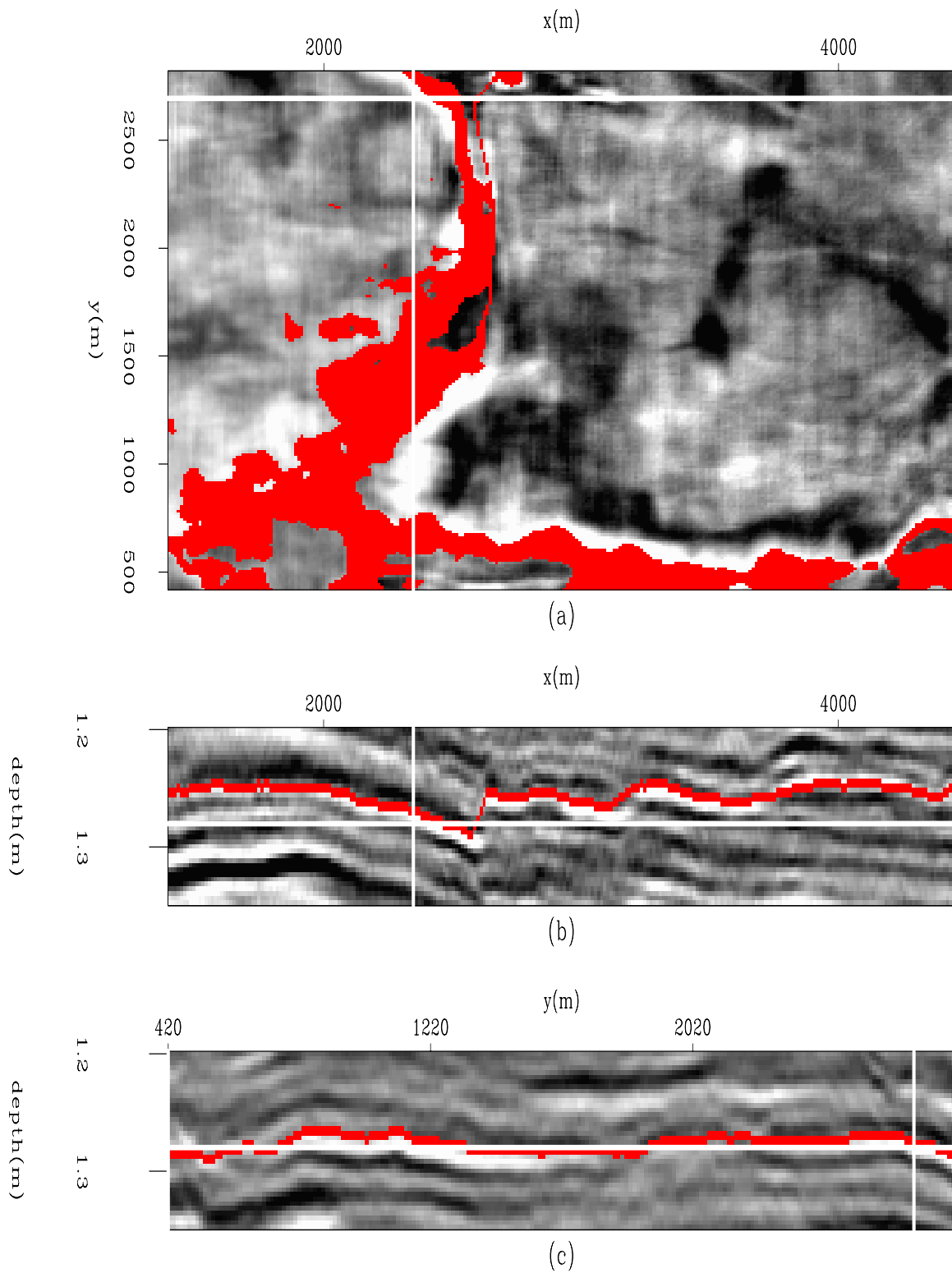


Figure 13: The result of overlaying a tracked horizon on the image in Figure 10. (a) The time slice at time=1.28 s. (b) An in-line section at $y=2693$ m. (c) A cross-line section at $x=2348$ m.

`jesse1-shoal.horizon_overlay` [ER]

REFERENCES

- Bienati, N., and Spagnolini, U., 1998, Traveltime picking in 3d data volumes: 60th EAGE Meeting, Extended Abstracts.
- Bienati, N., and Spagnolini, U., 2001, Multidimensional wavefront estimation from differential delays: *IEEE Trans on Geoscience and Remote Sensing*, , no. 3, 655–664.
- Bienati, N., Nicoli, M., and Spagnolini, U., 1999a, Automatic horizon picking algorithms for multidimensional data: 61st EAGE Meeting, Helsinki, Extended Abstracts.
- Bienati, N., Nicoli, M., and Spagnolini, U., 1999b, Horizon picking for multidimensional data: an integrated approach: Proc. 6th International Congress of the Brazilian Geophysical Society, Rio de Janeiro.
- Blinov, A., and Petrou, M., 2003, Reconstruction of 3d horizons from 3d seismic data sets: SPIE 10th International Symposium on Remote sensing, Remote Sensing fro environmental monitoring, GIS applications and Geolgy III.
- Claerbout, J. F., 1992, *Earth Soundings Analysis: Processing Versus Inversion*: Blackwell Scientific Publications.
- Claerbout, J., 1999, Geophysical estimation by example: Environmental soundings image enhancement: Stanford Exploration Project, <http://sepwww.stanford.edu/sep/prof/>.
- Farlow, S. J., 1993, *Partial differential equations for scientists and engineers*: Dover Publications.
- Fomel, S., 2002, Applications of plane-wave destruction filters: *Geophysics*, **67**, no. 6, 1946–1960.
- Ghiglia, D. C., and Romero, L. A., 1994, Robust two-dimensional weighted and unweighted phase unwrapping that uses fast transforms and iterative methods: *Optical Society of America*, **11**, no. 1, 107–117.
- Guitton, A., Claerbout, J. F., and Lomask, J. M., 2004, First order interval velocity estimates without picking: 74th SEG Meeting, Extended Abstracts.
- Guitton, A., Lomask, J., and Fomel, S., 2005, Non-linear estimation of vertical delays with a quasi-Newton method: *SEP-120*, 167–178.
- James, H., Peloso, A., and Wang, J., 2002, Volume interpretation of mult-attribute 3d surveys: *First Break*, **20**, no. 3, 176–180.
- Lee, R., 2001, Pitfalls in seismic data flattening: *The Leading Edge*, **20**, no. 01, 160–164.
- Leggett, M., Sandham, W. A., and Durrani, T. S., 1996, 3d horizon tracking using artificial neural networks: *First Break*, **14**, no. 11, 413–418.

Lomask, J., 2003a, Flattening 3d seismic cubes without picking: 73th SEG Meeting, Extended Abstracts.

Lomask, J., 2003b, Flattening 3-D data cubes in complex geology: SEP-**113**, 247-260.

Stark, T. J., 2004, Relative geologic time (age) volume- relating every seismic sample to a geologically reasonable horizon: *The Leading Edge*, **23**, no. 9, 928-932.

Flattening without picking faults

Jesse Lomask, Antoine Guitton, and Alejandro Valenciano¹

ABSTRACT

We show that iteratively re-weighted least squares (IRLS) can flatten data cubes with vertically-oriented faults without having to pick the faults. One requirement is that the faults need to have at least part of their tip-lines (fault terminations) encased within the 3D cube. We demonstrate this method's flattening ability on a faulted 3D field data-set.

INTRODUCTION

Flattening algorithms (Lomask and Claerbout, 2002; Lomask, 2003; Lomask et al., 2005) are able to flatten seismic data cubes with faults by summing the dips into time shifts around the faults and ignoring the dips across the faults. In order to know which dips to ignore and which dips to honor during inversion, we require a fault indicator (data residuals weight that throw away bad dips). This indicator could be either manually picked or automatically generated by an automatic fault detector.

While the smoothness of the summed time shifts are often justifiable in non-faulted areas, the time shifts can change abruptly across the faults. In these situations, we desire an inversion technique that yields smooth time shifts in non-faulted areas while preserving sharp time shifts across the faults. In addition, no pre-defined fault indicator should be supplied.

In this paper, we present an automatic edge-preserving method for flattening faulted data without requiring an input fault model. The method uses iterative re-weighted least-squares (IRLS). A Geman-McClure weight function (fault indicator) of data residuals is computed at each non-linear iteration to allow outliers in the data residuals.

The only requirements are that part of the fault tip-lines are encased in the data and that the faults are oriented vertically. The resulting weight generated by this IRLS method is a fault indicator cube that best flattens the data. This is an important difference from many traditional automatic fault detectors that are defined by local discontinuities.

¹**email:** lomask@sep.stanford.edu, antoine@sep.stanford.edu, valencia@sep.stanford.edu

METHODOLOGY

We modify the flattening algorithm described in Lomask et al. (2005). The key regression is this overdetermined system:

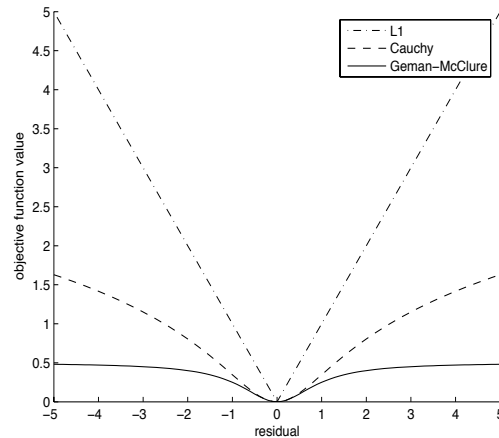
$$\nabla \tau = \mathbf{p}. \quad (1)$$

This equation means that we need to find a time-shift field $\tau(x, y, z)$ such that its gradient approximates the dip $\mathbf{p}(x, y, \tau)$. It is overdetermined because we are finding a single summed time shift field such that its two-dimensional gradient matches the dip in the x and y directions.

Imagine that after solving equation (1), the data residuals consist of spikes separated by relatively large distances. Then the estimated time shifts τ would be piecewise smooth with jumps at the spike locations (fault locations), which is what we desire. However, in solving Equation (1), we use the least-squares criterion – minimization of the ℓ_2 norm of the residual. Large spikes in the residual tend to be attenuated. In the model space, the solver smooths the time shifts across the spike location.

It is known that the ℓ_1 norm is less sensitive to spikes in the residual (Claerbout and Muir, 1973; Darche, 1989; Nichols, 1994). Minimization of the ℓ_1 norm makes the assumption that the residuals are exponentially distributed and have a “long-tailed” distribution relative to the Gaussian function assumed by the ℓ_2 norm inversion.

Figure 1: Comparison of the loss functions for the ℓ_1 , Cauchy, and Geman-McClure functions. Notice that the Geman-McClure is the most robust. [jesse2-2](#) [CR]

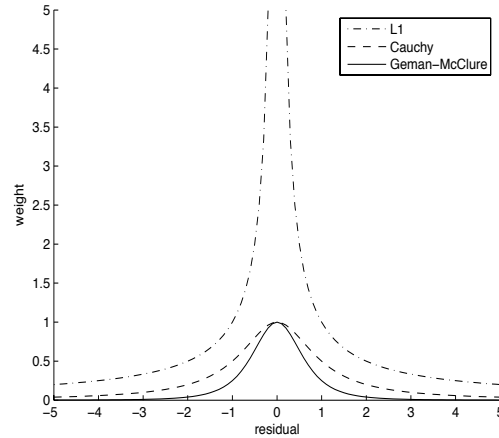


Here, we compute non-linear model residual weights which force a Geman-McClure distribution, another long-tailed distribution which approximates an exponential distribution. A comparison of the loss functions for the ℓ_1 , Cauchy (Claerbout, 1999), and Geman-McClure functions is shown in Figure 1. Notice that the Geman-McClure is the most robust in that it is the least sensitive to outliers. Our weighted regression now is the following over-determined system:

$$\mathbf{W}^{j-1} \nabla \tau^j = \mathbf{W}^{j-1} \mathbf{p}, \quad (2)$$

where \mathbf{W}^{j-1} is the weight computed at the previous non-linear iteration.

Figure 2: Comparison of weight functions for the ℓ_1 , Cauchy, and Geman-McClure functions. The Geman-McClure is most restrictive, this may be desirable for weighting faults. [jesse2-3](#) [CR]



Our method consists of recomputing the weights at each non-linear iteration, solving small piecewise Gauss-Newton linear problems. The IRLS algorithms converge if each minimization reaches a minimum for a constant weight. We perform the following non-linear iterations: starting with the weights $\mathbf{W}^0 = \mathbf{I}$, at the j^{th} iteration the algorithm solves

iterate {

$$\mathbf{r} = \mathbf{W}[\nabla \boldsymbol{\tau}_k - \mathbf{p}] \quad (3)$$

$$\Delta \boldsymbol{\tau} = (\nabla' \nabla)^{-1} \nabla' \mathbf{r} \quad (4)$$

$$\boldsymbol{\tau}_{k+1} = \boldsymbol{\tau}_k + \Delta \boldsymbol{\tau} \quad (5)$$

}

At every non-linear iteration j^{th} iteration we re-estimate our Geman-McClure weight function:

$$\mathbf{W}^{j-1} = \mathbf{diag} \left(\frac{1}{(1 + (\mathbf{r}^{j-1})^2 / \bar{r}^2)^2} \right) \quad (6)$$

where \bar{r} is an adjustable parameter. A comparison of weight functions for the ℓ_1 , Cauchy, and Geman-McClure functions is shown in Figure 2. Notice that the Geman-McClure creates the tightest, most precise weight. This should have the advantage of having a surgical-like effect of down-weighting spurious dips.

FIELD DATA EXAMPLE

We tested this method on the Chevron Shoal data shown in Figure 3. At first glance, the 2D in-line section does not appear to have much faulting. However, there is actually a nearly vertical fault near the center, and dip estimators will return incorrect estimates at faults.

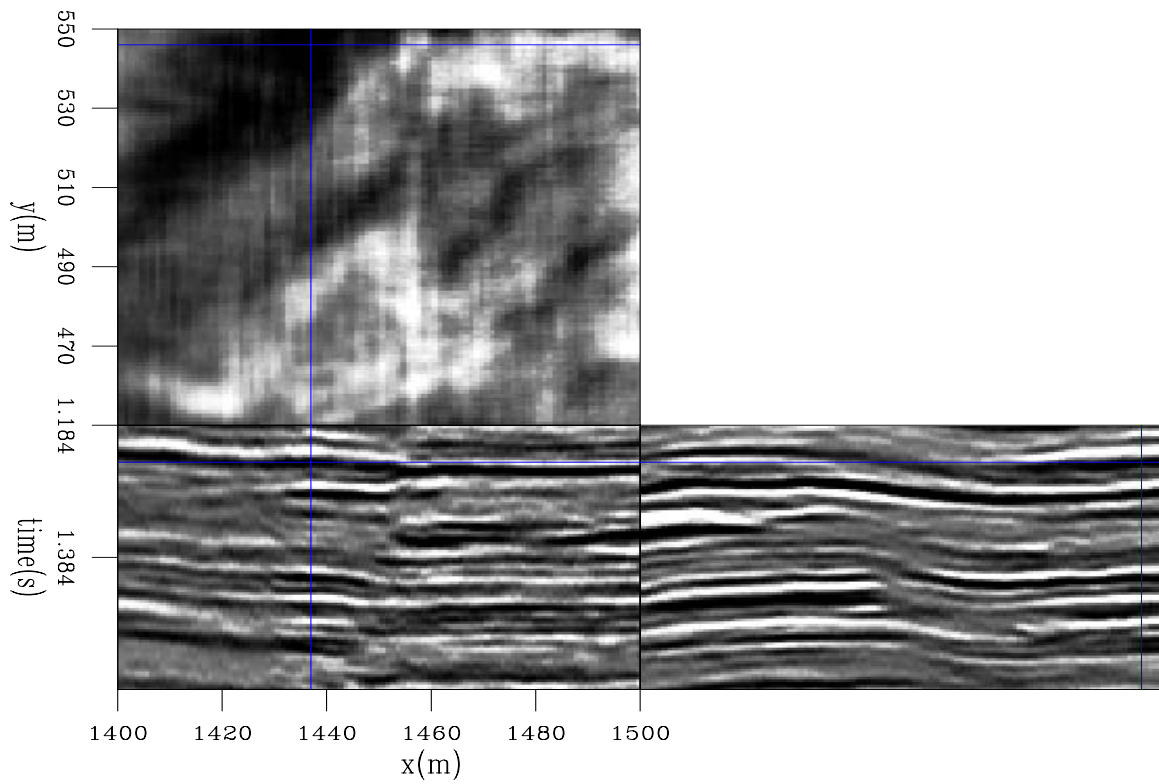


Figure 3: Faulted Chevron Gulf of Mexico data. Although it is difficult to see, the 2D vertical section shows fault with significant displacement, enough to cause our dip estimator to return erroneous values. `jesse2-dat` [ER]

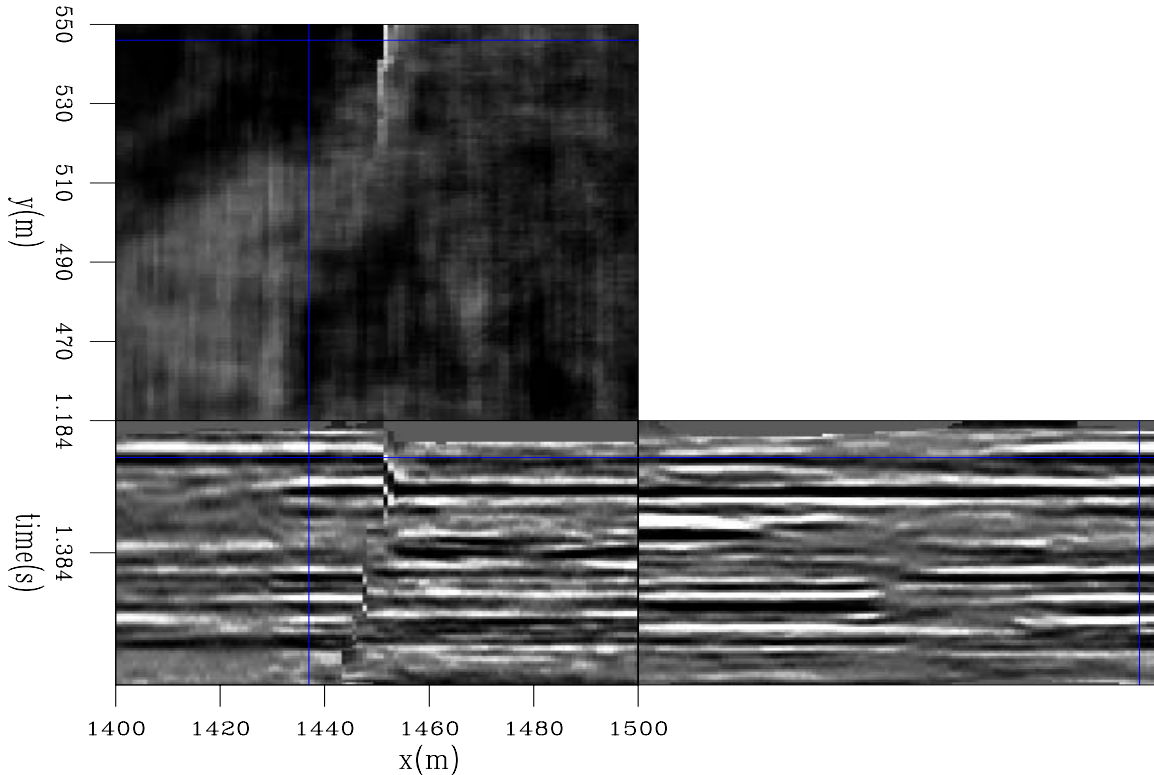


Figure 4: The result of flattening of Figure 3 `jesse2-flat` [ER]

We applied our IRLS flattening method to this data to get the result shown in Figure 4. The position of the fault is more obvious in this image because the data on either side were shifted by the flattening process.

The fault weight automatically created by this method is shown in Figure 5. It is, however, more insightful to overlay the fault weight on the original unflattened data as in Figure 6. Also, it is interesting to note that the fault appears to be segmented.

CONCLUSION

We presented an IRLS flattening approach able to flatten data cubes in the presence of laterally limited vertical faults. Our method uses iteratively re-weighted least-squares with the Geman-McClure function. The requirement that the faults terminate within the data is necessary so that dips can be summed around the faults in order to remove the structure.

For faults that do not terminate within the data cube, this method still may indicate their location. This is because dips estimated at faults tend to be more erratic than other dips away from the fault and are usually treated as outliers.

There are still several weaknesses and areas for improvement of this method. If the fault termination is close to the boundary of the data, this method has the unfortunate side effect

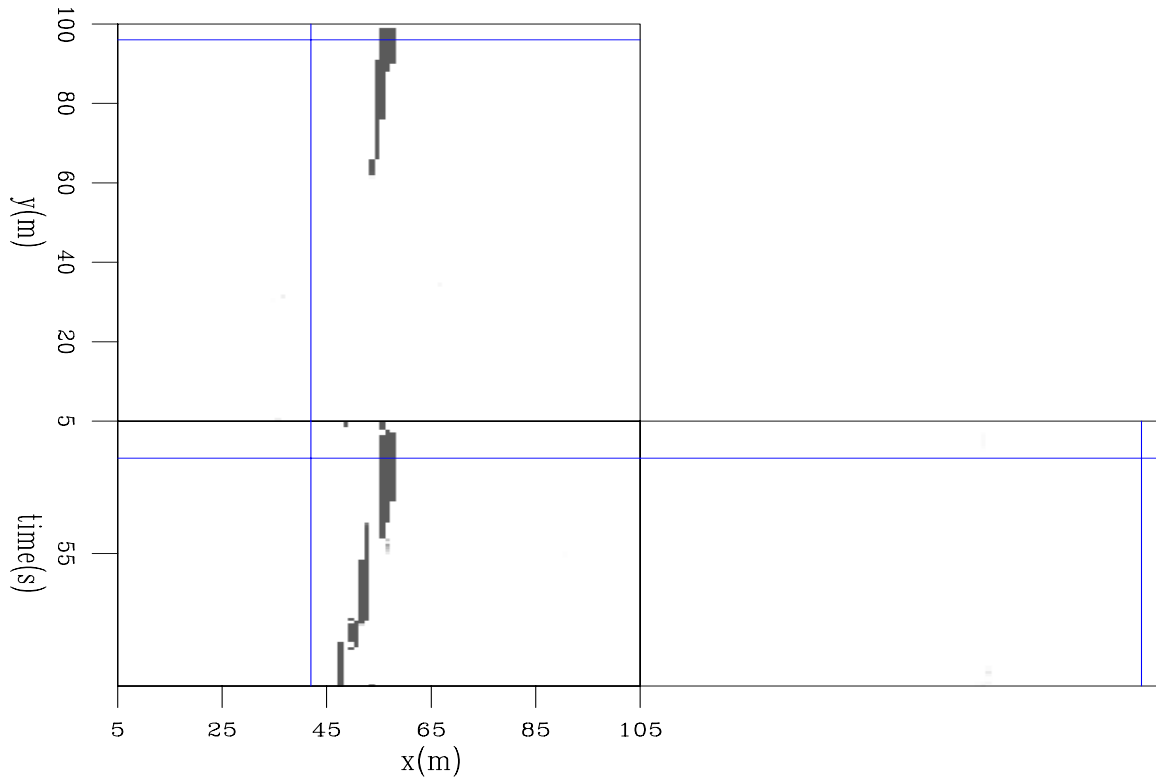


Figure 5: The fault weight automatically created by flattening Figure 3 `jesse2-wt` [ER]

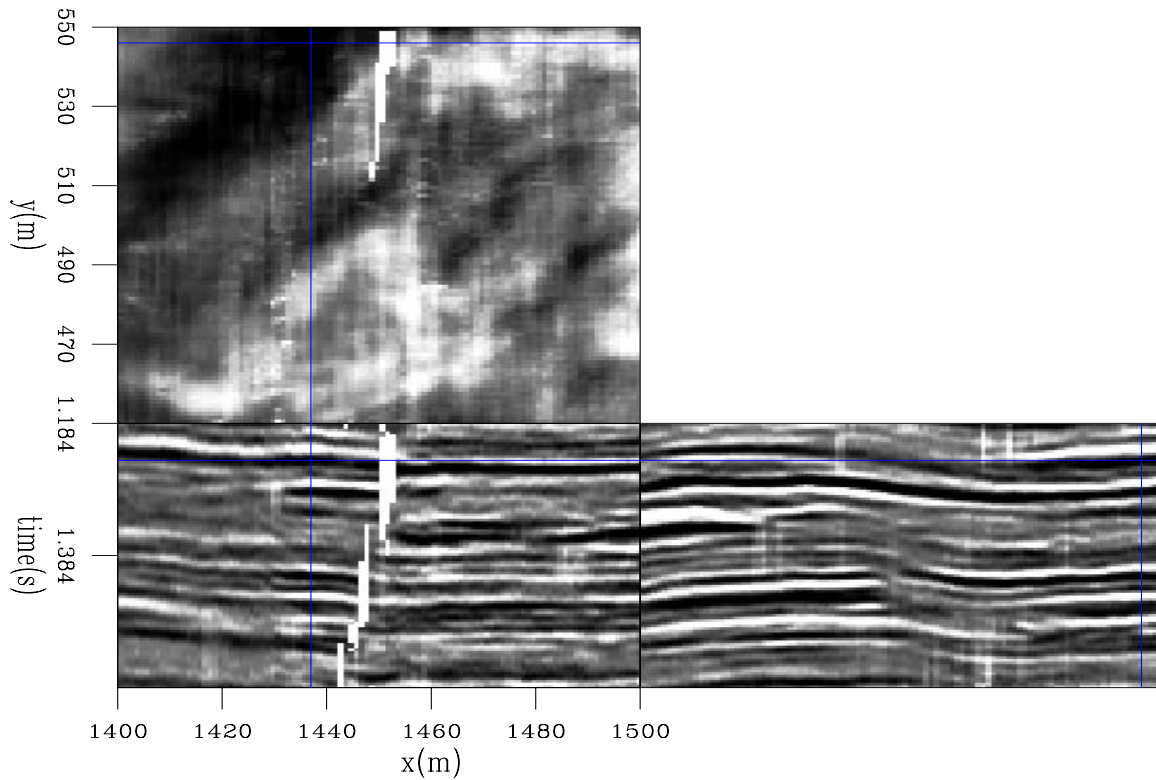


Figure 6: The input data with the `jesse2-wt.dat` [ER]

of connecting the fault to the data boundary, creating a separate fault block. It may also have the tendency to create false faults if there is significant noise. Lastly, we still may not have determined the best weight function.

ACKNOWLEDGMENT

We would like to thank Chevron for providing the data used in this paper.

REFERENCES

- Claerbout, J. F., and Muir, F., 1973, Robust modeling with erratic data: *Geophysics*, **38**, no. 5, 826–844.
- Claerbout, J., 1999, Geophysical estimation by example: Environmental soundings image enhancement: Stanford Exploration Project, <http://sepwww.stanford.edu/sep/prof/>.
- Darce, G., 1989, Iterative l_1 deconvolution: SEP-**61**, 281–302.
- Lomask, J., and Claerbout, J., 2002, Flattening without picking: SEP-**112**, 141–150.
- Lomask, J., Guitton, A., Fomel, S., and Claerbout, J., 2005, Update on flattening without picking: SEP-**120**, 137–158.
- Lomask, J., 2003, Flattening 3-D data cubes in complex geology: SEP-**113**, 247–260.
- Nichols, D., 1994, Velocity-stack inversion using L_p norms: SEP-**82**, 1–16.



Non-linear estimation of vertical delays with a quasi-Newton method

Antoine Guitton, Jesse Lomask, and Sergey Fomel¹

ABSTRACT

A local dip (or step out) between two adjacent traces embeds the necessary information to go from one reflection on one trace to the same reflection on the next. In more dimensions, i.e., 3-D, the same result is obtained between distant traces by integrating the local dips in all directions, thus obtaining relative delay maps useful for (1) automatic full-volume picking and (2) automatic flattening of horizons. The estimation of these maps from local dips is a non-linear process. In this paper, this problem is solved with a quasi-Newton technique for 2-D slices and 3-D cubes. Furthermore, the estimation of the relative delays is done globally in a least-squares sense for all reflectors at once. Synthetic and field data examples illustrate the ability of the algorithm to flatten horizon according to their geological time. As a natural extension of our algorithm, any horizon can also be picked automatically at no additional cost.

INTRODUCTION

From the estimation of local dips, Lomask (2003a) showed that vertical shifts (time or depth) can be estimated to flatten seismic data in 2-D or 3-D. The basic idea is to integrate local dips or step outs estimated from the data. This integration gives for every point in the data volume a relative vertical (time or depth) delay to one event present on a reference trace. This delay can be used for flattening, where each sample is shifted according to the delay value, or for picking, where one event (or many events) can be followed from the reference trace to everywhere in the data volume by simply stepping up or down according to the delay value. In addition, time/depth shift estimation can be used for many geophysical applications. For instance, Wolf et al. (2004) illustrate how RMS velocities can be estimated without picking. Similarly, Guitton et al. (2004) solve a tomographic problem by inverting the time delays.

Lomask (2003b) identified a non-linear relationship between the local dips and the relative delays. In his approach, however, this property was first ignored by solving simpler linear problems. The goal of this paper is to solve the non-linear problem exactly with a quasi-Newton approach called L-BFGS (Guitton and Symes, 2003). Solving the non-linear problem allows us to estimate relative time/depth shifts when the local dips are not constant with time or depth, a central assumption in the linear approach of Lomask (2003a).

¹**email:** antoine@sep.stanford.edu, lomask@sep.stanford.edu, sergey.fomel@beg.utexas.edu

This paper starts with a presentation of the theory of time/depth delay estimation in 2-D and 3-D. The quasi-Newton method is briefly introduced. Then, the proposed algorithm is tested on 2-D and 3-D data examples. They illustrate the accuracy of the method to compute relative time/depth delays and to perform event picking.

THEORY OF TIME/DEPTH DELAYS ESTIMATION

First consider a data volume $d(x, y, z)$ where x and y are the horizontal axes and z is the depth or time axis. Building on Lomask (2003b), a vertical (time or depth) delay function $\tau(x, y, z)$ is estimated by minimizing the following functional $J(\tau)$:

$$J(\tau) = \int \int \left[\left(p_x(x, y, z; \tau) - \frac{\partial \tau}{\partial x} \right)^2 + \left(p_y(x, y, z; \tau) - \frac{\partial \tau}{\partial y} \right)^2 \right] dx dy, \quad (1)$$

where p_x is the local step-out vector estimated in the x direction and p_y is the local step-out vector estimated in the y direction. Both vectors depend on τ , which makes the problem of finding the time/depth delays non-linear.

In this paper, we propose solving for $\tau(x, y, z)$ with a quasi-Newton method called L-BFGS (Guitton and Symes, 2003). The quasi-Newton method is an iterative process where the solution to the problem is updated as follows:

$$\tau_{k+1} = \tau_k - \lambda_k \mathbf{H}_k^{-1} \nabla J(\tau_k), \quad (2)$$

where τ_{k+1} is the updated solution at iteration $k + 1$, λ_k the step length computed by a line search that ensures a sufficient decrease of $J(\tau)$ and \mathbf{H}_k an approximation of the Hessian (or second derivative.) One important property of L-BFGS is that it requires the gradient of $J(\tau)$ only to build the Hessian. The gradient $\nabla J(\tau)$ of $J(\tau)$ can be found by introducing the Euler-Lagrange equation and is given by:

$$\nabla J(\tau) = -\frac{\partial^2 \tau}{\partial x^2} - \frac{\partial^2 \tau}{\partial y^2} + \frac{\partial p_x}{\partial x} + \frac{\partial p_y}{\partial y} + \frac{1}{2} \frac{\partial p_x^2}{\partial \tau} + \frac{1}{2} \frac{\partial p_y^2}{\partial \tau} \quad (3)$$

The 2-D case is a simple extension of this result where the terms in y are dropped. In practice, the last four terms of the gradient in equation (3) can be precomputed and evaluated at $\tau_k(x, y, z)$ when needed for the BFGS update. This saves a lot of computational effort. Note that the relative vertical (time or depth) delays are computed with respect to a reference trace chosen a priori in the data volume. A weight that would throw-out fitting equations at fault locations can also be incorporated easily in both the gradient and objective function.

The most important components of this time/depth delay evaluation technique are the dip fields p_x and p_y . In our implementation, we use the method of Fomel (2002) to estimate both. This technique estimates local dips from adjacent traces without slant-stacking. It also gives one dip value only for each data point. Next, 2-D and 3-D data examples illustrate the flattening technique.

2-D DATA EXAMPLES

The 2-D algorithm, a simple extension of the 3-D algorithm, is illustrated first on five synthetic (Figures 1 to 5) and one field data examples (Figure 6). All these figures are organized as follows: panel (a) shows the input data, panel (b) shows the estimated dip field using Fomel's technique (Fomel, 2002), (d) shows the picking result where the seed point starts from the reference trace every ten samples in time/depth, and (d) shows the flattening result. The field data example is a 2-D slice extracted from the Elf (now Total) L7D dataset after common-azimuth depth migration (Vaillant et al., 2000). All these examples illustrate that the time/depth delay estimation process is very accurate and robust.

3-D DATA EXAMPLES

The 3-D algorithm is tested on two datasets from the Gulf of Mexico. Figures 7a, 7b, and 7c show the input data, the picked reflector, and the flattening result for the first dataset. The size of this dataset is 100x100x100 samples. After flattening in Figure 7c, a channel is now clearly visible. Note that the picked reflectors in Figure 7b follow extremely well the true reflectors. Again, this result is obtained at no cost and is readily available from the estimation of $\tau(x, y, z)$.

Figures 8a, 8b, and 8c show the input data, the picked reflector, and the flattening result for the second dataset. The size of this dataset is 200x200x200 samples. It features more complicated structures such as a large salt body on the left (shown as SF) and faults. Nothing was done to pick the faults, as suggested by (Lomask et al., 2005). Nevertheless, the flattening result in Figure 8c highlights one channel on the depth slice that was not previously visible. The picking result in Figure 8b is also very accurate.

CONCLUSION

Estimating time/depth delays from dip fields is a non-linear problem. A quasi-Newton technique was introduced to solve it. Several 2-D and 3-D examples illustrate the efficiency of this method to flatten and automatically interpret seismic horizons without any picking.

ACKNOWLEDGEMENTS

We thank ChevronTexaco for providing the dataset used in the first 3-D example, and Joe Reilly at ExxonMobil for the second 3-D dataset.

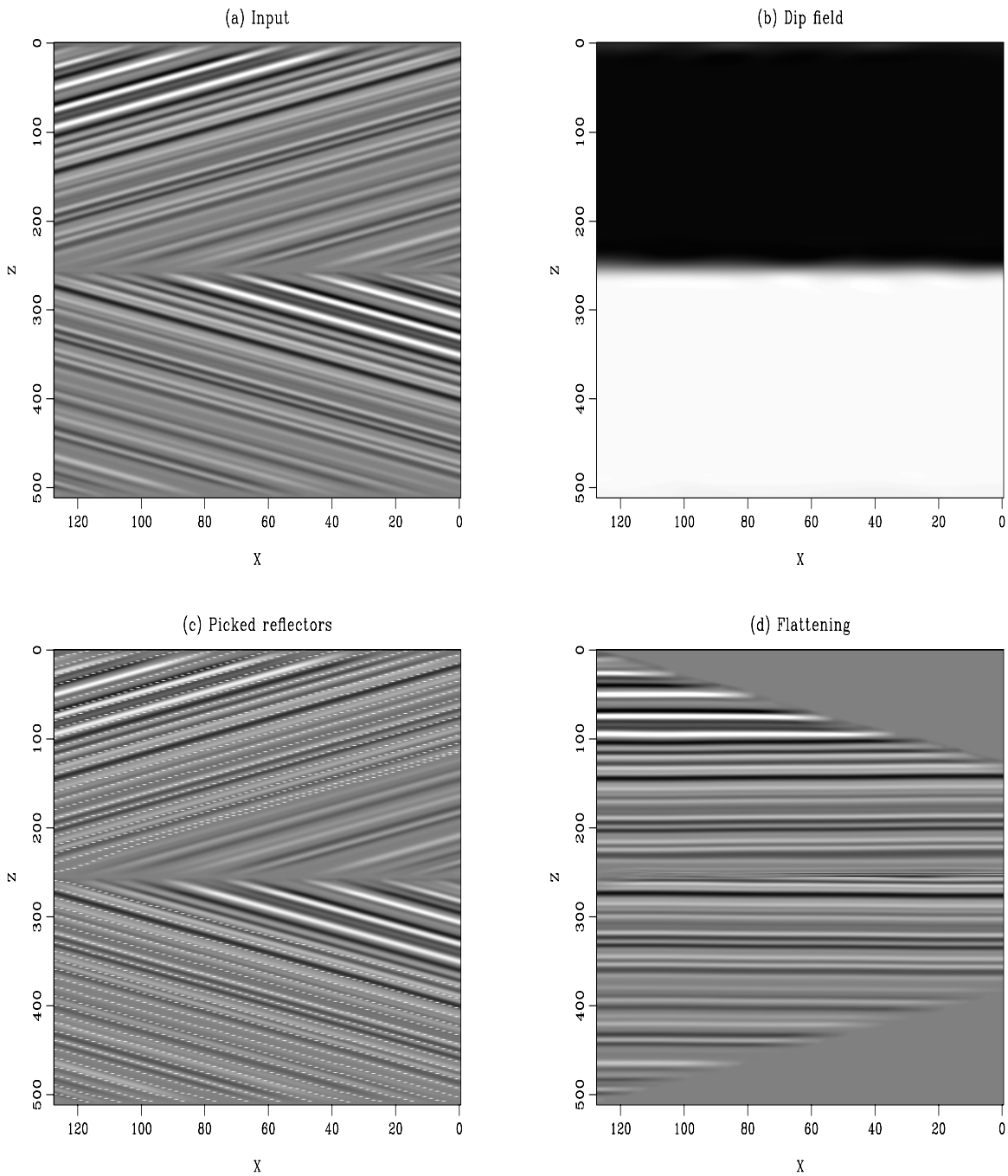


Figure 1: (a) Model. (b) Estimated dips. (c) Automatic picking of few horizons. (d) Flattening result. The first trace is used for reference. [antoine1-unconformity](#) [ER]

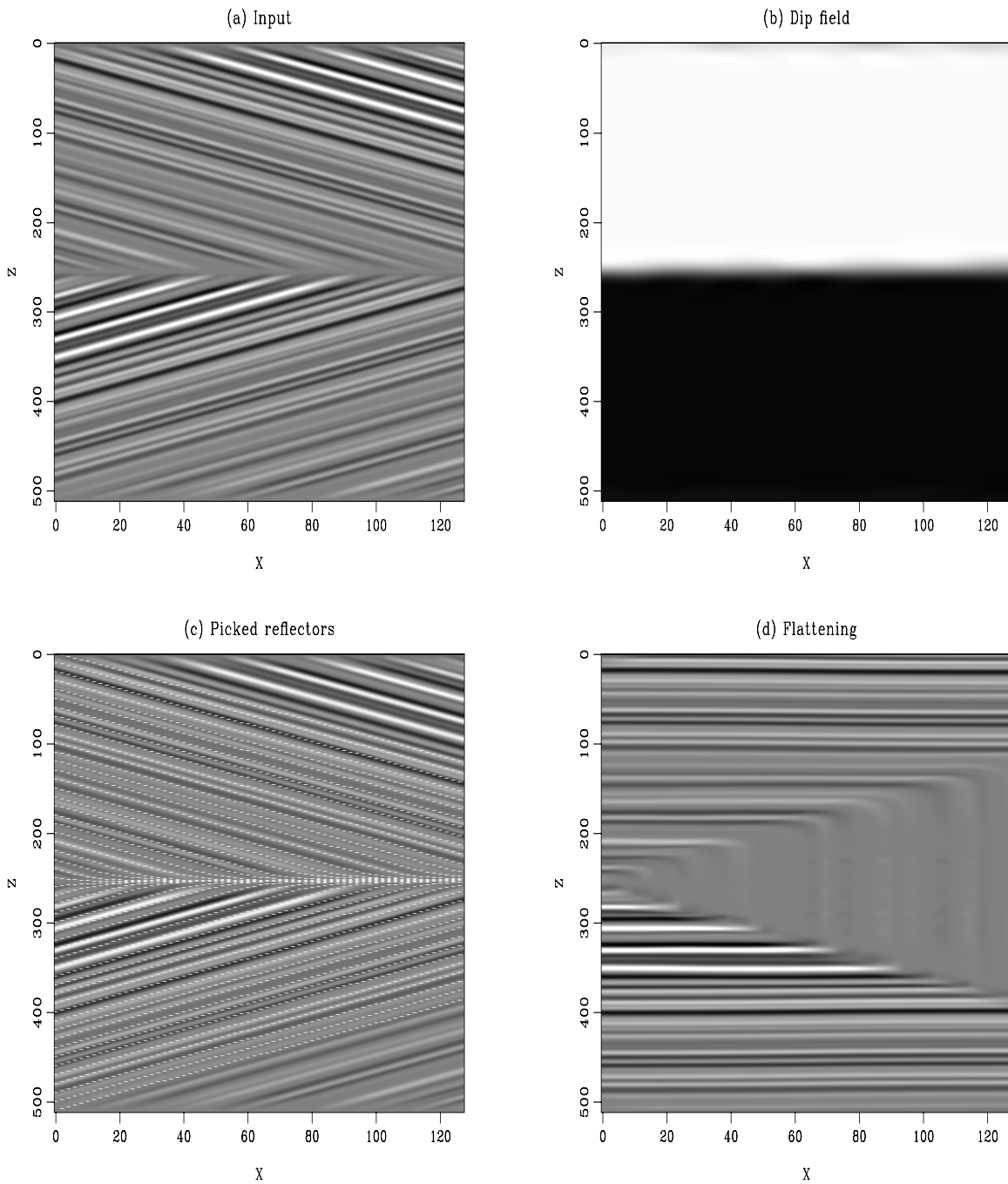


Figure 2: (a) Model. (b) Estimated dips. (c) Automatic picking of few horizons. (d) Flattening result. The first trace is used for reference. [antoine1-unconformity2](#) [ER]

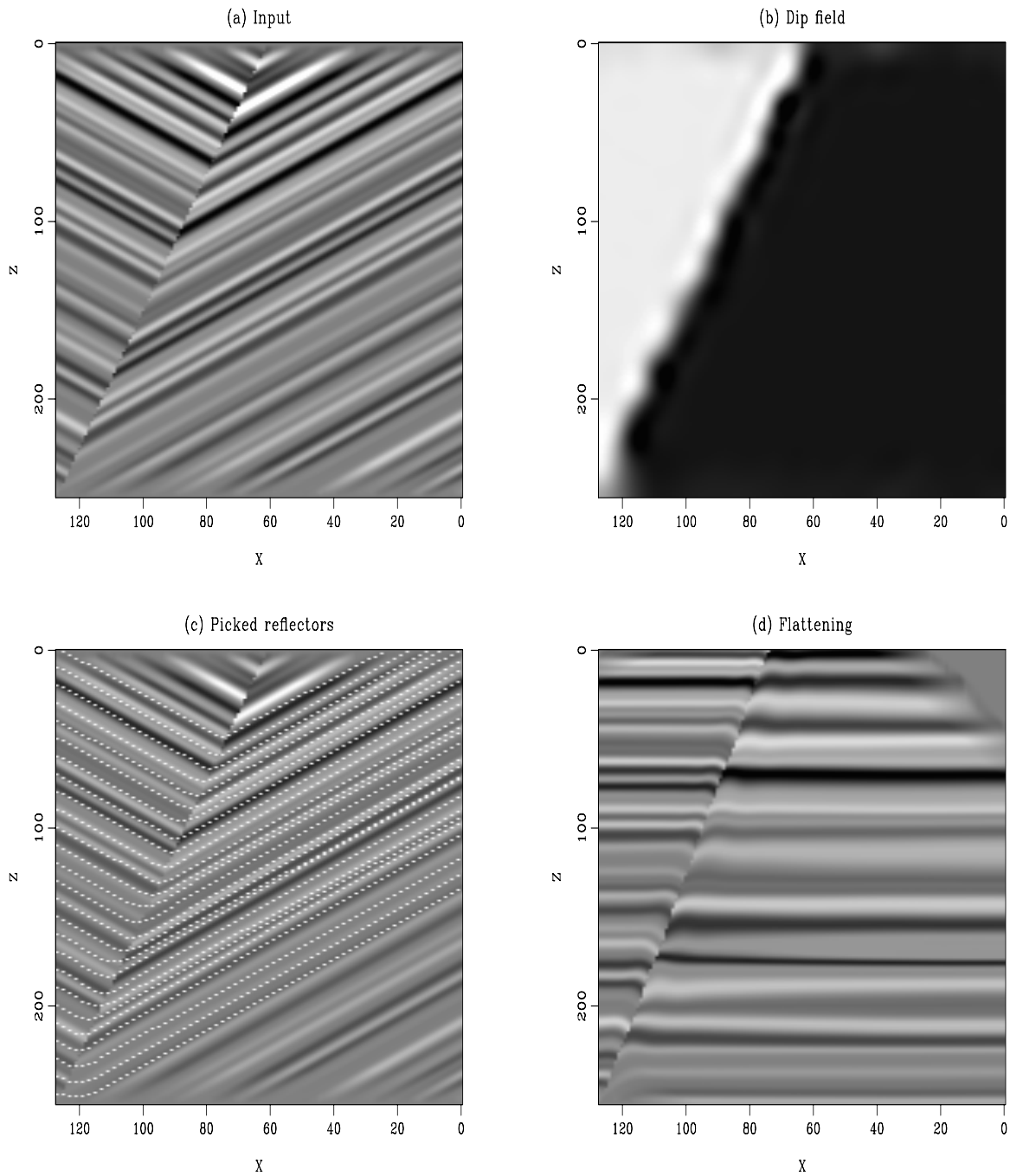


Figure 3: (a) Model. (b) Estimated dips. (c) Automatic picking of few horizons. (d) Flattening result. The smoothness of the estimated dips introduce small errors in the flattening result. The first trace is used for reference. `antoine1-unconformity3` [ER]

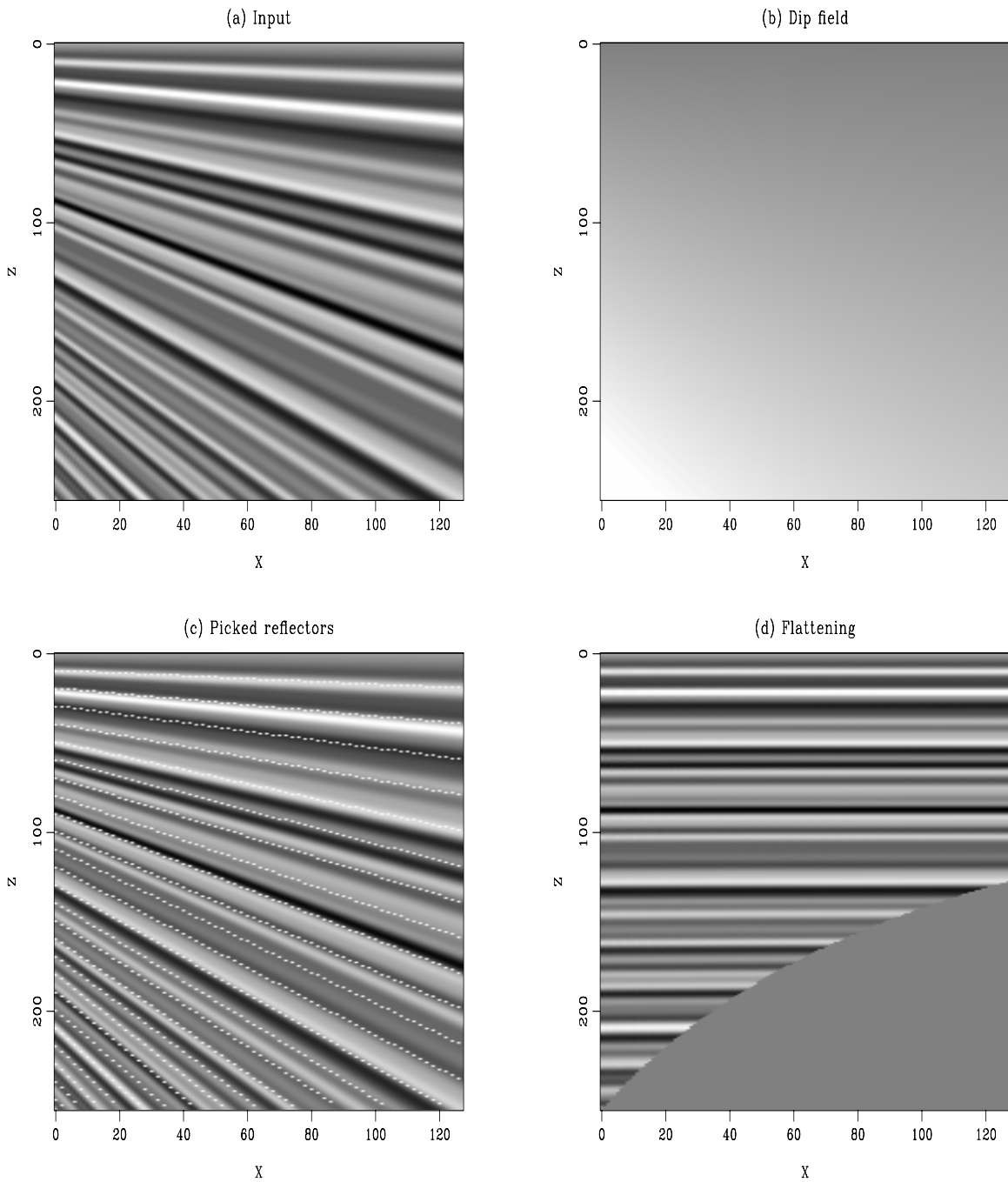


Figure 4: (a) Model. (b) Estimated dips. (c) Automatic picking of few horizons. (d) Flattening result. The first trace is used for reference. antoine1-thinning3 [ER]

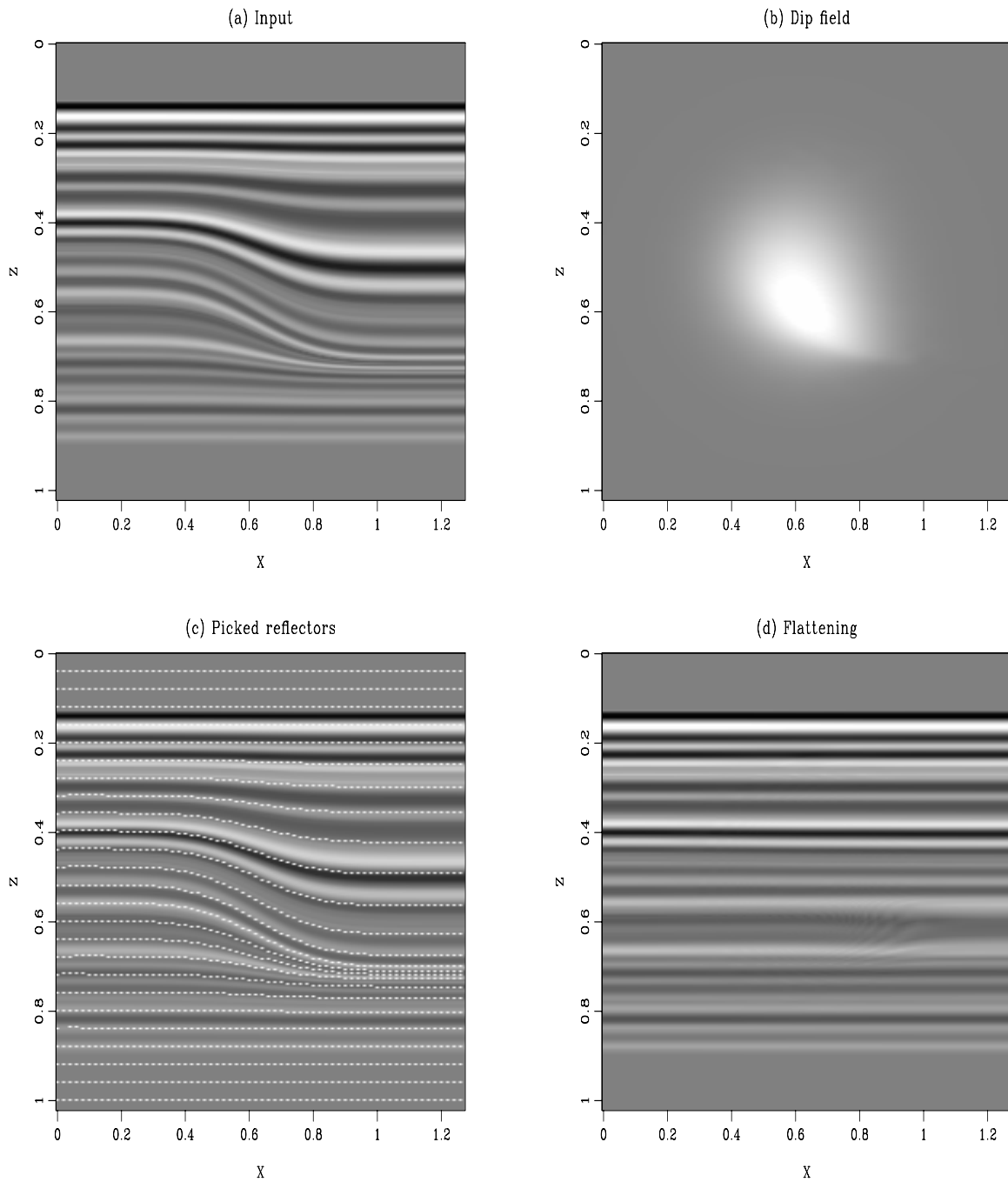


Figure 5: (a) Model. (b) Estimated dips. (c) Automatic picking of few horizons. (d) Flattening result. The first trace is used for reference. `antoine1-down_lap2D` [ER]

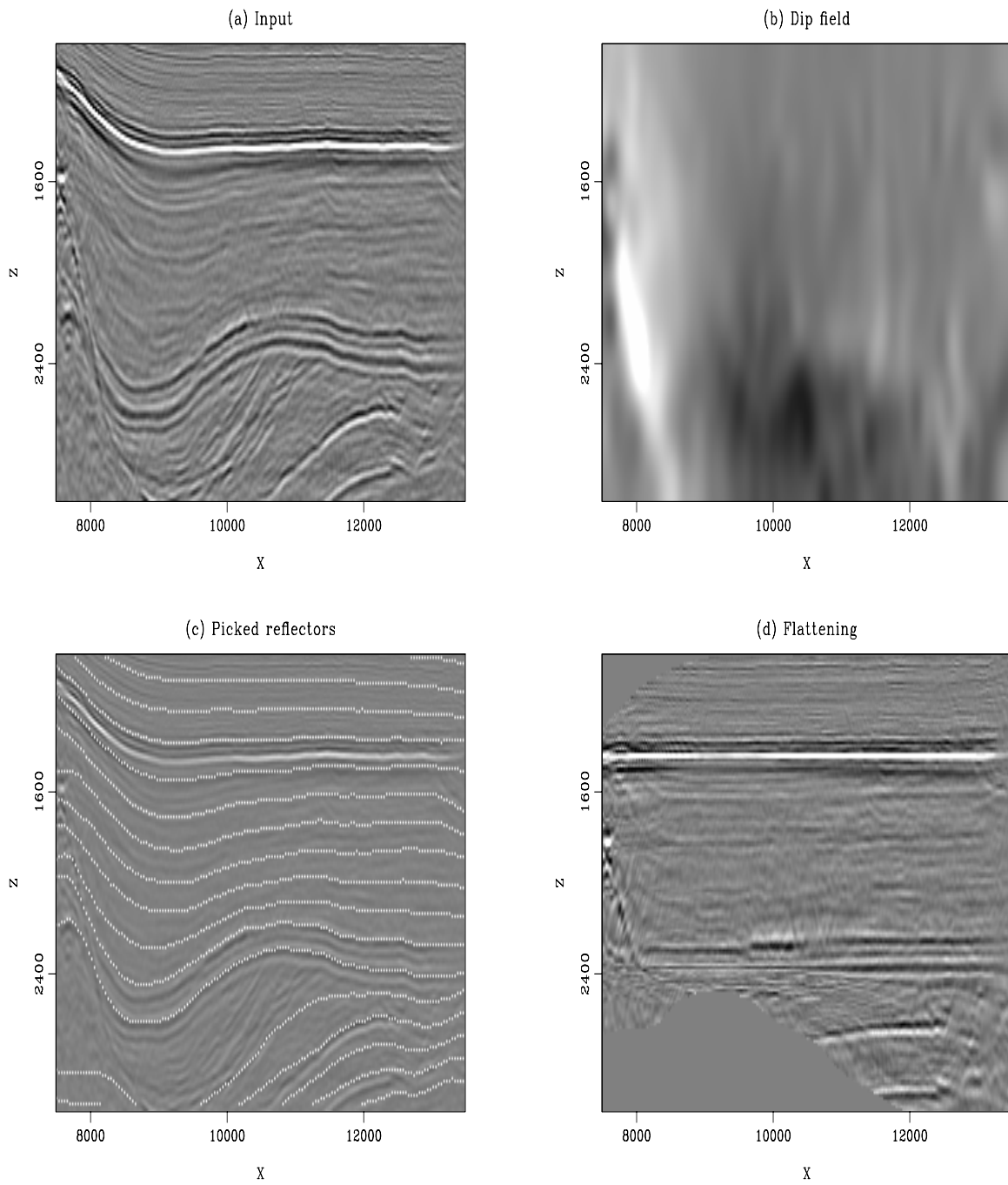


Figure 6: (a) Model. (b) Estimated dips. (c) Automatic picking of few horizons. (d) Flattening result. The picked horizons follow extremely well the structure of the data. The trace at $X=12000$ is used for reference. [antoine1-elf2D](#) [ER]

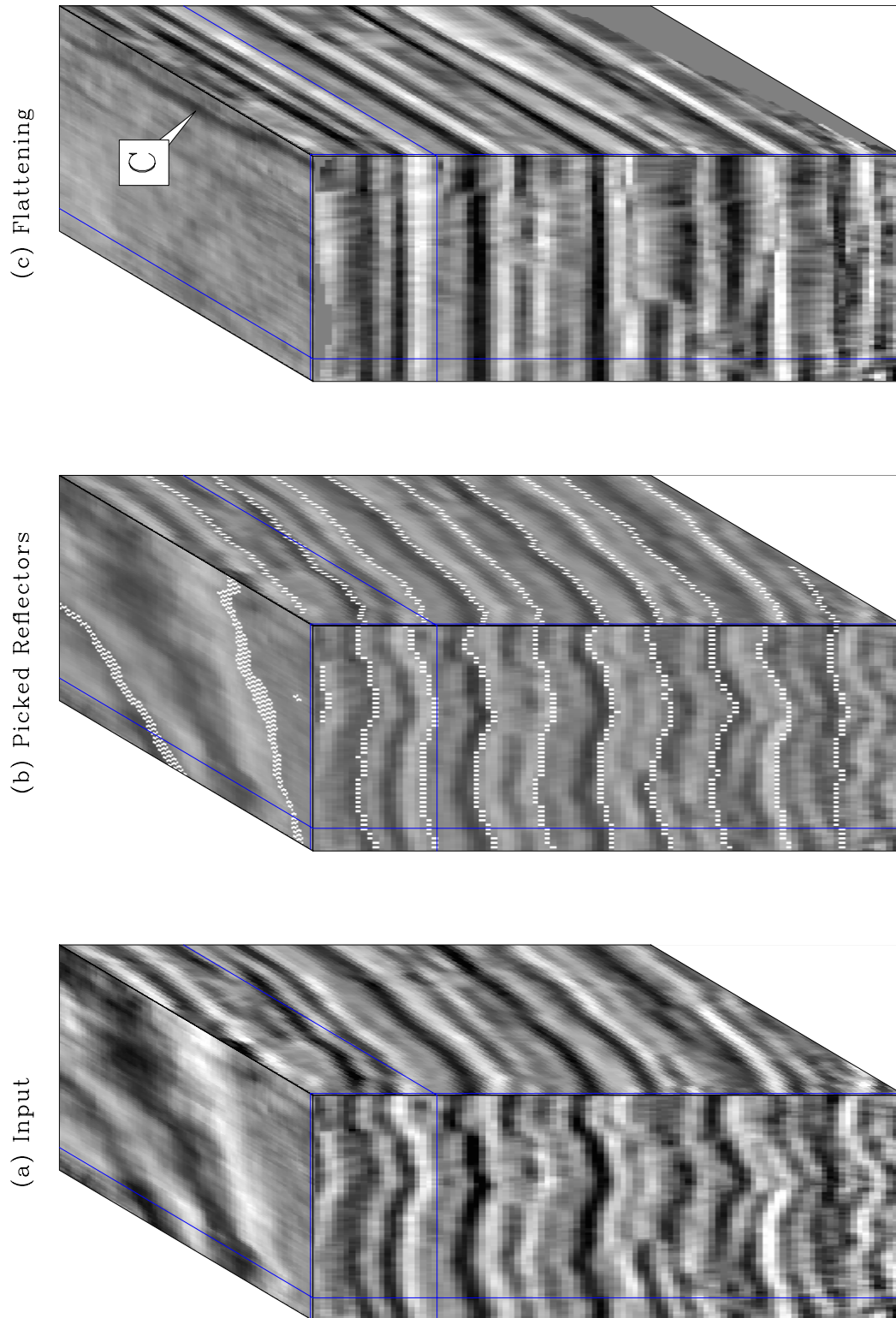


Figure 7: (a) Model. (b) Automatic picking of few horizons. (c) Flattening result. The picked horizons follow extremely well the structure of the data. On the time slice (top panel) a channel (marked as C), previously unseen in the data, is revealed by the flattening process.

`antoine1-3D-data-shoal-test` [CR]

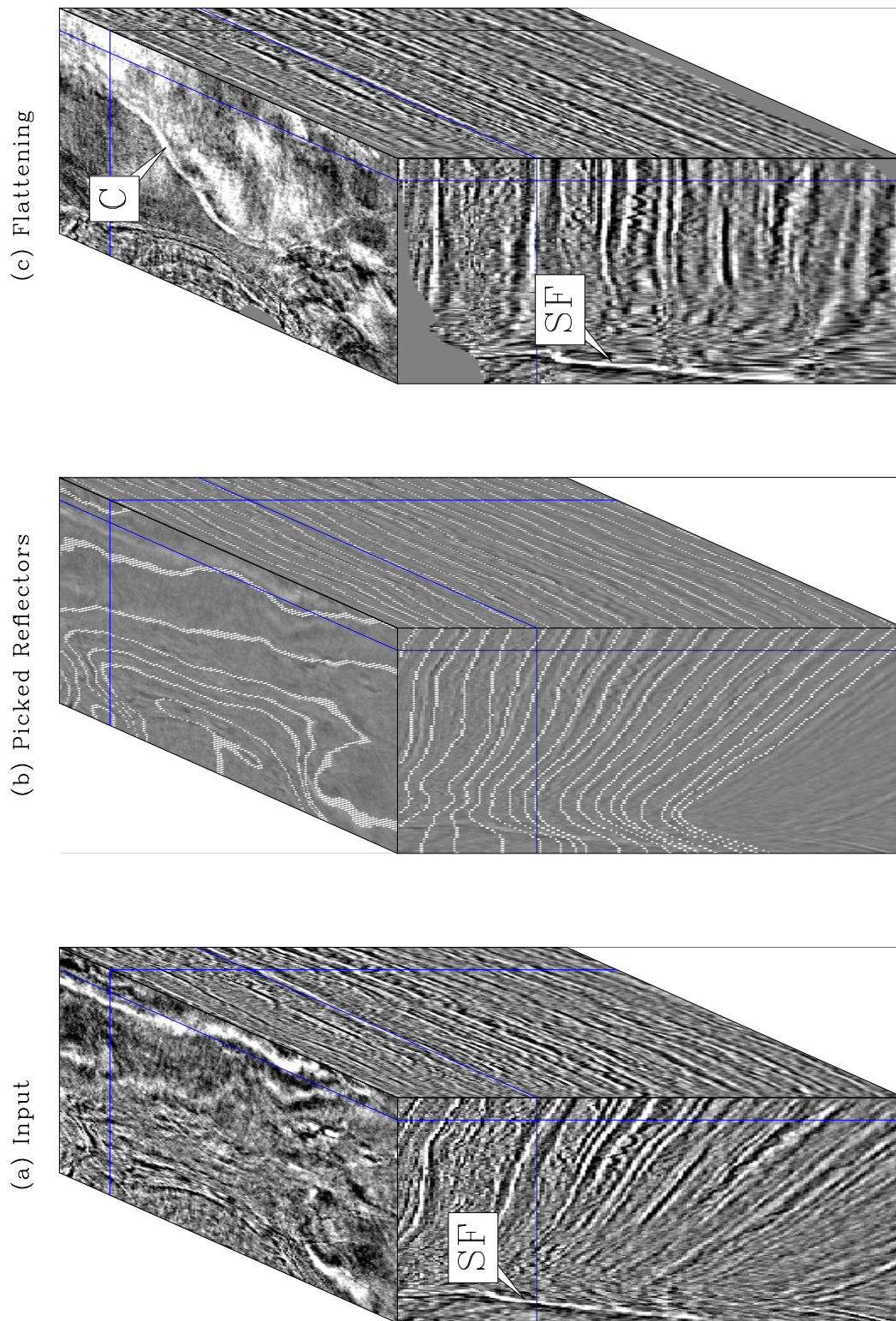


Figure 8: (a) Model. (b) Automatic picking of few horizons. (c) Flattening result. On the depth slice (top panel) a channel (marked as C), previously unseen in the data, is revealed by the flattening process. Arrow SF shows the salt flanks. [antoine1-3D-ExxonMobil-data](#) [CR]

REFERENCES

- Fomel, S., 2002, Applications of plane-wave destruction filters: *Geophysics*, **67**, no. 06, 1946–1960.
- Guitton, A., and Symes, W., 2003, Robust inversion of seismic data using the Huber norm: *Geophysics*, **68**, no. 4, 1310–1319.
- Guitton, A., Claerbout, J., and Lomask, J., 2004, First-order lateral interval velocity estimates without picking: *in* 74th Ann. Internat. Mtg. Soc. of Expl. Geophys., 2339–2342.
- Lomask, J., Guitton, A., and Valenciano, A., 2005, Flattening without picking faults: *SEP-120*, 159–166.
- Lomask, J., 2003a, Flattening 3D seismic cubes without picking: *Soc. of Expl. Geophys.*, 73rd Ann. Internat. Mtg., 1402–1405.
- Lomask, J., 2003b, Flattening 3-D data cubes in complex geology: *SEP-113*, 247–260.
- Vaillant, L., Calandra, H., Sava, P., and Biondi, B., 2000, 3-D wave-equation imaging of a North Sea dataset: Common-azimuth migration + residual migration: *Soc. of Expl. Geophys.*, 70th Ann. Internat. Mtg, 874–877.
- Wolf, K., Rosales, D. A., Guitton, A., and Claerbout, J., 2004, Robust moveout without velocity picking: *in* 74th Ann. Internat. Mtg. Soc. of Expl. Geophys., 2423–2426.

Short Note

Image segmentation with bounds

Jesse Lomask and Biondo Biondi¹

INTRODUCTION

Image segmentation (Shi and Malik, 2000; Hale and Emanuel, 2003, 2002) for tracking salt boundaries (Lomask and Biondi, 2003; Lomask et al., 2004) is extremely memory intensive. Memory saving measures must be implemented in order to consider applying this technique to 3D seismic cubes. If coarse bounds can be picked, either manually or using another automatic algorithm, this image segmentation algorithm can then be used to partition between the bounds. Unfortunately, the quality of the segmentation result is strongly affected by the shape of the image. For example, elongated images are more likely to be partitioned along their shortest dimension.

In this note, we present one such memory saving technique and demonstrate its ability to pick a salt boundary on a 2D seismic section. By imposing bounds, we significantly reduce the size of the problem and, as a result, increase efficiency and robustness. Also, errors created by segmenting thin images can be rectified with novel boundary conditions described here.

METHODOLOGY

Normalized cuts image segmentation partitions images into two groups. To do this, it first creates weights relating each sample to every other sample along paths within local neighborhoods. It then finds the cut that partitions the image into two groups, A and B , by minimizing the normalized cut:

$$N_{\text{cut}} = \frac{\text{cut}}{\text{total}_A} + \frac{\text{cut}}{\text{total}_B} \quad (1)$$

where cut is the sum of the weights cut by the partition. total_A is the sum of all weights in Group A , and total_B is the sum of all weights in Group B . Normalizing the cut by the sum of all the weights in each group prevents the partition from selecting overly-small groups of nodes.

¹email: lomask@sep.stanford.edu, biondo@sep.stanford.edu

The minimum of N_{cut} can be found by solving the generalized eigensystem:

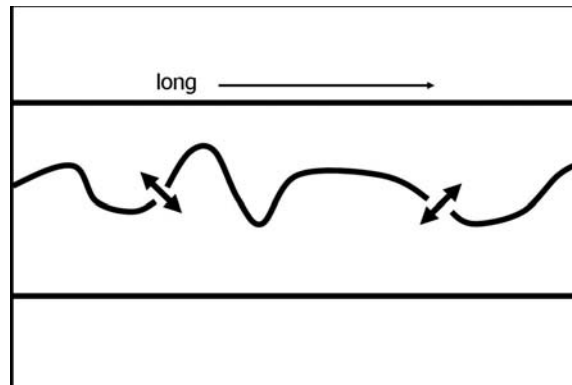
$$(\mathbf{D} - \mathbf{W})\mathbf{y} = \lambda\mathbf{D}\mathbf{y}, \quad (2)$$

created from a weight matrix (\mathbf{W}) and a diagonal matrix (\mathbf{D}), with each value on the diagonal being the sum of each column of \mathbf{W} . The eigenvector (\mathbf{y}) with the second smallest eigenvalue (λ) is used to partition the image by taking all values greater than zero to be in one group, and its complement to be in the other. For a more detailed description, please see Shi and Malik (2000).

For application to seismic salt interfaces, we merely apply the algorithm to instantaneous amplitude. Several cost saving techniques are explored in Lomask et al. (2004).

By applying bounds we greatly reduce the size of the problem. These initial rough bounds can be found by first running the algorithm with small search neighborhoods and coarse sampling.

Figure 1: A cartoon of a masked salt boundary. It is long and thin with a discontinuous salt boundary snaking across it. [jesse3-pic2](#) [NR]



Unfortunately, the normalized cut segmentation method tends to partition elongated images along their shortest dimension. For instance, Figure 1 is a cartoon of an elongated image with a salt boundary snaking across it. If the segmentation algorithm were to function as hoped, the minimum cut would be found along the salt boundary. However, because the salt boundary is discontinuous, it is likely that the minimum of the normalized cut in equation (1) will be found by cutting the image vertically where the image is thin.

To correct this problem, we exploit the fact that the upper boundary will necessarily be in Group *A* and the lower boundary will be in Group *B*. In other words, we want to force the segmentation algorithm to put the coarsely picked bounds in different groups.

We can enforce this constraint during the creation of the weight matrix (\mathbf{W}). Recall that this matrix contains weights relating each sample to every other sample along paths within a neighborhood. For any given sample, if its search neighborhood happens to cross a coarse boundary, it becomes weighted to every other sample near the boundary. This can be imagined by wrapping the image on a globe so that both the upper and lower bounds collapse to points at the poles (see Figure 2). When estimating the weight matrix, every time a path crosses the north or south pole, it continues down the other side. In Cartesian space, this can be seen in the cartoon in Figure 3.

Figure 2: A cartoon illustrating global bounds. The image is stretched onto a sphere and the upper and lower boundaries of the mask collapse to points. [jesse3-pic6](#) [NR]

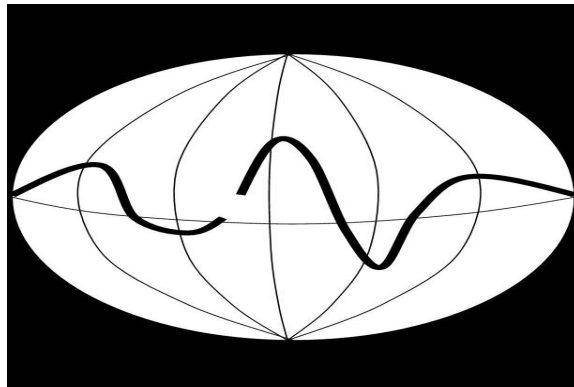
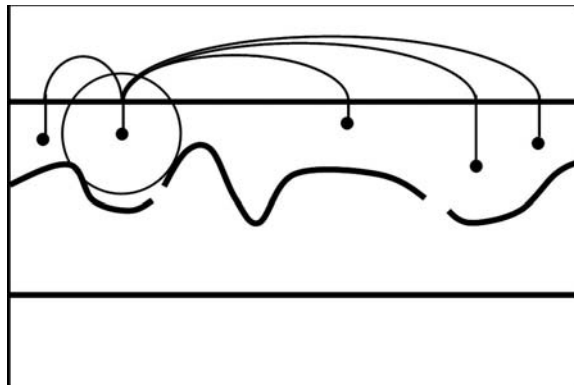


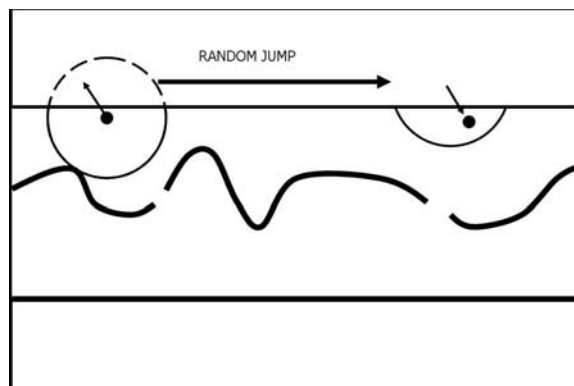
Figure 3: A cartoon illustrating idealized global bounds. When the search area for a node reaches outside the mask (as shown by the circle on the left), it becomes connected to all points along the boundary. [jesse3-pic5](#) [NR]



This “Global” bounds approach is completely impractical because it creates as many new weights as are saved by the size reduction of the problem.

A more practical approach that is still essentially the same concept is “Random” bounds. This is illustrated in Figure 4. Every time a path crosses a bound, it jumps a random distance along the boundary.

Figure 4: A cartoon illustrating the more practical random bounds. When the search area for a node reaches outside the mask (as shown by the circle on the left), it is connected to a single node a random distance along the boundary. [jesse3-pic4](#) [NR]



We have implemented and tested this random bounds method and found that it works well in our preliminary test cases.

FIELD TEST CASE

We tested this method on a 2D section taken from a Gulf of Mexico data set provided by WesternGeco.

Figure 5 shows a base of salt reflection. Although it is discontinuous, the human eye can see how it should be picked without too much uncertainty.

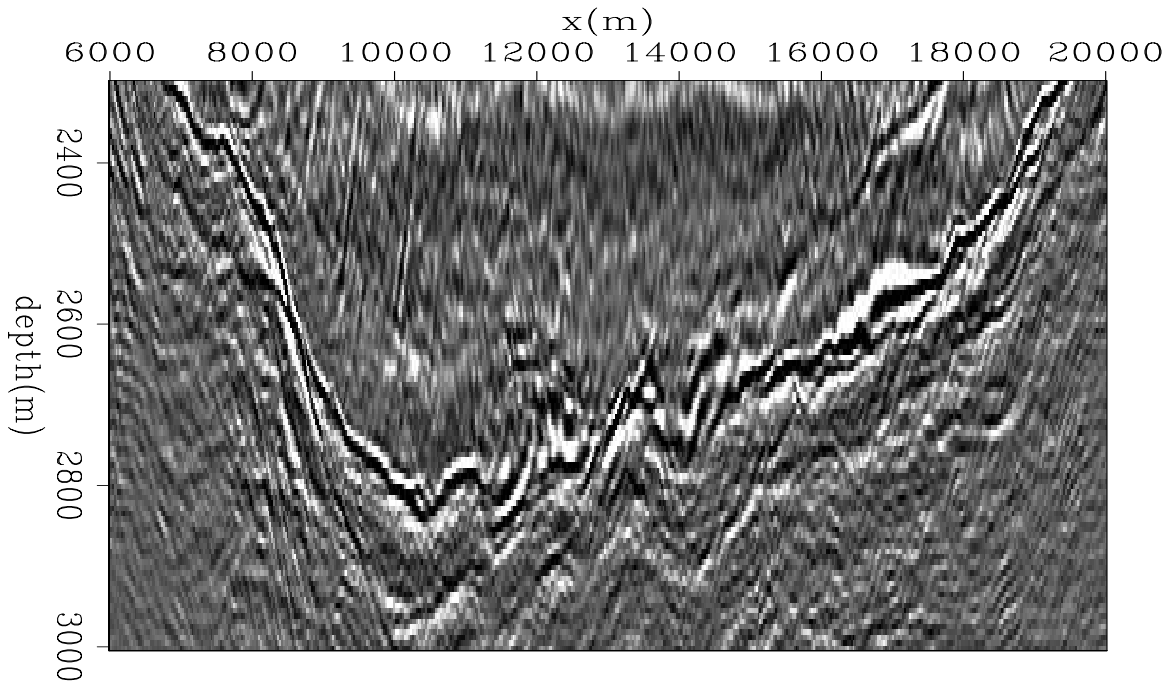


Figure 5: A 2D seismic section with a salt boundary from the Gulf of Mexico. `jesse3-gom.data` [ER]

We first ran the standard segmentation method on the entire image in Figure 5 with a short search distance and coarse sampling. We then shifted the result up and down 20 samples to get the mask shown in Figure 6.

Now our image is thinner and defined by that mask. We ran the standard segmentation method on the masked area. The resulting eigenvector (y) used to partition the image is shown in Figure 7. In principle, this eigenvector would be clipped to track the salt. Unfortunately, it is dominated by a low frequency trend and will create an erroneous vertical cut.

The eigenvector result of applying the random bounds approach is shown in Figure 8. It is clear that the salt interface can be gleaned from this image.

The resulting tracked salt boundary is displayed in Figure 9. It does an excellent job of tracking the salt boundary. The base salt tracking result is also overlain on the full 2D section in Figure 10.

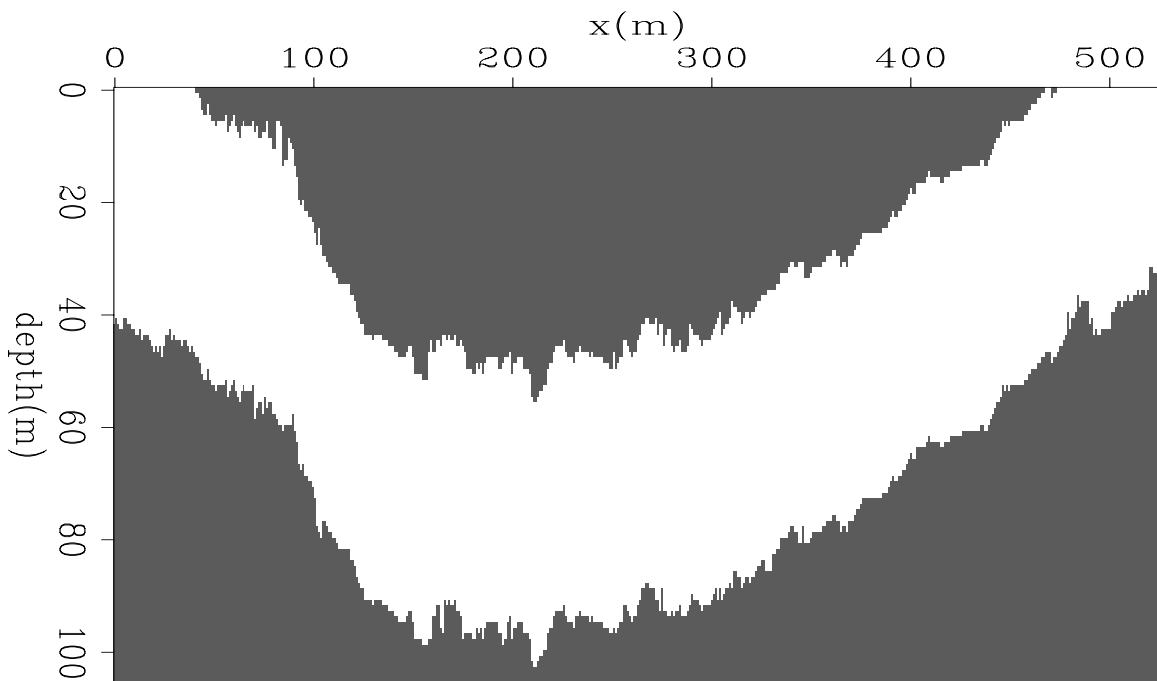


Figure 6: A binary mask defining the bounds of the salt boundary. This was generated by first running the image segmentation method on the entire image with short search distances and sparse sampling. In this case, the mask reduces the size of the problem by a factor of 2.

`jesse3-gom.mask_in` [ER]

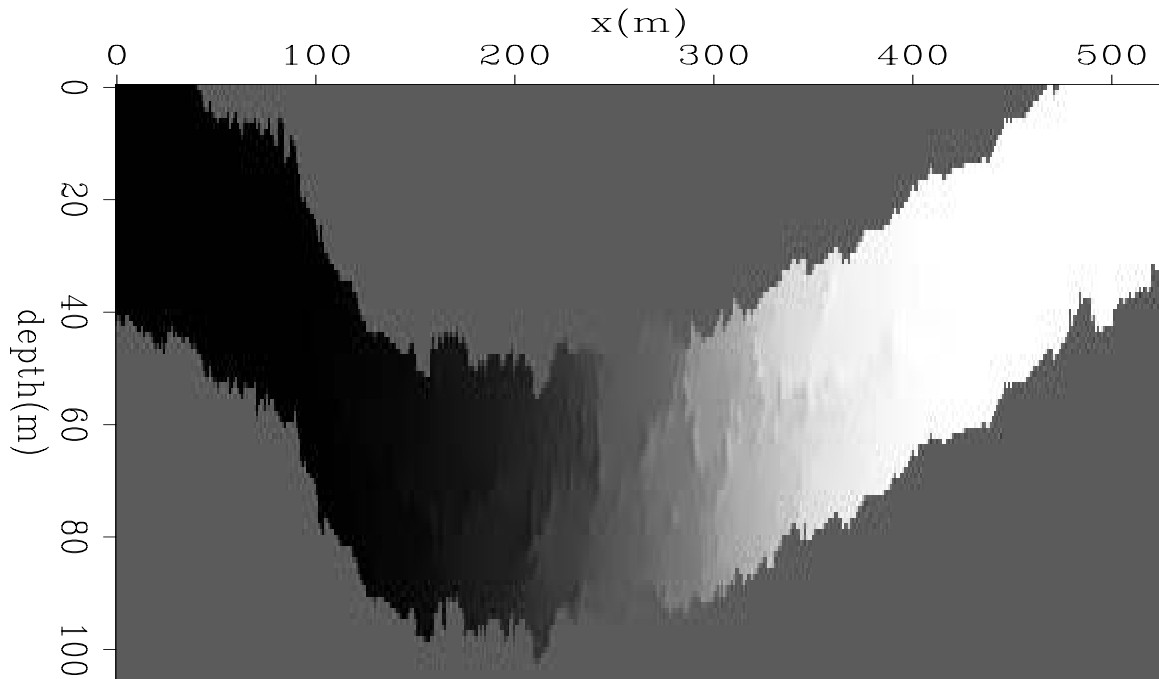


Figure 7: The eigenvector that is used to partition the image using our old segmentation algorithm after the mask in Figure 6 is applied. Hints of the salt boundary can be seen but is obscured by the overall low frequency trend from left to right. This will not produce a satisfactory segmentation result. `jesse3-gom.eig_nrand` [ER]

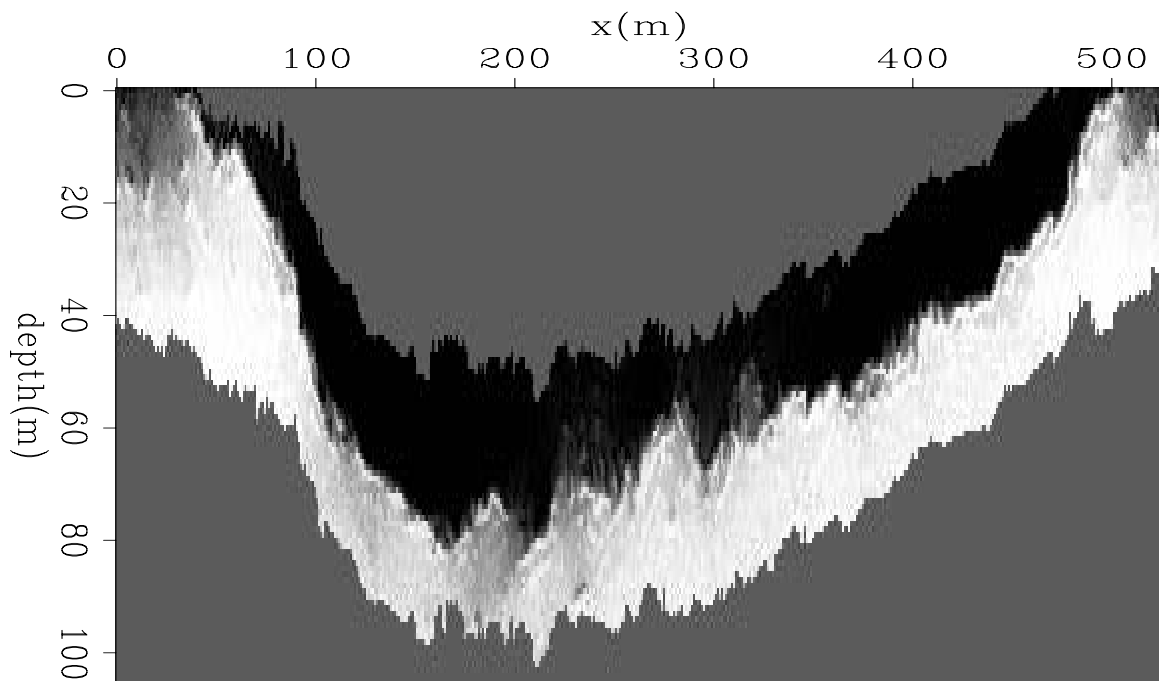


Figure 8: The eigenvector that is used to partition the image using our new approach with random bounds. The salt boundary is conspicuous in this image and can be extracted easily. `jesse3-gom.eig_rand` [ER]

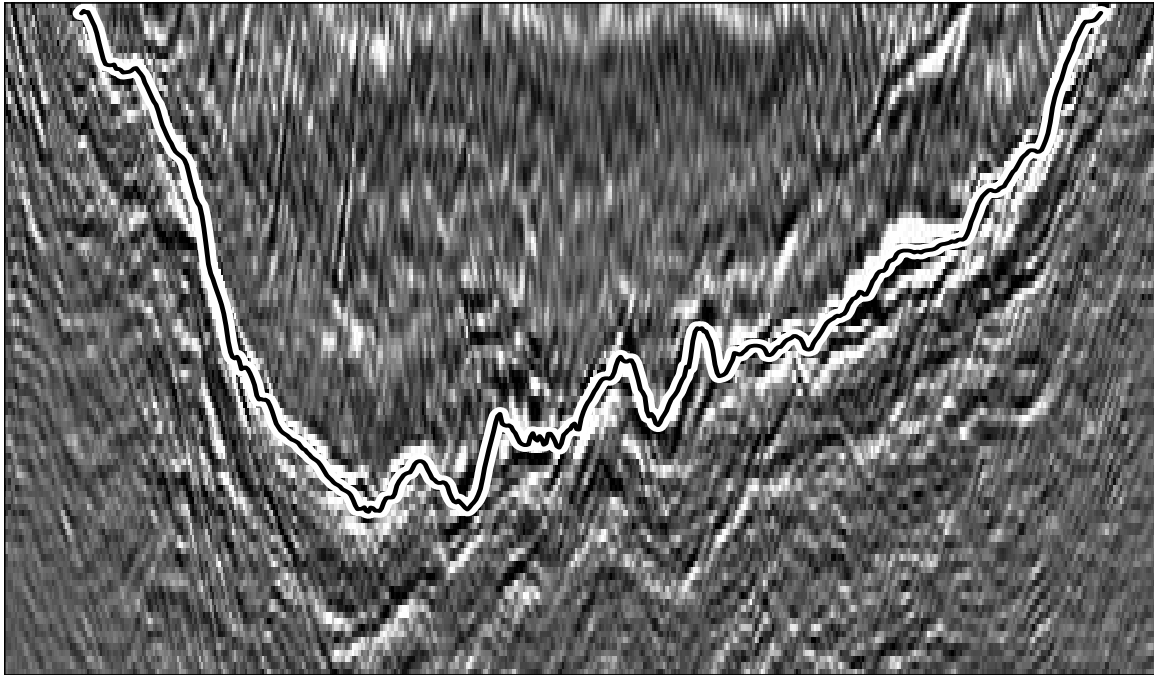


Figure 9: The boundary is garnered from the image in Figure 8 and overlain on the original base of salt data. It does a very good job of tracking the boundary. `jesse3-gom.horiz2` [ER]

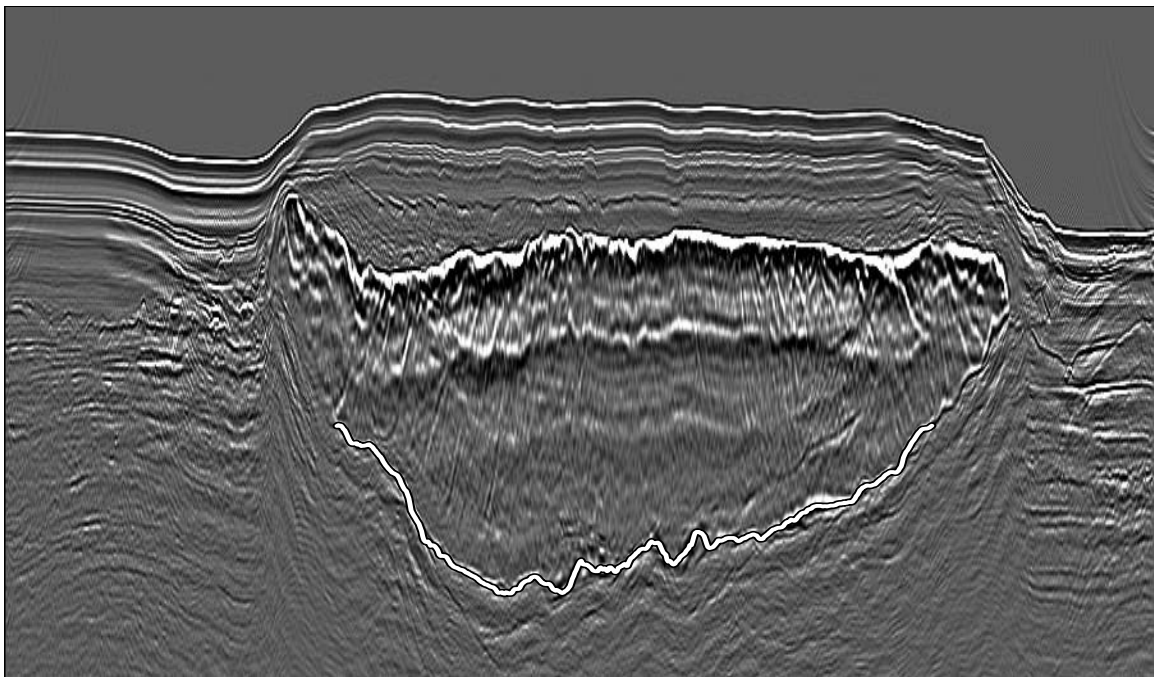


Figure 10: The boundary is overlain on a larger 2D section. `jesse3-gom_horiz2_full` [ER]

CONCLUSIONS

In this note, we presented a modification of image segmentation that allows narrow bounds to be introduced. We then demonstrated its effectiveness on a 2D field data set from the Gulf of Mexico. Now, armed with this new tool, tackling the 3D problem is one step closer.

ACKNOWLEDGMENT

We would like to thank WesternGeco for providing the field data used in this paper. We would also like to thank Dave Hale for his insightful suggestions.

REFERENCES

- Hale, D., and Emanuel, J. U., 2002, Atomic meshing of seismic images: Soc. of Expl. Geophys., Expanded Abstracts, 2126–2129.
- Hale, D., and Emanuel, J. U., 2003, Seismic interpretation using global image segmentation: Soc. of Expl. Geophys., Expanded Abstracts, 2410–2413.
- Lomask, J., and Biondi, B., 2003, Image segmentation for tracking salt boundaries: SEP-**114**, 193–200.
- Lomask, J., Biondi, B., and Shragge, J., 2004, Improved image segmentation for tracking salt boundaries: SEP-**115**, 357–366.
- Shi, J., and Malik, J., 2000, Normalized cuts and image segmentation: IEEE Trans on Pattern Analysis and Machine Intelligence, **22**, no. 8, 838–905.

Data regularization: inversion with azimuth move-out

Robert G. Clapp¹

ABSTRACT

Data regularization is cast as a least-squares inversion problem. The model space is a five-dimensional (t, cmpx, cmpy, hx, hy) hypercube. The regularization minimizes the difference between various (t, cmpx, cmpy) cubes by applying a filter that acts in (hx,hy) plane. Azimuth Move-out is used transform the cubes to the same (hx,hy) before applying the filter. The methodology is made efficient by a Fourier-domain implementation, and preconditioning the problem. The methodology, along with two approximations is demonstrated on 3-D dataset from the North Sea. The inversion result proves superior at a reasonable cost.

INTRODUCTION

The irregularity of seismic data, particularly 3-D data, in both the model domain (in terms of subsurface position and reflection angle) and the data domain (in terms of midpoint, offset, and time) cause imaging problems. The most effectively family of multiple removal methods, SRME (Verschuur et al., 1992) rely on data regularity. The standard marine acquisition technology results in empty bins in the cross-line direction.

Migration methods also desire a greater level of regularity than is often present in seismic surveys. There are two general approaches to deal with this problem. One approach is to treat the imaging problem as inverse problem. In this case is the adjoint of the migration operator. Ronen and Liner (2000); Duquet and Marfurt (1999); Prucha et al. (2000) cast the problem as such and then try to solve it with an iterative solver. These approaches have shown promise but are in many cases prohibitively expensive, and rely on an accurate subsurface velocity model.

Another approach is to try to regularize the data. AMO provides an effective regularization tool (Biondi et al., 1998). AMO is generally applied as an adjoint to create a more regularized volume. These regularized volumes still often contain in 'acquisition footprint' or more subtle amplitude effects. Chemingui (1999) used a logstretch transform to make the AMO operator stationary in time. He then cast the regularization problem as a frequency by frequency inversion problem using a Kirchoff-style AMO operator. He showed that acquisition footprint could be significantly reduced. The downside of this approach is relatively high cost of Kirchoff implementation and the difficulty with a frequency-by-frequency approach to a global inversion problem.

¹email: bob@sep.stanford.eda

Biondi and Vlad (2001) built on the work of Fomel (2001). They set up an inverse problem relating the irregular input data to a regular model space. They regularized the problem by enforcing consistency between the various (t,cmpx,cmpy) cubes. The consistency took two forms. In the first a simple difference between two adjacent in-line offset cubes was minimized. In the second the difference was taken after transforming the cubes to the same offset AMO. For efficiency the model was preconditioned with the inverse of the regularization operator (Fomel et al., 1997). Instead of solving the least squares inverse problem, the Hessian is approximated by a diagonal operator computed from a reference model (Claerbout and Nichols, 1994; Rickett, 2001; Clapp, 2003a).

In this paper I examine and extend the work in Biondi and Vlad (2001) and Clapp (2003b). I compare the result of using the AMO operator as an adjoint, using a diagonal operator to approximate the Hessian, and doing a full inverse. I show that applying the inverse proves to be significantly better. In the paper I begin the paper by going the general methodology, I then discuss how to implement it effectively on a Beowulf cluster.

ADJOINT IMPLEMENTATION

To map the irregular recorded seismic data onto the regular mesh is a far from trivial. A common approach in industry is to think of the problems in the same way we approach Kirchhoff migration, namely to loop over data space and spread into our regular model space. The spreading operation can be governed by something like AMO (Biondi et al., 1998), which maps data from one offset vector to another. If we think of the AMO operator \mathbf{T} as mapping from the regular model space \mathbf{m} to the irregular data space \mathbf{d} , our estimation procedure becomes,

$$\mathbf{m} = \mathbf{T}'\mathbf{d}. \quad (1)$$

The wavenumber domain AMO operator works on a regular sampled cube, so the problem is more complicated. We first must map the data to a regular sampled space by applying the interpolation operator \mathbf{L}' . The regular sampled cube \mathbf{s} is now a full five dimensional volume (t,cmpx,cmpy,hx,hy). We can produce the model \mathbf{m} at a given (hx,hy) by summing nearby cubes (t,cmpx,cmpy) that have transformed to our desired (hx,hy) through AMO. To write this in a mathematical form we need to make some definitions. We will define ihx and ihy as the offset indicies of the expanded space \mathbf{s} . These indicies correspond to the half-offset hx and hy. The output space, \mathbf{m} , is defined as a coralary ihx' and ihy' which also correspond to hx and hy. The notation $\mathbf{m}(ihx',ihy')$ correspond to the 3-D subcube (t,cmpx,cmpy) at the given ihx' and ihy' . Finally $\mathbf{T}_{\mathbf{x}_1 \Rightarrow \mathbf{x}_2}$ refers to transforming the cube through AMO from the offset vector \mathbf{x}_1 to \mathbf{x}_2 , nx and ny is the region in sampling of \mathbf{s} that we wish to sum over; and dhx and dhy is the sampling of the cube in hx and hy respectively. We obtain

$$\mathbf{m}(ihx',ihy') = \sum_{iy=-ny}^{ny} \sum_{ix=-nx}^{nx} \mathbf{T}_{(hx+ixd hx,hy+iyd hy) \Rightarrow (hx,hy)} \mathbf{s}(\mathbf{ix} + \mathbf{ihx}, \mathbf{iy} + \mathbf{ihy}). \quad (2)$$

In we to write our regularization problem in the form of equation (2), \mathbf{S} is a spraying operation where the columns of the matrix are defined by equation (1). We then obtain or model by applying

$$\mathbf{m} = \mathbf{S}'\mathbf{L}'\mathbf{d}. \quad (3)$$

The formulation suffers from all of the usual problems associated with applying an adjoint operation. We are spraying into a regular mesh, but the data is not regular. Areas with higher concentration of data traces will tend to map to artificially higher amplitudes in the model space. In the Kirchoff formulation we can do some division by hit count to help minimize this effect. Because we are operating in the wave number domain we can't normalize by something as simple as hit count. We can accomplish something similar by following the approach of Claerbout and Nichols (1994) and Rickett (2001). We approximate the Hessian of the least squares solution,

$$\mathbf{m} = (\mathbf{S}'\mathbf{L}'\mathbf{S})^{-1} \mathbf{S}'\mathbf{L}'\mathbf{d}, \quad (4)$$

by the diagonal operator \mathbf{W} . We form \mathbf{W} by

$$\mathbf{W}^{-1} = \text{diag}[(\mathbf{S}'\mathbf{L}'\mathbf{S}\mathbf{1} + \alpha)], \quad (5)$$

where $\mathbf{1}$ is a vector of 1s, α is a stabilization term, and $\text{diag}[]$ map the vector to the diagonal of the matrix. We scale our adjoint solution by \mathbf{W} obtaining

$$\mathbf{m} = \mathbf{W}\mathbf{S}'\mathbf{L}'\mathbf{d}. \quad (6)$$

Implementation

There are several issues that must be considered when implementing AMO in this form. The large volume of data that we are dealing with means that the problem must be parallelized. The problem can be parallelized in several different ways. While it is possible to split in the (cmpx, cmpy) plane, boundary effect are a concern because the operator is applied in the wave-number domain. Because the operator is applied in the frequency domain parallelizing over frequency seems a natural choice. The problem with dividing the problem along the frequency axis is that the intermediate space \mathbf{s} can become enormous, even for fairly small datasets, which would require some level of patching along other axes. In addition it requires a troubling transpose. The input data has its inner axis as time, while we want the outer axis to be frequency. For multi-gigabyte this can be quite time consuming. For this reason I chose to parallelize offset. Each process is assigned an output (hx,hy) range. It takes the input that range plus the additional summation range implied by equation (2).

The parallel job is controlled by the library described in Clapp (2005). Each node receives a SEP3D (Biondi et al., 1996) volume corresponding to its output space and the summation region implied by (2). The serial code first NMOs, log-stretches, and converts to frequency its data volume. The data volume is transposed and equation (6) is applied. The regularized frequency slices are transposed, inverse Fourier transformed, and has inverse NMO applied to it. Finally the data is recombined to form the regularized volume.

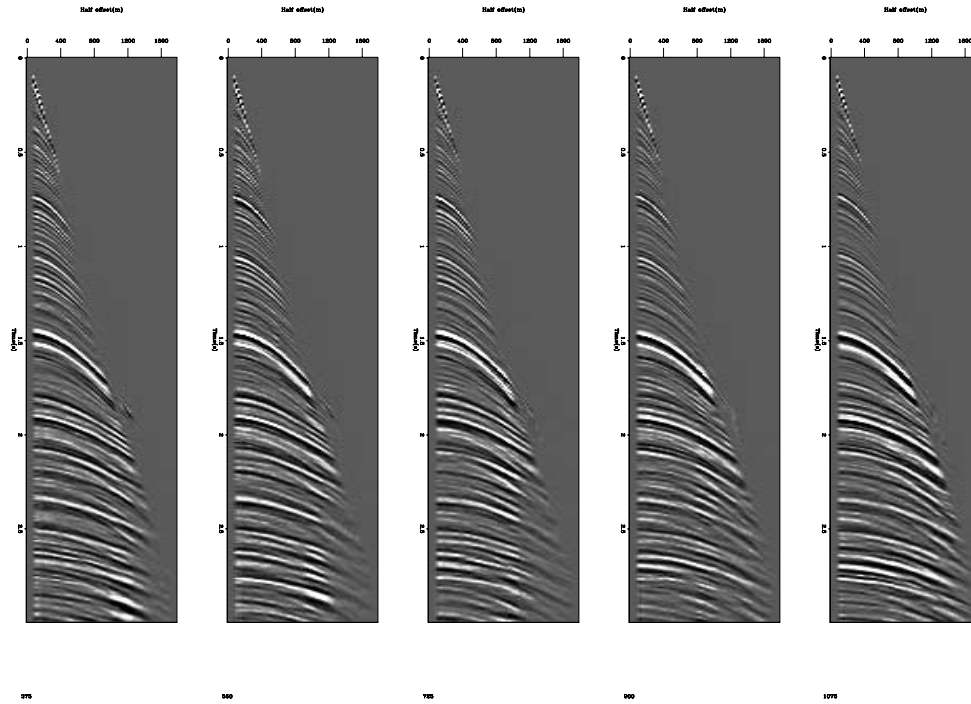


Figure 1: Five CMP gathers from the regularized dataset. Note the overall smoothness of the result. `bob2-adj.cmp` [CR]

Results

The methodology was applied on a 3-D marine dataset from the North Sea. The output model space was limited to $h_x = 0$, n_y of equation 2 was set to the entire h_y range, and n_x was set to 1. Figure 1 shows five CMP gathers from a relatively simple geologic portion of the dataset. The overall result is satisfactory and event continuity is quite good. Note the brightening and dimming as a function of offset in the lower portion of the second and third panels. The correction factor, equation (5) does not sufficiently emulate the inverse Hessian to remove all of acquisition artifacts.

REGULARIZING OVER OFFSET

There is a notable drawback from the approach described above. The operator \mathbf{S} can be quite costly, We are doing $n_x \times n_y$ AMO transforms for every output (h_x, h_y) . If we are only interested in a common azimuth dataset $h_y = 0$, the cost is acceptable as long as n_y is fairly small. If we want any cross line offset output the cost isn't acceptable. In addition \mathbf{S} is a modified version (because of the AMO transform) of a small 2-D box car filter. If you desire additional smoothness in the in-line offset direction (to suppress amplitude variations) we must try a different approach.

Biondi and Vlad (2001) proposed reducing the dimensionality of the problem by ignoring the azimuth direction. They added a smoothness constraint to the problem by applying a Leaky derivative \mathbf{D} operator between AMO transformed (t,cmpx,cmpy) cubes setting up the minimization,

$$Q(\mathbf{m}) = \|\mathbf{d} - \mathbf{Lm}\|^2 + \epsilon^2 \|\mathbf{Dm}\|^2, \quad (7)$$

where ϵ controls the weighting between the two goals. They preconditioned the problem with the inverse of \mathbf{D} , leaky integration between AMO transformed cubes \mathbf{C} and applied the same Hessian approximation to obtain the approximation

$$\mathbf{m} = \mathbf{CWC}'\mathbf{L}'\mathbf{d}, \quad (8)$$

where \mathbf{C} is the inverse of \mathbf{D} and

$$\mathbf{W}^{-1} = \text{diag}[\mathbf{C}'\mathbf{L}'\mathbf{LC}\mathbf{1} + \epsilon^2]. \quad (9)$$

Clapp (2003b) noted that ignoring the azimuth removed some of the advantage of using the AMO operator and suggested that \mathbf{C} should be applying polynomial division with a 2-D filter operating in the the (hx,hy) plane. For this exercise I chose a small helical derivative for my 2-D filter (Claerbout, 1999).

Implementation

Implementing this method proves to be more problematic then the adjoint case. The added difficulty is caused by the 2-D filter. In order to parallelize over offset we would have to have significant inter-processor communication. This is problematic from both stability, we must rely all of the nodes remaining up, and efficiency, both the cost of sending the data and the delay caused by machine A needing data from B which needs data from C. As a result I decided to parallelize over frequency. As mentioned before this also has drawbacks. An entire (cmpx,cmpy,hx,hy) hypercube can not be held in memory for large problems, so we must do patching along some other axes.

The necessary transposes (to move from an inner time axis, to an outer frequency and back) complicate matters. The data are initially broken along the trace axis. The local datasets are NMOed, FFTed, and transposed. The transposed data is then recombined with frequency the outer axis. The procedure is significantly faster then performing the transpose on a single machine where disk IO dominates. By using multiple nodes which can each do the transpose in-core, or nearly core, the entire processing drops to minimally more than distributing and collecting the data.

Frequency blocks are then distributed to the nodes and equation (8) is applied. The data is then collected and re-split along the cmpx axis. The new regularized frequency slices are transposed, inverse FFTed, inverse NMOed, and recombined to form the output volume.

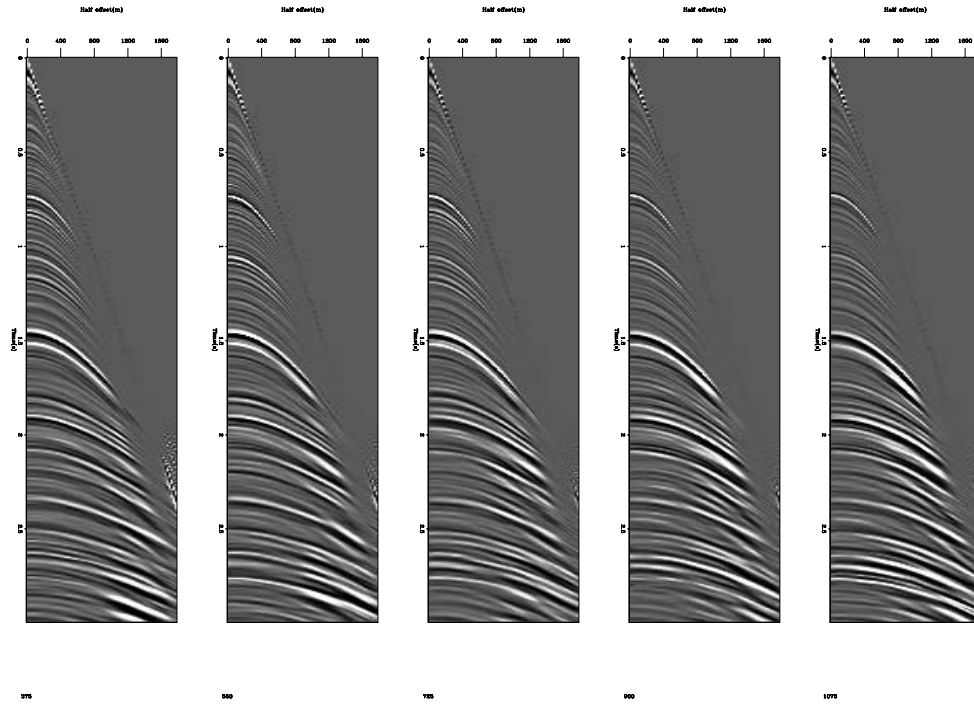


Figure 2: The same five CMP gathers from Figure 1 estimated by applying equation (8). Note the reduced frequency content in the image. `bob2-approx0.cmp` [CR]

Results

Equation 8 was applied to the 3-D marine dataset. Figure 2 shows the same five CMP gathers as Figure 1. The CMP gathers were created by AMO stacking to zero hy ,

$$\mathbf{m}(hy = 0, ihx) = \sum_{hy} \mathbf{T}_{(hx,hy+iydhy) \Rightarrow (hx,0)} \mathbf{m}(ihy, ihx). \quad (10)$$

The resulting CMP gathers show a reduction in the dimming and brightening as function of offset but also show notable reduction in frequency content. The approximation is more economical in forming a full 5-D space than the adjoint formulation and produces a greater continuity in the offset plane. On the other hand, noticeable brightening and dimming can still be seen. In addition transfer times, due to the transposes, dominate the processing time.

INVERSION

Instead of approximating the Hessian with a diagonal matrix we can attempt to estimate the least squares inverse using a conjugate gradient solver. The model is preconditioned by using polynomial division to apply the helical derivative and the new preconditioned variable \mathbf{p} is estimated through

$$Q(\mathbf{p}) = \|\mathbf{d} - \mathbf{L}\mathbf{C}\mathbf{p}\|^2 + \epsilon^2 \|\mathbf{p}\|^2, \quad (11)$$

where $\mathbf{m} = \mathbf{Cp}$.

Implementation

The implementation follows the same form as the approximate solution. The data is converted to frequency and distributed to the nodes. The inversion is done on the distributed files. Vector operations (scale, add, dot product) are calculated with MPI based routines. After the model has been estimated the data is redistributed for conversion back to time.

Results

Ten conjugate gradient iterations with $\epsilon = 0$ were applied. Figure 3 shows the same five CMP gathers shown in the previous two sections. The frequency content is restored compared to the result seen in Figure 2. In addition the brightening and dimming seen in the result of the previous two methods are almost completely removed.

CONCLUSION

Three different methods to regularize seismic data with a wavenumber based AMO operator are described. The adjoint implementation is the most efficient for creating a Common Azimuth but inefficient for creating multi-azimuth data. The adjoint approach also shows noticeable amplitude dimming and brightening due to acquisition geometry. Formulating the regularization problem as an inverse problem and then approximating the Hessian with a diagonal operator provides better results. The cost and memory requirements are significantly increased but multi-azimuth data comes for free. Estimating the model with a conjugate gradient solver produces the best results. Amplitude artifacts are virtually eliminated and the frequency content is noticeably improved.

ACKNOWLEDGMENTS

I would like than TotalFinaElf for providing the data used in this paper.

REFERENCES

- Biondi, B., and Vlad, I., 2001, Amplitude preserving prestack imaging of irregularly sampled 3-D data: SEP-110, 1-18.
- Biondi, B., Clapp, R., and Crawley, S., 1996, Seplib90: Seplib for 3-D prestack data: SEP-92, 343-364.

- Biondi, B., Fomel, S., and Chemingui, N., 1998, Azimuth moveout for 3-D prestack imaging: *Geophysics*, **63**, no. 2, 574–588.
- Chemingui, N., 1999, Imaging irregularly sampled 3D prestacked data: SEP-101.
- Claerbout, J., and Nichols, D., 1994, Spectral preconditioning: SEP-82, 183–186.
- Claerbout, J., 1999, Geophysical estimation by example: Environmental soundings image enhancement: Stanford Exploration Project, <http://sepwww.stanford.edu/sep/prof/>.
- Clapp, M. L., 2003a, Illumination compensation: Model space weighting vs. regularized inversion: SEP-113, 369–378.
- Clapp, R. G., 2003b, AMO regularization: Effective approximate inverses for amplitude preservation: SEP-114, 159–170.
- Clapp, R. G., 2005, Inversion and fault tolerant parallelization using Python: SEP-120, 41–62.
- Duquet, B., and Marfurt, K. J., 1999, Filtering coherent noise during prestack depth migration: *Geophysics*, **64**, no. 4, 1054–1066.
- Fomel, S., Clapp, R., and Claerbout, J., 1997, Missing data interpolation by recursive filter preconditioning: SEP-95, 15–25.
- Fomel, S., 2001, Three-dimensional seismic data regularization: Ph.D. thesis, Stanford University.
- Prucha, M. L., Clapp, R. G., and Biondi, B., 2000, Seismic image regularization in the reflection angle domain: SEP-103, 109–119.
- Rickett, J., 2001, Model-space vs data-space normalization for finite-frequency depth migration: SEP-108, 81–90.
- Ronen, S., and Liner, C. L., 2000, Least-squares DMO and migration: *Geophysics*, **65**, no. 5, 1364–1371.
- Verschuur, D. J., Berkhout, A. J., and Wapenaar, C. P. A., 1992, Adaptive surface-related multiple elimination: Adaptive surface-related multiple elimination:, *Soc. of Expl. Geophys., Geophysics*, 1166–1177.

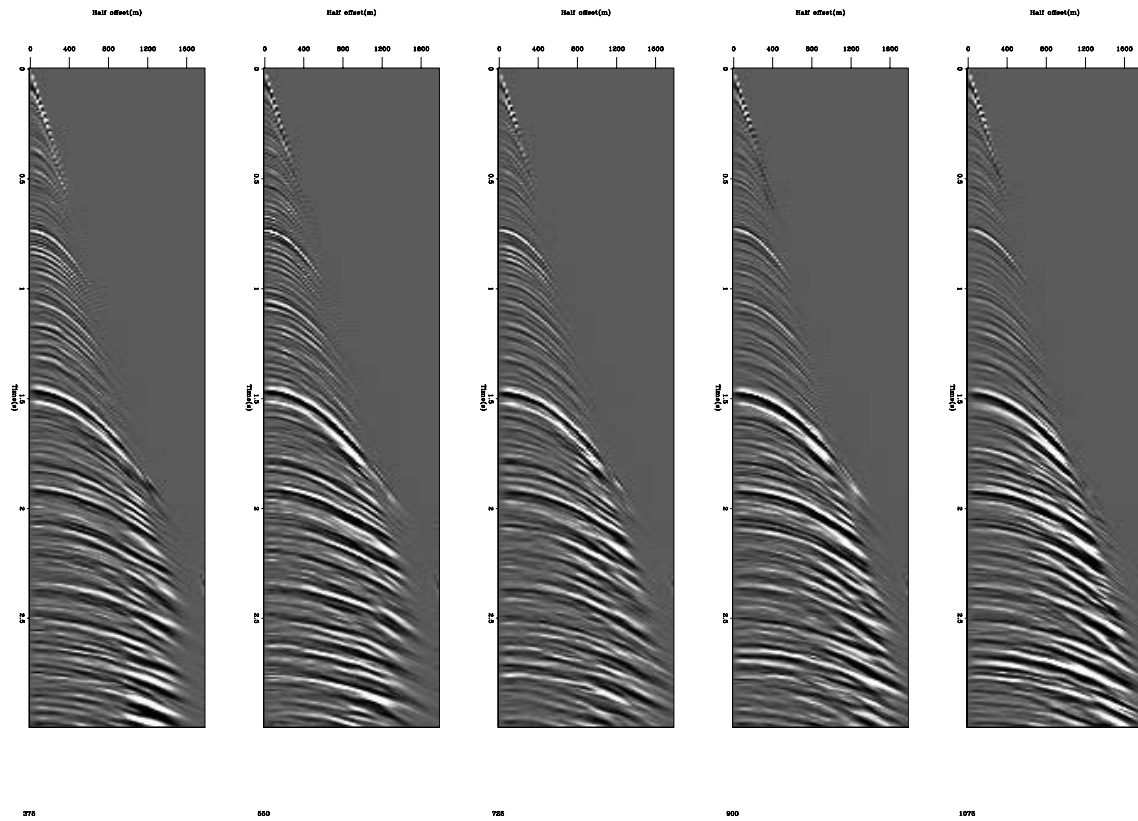


Figure 3: The result of ten iterations minimizing equation (11). Note the improved frequency content compared to Figure 2 and the decreased dimming and brightening of both Figure 1 and Figure 2. `bob2-inv0.cmp` [CR]



Interpolation and signal extraction of teleseismic wavefields with the linear radon transform

Charles K. Wilson and Antoine Guitton¹

ABSTRACT

We present a new method for data interpolation and signal/noise separation of teleseismic wavefields recorded by regional seismic arrays. The method exploits the plane wave nature of direct arrivals and receiver-side arrivals from regional scale structure by decomposing the recorded wavefield into a plane wave basis using the linear radon transform. Casting the radon transform as an inversion problem allows the incorporation of time dependent weighting schemes and model variance tuning which are helpful in minimizing artifacts related to the transform process while enhancing lower amplitude arrivals. Following radon transformation, we mute portions of the radon panel that represent plane waves with significantly different moveout ($\sim \pm 1$ s/km) relative to the direct arrival. Transformation back to the data domain from the muted radon domain gives the original signal without (1) plane waves following undesired moveouts, (2) white ambient noise, and/or (3) arrivals not represented well by plane waves (diffractions). Interpolation follows from the inverse data spray operation computed upon return to the data domain and the implicit assumption that a plane wave basis provides the most compact representation of the teleseismic wavefield.

INTRODUCTION

The growing abundance of densely sampled recordings of the teleseismic wavefield from regional scale portable and permanent seismic arrays demands the employment of more sophisticated array processing algorithms previously developed for seismic exploration. Most of the effort to date has concentrated on depth imaging algorithms using forward-scattered arrivals and free-surface multiples (Dueker and Sheehan, 1997; Sheehan et al., 2000; Rondenay et al., 2001; Aprea et al., 2002; Poppeliers and Pavlis, 2003; Wilson et al., 2003; Wilson and Aster, 2004). We suggest that imaging efforts in the absence of other preprocessing steps often are misguided. Seismic imaging algorithms are developed for noise-free datasets with an ideal distribution of source-receiver geometries that illuminate the imaging target from all angles. Even exploration data collected using industry standard acquisition geometries and well-controlled local sources with clean, easily modeled source functions are plagued by noise and incomplete illumination. To overcome these acquisition shortcomings, industry processing flows usually

¹email: wilsonck@sep.stanford, antoine@sep.stanford.edu

begin with different combinations of deconvolution, data interpolation and regridding, surface static corrections, datuming, and spatial/temporal filtering (Yilmaz, 1997).

Although many arrivals in the teleseismic wavefield have comparable and sometimes better signal-to-noise ratios than exploration experiments, all teleseismic imaging experiments suffer from sparse, incomplete, and irregular angular and spatial sampling (e.g. limited range of source-receiver offsets and azimuths). These difficulties hamper imaging efforts and require the employment of preprocessing steps similar to those used by the exploration industry. Deconvolution in the form of traditional "receiver function analysis" is of course widely employed to enhance receiver-side converted arrivals (Phinney, 1964; Langston, 1977). Initial attempts to use f-k (Wilson and Aster, 2004) or Karhunen-Loeve (Rondenay et al., 2001) filtering on teleseismic data have shown promise although it may not be the best method of signal extraction because of lack of spatial frequency resolution and inability to cope with time variable (non-stationary) signals. Other preprocessing efforts have used the predicted teleseismic P-wave slowness for a given arrival to separate signal from near surface scattering (Jones and Phinney, 1998; Wilson et al., 2003, 2004) and to interpolate data traces (Poppeliers and Pavlis, 2003). However, besides deconvolution, none of these or other widely used industry standard preprocessing steps have become commonplace in teleseismic imaging practice despite its apparent necessity.

It is likely that the exclusion of these preprocessing steps is largely historical. Initial analysis of teleseismic conversions was performed with a single set of three component seismograms recorded by an isolated station (Phinney, 1964; Langston, 1977). To avoid scattering from short wavelength features that depend strongly on back-azimuth, seismograms from single stations were routinely low-pass filtered to remove everything except energy primarily sensitive to structure with long spatial wavelengths (long temporal wavelengths). After the introduction of three component seismic arrays and with the birth of programs like IRIS-PASSCAL (<http://www.iris.edu>), data processing still followed the path devised for single isolated stations with the only difference being that the point measurements made by individual stations were now closer together. Much of the information about the lithospheric structure beneath the stations was discarded through temporal filtering and the absence of array-based processing. To extract the most information about lithospheric structure from increasingly more dense seismic arrays we must reexamine standard teleseismic data preprocessing flows prior to application of imaging algorithms.

For this reason, we have introduced a new method for signal/noise separation and data interpolation using an inverse formulation of the linear radon transform based on previous work applied to industry data (Sacchi and Ulrych, 1995; Guitton and Symes, 2003). This paper will begin by defining signal and noise for wavefields produced by teleseismic earthquakes. After definition, we will show how differences in the basic moveout and geometry of the signal and noise wavefields can be used to separate them through projection of the data space onto a plane wave basis (linear radon domain). Our choice of separation through linear radon transform also gives us the added advantage of automatic data interpolation of spatially coherent plane wave arrivals upon return to the data domain. We show application of this technique to one synthetic and one recorded dataset with differing receiver spacing, target depths, and structural geometry.

COMPONENTS OF THE TELESEISMIC WAVEFIELD

The complete teleseismic wavefield (U_{total}) recorded at the surface can be represented as a linear combination of the impinging source wavefield (u_{src}), a specularly scattered wavefield (u_{spec}), a diffracted wavefield (u_{diff}), and an ambient noise wavefield (n) present at all times.

$$U_{total} = \underbrace{u_{src} + u_{spec}}_{SIGNAL} + \underbrace{u_{diff} + n}_{NOISE} \quad (1)$$

We assume either an isotropic character for the ambient noise (n) or that the highest amplitude components of the ambient noise wavefield (e.g. microseismic noise) do not follow the dominant moveout of teleseismic P wavefields. The specularly scattered portion of the wavefield contains plane wave arrivals generated at laterally continuous structures with little to no structural dip (arrivals marked A on Figure 1). The diffracted wavefield (arrivals marked B on Figure 1) consists of non-planar arrivals generated by point scatterers and short wavelength structures ($\leq 1/2$ of the array aperture). For certain point scatterers, diffracted energy will arrive as plane waves that may appear as specularly scattered arrivals (arrivals marked C on Figure 1). In these instances, there will be no way to discriminate between a specularly scattered arrival from a planar, sub-horizontal interface and a diffraction except by comparing the scattered arrival slowness to that of the direct arrival.

THEORY OF NOISE ATTENUATION AND DATA INTERPOLATION USING RADON TRANSFORMS

Radon transforms are simple summations along predefined trajectories of the input data. These trajectories are controlled by a single parameter that defines the geometry of the summation trajectory. Various trajectories are chosen based on the input data with the most popular being the linear radon transform, the parabolic radon transform, or the hyperbolic radon transform. The choice of transform depends exclusively on the data to be processed. For instance, parabolic radon transforms are chosen for multiple attenuation of common mid-point gathers after normal move-out (Foster and Mosher, 1992). Hyperbolic radon transforms are most commonly used for producing velocity panels from seismic reflections following hyperbolic moveout (Taner and Koehler, 1969) but they can also be used for noise attenuation (Foster and Mosher, 1992) and data interpolation (Hindriks and Duijndam, 1998; Trad et al., 2002). In the teleseismic case, the plane wave nature of the data makes the use of linear radon transform a natural choice to process the data.

With the application of the linear radon transform we hope to extract the signal from the total wavefield and to interpolate the wavefield on return to the data domain. First, we intend to separate the signal and source wavefields from diffracted and ambient noise wavefields based on differences in slowness and wavefield curvature. Arrivals with a planar moveout will map well into the linear radon domain (see Figures 1 and 2). However, the diffuse ambient noise

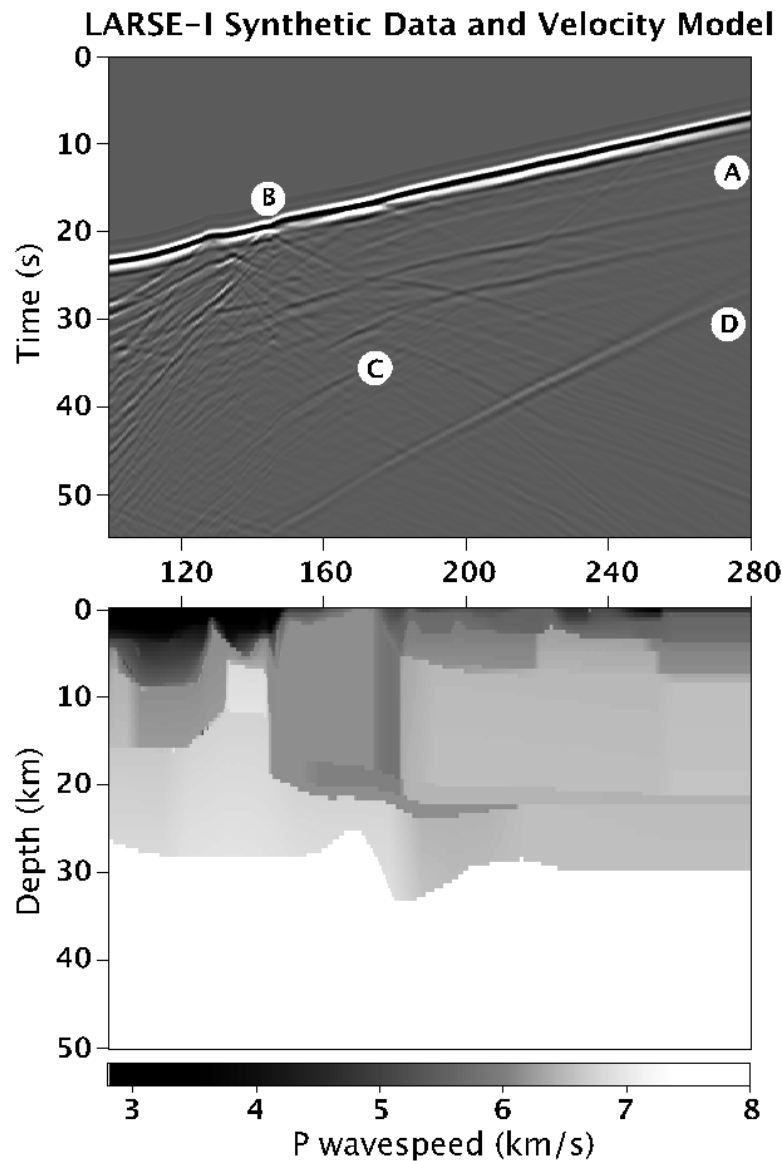


Figure 1: Synthetic seismograms (a) calculated from the LARSE-I velocity model (Baheer et al., 2004) (b) generated by a steeply dipping incident plane wave from the base of the model (approximation of actual teleseismic source-receiver geometry). The arrivals marked (A) represent specularly scattered arrivals from laterally coherent structures. Notice these arrivals follow a similar moveout to the direct arrivals. Diffractions from both the bottom of the basin (B) and Moho topography (C) show a clearly different moveout and are slightly less planar than the direct arrival. The side reflection related to the boundary conditions of the synthetic model, marked as (D), approximates source-side scattered phases that have similar moveout to the direct arrival, such as pP. charlie1-Data+Model [NR]

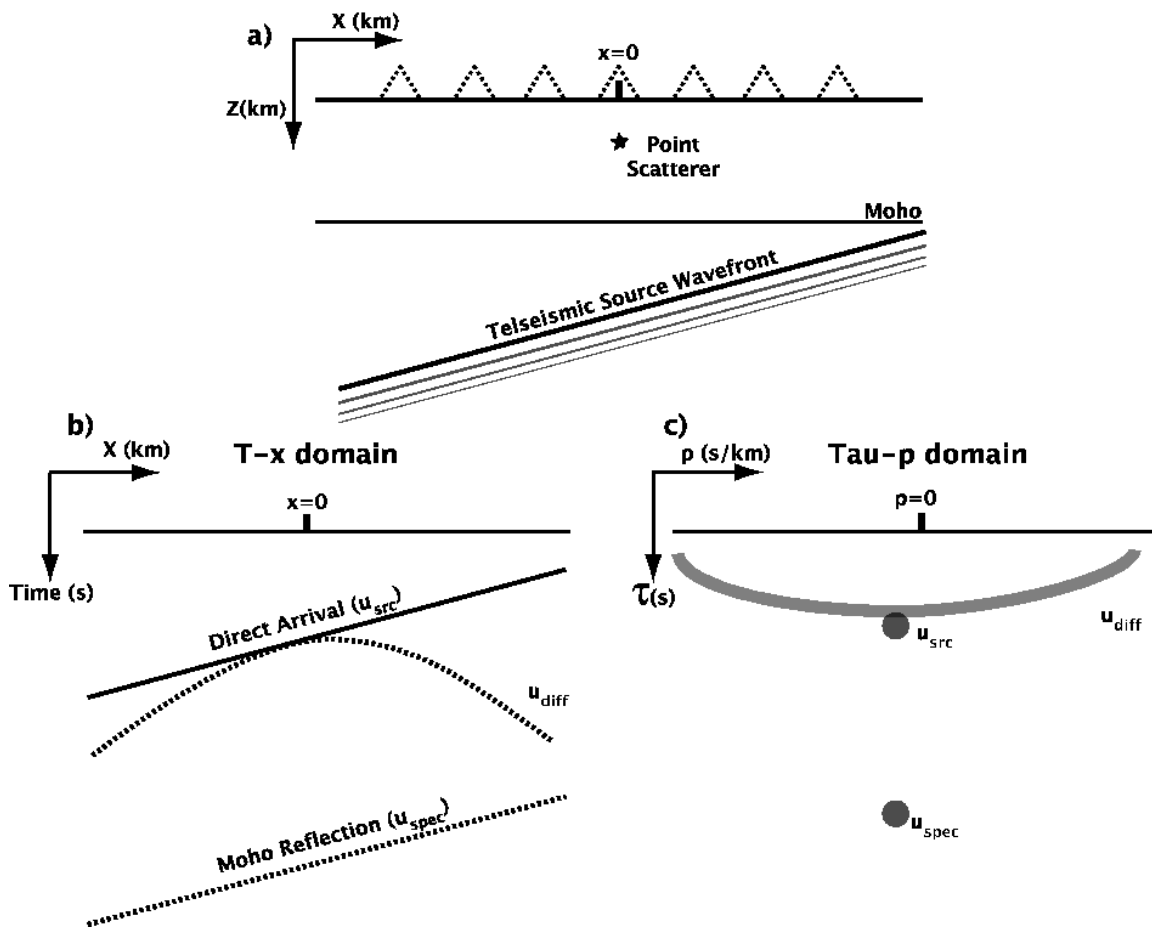


Figure 2: Figure showing representation of the teleseismic wavefield in the physical domain (a), the data domain (b), and the linear τ - p domain (c). By applying the linear radon transform we can differentiate between specularly scattered and diffracted waves as shown in (c).

charlie1-TeleGeometry [NR]

wavefield and diffracted arrivals will have near zero amplitude after transformation because they are not represented well as plane waves. In the radon domain, coherent plane wave arrivals that do not follow the expected moveout of specularly scattered waves (e.g. P to Rg scattering from the surface and basin bottom topography) are assumed to be noise and muted. On return to the data domain, we will automatically interpolate the wavefield to a regularly sampled grid because of the plane wave representation of the wavefield and the loss of spatial reference in the radon domain.

Implementation of the linear radon transform

In this section, we show the details of the linear radon transform and how it can be cast as an inverse problem. The forward transformation maps the radon domain $m(\tau, s)$ into the data space $d(t, x)$ (recorded data) as follows:

$$d(t, x) = \sum_{s=s_{min}}^{s_{max}} m(\tau = t - sx, s), \quad (2)$$

and the adjoint transformation

$$m(\tau, s) = \sum_{x=x_{min}}^{x_{max}} d(t = \tau + sx, x), \quad (3)$$

where t is the time, x the station location (x_{min} and x_{max} being the offset range), s the slowness (s_{min} and s_{max} being the range of slownesses investigated), and τ the travel time at x_{min} (the first trace is the origin of the summation path).

Equation (2) can be rewritten in a more compact way by introducing the forward linear radon transform operator \mathbf{L} , the model space vector \mathbf{m} (which contains all the $m(\tau, s)$ points) and the data vector \mathbf{d} (which contains all the $d(t, x)$ points):

$$\mathbf{d} = \mathbf{Lm}. \quad (4)$$

Therefore, the goal is to minimize the difference between the input data \mathbf{d} and the modeled data via the linear radon transform operator as follows:

$$\mathbf{0} = \mathbf{r}_d = \mathbf{Lm} - \mathbf{d}, \quad (5)$$

where \mathbf{r}_d is called the data residual. As explained before, the data are irregularly spaced and traces may be missing. A mask \mathbf{M} is introduced in equation (5) such that only the recorded data are considered in the residual:

$$\mathbf{0} = \mathbf{r}_d = \mathbf{M}(\mathbf{Lm} - \mathbf{d}), \quad (6)$$

where \mathbf{M} is a diagonal operator that equals one where data are known and zero where they are unknown (at the missing traces). Finally, we estimate the radon domain by minimizing the objective function

$$f(\mathbf{m}) = \|\mathbf{r}_d\|^2, \quad (7)$$

which gives a least-squares estimate of the model parameters. Note that with the linear radon transform, the model space \mathbf{m} can be estimated without inversion by introducing the so-called rho filter (Yilmaz et al., 1987), usually estimated in the Fourier domain. With missing traces, the rho filter is not appropriate anymore and inversion is required. In the next section, we describe how a sparse radon domain can be estimated with inversion.

Sparse inversion

For noise attenuation and data interpolation with radon transforms, numerous authors have shown that the inclusion of sparseness constraints during transformation into the radon domain improves the final result (Sacchi and Ulrych, 1995; Herrmann et al., 2000; Trad et al., 2003). The goal is to obtain a solution with minimum entropy (Burg, 1975). This property is important because radon transforms suffer from decreases in resolution due to the limited aperture of the data, creating transformation artifacts known as butterfly patterns (Kabir and Marfurt, 1999). The sparse inversion attenuates these effects by minimizing energy that does not focus well in the radon domain.

In this paper, we use the method of (Sacchi and Ulrych, 1995) to estimate a sparse model \mathbf{m} . This technique imposes a Cauchy form probability-density function to the model parameters. This long-tailed probability-density function isolates the most energetic components of the radon domain and ignores the smallest, thus giving a minimum entropy solution. Note that other techniques such as stochastic inversion (Thorson and Claerbout, 1985) are also available.

To obtain a sparse radon domain \mathbf{m} , a regularization term, i.e., the Cauchy function, is introduced in equation (7) as follows:

$$f(\mathbf{m}) = \|\mathbf{r}_d\|^2 + \epsilon^2 \sum_{i=1}^N \ln \left(1 + \frac{m_i^2}{\gamma^2} \right), \quad (8)$$

where N is the number of parameters to be estimated, ϵ the Lagrange multiplier and γ a parameter controlling the amount of sparseness in the model. Both ϵ and γ are estimated by trial and error. Whereas solving for \mathbf{m} in equation (7) is a linear problem, solving for \mathbf{m} equation (8) is not. Therefore, we use a quasi-Newton method to minimize iteratively the objective function in equation (8) (Guitton and Symes, 2003).

To demonstrate the effectiveness of the sparse radon transform for signal noise separation, we show the representation of the data panel from Figure 1 in the f-k domain (a), the radon domain (b), and the sparse radon domain (c). Much of the energy in the synthetic data panel follows linear moveout. Therefore, the dominant factor in real data for signal/noise separation becomes the moveout of the scattered arrival compared to the direct arrival. f-k filtering is effective at isolating energy with differing dips with proper spatial sampling but is unable to isolate the energy in time regardless of sampling geometry. The side reflection and the direct arrival are colocated in f-k space and can not be separated. In the radon domain, the side reflection and the direct arrivals map to distinctly different dips for different τ 's. But, without sparseness constraints many spurious artifacts are introduced from unwanted arrivals. The

shaded region near zero slope represents an example radon mute that would remove the side reflection without reducing energy following the moveout of the direct arrival.

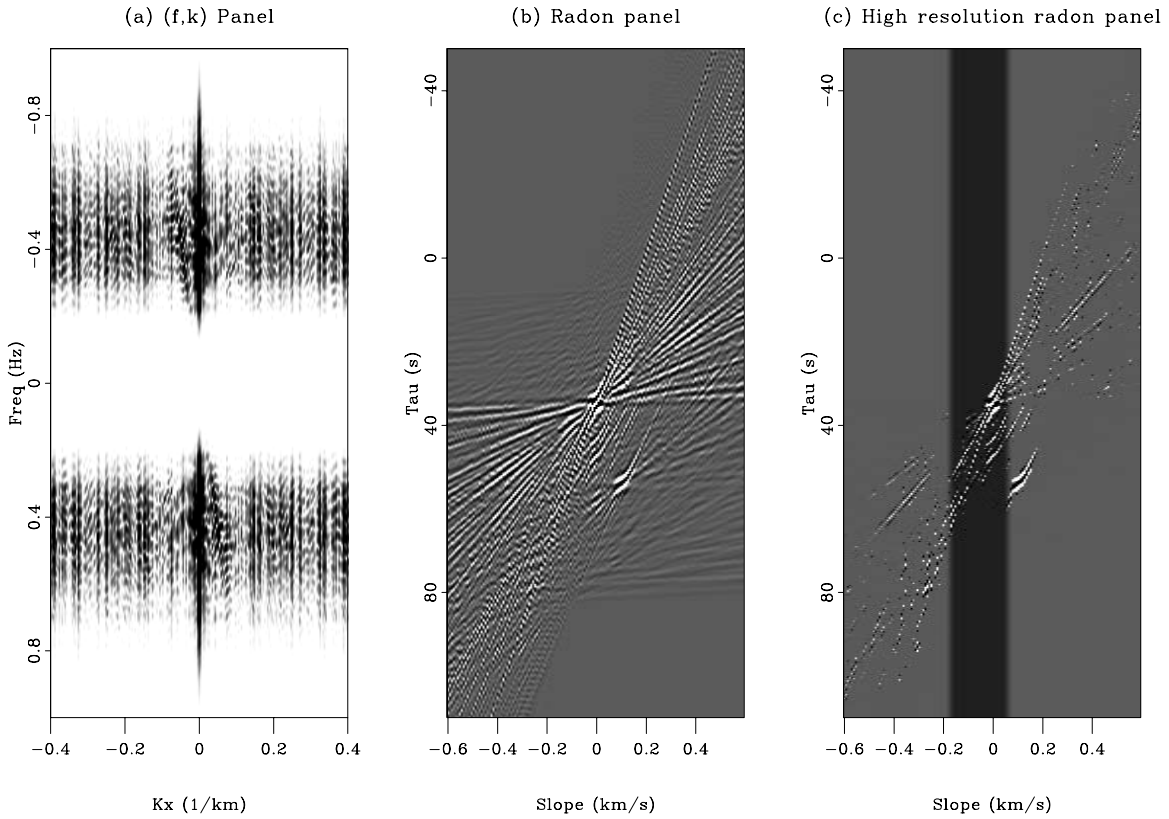


Figure 3: Figure showing representation of the synthetic teleseismic wavefield shown in 1 in the f-k domain (a), the radon domain (b), and the sparse linear radon domain (c). The letters denote arrival location identified in Figure 1. The f-k domain allows the isolation of distinct dips but does not offer a way to isolate different dips in time (e.g. time variable dip filter). The standard linear radon domain offers the possibility of separating dips as a function of time but introduces artifacts related to the transform. The sparse linear radon transform (c) allows us to isolate energy in time as in (b) while minimizing artifacts introduced from the transform. The shaded region indicates the radon mute used for the synthetic example shown in Figure 5.

`charlie1-complarse-fp-tp` [NR]

Data interpolation and noise removal

Applying a mask in equation (6) eliminates the contribution of the empty traces in the model space, making them invisible to the inversion. Therefore, by simply remodeling a data panel from the estimated model $\hat{\mathbf{m}}$ after inversion without the mask, the missing traces are reconstructed. Then, the interpolated data vector \mathbf{d}_{int} can be estimated as follows:

$$\mathbf{d}_{\text{int}} = \mathbf{d} + (\mathbf{I} - \mathbf{M})\mathbf{L}\hat{\mathbf{m}}, \quad (9)$$

where \mathbf{I} is the identity matrix. Now, for the noise removal, we simply (1) apply a mute \mathbf{K} in the radon domain that isolates and preserves the signal, and (2) transform the muted panel in the data space as follows:

$$\mathbf{n}_{\text{est}} = \mathbf{MLK}\hat{\mathbf{m}}, \quad (10)$$

where \mathbf{n}_{est} is the estimated signal (specular reflections and impinging source). The estimated noise \mathbf{n}_{est} (diffracted energy and ambient noise) is obtained by subtracting the estimated signal from the input data:

$$\mathbf{s}_{\text{est}} = \mathbf{d} - \mathbf{MLK}\hat{\mathbf{m}}. \quad (11)$$

Note that the estimated noise and signal in equations (10) and (11) are for the non-interpolated data. To compute the estimated noise and signal for the interpolated data, \mathbf{M} must be removed in equations (10) and (11) and \mathbf{d} must be replaced by \mathbf{d}_{int} in equation (11).

SYNTHETIC TEST: DATA INTERPOLATION AND SIGNAL EXTRACTION

In this section, we show the results of applying the sparse linear radon transform to synthetic teleseismic waveforms calculated with a velocity model (Figure 1) from the LARSE-I experiment (Baher et al., 2004). This model presents several real challenges in the form of large gradients in wavespeed found at the bottom of the Los Angeles basin, in the mid and the lower crust beneath the surface trace of the San Andreas, and at the base of the San Gabriel Mountains. After synthetic calculation, we extracted seismograms with actual station event geometries recorded during the experiment. This provides us a test dataset where we have prior knowledge of the crustal structure for assistance in identification of signal and noise phases and accurately sampled data for later comparison following interpolation.

Figure 4 shows the results of interpolation (c) of the resampled (b) data panel presented in (a) using the high resolution linear radon transform. The resampled synthetic data panel mimics the actual recording geometry used in the LARSE-I experiment and demonstrates the effect of wavefield aliasing due to irregular and coarse sampling. Despite the somewhat extreme spatial aliasing, the interpolated wavefield (c) contains many of the major features seen in (a) including the specularly scattered phases seen clearly between 200-240 km (see Figure 1 for a more complete description), the high amplitude laterally coherent source wavefield, and the side reflection starting at 50 seconds at 280 km. In regions of especially sparse sampling, the amplitude of the interpolated data is slightly lower than in the original data panel and several butterfly artifacts can be identified. This suggests that finer, regular sampling would produce a more accurate and smooth data interpolation for many cases. Diffracted phases with large dips scattered from the basin bottom and the sharp Moho topography are severely aliased after resampling. For this example, we have applied a mute in the radon domain to regions outside of $-0.18/0.05$ s/km. This mute effectively removes surface scattered phases with large negative slopes and the side reflection with a positive slope near 0.1 s/km (Figure 5).

In Figure 5, we show the estimated signal from the synthetic data panel using both the linear radon transform (a and b) and standard f-k filtering (c). The comparison of the filtered signal using the interpolated traces (b) and all traces demonstrates how incomplete and

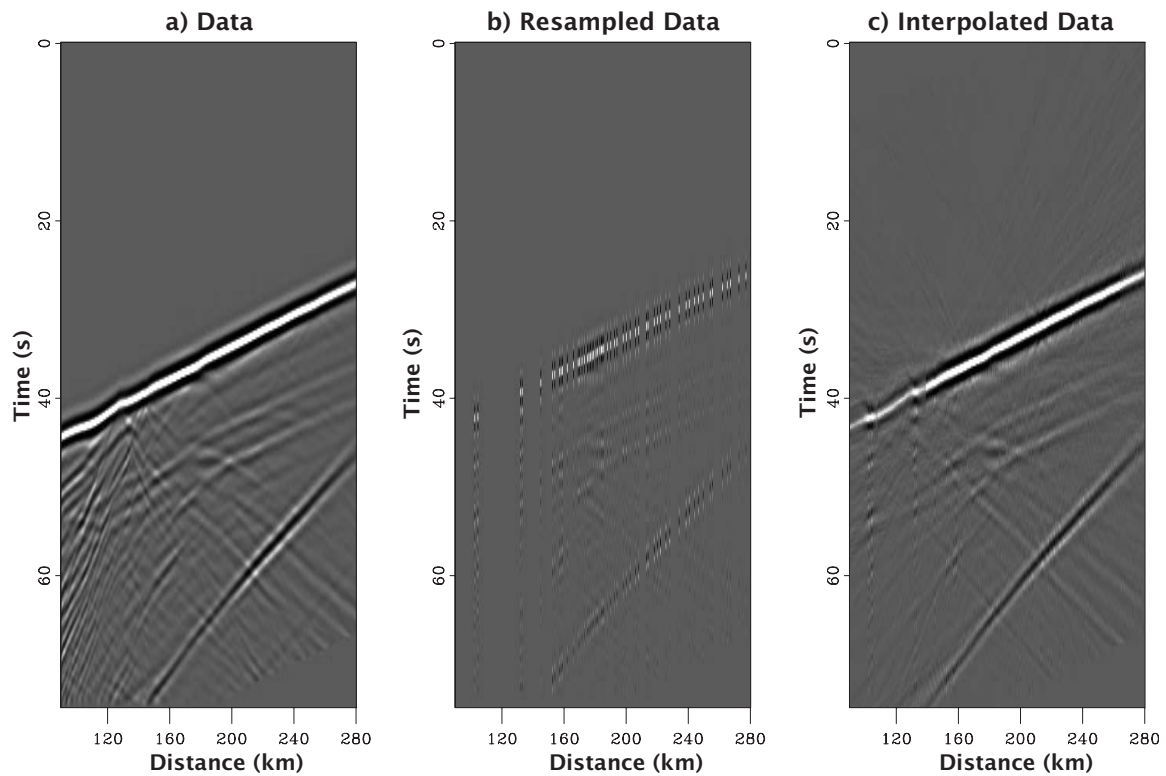


Figure 4: Results of interpolation (c) of synthetic data (a) decimated to station spacing similar to that employed in the LARSE experiment (b). The decimated data panel shows how spatial aliasing can significantly hamper the ability to recover structure easily seen in the data in panel (a). Interpolation recovers many of the major planar arrivals especially in the regions with adequate sampling. charlie1-SynthData-Result [NR]

irregular spatial sampling (e.g most teleseismic experiments) severely effects all procedures attempting to estimate and filter dips. Both the f-k and high resolution linear radon transform produce good results when the wavefield is adequately sampled. Unfortunately, this is rare and f-k methods do not offer an interpolation method except in cases of evenly spaced sampling. The filtered, interpolated data shown in panel (b) retains the medium to long wavelength, laterally coherent structures with similar moveout to the direct arrival. The majority of contamination from shallow scattering occurs in the region between 100-140 km. This is also the region of the poorest sampling and makes dip filtering very difficult. Therefore, some of what might be considered signal is lost in this area.

The linear radon transform excels in a few important areas of the data panel when compared to the f-k filtered data panel. This is directly related to the superior dip and time resolution in the radon domain as compared to f-k space. For example, Moho diffraction tails seen between 160-180 km at ~50 seconds are lost in the f-k section and remain in both radon filtered sections. Depending on the imaging algorithm chosen these diffraction tails could be considered signal or noise. A tighter mute in the radon domain could remove these features if necessary. This type of flexibility is not available with f-k filtering. Also, note the presence of the side reflection in the f-k filtered sections and its absence in the Radon filtered panels. Identification of the side reflection can occur in the f-k domain however separating without removing signal is difficult without using other attributes such as arrival time.

Possibly the easiest way to determine the effectiveness of the filtering operation is to look at what remains after subtracting the filtered section from the raw data (see Figure 6). This provides a visual measure of what was removed and subsequently classified as noise. Figure 6 shows the difference panels from high resolution radon filtering of all traces (a) and interpolated traces (b) and f-k filtering of all traces (c). The f-k panel was most effective with the near surface scattered energy although, the diffraction tails absent from the signal panel 5 have reemerged here in the noise panel. Much of the major noise features are present on the noise estimates created with complete data panels (a and c). However, the interpolated data panel fails to identify a significant amount of energy from shallow features (near 40 s and between 100-140 km) as noise. Most likely this is because of dip ambiguities that result from coarse and irregular sampling. Ambiguous dips in a data panel are spread across a broader region in the radon domain and can not be completely muted.

APPLICATION TO CASCADIA TELESEISMIC DATA

The Cascadia seismic array deployed during 1993-1994 (Nabelek et al., 1993), recorded data that was later used to make remarkable images of the underlying subduction zone (Rondenay et al., 2001; Bostock et al., 2002). These data assisted in demonstrating the potential of producing high quality images with regularly and densely sampled teleseismic wavefields. We show the results of application of the high resolution linear radon transform to the P and Sv component for one event from the recorded data (Figure 7). We chose an example event from this dataset because of its dense, approximately regular sampling and because the scattered wavefield contains clearly discernible arrivals with time variable dips. We feel that although this dataset

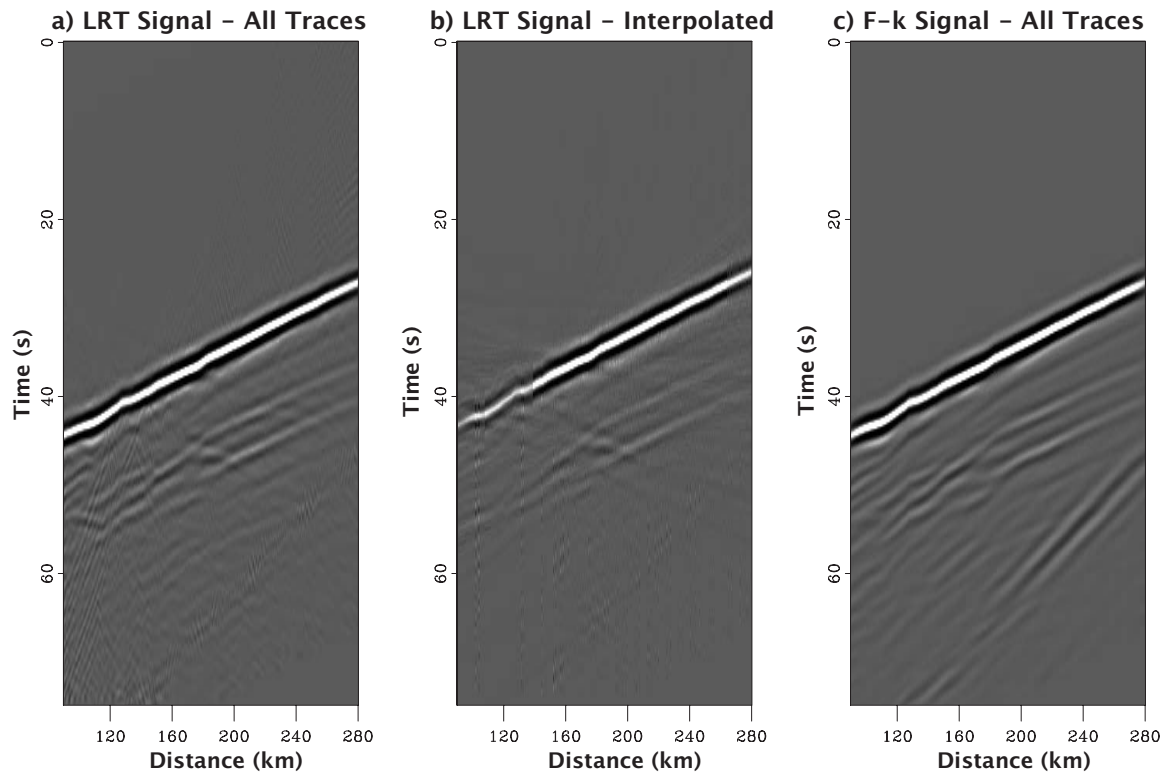


Figure 5: Comparison of signal panels calculated using the linear radon transform with all traces (a), linear radon transform with realistic station geometry (b), and f-k filtering using all traces. The results using the linear radon transform effectively muted the side reflection although this was not possible with f-k filtering without significantly degrading the signal. Diffraction tails from the complicated Moho topography between 160-200 km at 50 seconds have been removed by f-k filtering and replaced by artificial laterally continuous arrivals. The true character of these arrivals have not been modified by the radon algorithm although they could be removed with a modified mute window. charlie1-SynthSignal-Result [NR]

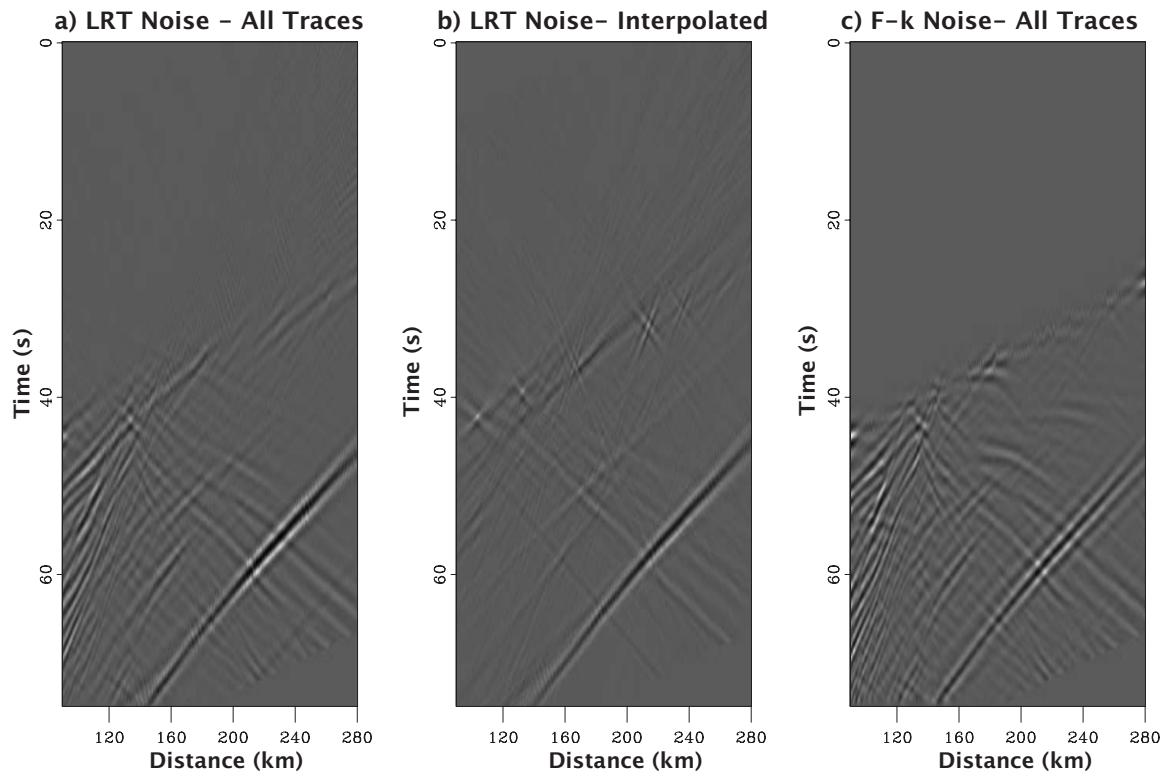


Figure 6: Comparison of noise panels calculated by subtracting results shown in Figure 5 from the original data panels shown in Figure 4. The truncated diffraction tails from the complicated Moho topography between 160-200 km at 50 seconds removed by f-k filtering have reappeared in the noise panels. The f-k filter was able to remove some of the energy from the side reflection (clearly seen in the noise panel) but this is still a significant arrival in Figure 5c. We prefer the noise estimation shown in (a) and (b) because we feel the character of the actual data and the noise have not been affected by spurious truncations and artifacts apparent in the f-k panels. charlie1-SynthNoise-Result [NR]

makes an excellent example it is not an isolated case and this method would be effective with other densely sampled datasets.

Figure 7 shows a high resolution radon panel of the P component (Figure 7a) followed by the recorded data (Figure 7b), the estimated signal (Figure 7c), and the estimate noise panel (Figure 7d). The radon panel (Figure 7a) shows the clearly focussed direct P arrival beginning centered around 0 s/km, near 30 seconds. It is followed by lower amplitude coda waves until near 120 seconds. At 120 seconds, there is a clear change in primary slowness to a peak centered at ~ 0.04 s/km. We interpret this arrival as pP because of its timiCASC-Png and its similar slowness and character to that of the direct arrival. After application of the radon mute (white panel in Figure 7c), the arrival was successfully removed and the underlying coda of the direct P arrival is recovered (Figure 7c). The estimated noise wavefield contains the majority of the energy from the later arrival as well as some low amplitude arrivals with negative dips recorded just after the direct arrival. By examining similarities between the signal and noise wavefields we can estimate cross-contamination of arrival dips in each wavefield and evaluate the quality of our taper parameters. In this case (Figure 7), the estimated signal and noise show little similarity and are comprised by a set of arrivals with distinctly different dips. This supposition is demonstrated by the clear separation of arrivals in the radon domain.

Figure 8 shows the same panels as in Figure 7 but for the Sv component from the same event. In this case, the small relative amplitude difference between diffracted noise and specularly scattered arrivals directly following the direct P arrival makes focusing energy in the radon domain difficult. Despite the limited focussing in the radon domain, application of the radon mute clearly separates arrivals with differing dips which are intermingled near 70 seconds (see panel 8b). These arrivals are visible as low amplitude radon peaks at 0.08 s/km near 45 seconds and 0.2 s/km at 70 seconds (8a). These represent the forward scattered and free-surface reflected arrivals from the dipping subducting slab below. By muting dips greater than 0.2 s/km we can remove this free-surface reflection as demonstrated in the estimated noise panel in Figure 8c. The absence of coherent features in the estimated noise panel (Figure 8d) other than the energy beginning between 60 and 90 seconds indicates that we the mute successfully separates the forward and back-scattered wavefields. This example also demonstrated the potential of using the radon transform as a wavefield separation technique regardless of the relative amplitude between the wavefields identified as signal and noise.

CONCLUSIONS

We have introduced a method of separating signal and noise and interpolating irregularly sampled data from regional scale teleseismic recordings using application of industry standard filtering algorithms based on the linear radon transform. With this method, we exploit the plane wave nature of much of the teleseismic wavefield useable for creating structural images of the lithosphere. Arrivals not following plane wave moveouts, within a desired dip range, are easily identified and removed from the recorded wavefield. Additionally, the linear radon transform provides a method for interpolation of planar arrivals that reside within the desired dip range.

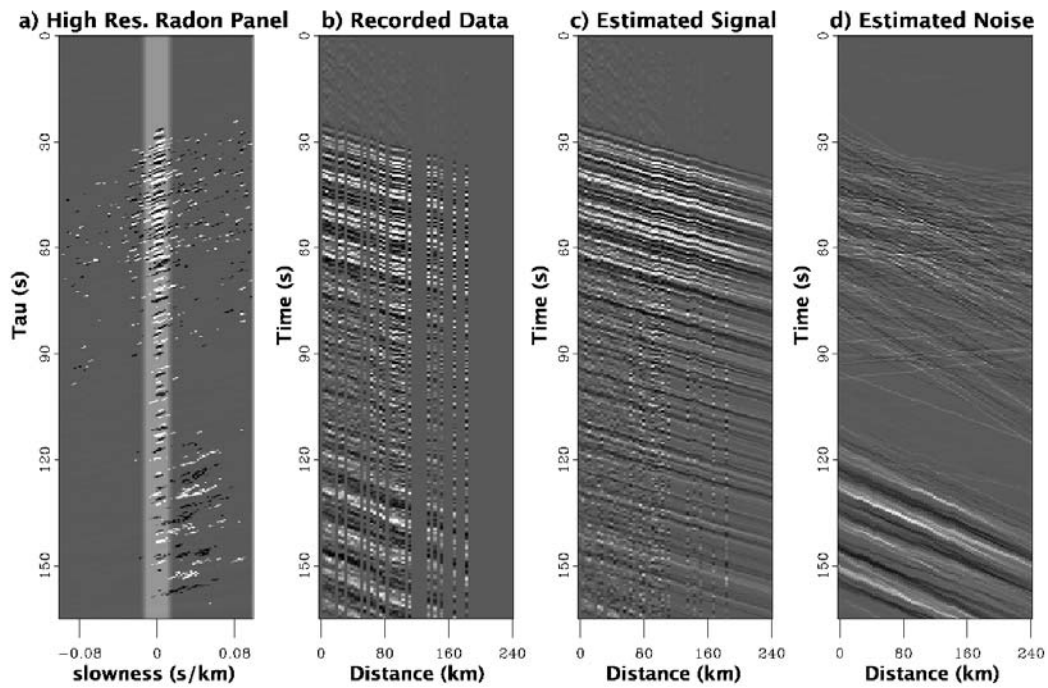


Figure 7: Figure showing the (a) high resolution radon panel of the P component, (b) the recorded data, (c) the estimated signal, and (d) the estimated noise panel (Figure 7d) for an event recorded by the Cascadia seismic array. This radon panel (a) shows how time variable dips can be used to separate wavefields that are coincident in time. The resulting interpolated panel (c) does not contain dips significantly different from that of the direct arrival (seen in panel (d)). [charlie1-CASC-P](#) [NR]

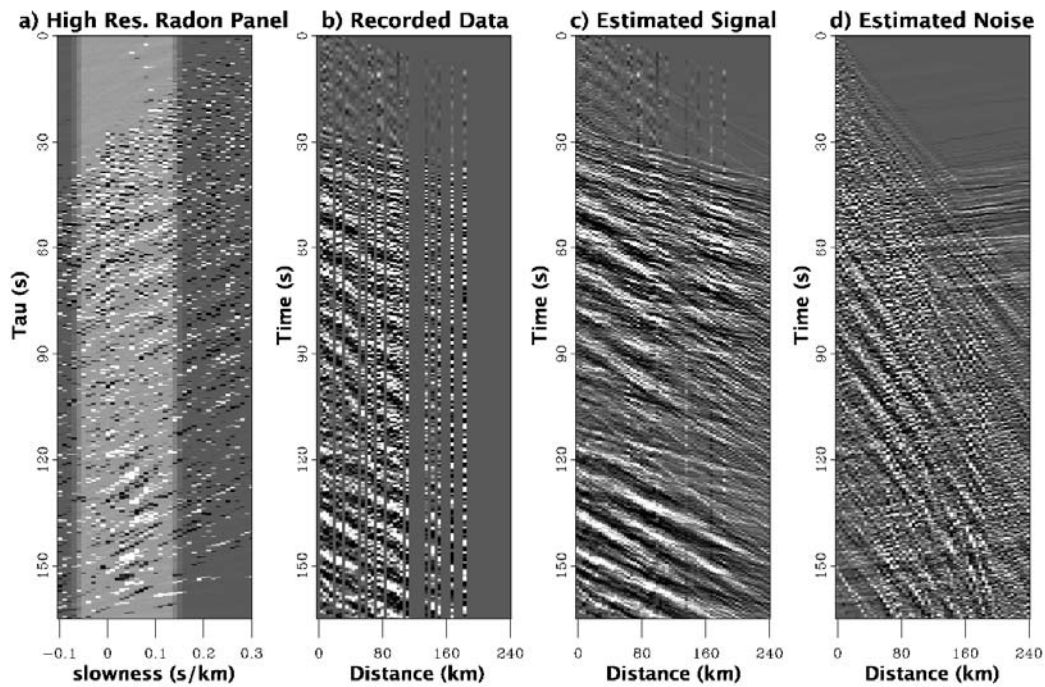


Figure 8: Figure showing the (a) high resolution radon panel of the Sv component, (b) the recorded Sv data, (c) the estimated signal, and (d) the estimated noise panel (Figure 8d) for an event recorded by the Cascadia seismic array. The radon panel appears to be poorly focussed until later τ . Despite the lack of focus, application of the radon mute allows the separation of the arrivals with clearly different dips near 60 seconds. `charlie1-CASC-Sv` [NR]

We have shown the method to be successful in interpolating real data and synthetic data with a real acquisition geometry created with a complicated wavespeed model. In addition, we have shown this method to be effective at isolating dips differing from the laterally coherent scattering and source related energy even in the presence of severe under sampling. We have demonstrated that our method is more effective than f-k filtering because it has superior dip resolution, allows the separation of dips as a function of time, and can handle (and interpolate) irregular wavefield sampling. Besides the algorithm development, the most important aspect of this study has been the recognition of the effect of current standard teleseismic wavefield acquisition geometries on dip filtering as well as standard seismic imaging methods. We hope that the examples shown in this paper will motivate denser deployments in the future to allow proper pre-processing and insure more accurate images than are presently possible.

REFERENCES

- Apra, C. M., Hildebrand, S., Fehler, M., Steck, L., Baldrige, W. S., Roberts, P., Thurber, C. H., and Lutter, W. J., 2002, Three-dimensional Kirchhoff migration: Imaging of the Jemez volcanic field using teleseismic data: *J. Geophys. Res.*, **107**, no. B10, doi: 10.1029/2000JB000097.
- Baher, S., Fuis, G., Wilson, C., Langenheim, V., and Murphy, J., 2004, The Onshore-Offshore LARSE I Transect: San Clemente Island to the Mojave Desert—Crustal blocks and the Moho: *Eos Trans. AGU*, **85** (47), Fall Meet. Suppl., Abstract S53B-0206.
- Bostock, M. G., Hyndman, R. D., Rondenay, S., and Peacock, S. M., 2002, An inverted continental Moho and serpentinization of the forearc mantle: *Nature*, **417**, no. 6888, 536–538.
- Burg, J. P., 1975, Maximum Entropy Spectral Analysis: Ph.D. thesis, Stanford University.
- Dueker, K. G., and Sheehan, A. F., 1997, Mantle discontinuity structure from midpoint stacks of converted P to S waves across the Yellowstone hotspot track: *J. Geophys. Res.*, **102**, no. B4, 8313–8327.
- Foster, D. J., and Mosher, C. C., 1992, Suppression of multiple reflections using the Radon transform: *Geophysics*, **57**, no. 03, 386–395.
- Guitton, A., and Symes, W., 2003, Robust inversion of seismic data using the Huber norm: *Geophysics*, **68**, no. 4, 1310–1319.
- Herrmann, P., Mojesky, T., Magesan, M., and Hugonnet, P., 2000, De-aliased, high-resolution Radon transforms: *Soc. of Expl. Geophys.*, 70th Ann. Internat. Mtg, 1953–1956.
- Hindriks, C. O. H., and Duijndam, A. J. W., 1998, Radon domain reconstruction of 3-D irregularly sampled VSP data: *Soc. of Expl. Geophys.*, 68th Ann. Internat. Mtg, 2003–2006.
- Jones, C. H., and Phinney, R. A., 1998, Seismic structure of the lithosphere from teleseismic converted arrivals observed at small arrays in the southern Sierra Nevada and vicinity, California: *J. Geophys. Res.*, **103**, no. B5, 10065–10090.

- Kabir, M. M. N., and Marfurt, K. J., 1999, Toward true amplitude multiple removal: The Leading Edge, **18**, no. 1, 66–73.
- Langston, C. A., 1977, Effect of Planar Dipping Structure on Source and Receiver Responses for Constant Ray Parameter: Bulletin of the Seismological Society of America, **67**, no. 4, 1029–1050.
- Nabelek, J., Li, X.-Q., Azevedo, S., Braunmiller, J., Fabritius, A., Leitner, B., Trehu, A. M., and Zandt, G., 1993, A high-resolution image of the cascadia subduction zone from teleseismic converted phases recorded by a broadband seismic array: Eos Trans. AGU, **74(43)**, **Fall Meet. Suppl.**
- Phinney, R. A., 1964, Structure of the Earth's Crust from Spectral Behavior of Long-Period Body Waves: J. Geophys. Res., **69**, no. 14, 2997–3017.
- Poppeliers, C., and Pavlis, G. L., 2003, Three-dimensional, prestack, plane wave migration of teleseismic P-to-S converted phases: 1. Theory: J. Geophys. Res., **108**, no. B2, art. no.–2112.
- Rondenay, S., Bostock, M. G., and Shragge, J., 2001, Multiparameter two-dimensional inversion of scattered teleseismic body waves 3. Application to the Cascadia 1993 data set: J. Geophys. Res., **106**, no. B12, 30795–30807.
- Sacchi, M. D., and Ulrych, T. J., 1995, High-resolution velocity gathers and offset space reconstruction: Geophysics, **60**, no. 04, 1169–1177.
- Sheehan, A. F., Shearer, P. M., Gilbert, H. J., and Dueker, K. G., 2000, Seismic migration processing of P-SV converted phases for mantle discontinuity structure beneath the Snake River Plain, western United States: J. Geophys. Res., **105**, no. B8, 19055–19065.
- Taner, M. T., and Koehler, F., 1969, Velocity spectra - Digital computer derivation and applications of velocity functions: Geophysics, **34**, no. 06, 859–881.
- Thorson, J. R., and Claerbout, J. F., 1985, Velocity stack and slant stochastic inversion: Geophysics, **50**, no. 12, 2727–2741.
- Trad, D., Ulrych, T. J., and Sacchi, M. D., 2002, Accurate interpolation with high-resolution time-variant Radon transforms: Geophysics, **67**, no. 2, 644–656.
- Trad, D., Ulrych, T., and Sacchi, M., 2003, Latest views of the sparse Radon transform: Geophysics, **68**, no. 1, 386–399.
- Wilson, D. C., and Aster, R. C., 2004, Receiver function seismic imaging of the crust and upper mantle using frequency-wavenumber filtering and regularized multimode kirchhoff migration: Eos Trans. AGU, **85(47)**, Fall Meet. Suppl., Abstract S33A-1090.
- Wilson, C. K., Jones, C. H., and Gilbert, H. J., 2003, Single-chamber silicic magma system inferred from shear wave discontinuities of the crust and uppermost mantle, Coso geothermal area, California: J. Geophys. Res., **108**, no. B5, art. no.–2226.

Wilson, C. K., Jones, C. H., Molnar, P., Sheehan, A. F., and Boyd, O., 2004, Distributed deformation in the lower crust and upper mantle beneath a continental strike-slip fault zone: Marlborough Fault System, South Island, New Zealand: *Geology*, **32**, 837–840.

Yilmaz, O., Chambers, R., Nichols, D., and Abma, R., 1987, Fundamentals of 3-D Migration: *The Leading Edge*, **6**, 22–30.

Yilmaz, O., 1997, Seismic Data Processing:, volume 2 of **Investigations in Geophysics** Society of Exploration Geophysics, Tulsa, Oklahoma.



Focusing-effect AVO/AVA: overview of results and assessment of problems

*Ioan Vlad*¹

ABSTRACT

Small-scale heterogeneities in the Earth produce visible focusing of seismic wavefield amplitudes with offset, but minimal variations in traveltimes. These effects are called Focusing-Effect AVO (FEAVO) or AVA (FEAVA) for avoiding confusion with lithology-caused AVO/AVA. FEAVO/FEAVA is not an unpredictable phenomenon that occurs at random. It appears in a number of well-defined geological settings, it can be modeled with appropriate precautions, it can be identified by its spatially predictable patterns, and can be removed in a manner that takes into account the specific physics involved. This paper summarizes work published over the course of several years in seven different SEP reports, providing an overview of the results obtained up to date and an assessment of the most critical problems to be solved.

INTRODUCTION

Amplitudes of reflected seismic waves have concerned geophysicists since the beginnings of the profession (Gutenberg, 1936). However, until the advent of digital recording in the late sixties, efforts in this direction were mainly theoretical (Bortfeld, 1961). “Bright-spot” technology started a first wave of applied amplitudes research in the early seventies (Craft, 1973), and the emergence of Amplitude Variation with Offset (AVO) techniques (Shuey, 1985) assured amplitudes a solid place in the geophysicist’s toolbox. The line of research to which this paper belongs was started by Kjartansson (1979).

Kjartansson observed that zones with amplitudes too large to be explained by lithological contrasts at the reflector or by tuning were correlated in a predictable way in the prestack data volume, and he provided a conceptual explanation for it. I will call these phenomena Focusing-Effect AVO/AVA (FEAVO/FEAVA).² The section that follows after the Introduction will describe them in detail. The important thing to note, and the motivation for this work, is that: (1) those anomalous amplitudes are caused by wavefield focusing through velocity or absorption lenses, (2) that they impede proper AVO/AVA analysis or any other amplitude analysis techniques, and that therefore (3) they should be removed from the seismic image. Work on this subject has been published sporadically, especially at SEP, ever since Kjartansson’s

¹**email:** nick@sep.stanford.edu

²The name FEAVA will be used only when referring specifically to the angle domain.

paper. The most recent publications related to this topic are Vlad and Biondi (2002), Vlad et al. (2003a), and Vlad (2002; 2003; 2004a; 2004b; 2005). While these articles dealt with highly specific details, the material that follows will provide an overview of the current state of knowledge about FEAVO and its removal, with assessments of the problems that remain to be solved, in highlighted paragraphs.

FEAVO DESCRIPTION

Geologic setting

FEAVO effects are caused by focusing through velocity or absorption heterogeneities smaller than the Fresnel zone (Spetzler et al., 2004) – too small to be resolved by velocity analysis methods currently employed in production settings, too small to send the energy outside the aperture of the seismic survey, but not so small and sharp that they would simply cause a diffraction. This means roughly “a few tens of meters”. White et al. (1988) shows analytically that it is more likely that the interfaces are smooth rather than sharp. Highly visible FEAVO effects appear easily in the presence of velocity contrasts as small as 2%, and no absorption (Vlad, 2004a). Examples of such heterogeneities include:

(1) Irregular interfaces between spatially extended media with different velocity and/or absorption characteristics: (a) channels on the sea bottom caused by currents, former rivers, or glaciers; (b) positive landforms on sea bottom such as moraines (North Sea); (c) Irregular thickness of permafrost; (d) low-velocity eolian, fluvial or marine sediment covering karst features or other irregular erosion surfaces; (e) interfaces of plastic clay or salt bodies. In this case FEAVO can be hard to see because of the much more powerful illumination effects caused by interface undulations of a larger spatial wavelength than those which cause FEAVO.

(2) Small lenticular bodies of contrasting properties with the surrounding medium. They may be filled with gas, in which case absorption would play an important role. They can be small in all directions, as would be the case with filled peat bogs, or they can be elongated along one direction, such as gas sand-filled river channels (small in cross-section) or lenses formed by gas-liquid contact inside a fold associated with normal listric faulting, (left panel in Figure 1).

(3) Termination of a relatively thin layer of highly contrasting properties with the surrounding medium, either by tapering off stratigraphically (right panel in Figure 1), or by ending abruptly against a fault (Hatchell, 1999, 2000a,b). The latter case, illustrated by Figure 2, is interesting because it may occur much deeper (thousands of meters) than the previously described ones, and the bodies causing the FEAVO anomalies may have much sharper interfaces.

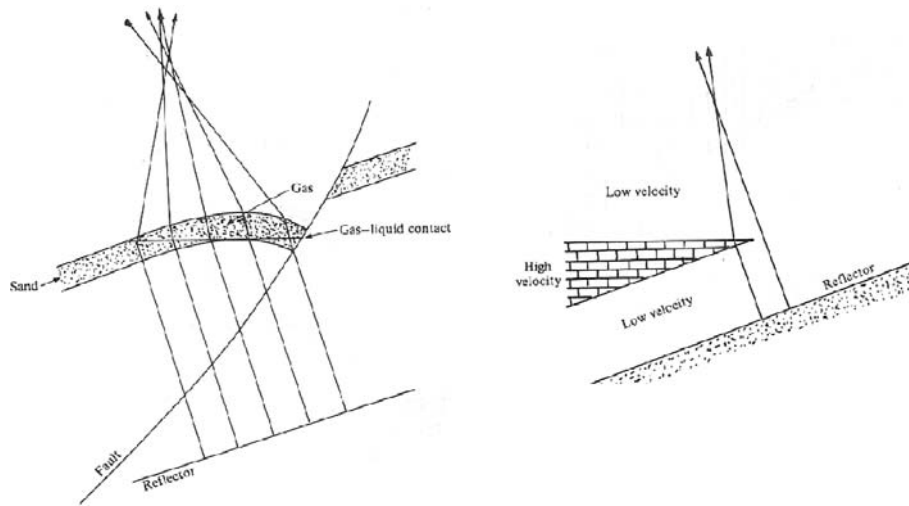


Figure 1: Examples of geologic settings which may cause focusing. From Sheriff and Geldart (1995). [nick2-sheriff](#) [NR]

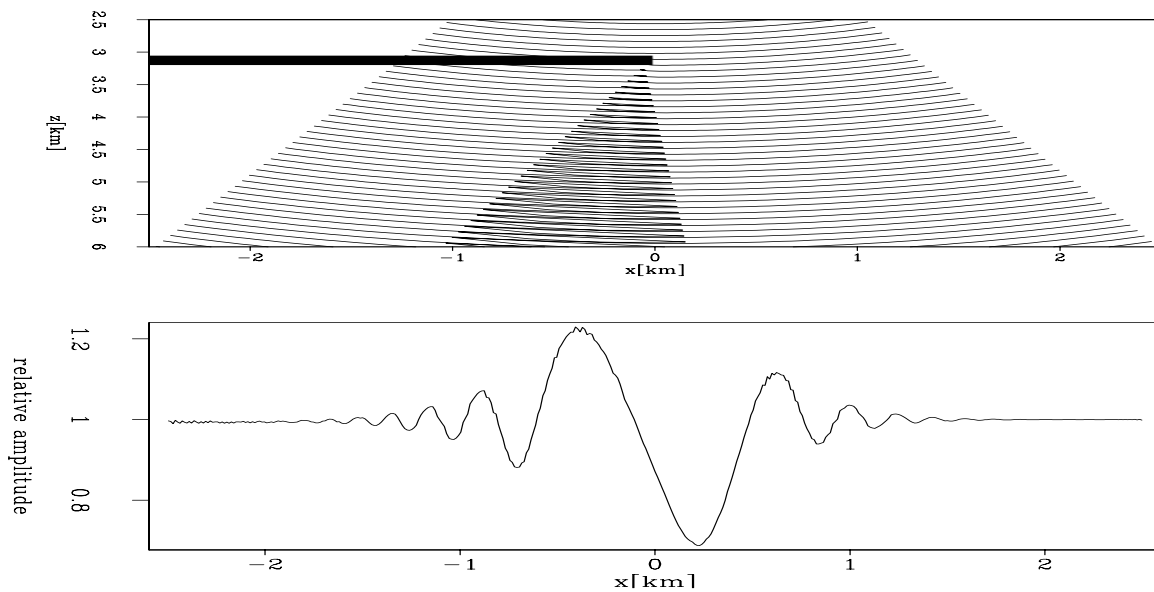


Figure 2: **Top:** Velocity model and isochrones for a shot at (0,0). The background is 1830m/s and the slab is 1647m/s. No absorption, pseudospectral two-way method. **Bottom:** The shot is downward continued through the velocity model with the slab and without the slab to simulate the seismograms that a horizontal strings of geophones would record at a depth of 6000m. At each x location, the plotted value is the ratio between the highest amplitude obtained at that location without the slab and with the slab. The end of the slab induces focusing. The dispersion is just a numerical effect. From Vlad and Tisserant (2004). [nick2-g3_sep120](#) [CR]

Needed: realistic modeling of these FEAVO-causing geologic settings with a variety of plausible parameters (shape, size, depth, velocity, Q), in 2-D and 3-D, in order to estimate the range of parameters which results in FEAVO anomalies (source too small to be resolved by state-of-the-art velocity analysis methods used in production, yet too large and smooth to cause diffractions). This is a computationally-intensive task. The datasets obtained from modeling could be used as benchmarks for FEAVO detection and removal.

FEAVO effects in the data

The first sign of FEAVO that one may encounter in a dataset are subvertical streaks of alternating high and low amplitudes in constant-offset sections (left panel in Figure 3). At a closer inspection, the affected areas show traveltime departures from hyperbolicity as small as 2-3 ms (Carazzone et al., 1984) and as large as 20 ms (Kjartansson, 1979). An illustration of these effects is presented in the middle panel of Figure 3. The amplitudes in these areas may be easily three times larger than those in unaffected areas (White et al., 1988). The effects may be frequency-dependent and distort the wavelet (Stephens and Sheng, 1985; Vlad and Biondi, 2002).

Needed: modeling of purely-velocity and purely-absorption FEAVO, in order to investigate whether the frequency-dependent effects can serve to discriminate between FEAVO caused by absorption and that caused by velocity.

While the above-described effects are visible and are what started FEAVO research in the seventies, FEAVO's certain "signature" in the data domain (before migration) is the "Kjartansson V's". These shapes appear if we window a prestack 2-D line to roughly include the areas with anomalous amplitudes, then take the absolute value of each sample, *stack* the prestack dataset along the time axis and display the resulting midpoint-offset plot with an appropriate gain. "V" shapes become visible (right panel in Figure 3). This may not occur if the background velocity in the medium varies so strongly with midpoint as to distort these shapes too much.

The heuristic used by Kjartansson (1979) to explain the formation of the "V" shapes is presented in Figure 4. The "V" shapes are the result of stacking along the time axis surfaces which in constant velocity are described by

$$h = \frac{t}{t - t_a} \cdot |m - m_a| \quad (1)$$

A form of this equation is given by Rocca and Toldi (1982), with a simpler proof of another form in Vlad (2002). h is the half offset, t is traveltime, m is midpoint, t_a and m_a are the location of the heterogeneity that causes the focusing. Figure 5 gives a better view of the path of the FEAVO effects through the prestack dataset. The shape resembles the bow of a capsized boat. Its slope becomes asymptotically vertical with time and the opening of the "V"s becomes asymptotically 45° as the traveltime to the focusing source becomes negligible. It is visible

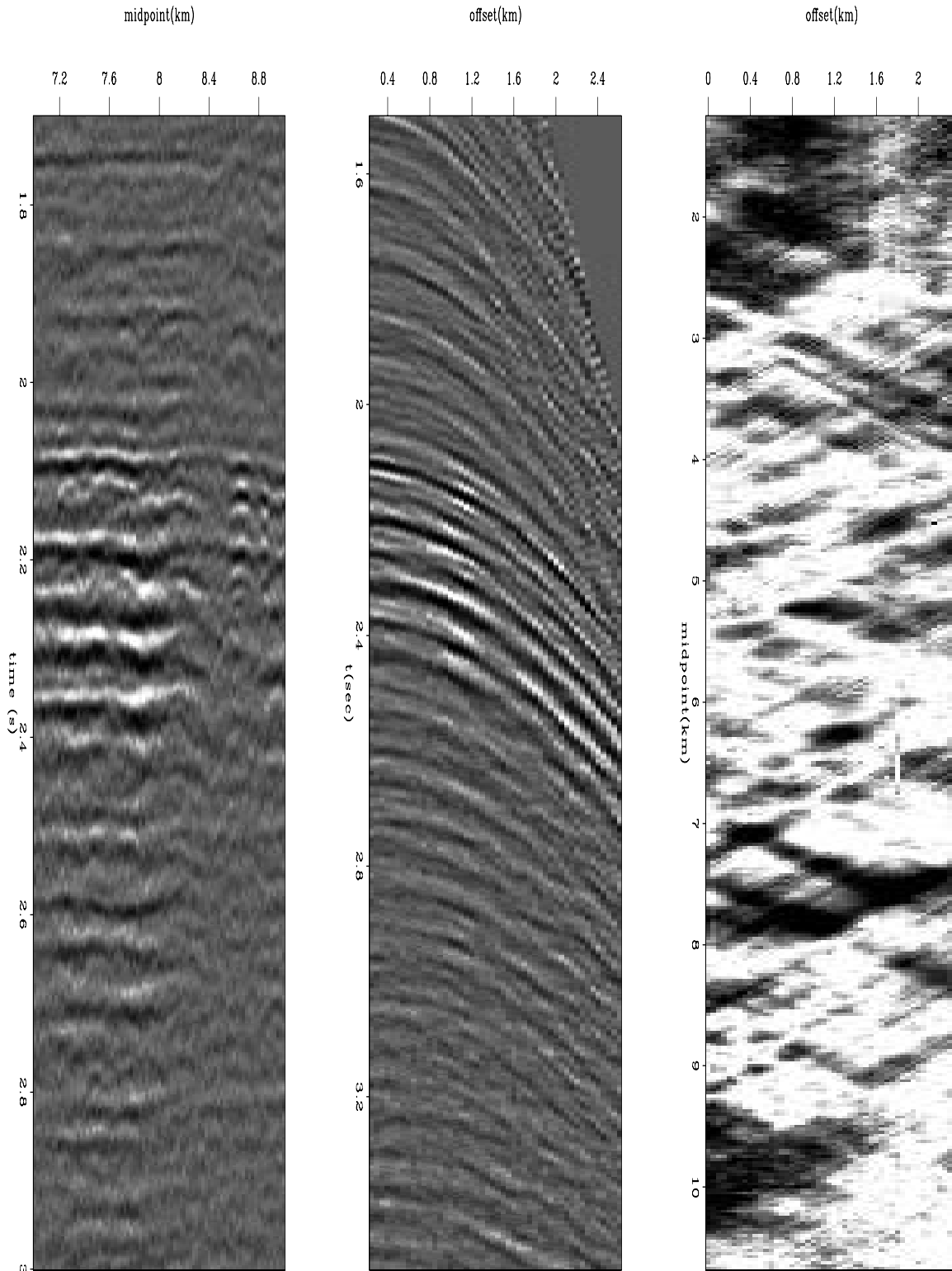


Figure 3: FEAVO in the data domain (before migration). Grand Isle dataset, also used by Vlad and Biondi (2002) **Left:** vertical amplitude streaks in constant-offset section. **Center:** Milisecond-sized departures from hyperbolicity. Most visible at 2.35s. **Right:** Kjartansson V's in the midpoint-offset space, after stacking the unsigned values along the time axis.

`nick2-new_prodef` [ER]

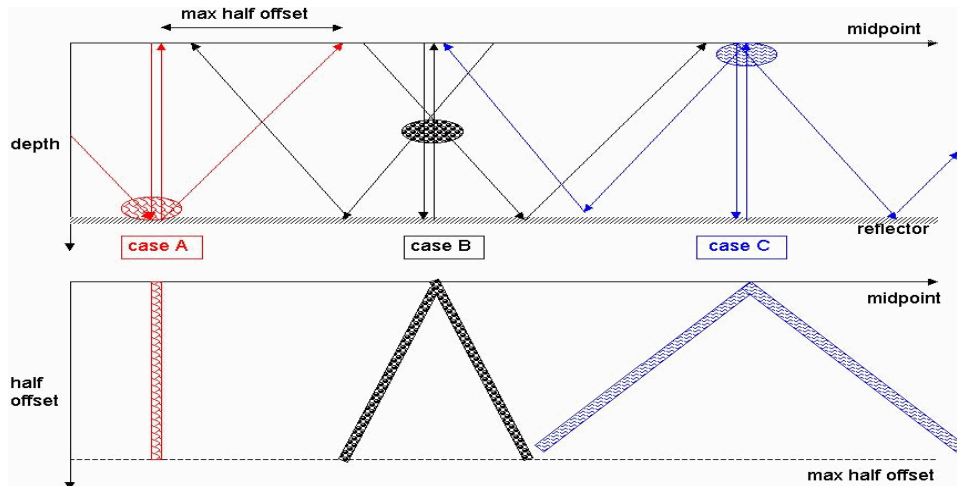


Figure 4: The physical explanation for the expression of FEAVO anomalies in midpoint-offset space Kjartansson “V”s. In the upper picture, the blobs are transmission anomalies and the arrows are raypaths for the zero offset and for the maximum offset recordings. For case A (anomaly on the reflector), only a single midpoint is affected, for all offsets. Case C (anomaly at the surface), is actually a static: its “footprint” is a pair of streaks slanting 45° from the offset axis. Case B (in between) gives a pair of streaks with angles smaller than 45° . From Vlad and Biondi (2002). [nick2-vilus](#) [NR]

now why stacking along the time axis a window in the middle of the prestack data volume would produce a “V”.

A subtle, little-studied aspect of FEAVO effects is the distribution of the anomalous amplitudes when the anomaly paths described above intersect reflectors, for which I will use the name “FEAVO microstructure”. Since an absorption-free, velocity-only “lens” conserves energy, any increase in amplitudes would have to be bordered by one or two shadow zones, and a decrease – by two illuminated zones. Finite-frequency wave theory predicts this for absorption-free media and ultrasonic experiments confirm it, as illustrated by Figure 4 of Spetzler et al. (2004). I am not aware of any equivalent studies for absorption. The existence or not of shadow/highlight border zones for absorption is important because it may offer an avenue of discriminating between absorption-caused FEAVO and velocity-caused FEAVO, a key issue when trying to remove focusing with methods based on the physics of the phenomena (not just image processing).

Needed: A theoretic/numeric study of the magnitude of the shadow/highlight effects bordering FEAVO with parameters likely to be encountered in real exploration surveys, including absorption.

The polarity of the FEAVO on a reflector depends on the polarity of the velocity anomaly causing the FEAVO (negative or positive with respect to the background) and on the polarity of the reflector itself. The rightmost “V” in the bottom panel of Figure 8 illustrates the depen-

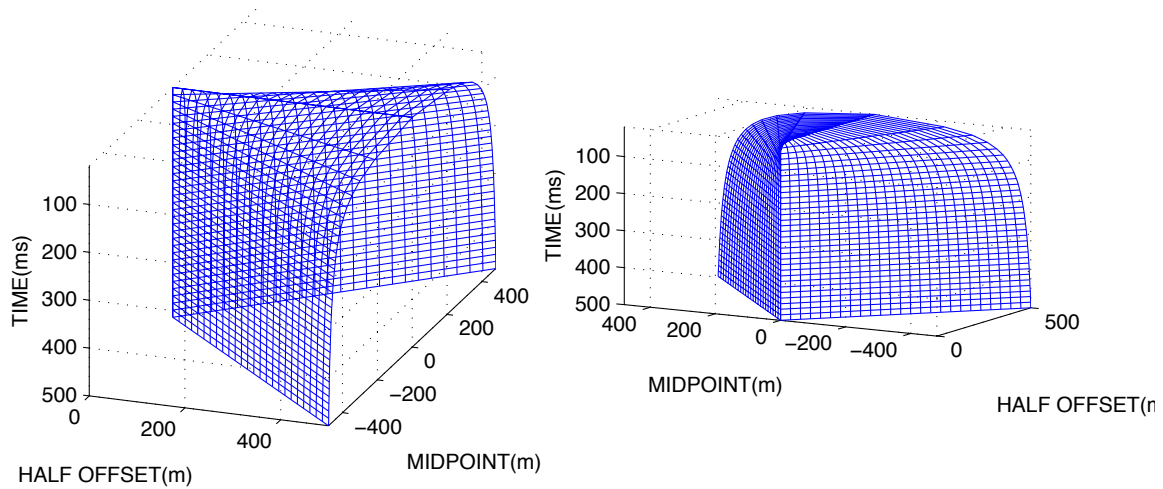


Figure 5: Path of FEAVO effects through the prestack data volume in constant velocity, flat reflectors. The source of focusing is at midpoint 0 and travelttime 20ms. Two views are provided for a better perception of the tridimensional surface. `nick2-feavo_data` [CR]

dence of the polarity of the “V”s on the sign of the velocity anomaly.³ This will have important consequences on the choice of FEAVO removal strategies, treated in a separate section towards the end of this paper.

FEAVA effects in the image

Simple algebraic manipulations of Equation 1 show that in Angle-Domain Common Image Gathers (ADCIGs), for constant velocity and flat reflectors, the shape of the FEAVA path is given by

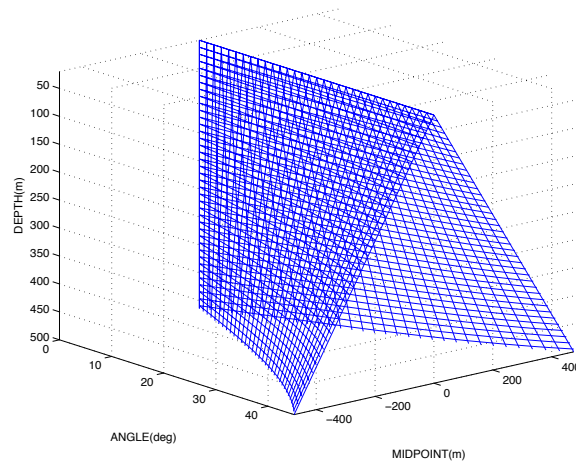
$$z = z_a + |m - m_a| \cot \theta, \quad (2)$$

where z is depth, z_a is the depth of the heterogeneity, m is midpoint, m_a is the location of the anomaly, and θ is the reflection angle (Vlad, 2002). Figure 6 plots this surface. The “Kjartansson V’s” are visible in the Grand Isle dataset after a $v(z)$ survey-sinking migration. Figure 7 shows two depth slices through the prestack image. The number of “V”s is particularly large in this dataset, making it less than suitable for isolating and studying a FEAVO instantiation free from interference. In a less crowded area of the figure, the circled upside-down “V” shows vertical continuity as well as borders of polarity opposite from that of the main image, as predicted by finite-frequency wave theory (Spetzler et al., 2004). Another property of data-domain FEAVO that gets carried over in the image domain is the dependence of the polarity of the effects on the sign of the velocity “lenses” (Figure 9). The effects along the described paths have a finite width, as exemplified by Figure 9. In the case of velocity-caused

³Assuming that one-way modeling produced morphologically correct effects – see more in the Modeling section.

Figure 6: FEAVO path in ADCIGs, constant velocity, flat reflectors, heterogeneity 20m deep. Unlike in the data domain, the shape keeps on opening with depth and the arms of the “V’s” are slightly curved.

`nick2-feavo_imag` [CR]



FEAVO, the width of the path is linked to both the magnitude and the size of the heterogeneity. It is not known to what extent there is a magnitude-size ambiguity in the case of absorption. For both cases it may be possible to put an upper bound on the spatial extent of the anomaly based on the width of the FEAVO path, and this can be used as regularization in inversion for the anomalies or as an aid in interpretation.

Needed: A study of the link between the magnitude (intensity) and size (spatial extent) of the FEAVO source and the width of the FEAVA effects. This applies to data-domain effects too.

Migration removes any focusing effects which did not send energy outside the survey aperture (Vlad, 2005), so it will be easier to study FEAVA effects in the image than in the data – there is simply much less misplaced energy to interfere with the object of study.⁴ To properly view (and extract) FEAVA, one must first resolve the background velocity well enough that there is no residual first-order curvature in ADCIGs. FEAVA effects, being caused by anomalies much smaller than the cable length, will manifest themselves as slight travelt ime wiggling accompanied by high/low amplitudes. Figure 9 shows a synthetic example obtained of FEAVA effects “in a pure state”, after all non-FEAVA energy has been removed.

The advantage of having less clutter in the image can be easily negated by a treatment of the data that emphasizes lack of noise over amplitude preservation. A comparison of Figure 2 in Vlad (2002) and Figure 6 in Vlad and Biondi (2002) shows an example of such an occurrence. Using an amplitude-preserving processing and imaging flow is critical for correctly imaging the effects. Smearing the FEAVO effects with amplitude-careless processing is not removing them, but sweeping the dirt under the rug, since this will result in undesired FEAVO energy contaminating now unknown areas. Also, FEAVO removal may need to take into account the physics of the phenomenon, which need to be preserved. Vlad et al. (2003b) and Vlad and Tisserant (2004) describe the implementation of an amplitude-preserving shot-profile migration. The processing done before migration needs to use amplitude-preserving algorithms too.

⁴Multiples can be more of a problem, though.

Needed: A study of the amplitude properties of the offset-to-angle transformation used in creating the ADCIGs, and in particular the role of the regularization ϵ , the variation of which has been observed to have significant results.

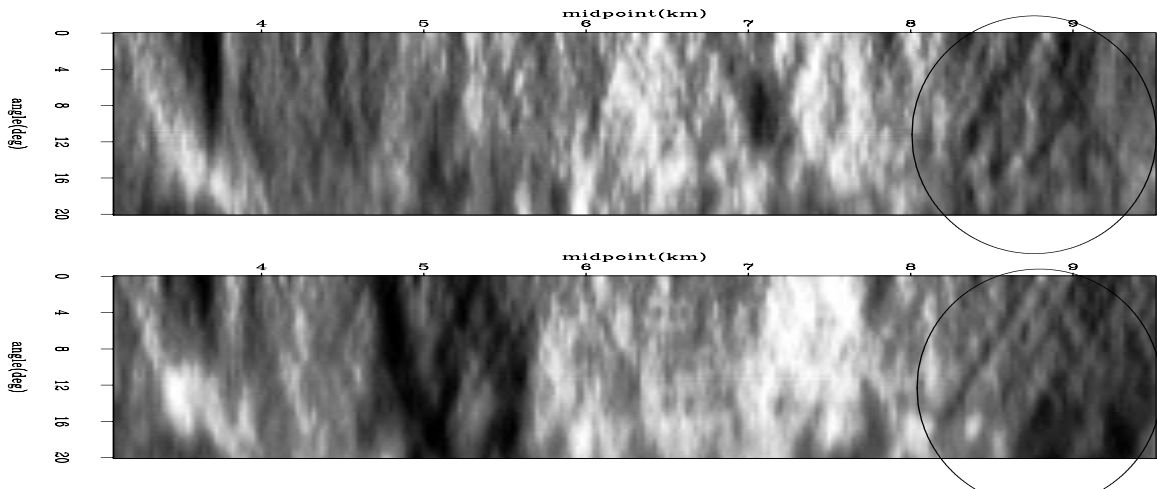


Figure 7: Depth slices 2.36km (top), 2.43km (bottom). Notice: (1) the slight opening of the upside-down, encircled “V” with depth, like in Figure 6; (2) its opposite-polarity borders; and (3) the rectangular shaded areas spanning all angles which may denote “legitimate”, reflector-caused AVO if reflectors are flat enough in this area. nick2-apslim [CR]

An important point to note is that there is no relationship whatsoever between amplitude variations caused by focusing and those caused by variation of incidence angle on the reflector (FEAVO vs. “legitimate” AVO). The total amplitude of a reflector will show a superposition of the two effects, but the effects are physically independent from each other. *FEAVO effects do not obey the \sin^2 dependence between amplitude and reflection angle given by Shuey (1985).* Figure 10 offers an illustration of this property, and the “FEAVO detection” and “FEAVO removal” sections explore its the applications.

FEAVO MIGRATION AND MODELING

Since velocity heterogeneities of the size of those which cause FEAVO break the high-frequency assumption of the ray theory (Woodward, 1990), wavefield extrapolation methods should be used to migrate and model FEAVO-affected data. Vlad (2005) has demonstrated qualitatively that one-way migration methods with the *correct* velocity model (containing the FEAVO-causing velocity lenses) eliminate all FEAVA effects from the image. The same publication shows in the same way that: (1) only FEAVO effects modeled with two-way schemes have a microstructure (i.e., width of the bordering shadows) identical to that of real data, but (2) the errors introduced by one-way modeling schemes are removed when migrating with one-way schemes *and the correct velocity model*. Thus the numerical experiments from Vlad et al.

(2003a), which show that migration with the correct velocity model removes FEAVA, keep their validity.

Needed: Mathematical proof of the conclusions of Vlad (2005), and further investigation for cases involving absorption.

Figure 8 shows the output of modeling FEAVO with a one-way scheme. While the synthetic dataset does feature the small traveltime anomalies associated with FEAVO, it does not exhibit the several-fold increase in amplitudes noticed in the real data and which got FEAVO discovered in the first place (Kjartansson, 1979; White et al., 1988). The magnitude of the velocity “lenses” (10% of the background) should have been sufficient to have caused it. It is unclear to what extent the lack of strong amplitude effects is caused by modeling with a one-way scheme in general (as discussed above) or by the amplitude characteristics of the particular one-way scheme employed. FEAVA effects obtained by modeling with a one-way scheme followed by migrating with the background velocity (Figure 9) have neither border shadows/highs as real data does (Figure 7), nor extremely high amplitudes. Modifications of the downward propagation operators designed to take into account vertical gradients in velocity (Vlad et al., 2003b) will not result in improvements in this case because the background velocity is constant. Having correct amplitudes of FEAVA effects, including their microstructure, is paramount to the success of any inversion-based removal procedure that inverts FEAVA into velocity/absorption anomalies, and any such procedure would need to be tested on a synthetic while being prototyped.

Needed: Extraction of “pure”, *correct* FEAVA effects by two-way modeling of FEAVA effects followed by two-way migration with the correct velocity, with the background velocity, and subtraction in ADCIGs. A comparison with the result of the equivalent one-way flow (Figure 9) will allow then to assess whether the errors introduced by the one-way problem are negligible or not.

Not only primaries are focused by the heterogeneities that caused FEAVO. Multiples are too. Vlad (2004a) uses numerical experiments on highly realistic data to present evidence towards the idea that, unlike FEAVO from primaries, FEAVO from multiples is not eliminated through simple migration that does not take multiples into account. It is easy to understand this intuitively: during a migration designed for primaries, the multiples wavefields do not pass through the focusing heterogeneities enough times for the focusing to be undone by the extrapolation operators. Another type of FEAVO that may not be eliminated by migration is the one caused by absorption. An absorption compensating-scheme, such as Lu et al. (2004), would need to be employed to eliminate FEAVO after an absorption model has been obtained through inversion.

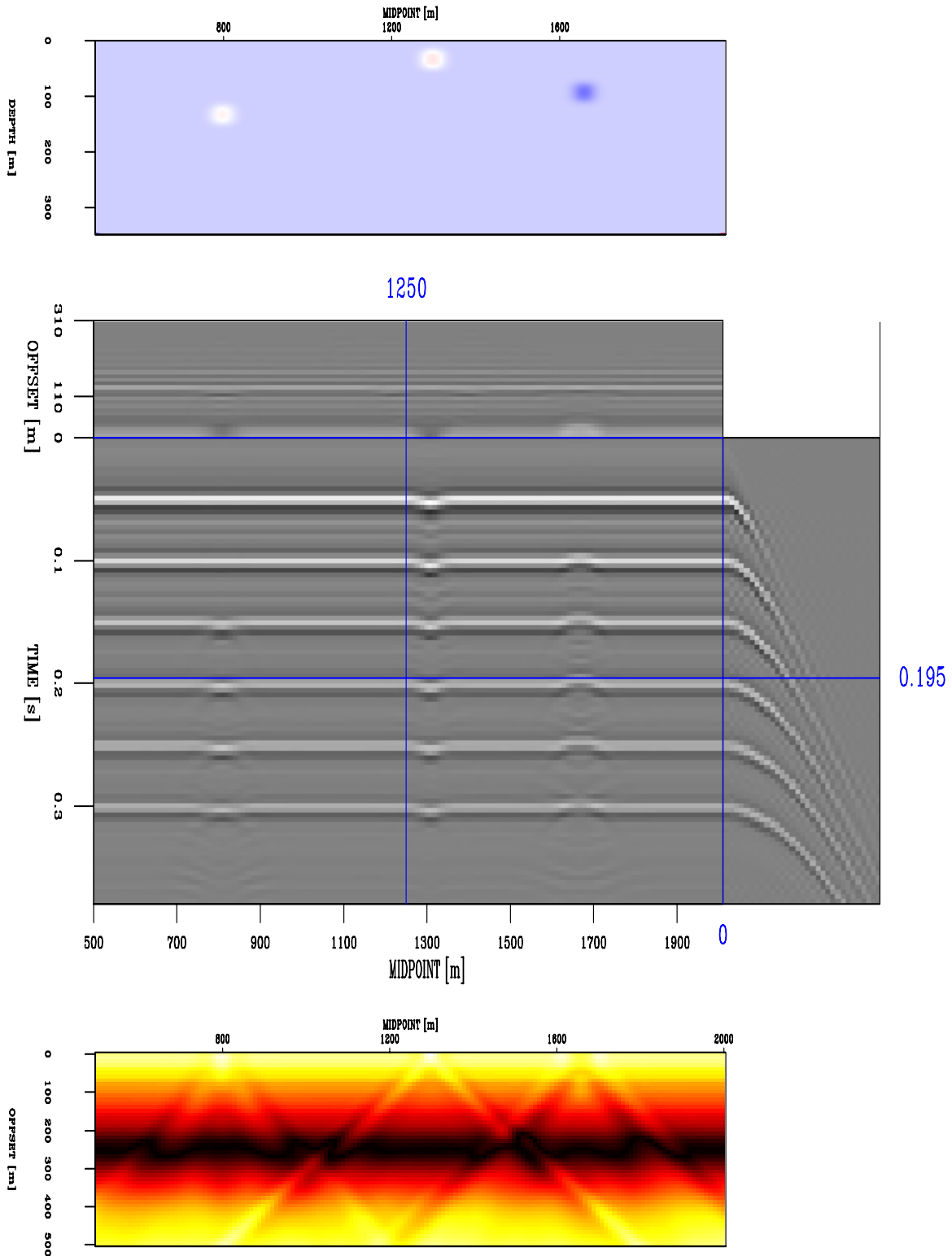


Figure 8: **Top:** Velocity model with 2000m/s background and anomalies with peak values, from left to right, of -153m/s, -188m/s and +231 m/s. **Middle:** Prestack data generated with one-way source-receiver upward continuation with two reference velocities. **Bottom:** “Kjartansson V’s”. From Vlad et al. (2003a). nick2-f1 [CR]

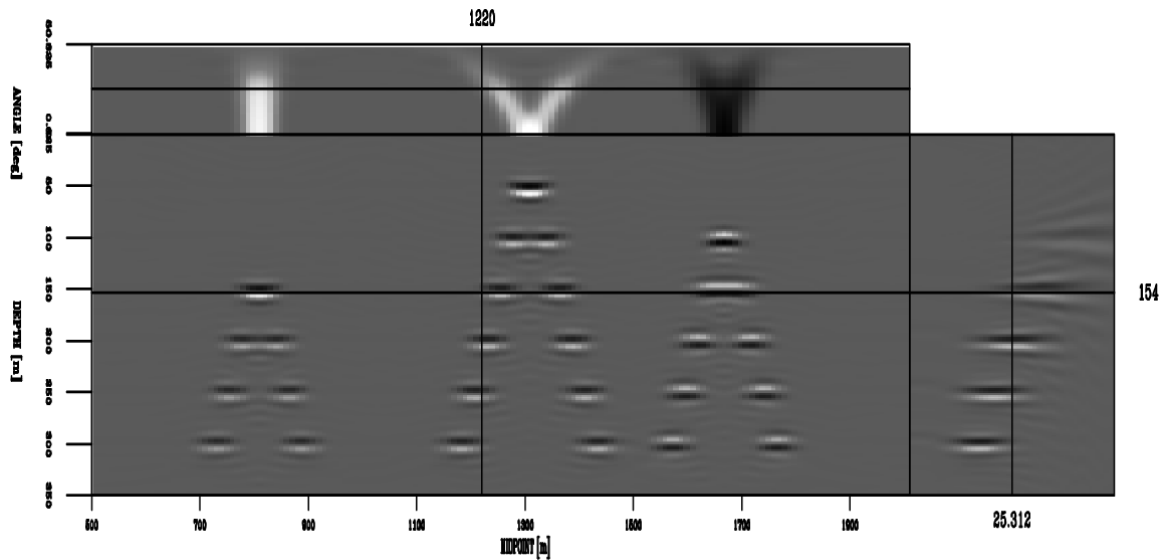


Figure 9: “Pure” FEAVA. Obtained by: (1) migrating the dataset shown in Figure 8 with the correct velocity; (2) migrating it with the background velocity; (3) subtracting the ADCIGs. From Vlad et al. (2003a). `nick2-f6_top` [CR]

FEAVA DETECTION

In order to remove FEAVO/FEAVA, or at least not to trust the amplitudes from the affected areas, one must be alerted to its existence. Visual inspection of zero-offset data for subvertical streaks of high energy provides a cue only in the case of the most powerful effects. “Kjartansson V’s” would provide a good diagnostic tool if it were not for today’s prestack data volumes which size in the terrabytes. Comparing stacks of near and far offsets is a good way of alerting that something is wrong (Hatchell, 2000a), but it does not highlight FEAVO specifically. Laurain et al. (2004) give a good way of quantitatively estimating the amplitudes due solely to propagation effects for a single reflector at a time. This method is even more labor-intensive than visually examining the prestack lines for “V”s. The worst one is to rely on the interpreter to realize if “something is wrong with the AVO” - he may just interpolate an intercept and gradient through the erratic values. What is needed is a quick, simple and robust way to signal the corruption of AVO by focusing.

Vlad (2004b) provides such a FEAVA detection method. The method is based on the fact that reflector-caused AVO for incidence angles $\theta < 30^\circ$ is very well described (Shuey, 1985) by

$$R(\theta) = I + G \sin^2(\theta), \quad (3)$$

where I and G depend only on the lithology at the reflector. If the amplitudes are picked at a single midpoint-depth location not affected by focusing and plotted as a function of the $\sin^2(\theta)$, the values will arrange close to a line with intercept I and gradient G . The presence of FEAVO causes the linear dependence to break, as exemplified on a simple synthetic in

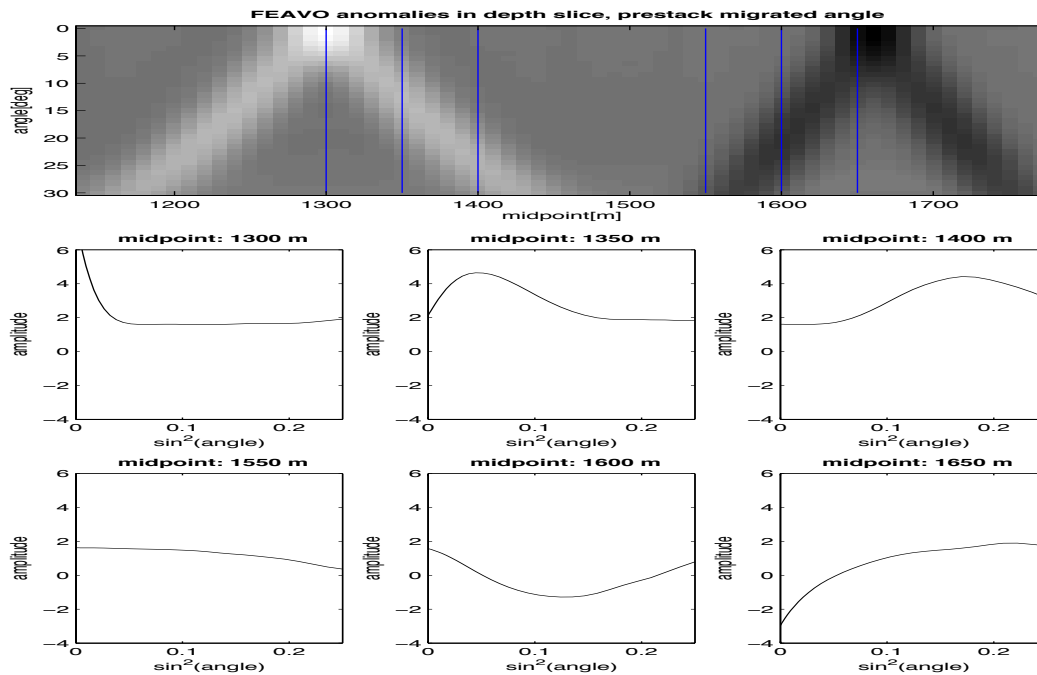


Figure 10: **Top panel:** Midpoint-angle depth slice from the prestack migrated synthetic dataset shown in Figure 9. From Vlad et al. (2003a). **Bottom panels:** Amplitudes at midpoints marked by vertical thin lines in the upper panel. From Vlad (2004b). `nick2-examine_FEAVO` [CR]

Figure 10. A direct estimate of the amount of FEAVA energy present at a (midpoint, depth) location can be obtained by measuring how much nonlinearity is in the dependence between amplitudes and $\sin^2(\theta)$. Simply interpolating a linear trend, subtracting it and computing the variance of the residual (Figure 11) provides a computationally cheap procedure with no knobs to turn. The “FEAVO attribute” output by this detector is “poststack-sized”, having no offset dimensions and no intensive human labor requirement for the visual examination. The vertical clustering of the affected areas in clusters under the source anomalies helps with the detection and possibly with the interpretation of the heterogeneities that cause FEAVA as well. Figure 12 shows a simple example obtained by migrating with the background velocity the synthetic dataset from Figure 8. The FEAVO effects are very visible – everything that is certainly not FEAVO has been eliminated. By contrast, when looking for vertical streaks or Kjartansson “V”s in the data without the help of the detector, the eye is distracted by the very large amount of amplitudes that cannot possibly be FEAVO, but are still in the picture. Figure 13 shows that the FEAVO detector functions well in a complex case, with subtle (2-3% variation from the background) velocity “lenses” which produce barely visible subvertical high amplitude streaks in the stack. The robustness of the FEAVO detector is confirmed by its behavior in the presence of multiples. In Figure 14 multiples are also weakly highlighted, but they are not vertically correlated like FEAVO and therefore they are not a serious source of noise.

The output of the detector could be improved in principle by subtracting an interpretation-based estimation of the lithology-caused AVO, instead of just the best fitting line. However,

Figure 11: FEAVA detection flowchart. From Vlad and Biondi (2004). `nick2-detect` [NR]

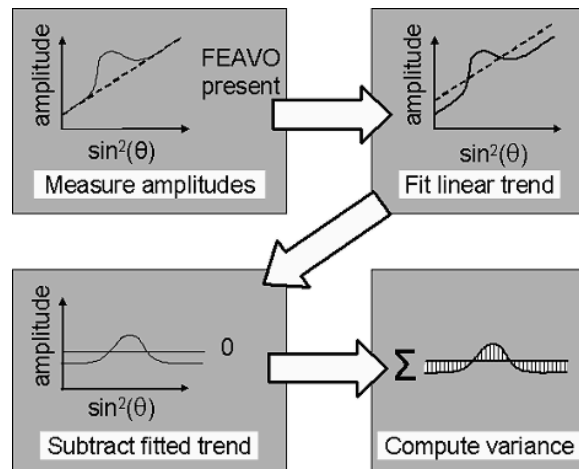


Figure 12: FEAVO anomalies flagged in the midpoint-depth space by the automatic detection procedure. The stars denote the location of the heterogeneities causing the focusing. From Vlad (2004b). `nick2-anoloc` [CR]

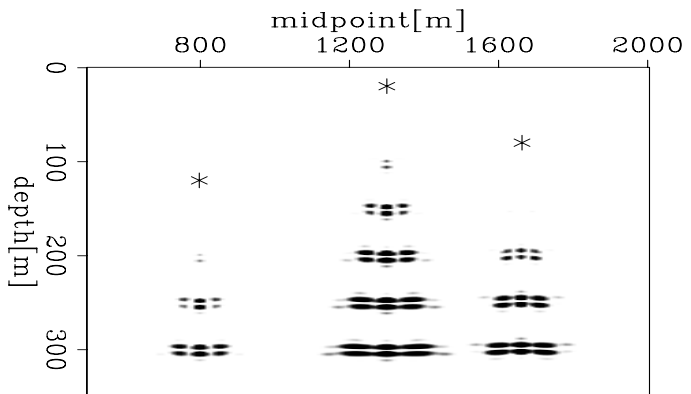
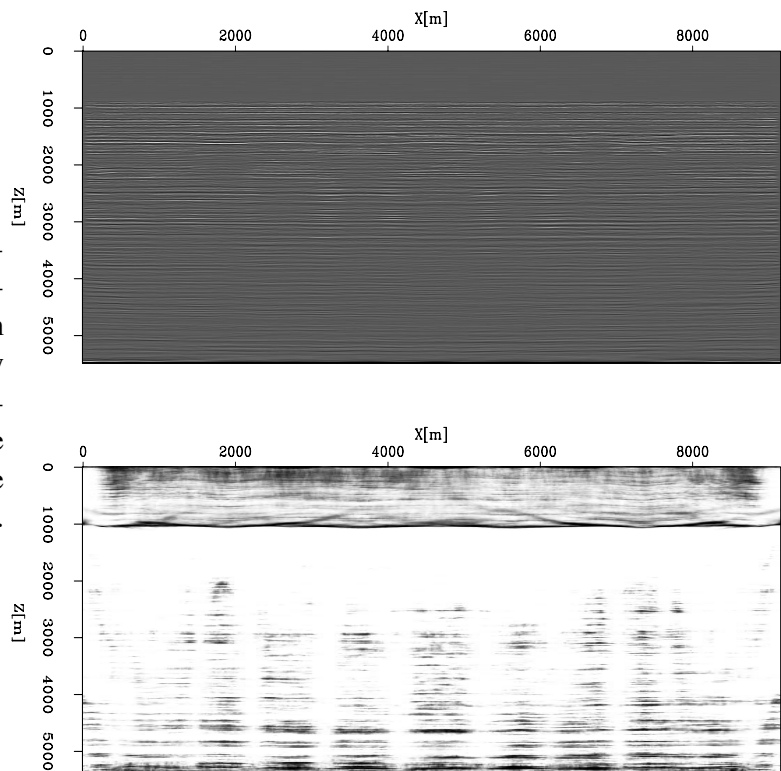


Figure 13: The FEAVO detector performs well on realistic data. Notice how barely visible focusing in the stack (top panel) is amplified by the detector (bottom panel). The erratic values in the upper part of the detector output are from above the sea bottom. From Vlad (2004a). `nick2-com_nomult_imag` [CR]



this would introduce complexity, expense and sources of errors for marginal gains. Simple as it is, the FEAVO detector works well independently for each midpoint, even when the rock-caused AVO is unknown, and even in the presence of multiples or limited aperture angles (Vlad, 2004a). A significant increase in complexity appears to be necessary, however, when trying to remove FEAVO from the data, which is the subject of the next section.

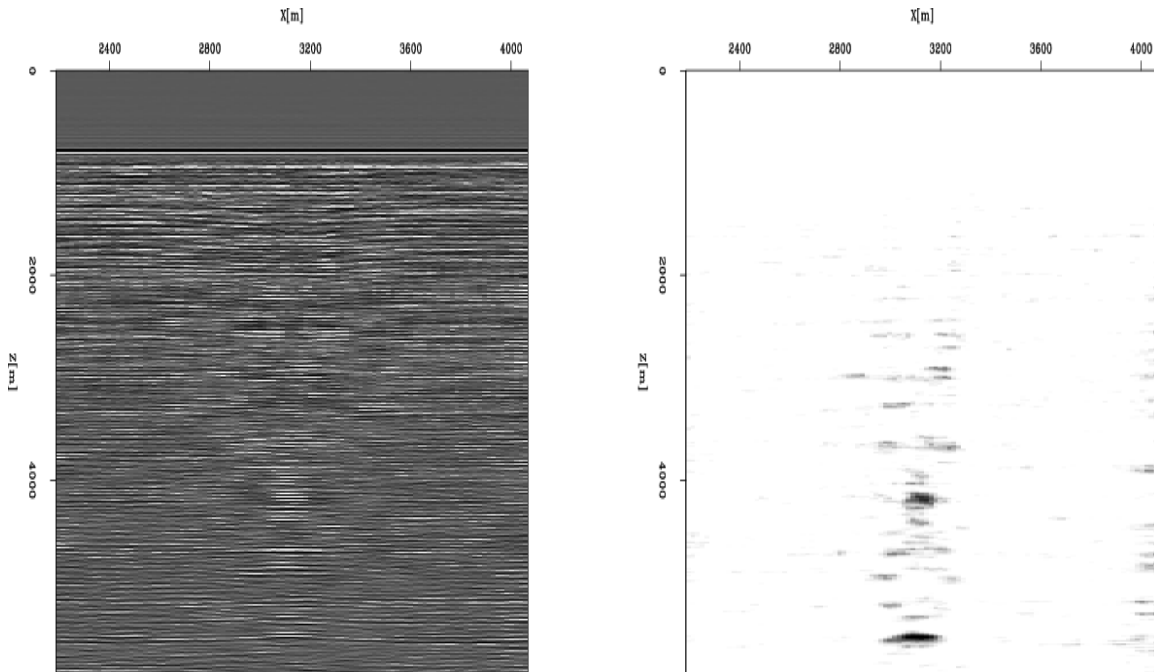


Figure 14: **Left:** $V(z)$ migration of FEAVO-affected data with internal multiples. The streak of energy in the center is barely visible. **Right:** Applying the FEAVO detector really highlights the focusing effects. From Vlad (2004a). [nick2-bg-refvel1top2](#) [CR]

FEAVA REMOVAL

No approach attempted up to date has managed to successfully remove all FEAVA effects from ADCIGs. Hatchell (2000a) states that AVO stack (crosscorrelate traces to get rid of the traveltime aspects of FEAVA, then stack) is effective in eliminating FEAVA from the stacked image. This, however, does not solve the problem of “contaminated” angle gather amplitudes which impedes AVA analysis.

Another avenue of approach consists of using the physics of FEAVO to generate a velocity/absorption anomaly section, and then to use it for imaging, which will eliminate FEAVO. Woodward (1987), Claerbout (1993), Bevc (1994), and Harlan (1994) follow the template laid out by Kjartansson (1979): (1) Generate a bidimensional midpoint-offset map of FEAVO effects as expressed in either the traveltime or the amplitude of unmigrated data. (2) Obtain the transmission anomaly section by inputting the map obtained at step 1 into an inverted operator. At first sight, the tomographic seismic amplitude correction in Harlan (1994) appears

quite successful, managing to eliminate the FEAVO effects along particular well-defined reflectors one at a time by computing transmission anomaly sections used to correct the amplitudes. Nevertheless, he states that the transmission anomaly sections generated for different reflectors appear inconsistent, and that simultaneous inversion did not improve things. For “cleaning” the FEAVO effect the process must be repeated for each particular reflector, and it involves picking, a process prone to errors in the case of weaker reflectors. Most of these approaches suffered because of using ray theory, and all of them because they were working in the data domain, before migration eliminates other propagation effects. Also, none of them used all the FEAVO characteristics described in a previous section at the same time. Since this information is not redundant, all is necessary to properly characterize the FEAVO sources.

Vlad and Biondi (2002), Vlad (2002) and Vlad et al. (2003a) propose an approach that follows the strategy of finding a correct velocity model and imaging with it to get rid of FEAVO. Vlad (2004b) refine it further. This method proceeds as follows:

(1) Find the background velocity sufficiently well to flatten the ADCIGs, except for FEAVA effects.

(2) Perform prestack depth migration and transformation to ADCIGs.

(3) Process the ADCIGs so that in the end they contain *only* FEAVA effects, in the manner of Figure 9. Areas where no focusing effects are present are zeroed. In areas where FEAVA is overimposed with “legitimate”, lithological AVA (everywhere else), the lithological AVA is found and subtracted, so that only FEAVA effects remain. The processed ADCIGs are called a “image perturbation”.

(4) The image perturbation is transformed from ADCIGs to offset, fed into the adjoint of wavefield-extrapolation migration, then becomes input for inverse linearized downward continuation. The end product is a velocity update.

(5) The velocity field is updated and a new iteration proceeds.

This is an adaptation of Wavefield-Extrapolation Migration Velocity Analysis (WEMVA), an iterative inversion method described by Sava (2004). Figure 15 provides a flowchart. In essence, WEMVA linearizes and inverts the whole process of transforming a dataset and a velocity model into ADCIGs.

This is a complex machinery which invites several questions. What can go wrong? How large are the errors introduced by the inverse linearized downward continuation? Vlad et al. (2003a) explore in detail the answers. Provided an optimal image perturbation (with the help of a synthetic dataset), WEMVA manages to produce velocity updates that eliminate FEAVO from the ADCIGs through migration. The only step left to accomplish is extracting the FEAVA-only image perturbation.

Vlad (2004b) deals specifically with this issue. The (revised since then) FEAVA extraction process from the ADCIGs consists of the following steps:

(1) **Detect:** Use the FEAVA detector to keep all that can possibly be FEAVA. Set a threshold and zero the rest of the values in the ADCIGs.

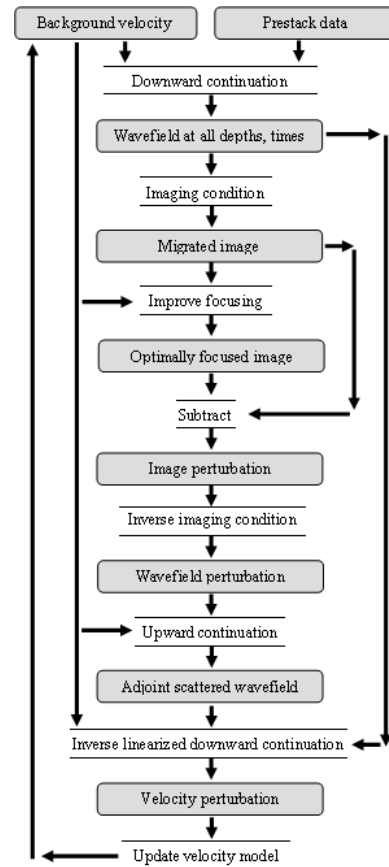


Figure 15: WEMVA flowchart.
From Vlad and Tisserant (2004).
`nick2-wemva` [NR]

(2) **Focus:** Take the absolute value/envelope of the output of (1) and run a weighed summation operator along precomputed velocity-dependent FEAVA surfaces. Semblance will not work because it will be attracted by higher coherence along the reflectors. The summation weights will consider the finite spatial extent of the FEAVA effects and may be negative in the exterior according to the extent of the bright/dim zones predicted by theory.

(3) **Filter** the output of (2) in the manner of Harlan (1986) to keep only the high semblance values.

(4) **Spread** back along the FEAVA surfaces, with weights, to obtain a weighted mask that indicates the probability of FEAVA presence in any voxel in ADCIGs. Zero everything in ADCIGs outside the mask.

(5) **Interpolate** reflector-caused lithological AVO inside the mask from values outside the mask and geologic information.

(6) Subtract the output of (5) from the corresponding unaltered values in ADCIGs at the respective locations.

Needed: a working implementation of the image perturbation extraction process described above.

FEAVA effects are a suitable input for WEMVA because the small traveltime effects makes them satisfy easily the Born approximation required from WEMVA inputs. There are variations of WEMVA which are not subject to the Born constraints (Sava and Symes, 2002), but they incorporate the image perturbation extraction step inside the inversion process, making it difficult to isolate errors that may appear during the design and prototyping of the FEAVA extraction procedure described above.

WEMVA coupled with FEAVA extraction in the manner described above has many strengths that previous approaches did not have. It considers every aspect of FEAVO, it uses wavefield-extrapolation methods, and it takes the input of the inversion from the image domain. Potential weaknesses lay in the subjectivity associated with the image perturbation extraction, with the cost (each linear solver iteration contains a prestack downward continuation and a prestack upward continuation; several solver iterations are required for a single step of WEMVA.) and with the fact that it does not consider absorption, which is likely to exist in real data.

CONCLUSIONS

This paper represents itself the conclusions of seven other papers on this topic over a period of three years. The work presented here is by no means finished. On the contrary, the main purpose of this paper was to collect in a single place the most meaningful information in order to allow a strategic view on the FEAVO problem. I believe that any physics-based approach to FEAVA removal needs first a solid foundation of knowledge about the characteristics of the phenomenon, especially in the image domain. This will allow building proper FEAVA extraction tools. No reason why WEMVA-based FEAVA removal should not work has been identified. In the past three years the amount of information on all aspects of the FEAVO problem has increased and I expect that to happen in the future.

ACKNOWLEDGMENTS

I thank Biondo Biondi for guidance and to Paul Sava for meaningful discussions. I thank Guojian Shan for the pseudospectral wave propagation code used in Figure 2. I thank Dr. Ralph Shuey of Gulf Science and Technology Company for making the Grand Isle dataset used in Figure 3 available to SEP (1978). I thank ChevronTexaco for providing the synthetic velocity model used for Figures 13 and 14 and the dataset in Figure 14.

REFERENCES

- Bevc, D., 1994, Datuming velocity from traveltime tomography: SEP-82, 145-164.
- Bortfeld, R., 1961, Approximations to the reflection and transmission coefficients of plane longitudinal and transverse waves: Geophys. Prosp., 09, no. 04, 485-502.

- Carazzone, J. J., Eriksen, E. A., and Rokhlin, V., 1984, Connection between phase and amplitude for the acoustic wave equation:, *in* 54th Ann. Internat. Mtg Soc. of Expl. Geophys. Expanded Abstracts, 738–740.
- Claerbout, J. F., 1993, Reflection tomography: Kjartansson revisited: SEP-79, 59–68.
- Craft, C., 1973, Detecting hydrocarbons: For years the goal of exploration geophysics: Oil and Gas Journal, **Feb. 19**.
- Gutenberg, B., 1936, The amplitudes of waves to be expected in seismic prospecting: Geophysics, **01**, no. 02, 252–256.
- Harlan, W. S., 1986, Signal-noise separation and seismic inversion: Ph.D. thesis, Stanford University.
- Harlan, W. S., 1994, Tomographic correction of transmission distortions in reflected seismic amplitudes: Soc. Expl. Geophys, 64th Annual Internat. Mtg., Soc. Expl. Geophys., Expanded Abstracts, 968–971.
- Hatchell, P., 1999, Fault whispers: Transmission distortions on prestack seismic reflection data: Soc. Expl. Geophys, 69th Annual Internat. Mtg., Soc. Expl. Geophys., Expanded Abstracts, 864–867.
- Hatchell, P., 2000a, Fault whispers: Transmission distortions on prestack seismic reflection data: Geophysics, **65**, no. 2, 377–389.
- Hatchell, P., 2000b, What causes distortions on prestack reflection seismic data?: World Oil, **221**, no. 11, 69–77.
- Kjartansson, E., 1979, Analysis of variations in amplitudes and traveltimes with offset and midpoint: SEP-20, 1–24.
- Laurain, R., Vinje, V., and Strand, C., 2004, Simulated migration amplitude for improving amplitude estimates in seismic illumination studies: The Leading Edge, **23**, no. 03, 240–245.
- Lu, R., Lovell, R., DawsonII, D., and Yu, Y., 2004, Compensation of the gas-cap attenuation with viscoacoustic wave-equation migration: A case study from west africa:, *in* 74th Ann. Internat. Mtg. Soc. of Expl. Geophys., 476–477.
- Rocca, F., and Toldi, J., 1982, Lateral velocity anomalies: SEP-32, 1–14.
- Sava, P., and Symes, W. W., 2002, A generalization of wave-equation migration velocity analysis: SEP-112, 27–36.
- Sava, P., 2004, Migration and velocity analysis by wavefield extrapolation: Ph.D. thesis, Stanford University.
- Sheriff, R. E., and Geldart, L. P., 1995, Exploration Seismology: Cambridge University Press.

- Shuey, R. T., 1985, A simplification of the Zoeppritz equations: *Geophysics*, **50**, no. 4, 609–614.
- Spetzler, J., Jocker, J., Smeulders, D., and Trampert, J., 2004, Validation of first-order wave diffraction theory by an ultrasonic experiment: *in* 74th Ann. Internat. Mtg. Soc. of Expl. Geophys., 2180–2183.
- Stephens, R. B., and Sheng, P., 1985, Acoustic reflections from complex strata: *Geophysics*, **50**, no. 7, 1100–1107.
- Vlad, I., and Biondi, B., 2002, Velocity estimation for seismic data exhibiting focusing-effect avo: *SEP-111*, 107–123.
- Vlad, I., and Biondi, B., 2004, Velocity estimation for seismic data exhibiting focusing-effect AVO: *Soc. of Expl. Geophys., Expanded Abstracts*, 2427–2430.
- Vlad, I., and Tisserant, T., 2004, Improving the amplitude accuracy of downward continuation operators (part 2): *SEP-115*, 81–88.
- Vlad, I., Biondi, B., and Sava, P., 2003a, Velocity estimation for seismic data exhibiting focusing-effect AVO (part 3): *SEP-114*, 101–110.
- Vlad, I., Tisserant, T., and Biondi, B., 2003b, Improving the amplitude accuracy of downward continuation operators: *SEP-113*, 163–176.
- Vlad, I., 2002, Velocity estimation for seismic data exhibiting focusing-effect avo (part 2): *SEP-112*, 47–64.
- Vlad, I., 2003, Frequency-dependent velocity analysis?: *SEP-114*, 119–124.
- Vlad, I., 2004a, The influence of multiples and imaging approximations on focusing-effect AVA detection and removal: *SEP-117*, 95–104.
- Vlad, I., 2004b, Velocity estimation for seismic data exhibiting focusing-effect avo (part 4): *SEP-115*, 265–272.
- Vlad, I., 2005, Migration and modeling of seismic data affected by focusing-effect AVO/AVA: *SEP-120*, 317–322.
- White, B. S., Nair, B., and Bayliss, A., 1988, Random rays and seismic amplitude anomalies: *Geophysics*, **53**, no. 07, 903–907.
- Woodward, M., 1987, Reflection tomography : Veas in midpoint offset space: *SEP-51*, 1–12.
- Woodward, M., 1990, Wave equation tomography: Ph.D. thesis, Stanford University.

Interpolating with data-space prediction-error filters

William Curry¹

ABSTRACT

The Madagascar sea elevation dataset presents a problem where data are collected along crossing tracks. These tracks are not straight, and are therefore irregular in the model space. Previous methods assumed that the data were regularly sampled in the model space coordinate system, or did not take into account the regularities in the acquisition of the data. Instead of attempting to find a prediction-error filter in the model space, I estimate two prediction-error filters in a coordinate system based on the data's spatial distribution, and show how to regularize the data with these filters with promising results. I then show how this strategy can be applied to 2D and 3D land surveys when data predicted by reciprocity is included.

INTRODUCTION

The Madagascar seasat sea level dataset is a collection of two passes of the GEOSAT satellite (ascending and descending) over a region of the Southwest Indian Ridge in the Indian Ocean. There is a densely-acquired region of the dataset in the south, which ranges from 40 to 70 degrees (E) longitude and 30 to 40 degrees (S) latitude, while the latitude of the sparsely-acquired data ranges from 20 to 40 degrees (S) latitude, as shown in Figure 1.

The satellite tracks are much like feathered marine geophone cables, sail lines, or shot lines in a 3D seismic survey. Any method that hopes to succeed on 3D seismic data should be able to deal with this toy problem.

Early work on this dataset at SEP (Ecker and Berlioux, 1995; Lomask, 1998, 2002) has mainly dealt with the systematic errors present in the dense dataset (Ecker and Berlioux, 1995), or with ways in which to use information in the dense portion of the data to regularize the missing bins in the northern, sparse portion of the data (Lomask, 1998, 2002). In the latter, it is assumed that the statistics of the data are stationary over both regions. More recent work has started to deal with the interpolation of only the sparse tracks (Curry, 2004; Lomask, 2004).

In this paper, only the lower half of the dataset (30 to 40 degrees (S) latitude) is examined, so that interpolation of the sparse tracks can be compared with the dense tracks. Here, a different approach is presented to dealing with the sparse track problem, where a pair of prediction-error filters (PEFs) are estimated directly on the two sets of tracks. This pair of

¹email: bill@sep.stanford.edu

filters is estimated in the data space, so that the issues of missing data and irregular geometry are no longer present. Once these filters have been estimated, they can be used in tandem to regularize the missing portions of the model space.

Extension of this method to incorporate non-stationary PEFs is quite straightforward. The similarities between the Madagascar data and a Colombian 2D seismic data line are noteworthy enough that this method should be applicable to 2D land data, where the two sets of tracks correspond to positive and negative offsets. The geometry of a 3D cross-swath land seismic survey also has similarities to the Madagascar data, where when data predicted by reciprocity is added irregular crossing tracks are present in `cmp_x`, `offset_x` space.

BACKGROUND

The Madagascar regularization problem has been approached using the following fitting goals (Lomask, 2002):

$$\begin{aligned} \mathbf{W} \frac{d}{dt} [\mathbf{Lm} - \mathbf{d}] &\approx \mathbf{0} \\ \epsilon \mathbf{Am} &\approx \mathbf{0}. \end{aligned} \quad (1)$$

In these fitting goals: \mathbf{W} corresponds to a weight for ends of tracks and spikes in the data, $\frac{d}{dt}$ is a derivative along each track used to eliminate low frequency variations along each track, \mathbf{L} is a linear interpolation operator that moves from values on a regular grid to the data points, \mathbf{m} is the desired gridded model, \mathbf{d} are the data points along the tracks, \mathbf{A} is a regularization operator, and ϵ is a trade-off parameter between the two fitting goals.

The regularization operator (\mathbf{A}) typically is a Laplacian, a prediction-error filter (PEF), or a non-stationary PEF (Crawley, 2000). When using a PEF, it first must be estimated on some training data, using a least-squares fitting goal,

$$\mathbf{W}(\mathbf{DKa} + \mathbf{d}) \approx \mathbf{0}, \quad (2)$$

in which \mathbf{W} is a weight to exclude equations with missing data, \mathbf{D} is convolution with the data, \mathbf{K} constrains the first filter coefficient to 1, \mathbf{a} is the unknown filter, and \mathbf{d} is a copy of the data.

In order to set a benchmark for how effective any interpolation of the sparse tracks is, a PEF is estimated using fitting goal (2) on the output of fitting goals (1) when using the dense tracks of the Madagascar dataset and a Laplacian regularization operator. The PEF is then used to interpolate the sparse tracks in the same area, using the same fitting goals (1), this time with the regularization being convolution with a PEF. This result provides an upper bound to what an ideal interpolation of the data would be if we already knew the answer. Any new result should be much better than the Laplacian regularization shown in Figure 2b.

PEFS IN THE DATA SPACE

Once we attempt to interpolate this dataset using only the sparse tracks, the above method no longer works, as no region would have enough contiguous data on which to estimate a PEF.

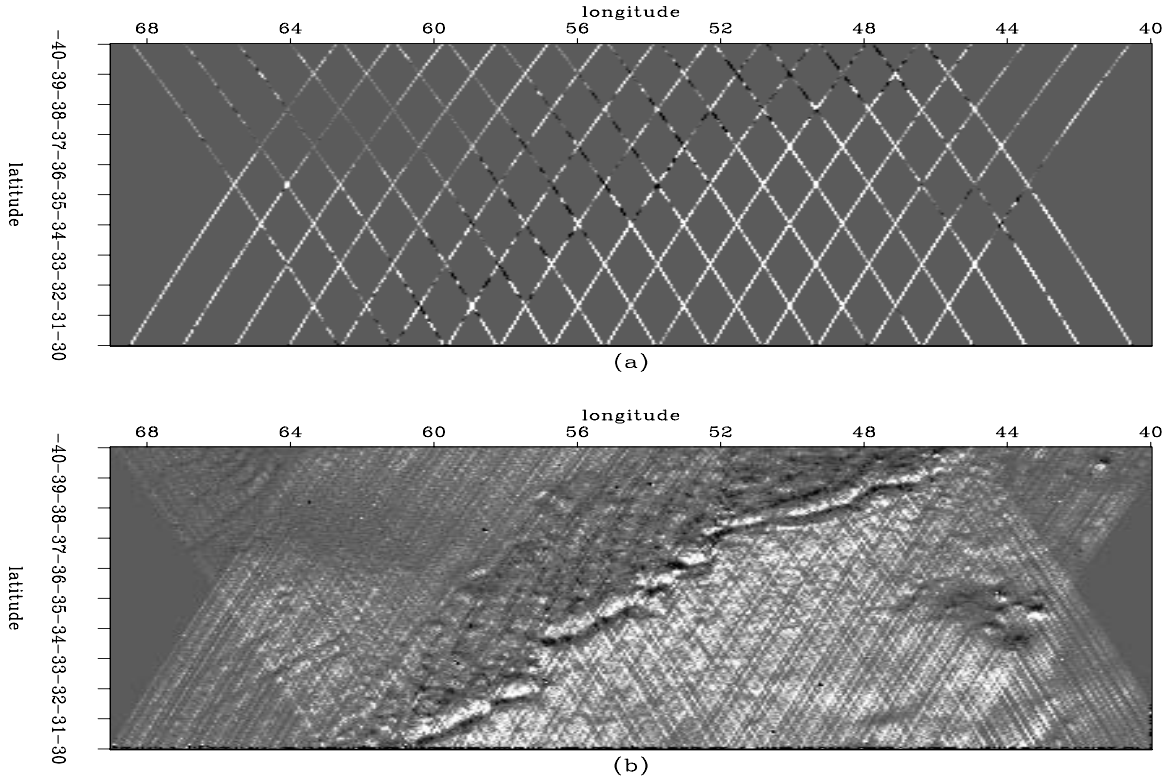


Figure 1: (a) sparse tracks. (b) dense tracks. `[bill1-data]` [ER,M]

In this case we will pay more attention to how our data are spatially distributed. The known data points in the model space are distributed along curved crossing tracks, making it very difficult to estimate a PEF in this space, as shown in Figure 1. However, in the data space of the fitting goals (1) of the previous section, the data are sampled in a regular space: a series of regularly-sampled tracks, as shown in Figures 3 and 4.

Since these data are collected in two series of one-dimensional tracks, it would be easiest to estimate a pair of one-dimensional PEFs on these two sets of tracks, as shown in the top halves of Figures 3 and 4.

We now have two PEFs which have been estimated in a data space, but the model which we wish to regularize with these PEFs is in a different space. This requires the introduction of two additional linear interpolation operators \mathbf{L}_1 and \mathbf{L}_2 , which pull bins from the model space into the ascending and descending track data spaces, respectively. The mappings used for these operators are shown in Figure 5. Now that we have both two prediction-error filters for regularizations operators as well as linear interpolation operators that pull model points into the data space, we can put everything together in the following fitting goals,

$$\begin{aligned}
 \mathbf{W} \frac{d}{dt} [\mathbf{Lm} - \mathbf{d}] &\approx \mathbf{0} \\
 \epsilon \mathbf{A}_1 \mathbf{L}_1 \mathbf{m} &\approx \mathbf{0} \\
 \epsilon \mathbf{A}_2 \mathbf{L}_2 \mathbf{m} &\approx \mathbf{0},
 \end{aligned} \tag{3}$$

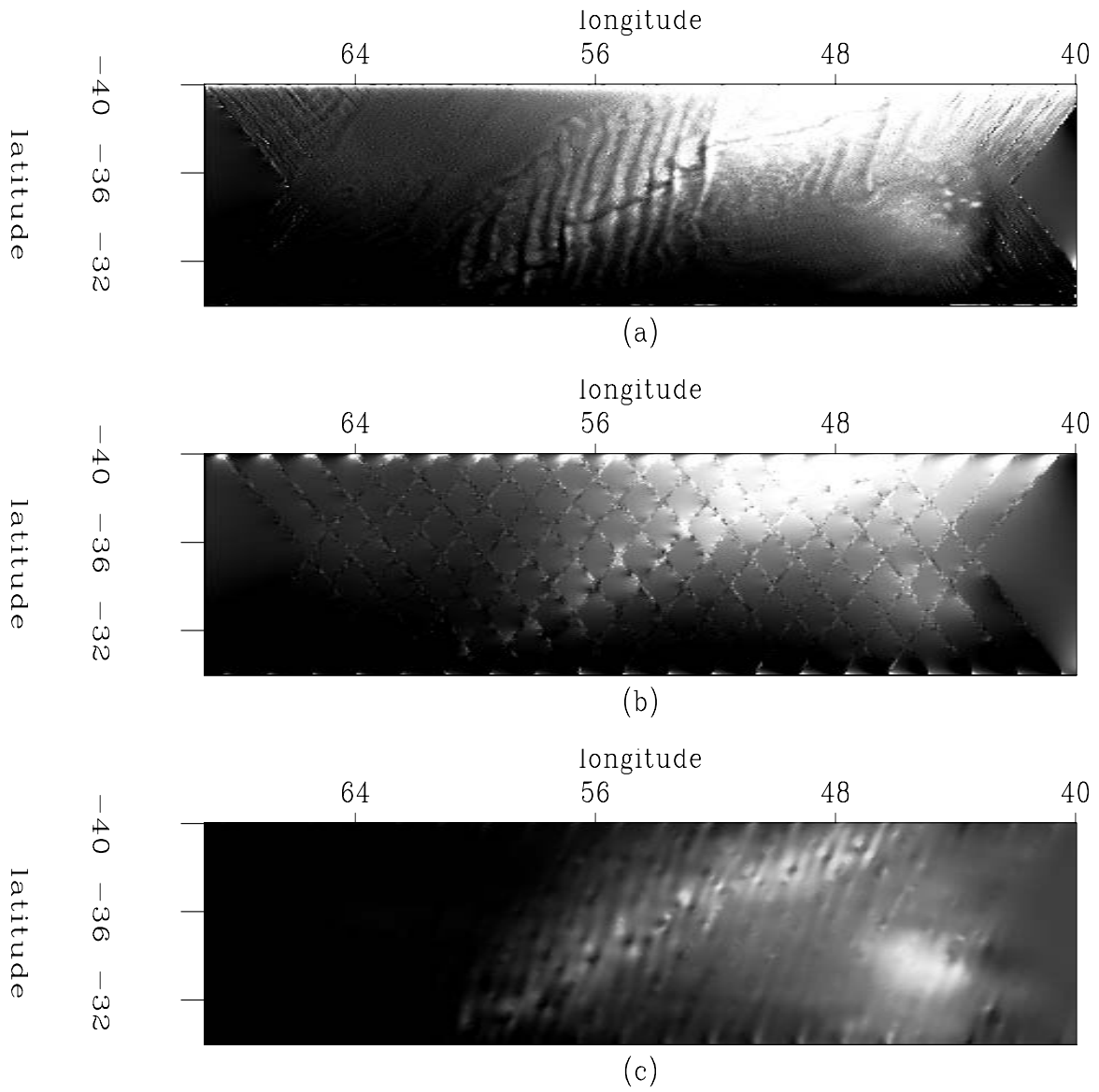


Figure 2: (a) dense data regularized with a Laplacian. (b) sparse data regularized with a Laplacian. (c) sparse data regularized with a PEF trained on the top. `bill1-best` [ER,M]

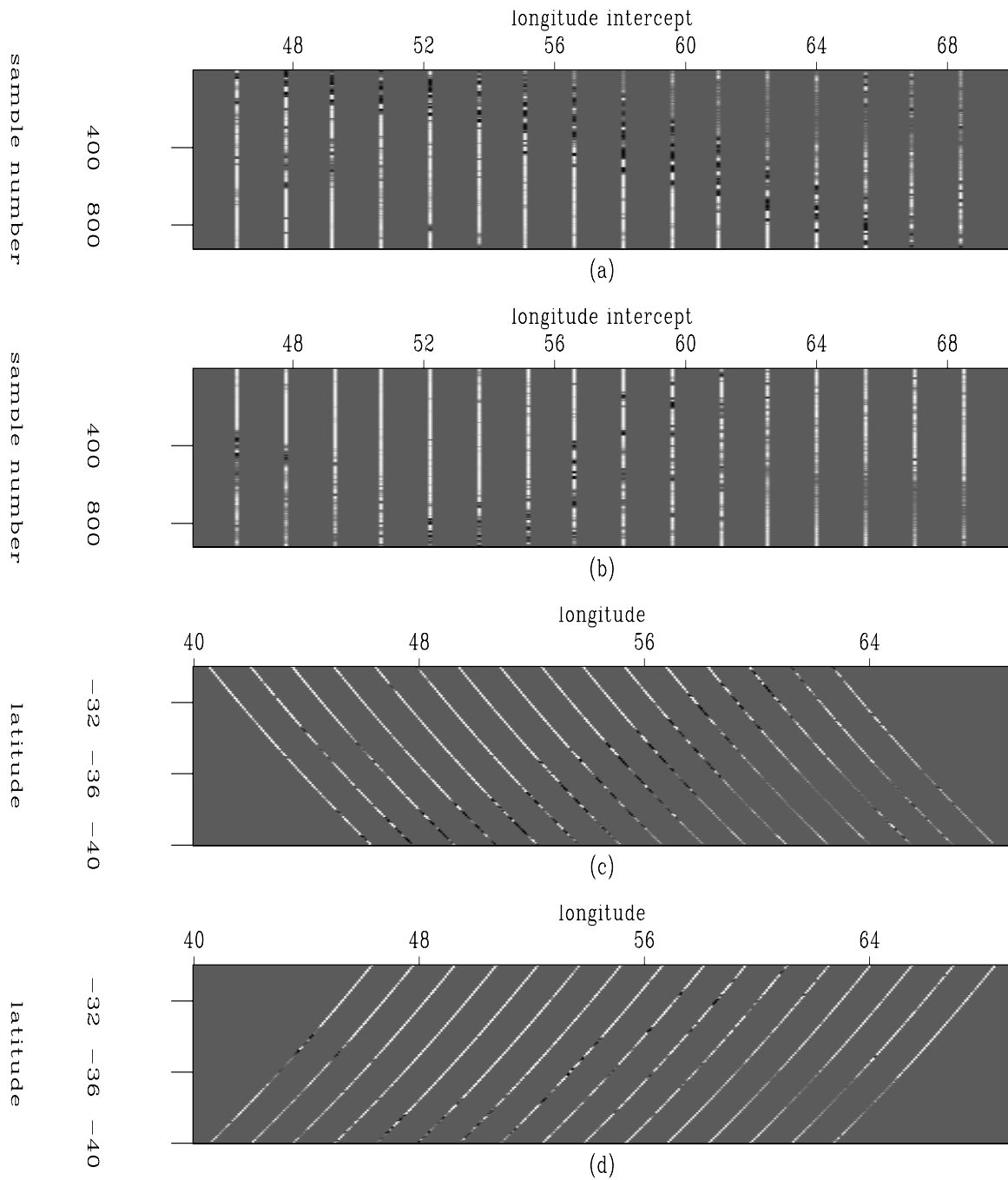


Figure 3: Sparse tracks, (a) ascending and (b) descending in model space, and (c) ascending and (d) descending tracks in data space. `bill1-sptracks` [ER,M]

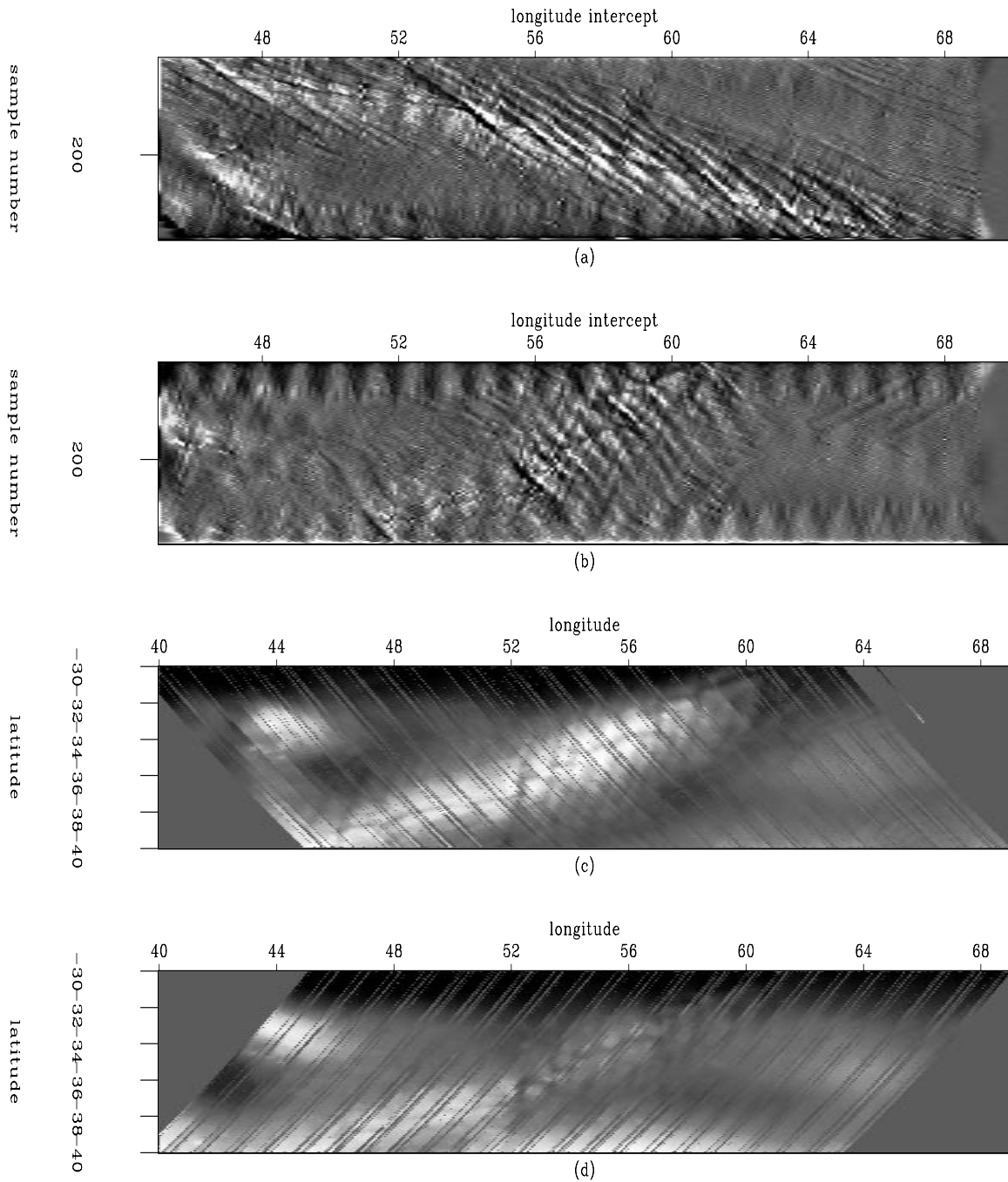


Figure 4: Dense tracks, (a) ascending and (b) descending in model space, and (c) ascending and (d) descending tracks in data space. `bill1-detracks` [ER,M]

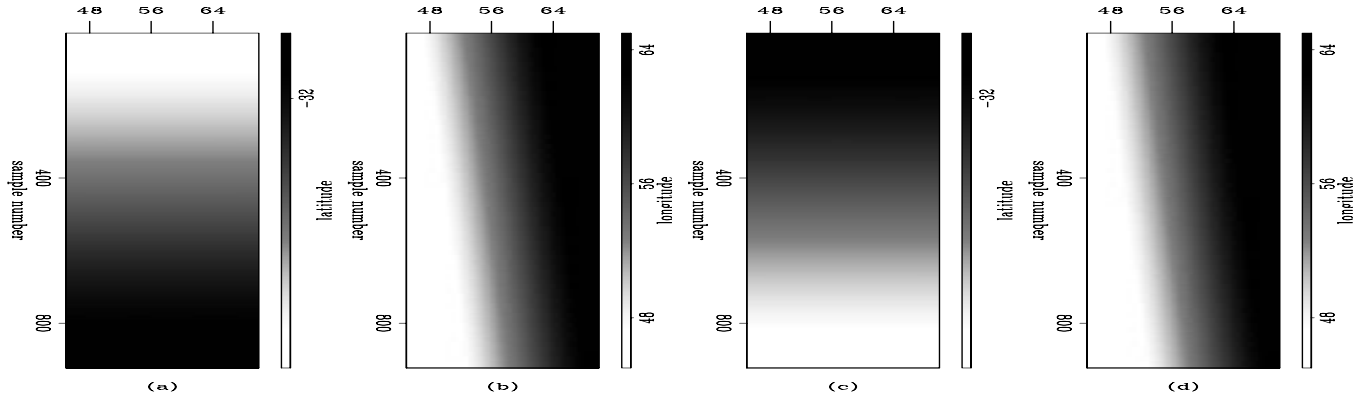


Figure 5: Mappings from data space to model space, all shown in data space. From the top down: ascending tracks latitude, ascending tracks longitude, descending tracks latitude, descending tracks longitude. `bill1-maps` [ER,M]

where \mathbf{L} pulls model points (\mathbf{m}) to where we have data (\mathbf{d}), \mathbf{A}_1 and \mathbf{A}_2 are 1D PEFs that are estimated on the ascending and descending tracks in the data space, respectively, and \mathbf{L}_1 and \mathbf{L}_2 are linear interpolation operators that pull model points into the ascending and descending track data spaces, respectively. ϵ is a tradeoff parameter between the data fitting and model styling goals.

The 1D PEFs can also be replaced by 2D PEFs that are estimated by scaling the filter so that it covers multiple sparse tracks. If this approach is taken, the interpolation can occur in the data space where the PEFs are estimated (using a single PEF for each of the two track spaces), or in the model space (using both PEFs simultaneously). The more straightforward data-space interpolation is shown in Figure 6.

Figures 6a and b are simply the interpolation of the data space with 2D PEFs estimated on the sparse tracks. Figures 6c and d are those interpolated results mapped back to the model space by using fitting goals (1), where the input data are now the interpolated sets of tracks in the first two panels. Since fitting goals (1) were applied when generating the new tracks, the track derivative is no longer necessary.

The results are mixed, as Figure 6c shows that the trend of the ridge was correctly identified by the PEF estimated on the ascending tracks. The PEF estimated on the descending tracks did not fare so well, as the direction of the ridge in the interpolated tracks of Figure 6d does not match the densely sampled tracks in Figure 4d. This is because the descending tracks are oblique to the structure, so the structure is aliased beyond the point where a spaced PEF can interpolate accurately. In either case, the result is better than that obtained with a Laplacian, and in the case of the ascending tracks is not that far from the PEF estimated on a fully-sampled model space shown in Figure 2c.

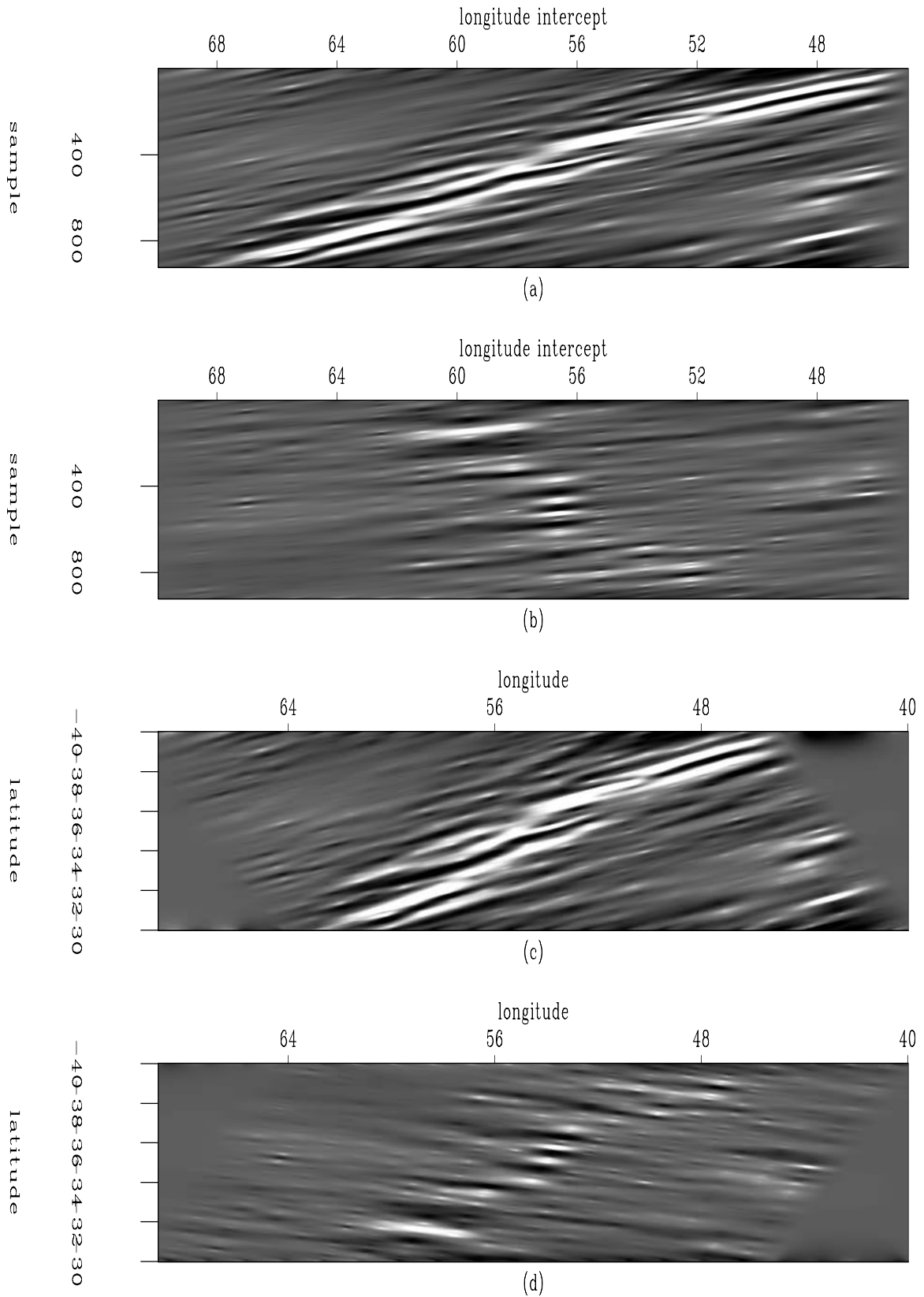


Figure 6: Interpolation of the two different track spaces (a) and (b). (c) and (d) contain the same results mapped into model space. The correct strike of the ridge is identified by the ascending tracks but not the descending tracks. `bill1-dataspinterp` [ER,M]

CONCLUSIONS AND FUTURE WORK

By estimating a pair of PEFs in the data space, the problem of irregular data acquisition has been avoided. The actual interpolation can be performed in either the data space (track coordinates) or the model space (latitude and longitude). The results turned out to be much better for the ascending tracks than for the descending tracks.

Crossing tracks are also present in land seismic data, where due to reciprocity the negative offsets in the split-spread land experiment cross. In 2D this happens in cmp - absolute offset space as shown in Figure 7, and in 3D this also happens, but in cmp_x - offset_x and cmp_y - offset_y spaces.

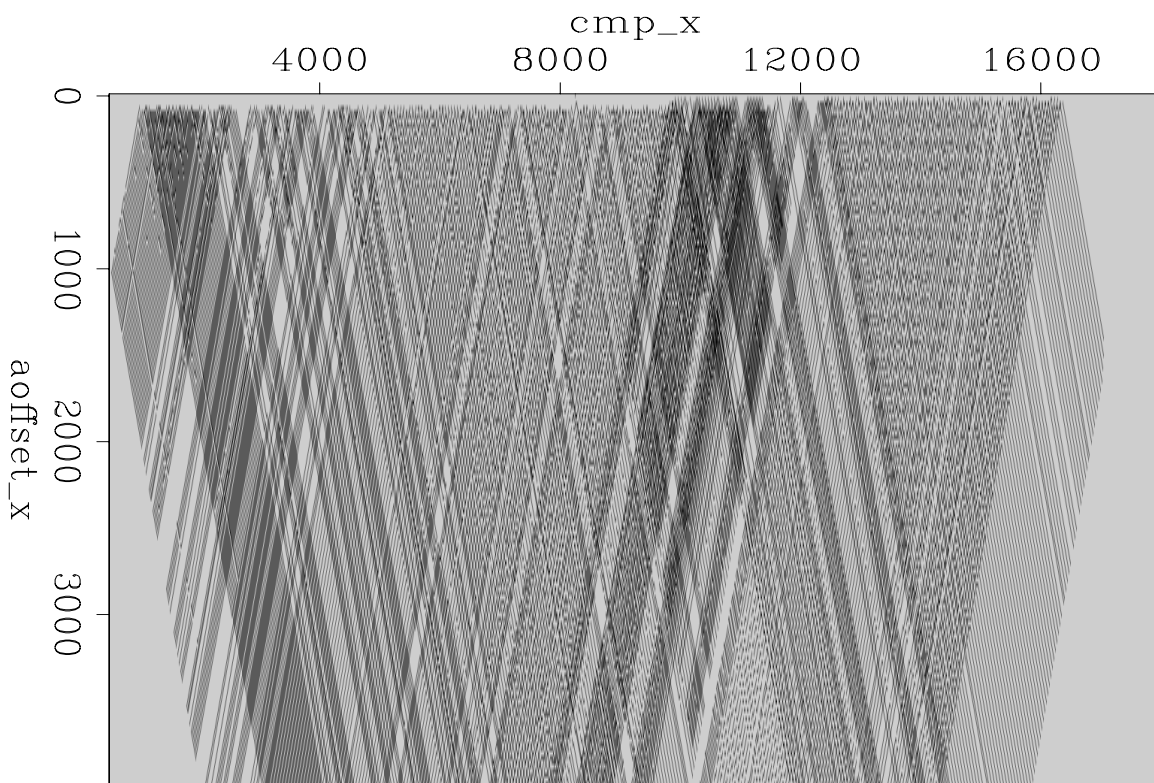


Figure 7: Fold map of an irregularly-sampled 2D land survey in cmp and absolute offset. Similar patterns of crossing tracks are also present in this survey due to reciprocity. [bill1-hulia](#) [ER]

REFERENCES

- Crawley, S., 2000, Seismic trace interpolation with nonstationary prediction-error filters: Ph.D. thesis, Stanford University.
- Curry, W., 2004, Regularizing Madagascar: PEFs from the data space?: SEP-115, 347-356.

Ecker, C., and Berlioux, A., 1995, Flying over the ocean southeast of Madagascar: SEP-**84**, 295–306.

Lomask, J., 1998, Madagascar revisited: A missing data problem: SEP-**97**, 207–216.

Lomask, J., 2002, Madagascar satellite data: An inversion test case: SEP-**111**, 337–349.

Lomask, J., 2004, Estimating a 2D stationary PEF on sparse data: SEP-**117**, 129–140.

Short Note

Non-stationary PEFs and large gaps

William Curry¹

INTRODUCTION

Prediction-error filters (PEFs) may be used to interpolate missing data, either to increase the sampling of data that are regularly-sampled (Spitz, 1991), as well as to interpolate larger gaps in data (Claerbout, 1992, 1999). In addition to using multi-dimensional PEFs, non-stationary PEFs (Crawley et al., 1998) have been used to interpolate regularly-sampled data (Crawley, 2000). Non-stationary PEFs have not been successfully used to interpolate large holes in data.

With the assumption of stationarity, a large hole in the data does not adversely affect PEF estimation as long as there are sufficient contiguous data present to constrain the data elsewhere. However, when non-stationary PEFs are used to interpolate data, there is a large gap in the PEF coefficients as well as in the data. In the stationary case those filter coefficients were assumed to be known, but in the non-stationary case that assumption is no longer valid.

For a simple non-stationary test case, a herringbone pattern has previously been used to test interpolation and simulation methods in geophysics with stationary PEFs (Brown, 1999; Claerbout, 1999) as well as more recently in the geostatistical community as a test case for multiple-point geostatistics (Journel and Zhang, 2005).

Estimation of a non-stationary PEF is an under-determined problem, so a regularization term is added to the estimation which ensures spatial smoothness of filter coefficients. This regularization term looks a lot like an isotropic interpolation, but this paper shows that the isotropic interpolation of filter coefficients is not a successful approach.

A much simpler method is to replace the unknown filter coefficients with the regularized filter coefficients from the nearest known filter, which is tantamount to a nearest-neighbor type of interpolation of filters. This wreaks substantially less havoc than other attempts to interpolate filters, as it does not manipulate PEF coefficients.

The herringbone pattern used in this paper has an obvious preferential direction, so by only regularizing and searching for a nearest-neighbor vertically a much better result can be produced. For seismic data this direction would be along radial lines in the cmp domain.

¹email: bill@sep.stanford.edu

Manipulating non-stationary filters during the estimation process with regularization terms to fill in missing filters appears to be ineffective. Instead, using a very simple method which uses the nearest known portion of the non-stationary PEF to interpolate shows promising results for a simple test case. By incorporating some prior information of which PEF to use, a much better interpolated result can be obtained.

BACKGROUND

Estimation of a stationary PEF can be phrased as a least-squares problem, where the following fitting goal is minimized with respect to an unknown filter \mathbf{f} :

$$\mathbf{W}(\mathbf{DKf} + \mathbf{d}) \approx \mathbf{0}, \quad (1)$$

in which \mathbf{W} is a weight to exclude equations with missing data, \mathbf{D} is convolution with the data, \mathbf{K} constrains the first filter coefficient to 1, \mathbf{f} is the unknown filter, and \mathbf{d} is a copy of the data.

Once the PEF has been estimated, it can then be used to interpolate missing data by solving another inverse problem:

$$\mathbf{Lm} - \mathbf{d} \approx \mathbf{0} \quad (2)$$

$$\epsilon \mathbf{Fm} \approx \mathbf{0}, \quad (3)$$

where \mathbf{L} is a selecting operator that selects the known data within the interpolated model \mathbf{m} , \mathbf{d} is the known data, ϵ is a scaling factor, and \mathbf{F} represents convolution with the newly-found PEF. The output model \mathbf{m} is referred to as the restored data.

Instead of a restored version of the data, multiple equiprobable realizations (Clapp, 2000) of the missing data can be generated by changing fitting goal (3) to

$$\epsilon \mathbf{Fm} \approx \sigma \mathbf{n}, \quad (4)$$

where instead of desiring the output of the filter convolved with the model to be zero, we now choose for it to be equal to random noise \mathbf{n} scaled by a factor σ . Multiple realizations of the interpolation can be generated by using different random numbers for \mathbf{n} that are identically distributed. This noise is only introduced where the data are missing, as the residual of fitting goal (3) will already look like random noise where data are present.

In geostatistical language, the restored data is very similar to an E-type, which is the same as an average of multiple realizations (or simulations) of the result generated by fitting goals (2) and (4). Dividing random noise by the PEF, which is the same as solving fitting goal (4) is equivalent to an unconditional simulation, where no data constrain the output.

All of the previous theory has been utilized for stationary PEFs. A non-stationary PEF can be estimated by a fitting goal similar to fitting goal (1), except that instead of the PEF having a single set of coefficients, the PEF now has a separate set of coefficients for each data point.

Since there are now many more unknown filter coefficients than known data, a regularization term needs to be added to constrain the problem:

$$\epsilon \mathbf{A} \mathbf{f} \approx \mathbf{0}, \quad (5)$$

where \mathbf{f} is the unknown non-stationary PEF and \mathbf{A} is a regularization operator that acts over space for each filter coefficient independently, and is typically either a Laplacian or helix derivative (Claerbout, 1999). Fitting goals (3) and (4) can be used with a non-stationary PEF \mathbf{f} in the place of a stationary PEF.

APPLICATION TO HERRINGBONE DATA

The methods described above were applied to the herringbone synthetic. The fully-sampled data as well as the data with the hole are shown in Figure 1.

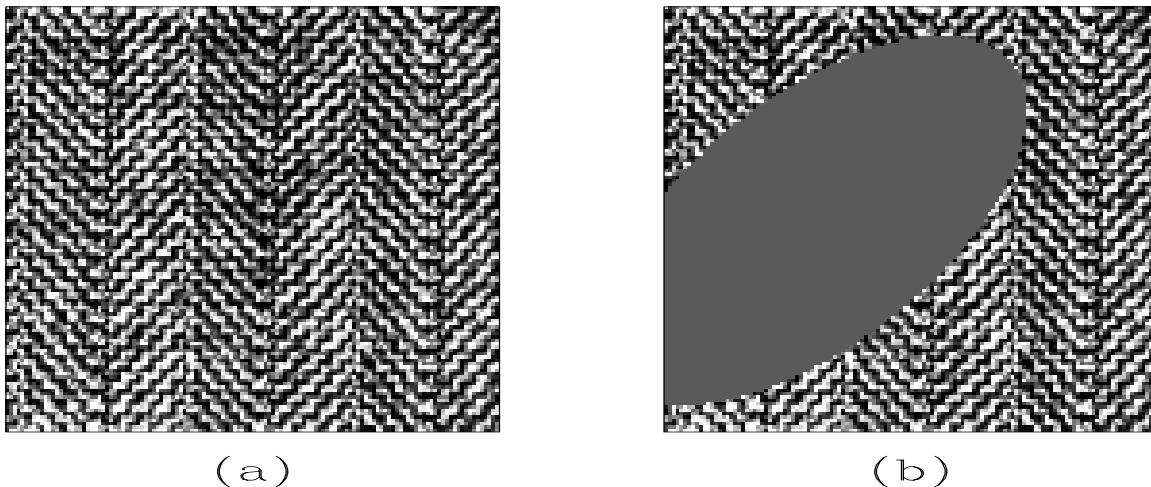


Figure 1: The herringbone data, (a) original data, and (b) data with hole. bill2-herr-orig [ER,M]

As a starting point, the hole was interpolated using a stationary PEF that was 9×4 coefficients, shown in Figure 2a. We can see how well the PEF has characterized the data by convolving the PEF with either the original data or the interpolated result. The result of convolving the PEF with the interpolated result is shown in Figure 2b. As has been previously noted, the PEF appears to miss the spines of the herringbone pattern, but gets the two slopes relatively well. When examining the result of random noise divided by that same stationary PEF (shown in Figure 2c) we can see the problem with the assumption of stationarity in that the two slopes present in the herringbone pattern are co-located throughout the simulation.

The problems with co-located dips due to the assumption of stationarity can be avoided by using a non-stationary PEF. A 9×2 non-stationary PEF (with a total of about 16,000 filter coefficients) was estimated on the known data and then used to interpolate the missing data. As we can see from Figure 3a, the result is nearly perfect, which shouldn't be surprising given

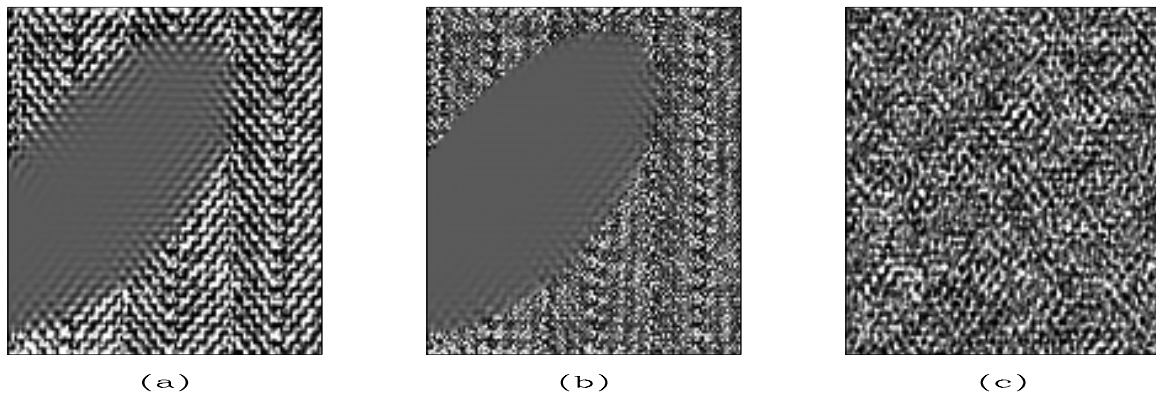


Figure 2: Stationary PEF result, (a) interpolated data, (b) interpolated data convolved with PEF, and (c) random noise divided by PEF. [bill2-herr-stat](#) [ER,M]

that the non-stationary PEF was estimated on the answer. Still, the restored version appears to have little of the problems of the interpolation smoothly decaying to zeros that was present in the stationary case. When convolving the PEF with the full dataset, we can see from the relative strength of the edge effects (in Figure 4b) that the filter perfectly captured the data. When we remove the edge effects, we see no trace of the spine of the herringbone, and the result looks very random as seen in Figure 4c.

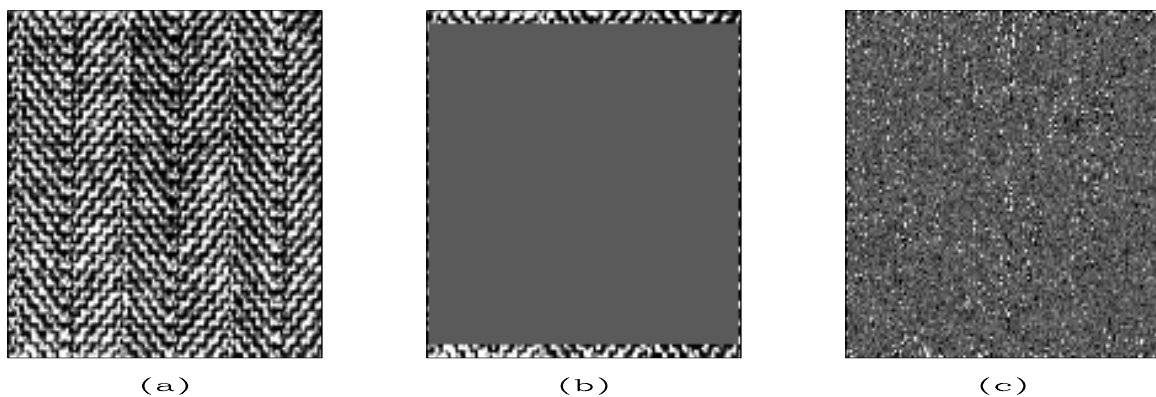


Figure 3: Non-stationary PEF results, where the PEF is estimated on the complete data. (a) interpolated result. (b) PEF convolved with original data. (c) PEF convolved with original data with edge effects removed, and the result scaled. [bill2-herr-ns-known](#) [ER,M]

The previous test was a demonstration of the effectiveness of a non-stationary PEF as a container for information, but we had the answer before attempting to solve the problem. Next, we must resolve the issue of non-stationary PEFs with holes in them, which happens when we do not have the answer.

A more realistic starting point would be to estimate a PEF on the data with the hole and hope that the regularization term in fitting goal (5) would act as a method of interpolating the PEF in areas with missing data. As we can see from the results in Figure 4, this is clearly not the case. The restored data using a stationary PEF extends much further into the gap than

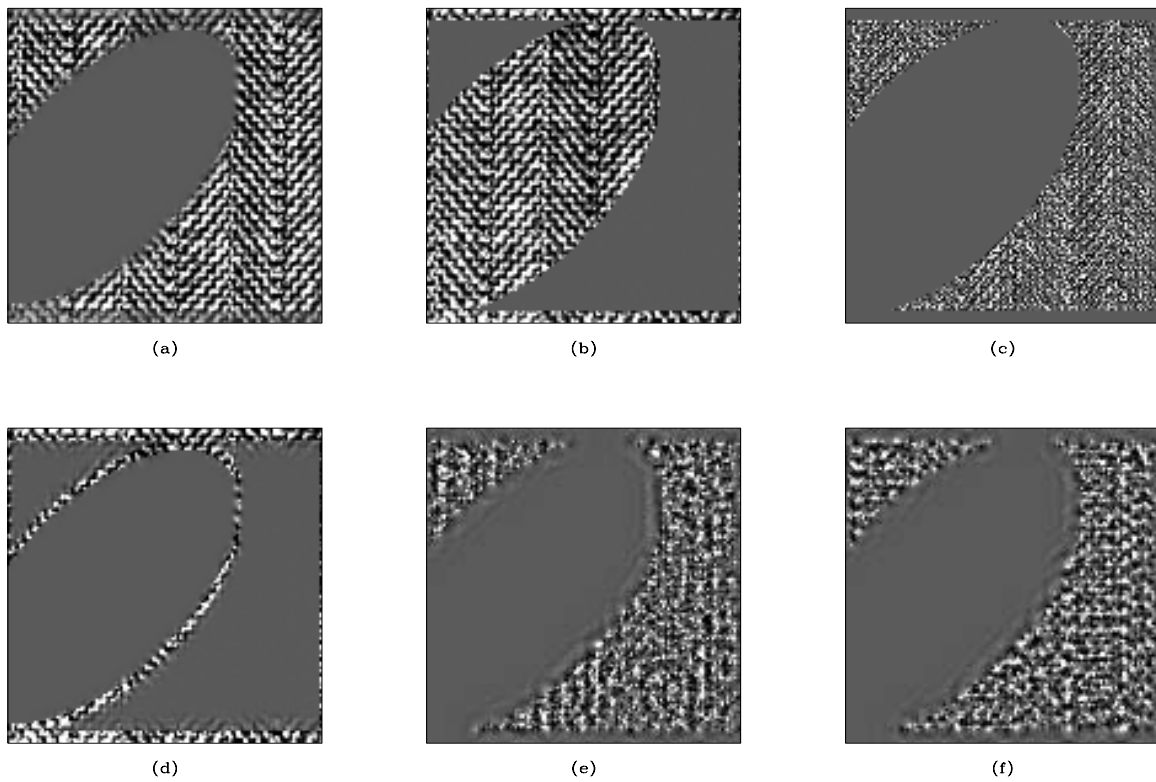


Figure 4: Non-stationary PEF results, where the PEF is estimated on the data with the hole. (a) The interpolation result using a filter with a hole in it. (b) non-stationary PEF convolved with original data. (c) non-stationary PEF convolved with interpolated result. (d) PEF from full data convolved with data with hole. (e) and (f): sections from a single filter lag for the model residual of fitting goal 5 `bill2-herr-ns-unknown` [ER,M]

the non-stationary PEF does. If we look at the model residual from fitting goal (5) shown in Figures 4e and f, we can start to see why. This is a portion of the model residual for two non-stationary filter coefficients over the entire space of the non-stationary PEF. We can see that as we move within the gap that the residual drops to zero, as the filter coefficients are also zero within this area. Relying upon the filter regularization to fill in gaps in the non-stationary filter does not put filters in holes.

We can also look at the performance of the PEFs by looking at the random realizations as well as random noise divided by the non-stationary PEF, both shown in Figure 5. These results mostly confirm what we already know from Figure 4, however it is surprising to see that Figures 4b and c, which use the full data, are not as consistent as expected. The areas which contain the herringbone pattern are non consistent from simulation to simulation. This is not the case with the stationary PEF result of Figure 2c.

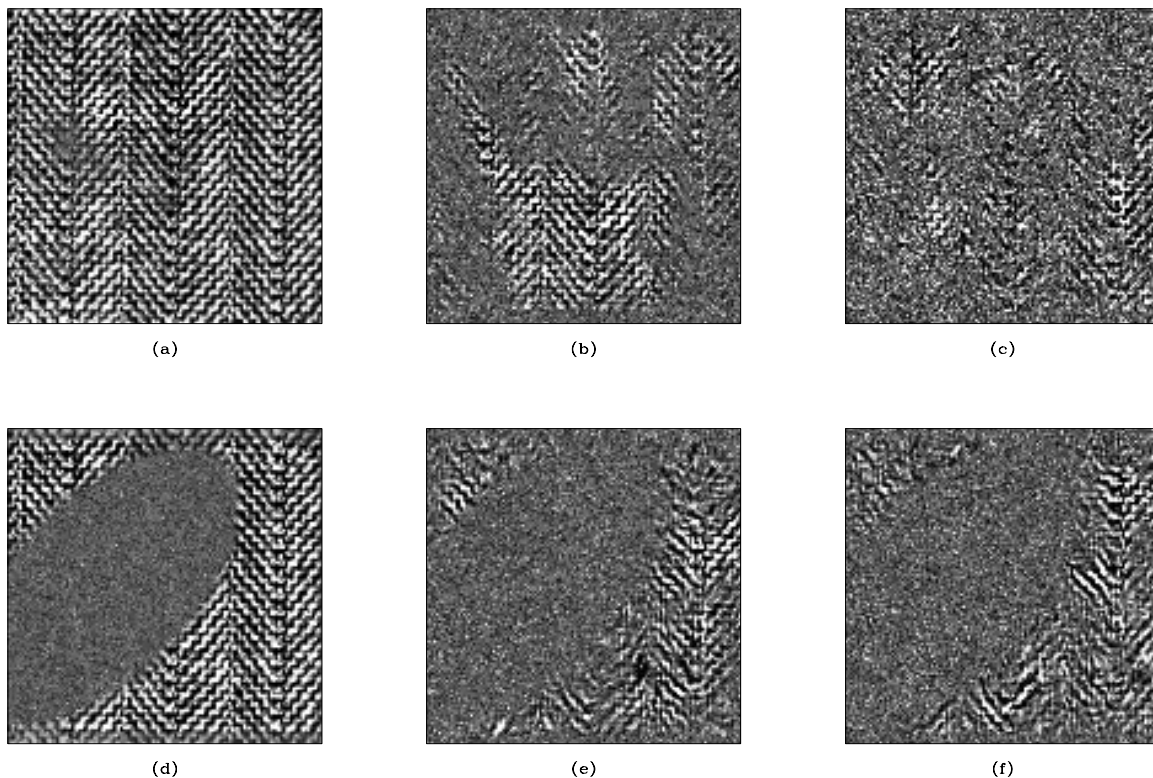


Figure 5: (a) random realization of interpolation, (b) and (c) two sets of random numbers deconvolved with the PEF estimated on the complete data. (d) to (f): same as (a) to (c), except for a PEF estimated on the data with the hole. `bill2-herr-realiz` [ER,M]

Instead of interpolating filter coefficients by relying on an isotropic roughener for regularization, a much simpler approach is taken. After the non-stationary PEF is estimated, the filter coefficients in areas with missing data are simply interpolated in a nearest-neighbor fashion with the nearest filter coefficients that are constrained by data. The results of using this method are shown in Figure 6. On the first panel (a), we can see that the signal that we want to destroy with our filter is partially gone, and the output looks much more random than before. On the second panel (b), we see that the interpolated result is better than any of the previous attempts.

While there is only a single dip in any location, these dips are not in the correct locations as they do not follow the vertical spine of the herringbone. On the third panel (c), a single filter lag plotted with respect to space, we can clearly see the difference between filter coefficients that have been estimated on data, and those that have been interpolated from neighboring area with data.

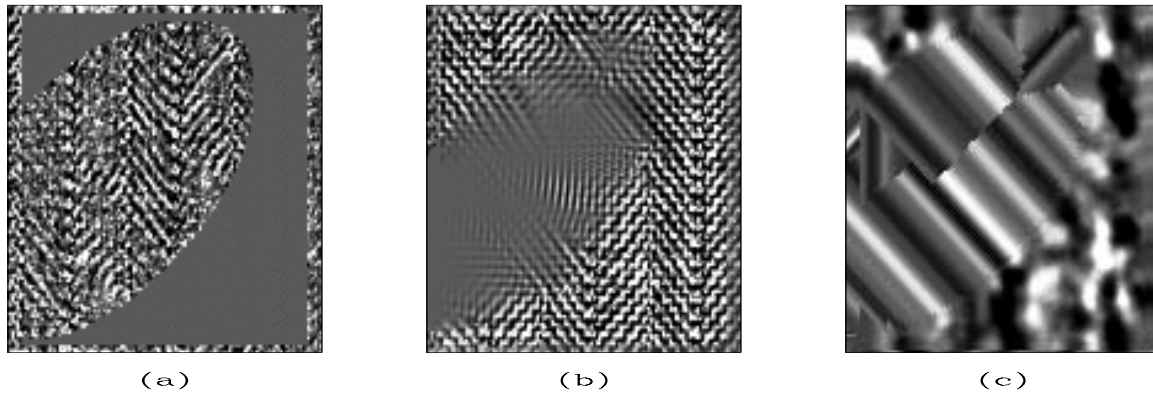


Figure 6: Results for PEF estimation with isotropic regularization and an isotropic nearest-neighbor search. (a) Convolution of the PEF with the fully-sampled data. (b) Interpolation with the PEF. We can see that the dips are no longer co-located, but do not match the spine of the herringbone pattern. (c) Filter coefficients from a single filter lag. We can see the isotropic smoothing of the filter coefficients as well as nearest neighbor smearing. bill2-herr-better [ER,M]

If we examine the mappings between the areas with no data and their nearest neighbors as shown in Figures 7a and b, we can see that the mappings do not correspond to the vertical trend present in the herringbone data. If we alter the nearest-neighbor interpolation so that no points outside of the vertical direction are considered, with the result shown in Figures 7c and d.

In addition to changing the filter interpolation so that it acts in a preferential direction, the regularization of the filter has been changed from an isotropic Laplacian to a derivative in the vertical direction. The results of using both of these new methods is shown in Figure 8. The first panel (a) shows how the missing signal is better attenuated with this method. The second panel (b) is the interpolation result, which is far superior to any other method shown in this paper. The correct dips are present in the correct locations. The amplitude of the interpolated result is not as uniform as would be desired, however. Finally, in the third panel (c), we can see that the interpolated filter coefficients are much more difficult to identify than with the previous method. The only obvious artifact is the seam caused by the nearest-neighbor interpolation when the interpolated data switched from one side of the gap to the other.

CONCLUSIONS AND FUTURE WORK

When making the jump from stationary to non-stationary interpolation, the issue of interpolating large gaps becomes a much more difficult problem. In addition to worrying about the

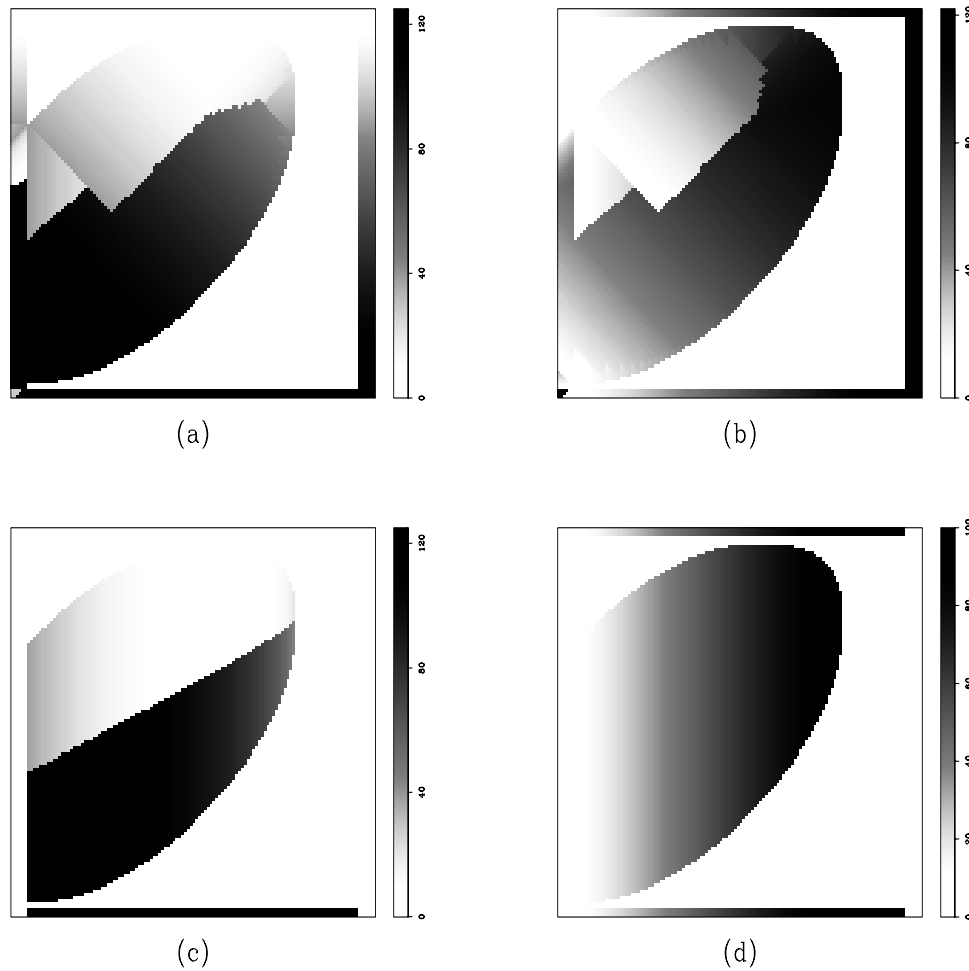


Figure 7: Nearest-neighbor coordinates of closest filters. (a) and (b): y and x locations (respectively) of nearest neighbors for missing data with an isotropic search. (c) and (d), the same, but when searching only vertically. `bill2-near` [ER,M]

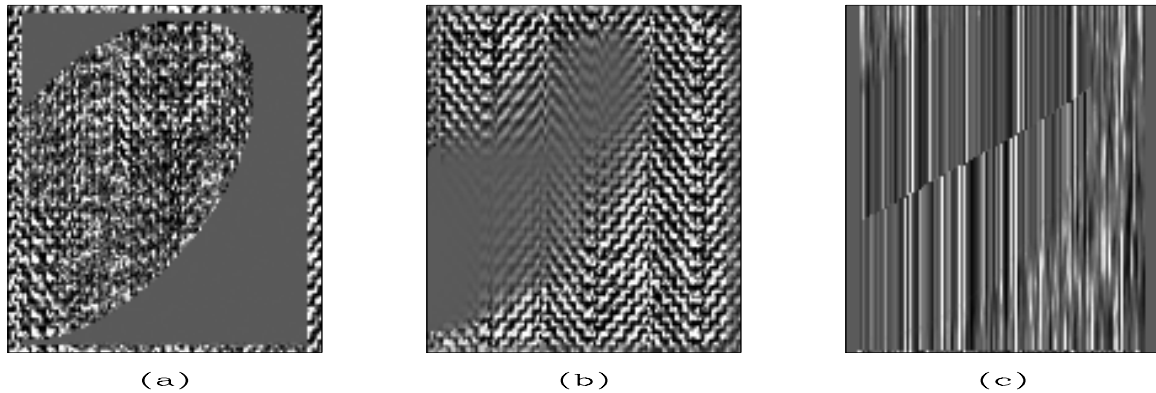


Figure 8: Results for PEF estimation with a vertical derivative for regularization and a vertical nearest-neighbor search for missing coefficients. (a) Convolution of the PEF with the fully-sampled data. We can see that the result is more white than in Figure 6. (b) Interpolation with the PEF. Again, the result is better than in Figure 6. The dips are all in the correct locations, but the amplitude is not as high as it should be. (c) Filter coefficients from a single filter lag. The nearest-neighbor interpolated filter coefficients are now much harder to distinguish from the area where the PEF is estimated from local data. [bill2-herr-best](#) [ER,M]

continuity of the estimate, estimating the value of the filter in the hole is also a problem.

Interpolating filter coefficients with a Laplacian or helical derivative clearly is not a viable approach. A method that preserves the filters, such as nearest neighbor interpolation of filter coefficients proves to be more feasible. When that method incorporates prior information in terms of a preferred direction of regularization and interpolation, the result is greatly improved.

In the future, this method can be applied to large gaps in seismic data, where the preferred direction is either radial lines or Snell rays.

REFERENCES

- Brown, M., 1999, Texture synthesis and prediction error filtering: SEP-100, 211–222.
- Claerbout, J. F., 1992, Earth Soundings Analysis: Processing Versus Inversion: Blackwell Scientific Publications.
- Claerbout, J., 1999, Geophysical estimation by example: Environmental soundings image enhancement: Stanford Exploration Project, <http://sepwww.stanford.edu/sep/prof/>.
- Clapp, R. G., 2000, Regularizing tomography with non-stationary filters: SEP-103, 47–60.
- Crawley, S., Clapp, R., and Claerbout, J., 1998, Decon and interpolation with nonstationary filters: SEP-97, 183–192.
- Crawley, S., 2000, Seismic trace interpolation with nonstationary prediction-error filters: Ph.D. thesis, Stanford University.

Journel, A., and Zhang, T. Geostatistics for spatial phenomena, course notes:, 2005.

Spitz, S., 1991, Seismic trace interpolation in the F-X domain: *Geophysics*, **56**, no. 06, 785–794.

ADCIGs for forward-scattered wavefields

Jeff Shragge, Brad Artman, and Biondo Biondi¹

ABSTRACT

We extend the 2-D theory of angle-domain common-image gathers (ADCIGs) to forward-scattered wavefields, and present a method for extracting reflectivity as a function of either the reflected or converted-wave receiver-side scattering angle. We use the shot-profile configuration of wave-equation migration along with planar source and receiver wavefields to generate an analytic hyper-plane surface in the intermediate offset-domain common-image gather space. Geometrical relations and partial derivatives of the hyper-plane function generate six constraint equations for the unknown six parameters, allowing us to solve for the source- and receiver-side reflection angles and geologic dip angle. Results of numerical experiments indicate that information on wavefield focusing is present in forward-scattered ADCIGs, which suggests that this algorithm may be useful tool for improving wave-equation based tomography of transmission wavefields.

INTRODUCTION

Conventional seismic exploration surveys acquire P -wave reflection data with surface-based acquisition geometry. Increasingly, though, non-conventional surveys provide additional and complementary constraints on the seismic imaging process. One non-conventional survey example is massive 3-D vertical seismic profiling (VSP), which generates increased subsurface ray coverage and affords enhanced resolution of complex geologic structure (Payne et al., 1994; Bicquart, 1998; Sullivan et al., 2003). A second example is the use of long-offset refracted waves in conventional reflection surveys to improve migration velocity analysis (MVA) through wavefield inversion (Pratt, 1999; Sirgue and Pratt, 2004). Non-conventional surveys often incorporate alternative acquisition geometry and/or novel sources such as in passive seismic imaging; many are designed to measure forward-scattered energy with sufficient spatial sampling to permit wavefield-based processing. Hence, a careful examination the utility of forward-scattered wavefields in the seismic imaging process is warranted.

The forward-scattering scenario arises when a source wavefield interacts with discontinuous structure generating a secondary scattered wavefield of diffracted and converted energy that propagates sub-parallel to the source wavefield. Importantly, because these two wavefields travel in similar directions, and thereby sample the subsurface in a similar way, they contain important velocity profile information in both absolute (i.e., direct waves) and relative (i.e., differential) travel-times. The utility of this information for velocity analysis and/or

¹email: jeff@sep.stanford.edu, brad@sep.stanford.edu, biondo@sep.stanford.edu

imaging is well-known, and is used frequently in many branches of seismology (Langston, 1977; VanDecar, 1991; Bostock et al., 2001; Sheley and Schuster, 2003).

Most forward-scattering MVA and imaging methods do not process entire wavefield records, and instead rely on the analysis of picked relative or global traveltimes. Analogous to conventional reflection seismic processing, though, significant MVA and imaging improvements should be achievable by moving from forward-scattered traveltime-based processing to forward-scattered wavefield inversion methods. However, before we can test this assertion, a number of forward-scattering MVA and imaging tools must be developed - in particular, the forward-scattering equivalent of the angle domain common image gather (ADCIG) (Prucha et al., 1999; Sava and Fomel, 2003a; Biondi, 2005; Rosales and Biondi, 2005)

In this paper, we modify existing 2-D ADCIG theory to account for the differences arising in the forward-scattering scenario. We use the shot-profile configuration of wave-equation migration to provide a ADCIG framework for both forward-scattered diffracted ($P - P$) and converted ($P - S$) wavefields. We begin by reviewing the wavefield extrapolation and imaging condition steps of shot-profile migration. We then specify planar source and receiver wavefields, and generate parametric surfaces in the intermediate offset-domain common-image gather (ODCIG) space. Subsequently, we show how to transform ODCIGs to their angle domain representation, and detail how to compute angle-dependent source- and receiver-side reflectivity and the geologic dip angle directly from the ODCIG volume. We then apply the approach to a synthetic teleseismic plane-wave data set (Shragge, 2003). This data set is comprised of elastic wavefields, which allows us to test our ADCIG theory for both $P - P$ and $P - S$ forward-scattered scenarios.

SHOT-PROFILE MIGRATION

Shot-profile migration reconstructs the subsurface reflectivity profile by approximately reconstructing the physics of wave-propagation and scattering that generated individual shot records. Central to this formulation is the notion of two independent wavefields: a source wavefield, S , that interacts with discontinuous structure to generate a scattered receiver wavefield, R . The shot-profile migration algorithm consists of two processing steps. The first step is the independent propagation of the S and R wavefields. The second step combines wavefields S and R in a physical imaging condition to generate a map of subsurface reflectivity.

The first shot-profile migration step is an independent extrapolation of S and R , which requires the recursive solution of (Claerbout, 1985),

$$\begin{aligned} S(x_s, z_s + \Delta z_s; \omega) &= S(x_s, z_s; \omega) e^{\pm i k_{z_s} \Delta z_s}, \\ R(x_r, z_r + \Delta z_r; \omega) &= R(x_r, z_r; \omega) e^{-i k_{z_r} \Delta z_r}, \end{aligned} \quad (1)$$

where k_{z_s} and k_{z_r} are the source and receiver vertical wavenumbers from the wave-equation dispersion relationship, Δz_s and Δz_r are depth step intervals, and ω is angular frequency. Successive applications of the complex exponential operators in Equation (1) generate the full S and R wavefield volumes, $S(\mathbf{x}_s; \omega)$ and $R(\mathbf{x}_r; \omega)$, at all source, \mathbf{x}_s , and receiver, \mathbf{x}_r , points in model space.

The source wavefield extrapolation operator in Equation (1) includes symbol \pm to distinguish between forward- and backscattering migration scenarios. This parameter explains the causality arguments illustrated in Figure 1. The four panels represent the forward (i.e., modeling) and adjoint (i.e., migration) propagation of wavefields for both the forward- and backscattered scenarios. Causal propagation is indicated with a forward time-arrow and a positive sign in the extrapolation operator.

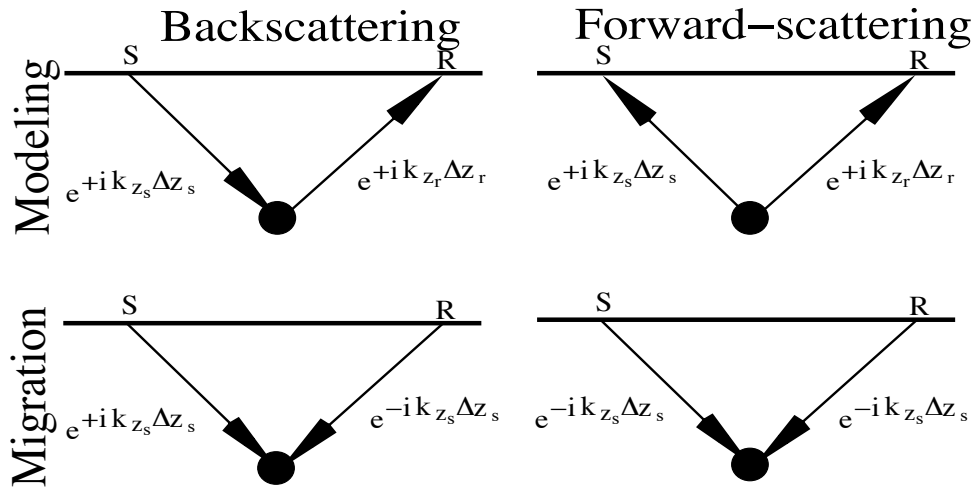


Figure 1: Sketch representing causality arguments for forward- and backscattering scenarios. Time-arrows and positive extrapolation operators indicate causal propagation. Upper left: Backscattered modeling; lower left: backscattered migration; upper right: forward-scattered modeling; and lower right: forward-scattered migration. Note the differing extrapolation operators required for migration that arise from causality arguments. jeff2-FSBS [NR]

In backscattered modeling (upper left), a surface-excited source wavefield propagates to a point scatterer and then diffracts as a scattered wavefield, R , upward to the surface. Migrating backscattered wavefields (lower left) propagates R backward in time into the subsurface, which requires reversing the direction of the receiver time arrow and the sign of the receiver extrapolation operator. In forward-scattered modeling (upper right), an upgoing source wavefield impinging from below interacts with the point scatterer, again generating an upgoing scattered wavefield, R . Migrating forward-scattered waves (lower right) requires propagating both S and R backward in time into the subsurface, which reverses the direction of the two time arrows and the signs of both extrapolation operators.

The second shot-profile migration step generates an image, I , of subsurface reflectivity through an evaluation of a physical imaging condition (Claerbout, 1971). The most basic imaging condition extracts the zero-lag coefficient of the correlation of wavefields S and R . An important extension includes an additional image-space dimension, subsurface half-offset \mathbf{h} , generated by shifting S and R in opposing directions by distance \mathbf{h} prior to correlation (Rickett and Sava, 2002). We emphasize that \mathbf{h} is not equivalent to the surface offset parameters often encountered in shot-geophone or Kirchhoff migration approaches. We write this step with the

following equation,

$$I(\mathbf{x}, \mathbf{h}) = \sum_{\omega} [\delta(\mathbf{x}_s - \mathbf{x} - \mathbf{h}) * S(\mathbf{x}_s; \omega)] [\overline{R(\mathbf{x}_r; \omega)} * \delta(\mathbf{x}_r - \mathbf{x} + \mathbf{h})], \quad (2)$$

where \mathbf{x} is the spatial variable of image-space, \overline{R} is the complex conjugate of R , and $*$ indicates convolution. The resulting image volume is termed an offset-domain common-image gather (ODCIG). In general, the shifting operation can be oriented in any direction; however, generating a complete 2-D ODCIG volume requires shifts in only two orthogonal directions. For computational simplicity, this is usually done along the horizontal (HODCIGs) and vertical (VODCIGs) axes (Biondi and Symes, 2004).

PLANE-WAVE ODCIGS

In this section, we examine the ODCIG volumes generated by forward-scattered wavefields. For simplicity, we illustrate these concepts using plane-wave S and R wavefields. We also assume that S and R propagate at constant, though not necessarily equal, slownesses (i.e., reciprocal of velocity). These idealizations allow us to generate an analytic surface in ODCIG space for both $P - P$ diffracted and $P - S$ converted waves. We specify planar S and R wavefields in constant velocity media using source and receiver ray parameter vectors, \mathbf{w}_s and \mathbf{w}_r , defined by,

$$\mathbf{w}_s = [p_s, q_s] = s_s [\sin \beta_s, \cos \beta_s] \quad \text{and} \quad \mathbf{w}_r = [p_r, q_r] = s_r [\sin \beta_r, \cos \beta_r], \quad (3)$$

where p_s and p_r are the source and receiver horizontal ray parameters, q_s and q_r are the source and receiver vertical ray parameters, and s_s and s_r are the source and receiver wavefield propagation slownesses, respectively. Also, we use a convention where angles are defined clockwise positive with respect to the vertical depth axis.

Forward-scattered S and R wavefields must satisfy the causality arguments illustrated in Figure 1, which requires a negative sign in the source and receiver extrapolation operators. Using the aforementioned assumptions, we generate the following extrapolated S and R wavefield volumes,

$$S(\mathbf{x}_s; t) = \delta(t + \mathbf{w}_s \cdot \mathbf{x}_s) \quad \text{and} \quad R(\mathbf{x}_r; t) = \delta(t + \mathbf{w}_r \cdot \mathbf{x}_r). \quad (4)$$

Applying a Fourier transform over the t -axis of both S and R yields,

$$S(\mathbf{x}_s; \omega) = \exp(-i\omega \mathbf{w}_s \cdot \mathbf{x}_s) \quad \text{and} \quad R(\mathbf{x}_r; \omega) = \exp(-i\omega \mathbf{w}_r \cdot \mathbf{x}_r). \quad (5)$$

Evaluating the imaging condition in Equation (2) with the wavefields in Equation (5) generates the following image-space volume,

$$\begin{aligned} I(\mathbf{x}, \mathbf{h}) &= \sum_{\omega} \delta(\mathbf{x}_s - \mathbf{x} - \mathbf{h}) * \exp(-i\omega \mathbf{w}_s \cdot \mathbf{x}_s) [\overline{\exp(-i\omega \mathbf{w}_r \cdot \mathbf{x}_r)} * \delta(\mathbf{x}_r - \mathbf{x} + \mathbf{h})], \\ &= \sum_{\omega} \exp(-i\omega [\mathbf{x} \cdot (\mathbf{w}_s - \mathbf{w}_r) + \mathbf{h} \cdot (\mathbf{w}_s + \mathbf{w}_r)]) \cdot \\ &= \delta[\mathbf{x} \cdot (\mathbf{w}_s - \mathbf{w}_r) + \mathbf{h} \cdot (\mathbf{w}_s + \mathbf{w}_r)]. \end{aligned} \quad (6)$$

The non-zero δ -function argument,

$$x(p_r - p_s) + z(q_r - q_s) - h_x(p_r + p_s) - h_z(q_r + q_s) = 0, \quad (7)$$

represents an analytic forward-scattered ODCIG hyper-plane surface. Importantly, this surface interrelates source and receiver plane-wave angles, propagation slownesses and image-space variables, \mathbf{x} and \mathbf{h} . In the next section, we manipulate this formula to generate constraint equations that help isolate the receiver-side contribution to the total reflection angle.

FROM ODCIGS TO ADCIGS

An ODCIG can be transformed to another image-space volume, termed an angle-domain common-image gather (ADCIG), representing reflectivity as a function of reflection angle. Sava and Fomel (2003b) present a post-imaging, Fourier-domain transform between these spaces appropriate for conventional reflection wavefields. However, as discussed by Rosales and Rickett (2001), this transform does not hold for converted waves because Snell's Law partitions the total reflection angle into unequal source- and receiver-side reflection contributions.

Figure 2 illustrates the generalized geometry of the forward-scattering scenario for a sub-surface geologic discontinuity, $\bar{\mathbf{I}}$, oriented at geologic dip angle, α , with normal, $\bar{\mathbf{n}}$. An upgoing planar source wavefield propagating at angle β_s to the upward vertical has already interacted at $\bar{\mathbf{I}}$ to generate an upgoing, planar wavefield propagating at angle β_r . For $P - P$ interactions, Snell's Law requires that total reflection opening angle, 2γ , is split equally between the source- and receiver-side reflection angles (i.e., $\gamma = \gamma_r = \gamma_s$). For $P - S$ conversions, Snell's Law requires that angle 2γ is not bisected into equal components, leaving γ_s unequal to γ_r . Hence, additional constraint equations must be included to isolate the receiver-side reflectivity contributions.

Generating Constraint Equations

Generating ADCIGs for forward-scattered wavefields requires specifying reflectivity as a function of either the source-side, γ_s , or receiver-side, γ_r , reflection angles. Either choice, though, requires isolating one angle from a system with 6 free parameters: $\beta_s, \beta_r, \gamma_s, \gamma_r, \alpha$, and γ . Hence, solving for, say, γ_r requires specifying 6 constraint equations.

Three constraint equations are specified by geometric relationships (c.f. Figure 2). The first constraint equation is a local conservation of reflection angle given by,

$$2\gamma = \gamma_s + \gamma_r. \quad (8)$$

The second and third constraint equations derive from a global conservation of reflection angle arguments that relate the S and R plane-wave angles, geologic dip, and the source- and receiver-side reflection angles through (Biondi, 2005),

$$\beta_s = \alpha - \gamma = \alpha - \frac{\gamma_s + \gamma_r}{2}, \quad (9)$$

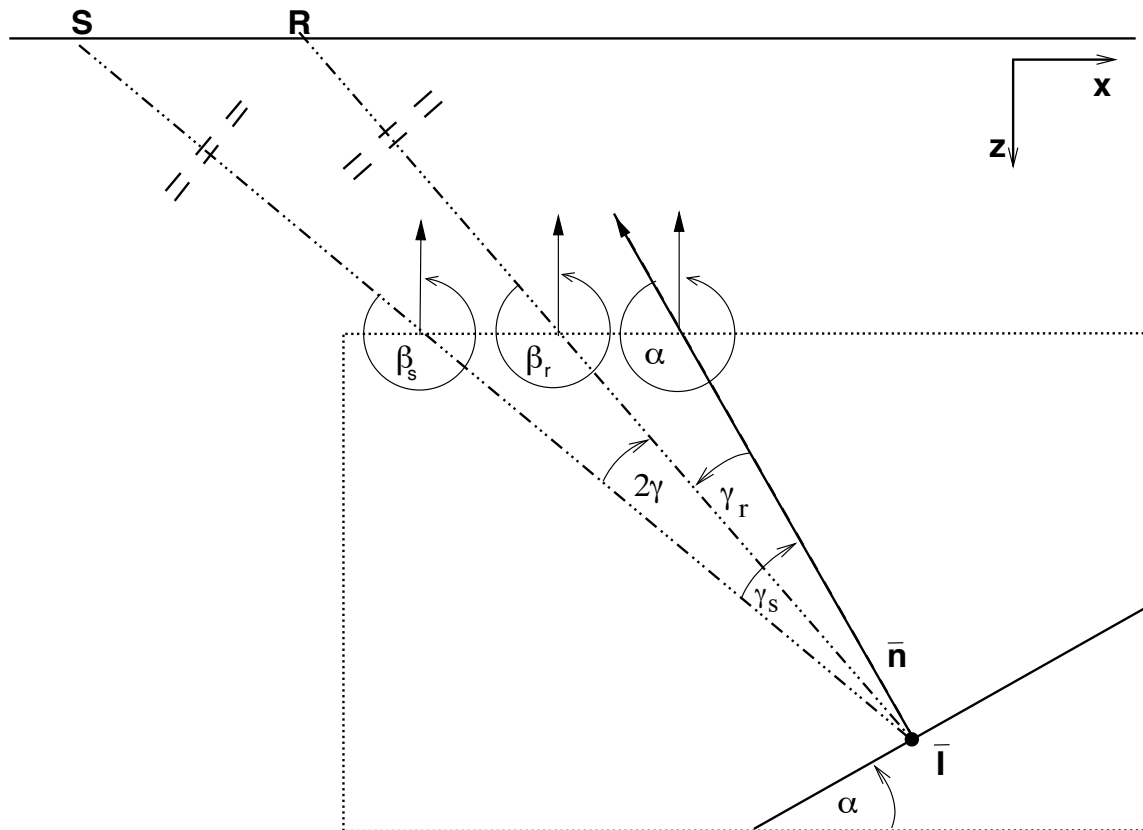


Figure 2: Sketch denoting the forward-scattered converted wave scenario. An ongoing planar source wavefield propagating at angle β_s has already interacted with surface \bar{I} to generate an ongoing planar scattered wavefield, R , propagating at angle β_r . The total reflection angle, 2γ , is partitioned into source- and receiver-side reflection angles, γ_s and γ_r , according to Snell's Law. Arrows are included on angles to show the sense of rotation, where (counter)clockwise angles are taken here to be (negative) positive quantities. jeff2-cig-simple-v4 [NR]

and,

$$\beta_r = \alpha + \gamma = \alpha + \frac{\gamma_s + \gamma_r}{2}. \quad (10)$$

Snell's Law provides a fourth physical constraint equation by relating the source- and receiver-side reflection angles with the local propagation slownesses,

$$s_s \sin \gamma_s = s_r \sin \gamma_r, \quad (11)$$

which can be rewritten using Equation (10) as,

$$\tan \gamma_r = \frac{\sin 2\gamma}{\frac{s_r}{s_s} + \cos 2\gamma}. \quad (12)$$

Constraint equations (8-11) do not incorporate physical observables measured from the generated image volume. However, we can calculate image-space dips in both the horizontal subsurface half-offset, $\frac{\partial z}{\partial h_x}$, and midpoint, $\frac{\partial z}{\partial x}$, directions. Thus, the final two constraint equations relating measured dips to free parameters can be obtained by taking the appropriate partial derivatives of the parametric hyper-plane surface in Equation (7),

$$\left. \frac{\partial z}{\partial h_x} \right|_{x,h_z} = \frac{p_r + p_s}{q_r - q_s} = \frac{s_r \sin(\alpha + \gamma) - s_s \sin(\alpha - \gamma)}{s_r \cos(\alpha + \gamma) + s_s \cos(\alpha - \gamma)}, \quad (13)$$

and

$$\left. \frac{\partial z}{\partial x} \right|_{z,h_z} = -\frac{p_r + p_s}{q_r + q_s} = -\frac{s_r \sin(\alpha + \gamma) + s_s \sin(\alpha - \gamma)}{s_r \cos(\alpha + \gamma) + s_s \cos(\alpha - \gamma)}. \quad (14)$$

We rewrite Equations (13) and (14) using the trigonometric angle addition and subtraction rules,

$$\left. \frac{\partial z}{\partial h_x} \right|_{x,h_z} = \frac{(s_r - s_s) \cos \alpha \sin \gamma + (s_r + s_s) \sin \alpha \cos \gamma}{(s_r - s_s) \cos \alpha \cos \gamma + (s_r + s_s) \sin \alpha \sin \gamma}, \quad (15)$$

and,

$$\left. \frac{\partial z}{\partial x} \right|_{z,h_z} = -\frac{(s_r + s_s) \cos \alpha \sin \gamma + (s_r - s_s) \sin \alpha \cos \gamma}{(s_r - s_s) \cos \alpha \cos \gamma - (s_r + s_s) \sin \alpha \sin \gamma}, \quad (16)$$

which we rearrange to yield,

$$\left. \frac{\partial z}{\partial h_x} \right|_{x,h_z} = \frac{\phi \tan \gamma + \tan \alpha}{\phi - \tan \alpha \tan \gamma} \quad \text{and} \quad \left. \frac{\partial z}{\partial x} \right|_{z,h_z} = -\frac{\tan \gamma + \phi \tan \alpha}{\phi - \tan \alpha \tan \gamma}, \quad (17)$$

where ϕ is a "normalized difference" of slownesses given by, $\phi = \frac{s_r - s_s}{s_r + s_s}$. Solving for $\tan \gamma$ and $\tan \alpha$ leads to,

$$\tan \gamma = \frac{\phi \frac{\partial z}{\partial h_x} - \tan \alpha}{\phi + \frac{\partial z}{\partial h_x} \tan \alpha} \quad \text{and} \quad \tan \alpha = \frac{\tan \gamma + \phi \frac{\partial z}{\partial x}}{\frac{\partial z}{\partial x} \tan \gamma - \phi}, \quad (18)$$

where the parameters held constant during partial differentiation are no longer explicitly written. These two expressions can be manipulated to specify independent equations for reflection angle, γ ,

$$\tan^2 \gamma \left[\phi \frac{\partial z}{\partial x} + \frac{\partial z}{\partial h_x} \right] + \tan \gamma [1 - \phi^2] + \phi \left[\phi \frac{\partial z}{\partial h_x} + \frac{\partial z}{\partial x} \right] = 0, \quad (19)$$

and true geologic dip, α ,

$$\tan^2 \alpha \left[\phi \frac{\partial z}{\partial h_x} - \frac{\partial z}{\partial x} \right] + \tan \alpha [1 + \phi^2] + \phi \left[\phi \frac{\partial z}{\partial x} + \frac{\partial z}{\partial h_x} \right] = 0. \quad (20)$$

When source and receiver propagation slownesses are equal (i.e., $\phi = 0$), these quadratic equations reduce to,

$$\frac{\partial z}{\partial h_x} = -\cot \gamma \quad \text{and} \quad \frac{\partial z}{\partial x} = -\cot \alpha. \quad (21)$$

which is similar to the expressions derived for the backscattered case save for a $\pi/2$ phase rotation (i.e., $\tan x = \cot(\pi/2 - x)$). Finally, the solution for the receiver-side reflection angle, γ_r , is obtained from angle γ through the relation specified in Equation (12).

In Equations (13) and (14), we differentiated with respect to variables, x and h_x . This choice was one step in the development of horizontal ADCIGs. Equally, we can create vertical ADCIGs by developing two constraint equations from partial derivatives with respect to vertical variables, z and h_z , holding horizontal variables x and h_x constant. Vertical ADCIGs are then generated through introduction of these functions into Equations (15-20). Biondi and Symes (2004) detail situations where it is more advantageous to use vertical ADCIGs than their horizontal counterparts. In particular, vertical ADCIGs provide better spatial resolution for scenarios where the wavefield propagation direction is oriented at steep angles to the geologic dip-field.

NUMERICAL EXAMPLES

In this section, we present numerical tests of the theory developed above. We provide the proof-of-concept using a plane-wave teleseismic data set (Shragge, 2003). This data set is comprised of elastic wavefields, which allows us to test both the diffracted and converted scattering scenarios. The idealized model, shown in Figure 3, is comprised of three materials with differing elastic properties. A low-velocity crustal layer (white) overlies a faster upper mantle (dark gray). At the location of the suture, crustal material from the lithospheric block to the left bifurcates, with the lower segment descending into the mantle. At the depth of approximately 40 km, the relict (black) converts to velocities and density higher than the surrounding mantle (with a proportionally greater increase in shear-wave velocity) and thereafter folds and thins to the right of the model. Structural dips in the model are generally quite low (i.e., less than 20°); however, sub-vertical discontinuities are present in the zone of short-wavelength structure between $x=120$ and $x=160$.

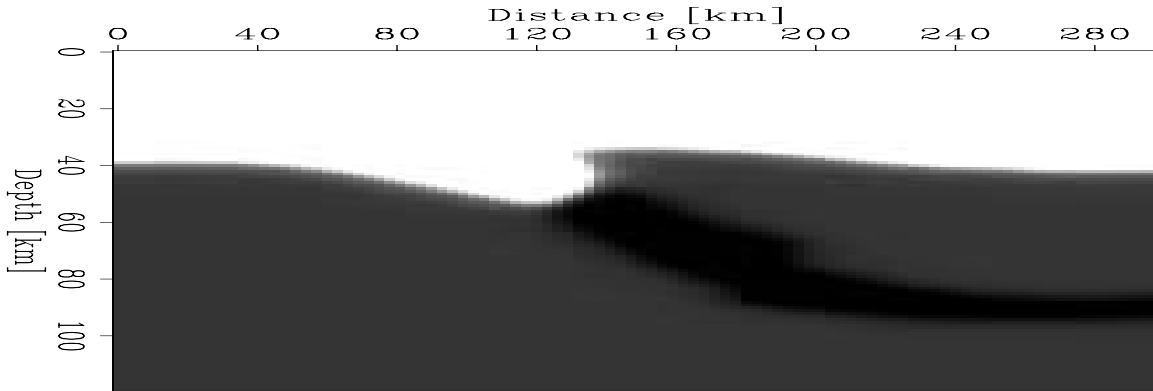


Figure 3: Smoothed version of structural model used in test. `jeff2-Vel` [ER]

Several sets of two-component seismograms were computed through this model using a 2-D, elastic pseudo-spectral finite-difference code (Kosloff et al., 1990). The seismograms comprise a suite of plane P -wave sources interacting with the model over a range of incident horizontal slownesses, $p_s = [\pm 0.05, \pm 0.06, \pm 0.07] \text{skm}^{-1}$. We rotated the output data from the computational orientation (i.e., $\mathbf{U} = [U_1, U_3]$) to a wave-vector orientation (i.e., $\mathbf{w} = [P, SV]$) via the free-surface transfer matrix (Kennett, 1991).

Figure 4 presents examples of P -wave (top panels) and S -wave (bottom panels) data sections. The left and right panels show data for plane-wave sources incident from the left and right sides of the model in Figure 3, respectively. We are interested in imaging are the $P - P$ diffracted waves from the zone of short wavelength structure immediately following the plane-wave arrival, and the $P - S$ diffracted and converted waves arriving shortly thereafter.

This vector-wavefield processing yields P - and S -wave data sections appropriate for use in shot-profile migration (Shragge et al., 2005). We migrated the data sections for both $P - P$ and $P - S$ scattering modes. We present the image volumes in Figures 5 and 6, where horizontal and vertical ADCIGs are shown in the upper and lower panels, respectively. The upper panel of Figure 5 shows a vertical streak around 130 km in midpoint. This indicates that because of the low geologic dip angles in this model, horizontal ADCIGs computed from forward-scattered $P - P$ migrations afford low resolution of the imaged structure, and are not likely to be useful either for MVA or imaging.

In addition, we computed vertical ADCIGs using the method described in the above section (i.e., by replacing horizontal variables x and h_x with vertical variables z and h_z). The vertical ADCIG shown in the lower panels have a slightly better spatial localization of energy. Note that migrated energy in panel d) focuses about 90° , which is the forward-scattered equivalent of a zero-offset reflection. Also imaged is a cross-hair pattern about the target zone in panel c) that is directly analogous to smearing commonly observed in tomographic images that derives from limited ray coverage.

The migration results for forward-scattered $P - S$ conversions are shown in Figure 6. However, we have not yet fully implemented Equation (19), and use Equation (21) as a proxy

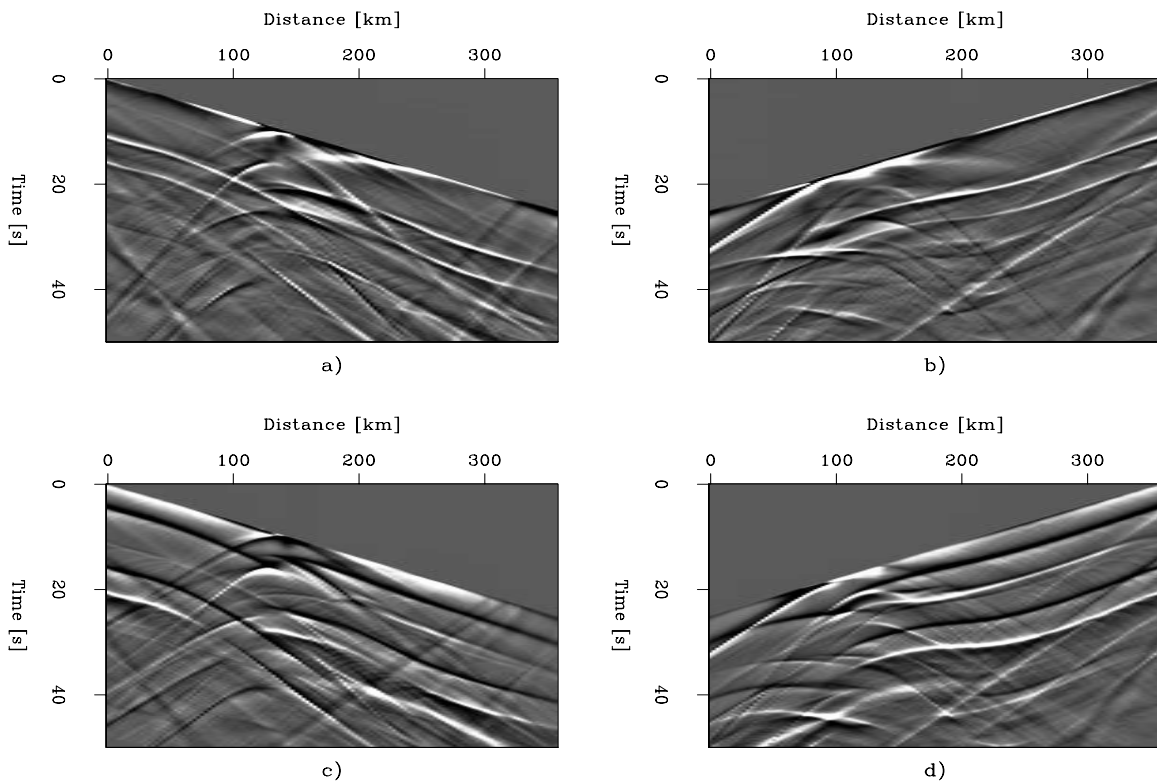


Figure 4: Examples of plane-wave data used in migration and ADCIG test. a) left-incident P-wave; b) right-incident P-wave; c) left-incident S-wave; and d) right-incident S-wave.

`jeff2-data` [ER]

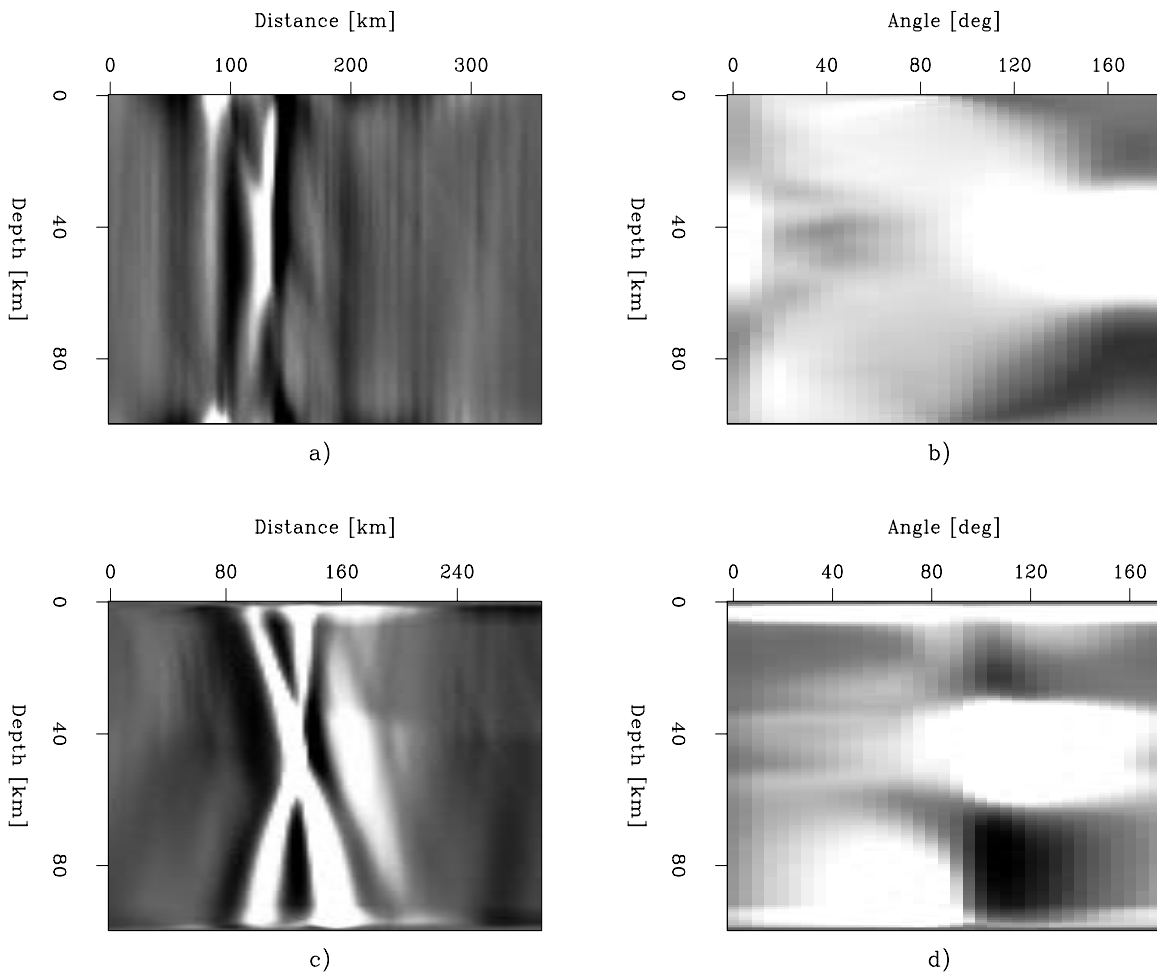


Figure 5: ADCIGs for forward-scattered $P - P$ diffracted wavefields. a) slice through horizontal ADCIG volume at angle 150° ; b) slice through horizontal ADCIG volume at $x=126$ km; c) slice through vertical ADCIG at angle 110° ; and d) slice through vertical ADCIG at $x=126$ km. Note that the vertical ADCIGs has a slightly better spatial localization of energy.

jeff2-Q1 [ER]

instead. This is not too grievous of an approximation, as shown by Rosales and Biondi (2005). Hence, angles are not exactly in the correct position. Future work will implement the appropriate expressions. The upper panels show the $P - S$ horizontal ADCIG. Panel b) exhibits clusters of energy on both sides of the 90° mark. These represent groups of 3 plane-waves impinging from the right and left sides of the model that are mapped to different sides of the 90° normal axis. Relative to the equivalent panels in Figure 5, the forward-scattered horizontal ADCIG indicates that forward-scattered converted waves afford significantly higher resolution than $P - P$ diffractions. This observation is a consequence of the direct link between increased differential arrival times and improved spatial resolution. The vertical ADCIG vol-

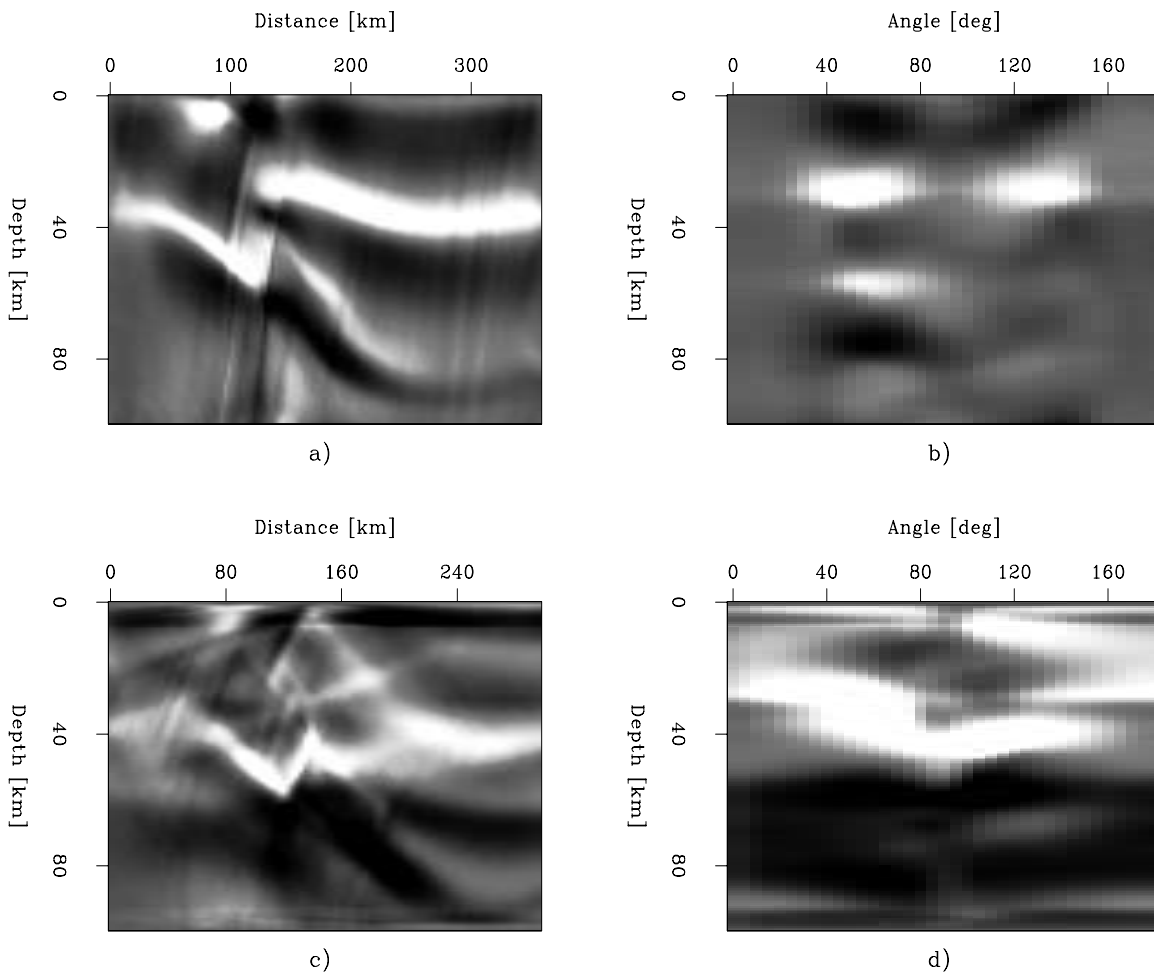


Figure 6: ADCIGs for forward-scattered $P - S$ converted wavefields. a) slice through horizontal ADCIG volume at angle 55° ; b) slice through horizontal ADCIG volume at $x=174$ km; c) slice through vertical ADCIG at angle 90° ; and d) slice through vertical ADCIG at $x=138$ km. jeff2-Q2 [ER]

ume, shown in the lower panels, again affords better resolution of sub-vertical structure than sub-horizontal interfaces. The zone of short-wavelength structure is better imaged than its counterpart in Figure 5, and has better angle-domain localization.

DISCUSSION AND FUTURE WORK

The numerical tests illustrate that forward-scattered wavefield imaging can lead to interpretable ADCIG volumes. In particular, we show that vertical ADCIGs are able to resolve geologic dips oriented sub-parallel to the plane-wave propagation direction. Conversely, horizontal ADCIGs are shown to afford little resolution to flat-lying reflectors. This data set, though, does not provide an ideal test of the forward-scattered imaging approach. The shots are both limited in number and distribution of wavenumbers within each shot-record. Higher frequency content of the data is required before the spatial resolution of forward-scattered ADCIGs is fully assessed. In the future, we will apply the methodology to data sets containing forward-scattered waves, potentially including cross-hole seismic, VSP, and long-offset surface reflection data.

CONCLUDING REMARKS

We extend the 2-D ADCIG theory to include forward-scattered wavefields comprised of $P - P$ diffracted and $P - S$ scattering. We develop a series of six equations for the six unknown parameters, which allows us to estimate either the source- or receiver-side, angle-dependent reflectivity directly from ADCIGs volumes. Numerical tests illustrate forward-scattered wavefields are useful for imaging. This observation motivates further testing of the developed algorithms on field data scenarios, including cross-hole seismic, VSP, and long-offset reflection data. Results of numerical experiments indicate that information on wavefield focusing is present in forward-scattered ADCIGs, which suggests that this algorithm may be useful tool for improving wave-equation based tomography of transmission wavefields.

ACKNOWLEDGMENTS

We would like to thank Charlie Wilson for helpful discussions early on in the development.

REFERENCES

- Bicquart, P., 1998, Application of Kirchhoff depth migration to 3D VSP: 68th Ann. Internat. Mtg., Soc. of Expl. Geophys., Expanded Abstracts, 389–392.
- Biondi, B., and Symes, W., 2004, Angle-domain common-image gathers for migration velocity analysis by wavefield-continuation imaging: *Geophysics*, **69**, 1283–1298.
- Biondi, B., 2005, Angle-domain common image gathers for anisotropic migration: SEP-120, 77–104.
- Bostock, M., Rondenay, S., and Shragge, J., 2001, Multi-parameter two-dimensional inversion of scattered teleseismic body waves, 1. Theory for oblique incidence: *J. Geophys. Res.*, **106**, 30771–30782.

- Claerbout, J., 1971, Toward a unified theory of reflector mapping: *Geophysics*, **36**, 467–481.
- Claerbout, J., 1985, *Imaging the Earth's Interior*: Stanford University.
- Kennett, B., 1991, The removal of free surface interactions from three-component seismograms: *J. Geophys. Res.*, **104**, 153–163.
- Kosloff, D., Kessler, D., Filho, A., Tessmer, E., Behle, A., and Strahilevitz, R., 1990, Solution of the equations of dynamic elasticity by a Chebychev spectral method: *Geophysics*, **55**, 734–748.
- Langston, C., 1977, Corvallis, Oregon, crustal and upper mantle structure from teleseismic P and S waves: *Bull. Seism. Soc. Am.*, **67**, 713–724.
- Payne, M., Eriksen, E., and Rape, T., 1994, Considerations for high-resolution VSP imaging: *The Leading Edge*, **3**, 173–179.
- Pratt, R., 1999, Seismic waveform inversion in the frequency domain, Part 1: Theory and verification in a physical model: *Geophysics*, **64**, 888–901.
- Prucha, M., Biondi, B., and Symes, W., 1999, Angle-domain common-image gathers by wave-equation migration: 69th Ann. Internat. Meeting, Soc. of Expl. Geophys., Expanded Abstracts, 824–827.
- Rickett, J., and Sava, P., 2002, Offset and angle-domain common image-point gathers for shot profile migration: *Geophysics*, **67**, 883–889.
- Rosales, D. A., and Biondi, B., 2005, Converted-mode angle-domain common-image gathers for migration velocity analysis: SEP-**120**, 283–296.
- Rosales, D., and Rickett, J., 2001, *ps*-wave polarity reversal in angle domain common-image gathers: SEP-**108**, 35–44.
- Sava, P., and Fomel, S., 2003a, Angle-domain common image gathers by wavefield continuation methods: *Geophysics*, **68**, no. 3, 1065–1074.
- Sava, P., and Fomel, S., 2003b, Angle-domain common-image gathers by wavefield continuation methods: *Geophysics*, **68**, 1065–1074.
- Sheley, D., and Schuster, G., 2003, Reduced-time migration of transmitted P-S waves: *Geophysics*, **68**, 1695–1707.
- Shragge, J., Artman, B., and Wilson, C., 2005, Shot profile migration of teleseismic wavefields: Submitted to *Geophysics*.
- Shragge, J., 2003, Phase-shift migration of approximate zero-offset teleseismic data: SEP-**113**, 145–156.
- Sirgue, L., and Pratt, R., 2004, Efficient waveform inversion and imaging: A strategy for selecting temporal frequencies: *Geophysics*, **69**, 231–248.

Sullivan, C., Ross, A., J., L., Urban, D., Hornby, B., West, C., Garing, J., Paulsson, B., Karrenbach, M., and Milligan, P., 2003, A 3D massive VSP survey at Milne Point, Alaska: 73rd Ann. Internat. Mtg., Soc. of Expl. Geophys., Expanded Abstracts.

VanDecar, J., 1991, Upper-mantle structure of the Cascadia subduction zone from non-linear teleseismic travel-time inversion: Ph.D. thesis, 165 pp., Univ. of Wash., Seattle.



Short Note

Time windowing passive seismic data in the frequency domain

Brad Artman¹

INTRODUCTION

One of the principle obstacles to the utility of passive seismic data is its bulk. With several hundred to thousands of geophones, we are able to generate mountains of data in a very short time. The simplest method of trimming down this volume is to keep only the recorded wave-field around times when usable source energy is known to be present. In the case of teleseismic imaging, or when utilizing unconventional, but known sources, this is easily done. However, if one hopes to image with the truly ambient noise field, time windowing amounts to removing needed signal.

After cross-correlation of passive traces, one can produce shot-gathers equivalent to an active source experiment. Having done so, we realize that most of the recording time axis can be discarded and maintain only enough time/lag samples to keep the reflection from the deepest subsurface structure of interest. As most of the processing of seismic data is accomplished in the Fourier-domain, I will consider the procedure and ramifications of time windowing after data have been transformed to frequency.

1D EXAMPLE

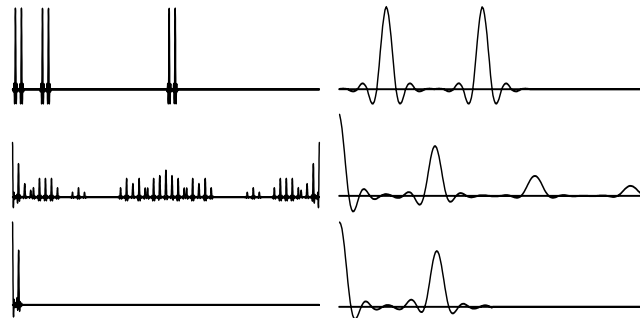
Windowing in the time domain is equivalent to subsampling in the dual domain. The first trace in Figure reffig:freq is a time signal that might correspond to several identical subsurface sources below a single layer in the earth. It is many thousands of samples long. The second trace is its autocorrelation calculated using all data in the frequency domain multiplication. We recognize the auto-correlation to be symmetric, and could have truncated the result after half of the samples. Also, because each event correlates with all the others, many correlation peaks appear at late time. These late events contain information about similarity of the earth's impulse response recovered by each independent source function. Mathematically, this is a chain of many convolutions of complicated functions and very difficult to understand or utilize. They do not fit into the framework of passive seismic imaging by representing the kinematics of a reflection gather. So I discard them. In this case, the "deepest subsurface

¹email: brad@sep.stanford.edu

reflector of interest” is the second peak of the output correlation. The correlations after this could be what Schuster et al. (2004) call *other terms*.

Instead of truncating the auto-correlation in the time-domain, the last trace was calculated by decimating the Fourier transform of the signal before multiplication. The trace was padded with zeros to facilitate plotting with the previous traces. The number of frequencies used to produce the second autocorrelation was 8 times fewer than the Fourier representation of the input. As long as the level of decimation maintains support for the time window desired for the final result, we can subsample the input after transforming to the frequency domain and before subsequent processing.

Figure 1: Idealized signal of three identical subsurface sources, its auto-correlation, and autocorrelation after subsampling the frequency axis by a factor of 4. Right panel is zoomed in view. `brad1-freq` [ER]



SYNTHETIC SEISMIC EXAMPLE

The seismic example was designed to mimic the passive seismic experiment and reflects the injection of a few simple but very important assumptions about the nature of the subsurface noise-field. These assumptions immediately move us away from the truly random ambient noise experiment. Strictly, I am assuming that the length of any particular subsurface source is fairly short in duration *i.e.* less than a few seconds) and randomly distributed throughout the recording time of the experiment. Cross-talk between sources and their reflections about the subsurface will be introduced under these assumptions if the subsurface sources are not completely uncorrelated. Some degree of correlation will arise if they are not separated in time by at least the two-way traveltime to the deepest reflector and if the sources have correlable waveforms.

Previously, I have manufactured synthetic passive data by convolving transmission wavefields from individual sources with different, long, random traces. The signal to noise ratio of the result can in this case be shown to improve with the square root of the number of time samples in the random source function and the square root of the number of transmission wavefields, that is number of sources, used. There are however important physical implications to modeling in this manner. Specifically, it implies many sources exploding simultaneously with infinite duration and perfect distribution of energy during this entire period. A more reasonable experiment instead is one where the sources have durations of less than a few seconds, and are randomly distributed during the course of the recording interval.

The synthetic examples presented here are generated with random source time functions

no longer than 3 seconds and a random bulk time shift. This facilitates the exploitation of this subsampling strategy to its limit. Under these assumptions, increasing the signal-to-noise ratio of the image will require recording more subsurface sources or allowing the sources to ring for longer than 3 seconds. In either case, the signal to noise ratio will increase with the square root of the quantity considered.

Figure 2 explores the use of Fourier subsampling on the migration results of the synthetic passive data. Three data volumes were created and imaged without first cross-correlating the traces (Artman et al., 2004). All three panels used 280 subsurface energy sources. The first panel was modeled with a total experimental duration of 8 seconds. The second and third panels assumed the recording time was 260 seconds. The first and second panel directly migrated all the data from the entire recording duration. They are identical to within machine precision. The third panel subsampled the 260 second data set in the Fourier domain to a level that will only support 4 seconds of an inverse Fourier transform. This image is identical to the others.

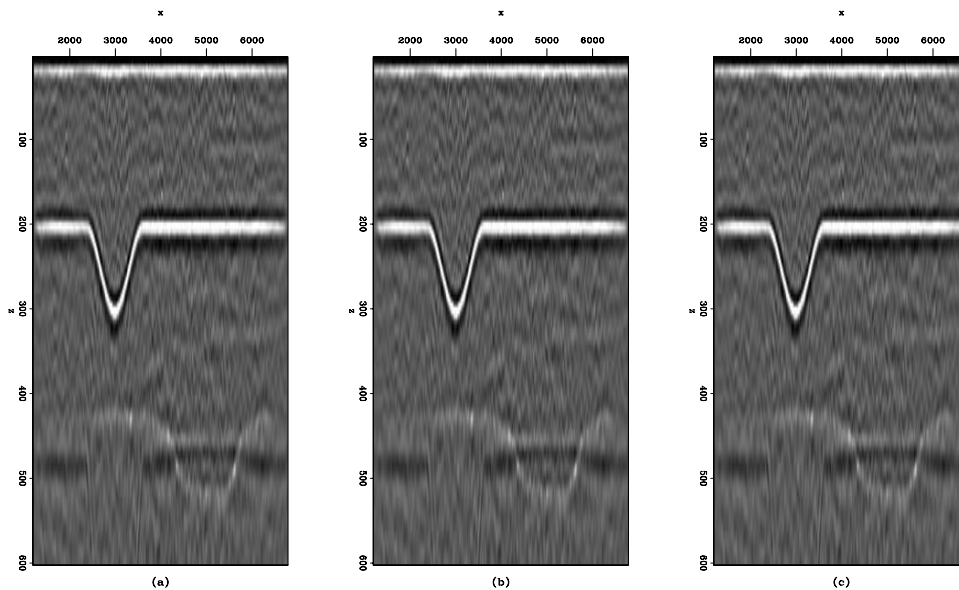


Figure 2: Identical imaging results from direct migration of modeled passive data from 280 subsurface sources (of random duration between 50 and 3000 ms) collected over 8 (panel (a)) and 260 (panels (b)) seconds and a version of the long data subsampled by a factor of 32 in the frequency domain (panel (c)). `brad1-migsub` [CR]

COST IMPLICATIONS

Considering a data set with n_x receivers with n_t time samples, Table lists the number of operations required to construct shot-gathers by cross-correlating the traces of the transmission wavefield and migration of either the raw volume or the data volume produced by correlation. Under the conditions presented above, the n_{ts} time samples needed for the shot-gathers is

the same as the number of frequencies required for direct migration. This will be orders of magnitude less than the n_t time samples collected during a passive seismic experiment in most cases. Finally, it is possible that not all receiver stations need be correlated when processing a large, high frequency experiment. ν will be a subsampling factor, less than 1, that controls the number of traces in, or aperture of, the correlated shot-gathers.

Migration costs scale according to the size of the input data set and the size of the image domain through which the data is extrapolated. X will represent a scalar multiplier due to the computer overhead costs of the migration strategy used. This will vary from a factor of 5 to n_x depending on the algorithm and accuracy required, but will be common to either direct migration or the migration of the correlated shot-gathers.

The size of the image space is assumed to be n_x samples areally by n_z samples in depth. No inverse Fourier transforms are required to prepare for migration, as the shot-gathers are needed to be functions of frequency for many migration algorithms. Also, I assume that the field passive seismic data fulfills the model of short source functions unevenly dispersed along the time axis of the duration of data collection.

	operations
Multiply	$\nu n_x^2 n_{ts}$
Gather Mig.	$(X n_z n_x) n_{ts} \nu n_x^2 \log n_x$
Raw Mig.	$(X n_z n_x) n_{ts} n_x \log n_x$

Table 1: Operation counts for migrating passive seismic data. X represents the a scalar multiplier of migration overhead. n_x is the number of receivers. n_t is the length of the time axis of the passive experiment. n_{ts} is the length of the time axis associated with the two-way travelttime to the deepest reflector of interest.

With these costs in mind, the ratio of the sum of the first two rows to the last must be balanced to decide which choice requires the least amount of computation operations. When $\nu = 1/n_x$, the costs of producing an image by either method is the same. The meaning of this situation is shot-gathers of one trace, *i.e.* a constant-offset (post-stack sized) migration. Thus, the passive seismic experiment acts similarly to a natural phase-encoding of active seismic shot-gathers that (Romero et al., 2000) explains as a method to reduce the cost of shot-profile migration schemes. This can be thought of as performing a full prestack migration for the cost of a zero-offset migration.

Therefore, if it is appropriate to assume that potential subsurface seismic sources are reasonably short in duration, and that the length of the passive experiment is dictated by the requirement to collect a sufficient number of them to illuminate our image space, we can save substantial computation cost, orders of magnitude, by migrating the raw data directly. Even if one is concerned that such a severe decimation of the frequency axis might be detrimental, many safety multiples can be carried without affecting the speed-up of direct migration of the data.

CONCLUSION

I have used Fourier sampling theory to apply a time window to correlated passive seismic data. Under a reasonable (I believe) set of assumptions, the initial Fourier transform of the raw data acts to redistribute the energy of late time arrivals toward the origin of the frequency axis, which effectively handles the zero-time problem of passive imaging. The multiplication (by conjugate traces) handles the waveform comparison problem.

In practice, we can avoid many calculations associated with the long time axis of transmission wavefields by exploiting the fact that the fine increments of the Fourier domain contain the information in the late times of the input data. Acknowledging that we are incapable of using the late time correlations within the framework of conventional seismic processing algorithms, this information can (and probably should) be removed after correlation. Conveniently, since the correlation is performed in the frequency domain with point-to-point multiplications, this extra information can be removed immediately upon its initial transform to the Fourier domain, and before any further processing is performed. This holds true for direct migration or manufacture of modeled shot-gathers from a transmission wavefield.

REFERENCES

- Artman, B., Draganov, D., Wapenaar, C., and Biondi, B., 2004, Direct migration of passive seismic data: 66th Conference and Exhibition, EAGE, Extended abstracts, P075.
- Romero, L. A., Ghiglia, D. C., Ober, C. C., and Morton, S. A., 2000, Phase encoding of shot records in prestack migration: *Geophysics*, **65**, no. 02, 426–436.
- Schuster, G., Yu, J., Sheng, J., and Rickett, J., 2004, Interferometric/daylight seismic imaging: *Geophysics Journal International*, **157**, 838–852.



Short Note

Converted-wave common-azimuth migration

*Daniel A. Rosales and Biondo Biondi*¹

INTRODUCTION

Multicomponent seismic data may hold a wealth of information for oil exploration and reservoir characterization. Multicomponent seismic contains energy from converted waves that is not seen in conventional seismic; therefore, the development of new techniques to process converted-wave data is important. Much progress has been made in many areas of converted-wave seismic processing, such as stacking, DMO, migration and velocity analysis (Tessmer and Behle, 1988; Iverson et al., 1989; Huub Den Rooijen, 1991; Alfaraj, 1992; Harrison and Stewart, 1993). However, more advanced techniques for single-mode PP seismic still have few converted-wave counterparts.

Common-azimuth migration is an efficient and robust technique for obtaining accurate single-mode PP 3-D seismic images. This technique takes advantage of the reduced dimensionality of the computational domain. It assumes that the data have only the zero cross-line offset; that is, all the traces in the data share the same azimuth (Biondi and Palacharla, 1996). Due to the growing number of 3-D multicomponent seismic data sets in areas where an accurate processing is required to obtain better subsurface images and/or estimate rock properties, wavefield-based continuation methods, such as common-azimuth migration, for converted-mode data are of great importance and are very much needed in the oil industry today.

Converted-wave common-azimuth migration is very similar to conventional common-azimuth migration. However, it uses different propagation velocities for different wavefields. We compare the differences between single-mode and converted-mode common-azimuth migration.

CONVERTED-WAVE COMMON-AZIMUTH MIGRATION

Point-scatterer geometry is a good starting point to discuss converted-waves prestack common-azimuth migration. The equation for the travel time is the sum of a downgoing travel path with

¹email: daniel@sep.stanford.edu, biondo@sep.stanford.edu

P-velocity (v_p) and an upcoming travel path with S-velocity (v_s),

$$t = \frac{\sqrt{z^2 + \|\mathbf{s} - \mathbf{x}\|^2}}{v_p} + \frac{\sqrt{z^2 + \|\mathbf{g} - \mathbf{x}\|^2}}{v_s}, \quad (1)$$

where \mathbf{s} and \mathbf{g} represent the source and receiver vector locations and \mathbf{x} is the point-scatterer sub-surface position. Common-azimuth migration is a wavefield-based, downward-continuation algorithm. The algorithm is based on a recursive solution of the one-way wave equation (Claerbout, 1985). The basic continuation step used to compute the wavefield at depth $z + \Delta z$ from the wavefield at depth z can be expressed in the frequency-wavenumber domain as follows:

$$P_{z+\Delta z}(\omega, \mathbf{k}_m, \mathbf{k}_h) = P_z(\omega, \mathbf{k}_m, \mathbf{k}_h) e^{ik_z \Delta z}. \quad (2)$$

After each depth-propagation step, the propagated wavefield is equivalent to the data that would have been recorded if all sources and receivers were placed at the new depth level (Schultz and Sherwood, 1980). The wavefields are propagated with two different velocities, a P-velocity for the downgoing wavefield and an S-velocity for the upcoming wavefield. The basic downward continuation for converted waves is performed by applying the Double-Square-Root (DSR) equation:

$$k_z(\omega, \mathbf{k}_s, \mathbf{k}_g) = \text{DSR}(\omega, \mathbf{k}_s, \mathbf{k}_g) = -\sqrt{\frac{\omega^2}{v_p^2(\mathbf{s}, z)} - \mathbf{k}_s^2} - \sqrt{\frac{\omega^2}{v_s^2(\mathbf{g}, z)} - \mathbf{k}_g^2}, \quad (3)$$

or in midpoint-offset coordinates,

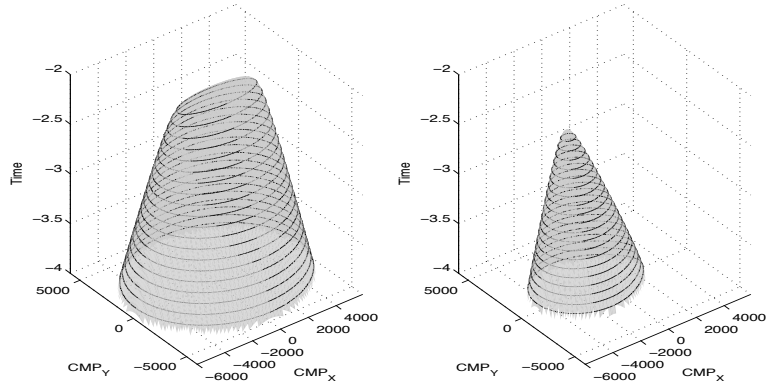
$$\text{DSR}(\omega, \mathbf{k}_m, \mathbf{k}_h) = -\sqrt{\frac{\omega^2}{v_p^2(\mathbf{s}, z)} - \frac{1}{4}(\mathbf{k}_m - \mathbf{k}_h) \cdot (\mathbf{k}_m - \mathbf{k}_h)} - \sqrt{\frac{\omega^2}{v_s^2(\mathbf{g}, z)} - \frac{1}{4}(\mathbf{k}_m + \mathbf{k}_h) \cdot (\mathbf{k}_m + \mathbf{k}_h)}. \quad (4)$$

The common-azimuth downward-continuation operator takes advantage of the reduced dimensionality of the data space, which results from using a common-azimuth resorting of the data. Rosales and Biondi (2004) discuss how to do this resorting for converted-wave data. The general continuation operator can then be expressed as follows (Biondi and Palacharla, 1996):

$$\begin{aligned} P_{z+\Delta z}(\omega, \mathbf{k}_m, k_{x_h}, y_h = 0) &= \int_{-\infty}^{+\infty} dk_{y_h} P_z(\omega, \mathbf{k}_m, k_{x_h}, y_h = 0) e^{-ik_z \Delta z} \\ &= P_z(\omega, \mathbf{k}_m, k_{x_h}, y_h = 0) \left\{ \int_{-\infty}^{+\infty} dk_{y_h} e^{-ik_z \Delta z} \right\} \\ &\approx P_z(\omega, \mathbf{k}_m, k_{x_h}, y_h = 0) A(\omega, \mathbf{k}_m, k_{x_h}) e^{-i\hat{k}_z \Delta z}. \end{aligned} \quad (5)$$

Since common-azimuth data is independent of k_{y_h} , the integral can be pulled inside and analytically approximated by the stationary-phase method (Bleistein, 1984). The application of the stationary-phase method is based on a high-frequency approximation. By geometrical means we derive the stationary-path approximation for converted waves.

Figure 1: Summation surfaces for a constant medium with a P-velocity of 3000 m/s, an S velocity of 1500 m/s, and an offset of 2 km. Left: PP summation surface. Right: PS summation surface. daniel1-impcheops [CR]



The expression for \hat{k}_z comes from substituting the stationary-path approximation into the expression for the full DSR of equation (4):

$$\hat{k}_z = \text{DSR}[\omega, \mathbf{k}_m, k_{hx}, \hat{k}_{hy}(z), z] \quad (6)$$

where

$$\hat{k}_{hy}(z) = k_{ym} \frac{\sqrt{\frac{\omega^2}{v_s^2(\mathbf{g}, z)} - \frac{1}{4}(k_{xm} + k_{xh})^2} - \sqrt{\frac{\omega^2}{v_p^2(\mathbf{s}, z)} - \frac{1}{4}(k_{xm} - k_{xh})^2}}{\sqrt{\frac{\omega^2}{v_s^2(\mathbf{g}, z)} - \frac{1}{4}(k_{xm} + k_{xh})^2} + \sqrt{\frac{\omega^2}{v_p^2(\mathbf{s}, z)} - \frac{1}{4}(k_{xm} - k_{xh})^2}}. \quad (7)$$

IMPULSE RESPONSE

Figure 1 presents the summation surfaces [equation (1)] for an impulse response at a depth of 500 m, a P-velocity of 3000 m/s, an S-velocity of 1500 m/s, and an in-line offset of 3000 m. The left panel shows the single-mode PP summation surface, and the right panel shows the converted-mode PS summation surface. Similarly, Figure 2 shows the spreading surfaces; that is, the theoretical solution for depth of equation (1), Appendix A shows the calculations. The left panel presents the single-mode PP spreading surface, the center panel shows the converted-mode PS spreading surface, and the right panel compares the contour lines for both spreading surfaces.

Figure 3 shows the common-azimuth impulse response for a constant P-velocity of 2500 m/s, and a constant S-velocity of 1250 m/s, and an in-line offset of 200 m. The left panel exhibits the response for the single-mode PP common-azimuth migration operator, and the right panel exhibits the response for the converted-mode PS migration operator.

CONCLUSIONS

We presented the converted-mode PS 3-D common-azimuth migration operator. The difference between this operator and the single-mode PP operator is the use of two different veloc-

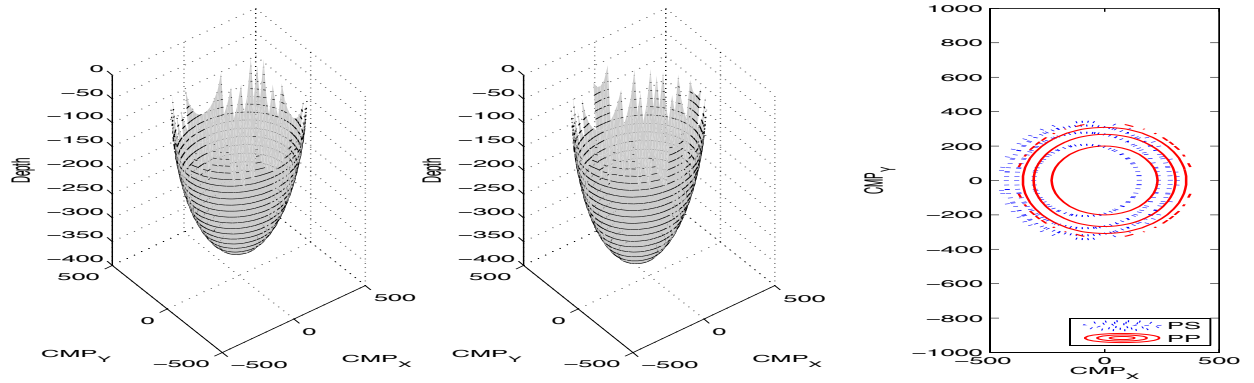
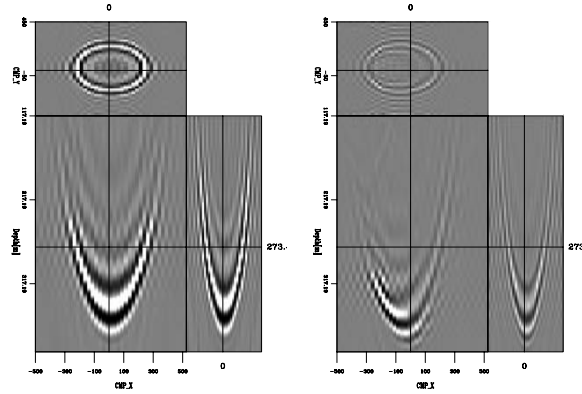


Figure 2: Spreading surfaces for an impulse at 0.320 s PP traveltime and 0.480 s PS traveltime, an offset of 200 m, and assuming constant P-velocity of 2500 m and S-velocity of 1250 m. Left: PP spreading surface. Center: PS spreading surface. Right: contour lines comparison from both spreading surfaces. [daniel1-imptheory](#) [CR]

Figure 3: Impulse response for a point diffractor at 0.320 s PP traveltime and 0.480 s PS traveltime, and in a constant-velocity medium with a P-velocity of 2500 m/s and S-velocity of 1250 m/s. Left: presents the single-mode PP. Right: panel presents the converted-mode PS. [daniel1-imp.resp](#) [CR]



ity fields. Therefore, a more careful implementation is needed to ensure the correct velocity model. We demonstrate that the subsurface area covered by the PS common-azimuth migration operator is different than that covered by the PP common-azimuth migration operator; therefore, only the area that the two surfaces share can be used for rock-properties analysis based on the two complementary images. This might have important impacts on the reservoir-characterization process.

APPENDIX A

This section derives the exact solution for the common azimuth prestack migration for a reflecting point within an homogeneous Earth. The total travel time is

$$t_D = \frac{\sqrt{z_\xi^2 + \|\xi_{xy} - \mathbf{m} + h_D\|^2}}{v_s} + \frac{\sqrt{z_\xi^2 + \|\xi_{xy} - \mathbf{m} - h_D\|^2}}{v_p}. \quad (\text{A-1})$$

The following procedure shows how to go from $t_D(z_\xi, \mathbf{m}, \mathbf{h})$ to $z_\xi(t_D, \mathbf{m}, \mathbf{h})$:

$$t_D v_p = \phi \sqrt{z_\xi^2 + \|\xi_{xy} - \mathbf{m} + h_D\|^2} + \sqrt{z_\xi^2 + \|\xi_{xy} - \mathbf{m} - h_D\|^2}, \quad (\text{A-2})$$

where ϕ represents the P-to-S velocities ratio. If we make the following definitions,

$$\begin{aligned} 2A &= t_D v_p, \\ \alpha &= z_\xi + \|\xi_{xy} - \mathbf{m} + h_D\|^2, \\ \beta &= z_\xi + \|\xi_{xy} - \mathbf{m} - h_D\|^2, \end{aligned} \quad (\text{A-3})$$

(A-2) becomes

$$2A = \phi \sqrt{\alpha} + \sqrt{\beta}. \quad (\text{A-4})$$

We square both sides to get a new equation with only one square root:

$$4A^2 - (\phi^2 \alpha + \beta) = 2\phi \sqrt{\alpha\beta}. \quad (\text{A-5})$$

Squaring again to eliminate the square root, and combining elements, we obtain

$$16A^4 - 8A^2(\phi^2 \alpha + \beta) + (\phi^2 \alpha - \beta)^2 = 0. \quad (\text{A-6})$$

This expression is a 4th degree polynomial in z_ξ ; which is:

$$\begin{aligned} 0 &= 16A^4 - 8A^2((\phi^2 + 1)z_\xi^2 + \phi^2(\|\xi_{xy} - \mathbf{m} + h_D\|^2) + (\|\xi_{xy} - \mathbf{m} - h_D\|^2)^2) \\ &+ ((\phi^2 - 1)z_\xi^2 + \phi^2(\|\xi_{xy} - \mathbf{m} + h_D\|^2)^2 - (\|\xi_{xy} - \mathbf{m} - h_D\|^2)^2). \end{aligned} \quad (\text{A-7})$$

This can also be written as follows

$$\begin{aligned} 0 &= (\phi^2 - 1)^2 z_\xi^4 \\ &+ (2\phi^2(\|\xi_{xy} - \mathbf{m} + h_D\|^2)^2 - (\|\xi_{xy} - \mathbf{m} - h_D\|^2)^2(\phi^2 - 1) - 8(t_D v_p)^2(\phi^2 + 1))z_\xi^2 \\ &+ 16(t_D v_p)^4 - 8(t_D v_p)^2\phi^2(\|\xi_{xy} - \mathbf{m} + h_D\|^2)^2 + (\|\xi_{xy} - \mathbf{m} - h_D\|^2)^2 \\ &+ (\phi^2(\|\xi_{xy} - \mathbf{m} + h_D\|^2)^2 - (\|\xi_{xy} - \mathbf{m} - h_D\|^2)^2)^2 \end{aligned} \quad (\text{A-8})$$

This polynomial equation has 4 solutions, which take the following well known form:

$$z_\xi = \pm \sqrt{\frac{-b \pm \sqrt{b^2 - 4ac}}{2a}}, \quad (\text{A-9})$$

where

$$\begin{aligned} a &= (\phi^2 - 1)^2, \\ b &= 2\phi^2(\|\xi_{xy} - \mathbf{m} + h_D\|^2)^2 - (\|\xi_{xy} - \mathbf{m} - h_D\|^2)^2(\phi^2 - 1) - 8(t_D v_p)^2(\phi^2 + 1), \\ c &= 16(t_D v_p)^4 - 8(t_D v_p)^2\phi^2(\|\xi_{xy} - \mathbf{m} + h_D\|^2)^2 + (\|\xi_{xy} - \mathbf{m} - h_D\|^2)^2 \\ &+ (\phi^2(\|\xi_{xy} - \mathbf{m} + h_D\|^2)^2 - (\|\xi_{xy} - \mathbf{m} - h_D\|^2)^2)^2. \end{aligned} \quad (\text{A-10})$$

REFERENCES

- Alfaraj, M., 1992, Transformation to zero offset for mode converted waves by Fourier transform: 62nd Annual Internat. Mtg., Society Of Exploration Geophysicists, Expanded Abstracts, 974–977.
- Biondi, B., and Palacharla, G., 1996, 3-D prestack migration of common-azimuth data: *Geophysics*, **61**, 1822–1832.
- Bleistein, N., 1984, *Mathematical methods for wave phenomena*: Academic Press.
- Claerbout, J. F., 1985, *Imaging the earth's interior*: Blackwell Scientific Publications.
- Harrison, M. P., and Stewart, R. R., 1993, Poststack migration of P-SV seismic data: *Geophysics*, **58**, no. 8, 1127–1135.
- Huub Den Rooijen, P. G. M., 1991, Stacking of P-SV seismic reflection data using dip move-out: *Geophysical Prospecting*, **39**, no. 4, 585–598.
- Iverson, W. P., Fahmy, B. A., and Smithson, S. B., 1989, VpVs from mode-converted P-SV reflections: *Geophysics*, **54**, no. 7, 843–852.
- Rosales, D. A., and Biondi, B., 2004, Acquisition geometry regularization for multicomponent data: 74rd Annual Internat. Mtg., Society Of Exploration Geophysicists, Expanded Abstracts, 1162–1165.
- Schultz, P. S., and Sherwood, J. W. C., 1980, Depth migration before stack: *Geophysics*, **45**, 376–393.
- Tessmer, G., and Behle, A., 1988, Common reflection point data-stacking technique for converted waves: *Geophysical Prospecting*, **36**, no. 5, 671–688.

Converted-mode angle-domain common-image gathers for migration velocity analysis

Daniel A. Rosales and Biondo Biondi¹

ABSTRACT

Common-image gathers are very useful for velocity and petrophysical analysis. Wavefield-extrapolation methods produce Angle-Domain Common-Image Gathers (ADCIGs). For the conventional PP case, ADCIGs are a function of the opening angle. The representation of ADCIGs for PS data (PS-ADCIGs) is more elaborate than for conventional ADCIGs. In PS-ADCIGs, the P-to-S velocity ratio is a major variable in transforming the subsurface offset to the opening angle, and in transforming this opening angle to either the P-incidence or the S-reflection angle. Numerical studies show that when the P-to-S velocity ratio and image midpoint information are not incorporated the error in computing PS-ADCIGs is enough to introduce artifacts in the velocity model.

INTRODUCTION

Imaging is the combined process of migration and velocity analysis. The final image provides two important pieces of information about the subsurface: its structure and some of its rock properties. To obtain a reliable image, we need a reliable velocity model. Therefore, the image process becomes a combined procedure between migration and migration velocity analysis.

The final image by itself provides information about the accuracy of the velocity model. This information is present in the redundancy of the seismic data, that is in non-zero-offset images. The information is distributed along a 3-dimensional image space, for 2D seismic data; the coordinates of this space are $I(z_\xi, m_\xi, h)$. The subsets of this image for a fixed image point (m_ξ) with coordinates (z_ξ, h) are known as common-image gathers (CIG), or common-reflection-point gathers (CRP). If the CIGs are a function of (z_ξ, h) , the gathers are also referred to offset-domain common-image gathers (ODCIG). These gathers can also be expressed in terms of an opening angle γ , by transforming the offset axis (h) into the opening angle (γ) to obtain a common image gather with coordinates (z_ξ, γ) ; these gathers are known as Angle-Domain Common-Image Gathers (ADCIG) (de Bruin et al., 1990; Prucha et al., 1999; Brandsberg-Dahl et al., 1999; Rickett and Sava, 2002; Sava and Fomel, 2003; Biondi and Symes, 2004).

¹email: daniel@sep.stanford.edu, biondo@sep.stanford.edu

There are two kinds of ODCIGs: those produced by Kirchhoff migration, and those produced by wavefield-extrapolation migration, referred to from now on as wave-equation migration. There is a conceptual difference in the offset dimension between these two kinds of gathers. For Kirchhoff ODCIGs, the offset is a data parameter ($h = h_D$), and involves the concept of flat gathers. For wave-equation ODCIGs, the offset dimension is a model parameter ($h = h_\xi$), and involves the concept of focused events. In this paper, we will refer to these gathers as subsurface offset-domain common-image gathers (SODCIG).

There are problems observed with ODCIGs, which can be alleviated by parameterizing the offset axis into an angle axis to form angle-domain common image-gathers. Unlike ODCIGs, ADCIGs produced with either method have similar characteristics, since they describe the reflectivity as a function of the angle at the reflector.

Depending on the seismic experiment we are analyzing, the coordinates of the image space possess different information relevant to the experiment. We refer to a conventional seismic reflection experiment, where the source and the receiver have the same type of wave, as *single-mode* case. The transformation from ODCIGs to ADCIGs is a well-known process in the literature, and in this case the angle axis represents the true reflection angle.

A seismic experiment where the source and the receiver process different types of waves is known as multi-component seismic, throughout this paper, we refer to this experiment as *converted-mode* case, as for example the conversion from P wave into an S wave at the reflection point. This paper discusses the common-image gathers for this kind of experiment, focusing mainly on SODCIGs and their accurate transformation into ADCIGs. We validate our results by generalizing the concepts of Kirchhoff migration.

A final side product of our analysis is the ability to separate the final image into two parts, each one corresponding to a distinctive wave. Throughout this process, the velocity ratio between the different velocities plays an important role in the transformation. We present and analyze the kinematics of our equations and present some synthetic results.

KINEMATIC EQUATIONS

This section describes the kinematic equation that transforms a subsurface offset-domain CIG to an opening-angle-domain CIG, for the converted-mode case. The derivation follows the well-known equations for apparent slowness in a constant-velocity medium in the neighborhood of the reflection/conversion point. Our derivation is consistent with those presented by Fomel (1996); Sava and Fomel (2000); and Biondi (2005).

The expressions for the partial derivatives of the total traveltime with respect to the image

point coordinates are as follows (Rosales and Rickett, 2001a):

$$\begin{aligned}\frac{\partial t}{\partial m_\xi} &= S_s \sin \beta_s + S_r \sin \beta_r, \\ \frac{\partial t}{\partial h_\xi} &= -S_s \sin \beta_s + S_r \sin \beta_r, \\ -\frac{\partial t}{\partial z_\xi} &= S_s \cos \beta_s + S_r \cos \beta_r.\end{aligned}\quad (1)$$

Where S_s and S_r are the slowness (inverse of velocity) at the source and receiver locations. Figure 1 illustrates all the angles in this discussion. The angle β_s is the direction of the wave propagation for the source, and the angle β_r is the direction of the wave propagation for the receiver. Through these set of equations, we obtain:

$$\begin{aligned}-\frac{\partial z_\xi}{\partial h_\xi} &= \frac{S_r \sin \beta_r - S_s \sin \beta_s}{S_r \cos \beta_r + S_s \cos \beta_s}, \\ -\frac{\partial z_\xi}{\partial m_\xi} &= \frac{S_s \sin \beta_s + S_r \sin \beta_r}{S_s \cos \beta_s + S_r \cos \beta_r}.\end{aligned}\quad (2)$$

We define two angles, α and γ , to relate β_s and β_r as follows:

$$\alpha = \frac{\beta_r + \beta_s}{2}, \quad \text{and} \quad \gamma = \frac{\beta_r - \beta_s}{2}.\quad (3)$$

The meaning of the angles α and γ will become clear later in the paper; for now, we will refer to γ as the *full-aperture* angle. Through the change of angles presented on equation (3), and by following basic trigonometric identities, we can rewrite equations (2) as follows:

$$\begin{aligned}-\frac{\partial z_\xi}{\partial h_\xi} &= \frac{\tan \gamma + \mathcal{J} \tan \alpha}{1 - \mathcal{J} \tan \alpha \tan \gamma}, \\ -\frac{\partial z_\xi}{\partial m_\xi} &= \frac{\tan \alpha + \mathcal{J} \tan \gamma}{1 - \mathcal{J} \tan \gamma \tan \alpha}\end{aligned}\quad (4)$$

where,

$$\mathcal{J} = \frac{S_r - S_s}{S_r + S_s} = \frac{\phi - 1}{\phi + 1},\quad (5)$$

Figure 1: Angle definition for the kinematic equation of converted mode ADCIGs daniel2-angles [NR]

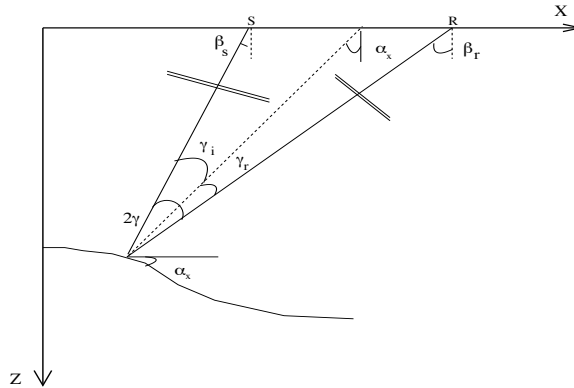
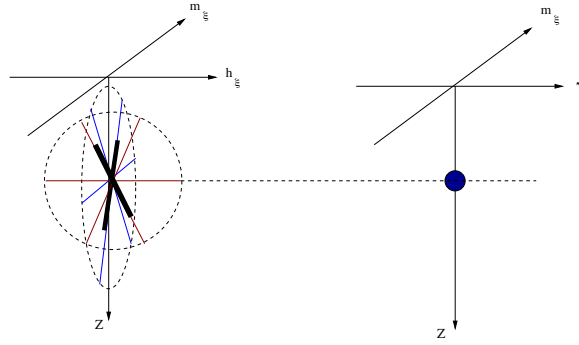


Figure 2: Slant stack angle transformation from SODCIGs to ADCIGs. This transformation allows lateral and vertical variation of \mathcal{S} . [daniel2-sketch](#) [NR]



and ϕ is the velocity ratio, as for example the P-to-S velocity ratio. This leads to quadratic equations for $\tan \alpha$ and $\tan \gamma$ as follows:

$$\begin{aligned} \left[\frac{\partial z_\xi}{\partial m_\xi} \mathcal{S} - \frac{\partial z_\xi}{\partial h_\xi} \mathcal{S}^2 \right] \tan^2 \gamma + [1 - \mathcal{S}^2] \tan \gamma + \frac{\partial z_\xi}{\partial m_\xi} \mathcal{S} - \frac{\partial z_\xi}{\partial h_\xi} &= 0, \\ \left[\frac{\partial z_\xi}{\partial h_\xi} \mathcal{S} - \frac{\partial z_\xi}{\partial m_\xi} \mathcal{S}^2 \right] \tan^2 \alpha + [1 - \mathcal{S}^2] \tan \alpha + \frac{\partial z_\xi}{\partial h_\xi} \mathcal{S} - \frac{\partial z_\xi}{\partial m_\xi} &= 0. \end{aligned} \quad (6)$$

Each equation has two solutions, which are:

$$\begin{aligned} -\tan \gamma &= \frac{\mathcal{S}^2 - 1 \pm \sqrt{(1 - \mathcal{S}^2)^2 - 4 \left[\frac{\partial z_\xi}{\partial m_\xi} \mathcal{S} - \frac{\partial z_\xi}{\partial h_\xi} \mathcal{S}^2 \right] \left[\frac{\partial z_\xi}{\partial m_\xi} \mathcal{S} - \frac{\partial z_\xi}{\partial h_\xi} \right]}}{2 \left[\frac{\partial z_\xi}{\partial m_\xi} \mathcal{S} - \frac{\partial z_\xi}{\partial h_\xi} \mathcal{S}^2 \right]}, \\ -\tan \alpha &= \frac{\mathcal{S}^2 - 1 \pm \sqrt{(1 - \mathcal{S}^2)^2 - 4 \left[\frac{\partial z_\xi}{\partial h_\xi} \mathcal{S} - \frac{\partial z_\xi}{\partial m_\xi} \mathcal{S}^2 \right] \left[\frac{\partial z_\xi}{\partial h_\xi} \mathcal{S} - \frac{\partial z_\xi}{\partial m_\xi} \right]}}{2 \left[\frac{\partial z_\xi}{\partial h_\xi} \mathcal{S} - \frac{\partial z_\xi}{\partial m_\xi} \mathcal{S}^2 \right]}. \end{aligned} \quad (7)$$

The first of equation (7) provides the transformation from subsurface offset-domain CIG into angle-domain CIG for the converted-mode case. This theory is valid under the assumption of constant velocity. However, it remains valid in a differential sense in an arbitrary-velocity medium, by considering that h_ξ is the subsurface half offset. Therefore, the limitation of constant velocity is on the neighborhood of the image. For $\mathcal{S}(m_\xi, z_\xi)$, it is important to consider that every point of the image $I(z_\xi, m_\xi, h_\xi)$ is related to a point on the velocity model with the same coordinates.

In order to implement this equation, we observe that this can be done by an slant-stack transformation as presented on Figure 2. Note that the contribution along the midpoints is a correction factor needed in order to perform the transformation. This allows us to do the transformation from SODCIGs to ADCIGs including the lateral and vertical variations of \mathcal{S} .

A Fourier domain look

It is also possible to implement the transformation to full-aperture angle in the Fourier domain. Although this transformation does not take into account the lateral and vertical variations of

\mathcal{S} , it's still an interesting exercise. We can link this theory with Fourier transform by knowing that:

$$\frac{\partial t}{\partial m_\xi} = \frac{k_{m_\xi}}{\omega}, \quad \frac{\partial t}{\partial z_\xi} = \frac{k_{z_\xi}}{\omega}, \quad \text{and} \quad \frac{\partial t}{\partial h_\xi} = \frac{k_{h_\xi}}{\omega} \quad (8)$$

From equations (8), it is well known that

$$\frac{\partial z_\xi}{\partial h_\xi} = \frac{k_{h_\xi}}{k_{z_\xi}}, \quad \text{and} \quad \frac{\partial z_\xi}{\partial m_\xi} = \frac{k_{m_\xi}}{k_{z_\xi}}. \quad (9)$$

Therefore, the Fourier equivalent for equations (7) is

$$\begin{aligned} -\tan \gamma &= \frac{\mathcal{S}^2 - 1 \pm \sqrt{(1 - \mathcal{S}^2)^2 - 4 \left[\frac{k_{m_\xi}}{k_{z_\xi}} \mathcal{S} - \frac{k_{h_\xi}}{k_{z_\xi}} \mathcal{S}^2 \right] \left[\frac{k_{m_\xi}}{k_{z_\xi}} \mathcal{S} - \frac{k_{h_\xi}}{k_{z_\xi}} \right]}}{2 \left[\frac{k_{m_\xi}}{k_{z_\xi}} \mathcal{S} - \frac{k_{h_\xi}}{k_{z_\xi}} \mathcal{S}^2 \right]}, \\ -\tan \alpha &= \frac{\mathcal{S}^2 - 1 \pm \sqrt{(1 - \mathcal{S}^2)^2 - 4 \left[\frac{k_{h_\xi}}{k_{z_\xi}} \mathcal{S} - \frac{k_{m_\xi}}{k_{z_\xi}} \mathcal{S}^2 \right] \left[\frac{k_{h_\xi}}{k_{z_\xi}} \mathcal{S} - \frac{k_{m_\xi}}{k_{z_\xi}} \right]}}{2 \left[\frac{k_{h_\xi}}{k_{z_\xi}} \mathcal{S} - \frac{k_{m_\xi}}{k_{z_\xi}} \mathcal{S}^2 \right]}. \end{aligned} \quad (10)$$

Equations (10) can be used to transform SODCIGs into *full-aperture* ADCIGs through stretching of the offset and midpoint axes, but this is only valid for a velocity-ratio function \mathcal{S} that is constant along the image ($I(z_\xi, m_\xi, h_\xi)$).

Transformation into independent angles

From equation (3) we established a relation between the propagation angles for the down-going and up-going plane-waves, β_s and β_r , respectively. Now, from Figure 1 it is easy to see that the propagation angles are related to: 1) the incidence angle of the down-going plane wave into the reflector (γ_i); 2) the reflection angle of the up-going plane wave (γ_r); and the structural dip (α_x). The relation among all the angles is

$$\beta_s = \alpha_x - \gamma_i, \quad \text{and} \quad \beta_r = \alpha_x + \gamma_r. \quad (11)$$

Combining equation (3) and (11), we can see the direct relation between the angles that we compute with relations (7) and/or (10) and the real structural dip, the incidence angle, and the reflection angle. That is:

$$\begin{aligned} 2\gamma &= \gamma_r + \gamma_i, \\ 2\alpha &= 2\alpha_x + (\gamma_r - \gamma_i). \end{aligned} \quad (12)$$

It is easy to note that the opening angle γ is the reflection angle and α is the geological dip when $\gamma_i = \gamma_r$, which is only valid for the single-mode case.

With these equations and Snell's law, we can convert the *full-aperture* angle (γ) obtained with equation (7) or (10) into the incidence angle (γ_i) or the reflection angle (γ_r):

$$\begin{aligned}\tan \gamma_i &= \frac{\phi \sin 2\gamma}{1 + \phi \cos 2\gamma}, \\ \tan \gamma_r &= \frac{\sin 2\gamma}{\phi + \cos 2\gamma}.\end{aligned}\quad (13)$$

Appendix A presents a full derivation of the same equations but with the perspective of the Kirchhoff approach. The reader is encourage to follow that demonstration.

NUMERICAL ANALYSIS

First, we analyze which one of the two solutions for $\tan \gamma$ is appropriate. For this, we plot both solutions for different values of the velocity ratio ϕ . Figure 3 presents such result. The right panel presents the positive solution surface, the left panel presents the negative one. The positive solution is more stable than the negative solution. Note that the solution for the quadratic system (7) is singular when $\phi = 1$. Thus, system (7) reduces to the known relation for single-mode case. The solid blue line at $\phi = 1$ represents this case. The negative solution is not well behaved for any of the values of ϕ . Figure 4 shows the first of equations (4), that is the

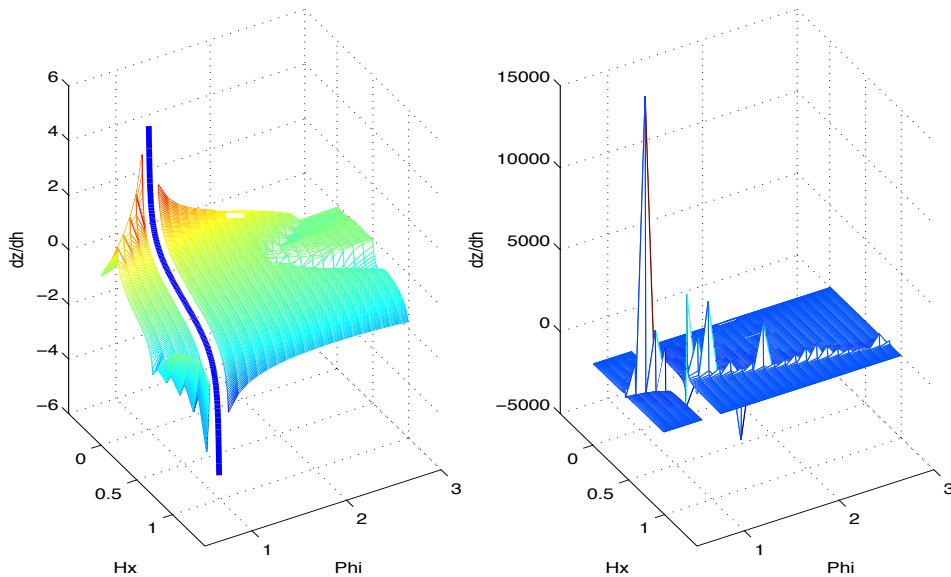


Figure 3: Both solutions for $\tan \gamma$ on equation (7). Left: Positive solution, the blue line at $\phi = 1$ corresponds to the single-mode case. Right: Negative solution. [daniel2-ang_cwv_2sols](#) [CR]

expression for the *full-aperture* angle as a function of α and the velocity ratio, ϕ . Remember that for the converted-mode case, α is related to the geologic dip (equation (12)), but it's not the dip itself. In order to understand better the previous plot, we take a look at Figure 5. This figure is a cut along $\phi = 2$ on Figure 4 (dotted line) and it's compared against the conventional

approach, which is $\tan \gamma$ equals the partial derivative of depth with respect to offset. If we omit the contribution of α and ϕ , we introduce a considerable error in the transformation from SODCIGs into ADCIGs for the converted-mode case. The first of equations (4) establishes

Figure 4: Full-aperture angle (γ) as a function of α and ϕ , from the first of equation (4).

`daniel2-ang_cwv_alpha` [CR]

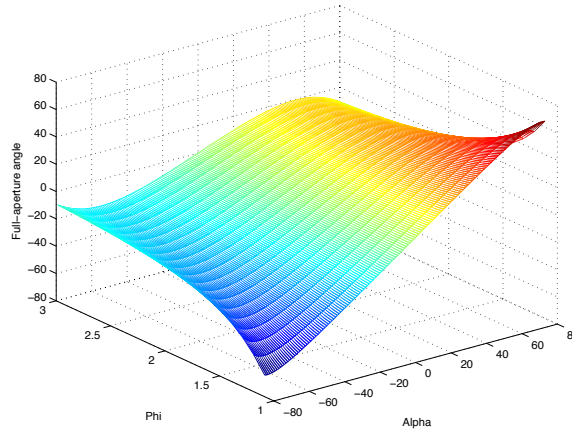
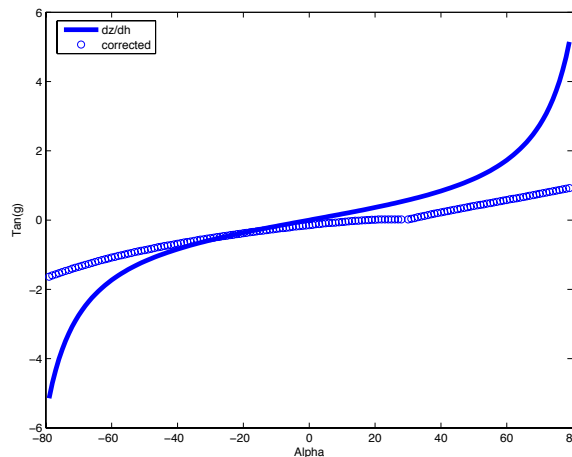


Figure 5: Difference between the conventional approach for $\tan \gamma$ (solid line) versus the transformation with the correction for α and ϕ (dotted line). This is a cut for $\phi = 2$ on Figure 4.

`daniel2-ang_cwv_diff` [CR]



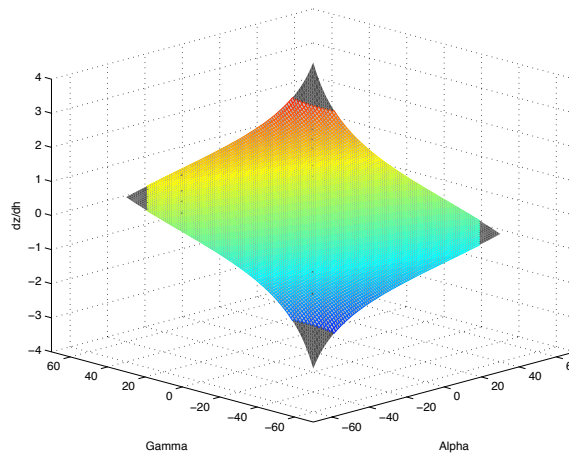
a relationship between $\tan \gamma$ and the partial derivative of depth with respect to offset. We derive this relation following a wave-equation approach. Appendix A shows that we can arrive at the same conclusion following an integral summation approach. Figure 6 summarizes both approaches. This figure presents two surfaces, both of them correspond to $\partial z / \partial h$. The color surface represents the computation with the integral summation approach (Appendix B); and the black surface represents the computation with the wave-equation approach (equation (4)). Both surfaces have a perfect match, this strongly suggests that equations (4) is accurate, and must be followed for an appropriate transformation from SODCIGs into ADCIGs for converted-mode seismic.

Synthetic model

A simple synthetic was created with constant velocity of $v_p = 2000$ and $v_s = 1000$, and varying dips. Figure 7 shows on the left the reflectivity model, and on the middle and right panels, one

Figure 6: Wave-equation approach compared with Integral summation approach. Both of them arrive to the same surface.

`daniel2-ang_cwv_wei_surf_comp`
[CR]



single mode PP CMP gather and one converted mode PS CMP gather. The PP-CMP gather presents four reflection hyperbolas, all of them centered at zero-offset. The PS-CMP gather also presents the four reflection hyperbolas, corresponding to the same events as in the PP-CMP gather, however, they are not centered at zero-offset, as it is expected for the converted-mode case. Also, the time axis for both synthetic data sets is different. The events on the PS CMP gather take longer to arrive, this is also a characteristic for the converted-mode case. The polarity flip is not included in this model, since it has been already discussed by Rosales and Rickett (2001b).

After wave-equation migration with the correct velocity model, the image is perfectly focused at zero subsurface offset, displayed on the left panel of Figure 8. Note, that both PP and PS sections, had the same SODCIG.

The middle and right panels of Figures 8 present the result of the transformation from SODCIGs into the single-mode ADCIG (center panel), and the converted-mode ADCIG (right panel). It is possible to observe that the angle range (i.e. before the start of the artifacts due to the transformation in the Fourier domain) for the converted-mode ADCIG is longer than for the single-mode ADCIG, as it is expected, since the angle-information contains both the incidence and reflection angle information.

CONCLUSIONS AND FUTURE WORK

The accurate transformation from subsurface offset-domain CIGs into angle-domain CIGs for the converted-mode case requires both the information along the midpoint axis and the velocity ratio. Omitting this information yields to errors in the transformation that might transform in wrong velocity updates. Two separate approaches to obtain the relation between the subsurface offset and the *full-aperture* angle corroborates the accuracy of our formulation.

For the converted-mode case, the angle axis of the final image ($I(z_\xi, m_\xi, \gamma)$), after the transformation, is neither the incidence nor reflection angle, but the average of both. The *full-aperture* angle gathers can be transformed into two separate angle gathers, each one represent-

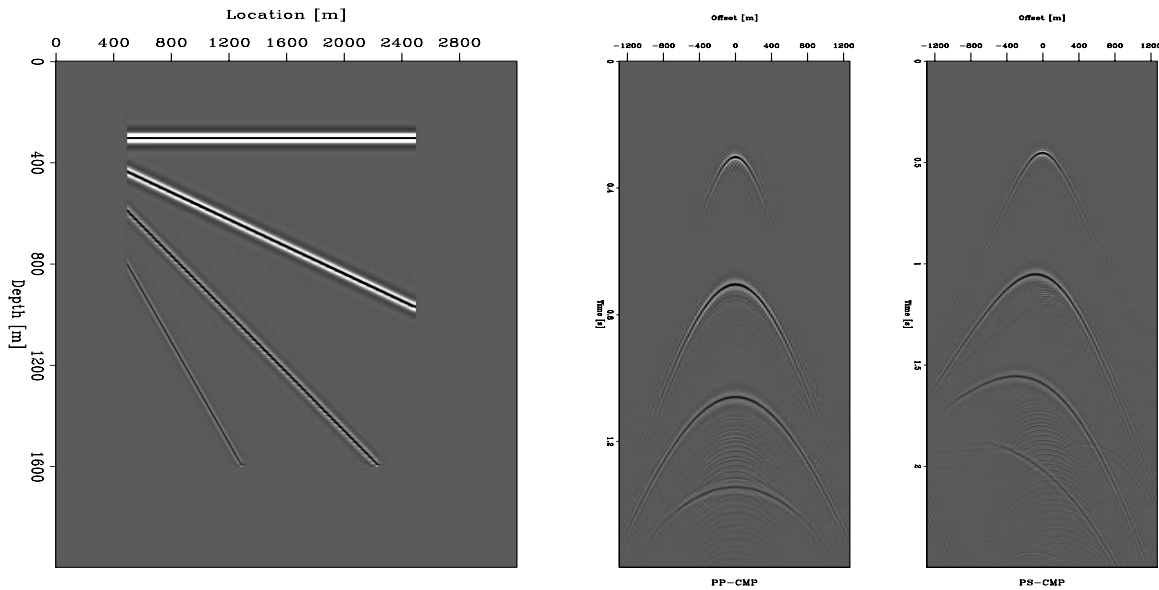


Figure 7: Synthetic data. Left: reflectivity model. Right panels: One single-mode PP CMP gather, and one converted-mode PS CMP gather. [daniel2-data](#) [CR]

ing the incidence and reflection angle. This transformations might bring useful information for the analysis of rock properties or velocity updates for the two different velocity models.

The transformation from SODCIGs into ADCIGs with a Fourier domain approach is accurate only for constant velocity. The general transformation needs to be done in the image space. Radon Transforms may provide to be a solution for this situation. The method will use the information along both the midpoint and subsurface offset axes in order to map the image into the *full-aperture* angle axis.

The next step is to analyze how errors in either P or S velocity models are transformed in the PS-ADCIGs. This will result in both a formulation for the residual moveout of converted mode data, and a methodology for vertical velocity updates of both P and S velocity models.

REFERENCES

- Biondi, B., and Symes, W., 2004, Angle-domain common-image gathers for migration velocity analysis by wavefield-continuation imaging: *Geophysics*, **69**, no. 5, 1283–1298.
- Biondi, B., 2005, Angle-domain common image gathers for anisotropic migration: *SEP-120*, 77–104.
- Brandsberg-Dahl, S., de Hoop, M. V., and Ursin, B., 1999, The sensitivity transform in the common scattering-angle/azimuth domain: 61st Ann. Internat. Mtg., Soc. Expl. Geophys., Expanded Abstracts, 1538–1541.

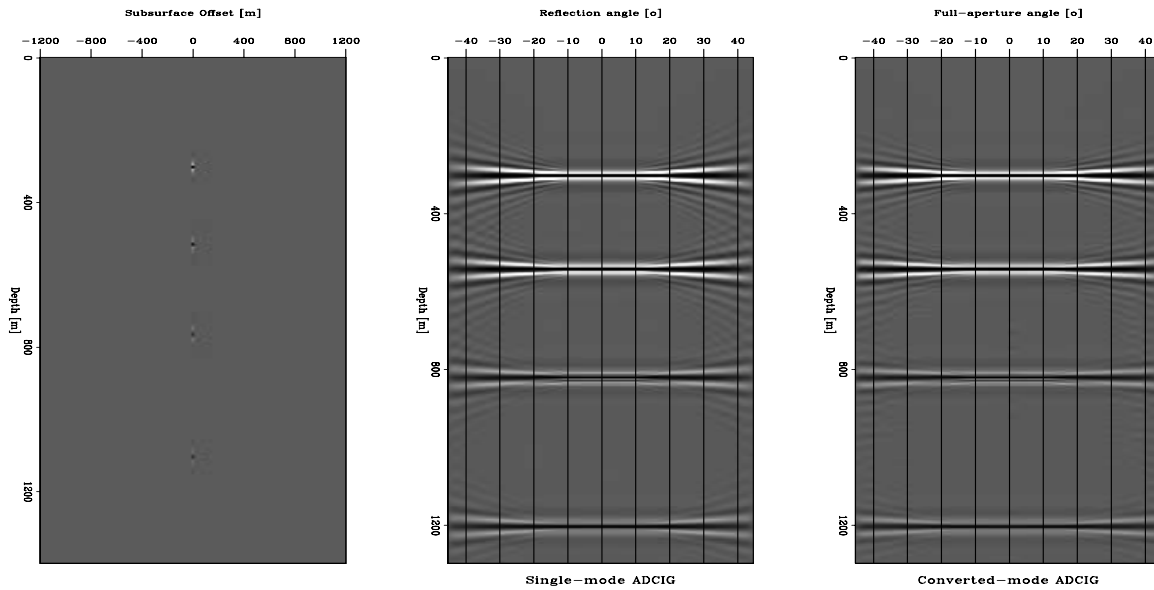


Figure 8: Subset of the image after migration. Left: one SODCIG gather. Right panels: the single-mode PP transformation to ADCIG, and the converted-mode transformation to ADCIG. daniel2-image [CR]

de Bruin, C. G. M., Wapenaar, C. P. A., and Berkhout, A. J., 1990, Angle-dependent reflectivity by means of prestack migration: *Geophysics*, **55**, no. 9, 1223–1234.

Fomel, S., and Prucha, M., 1999, Angle-gather time migration: *SEP-100*, 141–150.

Fomel, S., 1996, Migration and velocity analysis by velocity continuation: *SEP-92*, 159–188.

Prucha, M., Biondi, B., and Symes, W., 1999, Angle-domain common-image gathers by wave-equation migration: 69th Ann. Internat. Meeting, Soc. of Expl. Geophys., Expanded Abstracts, 824–827.

Rickett, J., and Sava, P., 2002, Offset and angle-domain common image-point gathers for shot-profile migration: *Geophysics*, **67**, 883–889.

Rosales, D., and Rickett, J., 2001a, *ps*-wave polarity reversal in angle domain common-image gathers: *SEP-108*, 35–44.

Rosales, D., and Rickett, J., 2001b, *PS*-wave polarity reversal in angle domain common-image gathers: 71st Annual Internat. Mtg., Expanded Abstracts, 1843–1846.

Sava, P., and Fomel, S., 2000, Angle-gathers by Fourier Transform: *SEP-103*, 119–130.

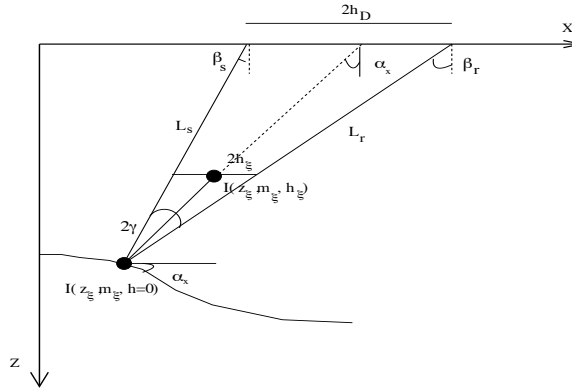
Sava, P., and Fomel, S., 2003, Angle-domain common-image gathers by wavefield continuation methods: *Geophysics*, **68**, no. 3, 1065–1074.

APPENDIX A

In this part, we obtain the relation to transform subsurface offset-domain common-image gathers into angle-domain common-image gathers for the case of PS data. To perform this derivation, we use the geometry in Figure 1 in order to obtain the parametric equations for migration on a constant velocity medium.

Following the derivation of Fomel (1996) and Fomel and Prucha (1999), and applying simple trigonometry and geometry to Figure A-1, we obtain parametric equations for migrating an impulse recorded at time t_D , midpoint m_D and surface offset h_D as follows:

Figure A-1: Parametric formulation of the impulse response. [daniel2-angles2](#) [NR]



$$\begin{aligned}
 z_\xi &= (L_s + L_r) \frac{\cos \beta_r \cos \beta_s}{\cos \beta_r + \cos \beta_s}, \\
 2h_\xi &= 2h_D + (L_s + L_r) \frac{\sin \beta_s \cos \beta_r - \sin \beta_r \cos \beta_s}{\cos \beta_r + \cos \beta_s}, \\
 m_\xi &= m_D - \frac{(L_s + L_r) \sin \beta_s \cos \beta_r + \sin \beta_r \cos \beta_s}{2 \cos \beta_r + \cos \beta_s}.
 \end{aligned} \tag{A-1}$$

where the total path length is:

$$\begin{aligned}
 t_D &= S_s L_s + S_r L_r, \\
 z_s - z_r &= L_s \cos \beta_s - L_r \cos \beta_r.
 \end{aligned} \tag{A-2}$$

From that system of equations, Biondi (2005) shows that the total path length is

$$L = \frac{t_D}{2} \frac{\cos \beta_r + \cos \beta_s}{S_s \cos \beta_r + S_r \cos \beta_s}. \tag{A-3}$$

Appendix A shows that we can rewrite system (A-1) as:

$$\begin{aligned}
 z_\xi &= \frac{(L_s + L_r) \cos^2 \alpha - \sin^2 \gamma}{2 \cos \alpha \cos \gamma}, \\
 2h_\xi &= 2h_D - (L_s + L_r) \frac{\sin \gamma}{\cos \alpha}, \\
 m_\xi &= m_D - \frac{(L_s + L_r) \sin \alpha}{2 \cos \gamma}.
 \end{aligned} \tag{A-4}$$

where α and γ follow the same definition as in equation (3). where, L in terms of the angles α and β is:

$$L(\alpha, \beta) = \frac{t_D}{(S_r + S_s) + (S_r - S_s) \tan \alpha \tan \gamma} \quad (\text{A-5})$$

Tangent to the impulse response

Following the demonstration done by Biondi (2005), the derivative of the depth with respect to the subsurface offset, at a constant image point, and the derivative of the depth with respect to the image point, at a constant subsurface offset are given by the following:

$$\left. \frac{\partial z_\xi}{\partial h_\xi} \right|_{m_\xi = \bar{m}_\xi} = - \frac{\left. \frac{\partial T}{\partial h_\xi} \right|_{m_\xi = \bar{m}_\xi}}{\left. \frac{\partial T}{\partial z_\xi} \right|_{m_\xi = \bar{m}_\xi}} = - \frac{\frac{\partial z_\xi}{\partial \alpha} \frac{\partial m_\xi}{\partial \gamma} - \frac{\partial z_\xi}{\partial \gamma} \frac{\partial m_\xi}{\partial \alpha}}{\frac{\partial m_\xi}{\partial \alpha} \frac{\partial h_\xi}{\partial \gamma} - \frac{\partial m_\xi}{\partial \gamma} \frac{\partial h_\xi}{\partial \alpha}}, \quad (\text{A-6})$$

and

$$\left. \frac{\partial z_\xi}{\partial m_\xi} \right|_{h_\xi = \bar{h}_\xi} = - \frac{\left. \frac{\partial T}{\partial m_\xi} \right|_{h_\xi = \bar{h}_\xi}}{\left. \frac{\partial T}{\partial z_\xi} \right|_{h_\xi = \bar{h}_\xi}} = - \frac{\frac{\partial z_\xi}{\partial \gamma} \frac{\partial h_\xi}{\partial \alpha} - \frac{\partial z_\xi}{\partial \alpha} \frac{\partial h_\xi}{\partial \gamma}}{\frac{\partial m_\xi}{\partial \alpha} \frac{\partial h_\xi}{\partial \gamma} - \frac{\partial m_\xi}{\partial \gamma} \frac{\partial h_\xi}{\partial \alpha}}, \quad (\text{A-7})$$

where the partial derivatives are:

$$\begin{aligned} \frac{\partial z_\xi}{\partial \alpha} &= - \frac{L}{\cos \alpha \cos \gamma} \left[\tan \alpha (\cos^2 \alpha + \sin^2 \gamma) + \frac{(S_r - S_s) \tan \gamma (\cos^2 \alpha - \sin^2 \gamma)}{\cos^2 \alpha} \right], \\ \frac{\partial z_\xi}{\partial \gamma} &= - \frac{L}{\cos \alpha \cos \gamma} \left[\tan \gamma (\cos^2 \alpha + \sin^2 \gamma) + \frac{(S_r - S_s) \tan \alpha (\cos^2 \alpha - \sin^2 \gamma)}{\cos^2 \gamma} \right], \\ \frac{\partial m_\xi}{\partial \alpha} &= - \frac{L}{\cos \gamma} \left[\cos \alpha - \frac{(S_r - S_s) \sin \alpha \tan \gamma}{\cos^2 \alpha} \right], \\ \frac{\partial m_\xi}{\partial \gamma} &= - \frac{L \sin \alpha}{\cos^2 \gamma} \left[\sin \gamma - \frac{(S_r - S_s) \tan \alpha}{\cos \gamma} \right], \\ \frac{\partial h_\xi}{\partial \alpha} &= - \frac{L \sin \gamma}{\cos^2 \alpha} \left[\sin \alpha - \frac{(S_r - S_s) \tan \gamma}{\cos \alpha} \right], \\ \frac{\partial h_\xi}{\partial \gamma} &= - \frac{L}{\cos \alpha} \left[\cos \gamma - \frac{(S_r - S_s) \tan \alpha \sin \gamma}{\cos^2 \gamma} \right]. \end{aligned} \quad (\text{A-8})$$

Figure A-2 presents the analytical solutions for the tangent to the impulse response. This was done for an impulse at a PS-travel time of 2 s, and a ϕ value of 2. The left panel shows the solution for equation (A-6). The right panel shows the solution for equation (A-7). The solid lines superimpose on both surfaces represents one section of the numerical derivative to the impulse response. The perfect correlation between the analytical and numerical solution validates our analytical formulations. This results supports the analysis presented with the kinematic equations.

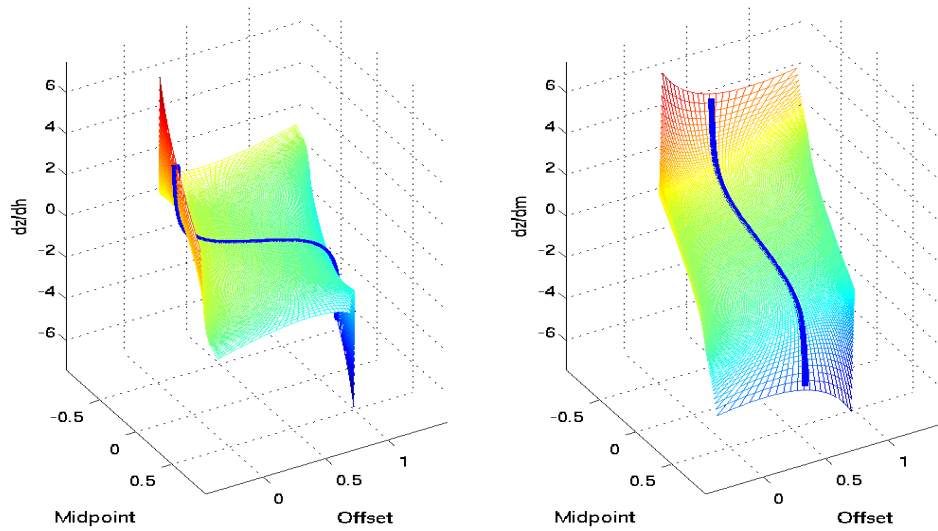


Figure A-2: Validation of the analytical solutions for the tangent to the impulse response, the surface represents the analytical solutions and superimpose is the cut with the numerical derivative. Left: For equation (A-6). Right: For equation (A-7) analytical solutions for the tangent of the spreading surface for different values of ϕ daniel2-ang_cwv_wei_surf [CR]

APPENDIX B

This section proves the equivalence between the parametric equations A-1, that is a direct result of trigonometry and geometry on the Figure A-1, with the parametric equations A-4, which the same equations presented by previous authors.

It is important to note that even though both parametric equations A-1 and A-4 are equivalent, the difference relies on the conceptual definitions of the angles involved.

The proof of this section is pure trigonometry, and the reader can safely skip this entire Appendix. However, this Appendix is here to show that the use of our equations is valid.

First, we rewrite β_s and β_r as function of α and γ by simple algebraic manipulation of equations 3.

$$\beta_s = \alpha - \gamma, \quad \text{and} \quad \beta_r = \alpha + \gamma. \quad (\text{B-1})$$

The first proof is the first parametric equation:

$$\begin{aligned}
 z_{\xi} &= (L_s + L_r) \frac{\cos \beta_r \cos \beta_s}{\cos \beta_r + \cos \beta_s} \\
 &= (L_s + L_r) \frac{\cos(\alpha + \gamma) \cos(\alpha - \gamma)}{\cos(\alpha + \gamma) \cos(\alpha - \gamma)} \\
 &= (L_s + L_r) \frac{(\cos \alpha \cos \gamma - \sin \alpha \sin \gamma)(\cos \alpha \cos \gamma + \sin \alpha \sin \gamma)}{2 \cos \alpha \cos \gamma} \\
 &= (L_s + L_r) \frac{\cos^2 \alpha \cos^2 \gamma - \sin^2 \alpha \sin^2 \gamma}{2 \cos \alpha \cos \gamma} \\
 &= (L_s + L_r) \frac{\cos^2 \alpha \cos^2 \gamma - \sin^2 \gamma + \sin^2 \gamma \cos^2 \alpha}{2 \cos \alpha \cos \gamma} \\
 &= (L_s + L_r) \frac{\cos^2 \alpha (\cos^2 \gamma + \sin^2 \gamma) - \sin^2 \gamma}{2 \cos \alpha \cos \gamma} \\
 &= \frac{(L_s + L_r) \cos^2 \alpha - \sin^2 \gamma}{2 \cos \alpha \cos \gamma}
 \end{aligned}$$

The second parametric equation is:

$$\begin{aligned}
 2h_{\xi} &= 2h_D + (L_s + L_r) \frac{\sin \beta_s \cos \beta_r - \sin \beta_r \cos \beta_s}{\cos \beta_r + \cos \beta_s} \\
 &= 2h_D + (L_s + L_r) \frac{\sin(\beta_s - \beta_r)}{2 \cos\left(\frac{\beta_s + \beta_r}{2}\right) \cos\left(\frac{\beta_r - \beta_s}{2}\right)} \\
 &= 2h_D + (L_s + L_r) \frac{\sin(-2\gamma)}{2 \cos \alpha \cos \gamma} \\
 &= 2h_D + (L_s + L_r) \frac{-2 \sin \gamma \cos \gamma}{2 \cos \alpha \cos \gamma} \\
 &= 2h_D - (L_s + L_r) \frac{\sin \gamma}{\cos \alpha}
 \end{aligned}$$

The third parametric equation is:

$$\begin{aligned}
 m_{\xi} &= m_D - \frac{(L_s + L_r) \sin \beta_s \cos \beta_r + \sin \beta_r \cos \beta_s}{2 \cos \beta_r + \cos \beta_s} \\
 &= m_D - \frac{(L_s + L_r) \sin(\beta_s + \text{angr})}{2 \cos\left(\frac{\beta_s + \beta_r}{2}\right) \cos\left(\frac{\beta_r - \beta_s}{2}\right)} \\
 &= m_D - \frac{(L_s + L_r) \sin(2\alpha)}{2 \cos \alpha \cos \gamma} \\
 &= m_D - \frac{(L_s + L_r) 2 \sin \alpha \cos \alpha}{2 \cos \alpha \cos \gamma} \\
 &= m_D - \frac{(L_s + L_r) \sin \alpha}{2 \cos \gamma}
 \end{aligned}$$

Orthogonal mesh generation for Riemannian wavefield extrapolation

Jeff Shragge¹

ABSTRACT

This paper presents a general method for generating 2D or 3D orthogonal coordinate systems. Developed coordinate systems are triplication free and appropriate for use in Riemannian wavefield extrapolation. This method exploits properties of potential function solutions of Laplace's equation. I show that certain specifications of a potential function's boundary conditions lead to a physical representation of equipotential surfaces where there are equivalent to extrapolation steps. Potential function solutions, obtained through conjugate gradient solvers, are used subsequently in a phase-ray-tracing procedure that generates geometric rays orthogonal to the equipotential surfaces. These rays collectively define an orthogonal coordinate system linked to the underlying Cartesian mesh through definable one-to-one mappings. The utility of this approach in generating coordinate systems is tested on a 2D model of rugged topography from the Canadian Foothills, and on 3D topography of the San Francisco Bay area.

INTRODUCTION

Wave-equation imaging is computed almost exclusively on Cartesian meshes both for computational simplicity and because imaged subsurface volumes are usually rectangular parallelepipeds. However, situations exist where performing wave-equation imaging on more generalized coordinate system meshes is warranted. For example, extrapolating wavefields directly from an undulating topographic surface (Shragge and Sava, 2004a), orienting the extrapolation axis of lower-order operators in the direction of wavefield propagation to improve higher angle accuracy (Sava and Fomel, 2004), or imaging with overturning waves not currently modeled by one-way extrapolation operators (Shan and Biondi, 2004). Employing non-Cartesian meshes, though, necessitates resolving these three issues: which coordinate system should be chosen? how is the preferred coordinate system generated? and what are the appropriate governing wavefield extrapolation equations for this coordinate system choice?

Non-Cartesian wavefield extrapolation theory has advanced in recent years in the context of both global and exploration seismology. All of these methods locally transform the coordinate system and the corresponding governing propagation equations to a more appro-

¹email: jeff@sep.stanford.edu

appropriate reference frame linked to an underlying Cartesian grid through one-to-one mappings. For example, Bostock et al. (1993) formulate an orthogonal, 2-D, plane-wave-centric coordinate system appropriate for propagating overturning teleseismic wavefields. Etgen (2002) and Shan and Biondi (2004) discuss the use of tilted coordinate systems that enable propagation of overturning waves with one-way extrapolation operators. Brandsberg-Dahl and Etgen (2003) and Sava and Fomel (2004) present generalized curvilinear coordinate and Riemannian metric formulations of the governing wavefield propagation equations, respectively.

Emerging with these developments are two classes of coordinate systems: those conformal with the propagating wavefield direction, and those conformal with pre-existing topology. Examples of the former include coordinate systems constructed by plane-wave decomposition (Bostock et al., 1993), and those generated using Eikonal equation ray-tracing (Sava and Fomel, 2004), whereas examples of the latter include a conformal mapping transform to incorporate surface topography (Shragge and Sava, 2004a). These methods, though, neither are universally applicable, nor always practical for 3D wavefield extrapolation. For example, ray-based methods can generate semi-orthogonal, triplicating coordinate systems that lead to numerical instability when propagating wavefields through coordinate system caustics. Another example is that the complex mathematics of conformal mapping surface topography does not extend easily to 3D. Hence, formulating a general approach for constructing 3D orthogonal coordinate systems appropriate for non-Cartesian wavefield extrapolation remains an open research topic.

This paper examines how potential function (PF) solutions of Laplace's equation, coupled with phase-ray tracing (Shragge and Sava, 2004b), can be used to generate orthogonal coordinate system meshes. Starting with appropriate PF boundary conditions, I generate a solution to Laplace's equation for any simply connected domain using conjugate gradient solvers (Claerbout, 1999). Importantly, the PF equipotentials define surfaces equivalent to wavefield extrapolation steps. The PF gradient field, by definition orthogonal to equipotentials, similarly forms geometric rays originating from the acquisition surface that collectively form a ray coordinate system. The most obvious example is the Cartesian coordinate system, where each depth step surface represents an equipotential surface, and each vertical line projecting downward defines a coordinate system ray. Mathematical properties of a PF also guarantee that the 3D orthogonality of equipotential coordinate systems. Hence, this approach constructs computational meshes conformal to 3D geometric boundaries, including undulating 2D topographic surfaces or deviated wells found in vertical seismic profiling.

I begin this paper by reviewing some important properties of PF solutions of Laplace's equation, and then outline an approach for defining a Laplace's equation appropriate for incorporating generalized topology of a solution domain. Subsequently, I show how modified phase-ray tracing generates a suite of geometric rays that collectively form a coordinate system mesh. I then demonstrate the utility of the approach by developing a 2D coordinate system for the Canadian Rocky Mountain Foothills model discussed in Shragge and Sava (2004a) and a 3D coordinate system conformal to the 2D topography of the San Francisco Bay area.

THEORY

This section discusses some important characteristics of PF solutions of Laplace's equation (Kellogg, 1953), and outlines how these properties can be exploited to generate orthogonal coordinate systems. Using the scenario of 2D wave-equation migration from topography, I present appropriate boundary conditions, detail a method for obtaining potential function solutions, and outline a ray-tracing approach. These three components collectively define and algorithm for computing a geometric coordinate system.

Laplace's Equation

The scalar form of Laplace's equation is the partial differential equation,

$$\nabla^2\phi = 0 \quad (1)$$

where ∇^2 is the second-order spatial derivative operator, and ϕ is the sought PF. Laplace's equation is a special case of the Helmholtz differential equation,

$$\nabla^2\phi + k^2\phi = 0, \quad (2)$$

when wavenumber $k = 0$. A physical interpretation of this observation is that PF ϕ is the zero-frequency solution of the frequency-domain wave-equation, and is independent of the velocity field and thereby solely a geometric construct. A harmonic PF satisfying Laplace's equation has a number of important properties that are valid either on the boundary of, or entirely within, the defining domain. Most relevant to this discussion are that a PF:

- is uniquely determined by either the values, or normal derivatives thereof, on the domain boundary;
- has an average value over a spherical neighborhood equal to the value at its center; hence, PFs do not have local maxima or minima in the domain;
- is curl-free (i.e., $\nabla \times \phi = 0$) ensuring non-overlapping, and at most simply connected, equipotential surfaces;
- gradient field is uniquely defined, locally orthogonal to the equipotential surfaces, and related to the PF through,

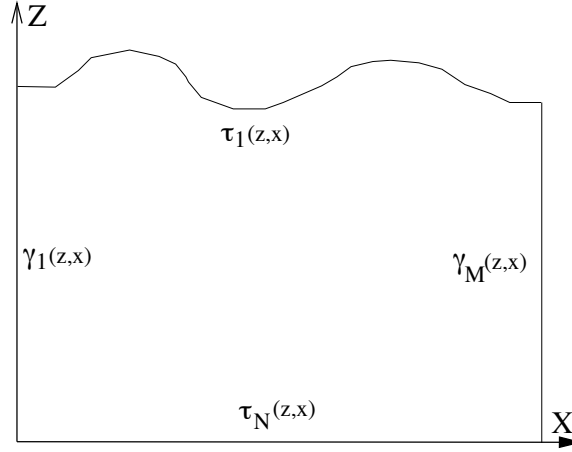
$$\phi(b) - \phi(a) = \int_a^b d\phi = \int_a^b \left(\frac{\partial\phi}{\partial x}dx + \frac{\partial\phi}{\partial y}dy + \frac{\partial\phi}{\partial z}dz \right). \quad (3)$$

Each of these properties make PF solutions of Laplace's equation an important tool for generating orthogonal coordinate systems.

Generating Potential Functions

Generating orthogonal coordinate system meshes from PFs requires ascribing a physical interpretation to equipotentials: they are equivalent to extrapolation steps. Similarly, the characteristics of the PF gradient field are intrinsically related to geometric coordinate system rays. Figure 1 illustrates these concepts for the example of 2D wave-equation migration from topography. This scenario requires extrapolating a wavefield comprised of M traces into the

Figure 1: Scenario of migration from topography. The upper and lower topographic surfaces are denoted $\tau_0(z, x)$ and $\tau_N(z, x)$, respectively. Connecting vertical lines are denoted $\gamma_1(z, x)$ (left) and $\gamma_M(z, x)$ (right). The upper and lower surfaces have equipotential values of $\phi(\tau_0) = 1$ and $\phi(\tau_N) = 0$, respectively, whereas both side boundaries have zero normal derivatives. jeff1-topocoord
[NR]



subsurface a total of N steps, which ideally occurs directly from the topographic surface. The upper boundary of the computational domain, denoted $\tau_0(z, x)$ in this figure, is the acquisition surface. The lower boundary, denoted $\tau_N(z, x)$, is the desired flat subsurface datum. These two bounding surfaces are connected by two curves, $\gamma_1(z, x)$ and $\gamma_M(z, x)$, extending between the first and last extrapolation levels.

Solving for a PF satisfying Laplace's equation first requires specifying appropriate boundary conditions. Because distinct upper and lower equipotentials are desired, these two surfaces must have different constant values. Thus, I choose the following boundary conditions,

$$\phi(\tau_0) = 1, \quad \phi(\tau_N) = 0, \quad \left. \frac{\partial \phi}{\partial \mathbf{n}} \right|_{\gamma_1} = 0, \quad \left. \frac{\partial \phi}{\partial \mathbf{n}} \right|_{\gamma_M} = 0, \quad (4)$$

where the derivative with respect to variable \mathbf{n} is in the direction outward normal to the surface represented by γ_1 and γ_M .

The Laplace's equation defined by the boundary conditions in Equation (4) is representable by a system of equations similar those commonly solved with conjugate gradient methods (Claerbout, 1999),

$$\mathbf{W}\mathbf{L}\mathbf{m} \approx 0 \quad (5)$$

subject to the following constraints,

$$(\mathbf{I} - \mathbf{W})(\mathbf{m} - \mathbf{m}_{bnd}) = 0, \quad (6)$$

where model vector \mathbf{m} is the sought PF solution, \mathbf{m}_{bnd} are the values on, and exterior to, the domain boundary, $\mathbf{L} = \nabla^2$ is a Laplacian operator matrix, \mathbf{W} is a mask operator indicating location of the boundary, and \mathbf{I} is the identity operator.

I use the following algorithm to obtain PF solution, \mathbf{m} :

1. Map the irregular topographic domain to a Cartesian mesh to generate vector \mathbf{m}_{bnd} ;
2. Fix the PF values on the boundary of, and external to, the mapped domain using the mask operator \mathbf{W} ;
3. Initialize the model vector with a starting guess (i.e., \mathbf{m}_0) exploiting the smooth variation of ϕ between the upper and lower surfaces (i.e., through linear interpolation of ϕ on $[1,0]$ between $\tau_0(z_0, x_0)$ and $\tau_N(z_1, x_0)$);
4. Solve system of equations in Equation (5) using a conjugate gradient algorithm (Claerbout, 1999), by allowing the solver to iterate until convergence is reached.

The resulting model vector, \mathbf{m} , is the desired potential function that can be input to the phase ray-tracing algorithm described below. Finally, as illustrated by the example below, this approach is directly applicable to 3D computational domains because conjugate gradient solvers still work in 3D after the geometry is unwrapped on to a helical coordinate system (Claerbout, 1999).

Potential function ray tracing

The next processing step involves tracing geometric coordinate system rays from the generated PF. The goal here is to develop an orthogonal, ray-based coordinate system related to an underlying Cartesian mesh through one-to-one mappings,

$$\begin{aligned} \tau &= \tau(z, x, y) \\ \gamma &= \gamma(z, x, y) \quad \text{where} \quad J = \frac{\partial(\tau, \gamma, \eta)}{\partial(z, x, y)} \neq 0, \\ \eta &= \eta(z, x, y) \end{aligned} \quad (7)$$

where τ is the wavefield extrapolation direction (equivalent to z in Cartesian), γ and η are the two orthogonal directions (equivalent to x and y in Cartesian), and J is the Jacobian of the coordinate system transformation. Recorded wavefield, $U(\tau_0, \gamma, \eta)$, is extrapolated from the acquisition surface defined by τ_0 into the subsurface along the rays coordinate system defined by triplet $[\tau, \gamma, \eta]$.

Geometric rays are traced by solving a first-order ordinary differential equation through integrating the PF gradient field along the gradient direction,

$$\delta\phi = \int_{a(z_0, x_0, y_0)}^{b(z_1, x_1, y_1)} \|\nabla\phi\|^{-1} \left[dz \frac{\partial\phi}{\partial z} + dx \frac{\partial\phi}{\partial x} + dy \frac{\partial\phi}{\partial y} \right], \quad (8)$$

where $a(z_0, x_0, y_0)$ is a known lower integration bound at equipotential $\phi(a)$, and $b(z_1, x_1, y_1)$ is an unknown upper integration bound located on equipotential surface, $\phi(b)$, and $\|\nabla\phi\|$ is the L^2 norm of the gradient function. The only unknown parameter is $b(z_1, x_1, y_1)$; hence, Equation (8) is an integral equation with an unknown integration bound. This approach is similar to phase-ray tracing method described in Shragge and Sava (2004b); however, in this case the integration step lengths are now unknown. Note also that the equipotentials of the upper and lower bounding surfaces in Equation (4) require PF steps of $\delta\phi = 1/N$.

The following approach locates unknown integration bound, b , on the next equipotential:

1. Numerically integrate Equation (8) on the interval $[a, a + \delta a]$ where δa is smaller than the expected step size, and test to see whether $\phi(a) - \phi(a + \delta a) > \delta\phi$; if yes goto step 3;
2. Numerically integrate Equation (8) on next interval $[a + \delta a, a + 2\delta a]$ and test whether $\phi(a) - \phi(a + 2\delta a) > \delta\phi$; if yes goto step 3; if no, repeat step 2 n times until true;
3. Linearly interpolate between points $a + (n - 1)\delta a$ and $a + \delta a$ to find the b corresponding to $\phi(b) = \phi(a) - \delta\phi$.

A geometric ray is initiated at a particular $[\gamma_0, \eta_0]$ on acquisition surface defined by τ_0 , and computed by integrating through each successive $\delta\phi$ step until the lower bounding surface τ_N is reached. This procedure is repeated for all γ and η acquisition points.

NUMERICAL EXAMPLES

2D Example - Canadian Foothills

The first test of the approach is on a 2D synthetic model characterized by rugged topography. This model is a merger of common geologic features from the Canadian Foothills in northeastern British Columbia, Canada (Gray and Marfurt, 1995). The velocity model, shown in Figure 2, consists of steep thrust fault planes and complex folds typical of a mountainous thrust region. The topographic boundary of interest is demarcated by the velocity model

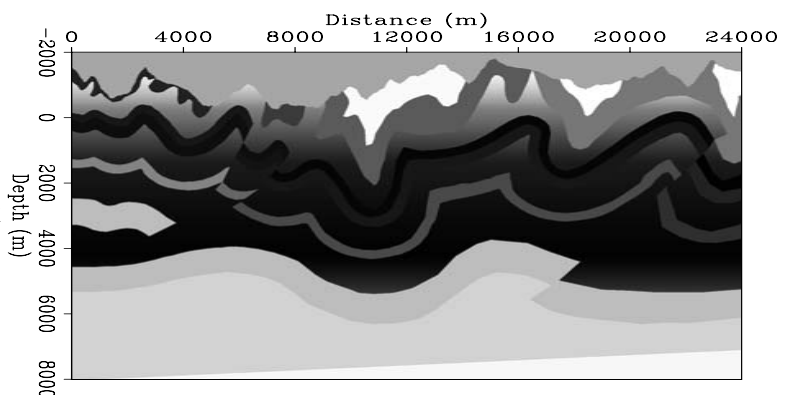


Figure 2: Example of 2D topography from the Canadian Foothills. Topographic surface is the first break in gray tone from the surface.

`jeff1-Foothills.vel` [ER]

discontinuity nearest to the surface. The total relief of the model's surface is approximately 1600 m.

Figure 3 shows the test results. The flat datum surface is at a depth of 10000 m. Left-hand panels show the case where surface topography amplitudes are scaled down by 50%. The top left panel shows the 2-D potential function obtained through solution of Equation (5).

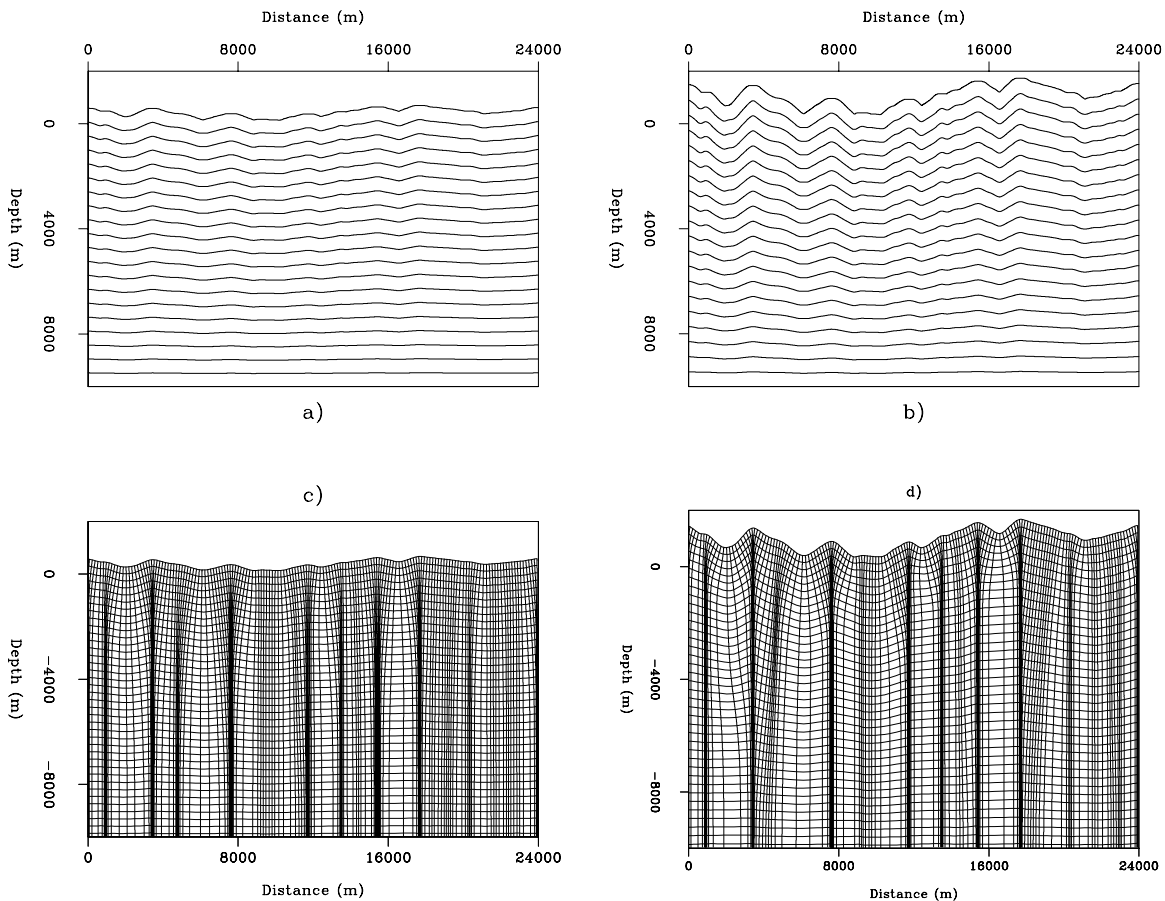


Figure 3: Potential functions and coordinate systems generated for the Canadian Foothills velocity model. a) Potential function with topography scaled down by 50%; b) Potential function with correct topography; c) coordinate system developed from the potential function of a); and d) coordinate system developed from the potential function of b). Note that increasing the amplitude of the topography tends to (de)focus the coordinate under topographic (lows) highs. `jeff1-Plot2D` [ER]

The PF is rougher nearer the surface, but smooths out to become uniform at the lower domain boundary. The bottom left panel shows the coordinate system ray-traced from the PF presented in the top left panel. Note that the coordinate system focuses beneath topographic maxima, and defocuses under topographic minima. This demands that the Jacobian value in Equation (7) diverge from unity.

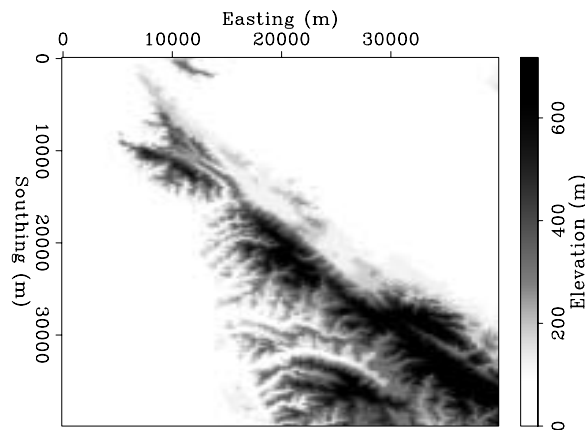
The right-hand panels of Figure 3 show results similar to those in the left-hand panels, except that the true topographic surface is restored. The top right panel shows a rougher PF,

which is expected due to the increased topographic rugosity. The bottom right panel presents the coordinate system ray-traced from the PF shown in the upper right panel. Relative to that the bottom left panel, this coordinate system exhibits increased focusing and defocusing under topographic maxima and minima, respectively.

3D Example - San Francisco Bay area Topography

Using the elevation map of the San Francisco Bay area illustrated in Figure 4, a second test was conducted to assess the applicability of the method in 3D. The maximum surface topographic relief is approximately 800 m; however, the elevation gradients and topographic wavelengths are significantly smaller and longer than the 2D test illustrated in Figure 2. The flat subsurface datum is set a depth of 8000 m. Figure 5 presents the slices through the 3D potential function

Figure 4: Elevation map of the San Francisco Bay area used in 3D testing. `jeff1-Bay.2D` [ER]



results. The top panel shows a depth slice at approximately zero elevation, whereas the lower two panels show slices along Easting (bottom left) and Southing (bottom right) directions. These profiles illustrate a PF that is smoother than the previous example.

Figure 6 shows the coordinate system generated along the same two slices shown in the panels b) and c) of Figure 5. The generated coordinate system much smoother than in the previous example, as expected from the smoothness of the PF. Figure 7 presents a perspective view of the ray-traced coordinate system results. The coordinate system rays are fairly straight, except in the region beneath topographic highs. Another way to visualize the ray coordinate system is to examine how the topography 'heals itself' at various τ steps. Figure 8 illustrates this for the τ_0 (top left), $\tau_{N/3}$ (top right), $\tau_{2N/3}$ (bottom left) and τ_N (bottom right) surfaces, where N is the total number of extrapolation steps. The sidebars show the elevation difference between the lowest and highest points of each equipotential surface. The greyscale intensity has been clipped according to the maximum elevation difference at τ_0 .

DISCUSSION AND FUTURE WORK

These examples indicate that the procedure developed in this paper can generate coordinate systems from potential function solutions of Laplace's equation. Tests were conducted on

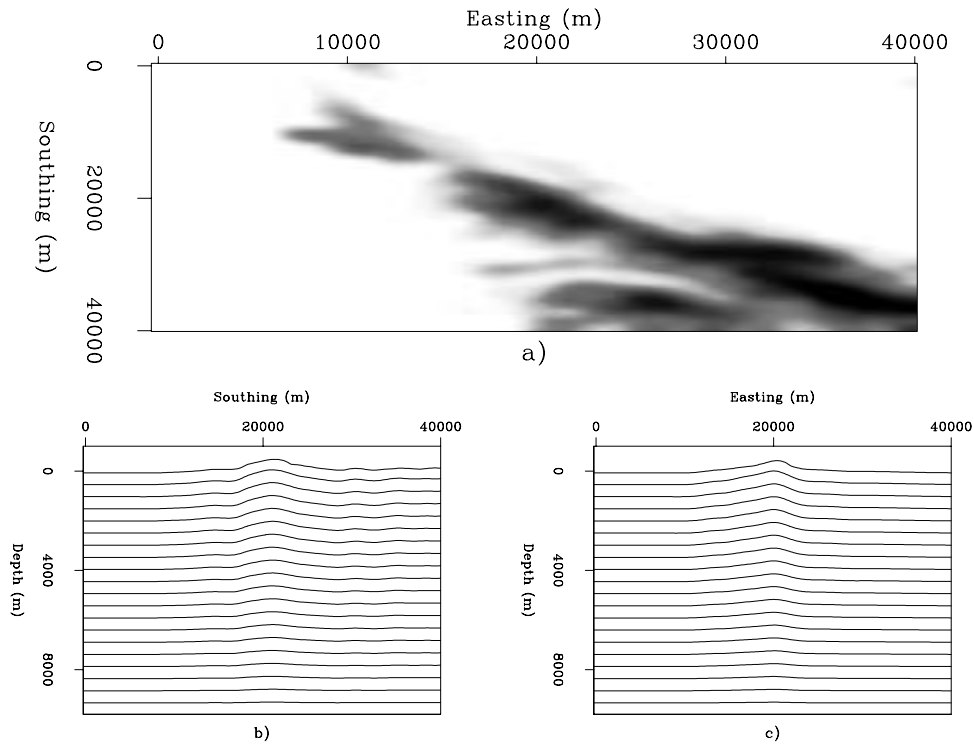


Figure 5: 3D potential function for San Francisco Bay area topography. a) depth slice of the potential function at approximately zero elevation; b) vertical slice along Southing 20 km; and c) vertical slice along Easting 20 km. Note that the potential function is smoother than the previous example indicating less coordinate system focusing. `jeff1-Pot3D` [ER]

surfaces exhibiting moderate-to-rough topography; hence, coordinate surfaces developed for smoother surfaces (e.g., deviated VSP wells) should be subject to less focusing than these examples. Thus, I assert that PF-derived smooth coordinate systems should be good for use in RWE.

However, as the 2D rugged topography example indicates, coordinate systems under rough topography generated by this approach probably are less well-suited for RWE. In particular, the 2D example probably reveals that coordinate system generated through the conformal mapping approach of Shragge and Sava (2004a) are probably better suited for RWE. This is because wavefield extrapolation on severely focused coordinate systems requires high extrapolation operator accuracy. However, the real test of whether coordinate systems generated by the above approach are appropriate for RWE ultimately lies in accuracy of resulting extrapolated wavefields and corresponding images.

CONCLUDING REMARKS

Generating 2D and 3D coordinate systems using geometric ray-tracing on potential function solutions of Laplace's equation is a viable approach. Because of certain properties of potential

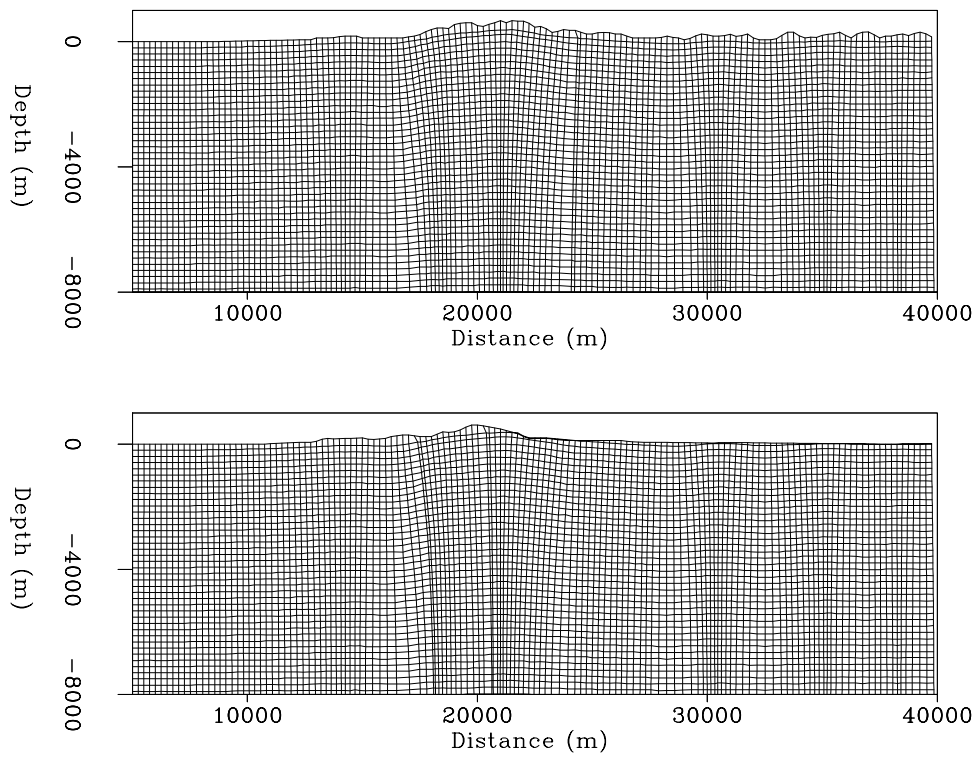


Figure 6: Cross-section of the 3-D coordinate system developed for the San Francisco Bay area topography. Left-hand panel: vertical slice along along Southings 20 km; and right-hand panel: vertical slice along Eastings 20 km. `jeff1-Ray.slice` [ER]

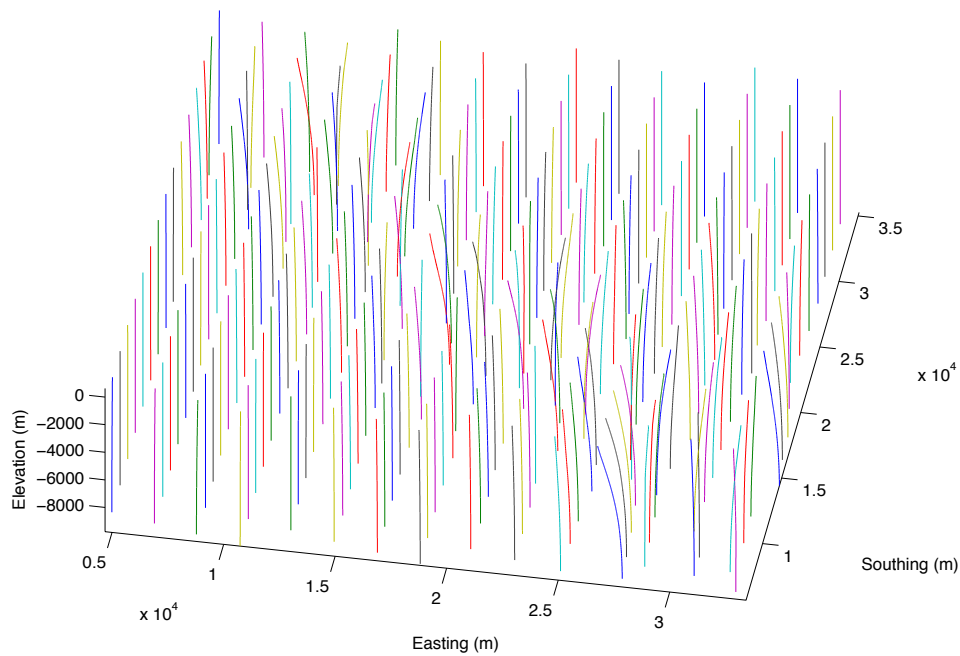


Figure 7: Perspective view of the ray-traced coordinate system developed from potential function in Figure 5. `jeff1-Rays3D` [CR]

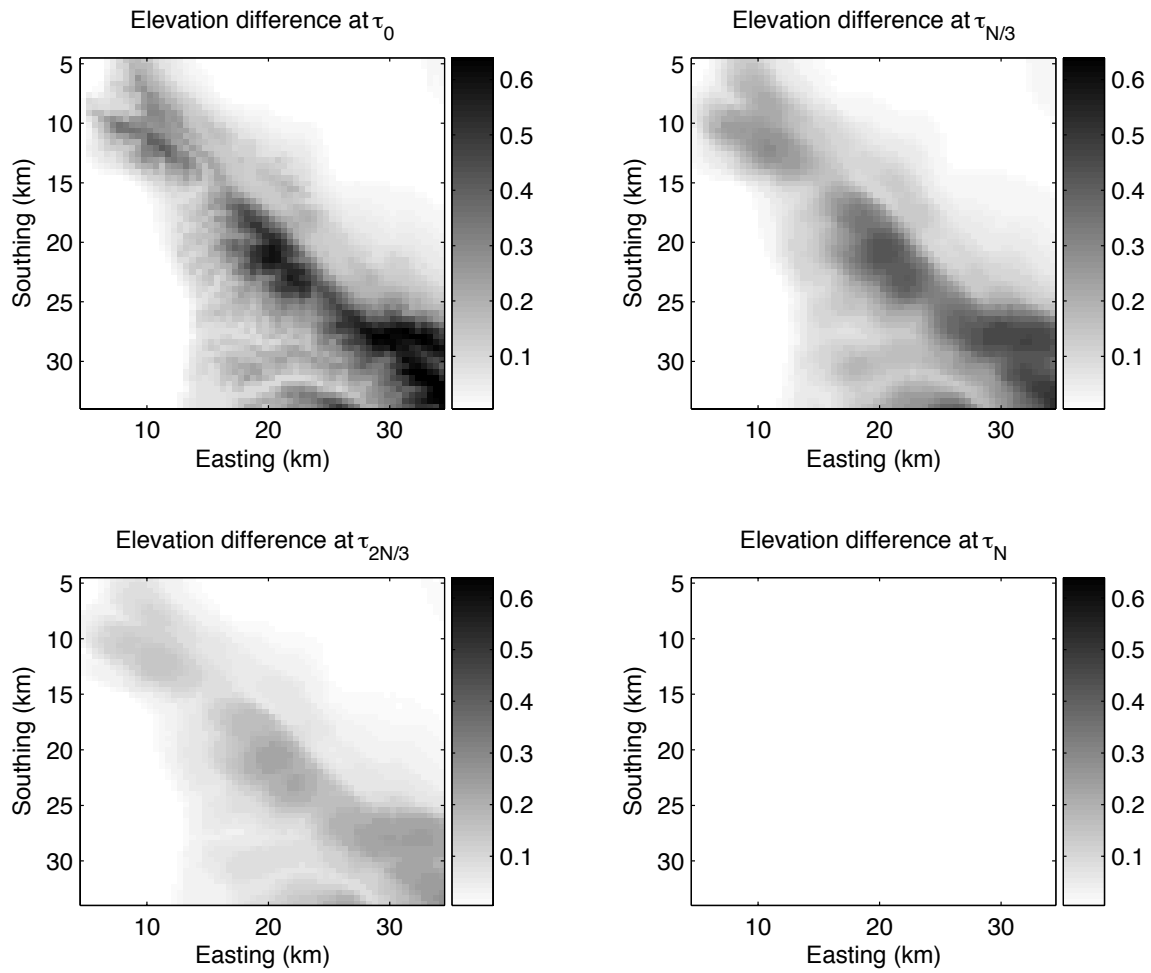


Figure 8: Illustration of topographic coordinate system healing through examination of single-extrapolation step elevation differences (in km). Top left: step τ_0 ; top right: step $\tau_{N/3}$; bottom left: step $\tau_{2N/3}$; and bottom right: step τ_N . Sidebar shows the elevation differences (in km), where the greyscale has clipped according to the peak elevation difference at τ_0 . [jeff1-Rays3D2](#) [CR]

functions, ray-traced coordinate systems are guaranteed to be orthogonal. Importantly, these coordinate systems are appropriate for 3D Riemannian wavefield extrapolation, and can be applied in numerous scenarios, including wave-equation migration directly from an undulating 2D topographic surface, and VSP imaging from deviated wells.

ACKNOWLEDGMENTS

Paul Sava assisted in the early development of the potential field approach. I would also like to thank Biondo Biondi and Brad Artman for helpful discussions.

REFERENCES

- Bostock, M., VanDecar, J., and Snieder, R., 1993, Modeling teleseismic P-wave propagation in the upper mantle using a parabolic approximation: *Bulletin of the Seismological Society of America*, **83**, 756–779.
- Brandsberg-Dahl, S., and Etgen, J., 2003, Beam-wave imaging: *Soc. of Expl. Geophys.*, Expanded Abstracts, 977–980.
- Claerbout, J., 1999, Geophysical estimation by example: Environmental soundings image enhancement: Stanford Exploration Project, <http://sepwww.stanford.edu/sep/prof/>.
- Etgen, J., 2002, Waves, Beams and Dimensions: an illuminating if incoherent view of the future of migration: *Soc. of Expl. Geophys.*, invited presentation.
- Gray, S., and Marfurt, K., 1995, Migration from topography: Improving the near-surface image: *J. Can. Soc. Expl. Geophys.*, **31**, 18–24.
- Kellogg, O., 1953, *Foundation of Potential Theory*: Dover Publications, Inc., New York.
- Sava, P., and Fomel, S., 2004, Seismic imaging using Riemannian wavefield extrapolation: Submitted to *Geophysics*.
- Shan, G., and Biondi, B., 2004, Wavefield extrapolation in laterally-varying tilted TI media: *SEP-117*, 1–10.
- Shragge, J., and Sava, P., 2004a, Incorporating topography into wave-equation imaging through conformal mapping: *SEP-117*, 27–42.
- Shragge, J., and Sava, P., 2004b, Adaptive phase-ray wavefield extrapolation: *SEP-115*, 13–28.

Short Note

Wavefield extrapolation in frequency-wavenumber domain for spatially-varying velocity models

Gabriel Alvarez and Brad Artman¹

INTRODUCTION

Mixed domain wavefield extrapolation methods can handle, to a large extent, spatial velocity variations by performing part of their computation in the ω - \mathbf{k} domain and part of the computation in the ω - \mathbf{x} domain. The best-known mixed domain methods are Phase Shift Plus Interpolation (PSPI) and extended split-step migration (Gazdag and Sguazzero, 1984; Stoffa et al., 1990; Biondi, 2004). They downward continue the wavefield in the ω - \mathbf{k} domain at each depth step with a series of reference velocities and then interpolate the wavefields in the ω - \mathbf{x} domain possibly after a split-step correction.

There are three main potential sources of error in mixed-domain algorithms: (1) the choice of the reference velocities, (2) the correction to account for the difference between the model velocity and the reference velocity at each spatial location, and (3) the accuracy of the interpolation of the wavefields.

In this paper, we present an alternative to ω - \mathbf{x} – ω - \mathbf{k} downward extrapolation that performs each depth extrapolation completely in the ω - \mathbf{k} domain, yet can handle arbitrary spatial variation of the migration velocities. The proposed algorithm eliminates the need for choosing reference velocities and requires no FFT's at each depth extrapolation level. Making the algorithm efficient, however, is still a research issue.

In the next section, we will present a brief overview of the standard ω - \mathbf{x} – ω - \mathbf{k} methods without getting into any specific implementation details. In the following section, we present our method, and in the last section, we discuss some implementation issues.

OVERVIEW OF MIXED-DOMAIN DOWNWARD EXTRAPOLATION

In this section, we will briefly review, from the mathematical point of view, the ω - \mathbf{x} – ω - \mathbf{k} algorithm. This will serve as the starting point for the presentation of the new extrapolation method in the next section.

¹email: gabriel@sep.stanford.edu, brad@sep.stanford.edu

Let \mathbf{W}^N be the wavefield at depth step N in the ω - \mathbf{k} domain and let \mathbf{W}_l^{N+1} be the wavefield extrapolated from depth step N to depth step $N + 1$ using reference velocity V_l . That is:

$$\mathbf{W}_l^{N+1} = \mathbf{W}^N e^{ik_{z_l} \Delta z},$$

where Δz is the depth of the N th layer and k_{z_l} is given by the dispersion relation:

$$k_{z_l} = \sqrt{\frac{\omega^2}{V_l^2} - |\mathbf{k}|^2} \quad (1)$$

with $|\mathbf{k}|$ being the magnitude of the horizontal wavenumber vector. PSPI handles the difference between the true velocity and the reference velocity by interpolating the downward-continued wavefields in the ω - \mathbf{x} domain based on the difference between the reference velocities and the model velocity at each \mathbf{x} position. The interpolated wavefield is therefore given by:

$$\mathbf{w}^{N+1}(j) = \sum_{l=1}^{n_v} \sigma_l \mathbf{w}_l^N(j)$$

where σ_l is an interpolation factor ($\sum_l^{n_v} \sigma_l = 1$), $\mathbf{w}_l^{N+1}(j)$ is the downward-continued wavefield in the ω - \mathbf{x} domain at the spatial location j , and n_v is the number of reference velocities.

Extended split-step adds a correction before the interpolation, the so-called ‘‘thin lens term’’:

$$e^{ik_{ssl}} \text{ where, } k_{ssl} = \frac{\omega}{V} - \frac{\omega}{V_l}$$

where V is the true model velocity. Depending on the choice and number of reference velocities, split-step can make significant improvements in accuracy compared to PSPI.

Other methods, such as pseudo-screen and Fourier finite-difference, increase the accuracy of the result by adding high-order spatial derivatives to the computation of the k_{z_l} term (Ristow and Ruhl, 1994; Huang et al., 1999; Xie and Wu, 1999; Biondi, 2004). The more accurate approximation of k_{z_l} relaxes the need for a large number of reference velocities such that with fewer reference velocities similar or even better accuracies can be obtained compared with split-step.

The last step in either of these methods is to Fourier transform the interpolated wavefield to the ω - \mathbf{k} space. This wavefield will then be the input to the propagation at the next depth step.

It should be clear that the accuracy of these methods, especially PSPI and extended split-step, is directly related to the accuracy of the wavefield interpolation and the number and choice of the reference velocities.

ω - \mathbf{K} DOWNWARD EXTRAPOLATION

The previous section suggests an alternative implementation of mixed-domain migration. To see this more clearly, assume that, at each depth step, we downward continue the wavefield

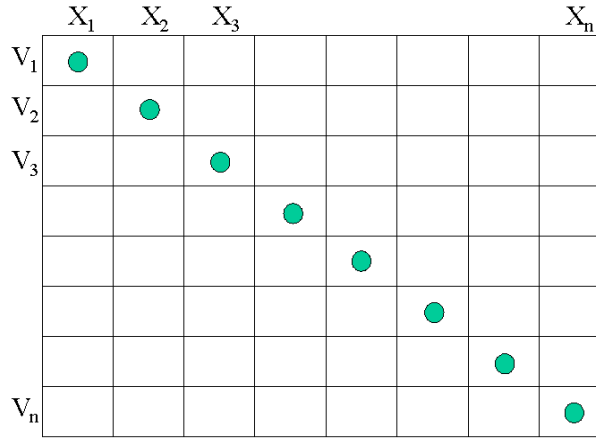
with the true velocities at that depth. In other words, compute $n_v = n_x$ wavefields, each one corresponding to the model velocity at each spatial location. No split-step correction or higher-order approximation of k_z would then be required. The wavefield interpolation in ω - \mathbf{x} domain reduces to a simple selection of the appropriate wavefield, operation that can be expressed as:

$$\mathbf{w}^{N+1}(j) = \sum_{l=1}^{n_v} \mathbf{w}_l^{N+1}(j) \delta_{lj} \quad (2)$$

where \mathbf{w}_l^{N+1} is the row of the array of wavefields extrapolated with the velocity V_l , and δ_{lj} is the Kronecker delta that selects from that row the corresponding $j = l$ component. Notice that, since we are extrapolating as many wavefields as there are spatial positions (traces), $n_v = n_x$. Figure 1 shows a schematic of the velocity selection. In the ω - \mathbf{k} domain, Equation (2)

Figure 1: Diagram illustrating velocity selection when there are many velocities as spatial locations.

`gabriel1-bin_vels1` [NR]



becomes:

$$\mathbf{W}^{N+1} = \sum_{l=1}^{n_v} \mathbf{w}_l^{N+1} \otimes e^{-ik_x \Delta x_l} \quad (3)$$

where $\Delta x_l = (l-1)\Delta x/n_x$ and we are using a single index to represent the spatial axis in order to simplify the notation. The symbol \otimes represents circular convolution.

Notice that Equation (3) was derived without any approximation. Let's make the computations more explicit in order to gain a better appreciation for what it means:

$$\mathbf{W}^{N+1}(j) = \sum_{l=1}^{n_v} \sum_{m=\langle n_x \rangle} \mathbf{w}_l^{N+1}(m) e^{-ik_x(j-m)\Delta x_l}$$

where $\langle m \rangle$ means that the summation is over the range n_x with modulus n_x . That is,

$$\mathbf{W}^{N+1}(j) = \sum_{l=1}^{n_v} \sum_{m=1}^{n_x} \mathbf{W}^N(m) e^{-ik_{z_l}(m)\Delta z} e^{-ik_x(\text{mod}(j-m, n_x))\Delta x_l}$$

Let $\tilde{m}_j = \text{mod}(j-m, n_x)$ and exchange the order of summation:

$$\mathbf{W}^{N+1}(j) = \sum_{m=1}^{n_x} \mathbf{W}^N(m) \sum_{l=1}^{n_v} e^{-i[k_{z_l}(m)\Delta z + k_x(\tilde{m}_j)]\Delta x_l}$$

This equation shows that in order to compute the j th component of the extrapolated wavefield in the ω - \mathbf{k} domain, we need to take the dot product of the wavefield at the previous depth step with a vector that contains all the velocity and interpolation information. That is,

$$\mathbf{W}^{N+1}(j) = \mathbf{W}^N \cdot \mathbf{f}_j \quad (4)$$

where \mathbf{f}_j is the vector given by

$$\mathbf{f}_j = \sum_{l=1}^{n_v} e^{-i[k_{z_l}(m)\Delta z + k_x(\tilde{m}_j)\Delta x_l]} \quad (5)$$

PRACTICAL IMPLEMENTATION

The algorithm described by equations 4 and 5 is theoretically attractive because it shows in one equation that downward extrapolation can be done entirely in the ω - \mathbf{k} domain, even for arbitrary spatial velocity variations. From the practical point of view, however, the algorithm is proportional, at each depth step and each frequency, to the cube of the spatial dimensions. Clearly, the cost is associated with the unreasonable demand that we extrapolated, at each depth step, as many wavefields as spatial positions. This is not really necessary, as we will see below.

Computation of the vertical wavenumber

Equation (5) contains all the velocity information in the data and can be precomputed, at least in part. Notice that, although we described the algorithm for $n_v = n\mathbf{x}$, that is not necessary because the range of velocities is limited and independent of the spatial dimensions of the data (although the velocities themselves vary spatially).

Start by binning the velocities in small bins, for example at 10 m/s (which would imply a maximum velocity error of 5 m/s, well below the likely error in the estimation of the velocities themselves) such that the vertical wavenumber k_{z_l} (that is, the dispersion relation), needs to be computed only a few hundred times and can thus be stored as a function of the horizontal wavenumber and the velocity. From the standpoint of the theoretical algorithm, all that changes is the selection process to choose the trace from the extrapolated wavefield that corresponds to the binned velocity at each spatial location. That is, instead of the selection being simply a multiplication by a Kronecker delta to choose $l = j$ as it was before, it is now a multiplication with a Kronecker delta, to select $l = p(j)$, that is, the wavefield that was migrated with the binned velocity corresponding to the bin of $V(j)$. Equation (2) can then be rewritten as:

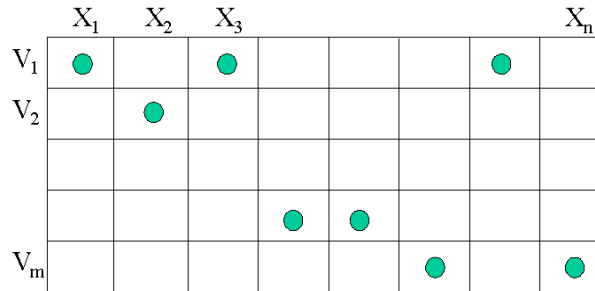
$$\mathbf{w}^{N+1} = \sum_{l=1}^{n_v} \mathbf{w}_l^{N+1} \sum_p \delta_{pl}.$$

The equation for the wavefield extrapolation then becomes:

$$\mathbf{W}^{N+1}(j) = \sum_{m=1}^{n_x} \mathbf{W}^N(m) \sum_{l=1}^{n_v} (e^{-ik_{z_l}(m)\Delta z} \sum_p e^{-ik_x(\tilde{m}_j)\Delta x_p}). \quad (6)$$

Notice that summation over l involves summing over all the binned velocities whereas summation over p involves selecting the different wavefield components that correspond to a given velocity. That is, p ranges over the spatial locations whose binned velocity is V_l for each l . Figure 2 shows the velocity selection. This time, since we don't have a wavefield migrated with each velocity, at each spatial location, it is likely that several locations correspond to the same wavefield, since they correspond to the same velocity bin. There is, obviously, just one possible velocity at each spatial location, but many spatial locations may share the same velocity. Also, it is possible for a particular velocity not to be required at a specific depth step.

Figure 2: Diagram illustrating velocity selection when there are fewer velocities than spatial locations. `gabriel1-bin_vels2` [NR]



Computation of the horizontal wavenumbers

The horizontal wavenumber term $k_x(\tilde{m}_j)$ can also be stored as a function of the circular-convolution index \tilde{m} since it does not depend on the data itself.

Subsampling in ω - \mathbf{k} Space

The previous subsections showed that the velocity part of the computation can be precomputed and therefore the cost of the algorithm becomes essentially quadratic in the spatial dimensions. For prestack 3D migration that is still too expensive. Notice however, that the algorithm doesn't have any significant approximation, since the velocities can be binned as finely as required by their intrinsic accuracy without significantly affecting the cost.

The question is whether we can reduce the computation time significantly by introducing reasonable approximations in the computation of each trace of the wavefield. It should be clear from Equation (6) that the cost of the algorithm comes from having to consider every single trace of the wavefield in the computation of every wavefield trace. We could, for instance, compute only every other wavefield trace in each of the axis of the ω - \mathbf{k} space. For 3D prestack migration that alone would reduce the computation cost to one sixteenth. The

extrapolated wavefield would then be interpolated at each depth step. Or, we can compute only say one in four traces in the *cmp* inline wavenumber axis and every trace in the cross-line offset wavenumber axis. This may be better since the *cmp* inline wavenumber axis is likely to be over-sampled whereas the *xline* offset wavenumber axis is not. Similarly, we may only consider traces of the wavefield in a given neighborhood for the computation of a given trace of the wavefield. If, for example, for the computation of each wavefield trace we use only the half traces closest to the trace being computed along each axis, again, for 3D prestack migration, that would imply a reduction of computation to only one sixteenth of the total computation. If we combine the two forms of computation savings we end up with an algorithm that may begin to be competitive with the mixed-domain algorithms, but that is simpler and more accurate in handling arbitrary lateral velocity variations.

Subsampling in the ω -**k** domain is akin to reducing the lateral extent of the wavefield in the ω -**x** domain. Whether this is acceptable and to what degree in each of the spatial axis is an unresolved issue at this point in our research. On physical grounds we can argue that the wavefield expands as it propagates so perhaps the approximation is valid at small depths but deteriorates at larger depths. Nothing prevents the subsampling to be a function of depth, making it an interesting issue to investigate further. Limiting the number of wavefield components that are actually used to the computation of another component may be acceptable in most cases since the wavefield is expected to be coherent in the ω -**k** domain. However, in specific, important cases, the wavefield may be irregular in the presence of sharp velocity discontinuities. In those cases it is not clear to what extent the approximation deteriorates.

Other issues

One advantage, that may be difficult to quantify, but that may none the less be significant is the simplicity of the algorithm. By doing away with the computation of FFT's, we are also implicitly simplifying the data access, which may be significant advantage for large datasets.

CONCLUSION AND FUTURE WORK

We have shown a theoretically attractive formulation of downward extrapolation in ω -**k** domain capable of handling arbitrary spatial velocity variations. The initial algorithm can be easily modified to make its cost quadratic in the spatial dimensions. This may be appropriate for 2D data or for post-stack 3D data but is certainly not good enough for prestack 3D data. By sacrificing some accuracy, yet to be quantified, we may be able to arrive to a competitive algorithm that is much easier to implement and whose accuracy can be improved at run time.

We need to research the issues of wavefield subsampling and the extent to which wavefield traces influence one another.

REFERENCES

- Biondi, B., 2004, 3-D Seismic Imaging: <http://sepwww.stanford.edu/sep/biondo/Lectures>.
- Gazdag, J., and Sguazzero, P., 1984, Migration of seismic data by phase-shift plus interpolation: *Geophysics*, **49**, no. 2, 124–131.
- Huang, L., Fehleri, M., and Wu, M., 1999, Extended local born fourier migration method: *Geophysics*, **64**, 1524–1534.
- Ristow, D., and Ruhl, T., 1994, Fourier finite-difference migration: *Geophysics*, **59**, no. 12, 1882–1893.
- Stoffa, P., Fokkema, J., de Luna Freire, R., and Kessinger, W., 1990, Migration of seismic data by phase-shift plus interpolation: *Geophysics*, **55**, no. 4, 410–421.
- Xie, X., and Wu, R., 1999, Improving the wide angle accuracy of the screen propagator for elastic wave propagation: 69th Ann. Internat. Mtg., Soc. of Expl. Geophys., Expanded Abstracts, 1863–1866.



Short Note

Migration and modeling of seismic data affected by focusing-effect AVO/AVA

Ioan Vlad¹

INTRODUCTION

Focusing-effect AVO or AVA is the phenomenon of velocity and/or absorption lenses creating substantial amplitude variations, but only small traveltimes anomalies (Kjartansson, 1979). The patterns thus created can interfere significantly with AVO/AVA caused by lithological contrasts at the reflector. To render amplitude analysis feasible, these patterns need to be removed from the image. I will use the acronym “FEAVO” to refer to focusing-effect AVO or AVA in general, reserving “FEAVA” only for specific references to the angle domain. These terms refer only to amplitudes focusing through heterogeneities smaller than the Fresnel zone, as formalized by Spetzler et al. (2004), and which do not cause energy to be lost by sending it outside the finite spatial extent of the seismic survey (i.e., “illumination problems”). Focusing can be positive (usual meaning of term) or negative (i.e., in the case of absorption).

Vlad and Biondi (2002), Vlad (2002), Vlad et al. (2003) and Vlad (2004) have conjectured that the key to removing FEAVO is creating an accurate velocity model that contains the lenses which cause the focusing, then performing one-way wavefield extrapolation migration with this velocity model. I will present a qualitative proof of this statement. I will also analyze the peculiarities of modeling FEAVO effects with one-way or two-way wavefield extrapolation algorithms.

MIGRATING FEAVO-AFFECTED DATA

I will use in my heuristic a constant background velocity model with a FEAVO-causing heterogeneity and a single horizontal reflector of reflectivity one. Since the small size of the heterogeneity localizes the effects it produces, it makes possible to indicate only the presence of focusing in a binary fashion (yes/no). The heterogeneity can be thought of either causing absorption or lens-like focusing by a small amount.

The presence of focusing will be reported to the appropriate *midpoint*, not to the receiver location. This is done because the midpoint coordinate is orthogonal to the offset coordinate

¹email: nick@sep.stanford.edu

in the prestack data space.

The figures below feature straight rays which may seem to indicate constant velocity. However, this takes place only for ease of drawing; the reasoning that follows does not require constant velocity. I will also consider a single signed offset h . The mental experiments to be performed below will be identical both for any other offset and for the prestack dataset taken together.

Figures 1 and 2 show a seismic experiment decomposed into two separate steps. In the

Figure 1: Single offset seismic experiment – part 1: propagation from sources to reflector, and graph with focusing at the reflector `nick1-f1` [NR]

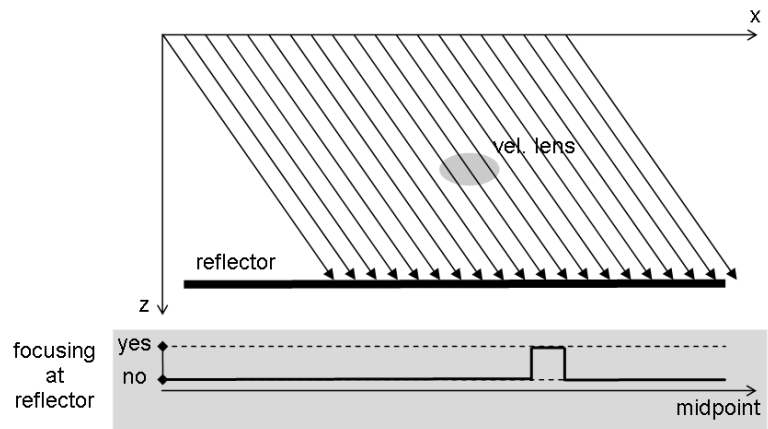
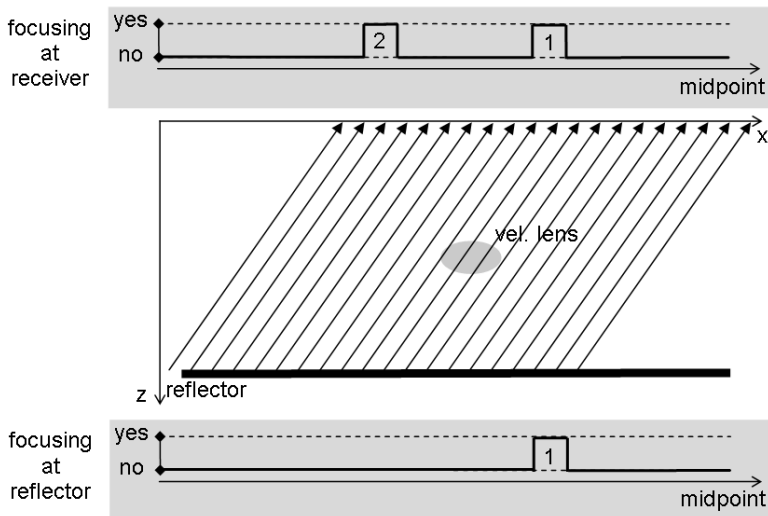


Figure 2: Single offset seismic experiment – part 1: graph with focusing at the reflector (bottom), propagation from the reflector to the receivers, and graph with focusing as recorded by receivers (top) `nick1-f2` [NR]

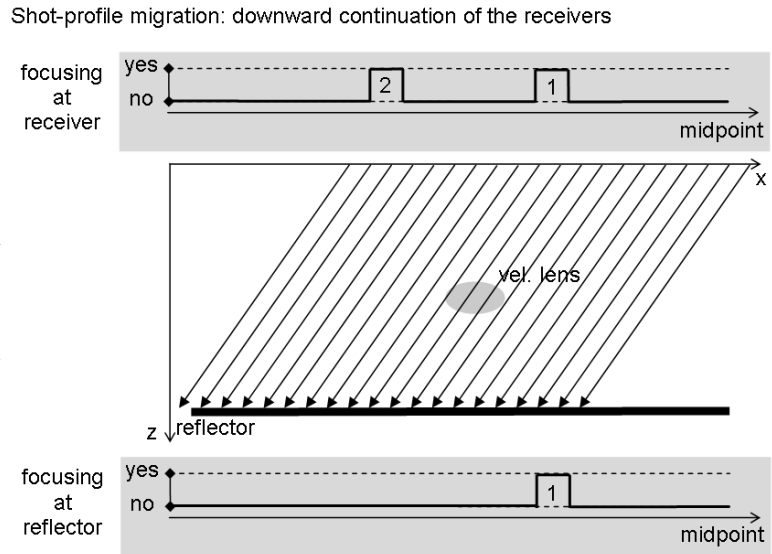


first step (Figure 1), the wavefield propagates from the sources to the reflector. Only a single midpoint local area is affected by focusing. In the second step (Figure 2), the wavefield propagates to the surface. Already existing focusing is preserved, and a new pass through the heterogeneity causes a second focusing area to appear. The focusing areas detected by the receivers at the surface are reported at the appropriate midpoints (not receiver locations) in the upper graph. The two midpoint local areas in which focusing is present are located at the intersection of the two arms of a midpoint-offset “Kjartansson V” (Kjartansson, 1979) with a line of constant offset h .

At this point one could make the argument that migration by definition recovers amplitudes at the reflector, and it cannot solve illumination problems, so effect 1 in Figure 2 will not be removed by migration, and one should instead try a regularized inversion that will smooth out small irregularities. Let us however examine more closely what happens with the energy from that offset when we do shot-profile migration using all shots.

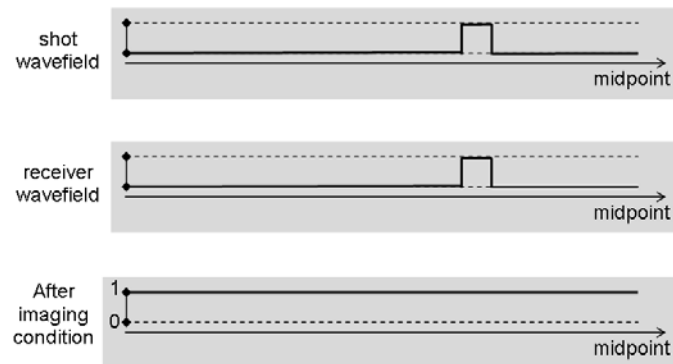
Downward continuation of the shots wavefields is properly described by Figure 1 and will produce at the reflector, as expected, the same focusing as the real experiment. Downward continuing the receivers (Figure 3) with the correct velocity (which includes both the background

Figure 3: Downward continuing the receivers in shot-profile migration: graph with focusing as recorded in the data (top), downward continuation with the correct velocity through the heterogeneity, and graph with residual focusing at the reflector (bottom) [nick1-f3] [NR]



and the heterogeneity) eliminates focusing area 2, but leaves focusing area 1 intact. What the objection stated in the previous paragraph failed to take into account, though, is the imaging condition (Figure 4). The imaging condition, taken as a black box, is not sensitive to the par-

Figure 4: The wavefields need only be *similar*, not *uniform*, in order for the imaging condition to produce a uniform-amplitude (no focusing) reflector. [nick1-f4] [NR]



ticular values of either the shot wavefield or the receiver wavefield, but to how close they are to each other. If at one location they are identical (for this idealized experiment we can use the word “identical”), it reports a reflection there with a probability (a.k.a. reflection coefficient) of 1. In our case (Figure 4) the shot wavefield and the receiver wavefield are identical in every point, and therefore the uniform value of 1 for reflectivity is recovered. Shot-profile migration with all sources therefore completely eliminates FEAVO from the image if the correct velocity

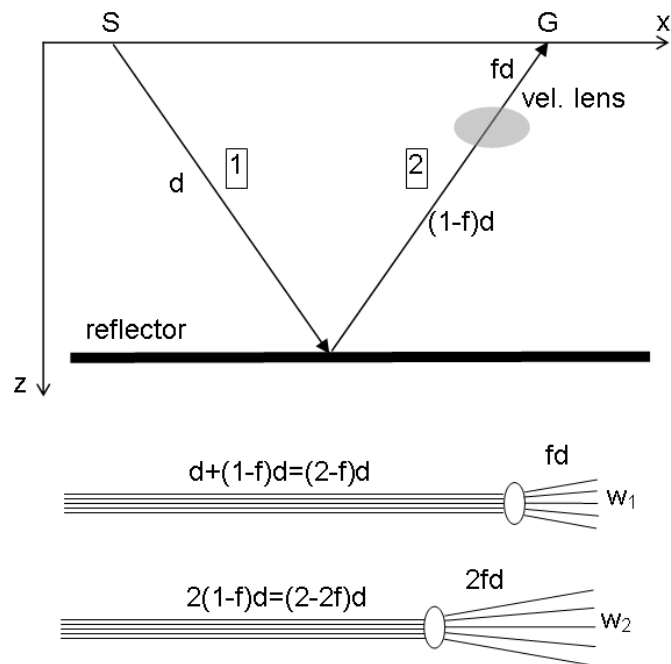
is provided. Survey-sinking migration, being mathematically equivalent to it (Biondi, 2003), also eliminates FEAVO if the velocity is provided.

MODELING FEAVO-AFFECTED DATA

It is not very straightforward why one-way wavefield extrapolation schemes would cause problems with modeling FEAVO, while they are fine for the adjoint of modeling, migration. There are however differences. Some operations can be irreversible (in the information theory meaning of the word) even if they have an adjoint. For example, summation of several values (“state 1”) into a single one (“state 2”) has the spreading of the sum as an adjoint. But a large quantity of information (all the frequencies except the zero one) was lost when summing, and spreading cannot recover that. State 2 simply has less information (and more entropy) than state 1, and anything we do to state 2 cannot reverse that (i.e. spreading only recovers the zero frequency). A related phenomenon happens during the imaging condition. Shot-profile migration, in the example previously described, has information on the source wavefield and receiver wavefield before they are combined during the imaging condition. The new state (after the imaging condition) has less information than the old one, and when trying to go back, we cannot recover lost information *without paying more* in computational expenses. What errors were introduced by the loss?

Exploding-reflector modeling with the one-way wave equation is a popular way of generating seismic data. At each depth level, the reflectivity values are spread to all offsets, added to the wavefield being upward propagated from below, then the wavefield is marched upwards to the next level. The fact that the wavefields travel along only a single propagation leg is accounted for by halving the velocity, effectively multiplying the traveltimes by two. This produces correct traveltimes, correct geometry of FEAVO patterns (Kjartansson V’s), and the FEAVO in the resulting data is eliminated by migration. The problem is that focusing, while localized when compared to the size of the survey, is not a binary condition. Figure 5 shows the details. If only pure absorption is involved, it would not matter whether the heterogeneity lied closer to the beginning than to the end of the travel path: multiplication of amplitudes by an absorption factor is commutative. But if velocity is at play, as it is often the case, then the microscale of the effects (assumed to be divergent in the figure) will look different if: (A) the wavefront goes along legs 1 and most of 2 and then encounters the velocity anomaly, as in the real experiment, or (B) it travels only along leg 2 in the numerical experiment and the traveltimes are multiplied by two. The microcharacter of the FEAVO effects will look different than for real data. This is a second-order effect only, but it is real. It can be ignored if the scope of the analysis is of a larger scale, but it can be important in particularly amplitude-sensitive processes, such as Wavefield-Extrapolation Migration Velocity Analysis, which inverts amplitude anomalies into velocity updates. There are only two cases when the approximations of one-way modeling are not a problem. The first is when the anomalies are purely due to absorption. The second case is when migrating the modeled data with the correct velocity and with an imaging algorithm close in accuracy (adjoint if possible) to the one used in modeling. In other cases, especially when studying the behavior of FEAVO itself, this effect should be taken into account. Two-pass one way or two-way wave equation algorithms should be used

Figure 5: Performing a real experiment or two-way modeling, in which the energy travels along leg (1) then along leg (2) produces a focused beam of width w_1 . This can be different from the beam of width w_2 produced by doubling traveltimes obtained by one-way modeling, even if at a scale at which the width of the beams is negligible, the travel paths are identical. [nick1-f5] [NR]



for FEAVO modeling in such cases.

CONCLUSIONS

This paper presented a qualitative proof that focusing-effect AVO/AVA (FEAVO/FEAVA) can be removed from the seismic image just by a single pass of one-way wavefield extrapolation migration. Modeling such data is more complicated. If just correct-velocity images of the modeled data were needed, then the data could be modeled with one-way exploding-reflector schemes. If data needed to be analyzed before migration, or if incorrect velocities were used for migration, then modeling should be done with a two-way scheme, or a two-pass, one-way one.

ACKNOWLEDGMENTS

I thank James Rickett, Biondo Biondi and Paul Sava for meaningful discussions.

REFERENCES

- Biondi, B., 2003, Equivalence of source-receiver migration and shot-profile migration: Equivalence of source-receiver migration and shot-profile migration:, Soc. of Expl. Geophys., Geophysics, 1340–1347.

- Kjartansson, E., 1979, Analysis of variations in amplitudes and traveltimes with offset and midpoint: SEP-**20**, 1–24.
- Spetzler, J., Jocker, J., Smeulders, D., and Trampert, J., 2004, Validation of first-order wave diffraction theory by an ultrasonic experiment:, *in* 74th Ann. Internat. Mtg. Soc. of Expl. Geophys., 2180–2183.
- Vlad, I., and Biondi, B., 2002, Velocity estimation for seismic data exhibiting focusing-effect avo: SEP-**111**, 107–123.
- Vlad, I., Biondi, B., and Sava, P., 2003, Velocity estimation for seismic data exhibiting focusing-effect AVO (part 3): SEP-**114**, 101–110.
- Vlad, I., 2002, Velocity estimation for seismic data exhibiting focusing-effect avo (part 2): SEP-**112**, 47–64.
- Vlad, I., 2004, Velocity estimation for seismic data exhibiting focusing-effect avo (part 4): SEP-**115**, 265–272.

Fourier-domain imaging condition for shot-profile migration

Brad Artman and Sergey Fomel¹

ABSTRACT

Cross-correlating up-coming and down-going wavefields inherently applies a spatial multiplication. This multiplication could be performed in the wave-number domain as a convolution. However, the full imaging condition, including subsurface offset, transforms to a Fourier domain equivalent that is also a lagged multiplication. This fact allows for the simple analysis of anti-aliasing criteria. Migrations with synthetic data with flat and dipping reflectors in a homogeneous medium are produced to evaluate the Fourier domain algorithm and shots from the Marmousi data set are shown as examples of its efficacy. Periodic replications in the image space are introduced when solving the imaging condition in the Fourier domain which make results unsatisfactory. The cost of computing the imaging condition in the Fourier domain is much higher than its space domain equivalent since very few subsurface offsets need to be imaged if the velocity model is reasonably accurate. Analysis of the Fourier domain imaging condition leads to the conclusion that anti-aliasing efforts can be implemented post-migration.

INTRODUCTION

Artman et al. (2003) introduced the advantages of a Fourier domain imaging condition for shot-profile migration in order to address aliasing problems due to unequal discretization of source and receiver acquisition geometries. It was posited, though not rigorously proven, that the details of the obvious implementation were also a lagged multiplication of the wavefields in the Fourier-domain.

When subsurface offset is introduced to the space-domain imaging condition, it is not a strict multiplication across the space axis. The lagged multiplication of the up- and down-going wavefields exist somewhere between simple multiplication and cross-correlation. By summing over the offset axis we are generating, we would be performing a rigorous correlation in space. Maintaining this axis invalidates the conventional relationships of operations in dual spaces that, in this case, results in symmetric (though not perfectly), imaging conditions in both the space and Fourier-domains.

In the theory below, we develop the imaging condition in terms of k_x and k_h . We then present synthetic migrations with the Fourier-domain imaging condition to show its equivalence with the space-domain imaging condition. There are, however, several key differences,

¹email: brad@sep.stanford.edu, sergey.fomel@beg.utexas.edu

associated with aliased replications, between the two results that can be seen by viewing the results in the $x - h$ plane at the depth of an imaging point. These have important ramifications for the use of this form of the imaging condition at shallow depths. Finally, by inspecting the form of the equation, we can see how the implementation of anti-aliasing criteria can be appropriately applied post-migration. This happy fact is beneficial because the Fourier-domain imaging condition is much more expensive to calculate than its space-domain equivalent.

THEORY

The space-domain shot-profile imaging condition including subsurface offset for shot-profile migration (Rickett and Sava, 2002) is

$$I(x, h)|_{\omega, z} = U(x + h) D^*(x - h), \quad (1)$$

Where I is the migrated image produced by cross-correlating the up-coming, U , and down-going, D , wavefields at every depth and frequency. Both x and h can be areal vectors. $*$ represents complex conjugation. To derive the Fourier-domain equivalent, we will perform a piece-wise proof and begin with the Fourier transform D^* to \hat{D}^* (neglecting Fourier scaling)

$$\hat{I}(x, h) = U(x + h) \int \hat{D}^*(k_s) e^{i k_s (x - h)} dk_s. \quad (2)$$

Continue by Fourier transforming the variable x to find

$$\hat{I}(k_x, h) = \int U(x + h) \int \hat{D}^*(k_s) e^{i k_s (x - h)} dk_s e^{-i x k_x} dx. \quad (3)$$

By reordering variables, the equivalent form

$$\begin{aligned} \hat{I}(k_x, h) &= \int \hat{D}^*(k_s) e^{-i k_s h} \int U(x - h) e^{-i x (k_x - k_s)} dx dk_s \\ &= \int \hat{D}^*(k_s) e^{i h (k_x - 2k_s)} \int U(x') e^{-i x' (k_x - k_s)} dx' dk_s \end{aligned} \quad (4)$$

is achieved. From here, we can recognize the inner integral is the Fourier transform of the wavefield U which can be replaced directly to yield

$$\hat{I}(k_x, h) = \int \hat{U}(k_x - k_s) \hat{D}^*(k_s) e^{i h (k_x - 2k_s)} dk_s. \quad (5)$$

With the use of the definition of offset, $k_h = k_x - 2k_s$, we can replace several of the above arguments with equivalent expressions to find

$$\hat{I}(k_x, h) = \frac{1}{2} \int \hat{U}\left(\frac{k_x + k_h}{2}\right) \hat{D}^*\left(\frac{k_x - k_h}{2}\right) e^{i h k_h} dk_h. \quad (6)$$

The last integral is recognized as an inverse Fourier transform, this time over the k_h variable. Using this fact, we arrive at the multi-dimensional (over x and h , which can be two-dimensional themselves) Fourier transform of the general shot-profile imaging condition

$$\hat{I}(k_x, k_h) = \frac{1}{2} \hat{U}\left(\frac{k_x + k_h}{2}\right) \hat{D}^*\left(\frac{k_x - k_h}{2}\right). \quad (7)$$

From this equation, the result that the Fourier-domain equivalent to the conventional space-domain imaging condition for shot-profile migration is again a lagged multiplication of the up-coming and down-going wavefields at each frequency and depth level. Evaluating the arguments inside the wavefields to produce a component of the image shows that the wavefields, in the wavenumber domain, will need to be interpolated by a factor of two to calculate the image space output. The Table 1 showing example calculations of the components of the image space looks like

		k_h		
		-1	0	1
k_x	-1	$\hat{U}(\frac{-2}{2})\hat{D}^*(0)$	$\hat{U}(\frac{-1}{2})\hat{D}^*(\frac{-1}{2})$	$\hat{U}(0)\hat{D}^*(\frac{-2}{2})$
	0	$\hat{U}(\frac{-1}{2})\hat{D}^*(\frac{1}{2})$	$\hat{U}(0)\hat{D}^*(0)$	$\hat{U}(\frac{1}{2})\hat{D}^*(\frac{-1}{2})$
	1	$\hat{U}(0)\hat{D}^*(\frac{2}{2})$	$\hat{U}(\frac{1}{2})\hat{D}^*(\frac{1}{2})$	$\hat{U}(\frac{2}{2})\hat{D}^*(0)$
	2	$\hat{U}(\frac{1}{2})\hat{D}^*(\frac{3}{2})$	$\hat{U}(\frac{2}{2})\hat{D}^*(\frac{2}{2})$	$\hat{U}(\frac{3}{2})\hat{D}^*(\frac{1}{2})$

Table 1: Layout of wavenumber components in Fourier-domain imaging conditions

SYNTHETIC TESTS

To test the above algorithm, synthetic data was generated and migrated with both the conventional space-domain and Fourier-domain imaging conditions. Images were created by migrating a single shot produced over a single reflecting layer within a constant velocity medium. The location, x , and offset, h , axes had the same extent and sampling. This is true for both implementations of the imaging condition.

Figure 1 shows the comparison of the space-domain impulse response to the Fourier equivalent developed above for the zero dip reflector. Both seem to provide identical results when viewed at subsurface offset $h = 0$ at the $x - z$ plane. The smile shapes are due to the limited extent of the acquisition along the surface. However, Figure 2 compares the algorithms across the $x - h$ plane at the depth of a correctly migrated image point. While at zero offset the two images are the same, the Fourier-domain implementation has obvious replications at the end of the dog-bone shaped energy distribution. Aliased energy is also introduced into the upper-right and lower-left corners of the image space. This periodicity is not encountered with the space-domain implementation.

By adding dip to the reflection point, the dog-bone shape in the $x - h$ plane becomes skewed. Figures 3 and 4 are produced with a reflector with 20° and 40° dip respectively. While the zero-offset image of the $x - z$ plane remains the same, the periodicity of the Fourier-

Figure 1: Migration impulse response through a constant velocity medium of both space-domain and Fourier domain implementation of the shot-profile imaging condition viewed at $h = 0$ on the $x - z$ image plane. `brad3-imp` [CR]

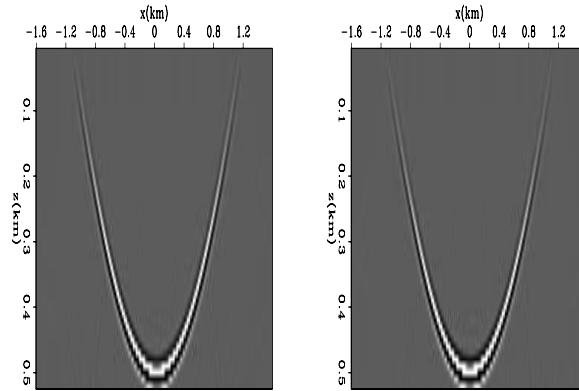
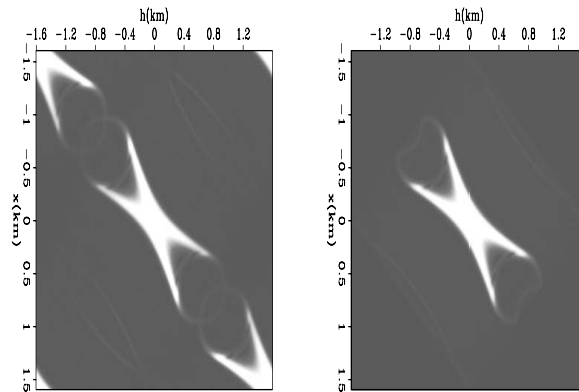
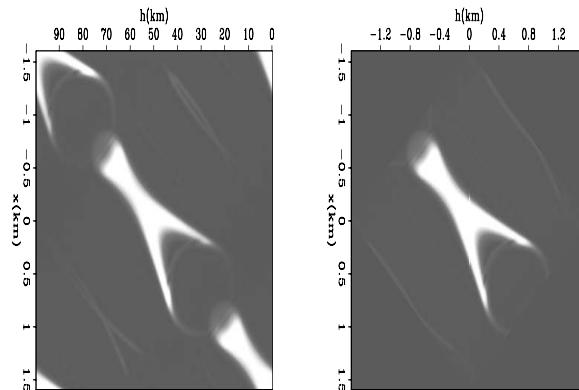


Figure 2: Migration impulse response through a constant velocity medium of both space-domain and Fourier domain implementation of the shot-profile imaging condition viewed at the depth of a focused image point on the $x - h$ image plane. `brad3-imp-comp` [CR]



domain algorithm is again visible as compared to the computation of the imaging condition in the space-domain. Notice that as dip increases, the saddle point of the dog-bone has moved away from zero offset and the image gives the sense of tipping into the page.

Figure 3: 20° dip reflector image comparison. Left is Fourier-domain implementation. Right is space-domain implementation. Image is extracted at the depth of a focused image point on the $x - h$ image plane. `brad3-imp-dip-comp` [CR]

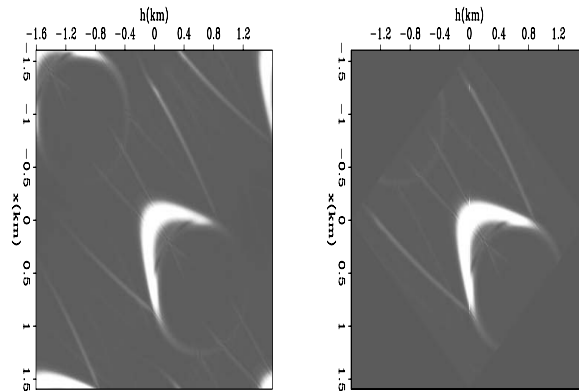


The onset of the replications are at precisely half the offset and surface location axes. To remove this type of artifact in the Fourier domain, interpolation of both axes by a factor of two would be required. From equation 7, we note that the wavefields have already required a factor of two interpolation to facilitate the algorithm. Interpolating the image by a factor of two again substantially increases memory consumption and computational effort for this implementation.

The first shot from the Marmousi synthetic data was migrated to examine the effects of the

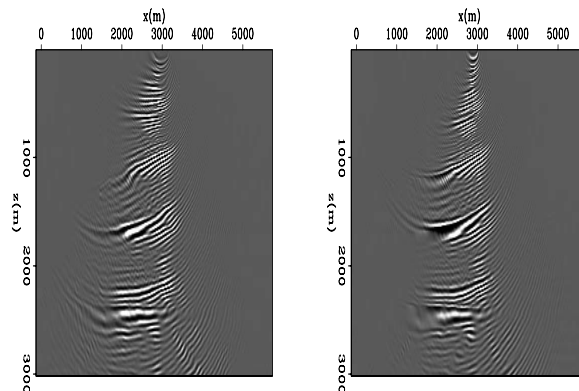
Figure 4: 40° dip reflector image comparison. Left is Fourier-domain implementation. Right is space-domain implementation. Image is extracted at the depth of a focused image point on the $x - h$ image plane.

`brad3-imp-dip-2-comp` [CR]



above periodicity injected into the image using the Fourier-domain imaging condition. Figure 5 compares the image from the first shot in the data computed with both space-domain and Fourier-domain imaging conditions. At great depth, the images are largely comparable, while at less than 1000 meters, the images are completely different. This is due to the combined effects of periodicity of the Fourier computed image and the steep dips of the model.

Figure 5: Images from the first shot in the Marmousi data set. Left panel computed with the Fourier-domain imaging condition, and the right panel with the conventional space domain algorithm. `brad3-marm.new` [CR]



Deeper in the section, the problem is less apparent and the Fourier domain imaging condition is much closer to the space-domain result. Figure 6 demonstrates how the zeroing of the evanescent waves through the course of the migration effectively limits the range of wavenumber energy allowed into the image. After the evanescent limitations are more restrictive than the effects of the Fourier domain periodicity, the artifacts begin to diminish.

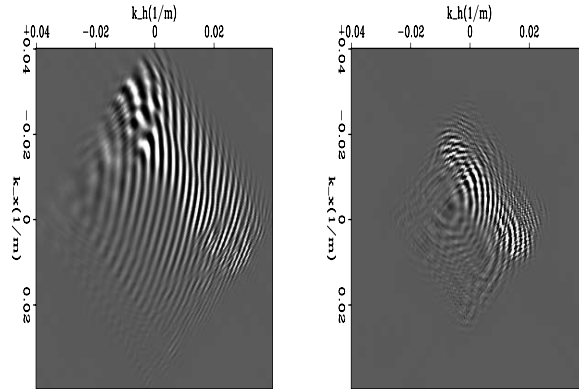
However, the images for a complex medium are definitely not strictly equivalent for the two alternative imaging condition implementations. By interpolating the k_x and k_h axes, it is possible to remove the limitation imposed by the periodicity at the memory/disk cost of $4n_x^2$ per depth level.

ANTI-ALIASING IMPLICATIONS

Figure 7 shows the impact on the image space of subsampling the shot axis by a factor of ten while migrating the flat reflector synthetic data described above. The left panel imaged with

Figure 6: Images from the first shot in the Marmousi data set. Depth slices, computed with the Fourier domain imaging condition, are extracted from $z = 250\text{m}$ and $z=1188\text{m}$.

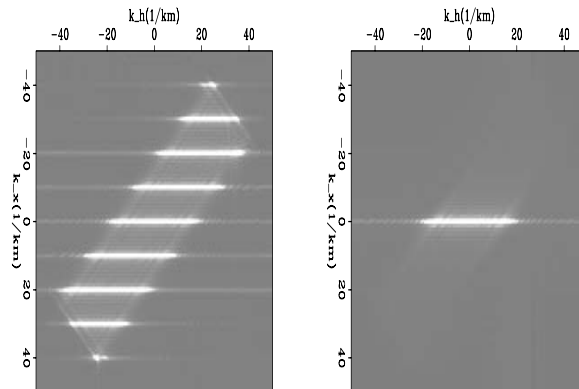
`brad3-dslice` [CR]



only every tenth shot, while right panel migrated shots at every receiver location. The shot-axis, which could be drawn at a 45° angle up and to the right, shows inappropriate replications (Rickett and Sava, 2002). The data are modeled with sufficient receiver density, that this level of decimation does not alias the receiver gathers. This is corroborated by the absence of aliased energy in the upper-left and lower right quadrants.

Figure 7: Left panel shows the wavenumber energy for a migrated flat reflector when using sources at every tenth receiver location. On the left, and all source locations.

`brad3-alias-flat` [CR]



From this simple example, we can see that the anti-aliasing restriction required for the decimated migration are sloped lines to remove energy from the upper-right and lower-left quadrants. In general, any of the four corners may experience aliased replications depending on the inequality between receiver and source sampling during acquisition. The form of the imaging condition in the Fourier domain as shown in equation 7 provides important insight into how to implement anti-aliasing criteria for shot-profile migration.

Limiting the image by neither constant k_x nor k_h will appropriately remove the aliased energy of Figure 7. Instead, one should limit the maximum bandwidth of both the \hat{U} and \hat{D}^* wavefields. Table 1 provides a convenient display of this fact. This will maintain the center diamond of appropriate energy. If the anti-aliasing bandlimit is applied to the image space instead of the two wavefields used to calculate it, there are two important conclusions: 1) the bandlimit should be the same for both the offset and location axes, and 2) the limit is a diamond shaped, not circular, filter on the $k_x - k_h$ plane.

CONCLUSION

The calculation of subsurface offset in the conventional space-domain imaging condition for shot-profile migration requires a series of lagged multiplications of the up-coming and down-going wavefields. Because it is not a simple multiplication, the development of its Fourier is required rather than axiomatically assuming it to take the form of a convolution. The result shown above has a very similar lagged multiplication form to its space-domain equivalent.

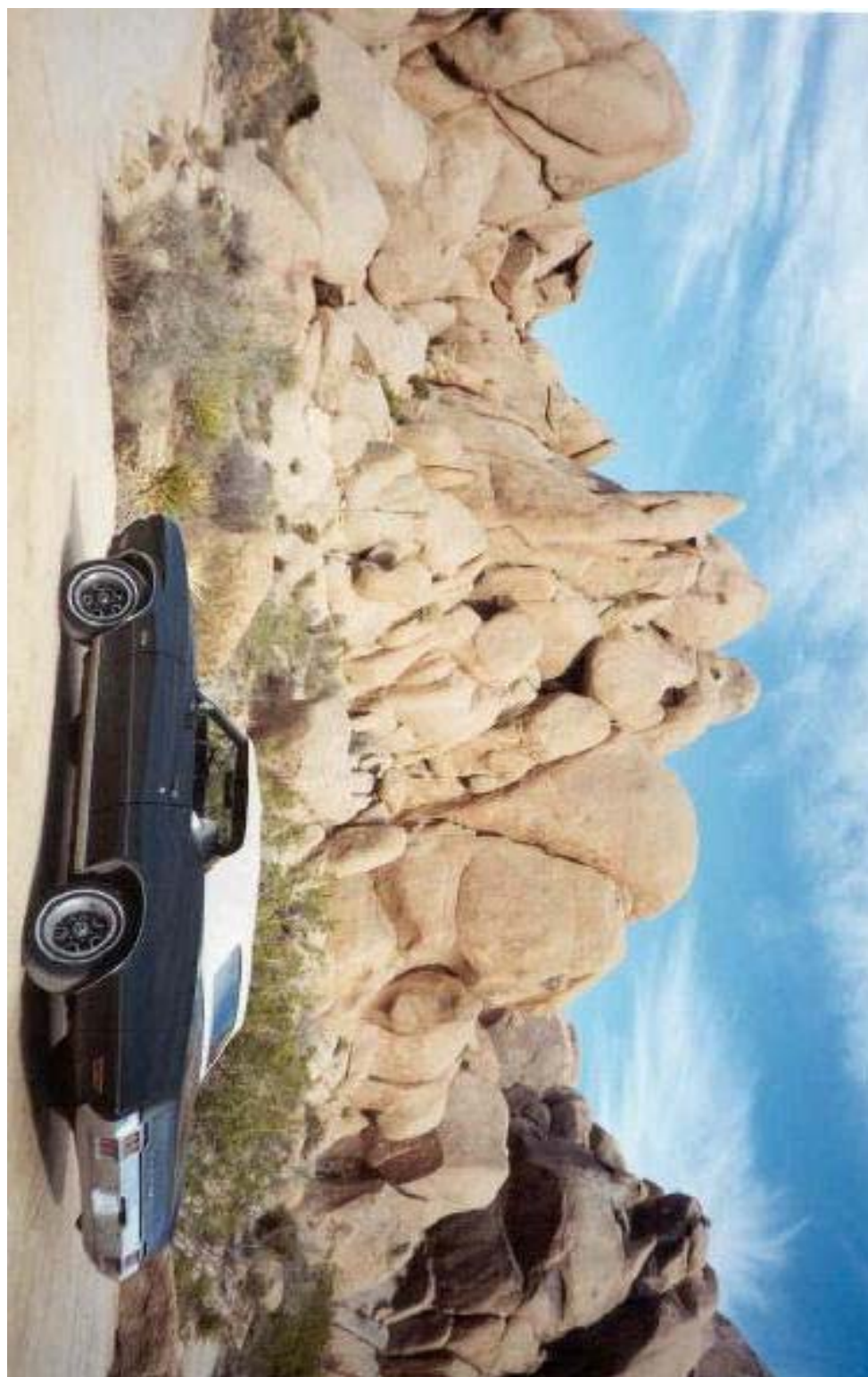
Several interpolations are required to implement the imaging condition as a function of wave number. First, the input wavefields, and then the calculated model space, must be twice finer sampled in wavenumber. Completely inadequate results are obtained for complex earth models if both interpolation steps are not honored. These steps increase the memory and computational demands of the method to unacceptable levels. Further, an equal number of offset-wavenumbers must be calculated to avoid aliasing as opposed to $O(10)$ for a space-domain implementation where one is reasonably confident in the accuracy of the velocity model.

Analyzing the form of the imaging condition allows us to make important conclusions about how to mitigate migration aliasing problems inherent with shot-profile migrations when the source and receiver sampling is unequal. Most importantly, anti-aliasing strategies can be implemented in the image domain after migration without needing to resort to the very expensive Fourier-domain imaging condition.

While the development of a Fourier-domain imaging condition for shot-profile migration has been presented, the periodicity of the process introduces unwanted artifacts into the image result. The form of the equation, however, provides rigor and understanding as to how to design anti-aliasing filters for data sets that do not have equal sampling of the source and receiver data axes. Further, these bandlimits can be applied on smaller post-migration volumes, possibly even during the course of converting subsurface offset to angle in the Fourier-domain at little to no additional cost.

REFERENCES

- Artman, B., Biondi, B., and Shragge, J., 2003, Operator aliasing in wavefield continuation migration: Soc. of Expl. Geophys., 73rd Ann. Internat. Mtg., 1091–1093.
- Rickett, J. E., and Sava, P. C., 2002, Offset and angle-domain common image-point gathers for shot-profile migration: Geophysics, **67**, no. 03, 883–889.



A self-adaptive algorithm for choosing reference velocities in the presence of lateral velocity variations

Huazhong Wang and Guojian Shan¹

ABSTRACT

Seismic wave propagation depicted with the perturbation theory has important and wide-spread uses in reflection seismology. As we know, in perturbation theory, wave propagation needs a reference velocity. The closer the reference velocity is to the true velocity, the more accurate the wave propagation is. However, it is not easy to choose reasonable reference velocities in the presence of severe lateral velocity variations. Assigning a reference velocity value at each spatial point is not computationally feasible, because there is a trade-off between the calculation cost and the number of reference velocities. We show that the accuracy of seismic wave propagation can be more easily improved by choosing a set of reasonable reference velocities rather than by optimizing a one-way wave propagator. Therefore, we introduce a self-adaptive approach to choose a set of reference velocities for an extrapolation layer, in the presence of lateral velocity variations. Through sorting the velocity data an array with increasing values, and by setting a threshold average-velocity ratio or velocity- variance ratio, we can choose a set of reasonable reference velocities for wavefield extrapolation. This method can also be used for image edge detecting. It is flexible and computationally cost-effective.

INTRODUCTION

Seismic migration is used to image recorded reflection and scatter events based on wave theoretical approaches, by de-propagating them to their true subsurface positions. Wave propagation and de-propagation is based on perturbation theory. Nowadays, prestack depth migration (**PSDM**) has become a most effective tool for imaging complex geological structures. Assuming the macro-velocity field is accurate enough, the migration operators or wave propagators should be competent for accurately expressing wave propagation in media with severe lateral velocity variations.

Stoffa et al. (1990) introduced a first-order split-step correction, which is accurate for flat reflectors. However, the accuracy of the migration operator for depicting wave propagation decreases as reflectors become steeper and the differences between the reference and migration velocities increase. Therefore, Ristow and Ruhl (1994) put forward the Fourier finite-difference (FFD) operator, and Huang et al. (1999) and Rousseau and de Hoop (2001) intro-

¹email: wang@sep.stanford.edu, shan@sep.stanford.edu

duced the generalized-screen propagator GSP, to compensate for high-order terms neglected when imaging steeply dipping reflectors with the Split-Step Fourier SSF operator. The FFD operator deals with the high-order terms in the frequency-space domain; the GSP processes them in the frequency-wavenumber domain. The FFD operator requires that the reference velocity is lower than the minimum velocity in an extrapolation layer, because the sign of the coefficients in the finite-difference equation can not be changed at different lateral points in a depth layer. Otherwise, calculation instability will occur. Therefore, even if a set of suitable reference velocities is given, the FFD operator cannot give a very good image.

Biondi (2002) modified the general FFD operator by introducing the interpolation of two wavefields: the first wavefield is obtained by applying the FFD correction, starting from a reference velocity lower than the medium velocity; the second wavefield is obtained by applying the FFD correction starting from a reference velocity higher than the medium velocity.

In fact, the high-order terms in wave-propagation perturbation theory are generated by the velocity perturbation between the true velocity and the reference velocity. If the reference velocity is chosen as close as possible to the true velocity, the SSF, FFD and GSP operators can accurately characterize the wave propagation in media with severe lateral velocity variations. Furthermore, the imaging quality can be improved with such propagators.

Assuming that the macro-velocity model for imaging is accurate enough, the main reason for most imaging errors is that the *one-way wave equation can not accurately characterize the wave propagation in the case of severe lateral velocity variations*. In such cases, steeply dipping reflectors cannot be clearly imaged. We can decrease these errors either by using an optimized, but complex propagator, or by choosing a set of reasonable reference velocities and using a simple propagator. We think that the latter is much more flexible and cost-effective. Of course, both approaches can be combined together.

Clapp (2004) proposed that the reference velocity can be selected by a generalized Lloyd method. The basic idea behind Lloyd's method is to iteratively improve the quantization of a function by looking at the velocity statistics of each region (such as mean, median, and variance), and then changing the boundaries of the regions at each iteration to find the solution which is optimal based on some criterion.

Now, we introduce a self-adaptive strategy for selecting a reasonable reference velocity in the presence of lateral velocity variations. The main steps include setting a threshold for the ratio between two adjoining reference velocities, sorting the velocity slice into an array, and detecting the edges of velocity regions using velocity averages and variances in the different regions. The resulting reference velocity field and the imaging results produced with it indicate that our approach is correct and effective. Meanwhile, the method is flexible in use, computationally efficient, and easy to program in either 2D or 3D. The approach can also be used for 2D or 3D image edge detecting. Numerical tests demonstrate that the method is effective.

WAVE PROPAGATOR CHARACTERIZED BY PERTURBATION THEORY

The Single-Square-Root (**SSR**) wavefield-extrapolation equation in the case of lateral velocity variation is of the following form (Claerbout, 1985):

$$\frac{\partial P(t, x, y, z)}{\partial z} = \pm \left[\frac{1}{v^2(x, y, z)} - \left(\frac{\partial t}{\partial x} \right)^2 - \left(\frac{\partial t}{\partial y} \right)^2 \right]^{\frac{1}{2}} \frac{\partial P(t, x, y, z)}{\partial t}. \quad (1)$$

The sign convention for the square root is negative for upcoming wavefield and positive for downgoing wavefield. We decompose the velocity field into two parts: the background velocity field and the velocity perturbation. In fact, we process the slowness field because the decomposition of the slowness is linear. The slowness field decomposition is defined as follows:

$$S(x, y, z) = \frac{1}{v(x, y, z)} = \frac{1}{v(z)} + \Delta S(x, y, z) = S_0(z) + \Delta S(x, y, z), \quad (2)$$

where $S_0(z)$ is the background slowness, $v(z)$ the background velocity and $\Delta S(x, y, z)$ is the slowness perturbation. We hope that the velocity perturbation $\Delta S(x, y, z)$ is as small as possible. Substituting the slowness-field-decomposition equation (2) into the wavefield-depth-extrapolation equation (1) and discarding the second-order terms of the slowness perturbation yields the following formula:

$$\frac{\partial P(t, x, y, z)}{\partial z} = \pm \left[\frac{1}{v^2(z)} + 2S_0(z)\Delta S(x, y, z) - \left(\frac{\partial t}{\partial x} \right)^2 - \left(\frac{\partial t}{\partial y} \right)^2 \right]^{\frac{1}{2}} \frac{\partial P(t, x, y, z)}{\partial t}. \quad (3)$$

Equation (3) can be rewritten as follows:

$$\frac{\partial P(t, x, y, z)}{\partial z} = \pm \left\{ \sqrt{\frac{1}{v^2(z)} - \left(\frac{\partial t}{\partial x} \right)^2 - \left(\frac{\partial t}{\partial y} \right)^2} \sqrt{1 + \frac{2S_0(z)\Delta S(x, y, z)}{\frac{1}{v^2(z)} - \left(\frac{\partial t}{\partial x} \right)^2 - \left(\frac{\partial t}{\partial y} \right)^2}} \right\} \frac{\partial P(t, x, y, z)}{\partial t}. \quad (4)$$

In simplicity, we define $A = \sqrt{\frac{1}{v^2(z)} - \left(\frac{\partial t}{\partial x} \right)^2 - \left(\frac{\partial t}{\partial y} \right)^2}$. Taylor-series expansion of the second square-root term in equation (4), neglecting second- and higher-order terms, yields

$$\frac{\partial P(t, x, y, z)}{\partial z} \approx \pm \left\{ A + \frac{S_0(z)\Delta S(x, y, z)}{A} \right\} \frac{\partial P(t, x, y, z)}{\partial t}. \quad (5)$$

Meanwhile, equation (5) can be rearranged as follows:

$$\begin{aligned} \frac{\partial P(t, x, y, z)}{\partial z} &= \pm [A] \frac{\partial P(t, x, y, z)}{\partial t} \\ &\pm \frac{S_0(z)}{A} \frac{\partial [\Delta S(x, y, z) P(t, x, y, z)]}{\partial t}. \end{aligned} \quad (6)$$

Transforming equation (6) into frequency-wavenumber domain gives

$$\frac{\partial P(\omega, k_x, k_y; z)}{\partial z} = \mp i k_0 k_z P(\omega, k_x, k_y; z) \mp \frac{i}{k_z} FT_{x,y} [\omega \Delta S(x, y, z) P(\omega, x, y; z)], \quad (7)$$

where $k_0 = \frac{\omega}{v(z)}$, $k_z = \sqrt{1 - \left(\frac{k_T}{k_0}\right)^2}$, $k_T = \sqrt{k_x^2 + k_y^2}$. Equation (7) can be split into two equations:

$$\frac{\partial P(\omega, k_x, k_y; z)}{\partial z} = \mp i k_0 k_z P(\omega, k_x, k_y; z) \quad (8)$$

and

$$\frac{\partial P(\omega, k_x, k_y; z)}{\partial z} = \mp \frac{i}{k_z} FT_{x,y} [\omega \Delta S(x, y, z) P(\omega, x, y; z)]. \quad (9)$$

Equation (8) downward extrapolates the wave field in the background velocity. Equation (9) describes the scattering wave propagation, which is caused by the slowness perturbation. The total wavefield is the summation of the background and scattering wavefields. When the vertical wavenumber k_z approaches zero, equation (9) has a singular point. To circumvent the problem, $\frac{1}{k_z}$ is expanded into a Taylor series:

$$\begin{aligned} \frac{1}{k_z} &= \frac{1}{\sqrt{1 - \left(\frac{k_T}{k_0}\right)^2}} = 1 + \frac{1}{2} \left(\frac{k_T}{k_0}\right)^2 + \frac{1 \cdot 3}{2 \cdot 4} \left(\frac{k_T}{k_0}\right)^4 + \cdots + \frac{(2n-1)!!}{2^n (n)!!} \left(\frac{k_T}{k_0}\right)^{2n} + \cdots \\ &= 1 + \sum_{n=1}^{\infty} \frac{(2n-1)!!}{2^n} \left(\frac{k_T}{k_0}\right)^{2n}. \end{aligned} \quad (10)$$

Substituting formula (10) into equation (9) gives,

$$\begin{aligned} \frac{\partial P(\omega, k_x, k_y, z)}{\partial z} &= \mp i \left\{ 1 + \sum_{n=1}^{\infty} \frac{(2n-1)!!}{2^n} \left(\frac{k_T}{k_0}\right)^{2n} \right\} FT_{x,y} [\omega \Delta S(x, y, z) P(\omega, x, y; z)] \\ &= \mp i FT_{x,y} [\omega \Delta S(x, y, z) P(\omega, x, y; z)] \\ &\mp i \sum_{n=1}^{\infty} \frac{(2n-1)!!}{2^n} \left(\frac{k_T}{k_0}\right)^{2n} FT_{x,y} [\omega \Delta S(x, y, z) P(\omega, x, y; z)]. \end{aligned} \quad (11)$$

Equation (11) is also split into two equations:

$$\frac{\partial P(\omega, x, y, z)}{\partial z} = \mp i \omega \Delta S(x, y, z) P(\omega, x, y; z) \quad (12)$$

and

$$\frac{\partial P(\omega, k_x, k_y, z)}{\partial z} = \mp i \sum_{n=1}^{\infty} \frac{(2n-1)!!}{2^n} \left(\frac{k_T}{k_0}\right)^{2n} FT_{x,y} [\omega \Delta S(x, y, z) P(\omega, x, y; z)]. \quad (13)$$

In the case of narrow propagation angles (near zero degree), $\frac{1}{k_z} \approx 1$ is satisfied, and equations (8) and (9) degrade to the split-step Fourier propagator (Stoffa, 1990):

$$\frac{\partial P(\omega, k_x, k_y; z)}{\partial z} = \mp i k_0 k_z P(\omega, k_x, k_y; z), \quad (14)$$

$$\frac{\partial P(\omega, x, y; z)}{\partial z} = \mp i \omega \Delta S(x, y, z) P(\omega, x, y; z). \quad (15)$$

Equations (8), (12) and (13) are combined to form the GSP (Huang et al, 1999). We can see that equation (13) deals with the wave propagation at high angles, which can be processed in either the frequency wavenumber domain (with the GSP operator) or frequency space domain (with the FFD operator). From the above derivation, we can see that the high-order terms of the slowness perturbation have been discarded twice, which works only under the condition of small slowness perturbation. Therefore, the slowness perturbation $\Delta S(x, y, z)$ should be as small as possible. However, using the velocity value at each spatial point as a reference velocity is impractical in calculation. Generally, the slowness perturbation is defined as

$$\Delta S(x_i, y_j, z) = S(x_i, y_j, z) - S_0(z) \quad (16)$$

We need to choose a set of reference velocities in an extrapolation step to maximize the accuracy of wave propagation.

SELF-ADAPTIVE REFERENCE VELOCITY CHOICE WITH LATERAL VELOCITY VARIATIONS

The background velocity or reference velocity should be chosen to match the true velocity distribution as closely as possible. The more closely the reference velocity field mimics the true velocity, the more accurately the wave-field propagation can be calculated and the higher the modeling and imaging quality will be. We redefine the velocity perturbation as

$$\Delta S(x_i, y_j, z) = S(x_i, y_j, z) - S_0^l(x_i, y_j, z), \quad (17)$$

where l is the index of the selected reference velocity. $S_0^l(x_i, y_j, z)$ means that there is a reference velocity with the index l at a spatial point (x_i, y_j) . In the extreme case, the maximum number of the reference velocities equals to the number of discrete spatial points in the extrapolation layer. Theoretically, every spatial point could be assigned a reference velocity, but that would entail a huge calculation cost. Generally, a set of reference velocities is chosen, with which the wavefield extrapolations are carried out. Then the extrapolated wavefields are merged together with some chosen methods (Gazdag and Sguazzero, 1984; Kessinger, 1992). However, it is difficult to choose a set of reasonable reference velocities for modeling and imaging, if the velocity laterally varies severely and irregularly. Therefore, we propose the following self-adaptive strategy for medium with lateral velocity variations. The procedure is as follows:

(1) Assign a threshold value of the ratio of two adjoining reference velocities, according to numerical experiments and experience. The threshold reflects how severe the lateral velocity variation is. Generally, we define the ratio to be greater than 1.0. Of course the threshold could be less than 1.0, but this would require sorting the discrete velocity values in decreasing order in the third step.

(2) Filter the 2D or 3D velocity slice of the depth layer with a median filter to eliminate possible wild velocity values.

(3) Sort the discrete velocity values into an array in increasing order.

(4) Set the summation value equal to zero, then sum the sorted discrete velocity values from left to right and point-by-point, calculating a cumulative velocity average, if a velocity

value is added, with the formula $v_{avg}^l = \frac{\sum_{k=1}^{K^l} v_k^{\tilde{m}}(x_i, y_j)}{K^l}$. Here, $\tilde{m} = 1, \dots, NX$ in the 2D case and $\tilde{m} = 1, \dots, NX \times NY$ in the 3D case, where \tilde{m} are the sequence numbers of the discrete velocity points that were disordered by sorting. K^l is the number of discrete velocity points in the l^{th} region, which is known after a dividing point is determined; l is the number of the reference velocity. If the ratio between the velocity value at the next point and the velocity average at the current point is greater than the preset threshold, we can judge that there exists a velocity boundary at the current point. This point is a dividing point between two velocity regions.

(5) Starting from the dividing point, repeat Step 4 to finding each successive dividing point until the end of the sorted velocity array is reached.

(6) Repeat Step 4 and Step 5. This time, the ratio between the cumulative velocity average at the current point and the velocity average at the adjacent and next point (which is calculated in the last iteration) is used, and if it is greater than the preset threshold value, the dividing point between two velocity regions is determined.

(7) If the velocity dividing points are not changed and the velocity averages are not changed, stop the iterative procedure. Otherwise, repeat Step 6.

We can see that the number of velocity regions is the number of chosen reference velocities. The velocity average in a velocity region is a reference velocity value. With the set of reference velocities, wavefield extrapolation is carried out with SSF, FFD, or GSP operators. For computational efficiency, the number of reference velocities should be kept small, usually less than 5 or 6. It should be mentioned that Step 6 and 7 are optional.

In order to merge extrapolated wavefield, the corresponding sequence number between the input discrete velocity slice and the sorted discrete velocity value should be recorded. This is important for the approach.

The approach can be used in 2D or 3D, poststack or prestack, and time or depth migration or modeling, as long as the seismic-wave propagation is characterized with perturbation theory. This method can be used for the image edge detecting as well.

If necessary, the velocity variances may be used as the criterion for dividing the velocity regions. Usually, it is sufficient to choose a set of reference velocities with velocity averages

for migration.

WAVEFIELD RECONSTRUCTION

Gazdag and Sguazzero (1984) use the following method for merging the extrapolated wavefield. Assume that the two extrapolated wavefields with the different reference velocities v_{ref}^1 and v_{ref}^2 are as follows:

$$P_1(x_i, y_j, z + \Delta z; \omega) = A_1 e^{i\theta_1}, \quad (18)$$

$$P_2(x_i, y_j, z + \Delta z; \omega) = A_2 e^{i\theta_2}, \quad (19)$$

where A_1 and A_2 , and θ_1 and θ_2 represent amplitude and phase, respectively. The merged wavefield at a spatial point is

$$P(x_i, y_j, z + \Delta z; \omega) = A e^{i\theta}. \quad (20)$$

The amplitude and phase of the merged wavefield is calculated with

$$A = \frac{A_1 (v_{ref}^2 - v(x_i, y_j, z + \Delta z)) + A_2 (v(x_i, y_j, z + \Delta z) - v_{ref}^1)}{v_{ref}^2 - v_{ref}^1}, \quad (21)$$

and

$$\theta = \frac{\theta_1 (v_{ref}^2 - v(x_i, y_j, z + \Delta z)) + \theta_2 (v(x_i, y_j, z + \Delta z) - v_{ref}^1)}{v_{ref}^2 - v_{ref}^1}. \quad (22)$$

where $v(x_i, y_j, z + \Delta z)$ is the velocity at the spatial point $(x_i, y_j, z + \Delta z)$. Kessinger (1992) shows that the wavefield at a spatial point can be directly replaced by the extrapolated wavefield with the reference velocity corresponding to the spatial point. The following formula is used for merging the extrapolated wavefields with SSF operator

$$P(x_i, y_j, z + \Delta z; \omega) = \delta(v_{ref}(x_i, y_j, z + \Delta z) - v_{ref}^l) e^{i\Delta s(x_i, y_j, z + \Delta z)\Delta z} FFT^{-1} [e^{ik_z \Delta z} P(x_i, y_j, z + \Delta z; \omega)], \quad (23)$$

where $v_{ref}(x_i, y_j, z + \Delta z)$ stands for the reference velocity at a spatial point (x_i, y_j) , v_{ref}^l is the member of the set of chosen reference velocities with the index l . The delta function $\delta(\bullet) = 1$ if $v_{ref}(x_i, y_j, z + \Delta z) = v_{ref}^l$; otherwise, $\delta(\bullet) = 0$. With this method, the extrapolated wavefield can be directly inserted into the relevant position without storing it. However, the amplitude and phase of the merged wavefield is not so accurate in the case of severe lateral velocity variations. We use quadratic interpolation to reconstruct the extrapolated wavefield with the

following equation:

$$P(x_i, y_j, z + \Delta z; \omega) = \delta(v_{ref}(x_i, y_j, z + \Delta z) - v_{ref}^l) \left\{ \begin{array}{l} \frac{(v(x_i, y_j) - v_{ref}^l)(v(x_i, y_j) - v_{ref}^{l+1})}{(v_{ref}^{l-1} - v_{ref}^l)(v_{ref}^{l-1} - v_{ref}^{l+1})} P^{l-1}(x_i, y_j, z + \Delta z; \omega) \\ + \frac{(v(x_i, y_j) - v_{ref}^{l-1})(v(x_i, y_j) - v_{ref}^{l+1})}{(v_{ref}^l - v_{ref}^{l-1})(v_{ref}^l - v_{ref}^{l+1})} P^l(x_i, y_j, z + \Delta z; \omega) \\ + \frac{(v(x_i, y_j) - v_{ref}^{l-1})(v(x_i, y_j) - v_{ref}^l)}{(v_{ref}^{l+1} - v_{ref}^{l-1})(v_{ref}^{l+1} - v_{ref}^l)} P^{l+1}(x_i, y_j, z + \Delta z; \omega) \end{array} \right\}, \quad (24)$$

where $P^{l-1}(x_i, y_j, z + \Delta z; \omega)$, $P^l(x_i, y_j, z + \Delta z; \omega)$ and $P^{l+1}(x_i, y_j, z + \Delta z; \omega)$ are the extrapolated wavefield at point (x_i, y_j) with the three adjacent reference velocities v_{ref}^{l-1} , v_{ref}^l and v_{ref}^{l+1} , respectively.

NUMERICAL TEST EXAMPLES

Now, we show some numerical examples of poststack depth migration results with the SSF operator, in which the reference velocity is chosen with the approach discussed above. Figure 1 is the 2D SEG/EAGE salt-dome model. Figure 2 shows the imaging result generated with the (SSF) operator with one reference velocity during one extrapolation step. The image is very noisy, especially in the inner part of the salt dome, and the small faults are vague and difficult to identify. In Figure 4, the reference velocity is chosen with the approach presented above, and the threshold of the ratio between two adjacent velocity steps is set to 1.3. We can see that the imaging noise is greatly attenuated, and the faults and the boundary are quite clear. Figure 3 and Figure 5 are similar to Figure 4, but with a threshold of 1.5 and 1.1. In Figure 5, the imaging quality is improved further, but the improvement is not sufficient to justify the increased number of reference velocities. In Figure 3, the imaging quality is not decreased obviously, which means that it is not necessary for the number of reference velocities to be too much. The reason why the noise appears on the right part of these images does not figure out. It remains a problem. The chosen reference velocity field, with the threshold set to 1.5, 1.3 and 1.1, is shown in Figure 6, 7, and 8, respectively. This choice satisfactorily characterizes the background variation of the true 2D SEG/EAGE salt-dome velocity model.

CONCLUSION AND DISCUSSION

We introduce the self-adaptive approach for choosing a set of reference velocities. The approach is quite flexible and of little calculation cost. It can be used for general image edge-detecting also. Numerical tests demonstrate that the method is effective. During the wavefield extrapolation, the wavefield merging remains a problem in the case of severe lateral velocity variation. Furthermore, by considering the velocity variance in a region, a better reference velocity choice can be reached.

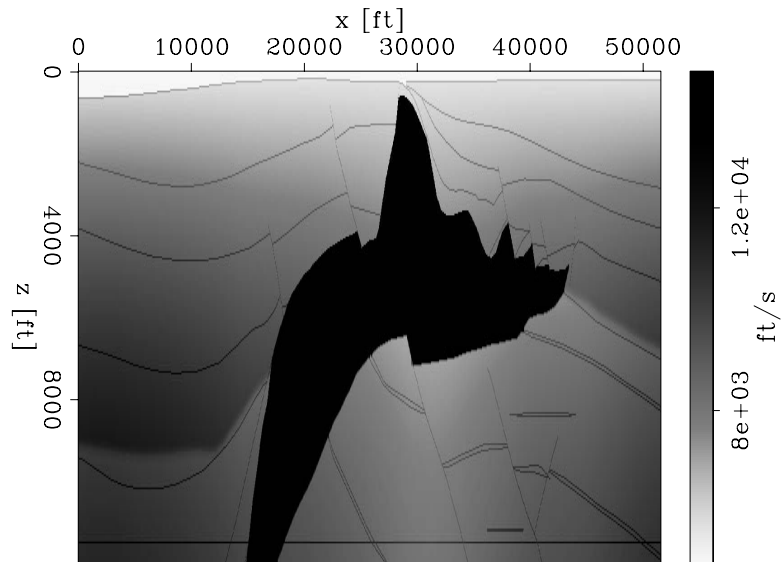


Figure 1: The 2D SEG/EAGE velocity model for the salt-dome example. `huazhong1-salt_model` [ER]

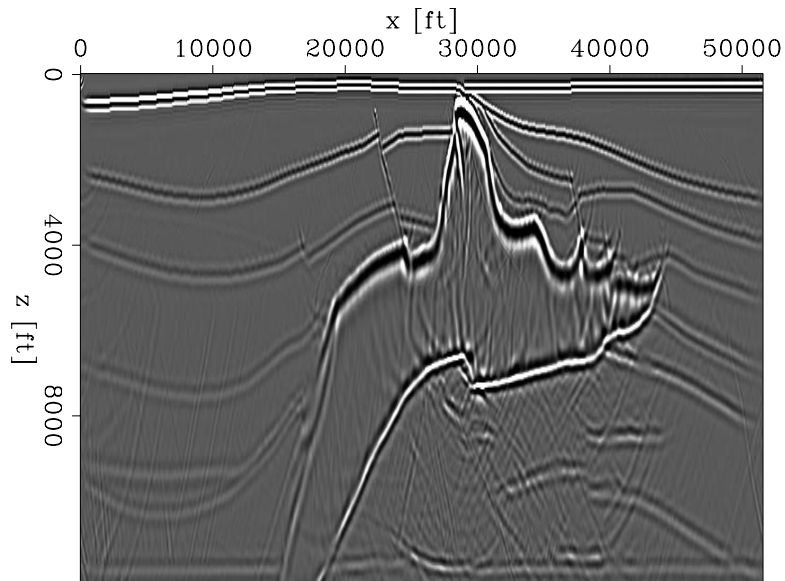


Figure 2: The imaging result of 2D poststack depth migration with one reference velocity during an extrapolation step. `huazhong1-single_ref_v` [ER]

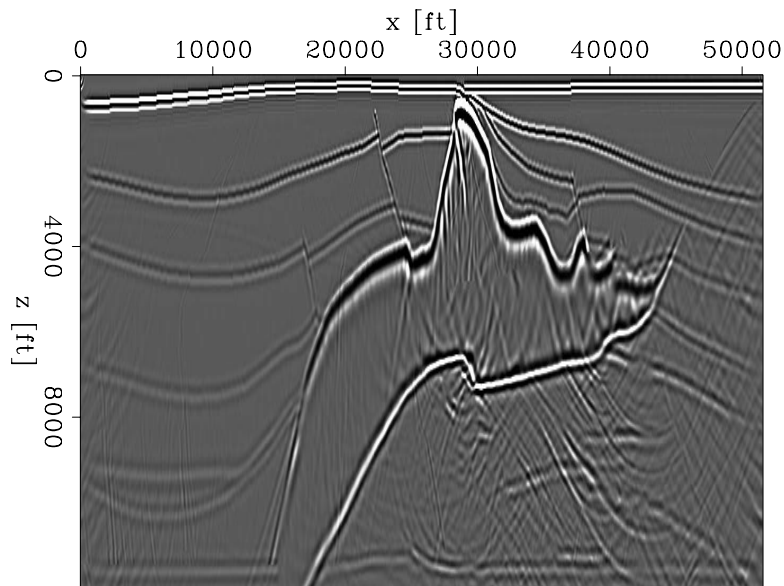


Figure 3: The imaging result of 2D poststack migration with a set of reference velocities during an extrapolation step with a threshold of 1.5. `huazhong1-multiple_ref_v1.5` [ER]

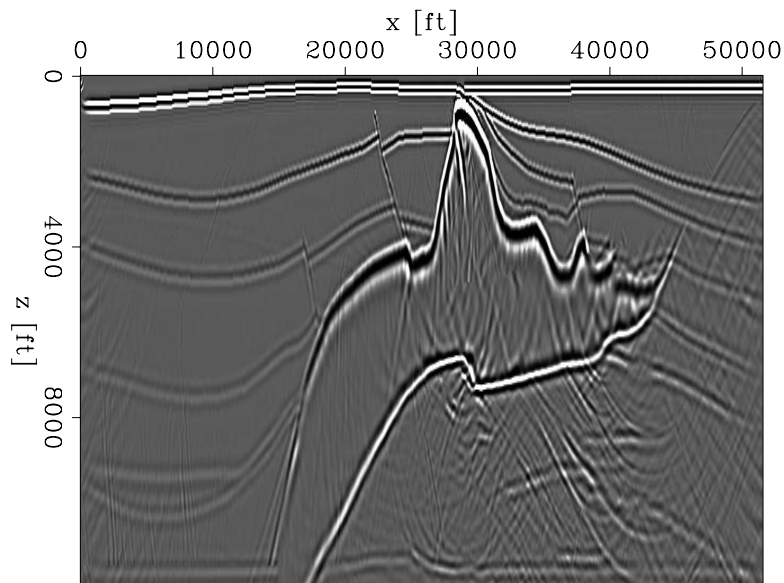


Figure 4: The imaging result of 2D poststack migration with a set of reference velocities during an extrapolation step with a threshold of 1.3. `huazhong1-multiple_ref_v1.3` [ER]

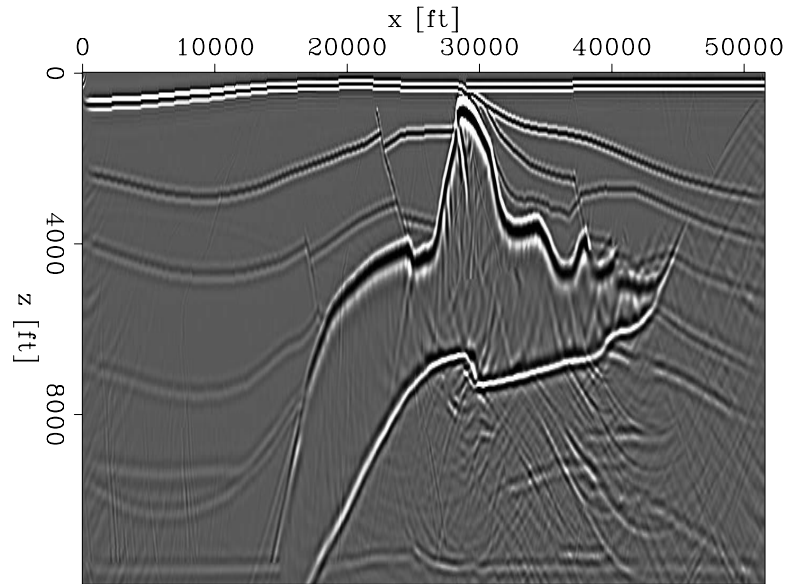


Figure 5: The imaging result of 2D poststack migration with a set of reference velocities during an extrapolation step with a threshold of 1.1. `huazhong1-multiple_ref_v1.1` [ER]

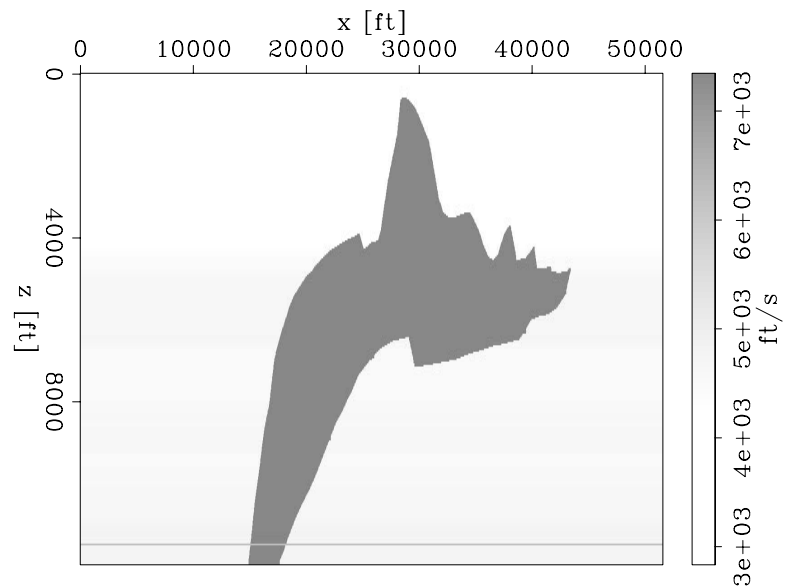


Figure 6: The chosen reference velocity field with a threshold of 1.5 which satisfactorily characterizes the background variation of the true 2D SEG/EAGE salt-dome velocity model. `huazhong1-reference_v1.5` [ER]

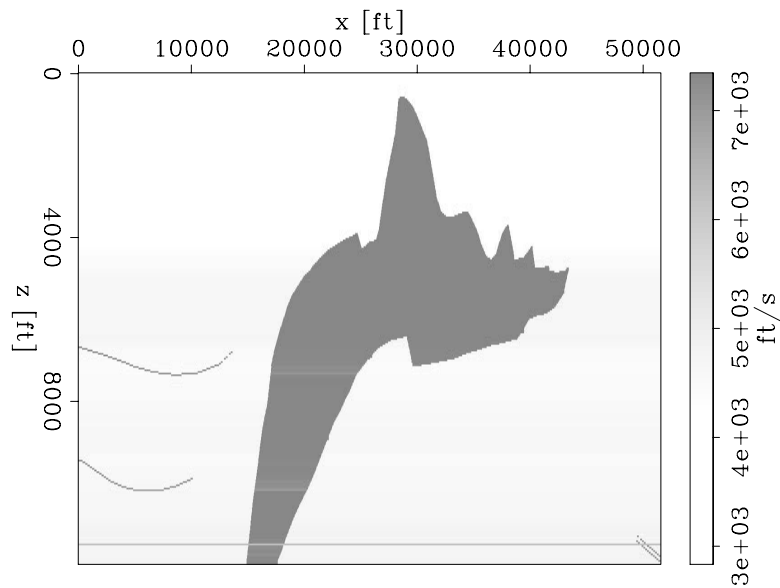


Figure 7: The chosen reference velocity field with a threshold of 1.3 which satisfactorily characterizes the background variation of the true 2D SEG/EAGE salt-dome velocity model.

`huazhong1-reference_v1.3` [ER]

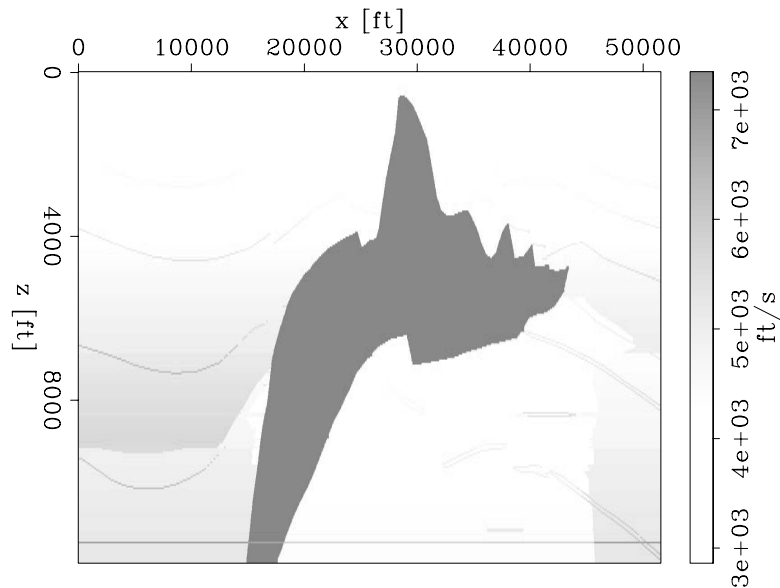


Figure 8: The chosen reference velocity field with a threshold of 1.1 which satisfactorily characterizes the background variation of the true 2D SEG/EAGE salt-dome velocity model.

`huazhong1-reference_v1.1` [ER]

ACKNOWLEDGEMENT

The first author thanks the SEP Group at Stanford University for providing an opportunity for him to serve as a visiting scholar.

REFERENCES

- Biondi, B., 2002, Stable wide-angle Fourier finite-difference downward extrapolation of 3-D wavefields: *Geophysics*, **67**, 872–882.
- Claerbout, J., 1985, *Imaging the earth's interior* Blackwell Scientific Publications, Oxford., 159–160.
- Clapp, R. G., 2004, Reference velocity selection by a generalized lloyd method: 74th Ann. Internat. Mtg., Soc. Expl. Geophys., Expanded abstracts, 981–984.
- Gazdag, J., and Sguazzero, P., 1984, Migration of seismic data by phase-shift plus interpolation: *Geophysics*, **49**, 124–131.
- Huang, L. Y., Fehler, M. C., and Wu, R. S., 1999, Extended local Born Fourier migration method: *Geophysics*, **64**, 1524–1534.
- Kessinger, W., 1992, Extended split-step Fourier migration *in* 62nd Ann. Internat. Mtg. Soc. of Expl. Geophys., 917–920.
- Ristow, D., and Ruhl, T., 1994, Fourier finite-difference migration: *Geophysics*, **59**, 1882–1893.
- Rousseau, J. H. L., and de Hoop, M. V., 2001, Modeling and imaging with the scalar generalized-screen algorithms in isotropic media: *Geophysics*, **66**, 1551–1568.
- Stoffa, P. L., Fokkema, J. T., de Luna Freire, R. M., and Kessinger, W. P., 1990, Split-step Fourier migration: *Geophysics*, **55**, 410–421.



Unified seismic-wave imaging - from data space to model space

Huazhong Wang and Guojian Shan¹

ABSTRACT

Under operator, matrix and inverse theory, seismic-wave imaging can be considered a unified process—mapping from data space to model space. The main topics in seismic-wave imaging include (1) seismic-data interpolation, regularization and redatuming, which mainly decrease the imaging noise; (2) seismic-wave illumination analysis, which predicts whether a target reflector can be imaged and evaluates the suitability of an acquisition configuration in the case of rugged topography and severe lateral velocity variations; and (3) seismic-wave migration/inversion imaging algorithms, which give an imaging result with the help of a wave propagator, known a macro-velocity model. The last and most important thing is to build an accurate macro-velocity model. All of the processes can be considered with the conjugate operator/matrix under least-squares theory. In this article, we review the following topics: (1) expression of data space and model space; (2) affiliation between data space and model space; (3) seismic-data preprocessing; (4) seismic-data illumination; (5) migration imaging and inversion imaging as least-squares inverse problems; (6) amplitude-preserving migration imaging with wavefield extrapolation; (7) migration velocity analysis and inversion and (8) some related topics. We express the imaging process with the operator or matrix theory and give some directions for further research.

INTRODUCTION

Seismic-wave imaging can be seen as a mapping from data space to model space. The objective is to position reflectors and to quantitatively estimate the physical parameters of the medium (such as reflectivity, P-wave velocity, S-wave velocity and density).

From the view of the historical development of seismic wave imaging, there are two ways to reach the goal. The first approach is seismic-wave migration technologies commonly used in the oil industry at present, which includes estimating low-wavenumber macro-velocity (with NMO+DMO velocity analysis, migration velocity analysis or travelttime tomography), positioning the reflectors and qualitatively estimating the reflectivity. However, quantitatively estimating reflectivities (which is called amplitude-preserving imaging or true-amplitude imaging) is currently much more actively pursued by the oil industry and academia. Seismic-wave illumination analysis, migration convolution, least-squares migration, and amplitude analysis of angle gathers are being given increased attention by many authors (Chavent and Plessix,

¹email: wang@sep.stanford.edu, shan@sep.stanford.edu

1999; Gray, 1997; de Bruin et al., 1990; Black et al., 1993; Bleistein et al., 1999; Nemeth et al., 2000; Brandsberg-Dahl et al., 2003). All of these endeavors aim for clearer imaging and more quantitative reflectivity. The second approach is seismic-wave inversion, which directly and quantitatively estimates the physical contrast parameters of rocks (such as P-wave impedance, S-wave impedance and density).

The advantages of the first approach are that reflectors can be positioned step by step, and that reflectivity estimation can take advantage of many signal/noise enhancement technologies, macro-velocity analysis techniques and migration imaging methods. The procedure can be easily controlled and adjusted, and its calculation cost can be afforded by present computer systems. The geological and lithological knowledge about a survey area can be easily used for adjusting the final imaging results. The disadvantage of this conventional approach is its lack of a unified theoretical framework. Therefore, it is difficult to guarantee the reliability of the quantitative estimation of reflectivities.

The second approach has two subcategories: direct inversion methods (Bleistein et al., 1987; Wu and Toksoz, 1987; Miller et al., 1987), and iterative inversion methods (Taratola, 1984; Mora, 1987, 1988; LeBras and Clayton, 1988; Chavent and Jacewitz, 1995; Pratt, 1999). Both have elegant theoretical expressions. However, the inverse problems are inherently ill-posed and the solutions are unstable and nonunique if the observed data set has certain flaws, including frequency band-limitation, aperture limitation, non-Gaussian noise, and/or an unknown source function. An unsuitable modeling algorithm or non-linearity between the observed data and geophysical parameters will also cause problems. In addition, the calculation costs of these methods often exceed the capacities of present computer systems. Until recently, only 2D inversion algorithms can be used in practice. The direct-inversion approach requires an analytical expression, which can be given analytically only in the case of constant background or slow background variance. Otherwise, the approach cannot produce a satisfactory result. Iterative inversion problems deal with either maximum-probability solutions for a Gaussian probability-density function or least-squares solutions of an l_2 -norm problem. These kinds of inverse problems need huge numbers of iterative modeling calculations.

At present, some trends indicate that standard seismic-wave migration imaging and inversion imaging are merging. The problem at the point of intersection is how to quantitatively estimate the reflectivity. How the shot and receiver configurations affect the imaging resolution and the amplitude of the estimated reflectivity is a question relevant to both imaging approaches.

We think that it is worthwhile to investigate how to generate amplitude-preserving common-image gathers with inversion imaging approaches, while also considering how to include seismic-wave-illumination effects and irregular data sets.

In this research proposal, we review the following topics: (1) expression of data space and model space; (2) relationship between data space and model space; (3) seismic-data pre-processing; (4) seismic-data illumination; (5) migration imaging and inversion imaging as a least-squares inverse problem; (6) amplitude-preserving migration imaging with wavefield extrapolation; (7) migration-velocity analysis or macro-velocity inversion and (8) some other related topics. We try to express the imaging process within the context of inverse theory and

give some directions for further research.

EXPRESSION OF DATA SPACE AND MODEL SPACE

First, we give a general expression of the data space and model space for seismic-data imaging. In general, seismic data acquired at the surface or in a well is presented as $\mathbf{d}(\vec{m}, \vec{h}, \omega)$ or $\mathbf{d}(\vec{s}, \vec{g}, \omega)$. We can use the following special variables to depict data space: azimuth, offset, and CMP coordinate, or azimuth, offset, shot-point coordinate and receiver-point coordinate respectively. These special variables completely define a data space or a seismic data set.

Model space can be characterized with as many different approaches as there are different applications. We define the model space as one which characterizes the interior of the earth, such as a velocity field, an impedance field, a stacked imaging volume, or common-image gathers, etc.. Basically, the model space is expressed as $\mathbf{m}(i\Delta x, j\Delta y, n\Delta z)$, with evenly discretized intervals. We usually present the velocity model or stacked imaging data volume in this form.

In some models, the subsurface floats in a velocity (or other physical parameter) field. The subsurface is a very important component of a physical parameter model, which shows the geometry of a geological structure. Reflectivities, for example, are defined in the subsurface. Therefore, common-image gathers and AVO/AVA analysis have a close relation to the subsurface. In fact, the subsurface plays a key role in macro-velocity model building (Mora, 1989; Cao et al., 1990; Pratt and Hicks, 1998). Angle gathers are expressed as $\mathbf{m}(i\Delta x, j\Delta y, \gamma(\alpha, \varphi), n\Delta z)$, where γ is an incident angle (between the incident ray and the normal ray of a reflector) or an emerging angle (between the emerging ray and the normal ray); φ is the azimuth angle; and α is the dipping angle of a reflector. In macro-velocity inversion, the model space is commonly expressed as $\mathbf{m}(r_{x_i}^k, r_{y_j}^k, v_{func}^k, r_{z_n}^k)$, where v_{func}^k is a velocity function attached to a reflector, which is given a concrete formula for each specific application; $r_{x_i}^k$ is the horizontal coordinate of i^{th} point on the k^{th} reflector, and $r_{x_i}^k$ and $r_{z_n}^k$ have a meaning similar to $r_{x_i}^k$.

How to evaluate data space and model space

What is a good observed data space? What is a good estimated model space? It is difficult to answer these two questions, because the answers depend on the practical applications. Up to now, the acquisition systems basically can be divided into three classes: Case \mathbf{d}_1 : Full-area acquisition system. A 3D survey area is discretized into a regular grid, and each grid point has a receiver point and a shot point. This is an ideal case, in which a data set has an even azimuth interval, offset interval and CMP interval. Such a data set is a complete one. In practice, to minimize acquisition costs, a receiver is put at each grid point, and the shot points are arranged depending on the on-site situations. Case \mathbf{d}_2 : Wide-azimuth acquisition system with partial sacrifice of cross-line aperture. The land acquisition system belongs to this category. It is difficult to maintain even azimuth intervals and even offset intervals because of complex

variations of the surface and near-surface, and the consideration of acquisition efficiency and costs. Commonly, we have to move the shot point to an advantageous location, sacrificing spatial regularization. Case \mathbf{d}_3 : Narrow-azimuth acquisition system with complete sacrifice of cross-line aperture. The present marine acquisition system belongs in this category. It is easy to achieve an even azimuth and even offset, but the data set is incomplete because it lacks the cross-line aperture. This acquisition system is not suitable in cases of complex structure variance along the cross-line direction. Similarly, we can divide the model space into three categories: Case \mathbf{m}_1 , with a flat surface and some flat subsurfaces; Case \mathbf{m}_2 , with a flat surface and some complex subsurfaces; and Case \mathbf{m}_3 , with a rough topography and some complex subsurfaces. Table 1 gives the relationship between the data space and model space in different cases.

	\mathbf{d}_1	\mathbf{d}_2	\mathbf{d}_3
\mathbf{m}_1	even azimuth interval, even offset interval and even CRP illumination; a complete data set	uneven azimuth interval, uneven offset interval and basically even CRP illumination;	even azimuth interval, even offset interval and even CRP illumination
\mathbf{m}_2	even azimuth interval, even offset interval and uneven CRP illumination	uneven azimuth interval, uneven offset interval and uneven CRP illumination	even azimuth interval, even offset interval and uneven CRP illumination
\mathbf{m}_3	even azimuth interval, uneven offset interval and uneven CRP illumination	uneven azimuth interval, uneven offset interval and uneven CRP illumination	even azimuth interval, uneven offset interval and uneven CRP illumination

From

the table, we know that wide-azimuth acquisition gives wider aperture in the cross-line direction. However, this also causes an uneven azimuth interval and uneven offset interval, which will result in a noisy image. Narrow-azimuth acquisition can give an even azimuth interval and even offset interval but sacrifices the cross-line aperture. Our conclusion can be summarized with following statements: In Case \mathbf{m}_1 , the regularization of the data space yields an even sampling of the model space. In a geologically symple medium, a good data set is one with an even azimuth interval, an even offset interval and an **even CMP interval**. In Cases \mathbf{m}_2 and \mathbf{m}_3 , a good data set is one with an even azimuth interval, an even offset interval and an **even CRP illumination**. In practice, even CRP illumination commonly means that a data set is irregular. There exists a trade-off between the even illumination and the regular data set. Since an irregular acquisition configuration generally yields a noisy image, a field data set should be preprocessed to be regular. On the other hand, bad illumination causes a vague image or no image, or yields false amplitude; therefore, the illumination deficiency should be compensated with other information from well-logging, rock physics or geology data. From the perspective of prestack imaging, assuming the macro-velocity model is accurate enough, a good model space can be defined as **one which has an amplitude-preserving angle gather on each point of a reflector at each azimuth**, which is the main goal of seismic-wave imaging (Shin and Min, 2001; Plessix and Mulder, 2004).

RELATIONSHIP BETWEEN DATA SPACE AND MODEL SPACE

Data space can be related to model space with the following formula:

$$\mathbf{d}(\vec{m}, \vec{h}, \omega) = L\mathbf{m}(\vec{m}, \gamma(\alpha, \varphi), n\Delta z), \quad (1)$$

where the modeling operator L can be a Green's function, a one-way or two-way wave equation, or a more complex wave equation suitable for wavefield extrapolation or modeling. Wavefield extrapolation and modeling operators were exhaustively studied by many authors (Hale, 1991c,a; Stoffa et al., 1990; Ristow and Ruhl, 1994; Huang et al., 1999; Biondi, 2002; Li, 1991; Docherty, 1991; Berkhout and Wapenaar, 1989; Wapenaar et al., 1989; Marfurt, 1984). However, prestack depth migration imaging is mostly implemented with one-way acoustic wave equations, which is one of the reasons it cannot achieve true-amplitude images. If a one-way wave equation is used for migration imaging, all wave phenomena except the primary reflection wave are processed as noise. In fact, if quantitative reflectivity is the objective of imaging, a two-way acoustic, or even elastic, wave equation should be used (Mora, 1988; Pratt, 1999; Pratt and Shipp, 1999).

SEISMIC DATA PREPROCESSING

As discussed above, seismic-wave imaging needs a suitable data set. In general cases, real data sets have some drawbacks. For example, the spatial sampling of land data commonly is too coarse and/or irregular; marine data sets commonly show feathering. Therefore, seismic-data preprocessing is necessary. Seismic-data preprocessing deals with the signal-to-noise enhancement, wavelet correction, seismic-data regularization and interpolation, and redatuming. The latter three terms are closely related to seismic-wave imaging. Seismic data regularization, interpolation and redatuming can be seen as a seismic-data mapping under the least-squares theory. An irregular seismic-data set from on-site field acquisition can be expressed as follows:

$$\mathbf{d}^{obs} = L\mathbf{m}, \quad (2)$$

where L is an ideal seismic-wave propagator, and \mathbf{m} is an ideal underground medium model. From the irregular observed seismic-data, an underground medium model can be estimated:

$$\hat{\mathbf{m}}_{inv} = [(\hat{L}^*)^T \hat{L}]^{-1} (\hat{L}^*)^T \mathbf{d}^{obs} \quad (3)$$

where \hat{L} is the practical seismic wave propagator, which can be written as a complex matrix. $(\hat{L}^*)^T$ is a conjugate transpose matrix of the matrix \hat{L} . Substituting the estimated model into equation (3), the estimated and regular data set can be found:

$$\hat{\mathbf{d}}_{reg} = L [(\hat{L}^*)^T \hat{L}]^{-1} (\hat{L}^*)^T \mathbf{d}^{obs}. \quad (4)$$

In equation (4), the ideal wave propagator L is unknown, but it can be replaced with the practical wave propagator \hat{L} . Therefore, equation (4) can be rewritten as

$$\hat{\mathbf{d}}_{reg} = \hat{L} [(\hat{L}^*)^T \hat{L}]^{-1} (\hat{L}^*)^T \mathbf{d}^{obs} = \hat{L} H^{-1} (\hat{L}^*)^T \mathbf{d}^{obs}, \quad (5)$$

where $H = (\hat{L}^*)^T \hat{L}$ is a Hessian matrix which acts as a filter. If we choose the filter as an ideal full-pass one, that is, $H = I$, equation (5) can be rewritten as

$$\hat{\mathbf{d}}_{reg} = \hat{L} (\hat{L}^*)^T \mathbf{d}^{obs}, \quad (6)$$

which is a general seismic data mapping frame. Up to now, the seismic data mapping can be implemented with $\mathbf{DMO} + \mathbf{DMO}^{-1}$ or $\mathbf{PSTM} + \mathbf{PSTM}^{-1}$ (Biondi et al., 1998; Canning and Gardner, 1996; Ronen, 1987; Bleistein et al., 1999).

Redatuming also can be carried out with equation (5). The formula for redatuming should be modified as follows:

$$\hat{\mathbf{d}}_{datum} = \hat{L}_2 \left[(\hat{L}_1^*)^T \hat{L}_1 \right]^{-1} (\hat{L}_1^*)^T \mathbf{d}^{obs} = \hat{L}_2 H^{-1} (\hat{L}_1^*)^T \mathbf{d}^{obs}, \quad (7)$$

where $\hat{\mathbf{d}}_{datum}$ is a new and regular data set extrapolated from a topographic surface to another surface which may be a horizontal or non-horizontal datum. \hat{L}_1^T is the propagator corresponding to the topographic surface, and \hat{L}_2 is the propagator to a horizontal datum. Now the Hessian matrix H has a relation to the topography and the acquisition configuration. Similarly, if the Hessian matrix is an ideal full-pass filter, equation (7) can be rewritten as

$$\hat{\mathbf{d}}_{datum} = \hat{L}_2 (\hat{L}_1^*)^T \mathbf{d}^{obs}. \quad (8)$$

However, if a suitable Hessian filter is chosen, the quality of data mapping will be improved further. Next, we discuss data regularization with common-offset prestack time migration and the necessity of anti-aliasing for processing land data sets.

Common-offset prestack time migration and data regularization

The time-distance relation for a shot-receiver pair is

$$\sqrt{(x - h_x)^2 + (y - h_y)^2 + z^2} + \sqrt{(x + h_x)^2 + (y + h_y)^2 + z^2} = vt_h, \quad (9)$$

where t_h is the two-way traveltimes of a non-zero-offset shot-receiver pair, h_x is the in-line component of the half-offset, and h_y is the cross-line component of the half-offset. For simplicity, the connection line of the shot and receiver points is parallel to the x -axis of the Cartesian coordinate system. Therefore, we have the following simple equation which delineates the isochron surface of the prestack migration:

$$\left(\frac{\hat{x}}{a_{\hat{x}}} \right)^2 + \left(\frac{\hat{y}}{a_{\hat{y}}} \right)^2 + \left(\frac{\hat{z}}{a_{\hat{z}}} \right)^2 = 1, \quad (10)$$

where $a_{\hat{x}}, a_{\hat{y}}$ and $a_{\hat{z}}$ are the half-lengths of the axes of the rotary isochron ellipse in the case of constant velocity. If $\hat{y} = \hat{z} = 0$, then $a_{\hat{x}} = \hat{x} = \frac{vt_h}{2}$; If $\hat{x} = \hat{z} = 0$, then $a_{\hat{y}} = \hat{y} = \sqrt{\left(\frac{vt_h}{2}\right)^2 - h^2} =$

$\frac{vt_n}{2}$; If $\hat{x} = \hat{y} = 0$, then $a_z = z = \sqrt{\left(\frac{vt_n}{2}\right)^2 - h^2} = \frac{vt_n}{2}$. The variable t_n is the two-way traveltime after NMO. Equation (10) can be rewritten as

$$\left(\frac{\hat{x}}{\frac{vt_n}{2}}\right)^2 + \left(\frac{\hat{y}}{\frac{vt_n}{2}}\right)^2 + \left(\frac{z}{\frac{vt_n}{2}}\right)^2 = 1. \quad (11)$$

Further, equation (11) can be changed into

$$\frac{\hat{x}^2}{1 + \left(\frac{2h}{vt_n}\right)^2} + \hat{y}^2 + z^2 = \left(\frac{vt_n}{2}\right)^2. \quad (12)$$

Defining $\hat{X}^2 = \frac{\hat{x}^2}{1 + \left(\frac{2h}{vt_n}\right)^2}$ yields:

$$\hat{X}^2 + \hat{y}^2 + z^2 = \left(\frac{vt_n}{2}\right)^2. \quad (13)$$

Equation (13) is in the form of a poststack migration. Therefore, prestack migration can be explained as a poststack migration on a post-NMO data set. We know that

$$k_{\hat{X}} = k_{\hat{x}} \sqrt{1 + \left(\frac{2h}{vt_n}\right)^2}. \quad (14)$$

Therefore, the dispersion relation of equation (13) is

$$\left(\frac{v}{2}\right)^2 [k_{\hat{X}}^2 + k_{\hat{y}}^2 + k_z^2] = \omega_n^2. \quad (15)$$

Substituting (14) into the above formula yields

$$\left(\frac{v}{2}\right)^2 \left[k_{\hat{x}}^2 \left(1 + \left(\frac{2h}{vt_n} \right)^2 \right) + k_{\hat{y}}^2 + k_z^2 \right] = \omega_n^2, \quad (16)$$

which can be rewritten as follows:

$$k_z = -\text{sgn}(\omega_n) \sqrt{\left(\frac{2\omega_n}{v}\right)^2 - \left(1 + \left(\frac{2h}{vt_n}\right)^2\right) k_x^2 - k_y^2}. \quad (17)$$

This is the dispersion relation of the common-offset prestack migration equation. In the time domain, the dispersion relation is

$$k_\tau = -\text{sgn}(\omega_n) \sqrt{\omega_n^2 - \left(\frac{v(\tau)}{2}\right)^2 \left[\left(1 + \left(\frac{2h}{v(\tau)t_n} \right)^2 \right) k_x^2 + k_y^2 \right]}. \quad (18)$$

Therefore, common-offset prestack time migration (PSTM) can be implemented with the following relation:

$$\mathbf{m}(\omega_\tau, k_x, k_y) = \int dt_n J \{ e^{-i\omega_\tau A t_n} \mathbf{d}(t_n, k_x, k_y, h) \}. \quad (19)$$

The term in the braces represents the wave-field extrapolation, and the integral at $t_n = 0$ serves to extract the imaging values. Then, the common-offset inverse PSTM is

$$\mathbf{d}(t_n, k_x, k_y, h) = \int d\omega_\tau \frac{1}{A} \{ e^{i\omega_\tau A t_n} \mathbf{m}(\omega_\tau, k_x, k_y) \}. \quad (20)$$

Similarly, the term in the braces represents the wave-field extrapolation, which is an inverse migration. The integral is an inverse Fourier transform.

In the presence of moderate lateral velocity variations, prestack time migration can be expressed as follows:

$$\begin{aligned} \mathbf{m}(\tau, m_x, m_y) &= \int dx_s \int dx_g W_1 e^{-i\omega[t-(t_s+t_g)]} \mathbf{d}(t, x_s, x_g, h), \\ &= \int dx_s \int dx_g W_1 \mathbf{d}(t, x_s, x_g, h) \delta(t = t_s + t_g), \end{aligned} \quad (21)$$

where $t = t_s + t_g = \sqrt{\left(\frac{m_x - h_x}{v_{rms}}\right)^2 + \left(\frac{m_y - h_y}{v_{rms}}\right)^2 + \left(\frac{\tau}{2}\right)^2} + \sqrt{\left(\frac{m_x + h_x}{v_{rms}}\right)^2 + \left(\frac{m_y + h_y}{v_{rms}}\right)^2 + \left(\frac{\tau}{2}\right)^2}$. W_1 is the amplitude weight, and τ is the two way traveltimes along the imaging ray.

The inverse PSTM is

$$\begin{aligned} \mathbf{d}(t, x_s, x_g, h) &= \int dm_x \int dm_y W_2 e^{-i\omega[t+(t_s+t_g)]} \mathbf{m}(\tau, m_x, m_y), \\ &= \int dm_x \int dm_y W_2 \mathbf{m}(\tau, m_x, m_y) \delta(t = -(t_s + t_g)). \end{aligned} \quad (22)$$

Bleistein and Stockwell (2000) give a general theory of data mapping. From here, we will develop some practical approaches for data mapping.

Aliasing and anti-aliasing

From the discretized data space, the discretized model space, and their relation formula,

$$\mathbf{d}(m_{x_i}, m_{y_j}, h_{x_k}, h_{x_l}, z_n, \omega) = L \mathbf{m}(m_{x_i}, m_{y_j}, n \Delta z), \quad (23)$$

some causes of aliasing can be clearly seen. The sources of aliasing can be divided into the following three types:

(1) Overly coarse sampling intervals. For example, $\Delta \vec{s}$ and/or $\Delta \vec{g}$, $\Delta \vec{m}$ and/or $\Delta \vec{h}$ are too coarse, where $\Delta \vec{s}$ and $\Delta \vec{g}$ are the shot-point and receiver-point intervals respectively, and $\Delta \vec{m}$ and $\Delta \vec{h}$ are the CMP and half-offset intervals, respectively.

(2) Unsuitable modeling or imaging operators, such as the integrated DMO operator (Hale, 1991b), or the Kirchhoff integral operator (Zhang et al., 2003; Biondi, 2001; Abma et al., 1999; Druzhinin, 1999).

(3) Insufficient output resolution, where the output spatial intervals, such as $\Delta\vec{m}$ and Δz are too coarse. We can analyze the aliasing in the cases of shot-gather migration, receiver-gather migration, common-offset gather migration, and midpoint half-offset domain migration.

Aliasing in shot gather migration is described by the following equation:

$$I(\vec{m}, z) = \sum_{S_k} \sum_{\omega} S^*(\vec{m}, z | S_k) R(\vec{m}, z | S_k), \quad (24)$$

where $S^*(\vec{m}, z | S_k)$ is the conjugate of the extrapolated shot wave-field; $R(\vec{m}, z | S_k)$ is the extrapolated receiver wave-field. S_k stands for the K^{th} common-shot gather. In general, single common-shot-gather imaging presents no aliasing, because the receiver-point interval is easily arranged regularly and small enough. However, imaging an entire 2D line or 3D area will present severe aliasing problems because of the irregular and large shot-point intervals.

Aliasing in receiver-gather migration is described by the following equation:

$$I(\vec{m}, z) = \sum_{R_k} \sum_{\omega} S_{sort}^*(\vec{m}^k, z | R_k) R_{sort}(\vec{m}^k, z | R_k), \quad (25)$$

where $S_{sort}^*(\vec{m}^k, z | R_k)$ is the extrapolated so-called shot wavefield, which corresponds to a specific receiver point; $R_{sort}(\vec{m}^k, z | R_k)$ is the extrapolated receiver wavefield, which is sorted from shot gathers. R_k stands for the K^{th} common-receiver-gather. In general, single common-receiver-gather imaging profiles are susceptible to aliasing.

Aliasing in midpoint half-offset domain migration follows equation (26):

$$I(\vec{m}, z) = \sum_h \sum_{\omega} U(\vec{m}, \vec{h}, \omega, z), \quad (26)$$

where $U(\vec{m}, \vec{h}, \omega, z)$ is the extrapolated wavefield with a double-square-root equation. Aliasing will result if $\Delta\vec{m}$ and/or $\Delta\vec{h}$ are too coarse.

Aliasing in common-offset-gather migration is described by the following equation:

$$I(\vec{m}, z) = \sum_{h_k} \sum_{\omega} U(\vec{m}, h_k, \omega, z), \quad (27)$$

where $U(\vec{m}, h_k, \omega, z)$ is the extrapolated wavefield with a double-square-root equation. Aliasing will result if $\Delta\vec{m}$ is too coarse.

In the case of rugged topography, the geometry of the acquisition configuration becomes more and more irregular, especially the shot-point coordinates. Therefore, antialiasing processing is necessary in redatuming, seismic data regularization and migration imaging for land-data imaging.

SEISMIC WAVE ILLUMINATION ANALYSIS

Seismic-wave illumination becomes increasingly problematic in regions with rugged topography and complex geological structure with severe lateral velocity variations. In these hostile cases, we think that seismic-wave illumination is much more important than seismic-data regularization. Without enough illumination for the target reflectors, regular seismic data can not guarantee a quality image.

Seismic-wave illumination is related to the macro-velocity model and the acquisition configuration, both of which are embodied in the Green's function. In fact, seismic-wave illumination analysis inherently is an issue of seismic-wave propagation and observation in the presence of complex velocity structure. Whether a seismic wave reaches a target reflector and whether the reflected wave is received are both important.

Wu and Chen (2002) analyze seismic-wave illumination with Beamlet Propagators. With directional illumination maps, the illumination of a reflector is demonstrated. Berkhout et al. (2001); Volker et al. (2001) discuss how the imaging resolution and amplitude are affected by the acquisition geometries with focal beams: emission-focusing and detection-focusing. However, neither methods deals with the compensation for illumination deficiency from the perspective of inverse imaging.

In least-squares inversion theory, the Hessian matrix—the second-order derivatives of the wavefield about the perturbation of a physical parameter—is given. The Hessian matrix is closely related to the seismic-wave illumination of a target reflector.

The two important issues of seismic-wave illumination analysis are (1) compensating for illumination deficiencies and (2) evaluating acquisition patterns and guiding their design.

Seismic-wave migration imaging can be represented by the following matrix equation:

$$\mathbf{m} = (\mathbf{L}^*)^T \mathbf{d}, \quad (28)$$

where

$$\mathbf{d} = (d_{x_1}, d_{x_2}, \dots, d_{x_n})^T, \quad (29)$$

and

$$\mathbf{m} = (m_{x_1}, m_{x_2}, \dots, m_{x_l})^T, \quad (30)$$

$$(\mathbf{L}^*)^T = \begin{pmatrix} L_{11}^* & L_{12}^* & \cdots & L_{1n}^* \\ L_{21}^* & L_{22}^* & \cdots & L_{2n}^* \\ \dots & \dots & \dots & \dots \\ L_{l1}^* & L_{l2}^* & \cdots & L_{ln}^* \end{pmatrix}. \quad (31)$$

The index l is the number of imaging points or scattering points along the in-line direction in the Z^{th} layer; n is the number of shot-receiver pairs; L_{ij}^* are the complex amplitudes of the

conjugate Green's functions corresponding to the imaging points. In the matrix $(\mathbf{L}^*)^T$, each row is a Green's function for an imaging point in the Z^{th} layer. In fact, equation (28) is the Kirchhoff integral migration formula expressed in matrix form.

However, if seismic-wave illumination is considered, the concept of double focusing (emission focusing and detection focusing) should be introduced into the general migration-imaging formula (28), following Berkhout's notation (Berkhout et al., 2001; Volker et al., 2001):

$$\mathbf{D}\mathbf{L}^U\mathbf{R}\mathbf{L}^D\mathbf{S} = \mathbf{d}^{obs}. \quad (32)$$

The matrix formula stands for the emission of a wavefield from the source S and the detection by the receivers D ; meanwhile the energy of the wavefield propagates downward to the reflector R with an ideal propagator \mathbf{L}^D , and is reflected back to the surface; \mathbf{L}^U is an ideal upward propagator.

Defining $\mathbf{F}^U = (\mathbf{D}^*)^T (\mathbf{L}^{*U})^T$ and $\mathbf{F}^D = (\mathbf{L}^{*D})^T (\mathbf{S}^*)^T$ gives us the formulae for detection focusing and emission focusing, respectively. Together, they represent the illumination of a point on a reflector.

We will analyze the seismic-wave illumination of a target reflector with the local Hessian matrix and compare this with the double-focusing approaches.

MIGRATION IMAGING AND INVERSION IMAGING AS A LEAST-SQUARES PROBLEM

Seismic-wave imaging can be expressed as a least-squares inversion problem,

$$\min V \mathbf{d}^{cal} - \mathbf{d}^{obs} V^2, \quad (33)$$

where, given an underground geological model characterized with some parameters such as P-wave velocity, S-wave velocity, and/or density, or a reflectivity image, we then create a synthetic data set which minimizes the "distance" between the calculated data set and the observed data set.

The solution of the inverse problem is expressed as follows:

$$\begin{aligned} \mathbf{m}_{inv}^{\hat{}} &= \left[(\hat{\mathbf{L}}^*)^T \hat{\mathbf{L}} \right]^{-1} (\hat{\mathbf{L}}^*)^T \hat{\mathbf{d}}^{obs} = \mathbf{H}^{-1} (\hat{\mathbf{L}}^*)^T \hat{\mathbf{d}}^{obs} \\ &= \mathbf{H}^{-1} \mathbf{m}_{mig}^{\hat{}}, \end{aligned} \quad (34)$$

or

$$\begin{aligned} \mathbf{m}_{inv}^{\hat{}} &= \left[(\hat{\mathbf{L}}^*)^T \hat{\mathbf{L}} \right]^{-1} (\hat{\mathbf{L}}^*)^T \hat{\mathbf{d}}^{reg} = \mathbf{H}^{-1} (\hat{\mathbf{L}}^*)^T \hat{\mathbf{d}}^{reg} \\ &= \mathbf{H}^{-1} \mathbf{m}_{mig}^{\hat{}}, \end{aligned} \quad (35)$$

or

$$\begin{aligned} \mathbf{m}_{inv}^{\hat{}} &= \left[(\hat{\mathbf{L}}^*)^T \hat{\mathbf{L}} \right]^{-1} (\hat{\mathbf{L}}^*)^T \hat{\mathbf{d}}^{datum} = \mathbf{H}^{-1} (\hat{\mathbf{L}}^*)^T \hat{\mathbf{d}}^{datum} \\ &= \mathbf{H}^{-1} \mathbf{m}_{mig}^{\hat{}}. \end{aligned} \quad (36)$$

Similarly, if we assume Hessian matrix is a unitary matrix, equation (35), (36), and (37) all degenerate to

$$\mathbf{\hat{m}}_{mig} = (\hat{L}^*)^T \hat{\mathbf{d}}^{obs}. \quad (37)$$

Migration imaging avoids the matrix inversion by replacing the general inverse with a conjugate-transpose operator $(\hat{L}^*)^T$. The advantage of the processing is to change an ill-posed inverse problem into a well-posed wavefield backpropagation problem, which is quite stable and robust (Ronen and Liner, 2000; Duquet et al., 2000; Chavent and Plessix, 1999; Nemeth et al., 1999; Chavent and Plessix, 1999). In fact, migration imaging mainly locates the reflector and gives only a qualitative estimate of the reflectivity. $(\hat{L}^*)^T$ is the two-way or one-way propagator, which commonly is expressed in the form of the conjugate Green's function.

In fact, the quantitative estimation of the reflectivity should take advantage of inverse imaging. If we consider the reflectivity imaging as a weighting summation, equation (37) gives an unsuitable weight function. Bleistein and Stockwell (2000) discuss in detail about how to choose a suitable weight function.

The inverse of the Hessian matrix is just a deconvolution operator, which modifies the unsuitable weight function of the migration imaging. Therefore, equation (35) can give more accurate estimate of the reflectivity than can the migration imaging (equation (37)).

If equation (35) is rewritten as

$$\hat{\mathbf{m}}_{inv} = \mathbf{H}^{-1} \hat{\mathbf{m}}_{mig}, \quad (38)$$

it is clear that Hessian matrix is a deconvolution operator, which improves the resolution of migration results (Hu et al., 2001). We will consider how to quantitatively estimate the reflectivity with inverse imaging and determine the conditions under which direct inverse imaging and iterative inverse imaging are equivalent.

RELATIONSHIP BETWEEN WAVEFIELD-EXTRAPOLATION IMAGING AND INVERSE IMAGING

At the scattering point, we can define a "distance" or norm as

$$E(R) = \sum_{\omega_{min}}^{\omega_{max}} (U_S - U_I R)^2 d\omega, \quad (39)$$

where R is the reflectivity, U_S is the wavefield downward extrapolated to a reflector, and U_I is the wavefield downward propagated to the reflector. The scattering wavefield U_S should be equal to or close to the convolution result between the wavefield U_I and the reflectivity. Letting

$$\frac{\partial E}{\partial R} = 0, \quad (40)$$

we have

$$-2 \sum_{\omega_{min}}^{\omega_{max}} (U_S(\omega) - U_I(\omega) R) U_I(\omega) d\omega = 0, \quad (41)$$

If the incident wavefield equals zero, equation (41) is satisfied. However this case has no physical meaning. If the incident wavefield does not equal zero, then,

$$R = \frac{\sum_{\omega_{min}}^{\omega_{max}} U_S}{\sum_{\omega_{min}}^{\omega_{max}} U_I}. \quad (42)$$

In the complex domain, we can rewrite equation (42) as

$$R = \frac{\sum_{\omega_{min}}^{\omega_{max}} U_S U_I^*}{\sum_{\omega_{min}}^{\omega_{max}} U_I U_I^*}. \quad (43)$$

If the incident wave is quite weak, the following regularization should be introduced:

$$R = \frac{\sum_{\omega_{min}}^{\omega_{max}} U_S U_I^*}{\sum_{\omega_{min}}^{\omega_{max}} (U_I U_I^* + \varepsilon)}, \quad (44)$$

where ε is the regularization coefficient. In fact, the reflectivity is related to the incident angle to a reflector of the plane-wave component of a seismic wave. Therefore, we should modify equation (44) into the following form to reach the angle gathers:

$$R(p) = \frac{\sum_{\omega_{min}}^{\omega_{max}} U_S(\omega, p) U_I^*(\omega, p)}{\sum_{\omega_{min}}^{\omega_{max}} (U_I(\omega, p) U_I^*(\omega, p) + \varepsilon)}, \quad (45)$$

where $U_S(\omega, p)$ and $U_I^*(\omega, p)$ are a scattering plane wavefield and an incident plane wavefield, respectively. In fact, the extrapolated wavefield can be defined as

$$U_S = (\hat{L}^*)^T \hat{\mathbf{d}}^{obs}. \quad (46)$$

Therefore, in the frequency domain, equation (44) can be rewritten as

$$R = \frac{\sum_{\omega_{min}}^{\omega_{max}} (\hat{L}^* U)^T \hat{\mathbf{d}}^{obs} (\hat{L}^* D)^T}{\sum_{\omega_{min}}^{\omega_{max}} (\hat{L}^D (\hat{L}^* D)^T + \varepsilon)}. \quad (47)$$

We will further discuss this topic later to clarify the relationship.

RELATED TOPICS

Angle gathers

Common-image gathers are closely related to the angle reflectivity, which can be used for AVA analysis or AVA inversion. Unfortunately, macro-velocity errors will cause amplitude aberrations in common-image gathers. Therefore, some traps in AVA analysis or inversion should be carefully avoided. However, residual depth or time differences are present in the common-image gathers if macro-velocity field has errors; these differences can be used for migration velocity analysis.

On the other hand, the amplitude-preserving common-image gathers may be generated from inverse imaging.

Wavefield propagator

In seismic-wave migration imaging, the conjugate-transpose matrix $(\hat{L}^*)^T$ stands for the back-propagation of the observed wavefield. Therefore, the wavefield propagators are the basis for seismic-wave imaging.

For constructing a wavefield propagator, we introduce the following methods: (1) a hybrid wavefield propagator, that is, the split-step-Fourier propagator plus optimal interpolation with a self-adaptive reference velocity choice; and (2) a local and directional wavefield propagator, which can be designed with the local Fourier transform and local plane wave/Gaussian beam, for target-oriented imaging (Hill, 2001, 1990; Soubaras, 2003).

MIGRATION VELOCITY ANALYSIS/INVERSION

The macro-velocity field has a decisive influence on seismic-wave imaging. Unfortunately, it is not easy to accurately estimate the velocity field from the seismic data. Up to now, the residual depth/time difference in the common-image gathers has been used for migration-velocity analysis (MVA) or inverting the macro-velocity distribution. However, in the case of complex topography and geological structures, MVA is not a successful approach. Therefore, seismic-wave imaging in complex survey areas has a long way to go. We propose the following approach to inverting the macro-velocity field. The norm is defined as

$$E = W_1 \left(U_S^{k+1} - U_S^k \right)^2 + W_2 \left(\Delta S_m^{k+1} - \Delta S_m^k \right)^2 + W_3 \left(R^{k+1} - R^k \right)^2, \quad (48)$$

where k stands for the iterative number; U_S is the calculated scattering wavefield. R is the position of the main reflectors, which can be identified from the migrated profile. ΔS_m is the slowness disturbance field. W_1, W_2 and W_3 are the different weights. According to Bleistein (2000,p.39), the calculated scattering wavefield can be given by

$$U_S(\vec{x}_g, \vec{x}_s, \omega) = \omega^2 \int_0^\infty \frac{\alpha(\vec{x})}{c^2(\vec{x})} U_I(\vec{x}, \vec{x}_s, \omega) g(\vec{x}, \vec{x}_g, \omega) d\vec{x}, \quad (49)$$

where $\alpha(\vec{x}) = \frac{c^2(\vec{x})}{c^2(\vec{x})} - 1$. Alternatively, the calculated scattering wavefield (Huang et al., 1999) also can be given by

$$\frac{\partial U_S(\omega, k_x, k_y, z)}{\partial z} = \frac{i}{k_z} FT_{x,y} [\omega \Delta S(x, y, z) U_I(\omega, x, y, z)], \quad (50)$$

where $\Delta S(x, y, z) = S(x, y, z) - S_{ref}(x, y, z)$ is the slowness disturbance, U_I is the incident wave field, and k_z is the vertical wavenumber. The incident wave field U_I can be calculated with the following equation:

$$\frac{\partial U_I(\omega, k_x, k_y, z)}{\partial z} = ik_0 k_z U_I(\omega, k_x, k_y, z). \quad (51)$$

where $k_0 = \frac{\omega}{v_r}$, $k_z = \sqrt{1 - \left(\frac{k_T}{k_0}\right)^2}$ and $k_T = \sqrt{k_x^2 + k_y^2}$.

DISCUSSION AND CONCLUSION

Migration algorithms extract the depth locations and relative amplitude behavior of reflectors in the earth from measured seismic data. However, these classic approaches cannot give a quantitative estimate of the reflectivity. In fact, seismic-wave imaging can be performed with the operator and matrix operations, based on least-squares inverse theory. The inverse imaging approaches have the potential to generate quantitative estimates of the reflectivity and to cope with seismic-data regularization and seismic-wave illumination. The ideas we proposed using these theories will open avenues for further research.

ACKNOWLEDGEMENT

The first author thanks the SEP Group at Stanford University for providing an opportunity for him to serve as a visiting scholar.

REFERENCES

- Abma, R., Sun, J., and Bernitsas, N., 1999, Antialiasing methods in Kirchhoff migration: *Geophysics*, **64**, 1783–1792.
- Berkhout, A. J., Ongkiehong, O., Volker, A., and Blacquièrè, G., 2001, Comprehensive assessment of seismic acquisition geometries by focal beams—Part I: Theoretical considerations: *Geophysics*, **66**, 911–917.
- Berkhout, A. J., and Wapenaar, C. P. A., 1989, One-way versions of the Kirchhoff integral: *Geophysics*, **54**, 460–467.

- Biondi, B., 2001, Kirchhoff imaging beyond aliasing: *Geophysics*, **66**, 654–666.
- , 2002, Stable wide-angle Fourier finite-difference downward extrapolation of 3-D wavefields: *Geophysics*, **67**, 872–882.
- Biondi, B., Fomel, S., and Chemingui, N., 1998, Azimuth moveout for 3-D prestack imaging: *Geophysics*, **63**, 574–588.
- Black, J. L., Schleicher, K. L., and Zhang, L., 1993, True-amplitude imaging and dip moveout: *Geophysics*, **58**, 47–66.
- Bleistein, N., C. J. K., and Stockwell, J. W. J., 2000, *Mathematics of multidimensional seismic imaging, migration, and inversion* Springer., Chapter 7.
- Bleistein, N., Cohen, J., and Jaramillo, H., 1999, True-amplitude transformation to zero offset of data from curved reflectors: *Geophysics*, **64**, 112–129.
- Bleistein, N., Cohen, J. K., and Hagin, F. G., 1987, Two and one-half dimensional Born inversion with an arbitrary reference: *Geophysics*, **52**, 26–36.
- Brandsberg-Dahl, S., de Hoop, M. V., and Ursin, B., 2003, Focusing in dip and AVA compensation on scattering-angle/azimuth common image gathers: *Geophysics*, **68**, 232–254.
- de Bruin, C. G. M., Wapenaar, C. P. A., and Berkhout, A. J., 1990, Angle-dependent reflectivity by means of prestack migration: *Geophysics*, **55**, 1223–1234.
- Canning, A., and Gardner, G. H. F., 1996, Regularizing 3-D data sets with DMO: *Geophysics*, **61**, 1103–1114.
- Cao, D., Beydoun, W. B., Singh, S. C., and Tarantola, A., 1990, A simultaneous inversion for background velocity and impedance maps: *Geophysics*, **55**, 458–469.
- Chavent, G., and Jacewitz, C. A., 1995, Determination of background velocities by multiple migration fitting: *Geophysics*, **60**, 476–490.
- Chavent, G., and Plessix, R. E., 1999, An optimal true-amplitude least-squares prestack depth-migration operator: *Geophysics*, **64**, 508–515.
- Docherty, P., 1991, A brief comparison of some Kirchhoff integral formulas for migration and inversion: *Geophysics*, **56**, 1164–1169.
- Druzhinin, A., 1999, Anti-aliased kirchhoff-helmholtz transformations: *Geophysical Prospecting*, **47**, 757–783.
- Duquet, B., Marfurt, K. J., and Dellinger, J., 2000, Kirchhoff modeling, inversion for reflectivity, and subsurface illumination: *Geophysics*, **65**, 1195–1209.
- Gray, S. H., 1997, True-amplitude seismic migration: A comparison of three approaches: *Geophysics*, **62**, 929–936.

- Hale, D., 1991a, 3-D depth migration via McClellan transformations: *Geophysics*, **56**, 1778–1785.
- , 1991b, A nonaliased integral method for dip moveout: *Geophysics*, **56**, 795–805.
- , 1991c, Stable explicit depth extrapolation of seismic wavefields: *Geophysics*, **56**, 1770–1777.
- Hill, N. R., 1990, Gaussian beam migration: *Geophysics*, **55**, 1416–1428.
- , 2001, Prestack Gaussian-beam depth migration: *Geophysics*, **66**, 1240–1250.
- Hu, J., Schuster, G. T., and Valasek, P., 2001, Poststack migration deconvolution: *Geophysics*, **66**, 939–952.
- Huang, L. Y., Fehler, M. C., and Wu, R. S., 1999, Extended local Born Fourier migration method: *Geophysics*, **64**, 1524–1534.
- LeBras, R., and Clayton, R. W., 1988, An iterative inversion of back-scattered acoustic waves: *Geophysics*, **53**, 501–508.
- Li, Z., 1991, Compensating finite-difference errors in 3-D migration and modeling: *Geophysics*, **56**, 1650–1660.
- Marfurt, K. J., 1984, Accuracy of finite-difference and finite-element modeling of the scalar and elastic wave-equations: *Geophysics*, **49**, 533–549.
- Miller, D., Oristaglio, M., and Beylkin, G., 1987, A new slant on seismic imaging - Migration and integral geometry: *Geophysics*, **52**, 943–964.
- Mora, P., 1988, Elastic wave-field inversion of reflection and transmission data: *Geophysics*, **53**, 750–759.
- , 1989, Inversion = migration + tomography: *Geophysics*, **54**, 1575–1586.
- Mora, P. R., 1987, Nonlinear two-dimensional elastic inversion of multioffset seismic data: *Geophysics*, **52**, 1211–1228.
- Nemeth, T., Sun, H., and Schuster, G. T., 2000, Separation of signal and coherent noise by migration filtering: *Geophysics*, **65**, 574–583.
- Nemeth, T., Wu, C., and Schuster, G. T., 1999, Least-squares migration of incomplete reflection data: *Geophysics*, **64**, 208–221.
- Plessix, R.-E., and Mulder, W. A., 2004, Frequency-domain finite-difference amplitude-preserving migration: *Geophys. J. Int.*, **157**, 975–987.
- Pratt, R. G., 1999, Seismic waveform inversion in the frequency domain, Part 1: Theory and verification in a physical scale model: *Geophysics*, **64**, 888–901.

- Pratt, R. G., and Shipp, R. M., 1999, Seismic waveform inversion in the frequency domain, Part 2: Fault delineation in sediments using crosshole data: *Geophysics*, **64**, 902–914.
- Pratt, R. G., S. C., and Hicks, G. J., 1998, Gauss-newton and full newton methods in frequency-space seismic waveform inversion: *Geophys. J. Int.*, **133**, 341–362.
- Ristow, D., and Ruhl, T., 1994, Fourier finite-difference migration: *Geophysics*, **59**, 1882–1893.
- Ronen, J., 1987, Wave equation trace interpolation: *Geophysics*, **52**, 973–984.
- Ronen, S., and Liner, C. L., 2000, Least-squares DMO and migration: *Geophysics*, **65**, 1364–1371.
- Shin, C., J. S., and Min, D., 2001, Improved amplitude preservation for prestack depth migration by inverse scattering theory: *Geophysical Prospecting*, **49**, 592–606.
- Soubaras, R., 2003, Angle gathers for shot-record migration by local harmonic decomposition: 73th Ann. Internat. Mtg., Soc. Expl. Geophys., Expanded abstracts, 889–892.
- Stoffa, P. L., Fokkema, J. T., de Luna Freire, R. M., and Kessinger, W. P., 1990, Split-step Fourier migration: *Geophysics*, **55**, 410–421.
- Tarantola, A., 1984, Inversion of seismic reflection data in the acoustic approximation: *Geophysics*, **49**, 1259–1266.
- Volker, A., Blacquièrre, G., Berkhout, A. J., and Ongkiehong, O., 2001, Comprehensive assessment of seismic acquisition geometries by focal beams – Part II: Practical aspects and examples: *Geophysics*, **66**, 918–931.
- Wapenaar, C. P. A., Peels, G. L., Budejicky, V., and Berkhout, A. J., 1989, Inverse extrapolation of primary seismic waves: *Geophysics*, **54**, 853–863.
- Wu, R., and Chen, L., 2002, Mapping directional illumination and acquisition-aperture efficacy by beamlet propagators: 72th Ann. Internat. Mtg., Soc. Expl. Geophys., Expanded abstracts, 1352–1355.
- Wu, R. S., and Toksoz, M. N., 1987, Diffraction tomography and multisource holography applied to seismic imaging: *Geophysics*, **52**, 11–25.
- Zhang, Y., Sun, J., and Gray, S., 2003, Aliasing in wavefield extrapolation prestack migration: *Geophysics*, **68**, 629–633.

Water-bottom and diffracted 2D multiple reflections in data space and image space

Gabriel Alvarez¹

ABSTRACT

Water-bottom multiples from a dipping interface have the same kinematics in a Common Midpoint (CMP) gather as a primary from a reflector with twice the dip at twice the perpendicular depth at the CMP location. When migrated with the velocity of the primaries, these multiples are overmigrated just as primaries migrated with higher velocity, and their moveout is thus predictable in image space. Diffracted multiples, on the other hand, have an apex-shifted moveout in CMP gathers and a more complicated, also apex-shifted, residual moveout in image space when migrated with the velocity of the primaries. I illustrate the moveout of water-bottom and diffracted multiples in image space with a simple 2D synthetic dataset.

INTRODUCTION

Recently, the increased interest in exploration in areas with rough salt bodies, such as the Gulf of Mexico, has sparked the interest in multiple attenuation methods that work in the image space (Sava and Guitton, 2003; Hargreaves and Wombell, 2004; Alvarez et al., 2004) as opposed to more traditional methods that work in the data space (Hampson, 1986) or Surface Related Multiple Elimination (SRME) methods (Verschuur et al., 1992; Verschuur and Berkhout, 1997) that require dense surface coverage of sources and receivers or demanding data interpolation and extrapolation.

The main advantage of the image space is that most of the complexity of the propagation for the primary reflections is handled by prestack depth migration such that the primary reflections in Angle-Domain Common-Image Gathers (ADCIGs) are flat or nearly flat if the migration is done with the velocity of the primaries. It is not immediately obvious, however, what is the residual moveout of the migrated multiples in ADCIGs. A reasonable approximation is to consider that the residual moveout of the migrated multiples is the same as that of the primaries when migrated with the wrong (higher) velocity (Biondi and Symes, 2004). This approach leads, in 2D, to a relatively simple and effective algorithm for the attenuation of the multiples in the image space (Sava and Guitton, 2003) and, with some modifications, can

¹email: gabriel@sep.stanford.edu

attenuate 2D diffracted multiples reasonably well (Alvarez et al., 2004). In this paper I present the equations for the image space coordinates of the water-bottom multiples in 2D ADCIGs and illustrate the migration of the multiples with a synthetic dataset.

The next section presents the kinematics of water-bottom and diffracted multiples in data space. The following section presents the equations to map the multiples from data space to image space. The last section illustrates the mapping of the multiples in image space, both in common subsurface offset common-image gathers and angle-domain common-image gathers for the simple synthetic dataset.

KINEMATICS OF MULTIPLES IN DATA SPACE FROM A 2D DIPPING INTERFACE

Water-bottom multiples

Consider a model with a dipping water-bottom in 2D. The raypath of the primary reflection can be easily computed using the concept of the image source as illustrated in Figure 1. The

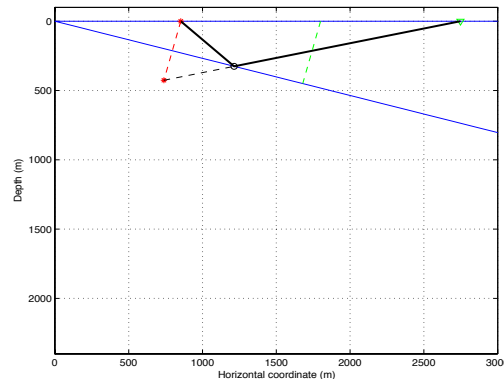


Figure 1: Construction of the primary reflection from a dipping interface.

[gabriel2-rayprim](#) [CR]

moveout of the primary reflection in the CMP domain is given by:

$$t_p = \sqrt{\left(\frac{2Z_D}{V}\right)^2 + \left(\frac{2h_D}{V_{NMO}}\right)^2} = \sqrt{t_0^2 + \left(\frac{2h_D}{V_{NMO}}\right)^2} \quad (1)$$

where t_p is the time of the primary, φ is the dip angle of the reflector, Z_D is the perpendicular distance between the surface and the reflector at the CMP location, h_D is half the source-receiver offset, V is the propagation velocity above the dipping reflector, $V_{NMO} = V/\cos\varphi$ is the normal moveout velocity and t_0 is the traveltime of the zero-offset reflection. This is obviously the equation of a hyperbola, as illustrated in Figure 4.

The raypath of the multiple reflection can be considered as a cascaded of two primary reflections as SRME methods do (Figure 2), but the traveltime of the multiple, t_m , can be computed more easily as the traveltime of an equivalent primary from a reflector dipping at

twice the dip angle of the actual reflector as illustrated in Figure 3. That is,

$$t_m = \sqrt{\left(\frac{2\hat{Z}_D}{V}\right)^2 + \left(\frac{2h_D}{\hat{V}_{NMO}}\right)^2} \tag{2}$$

where \hat{Z}_D is the perpendicular distance between the surface and the equivalent reflector with twice the dip at the CMP location and \hat{V}_{NMO} is now $V/\cos(2\varphi)$. Figure 4 corresponds to a CMP showing the primary and the multiple reflection. Obviously, they are both hyperbolas since the multiple has the same kinematics as a primary from a reflector dipping at twice the dip as indicated above.

Figure 2: Decomposition of the water-bottom multiple as a cascaded of two primary reflections. gabriel2-raymul1 [CR]

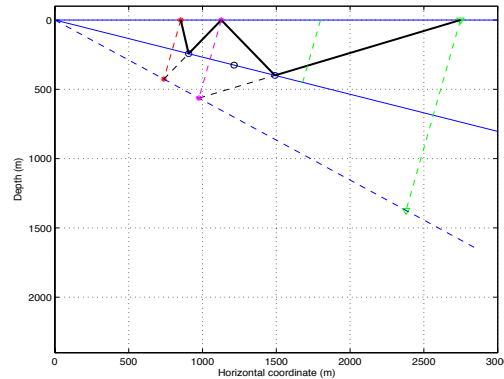


Figure 3: Multiple reflection as a primary from an equivalent reflector with twice the dip angle. gabriel2-raymul2 [CR]

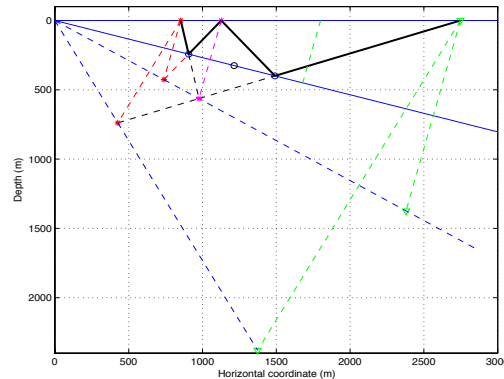
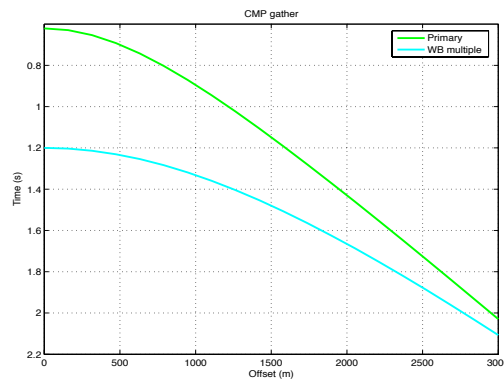


Figure 4: Moveout curves of primary and water-bottom multiple from a dipping interface on a CMP gather. gabriel2-moveouts1 [CR]



Diffracted multiples

Consider now a diffractor sitting on top of the water-bottom reflector at the lateral position x_d and depth z_d (Figure 5). The moveout of the primary diffraction is given by

$$t_d = t_s + t_g = \frac{1}{V} \left[\sqrt{(x_d - m_D + h_D)^2 + z_d^2} + \sqrt{(m_D + h_D - x_d)^2 + x_d^2} \right] \quad (3)$$

where t_s and t_g are traveltimes from the source and receiver to the diffractor, respectively, m_D is the horizontal position of the CMP gather and h_D is the half-offset between the source and the receiver. This is the equation of a hyperbola with apex at the horizontal position directly above the diffractor. Consider now the multiple that hits the diffractor on its second bounce on

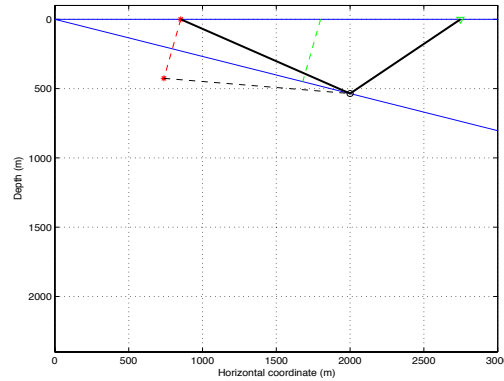


Figure 5: Image source construction for the primary diffraction.
gabriel2-rayprimdiff [CR]

the dipping reflector (source-side multiple), as shown in Figure 6. This multiple is no longer the equivalent of any primary, but we can compute its traveltime in the following way:

1. Form the image source.
2. Find the point at the surface such that the lines joining that point with both the image source and the diffractor intercept with the same angle with respect to the vertical (Snell's law).
3. Compute the raypath using the law of cosines and divide by the velocity to get the traveltime.

The coordinates of the image source (X_{is}, Z_{is}) are given by

$$X_{is} = X_s - 2Z_0 \sin \varphi, \quad (4)$$

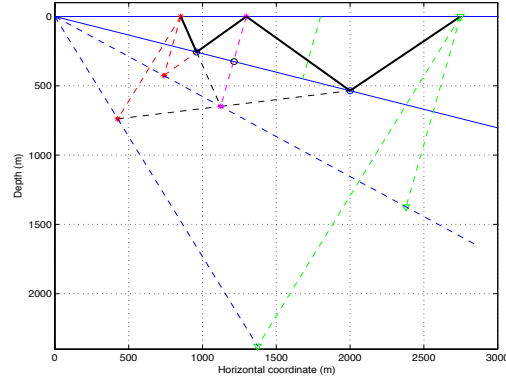
$$Z_{is} = 2Z_0 \cos \varphi, \quad (5)$$

where

$$Z_0 = Z_D - h_D \sin \varphi \quad (6)$$

is the perpendicular distance between the shot and the reflector. From the description of nu-

Figure 6: Diffracted multiple. Notice that the last leg of the multiple does not satisfy Snell's law. [gabriel2-raymuldiff](#) [CR]



meral 3. above, the surface coordinate of the multiple bounce at the surface is:

$$X_{ms} = \frac{X_{is}z_d + x_d Z_{is}}{Z_{is} + z_d}. \quad (7)$$

The aperture angle of the first bounce of the multiple is $\beta_s + \varphi$ where β_s is the takeoff angle of the multiple with respect to the vertical. The aperture angle at the surface bounce is $\beta_s + 2\varphi$ and can be easily computed as

$$\tan(\beta_s + 2\varphi) = \frac{x_d - X_{ms}}{z_d}. \quad (8)$$

The traveltme of the first leg of the multiple, in terms of β_s and the vertical distance between the source and the reflector, $Z_s = \frac{Z_D - h_D \sin \varphi}{\cos \varphi}$, is:

$$t_{m_1} = \frac{Z_s \cos \varphi}{V \cos(\varphi + \beta_s)}. \quad (9)$$

Similarly, repeated application of the law of sines gives the traveltme of the other three legs of the multiple

$$t_{m_2} = \frac{Z_s \cos \varphi \cos \beta_s}{V \cos(\varphi + \beta_s) \cos(2\varphi + \beta_s)}, \quad (10)$$

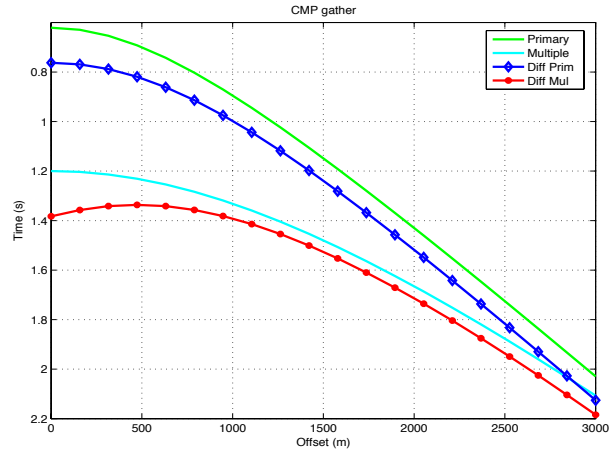
$$t_{m_3} = \frac{Z_s \cos \varphi \cos \beta_s}{V \cos(2\varphi + \beta_s) \cos(3\varphi + \beta_s)}. \quad (11)$$

The total arrival time of the diffracted multiple is therefore:

$$\begin{aligned} t_m &= \frac{Z_s \cos \varphi}{V \cos(\varphi + \beta_s)} \left(1 + \frac{\cos \beta_s}{\cos(2\varphi + \beta_s)} + \frac{\cos \beta_s \cos(2\varphi + \beta_s)}{\cos(2\varphi + \beta_s) \cos(3\varphi + \beta_s)} \right) + \frac{z_d}{V \cos \beta_r} \\ &= \frac{2Z_s \cos \varphi}{V \cos(\beta_s + 3\varphi)} + \frac{z_d}{V \cos \beta_r} \\ &= \frac{2(Z_D - h_D \sin \varphi) \cos \varphi}{\cos(\beta_s + 3\varphi)} + \frac{z_d}{V \cos \beta_r}, \end{aligned} \quad (12)$$

where $\tan \beta_r = \frac{m_D + h_D - x_d}{z_d}$ and β_r is the emergence angle of the diffracted multiple with respect to the vertical. Figure 7 compares the moveout of the diffracted multiple with that of the water-bottom multiple. Obviously, the apex of the diffracted multiple is not at zero offset.

Figure 7: Moveout curves of primary, water-bottom multiple, diffraction and diffracted multiple from a dipping interface on a CMP gather. [gabriel2-moveouts3](#) [CR]



WATER-BOTTOM MULTIPLE IN IMAGE SPACE

Given the kinematic equivalence between the water-bottom multiple and a primary from a reflector dipping at twice the dip angle, we can express the image space coordinates of the water-bottom multiple in terms of the data space coordinates by solving the system of equations presented by Fomel and Prucha (1999):

$$t_m = \frac{2\hat{Z}_\xi \cos \hat{\varphi} \cos \hat{\gamma}}{V \cos^2 \hat{\varphi} - \sin^2 \hat{\gamma}}, \quad (13)$$

$$h_D = \hat{Z}_\xi \frac{\sin \hat{\gamma} \cos \hat{\gamma}}{\cos^2 \hat{\varphi} - \sin^2 \hat{\gamma}}, \quad (14)$$

$$m_D = \hat{m}_\xi + \hat{Z}_\xi \frac{\sin \hat{\varphi} \cos \hat{\varphi}}{\cos^2 \hat{\varphi} - \sin^2 \hat{\gamma}}, \quad (15)$$

where $(\hat{X}_\xi, \hat{m}_\xi, \hat{\gamma})$ are the image space coordinates of the primary that is kinematically equivalent to the first order water-bottom multiple as mentioned in the previous section and $\hat{\varphi} = 2\varphi$. The formal solution of these equations, for the image space coordinates is:

$$\sin \hat{\gamma} = \frac{2h_D \cos 2\varphi}{V t_m} \rightarrow \tan \hat{\gamma} = \frac{2h_D \cos 2\varphi}{\sqrt{V^2 t_m^2 - 4h_D^2 \cos^2 2\varphi}}, \quad (16)$$

$$\hat{Z}_\xi = \frac{\cos(2\varphi)(V^2 t_m^2 - 4h_D^2)}{2\sqrt{V^2 t_m^2 - 4h_D^2 \cos^2(2\varphi)}}, \quad (17)$$

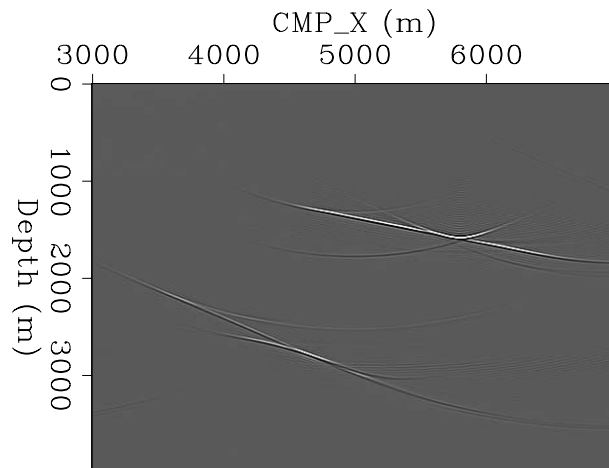
$$\hat{m}_\xi = m_D - \frac{V^2 t_m^2 \sin(2\varphi)}{2\sqrt{V^2 t_m^2 - 4h_D^2 \cos^2 \varphi}}. \quad (18)$$

These equations allow the computation of the impulse response of the water-bottom multiples in image space as a function of the aperture angle. More importantly, they are the starting point for understanding the kinematics of the data in 3D ADCIGs (Tisserant and Biondi, 2004), still a subject of research.

2D SYNTHETIC DATA EXAMPLE

To illustrate the migration of the multiples, I created a simple 2D synthetic model consisting of a water-bottom reflector dipping at 15 degrees. A diffractor sits on top of this reflector at a horizontal coordinate of 5600 m. The coordinate origin is the point at which the dipping reflector intercepts the surface. Two hundred CMP gathers were generated with 100 traces in an offset range from 0 to 3000 m. The first CMP corresponds to a horizontal position of 5000 m and the CMP interval is 10 m. Four events were simulated: primary reflection, water-bottom reflection, diffraction and diffracted multiple using the traveltimes equations presented before. I used a Ricker wavelet with peak frequency of 20 Hz. Figure 8 shows the zero

Figure 8: Zero subsurface-offset section extracted from the image obtained by migrating the data with a two constant-velocity layer model: 1500 m/s above the reflector and 2800 m/s below the reflector. `gabriel2-zsoff_mig_all` [CR]



subsurface offset section extracted from the image data migrated with a velocity model that consists of two constant velocity layers: 1500 m/s above the reflector and 2800 m/s below the reflector. Two reference velocities were used for the migration at each depth step. As expected, the water-bottom (primary) reflector and the diffraction are properly imaged since they were migrated with a velocity close to the true velocity. The water-bottom multiple and the diffracted multiple, on the other hand, have both been migrated. This can be seen more clearly in Figure 9, which shows four subsurface-offset common image gathers at four different horizontal locations: (a) $CMP_X=6280$ m, a primary location; (b) $CMP_X=5800$ m, diffractor location; (c) $CMP_X=4600$ m, a diffracted multiple location; and (d) $CMP_X=3600$ m, a water-bottom multiple location. The primary and the diffraction are well focused at zero subsurface offset, but not the multiples, since they were migrated with the wrong velocity.

There is, however, an important difference between the image of the water-bottom multiple and that of the diffracted multiple. This can be seen in Figure 10 that shows the zero-subsurface offset section but for the image obtained by migrating the data with constant water velocity (1500 m/s). The primary and the diffractor are both perfectly imaged since they were migrated with the exact velocity. The water-bottom multiple is also imaged perfectly as a primary with twice the dip of the real primary. The diffracted multiple, on the other hand, is still poorly imaged and does not show as a diffractor at all, since its kinematics do not match those of a primary reflection as explained before. Figure 11 shows the same image gathers as those in Figure 9. Notice the good focusing of the water-bottom multiple. Since the “natural” prestack

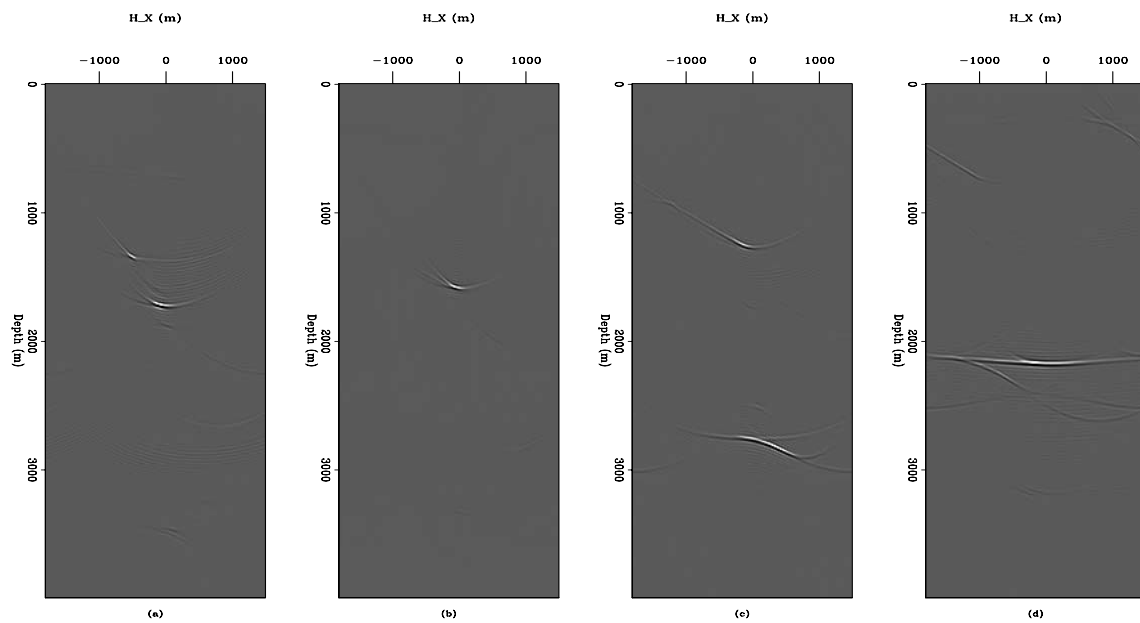


Figure 9: Subsurface-offset common-image gathers extracted from the image obtained by migrating the data with a two constant-velocity layer model. (a) at primary location (CMP_X=6280 m). (b) at the location of the diffractor (CMP_X=5800 m). (c) at a diffracted multiple location (CMP_X=4600 m) and (d) at a water-bottom multiple location (CMP_X=3600 m). `gabriel2-cigs1_all` [CR]

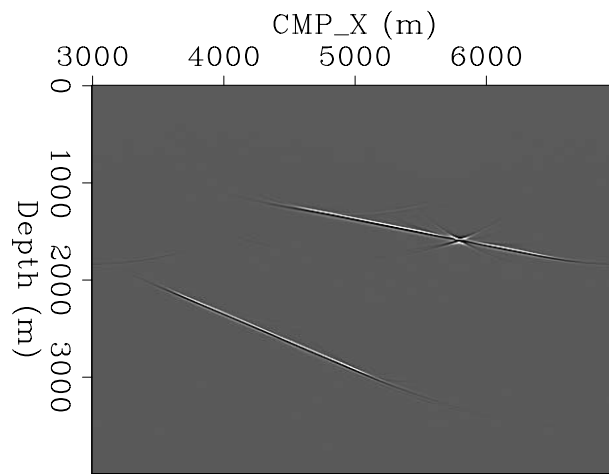


Figure 10: Zero subsurface-offset section extracted from the image obtained by migrating the data with constant water velocity. `gabriel2-zsoff_mig_all_const` [CR]

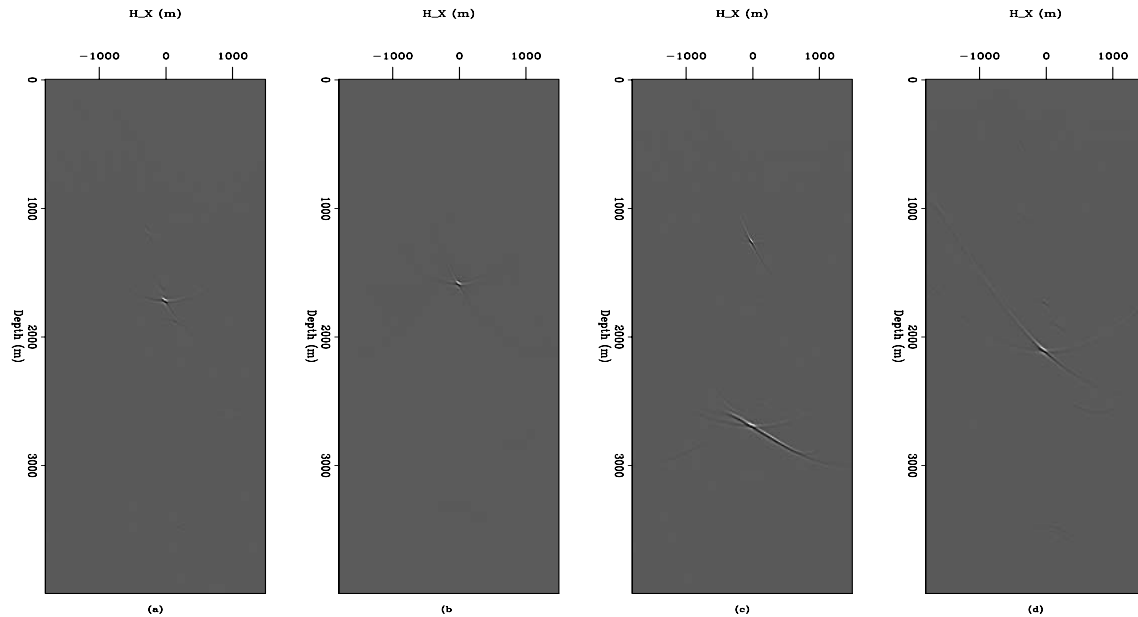


Figure 11: Subsurface-offset common image gathers extracted from the image obtained by migrating the data with constant water velocity. (a) at a primary location (CMP_X=6280 m). (b) at the location of the diffractor (CMP_X=5800 m). (c) at a diffracted multiple location (CMP_X=4600 m) and (d) at a water-bottom multiple location (CMP_X=3600 m). `gabriel2-cigs1_all_const` [CR]

domain of data migrated with wave-equation migration for velocity analysis is the aperture angle rather than the subsurface offset, it is worth looking at the results of the migration in this domain. Figure 12 shows angle-domain common-image gathers extracted from the image obtained by migrating the data with the two-velocity layer model at the same spatial locations as in Figure 9. The primary shows a good coverage of aperture angles. The diffraction samples even more aperture angles, since it is not restricted by Snell's law whereas the water-bottom multiple shows the characteristic overmigration. The diffracted multiple shows the expected, complicated apex-shifted moveout.

Finally, Figure 13 shows the angle-domain common-image gathers at the same spatial locations as in Figure 12 but corresponding to the data migrated with constant velocity. Notice how the moveout of the water-bottom multiple is flat like that of the primary but its range of aperture angles is much smaller as is intuitively obvious. The diffracted multiple shows focusing at its apex, located at an aperture angle of about 15 degrees.

CONCLUSIONS

I have demonstrated with a simple synthetic dataset that water-bottom multiples from a dipping interface behave as primaries generated by a reflector with twice the dip at twice the perpendicular depth at the CMP location. Therefore they can be perfectly migrated if the mi-

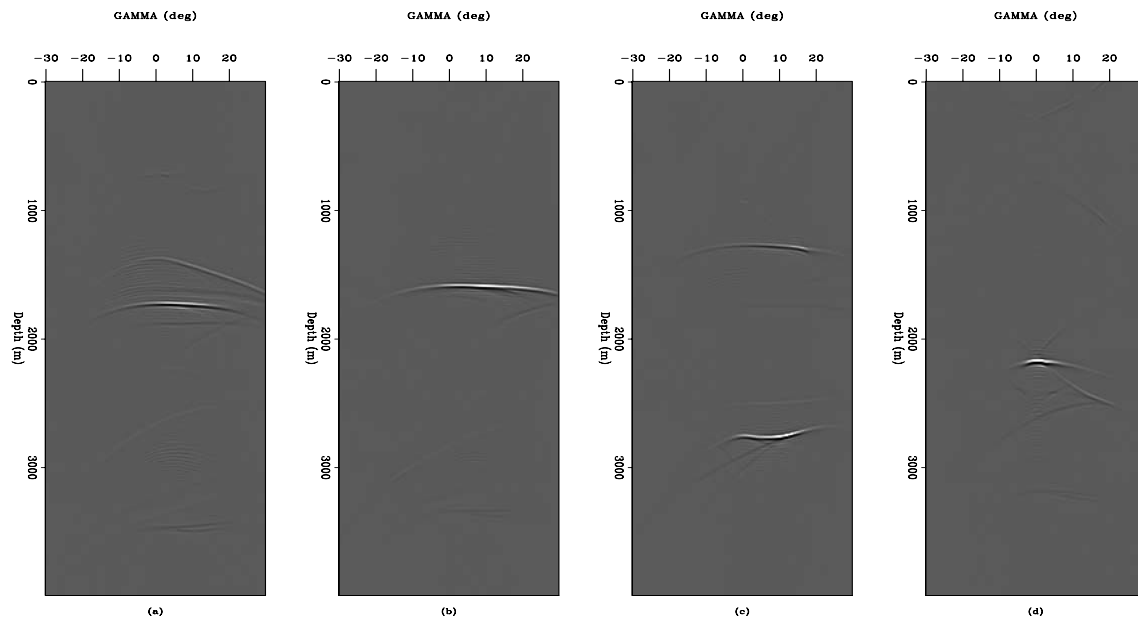


Figure 12: Angle domain common image gathers extracted from the image obtained by migrating the data with a two constant-velocity layer model. (a) at a primary location (CMP_X=6280 m). (b) at the location of the diffractor (CMP_X=5800 m). (c) at a diffracted multiple location (CMP_X=4600 m) and (d) at a water-bottom multiple location (CMP_X=3600 m).

`gabriel2-adcigs1_all` [CR]

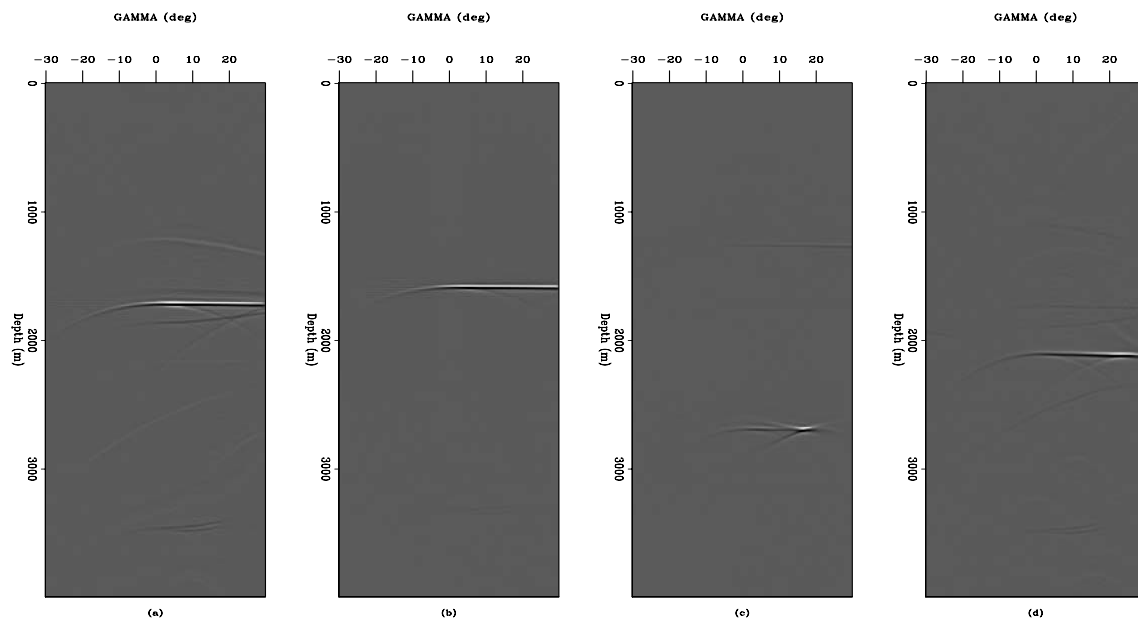


Figure 13: Angle domain common image gathers extracted from the image obtained by migrating the data with constant water velocity. (a) at a primary location (CMP_X=6280 m). (b) at the location of the diffractor (CMP_X=5800 m). (c) at a diffracted multiple location (CMP_X=4600 m) and (d) at a water-bottom multiple location (CMP_X=3600 m).

`gabriel2-adcigs1_all_const` [CR]

gration is done with the water velocity. The diffracted multiples, on the other hand, cannot be perfectly migrated because they do not correspond to an equivalent primary. Understanding how the multiples behave after migration, specially in 3D, is very important for the ultimate goal of attenuating the multiples in image space.

REFERENCES

- Alvarez, G., Biondi, B., and Guitton, A., 2004, Attenuation of diffracted multiples in angle-domain common-image gathers:, *in* 74th Ann. Internat. Mtg. Soc. of Expl. Geophys., 1301–1304.
- Biondi, B., and Symes, W., 2004, Angle-domain common-image gathers for migration velocity analysis by wavefield-continuation imaging: *Geophysics*, **69**, no. 5, 1283–1298.
- Fomel, S., and Prucha, M., 1999, Angle-gather time migration: *SEP-100*, 141–150.
- Hampson, D., 1986, Inverse velocity stacking for multiple elimination:, *in* 56th Ann. Internat. Mtg. Soc. of Expl. Geophys., Session:S6.7.
- Hargreaves, N., and Wombell, R., 2004, Multiple diffractions and coherent noise in marine seismic data:, *in* 74th Ann. Internat. Mtg. Soc. of Expl. Geophys., 1325–1328.
- Sava, P., and Guitton, A., 2003, Multiple attenuation in the image space: *SEP-113*, 31–44.
- Tisserant, T., and Biondi, B., 2004, Residual move-out analysis with 3d angle-domain common-image gathers: 74th Ann. Internat. Mtg., Soc. of Expl. Geophys., Expanded Abstracts, 2391–2394.
- Verschuur, D., and Berkhout, A., 1997, Estimation of multiple scattering by iterative inversion, part ii: practical aspects and examples: *Geophysics*, **62**, no. 5, 1596–1611.
- Verschuur, D., Berkhout, A., and Wapenaar, C., 1992, Adaptive surface-related multiple elimination: *Geophysics*, **57**, no. 9, 1166–1177.



Multiple attenuation: data space vs. image space - A real data example

Daniel A. Rosales and Antoine Guitton¹

ABSTRACT

Multiples can be attenuated either before or after the imaging process. Adaptive subtraction can be applied after migration to eliminate the multiples in the image space. We build a multiple model based on the sea floor reflection, that is kinematically correct. We then perform multiple attenuation to remove the water-bottom multiple in both the image space and the data space.

INTRODUCTION

Multiples are often the most significant impediment to the successful construction and interpretation of marine seismic and ocean bottom seismic data. There are several techniques for multiple removal. The selection of the most appropriate method depends on, among other factors, the geology, the acquisition methods and the processing costs. Examples of possible methods include: 1) multiple separation with a high-resolution hyperbolic Radon Transform (Lumley et al., 1995; Kostov and Nichols, 1995), which depends on a observable difference between the moveout of the primaries and multiples; and 2) surface-related multiple elimination (SRME) (Verschuur et al., 1992), which works better on areas with a difficult-to-distinguish difference between the moveout of the primaries and multiples.

Where to perform the multiple elimination, in the data space (before imaging) or in the image space (after imaging), is also a variable to consider when attenuating the multiples. Sava and Guitton (2003) conclude that multiples can be eliminated after migration, in the angle-domain, using Radon Transforms. Guitton (2004) suggests that the image space should be used as much as possible for the multiple-suppression process, since one of the final products of the seismic processing workflow is a migrated image. This paper compares the performance of surface-related multiple elimination in the data and image spaces.

For this purpose, we use a 2D/4C real data set, acquired with an ocean-bottom cable in the Mahogany field, located in the Gulf of Mexico. The dataset provides an interesting test, because conventional multiple-removal methods fail. There is not enough difference between the moveout of primaries and multiples, and the water depth is relatively shallow, thus producing strong multiple reflections at deep targets.

¹email: daniel@sep.stanford.edu, antoine@sep.stanford.edu

We first present a review of the theory behind multiple suppression by adaptive subtraction. Then, we present the results of multiple suppression both in the data space and in the image space. We conclude that multiple elimination in the image space yields a better final pre-stack image. However, the image space approach has a cost disadvantage, since a full migration of the multiple model is needed.

MULTIPLE ELIMINATION THEORY

The Delft approach (Verschuur et al., 1992) is able to remove surface-related multiples for any type of geology, as long as the receiver and source coverage at the surface is dense enough. One of the main advantages of the Delft method is that no subsurface information is required.

In this implementation of the Delft approach, we first create a kinematic model of the water-bottom multiple by convolving in time and space a water-bottom operator. We do this convolution such that the kinematics of all surface-related multiples are accurate. Then, the relative amplitudes of the first-order multiples are correct, but the amplitudes of higher-order multiples are over-predicted (Wang and Levin, 1994; Guitton et al., 2001).

Once a multiple model has been estimated, it is adaptively subtracted from the data. Note that, as pointed out by Berkhout and Verschuur (1997), this first subtraction step should be followed by more iterations. The goal of the iterative procedure is to better estimate and eliminate higher-order multiples (Verschuur and Berkhout, 1997). In this paper, we iterate only once and hope that the adaptive subtraction step is flexible enough to handle all the multiples at once.

We use non-stationary filtering technology for adaptive-subtraction (Rickett et al., 2001). The main advantage of these filters is that they are computed in the time domain and thus take the inherent non-stationarity of the multiples and the data into account. Therefore, it is possible to estimate adaptive filters locally that will give the best multiple attenuation result. Note that by estimating two-sided 2-D filters gives a lot of degrees of freedom for the matching of the multiple model to the real multiples in the data.

Thus, given a model of the multiples \mathbf{M} and the data \mathbf{d} , we estimate a bank of non-stationary filters \mathbf{f} such that

$$g(\mathbf{f}) = \|\mathbf{M}\mathbf{f} - \mathbf{d}\|^2 + \epsilon^2 \|\mathbf{R}\mathbf{f}\|^2 \quad (1)$$

is minimum. In equation (1), \mathbf{R} is the Helix derivative (Claerbout, 1998) that smooths the filter coefficients across micro-patches (Crawley, 2000) and ϵ is a constant to be chosen *a-priori*. Note that \mathbf{M} corresponds to the convolution with the model of the multiples \mathbf{m} (Robinson and Treitel, 1980). Remember that this model of the multiples is obtained by convolving in space and time the input data:

$$\mathbf{m}(\omega) = \mathbf{d}(\omega) * \mathbf{wb}(\omega), \quad (2)$$

where $*$ defines the convolution process detailed in Verschuur et al. (1992), and $\mathbf{m}(\omega)$, $\mathbf{d}(\omega)$, and $\mathbf{wb}(\omega)$ are the multiples model, the data, and the water-bottom operator for one frequency

(ω), respectively. In equation (1), the filters are estimated iteratively with a conjugate-gradient method.

The Delft approach is widely used in the industry and is known to give currently the best multiple attenuation results for complex geology (Dragoset and Jericevic, 1998). However, it has been shown that this method suffers from an approximation made during the adaptive filtering step. For instance, when “significant” amplitude differences exist between the primaries and the multiples, the multiple model might be matched to the primaries and not to the multiples. A solution to this problem is using the ℓ^1 norm in equation (1) (Guitton and Verschuur, 2002). Another assumption made in equation (1) is that the signal has minimum energy. Spitz (1999) illustrates the shortcomings of this assumption and advocates that a pattern-based method is a better way of subtracting multiples from the data.

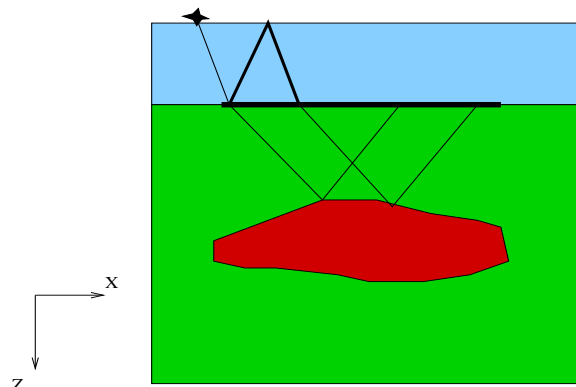
EXAMPLE

The data set that we use for our analysis corresponds to a 2D OBC experiment in the Gulf of Mexico, in the Mahogany field. Rosales and Guitton (2004) present the preprocessing for this data set. After combining the hydrophone and geophone components, we still have the multiples related to the water bottom. For this particular data set, we can consider the water bottom to be flat throughout the data (Herrenschmidt et al., 2001). Therefore, we can apply the Delft methodology to CMP gathers, for the elimination of the water-bottom multiples.

Multiples model

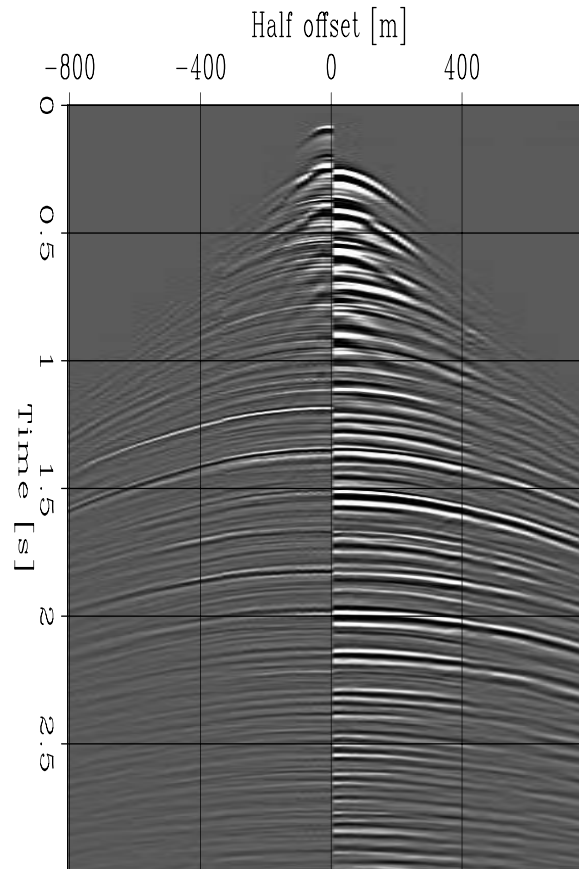
First, we need to obtain the multiples model. For this we create an operator that represents the reflection from the water surface to the water bottom and back (Figure 1) We obtain the operator from the data itself, by considering the water bottom a flat surface. We begin by isolating the first arrival, we then upward continue the first arrival to the water surface level. Figure 2 shows the comparison of one gather of our multiples model with the data itself.

Figure 1: Multiple operator. An OBC acquisition with the source at the surface and the receivers at the bottom. For this shallow experiment the water-bottom multiple is the most dominant multiple. daniel3-sketch
[NR]



The left side shows the multiples model and the right the data. Observe the good correlation between our data and the multiples model, not only at zero offset, but also in the moveout at far offset.

Figure 2: Multiples model compared against the data set. Left side corresponds to the data and right side to multiple model for the water-bottom. `daniel3-mult.model` [ER]



Data Space

We first applied adaptive subtraction to the Mahogany data set in data space. Since the water bottom is fairly shallow (approx. 118 m), the water-bottom multiples are the most dominant multiples in the data set. Figure 3 shows one CMP, between 2 s and 4 s. This figure shows, from top to bottom: A) the multiple model; B) the result of the adaptive subtraction, the estimated primaries; C) the filter obtained with the multiples model for performing the subtraction; and D) the original data set.

Many multiples were totally eliminated, while others were partially eliminated. The results are comparable throughout the data set. The shallow multiples, while they were partially eliminated, still retain some energy. As we will see in the next sections, this remaining energy will still interfere with an otherwise accurate final image.

Image Space

We now apply adaptive subtraction after migration. We perform split-step wavefield downward-continuation migration to go from the data to the image space. Both the original seismic data and the multiples model were migrated with the same algorithm. Because the velocity model is still an unknown at this stage of the processing, we use a simple, vertical-gradient velocity

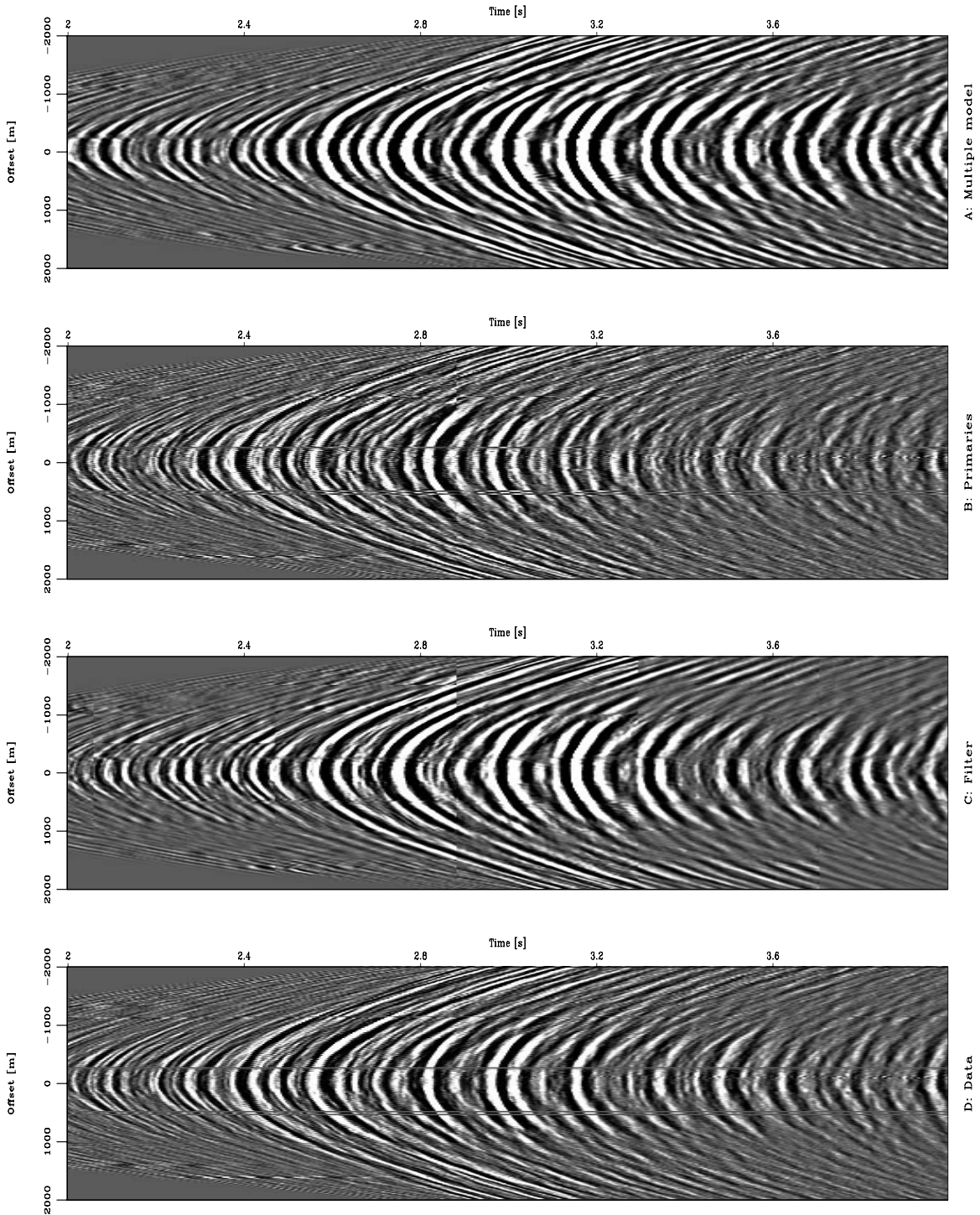


Figure 3: Data space multiple removal. From top to bottom: A) multiple model; B) Primaries; C) Filter; D) Data. [daniel3-dspace_4panel](#) [CR]

function. We use the same velocity model for the original data set and the multiples model. Since this particular data set corresponds to an OBC acquisition, both the original data set and the multiples model were re-datumed in order to have both sources and receivers at the same depth level before the migration.

Figure 4 shows one angle-domain common-image gather, following the same presentation scheme for the results in the data space. The figure shows, from top to bottom: A) the migrated multiples model; B) the result of adaptive subtraction in the image space, that is the primaries; C) the filter obtained with the migrated multiples model for performing the subtraction; and D) the migrated data set.

We first observe that both the migration of the entire data set and the migration of the multiples (panels A and D) have a residual curvature in the angle gathers because we have the correct velocity model. However, this is not an obstacle to performing the multiples subtraction in this domain, since both panels present the same residual moveout. After estimating the filter for performing the subtraction (panel C), we were able to eliminate almost all the multiples present in our multiples model.

Data space vs. Image space

To compare the results of multiple elimination in the data space directly to the multiple elimination in the image space, we transformed our data-space subtraction results into the image space. Figure 5 compares the same angle-domain common-image gathers for multiple removal in the data space and in the image space. The figure shows, from top to bottom: A) the migrated multiples model; B) the result of adaptive subtraction done in the data space, after migration; C) the result of adaptive subtraction done in the image space; and D) the migrated data set.

We observe that the multiples eliminated in the data space are also eliminated in the image space. However, some multiples were eliminated better in the image space, as, for example, the strong multiple at around 2800 m. Figure 6 compares the stack of the data space and image space results: from top to bottom, we have: A) the migration stack of the primaries obtained from the adaptive subtraction in the image space; B) the migration stack of the primaries obtained from the adaptive subtraction in the data space; and C) the migration stack of the original data set. Figure 7 compares the stack of migrated multiples models. From top to bottom, we have: A) the migrated multiple model; B) the estimated multiple section from the processing in the data space; and C) the estimated multiple section from the processing in the image space.

DISCUSSION AND CONCLUSIONS

Multiples are not always easy to eliminate with well-known methodologies, and many times we carry them into the imaging process. During velocity analysis, multiples interfere destructively with velocity model building. At this stage, primaries and multiples both have residual

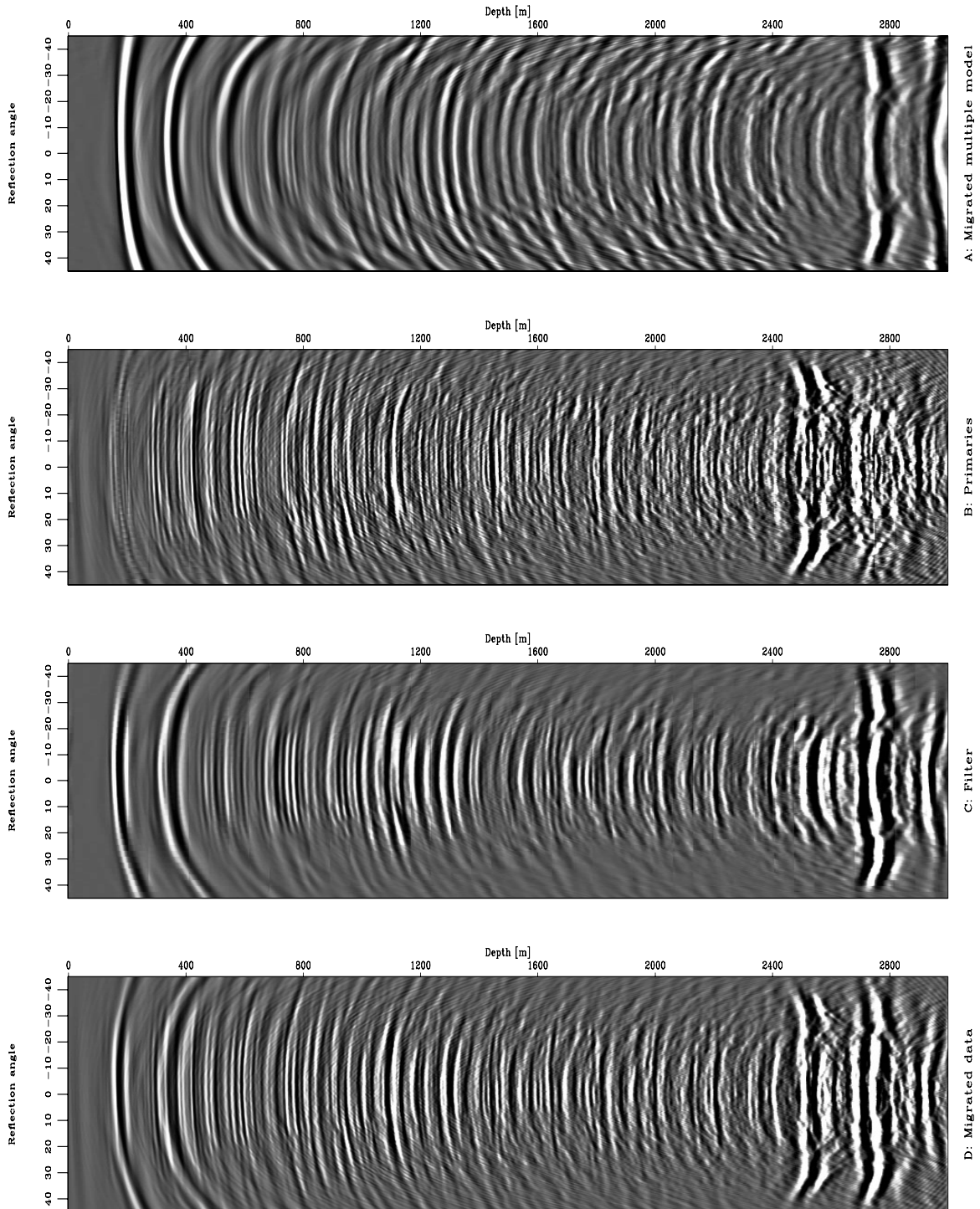


Figure 4: Image space multiple removal. From top to bottom: A) Migrated multiple model; B) Primaries; C) Filter; D) Migrated data. [daniel3-ispace_4panel](#) [CR]

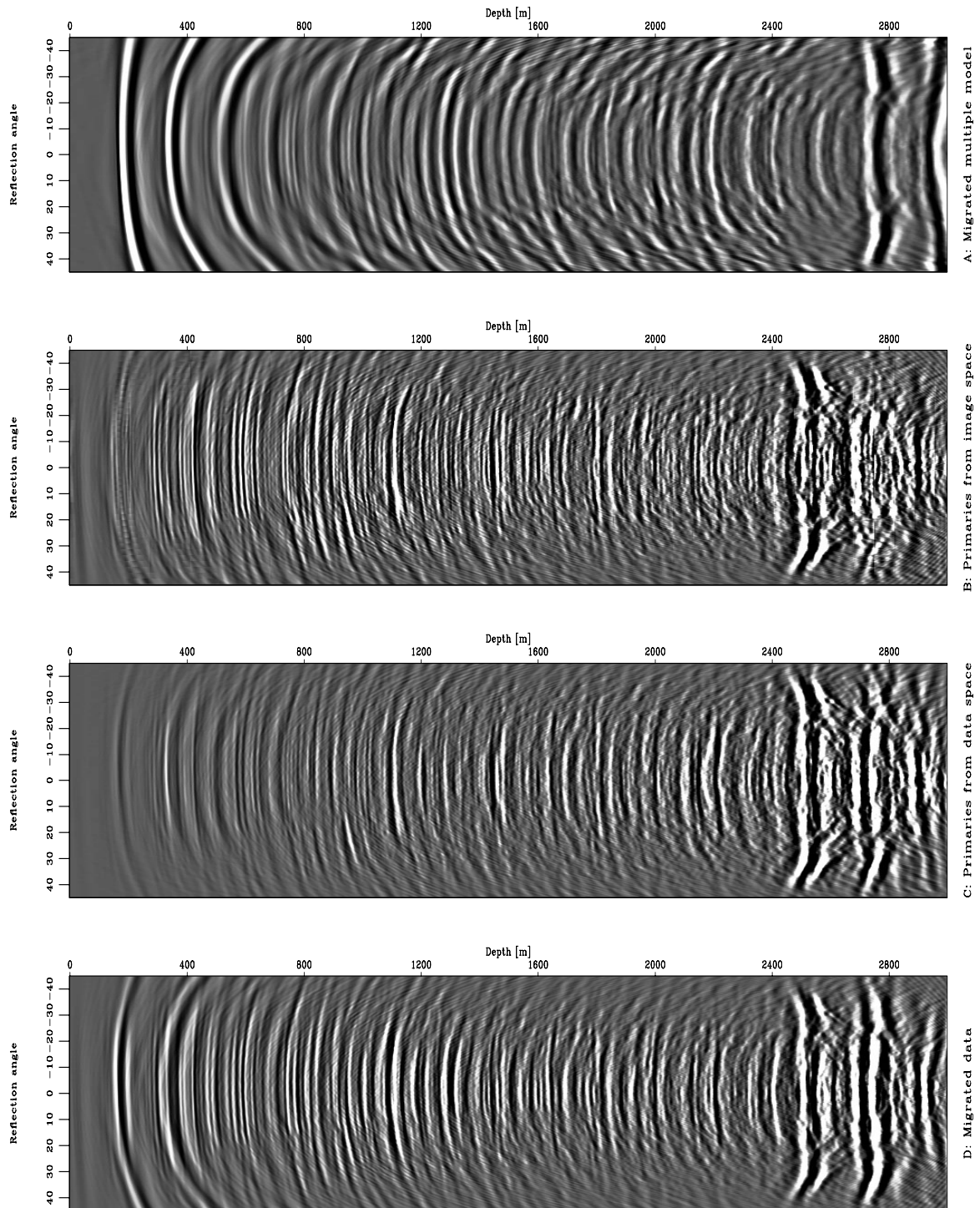


Figure 5: Comparison between multiple removal in the data space versus the image space. From top to bottom: A) Migrated multiple model; B) Primaries from the data space; C) Primaries from the image space; D) Migrated data. `daniel3-ispace_dspace` [CR]

moveouts that do not allow for a separation and elimination.

The shallow multiples are better eliminated in the image space. Since there is a very small coverage in offset for these multiples, when transformed to the image space and mapped into angle-domain common-image gathers, there is a wider distribution along the angle axis in the image space compared with the offset axis in the data space; therefore, subtraction performs better in the image space than in the data space.

For deeper multiples, although we were able to do a good job in the data space, there is still some energy remaining. The coherent noise is strong enough to produce an event in the image space that might interfere with future processing, such as, migration velocity analysis. Although, more detailed work can always be done in the data space to remove the multiples more carefully, the final stage and result are going to be in the image space. If we see coherent noise in the image space, we will be obligated to go back to the data space and re-process the data.

This re-processing is not needed if we do all our processing in the image space. The image space is where we want our final result to be coherent and interpretable. Furthermore, it is ideal for performing target-oriented processing and/or analysis, as, for example, focusing on an specific event or area to improve the image, like velocity or illumination problems.

REFERENCES

- Berkhout, A. J., and Verschuur, D. J., 1997, Estimation of multiple scattering by iterative inversion, part I: Theoretical considerations: *Geophysics*, **62**, no. 05, 1586–1595.
- Claerbout, J., 1998, Multidimensional recursive filters via a helix: *Geophysics*, **63**, no. 05, 1532–1541.
- Crawley, S., 2000, Seismic trace interpolation with nonstationary prediction-error filters: **SEP-104**.
- Dragoset, W. H., and Jericevic, Z., 1998, Some remarks on surface multiple attenuation: *Geophysics*, **63**, no. 02s, 772–789.
- Guitton, A., and Verschuur, E., 2002, Adaptive subtraction of multiples with the ℓ^1 -norm: **SEP-111**, 157–171.
- Guitton, A., Brown, M., Rickett, J., and Clapp, R., 2001, A pattern-based technique for ground-roll and multiple attenuation: **SEP-108**, 249–274.
- Guitton, A., 2004, Multidimensional multiple attenuation in complex geology: illustration on the Sigsbee2B dataset: **SEP-115**, 109–126.
- Herrenschmidt, A., Granger, P., Audebert, F., Gereaa, C., Etienne, G., Stopin, A., Alerini, M., Lebegat, S., and Boelle, J., 2001, Comparison of different strategies for velocity model building and imaging of PP and PS real data: *The Leading Edge*, **20**, no. 09, 984–995.

- Kostov, C., and Nichols, D., 1995, Moveout-discriminating adaptive subtraction of multiples: Soc. of Expl. Geophys., 65th Ann. Internat. Mtg, 1464–1467.
- Lumley, D. E., Nichols, D., and Rekdal, T., 1995, Amplitude-preserved multiple suppression: Soc. of Expl. Geophys., 65th Ann. Internat. Mtg, 1460–1463.
- Rickett, J., Guitton, A., and Gratwick, D., 2001, Adaptive Multiple Subtraction with Non-Stationary Helical Shaping Filters: Eur. Assn. Geosci. Eng., 63rd Mtg., Session: P167.
- Robinson, E. A., and Treitel, S., 1980, Geophysical signal analysis: Prentice-Hall, Inc.
- Rosales, D. A., and Guitton, A., 2004, Ocean-bottom hydrophone and geophone coupling: SEP-**115**, 57–70.
- Sava, P., and Guitton, A., 2003, Multiple attenuation in the image space: SEP-**113**, 31–44.
- Spitz, S., 1999, Pattern recognition, spatial predictability, and subtraction of multiple events: The Leading Edge, **18**, no. 1, 55–58.
- Verschuur, D. J., and Berkhout, A. J., 1997, Estimation of multiple scattering by iterative inversion, part II: Practical aspects and examples: Geophysics, **62**, no. 05, 1596–1611.
- Verschuur, D. J., Berkhout, A. J., and Wapenaar, C. P. A., 1992, Adaptive surface-related multiple elimination: Geophysics, **57**, no. 09, 1166–1177.
- Wang, Y., and Levin, S. A., 1994, An investigation into eliminating surface multiples: SEP-**80**, 589–602.

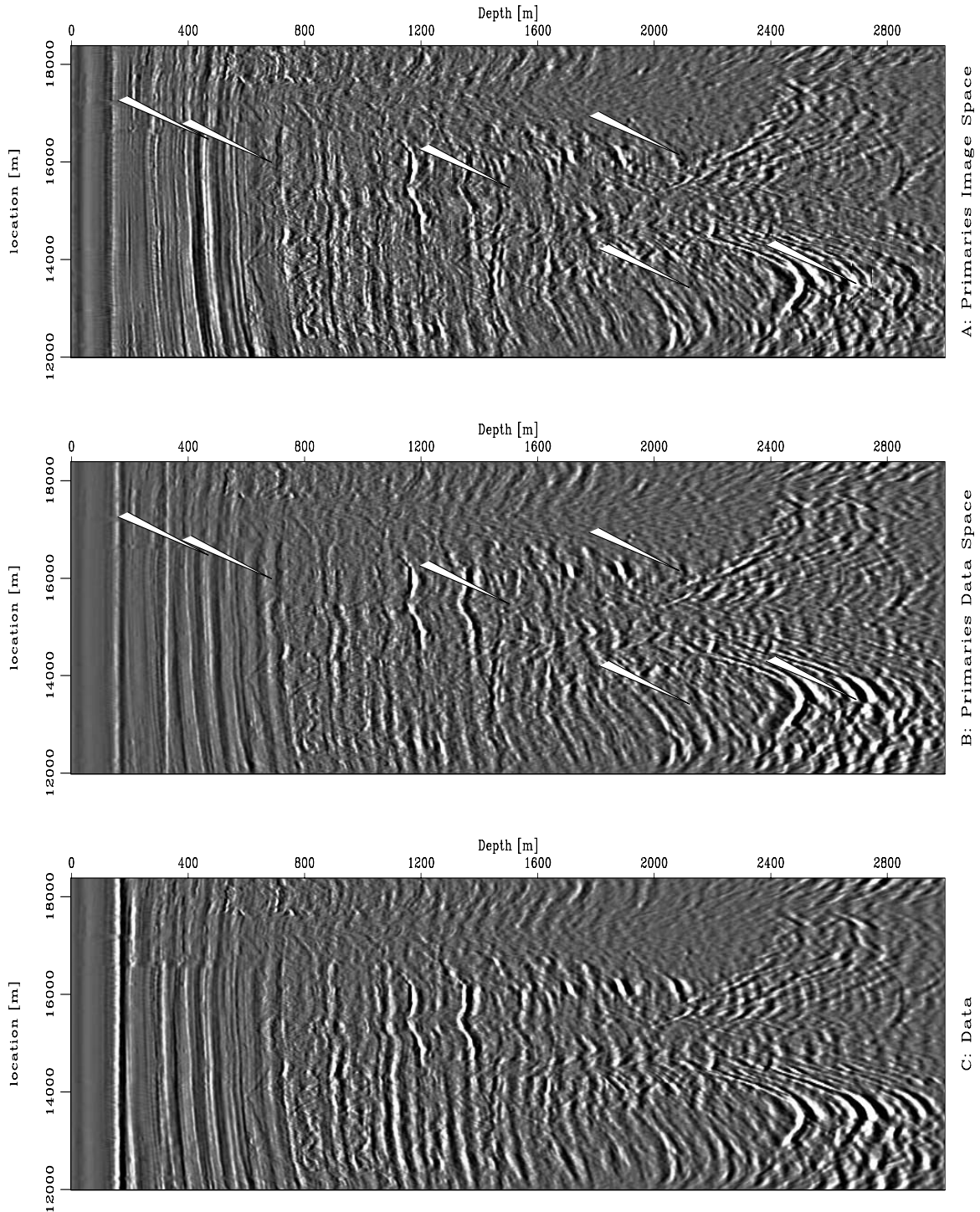
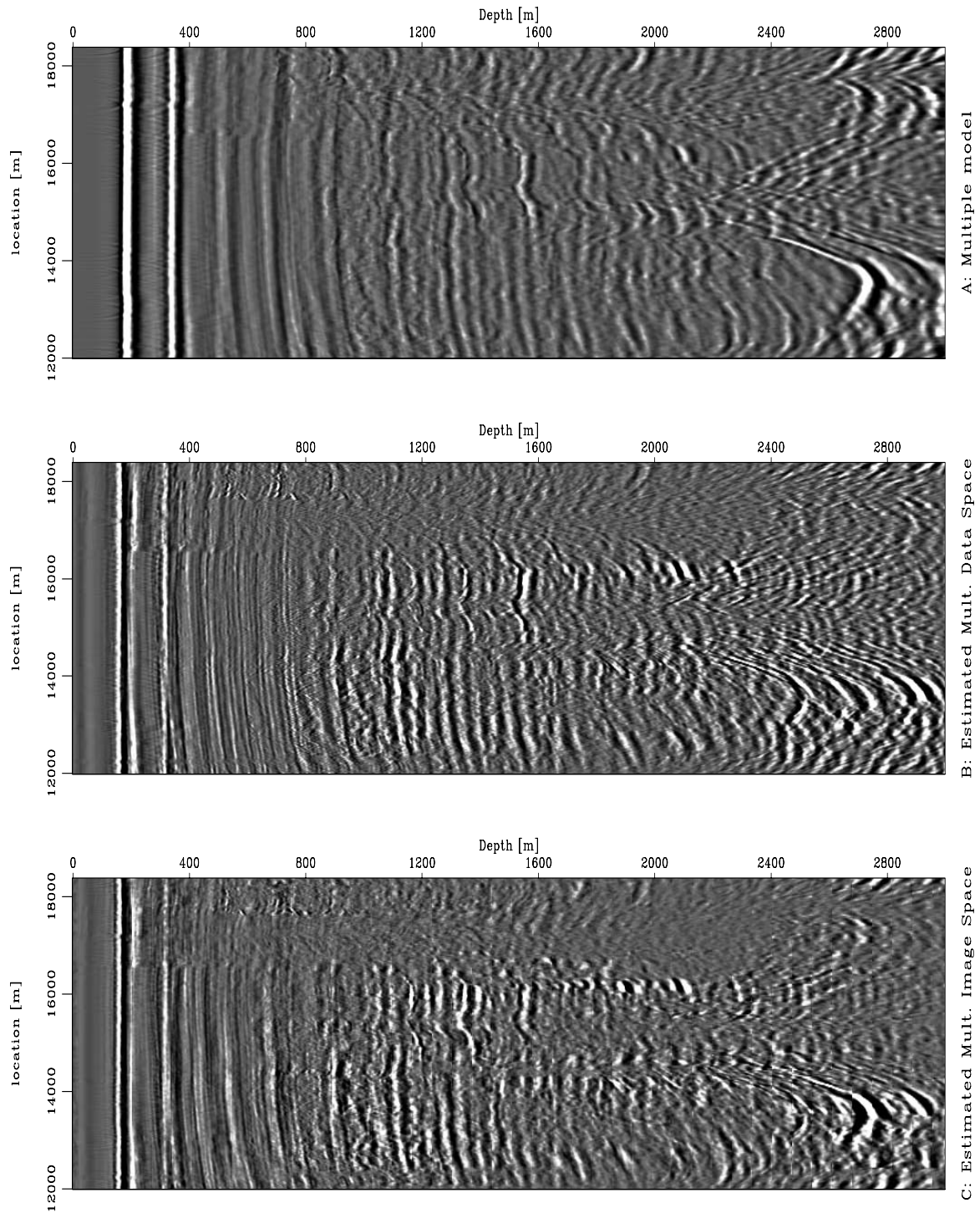


Figure 6: Comparison between multiple removal in the data space versus the image space. From top to bottom: A) Migrated stack of primaries from the image space processing; B) Migrated stack of the primaries from the data space processing; and C) Migrated stack of the entire data set. [daniel3-is_ds_stack](#) [CR]



Short Note

Sparse radon transforms with a bound-constrained approach

Antoine Guitton¹

INTRODUCTION

Radon transforms are popular operators for velocity analysis (Taner and Koehler, 1969; Guitton and Symes, 2003), noise attenuation (Foster and Mosher, 1992), and data interpolation (Hindriks and Duijndam, 1998; Trad et al., 2002). One property that is often sought in radon domains is sparseness, where the energy in the model space is well focused for each corresponding event in the data space. Sparseness is especially useful for multiple attenuation and interpolation. In practice, depending on the radon transform, sparseness can be achieved either in the Fourier (Herrmann et al., 2000) or time domain (Sacchi and Ulrych, 1995). To estimate sparse radon panels in the time domain, a regularization operator that enforces long-tailed probability density functions for the model parameters is often used. This regularization operator can be the ℓ^1 norm (Nichols, 1994) or the Cauchy norm (Sacchi and Ulrych, 1995).

In this paper, a new time-domain method is presented that yields sparse radon panels. This method estimates a sparse model by adding two models estimated independently with only positive or negative values obtained with a bound-constrained optimization technique. Therefore, by forcing the model to fall within a certain range of values, the null space and its effects are decreased.

In the section following this introduction, I introduce the problem of finding a bound-constrained model and its resolution by presenting the limited memory L-BFGS-B technique (Zhu et al., 1997). This method aims at finding a solution with simple bounds for linear or non-linear problems. Then, I introduce a method that estimates sparse radon domains. Finally, this technique is tested on a synthetic and field data examples and compared to the Cauchy regularization (Sacchi and Ulrych, 1995). They demonstrate that the proposed strategy yields sparse radon panels comparable to the Cauchy approach. One advantage of this new strategy is that the choice of parameters is much simpler; for instance, no Lagrange multiplier is needed. One drawback is that two inversions need to be carried out as opposed to one for the Cauchy method.

¹email: antoine@sep.stanford.edu

FINDING A MODEL WITH SIMPLE BOUNDS

In this section, I present the problem of finding simple bounds and the method that solves it.

The goal of bound-constrained optimization is to find a vector of model parameters \mathbf{m} such that we minimize

$$\min f(\mathbf{m}) \text{ subject to } \mathbf{m} \in \Omega, \quad (1)$$

where

$$\mathbf{m} \in \Omega = \{\mathbf{m} \in \mathfrak{R}^N \mid l_i \leq m_i \leq u_i\}, \quad (2)$$

with l_i and u_i being the lower and upper bounds for the model m_i , respectively. In this case, l_i and u_i are called simple bounds. They can be different for each point of the model space. The model vector that obeys equation (1) is called \mathbf{m}^* .

The sets of indices i for which the i th constraint are active/inactive are called the active/inactive sets $A(m)/I(m)$. Most of the algorithms used to solve bound constrained problems first identify $A(m)$ and then solve the minimization problem for the free variables of $I(m)$.

The L-BFGS-B algorithm

The L-BFGS-B algorithm is an extension of the quasi-Newton L-BFGS algorithm (Guitton and Symes, 2003) that yields a model constrained by simple bounds (Zhu et al., 1997). The L-BFGS algorithm is a very efficient algorithm for solving large scale problems. L-BFGS-B borrows ideas from trust region techniques while keeping the L-BFGS update of the Hessian and line search algorithms.

The L-BFGS-B algorithm is affordable for very large problems. The memory requirement is roughly $(12 + 2m)N$ where m is the number of BFGS updates kept in memory and N the size of the model space. In practice, $m = 5$ is a typical choice. Per iteration, the number of multiplications range from $4mN + N$ when no constraints are applied to m^2N when all variables are bounded. The program offers the freedom to have different bounds for different points of the model space. In addition, some points can be constrained while others are not.

There are three different stopping criteria for the L-BFGS-B algorithm. First the program stops when the maximum number of iterations is reached. Or, the program stops when the decrease of the objective function becomes small enough. Or, the program stops when the norm of the projected gradient (in a ℓ^∞ sense) is small enough.

Tests indicate that the L-BGFS-B algorithm ran in single precision with no constraints is not quite twice as slow as a conjugate gradient solver per iteration. This result is quite remarkable when considering that L-BFGS-B works for any type of non-linear (or linear) problem with line searches. In addition, the number of iterations needed to convergence is almost identical for both L-BFGS-B and the conjugate gradient solver. In the next section, I present a method to estimate sparse radon transforms.

ESTIMATING SPARSE RADON DOMAINS

Given a CMP gather \mathbf{d} and a radon transform operator \mathbf{L} , we want to minimize the least-squares objective function

$$f(\mathbf{m}) = \|\mathbf{Lm} - \mathbf{d}\|^2, \quad (3)$$

where \mathbf{m} is the unknown radon domain. The main idea of this paper is to decompose \mathbf{m} into its positive and negative parts by imposing simple bounds on \mathbf{m} with the L-BFGS-B algorithm. Therefore, the two problems

$$\min f(\mathbf{m}_{(-)}) \text{ subject to } \mathbf{m}_{(-)} \in]-\infty, 0[, \quad (4)$$

and

$$\min f(\mathbf{m}_{(+)}) \text{ subject to } \mathbf{m}_{(+)} \in [0, +\infty[, \quad (5)$$

need to be solved. Note that we could decompose \mathbf{m} into more subdomains as well. It is important to solve both problems of finding $\mathbf{m}_{(-)}$ and $\mathbf{m}_{(+)}$ independently, and not simultaneously as it can be done with linear programming techniques (Claerbout and Muir, 1973). Here, the main idea is to decrease the null space and its effects by constraining the model, similar to what is accomplished with the Cauchy regularization. Once the two models $\mathbf{m}_{(+)}$ and $\mathbf{m}_{(-)}$ are estimated with the L-BFGS-B algorithm, the sparse model is obtained by computing $\mathbf{m}_{\text{sparse}} = \mathbf{m}_{(-)} + \mathbf{m}_{(+)}$. In the following section, I illustrate this technique with a synthetic and real data example using the hyperbolic radon transform.

EXAMPLES

Figure 1a shows a synthetic CMP gather with five hyperbolas. First, the model is constrained to have positive values in Figure 1b. Note that this domain is artifacts free and extremely focused. Second, the model is constrained to have negative values in Figure 1c. Again, the model is very sparse. Finally, the sparse model obtained by adding Figures 1b and 1c is shown in Figure 1d. As expected, this model is very sparse compared to the radon panel obtained without sparseness constraints in Figure 1e. Now, this method is tested on one CMP gather from a marine dataset in the Gulf of Mexico. Here, the proposed method is also compared with the sparse result with the Cauchy regularization (Sacchi and Ulrych, 1995). Figure 2a shows the input data. The sparse models obtained by adding the bounded models and by using the Cauchy regularization are shown in Figures 2d and 2e, respectively. Both results are almost identical, with the new technique yielding a better panel. The residual, i.e., the difference between the input data and the remodeled data, is also very similar in both cases (Figures 2b and 2c).

CONCLUSION

A new method to estimate sparse radon panels has been presented. This method is based on (1) the decomposition of the model space into positive and negative values with a bound-

constrained optimization technique, and (2) the summation of the two estimated models. This decomposition has the property of reducing the null space and its effects. As illustrated with synthetic and field data examples, this method yields sparse radon panels and compares favorably with the Cauchy regularization technique. Compared to the Cauchy regularization, the proposed method is simpler to parametrize where, for instance, no Lagrange multiplier is estimated. However, more iterations are needed for the bound-constrained approach because two models are estimated independently.

ACKNOWLEDGMENTS

I would like to thank Westerngeco for providing the field data example.

REFERENCES

- Claerbout, J. F., and Muir, F., 1973, Robust modeling with erratic data: *Geophysics*, **38**, no. 05, 826–844.
- Foster, D. J., and Mosher, C. C., 1992, Suppression of multiple reflections using the Radon transform: *Geophysics*, **57**, no. 03, 386–395.
- Guitton, A., and Symes, W., 2003, Robust inversion of seismic data using the Huber norm: *Geophysics*, **68**, no. 4, 1310–1319.
- Herrmann, P., Mojesky, T., Magesan, M., and Hugonnet, P., 2000, De-aliased, high-resolution Radon transforms: *Soc. of Expl. Geophys., 70th Ann. Internat. Mtg*, 1953–1956.
- Hindriks, C. O. H., and Duijndam, A. J. W., 1998, Radon domain reconstruction of 3-D irregularly sampled VSP data: *Soc. of Expl. Geophys., 68th Ann. Internat. Mtg*, 2003–2006.
- Nichols, D., 1994, Velocity-stack inversion using L_p norms: *SEP-82*, 1–16.
- Sacchi, M. D., and Ulrych, T. J., 1995, High-resolution velocity gathers and offset space reconstruction: *Geophysics*, **60**, no. 04, 1169–1177.
- Taner, M. T., and Koehler, F., 1969, Velocity spectra - Digital computer derivation and applications of velocity functions: *Geophysics*, **34**, no. 06, 859–881.
- Trad, D., Ulrych, T. J., and Sacchi, M. D., 2002, Accurate interpolation with high-resolution time-variant Radon transforms: *Geophysics*, **67**, no. 2, 644–656.
- Zhu, H., Byrd, R. H., and Nocedal, J., 1997, Algorithm 778: L-BFGS-B, FORTRAN routines for large scale bound constrained optimization: *ACM Transactions on Mathematical Software*, **23**, 550–560.

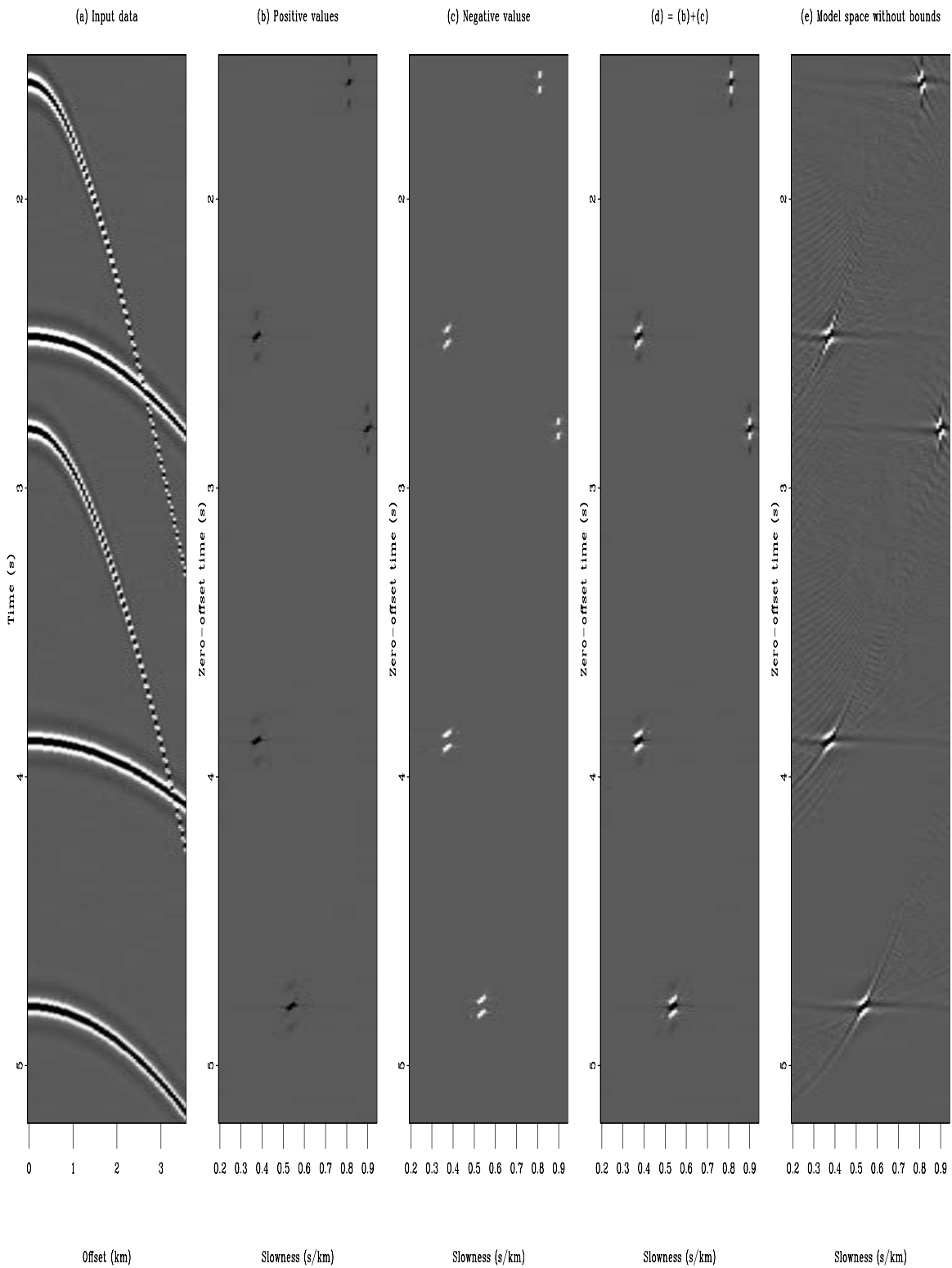


Figure 1: (a) Input data. Estimated model for (b) positive values and (c) negative values only. (d) Estimated sparse domain (b)+(c). (e) Estimated model without sparseness constraints.

antoine2-plusminus-nospike-HUBER [ER]

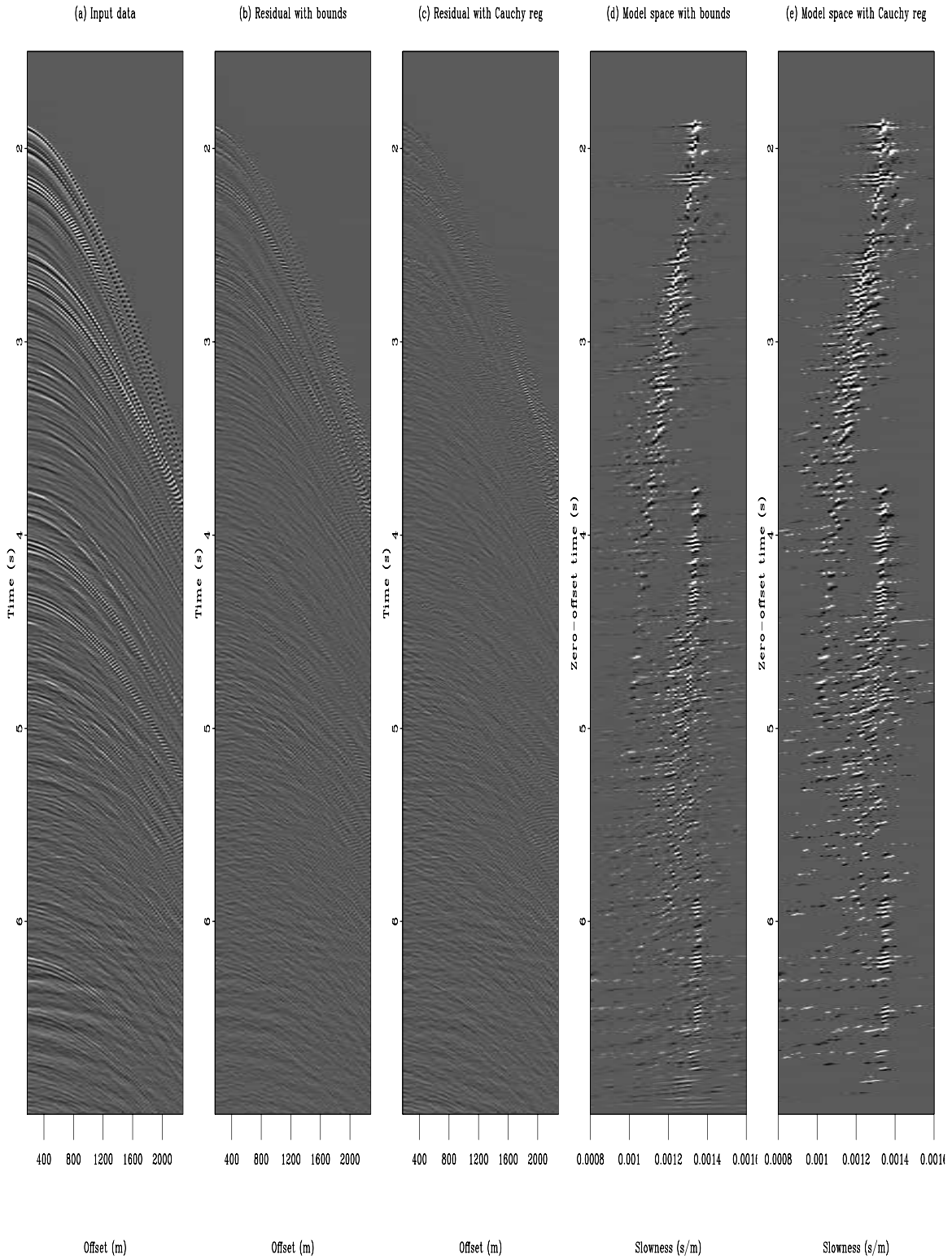


Figure 2: (a) Input CMP gather from a marine data experiment. Residual panels for the sparse model estimated with (b) the bounded models and (c) the Cauchy regularization. Sparse models estimated with (d) the bounded models and (e) the Cauchy regularization. `antoine2-cauchyres-gm2-HUBER` [ER]

Removal of linear events with combined radon transforms

Brad Artman and Antoine Guitton¹

ABSTRACT

We explore the classic signal and noise separation problem of removing linear events from shot-gathers through several inversion schemes using a combined modeling operator composed of both hyperbolic and linear radon transforms. Data are inverted simultaneously for both linear and hyperbolic moveout which provides two model-space outputs. These are forward modeled separately to provide an output data-space devoid of one of the model-space components. We employ this approach to analyze the removal of direct arrivals and ground-roll from shot-gathers. Inversion schemes used include: 1) bound-constrained, 2) Cauchy norm regularization, 3) Huber norm approximating the l_1 norm, and 4) the l_2 norm using linear least-squares. Synthetic tests and four field shot-gathers are used to demonstrate the approach. Methods 1, 2, and 3 are designed to provide sparse model-space inversions. In the real data examples, the least-squares solution is able to better achieve the signal to noise separation goal despite its model-space being often less appealing.

INTRODUCTION

Chen et al. (1999) introduces the idea that inversion problems solved with a sparseness constraint on the output model-space can be applied to data sets with an over-complete modeling operator. Over-complete means that the dictionary of transform kernels has (many) more terms than a strict basis transformation such as the standard DFT. For example, this could be realized by using several different modeling operators or even a over-sampled version of a single operator such as a Fourier transform with several times more frequency resolution than the compact support definition of DFT theory. Further, in Donoho and Huo (1999) the mathematics are presented to prove that the combined suite of model space kernels are orthogonal to each other if the inversion satisfies several requirements. Their goal is super-resolution during the analysis of a signal. These investigations are presented within the framework of inversion through linear programming techniques. Further, the papers imply that these desirable properties are realized with the use of an inversion methodology using a l^1 norm on the model-space. Artman and Sacchi (2003) made preliminary efforts to investigate these properties, but were stalled due to the instability and expense, when applied to the much larger and more complicated data domains of seismic data, of the linear programming technique. Trad et al. (2003) present results of such a combined operator inversion scheme using the Cauchy regularization.

¹email: brad@sep.stanford.edu, antoine@sep.stanford.edu

Guitton (2004) explores the novel result that two bound-constrained inversions (bounded by zero from below and above) contain orthogonal null-spaces. Therefore, summing the results of two such inversions can significantly enhance the sparseness of the model space compared to that produced by an inversion which is free to output both positive and negative values for the inverted model. The cost for this improvement is an extra inversion of identical size and cost. This characteristic is shared with the linear programming techniques used for the super-resolution problem, though the inversion algorithm is the L-BFGS.

We will compare the inverted models from several inversion schemes, and their concomitant data-space realizations. Inversion schemes that will be analyzed are: 1) bound-constrained (BC), 2) Cauchy norm regularization (Cauchy), 3) Huber norm approximating the l_1 norm (l_1), and 4) the l_2 norm using linear least-squares (l_2). The combined operator of Hyperbolic and Linear Radon Transforms will be used in all the inversion schemes on both synthetic data and three field shot gathers.

THEORY

The addition of a second simultaneous linear operator expands the usual linear inversion equations to the slightly more complicated linear operator (Claerbout, 1999),

$$\mathbf{L} = [\mathbf{L}_1 \ \mathbf{L}_2]$$

and a correspondingly longer model vector

$$\mathbf{m} = \begin{bmatrix} \mathbf{m}_1 \\ \mathbf{m}_2 \end{bmatrix}.$$

This simple introduction leads to the form of the inversion goals used here

$$[\mathbf{L}_h \mathbf{L}_l] \begin{bmatrix} \mathbf{m}_h \\ \mathbf{m}_l \end{bmatrix} = \mathbf{d} \quad (1)$$

$$\epsilon^2 \mathbf{I} \begin{bmatrix} \mathbf{m}_h \\ \mathbf{m}_l \end{bmatrix} = 0, \quad (2)$$

where subscripts h and l refer to the hyperbolic (HRT) and linear (LRT) radon transforms and we add identity operator regularization to provide damping.

SYNTHETIC EXAMPLES

The first concern when solving inversion problems with over-complete dictionaries is the potential for introduction of cross-talk (Claerbout, 1992) into the model-space. A synthetic data set was created to test the method to assure that this technique does not allow this to happen. Figure 1 shows the inverted models produced with the various methods compared to the least-squares solution. The first panel is a bandlimited model from which data were forward modeled, and the last four panels show the models produced by the various inversion procedures.

While the first two inversion schemes produce very sparse model-spaces with no cross-talk, the l_1 and l_2 products contain the familiar parabolas in the LRT domain due to data-space hyperbolas and ellipses in the HRT domain from the linear events in the data.

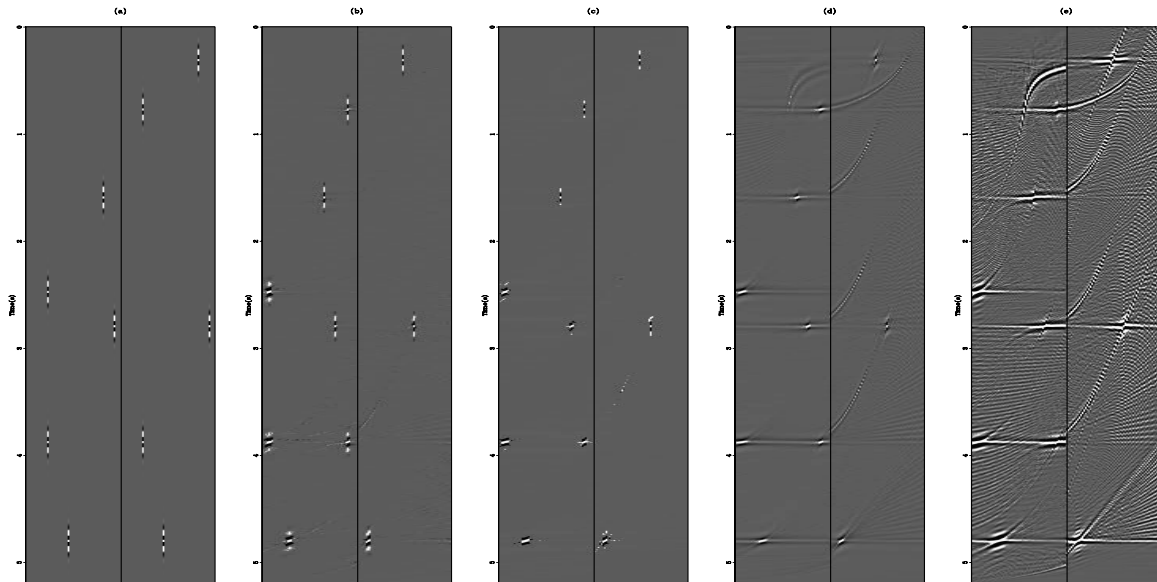


Figure 1: Synthetic model-space examples. The model-space contains both radon domains. Thus, half way across the slowness axis the plot changes from representing energy in the hyperbolic radon domain to events in the linear radon domain. The origin and sampling interval for both domains are the same in this example. Panel (a) is the band-limited model. Panel (b) shows the BC inversion result. Panel (c) shows the Cauchy result. Panel (d) shows the l_1 result. Panel (e) shows the l_2 result. `brad2-syn1` [CR]

The models produced by all the results are very good. The clip level is deliberately set very low to bring out artifacts. While the first two methods produce very sparse results, the l_1 and l_2 results contain sweeping artifacts and readily identifiable cross-talk between the two model domains.

Figure 2 shows the forward modeled data from the models produced from the various inversion techniques. The first panel is the starting data. Once again, the clip level has been set quite low to bring out the artifacts of the latter inversion schemes. Amazingly, the two sparse inversion schemes, especially the Cauchy inversion in panel (c), were able to remove much of the 0.000001 variance noise added to the data. A small amount of corrilary chatter can be seen in the Cauchy, l_1 , and l_2 data domains linear.

The inversion schemes designed for sparse model domains have produced models with no cross-talk between the two operators. The l_1 and l_2 inversions have allowed the transmission of energy between the two domains. However, the forward modeled data from all the methods show more than adequate results with only minor noise introduced in the immediate vicinity of the various events. Importantly, even the very steeply dipping events are well modeled despite being severely aliased. It should be noted however, that the first two schemes will not produce

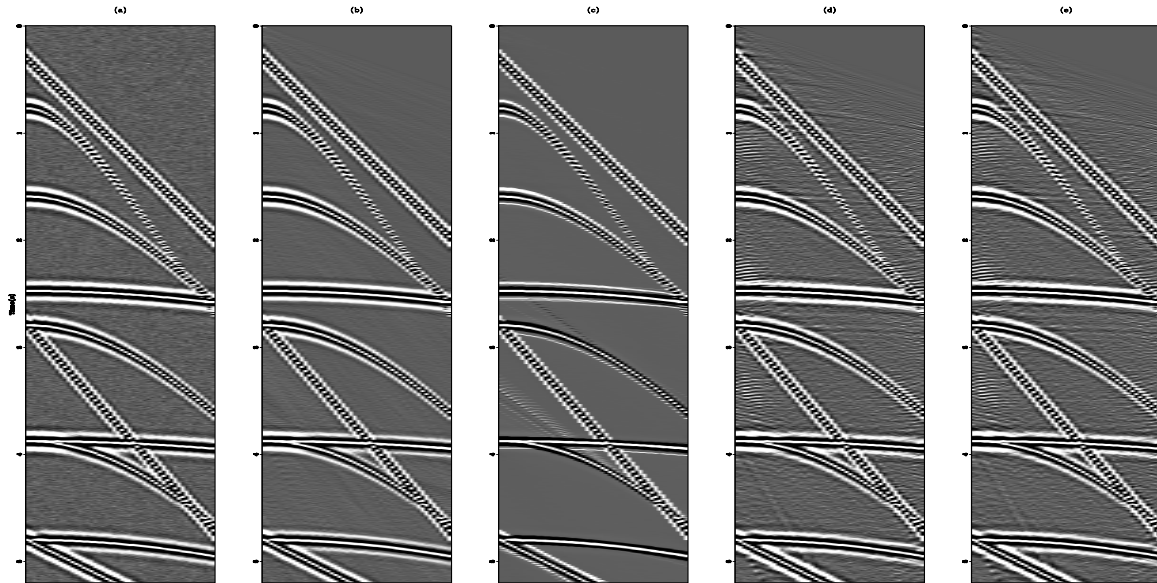


Figure 2: Forward modeled data from the inversion results presented in Figure 1. Panel (a) is the band-limited model. Panel (b) shows the BC inversion result. Panel (c) shows the Cauchy result. Panel (d) shows the l_1 result. Panel (e) shows the l_2 result. `brad2-syn2` [CR]

satisfactory data-space results given realistic split-spread gathers. Their short-comings are from linear events that do not continue completely across the entire data domain. The sparse model domains do not have sufficient freedom to add fictitious model energy to cancel events that do not exactly emanate from the origin of the shot (*ie.* exit the gather at $t = 0, x = 0$). Throughout this effort, only off-end gathers will be used.

NOISE SEPARATION IN FIELD DATA

Four shot-gathers are used to explore the efficacy of this method to remove linear events from shot-gathers. The paradigm is that linear events due to direct arrivals and ground-roll are noise and hyperbolic events due to subsurface reflectors should be maintained. The simple approach is to forward model only the linear model-space which can will then be directly subtracted from the data.

Figure 3 shows the data examples that will be used. They are shots 08, 14 and 25 from the Yilmaz shot-gathers. The three examples contain a nice compilation of common land data artifacts to be attacked through the removal of linear events. Direct arrivals, refractions, and ground-roll are all experienced to some degree both at early time and obscuring primaries late in the sections. A strong linear wavetrain dominates the early time of shot 08, Panel (a). Shot 14, Panel (b), has faint linear events at late time and several slopes at early time. The non-hyperbolic moveout at 5.2 seconds is a nice marker for judging the quality of the various inversion schemes. The obvious ground-roll in shot 25, Panel (c), is the main goal to eliminate.

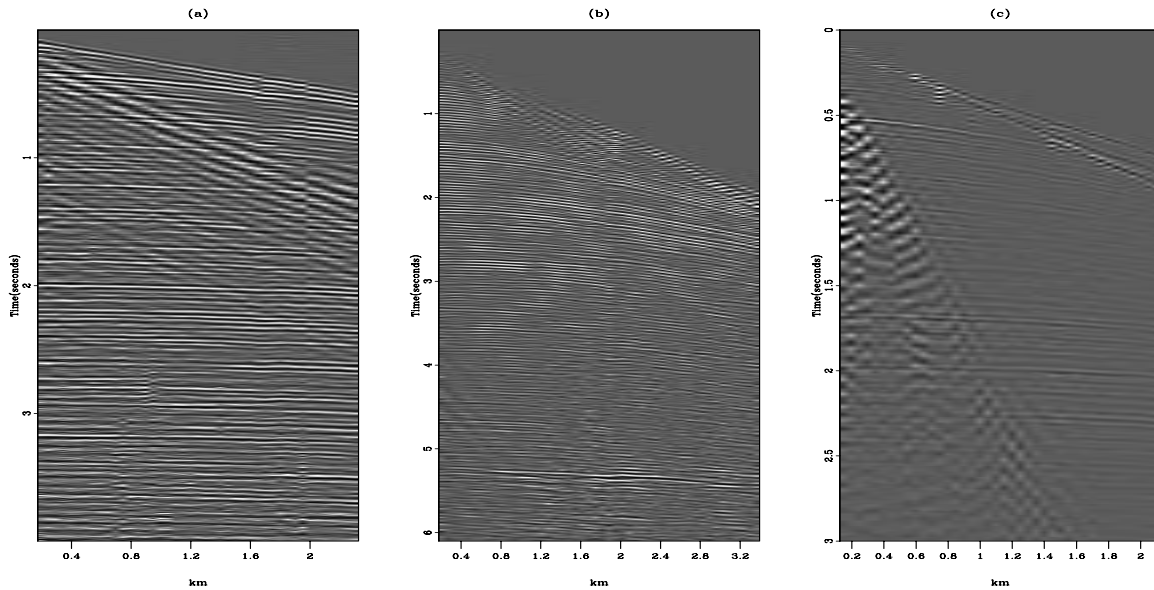


Figure 3: Shots from the Yilmaz data collection. Panel (a) is shot 08, Panel (b) is shot 14, Panel (c) is shot 25. `brad2-d` [ER]

Radon domain

Figure 4 through 6 contain the inverted model domains associated with the four techniques explored herein. Clearly the sparsity of the results decrease toward the right. Direct interpretation of the model domain would be easier and more accurate with the BC, Cauchy, and l_1 results. Distinct trains of energy in the hyperbolic and linear domains are visible. Without the clip set so low, the l_2 result is not as bad as these panels make it seem. A distinct fairway of energy, marginally larger than that presented in the l_1 result is visible. Velocity analysis of the gathers would likely be more accurate with the results that impose sparsity, especially at late times.

In general the l_1 inversion produced consistently better model space realizations. While the differences are often minor, the method provides consistent, stable, high quality results.

Data residuals

The data-space residuals of the inversion schemes are presented in Figures 7 through 9. The clip level in all cases are the same as the data in Figure 3. The sparse model-spaces produce residual panels less like the original data than the l_2 norm inversion. This results in data residuals often indistinguishable from the original data to the eye for the sparse schemes.

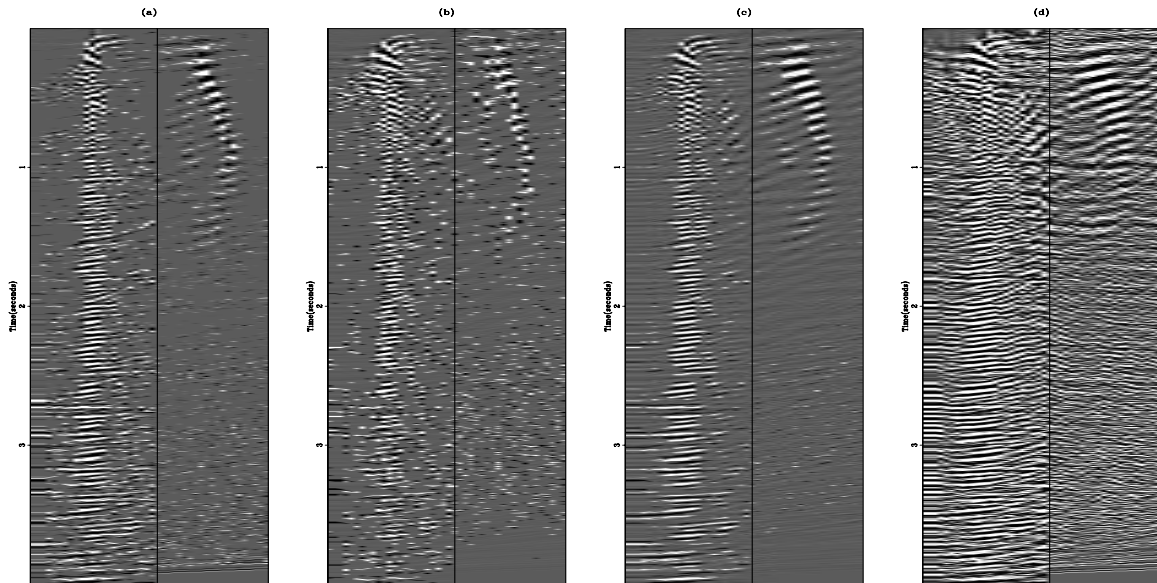


Figure 4: Model-space inversions of shot-gather 08 (Panel (a) from Figure 3). The first half of the panels is HRT space and the second half is LRT space. Panel (a) shows the BC, Panel (b) the Cauchy, Panel (c) the l_1 , and Panel (d) the l_2 inverted model spaces. [brad2-m.08](#) [ER]

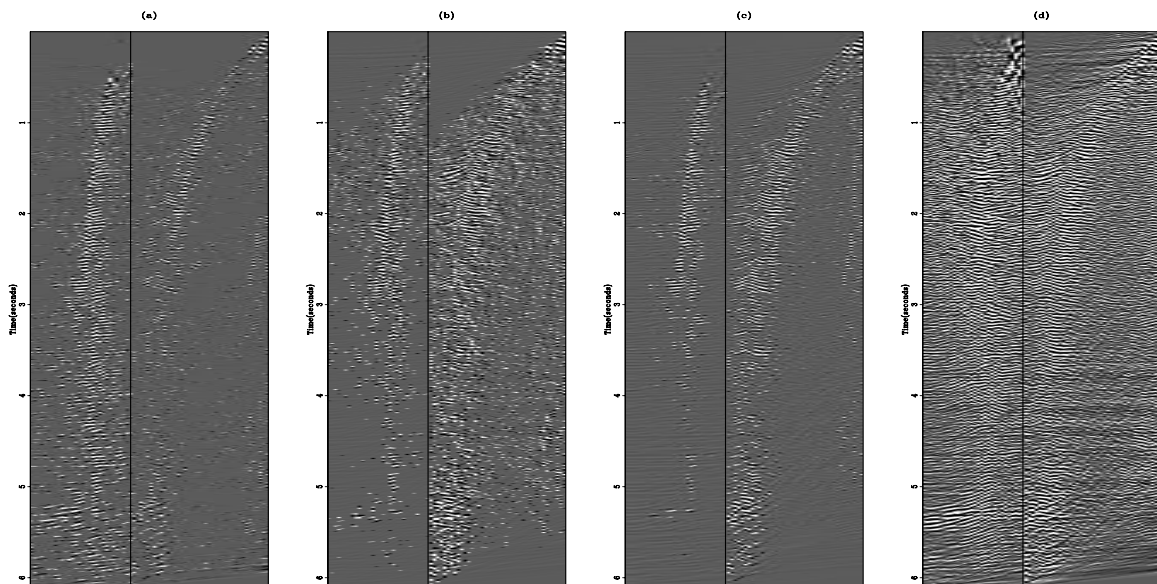


Figure 5: Model-space inversions of shot-gather 14 (Panel (b) from Figure 3). The first half of the panels is HRT space and the second half is LRT space. Panel (a) shows the BC, Panel (b) the Cauchy, Panel (c) the l_1 , and Panel (d) the l_2 inverted model spaces. [brad2-m.14](#) [ER]

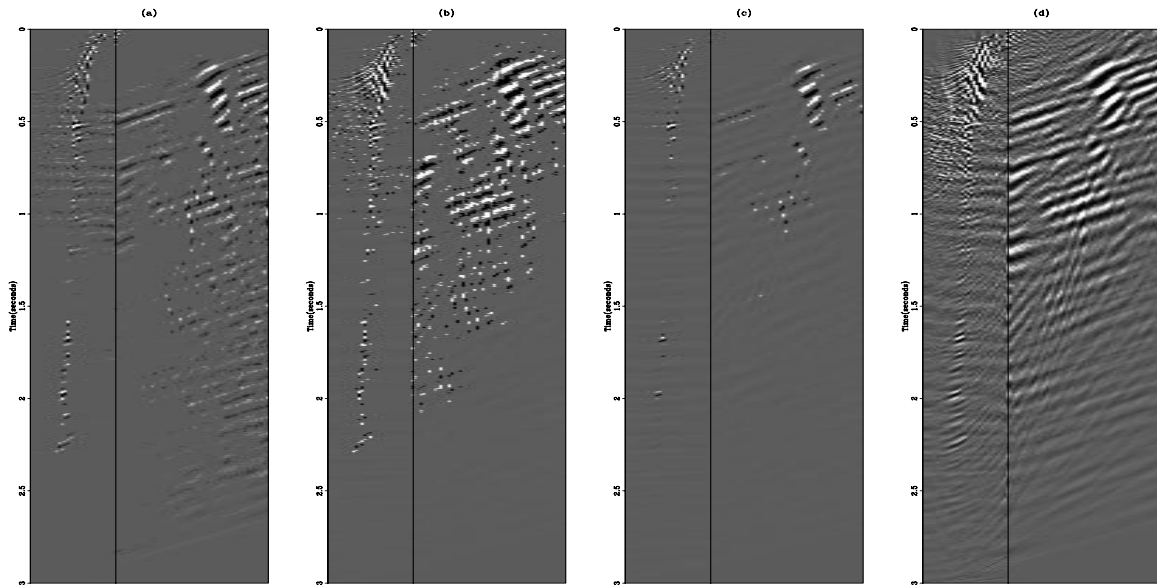


Figure 6: Model-space inversions of shot-gather 25 (Panel (c) from Figure 3). The first half of the panels is HRT space and the second half is LRT space. Panel (a) shows the BC, Panel (b) the Cauchy, Panel (c) the l_1 , and Panel (d) the l_2 inverted model spaces. `brad2-m.25r` [ER]

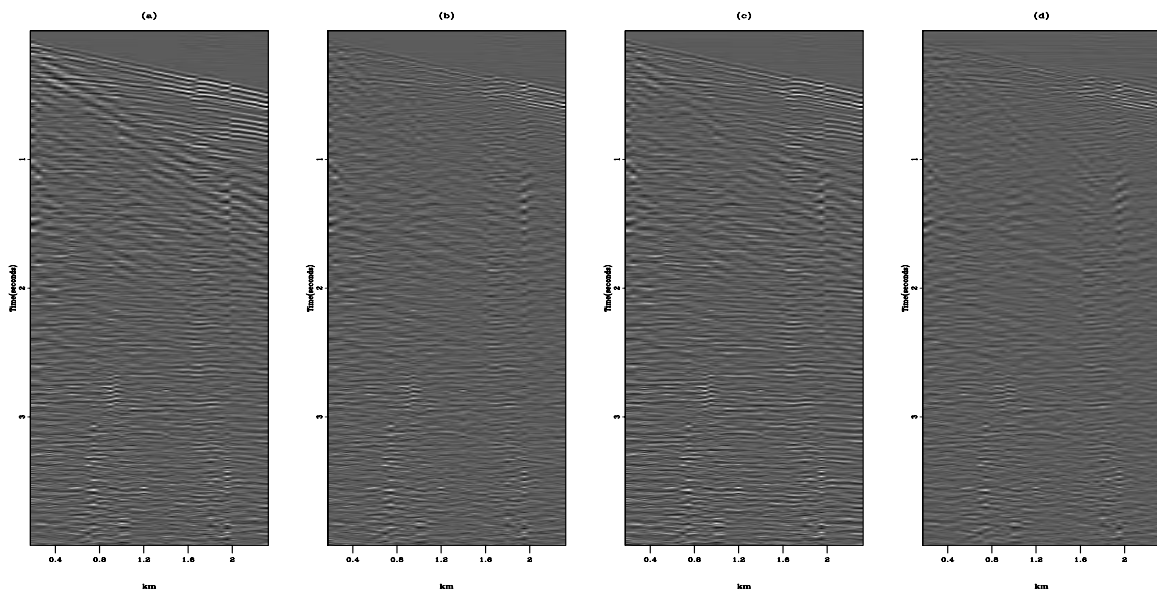


Figure 7: Data-space residuals of shot-gather 08 (Panel (a) from Figure 3). Panel (a) shows the BC, Panel (b) the Cauchy, Panel (c) the l_1 , and Panel (d) the l_2 inversion results. `brad2-r.08` [ER]

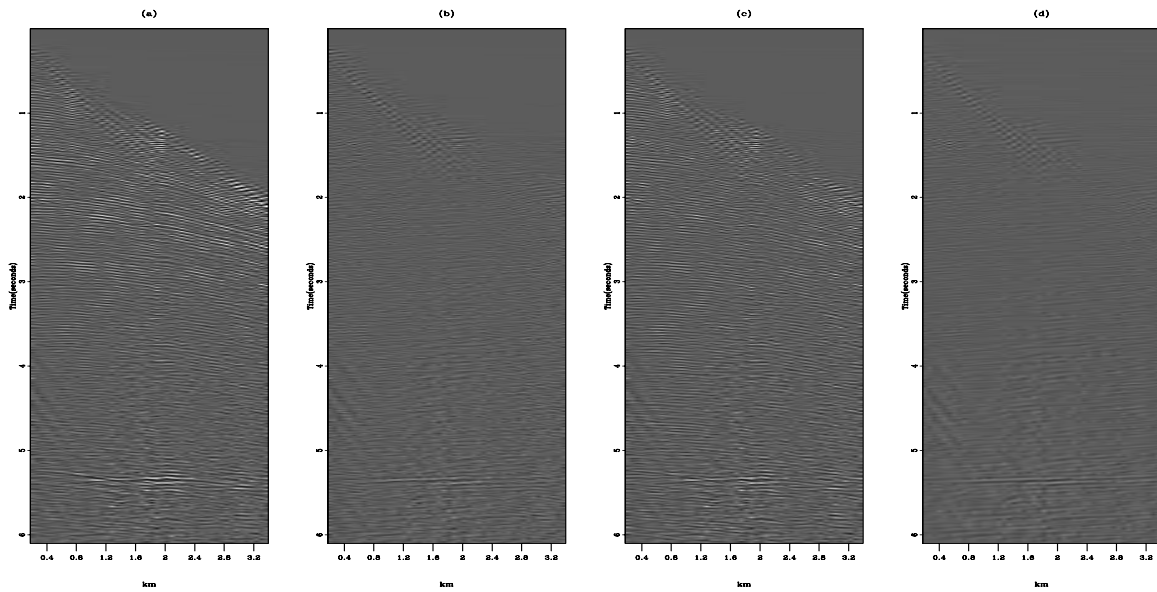


Figure 8: Data-space residuals of shot-gather 08 (Panel (b) from Figure 3). Panel (a) shows the BC, Panel (b) the Cauchy, Panel (c) the l_1 , and Panel (d) the l_2 inversion results. [brad2-r.14](#) [ER]

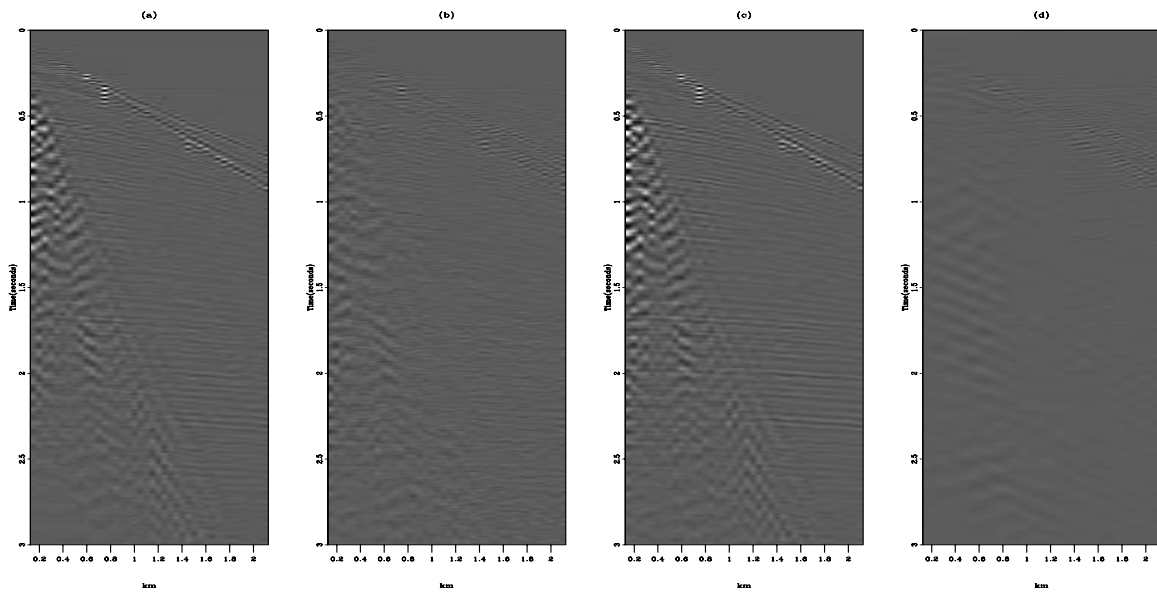


Figure 9: Data-space residuals of shot-gather 08 (Panel (c) from Figure 3). Panel (a) shows the BC, Panel (b) the Cauchy, Panel (c) the l_1 , and Panel (d) the l_2 inversion results. [brad2-r.25r](#) [ER]

Noise subtraction

Figures 10 through 12 show the efficacy of this simple signal to noise subtraction algorithm facilitated by the combined modeling operator inversion scheme presented here. Only the LRT model-space is forward modeled back into the data-space for subtraction from the original data. In every case the least-squares approach produces the best signal enhancement. Gather 14 produces a lot of acausal noise that could be muted, though the direct arrival was the main target for this gather. That being the case, it could also be considered a poor result.

The sparseness oriented schemes produce gathers with little to no improvement in signal-to-noise ratio while altering the amplitude variation, and sometimes kinematics, of the gathers.

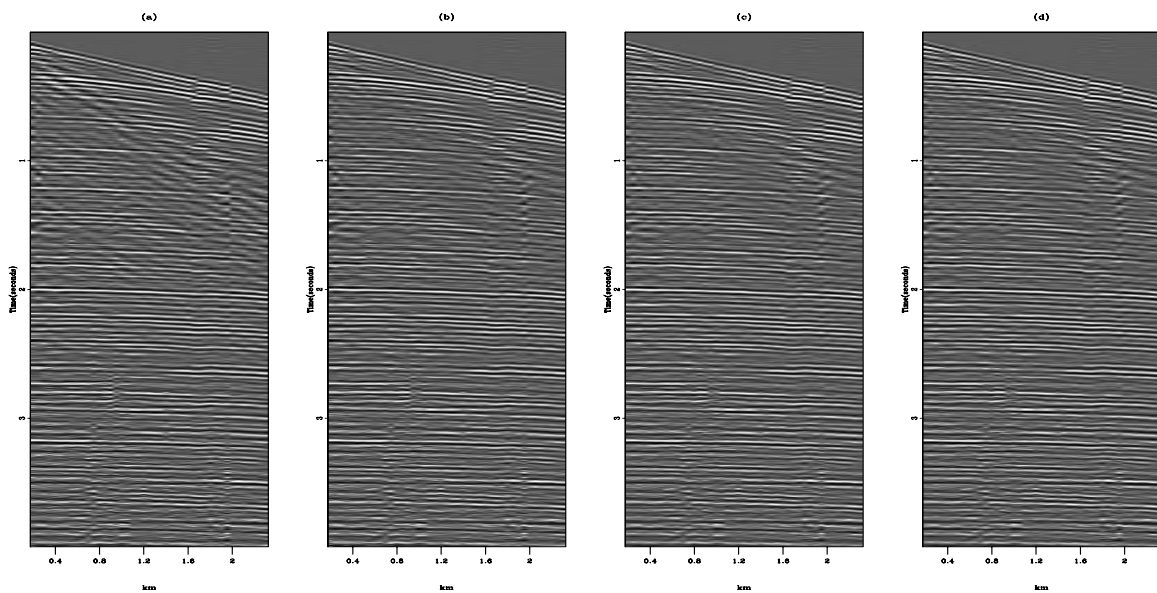


Figure 10: Signal estimate for shot-gather 08 (Panel (a) from Figure 3). Panel (b) shows the BC, Panel (c) the Cauchy, Panel (d) the l_1 , and Panel (e) the l_2 inversion results. brad2-s.08 [ER]

COMMENTS AND CONCLUSIONS

It will be noted that because the ground roll is very aliased and dispersive in these gathers, the linear radon operator has great difficulty describing these events with a single kernel in the model domain. While the least squares inversion will introduce energy into the model-space to combine these events, as well as cancel acausal energy above the direct arrival in the data-space, the sparse inversions are not capable of stopping events that do not cross the entire data-space. For this reason, only one-sided gathers have been used for this analysis.

These techniques are particularly sensitive to noisy, unbalanced traces. For this reason all gathers have been trace-balanced, gained as a function of time, and noisy traces zeroed. Last,

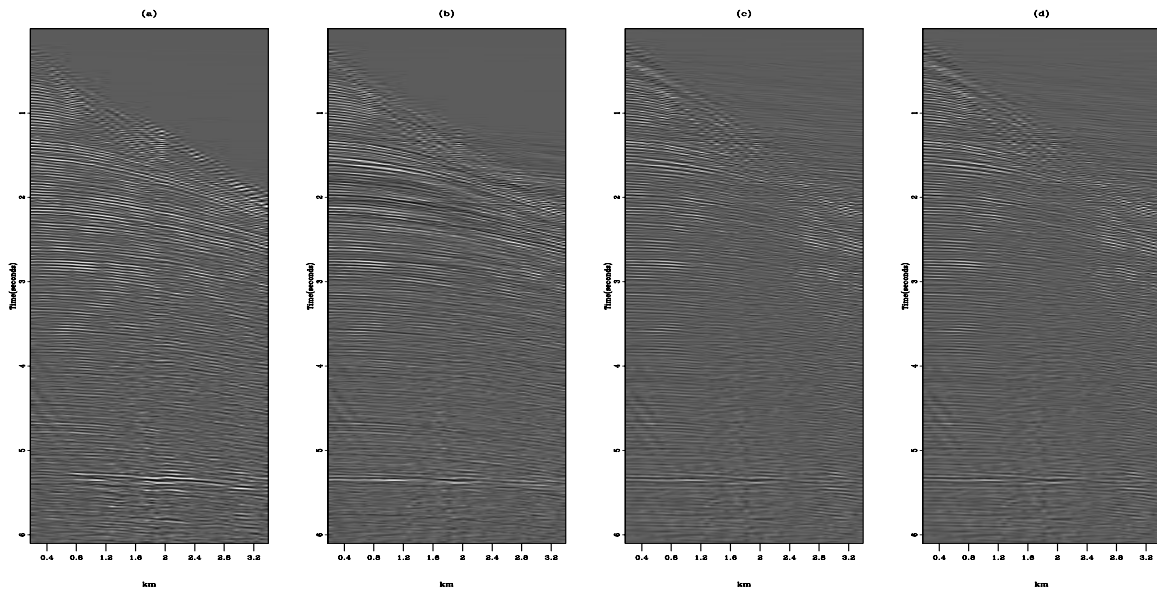


Figure 11: Signal estimate for shot-gather 14 (Panel (b) from Figure 3). Panel (b) shows the BC, Panel (c) the Cauchy, Panel (d) the l_1 , and Panel (d) the l_2 inversion results. [brad2-s.14](#) [ER]

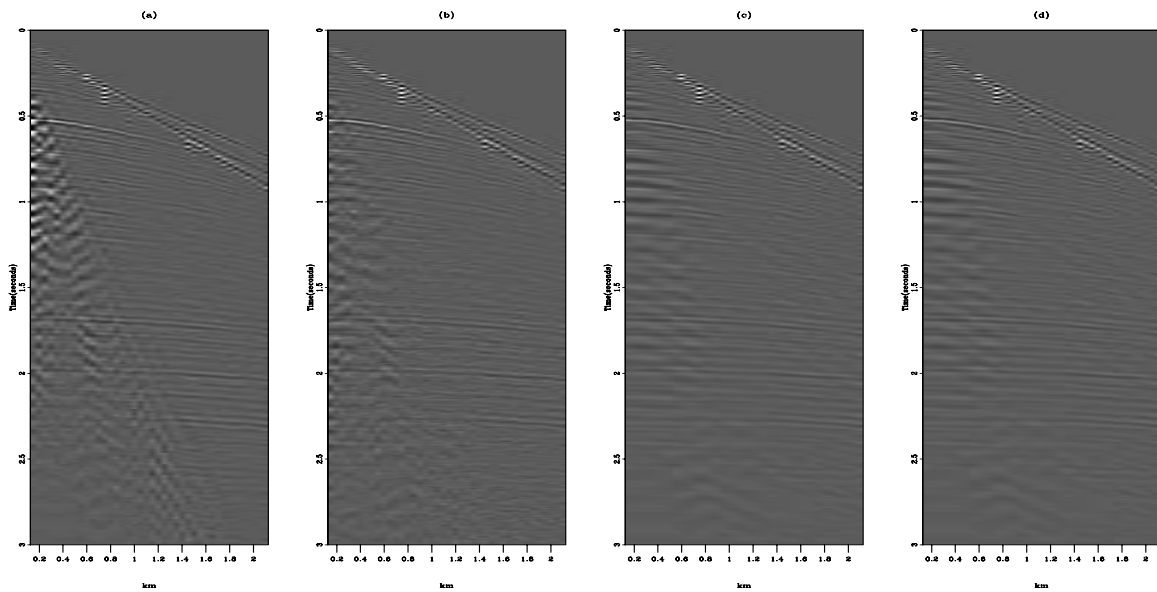


Figure 12: Signal estimate for shot-gather 25 (Panel (c) from Figure 3). Panel (b) shows the BC, Panel (c) the Cauchy, Panel (d) the l_1 , and Panel (d) the l_2 inversion results. [brad2-s.25r](#) [ER]

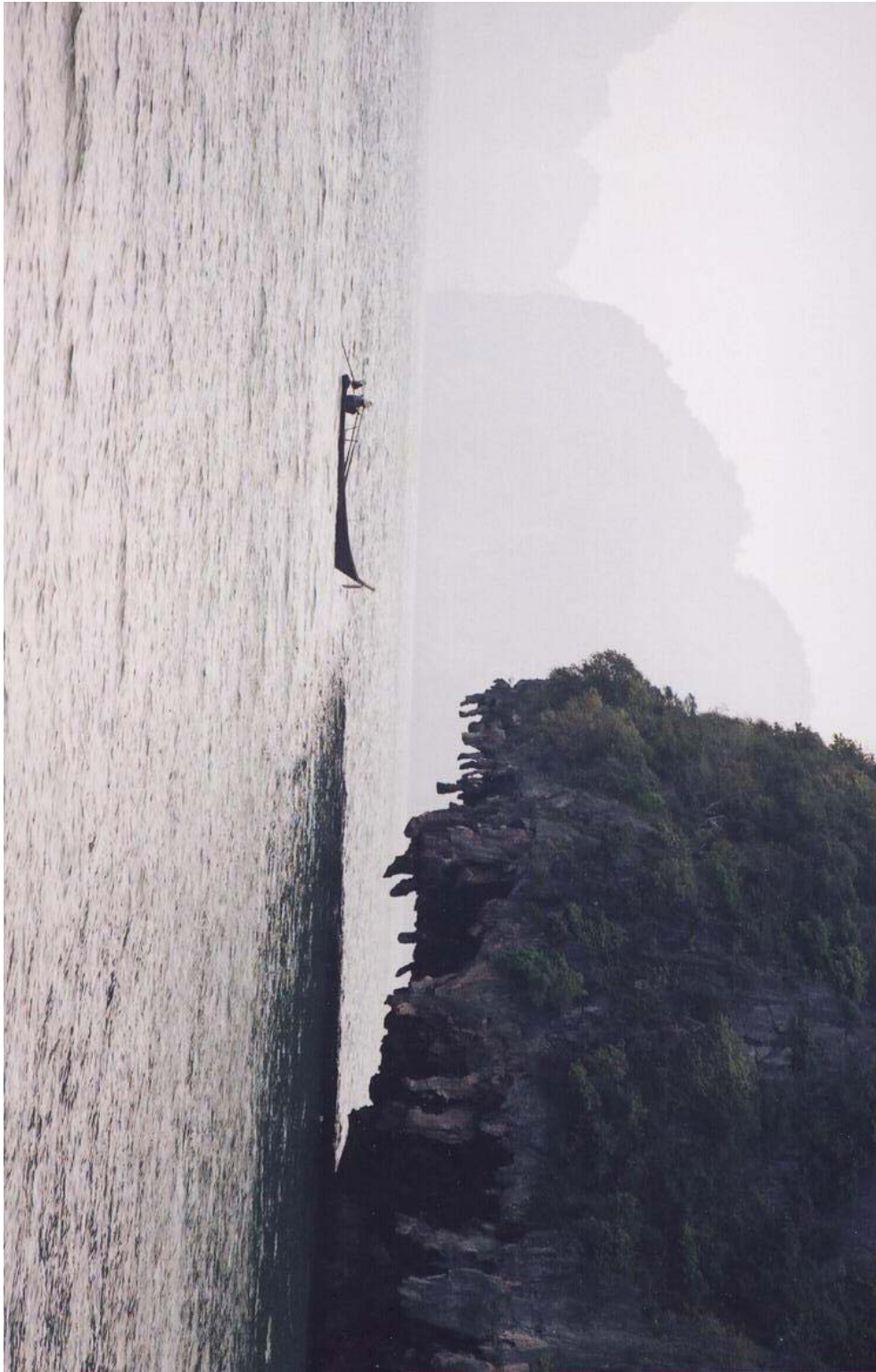
it should be noted that CMP-gathers should be used for this analysis instead of shot-gathers to insure that all of the subsurface hyperbolas do not have an apex shift.

While the bound-constrained, Cauchy, and l_1 inversion schemes produce a more pleasing model-space, this investigation shows it is of limited use in this application of separating the linear from hyperbolic events in a CMP gather. While the least-squares inversion does allow the introduction of cross-talk between the two model-spaces, the noise subtraction technique is better implemented within this framework. This conclusion can be evaluated in terms of the sometimes disparate goals of analysis versus synthesis. If analysis is the goal, the sparseness optimized inversion schemes clearly outperform the least-squares model product. Velocity picking would be much better performed with these results. Of the three, this exploration shows the l_1 scheme to be more tolerant in terms of the combined ease of parameter selection and quality of the model-space. For noise (linear event) separation, the least-squares solution enjoys both a high quality result and tolerance in terms of parameter selection. Further, the least-squares solution is much faster and requires fewer iterations. Purposefully halting the inversion after less than 30 iterations was important to avoid the inversion making efforts to fit the noise in the data. However, to realize a sparse model domain, at least 100 iterations were required for the other, slower, techniques. Full investigation into the ramifications of prematurely stopping the sparse inversion schemes was not performed.

For the purpose of removing linear events with a combined HRT-LRT inversion scheme a data-space solution is required. For this problem, the extra expense of fine-tuning the model-space is wasted.

REFERENCES

- Artman, B., and Sacchi, M., 2003, Basis pursuit for geophysical inversion: SEP-114, 137–150.
- Chen, S. S., Donoho, D. L., and Saunders, M. A., 1999, Atomic decomposition by basis pursuit: SIAM Journal on Scientific Computing, **20**, no. 1, 33–61.
- Claerbout, J. F., 1992, Earth Soundings Analysis: Processing Versus Inversion: Blackwell Scientific Publications.
- Claerbout, J., 1999, Geophysical estimation by example: Environmental soundings image enhancement: Stanford Exploration Project, <http://sepwww.stanford.edu/sep/prof/>.
- Donoho, D., and Huo, X. Uncertainty principles and ideal atomic decomposition: WWW, citeseer.nj.nec.com/donoho99uncertainty.html, June 1999. NSF grants DMS 95-05151 and ECS-97-07111.
- Guitton, A., 2004, Bound constrained optimization: application to the dip estimation problem: SEP-117, 51–62.
- Trad, D., Ulrych, T., and Sacchi, M., 2003, Latest views of the sparse Radon transform: Geophysics, **68**, no. 1, 386–399.



Using knowledge of microstructure to improve estimates and bounds on elastic constants and transport coefficients in heterogeneous media

James G. Berryman¹

ABSTRACT

The most commonly discussed measures of microstructure in composite materials are the spatial correlation functions, which in a porous medium measure either the grain-to-grain correlations, or the pore-to-pore correlations in space. Improved bounds based on this information such as the Beran-Molyneux bounds for bulk modulus and the Beran bounds for conductivity are well-known. It is first shown how to make direct use of bounds and spatial correlation information to provide estimates that always lie between these upper and lower bounds for any microstructure whenever the microgeometry parameters are known. Then comparisons are made between these estimates, the bounds, and two new types of estimates. One new estimate for elastic constants makes use of the Peselnick-Meister bounds (based on Hashin-Shtrikman methods) for random polycrystals of laminates to generate self-consistent values that always lie between the bounds. A second new type of estimate for conductivity assumes that measurements of formation factors (of which there are at least two distinct types in porous media, associated respectively with pores and grains for either electrical and thermal conductivity) are available, and computes new bounds based on this information. The paper compares and contrasts these various methods in order to clarify just what microstructural information — and how accurately that information — needs to be known in order to be useful for estimating material constants in random and heterogeneous media.

INTRODUCTION

A wide array of results is available for practical studies of the linear elastic constants of composite solid and/or granular materials, fluid suspensions, and emulsions. These results range from rigorous bounds such as the Voigt (1928), Reuss (1929), Hill (1952), and Hashin-Shtrikman (1962; 1963) bounds to the fairly popular and mostly well-justified [for sufficiently small concentrations of inclusions (Berryman and Berge, 1996)] approximate methods such as the explicit approximations of Kuster and Toksöz (1974) and Mori and Tanaka (Benveniste, 1987; Ferrari and Filipponi, 1991) and the implicit methods such as the differential effective medium (DEM) method (Cleary *et al.*, 1980; Norris, 1985) and the self-consistent (Hill, 1965;

¹email: berryman@sep.stanford.edu

Budiansky, 1965) or the coherent potential approximation for elastic composites (Gubernatis and Krumhansl, 1975; Korringa *et al.*, 1979; Berryman, 1980; 1982). Older reviews (Watt *et al.*, 1976) and both early (Beran, 1968; Christensen, 1979) and more recent textbooks and research monographs (Nemat-Nasser and Hori, 1993; Cherkaev, 2000; Milton, 2002; Torquato, 2002) survey the state of the art. So it might seem that there is little left to be done in this area of research. However, continuing problems with applications of these methods have included lack of sufficient information [such as the required spatial correlation functions (Torquato, 1980; Torquato and Stell, 1982; Berryman, 1985a)] needed to compute the most accurate bounds known and the failure of some of the explicit methods to satisfy the rigorous bounds in some limiting cases such as three or more constituents (Norris, 1989) or extreme geometries such as disk-like inclusions (Berryman, 1980). The best implicit schemes, even though they are known to be realizable and therefore cannot ever violate the bounds, are often criticized by some workers (Christensen, 1990) because the microgeometry generated implicitly by these methods does not represent the true microgeometry with any obvious fidelity. Nevertheless, it has been shown (Berge *et al.*, 1993; 1995) that knowing general features of the microgeometry such as whether one constituent can be classified as the host medium and others the inclusions, or whether in fact there is no one constituent that serves as the host can be sufficient information to decide on a model that can then be used successfully to study a class of appropriate composites (Berge *et al.*, 1993; 1995; Garboczi and Berryman, 2000; 2001). Some critics also point out that the iteration or integration schemes required to compute the estimates for implicit schemes are sufficiently more difficult to implement than those of the explicit methods that workers are often discouraged from trying these approaches for this reason alone.

Virtually all of the improved bounds (*i.e.*, improved beyond the bounds of Hashin and Shtrikman, which do not make direct use of microstructural information except for the volume fractions) require some information about the microstructure. But it has not been very clear just how precisely this information needs to be known in order for it to be useful. The present work will show for several examples how some general knowledge of microstructure can be used in more than one way to generate estimates. And since the predicted properties (at least in some cases) do not seem to depend too strongly on details beyond those readily incorporated, it gives some confidence that the methods can be successfully applied to real materials. One comparison we can make is between predictions and bounds on elastic constants for random polycrystals of laminates and the predictions of improved bounds based on spatial correlation functions for disks. It is clear that these models should both apply at least approximately to the same types of random composites, yet the microstructure is assumed to be organized rather differently. The random polycrystal is an aggregate of grains, each of which is a laminate material. These laminated grains are then jumbled together with random orientations so the overall composite is isotropic, even though the individual grains act like crystals having hexagonal symmetry. The improved bounds for composites with disk-shaped inclusions must have a microstructure that is at least crudely the same as the random polycrystal, since each layer of an individual grain could be seen as approximately disk-like. So one quantitative question we can ask is: How closely do these two models agree with each other, and if they are indeed close in value, what do we learn about the sensitivity of elastic constants to microstructure? Also, how does this information affect engineering efforts to design (Cherkaev, 2000; Torquato, 2002) new materials? Or, how does general knowledge of

the geology of a given region help us to choose good models of the rocks when we need to interpret our seismic data?

CANONICAL FUNCTIONS AND THE Y-TRANSFORM IN ELASTICITY

Canonical functions

To make progress towards our present goals, it will prove helpful to take advantage of some observations made earlier about both rigorous bounds and many of the known estimates for moduli of elastic composites (Berryman, 1982; 1995; Milton, 1987; 2002). In particular, it is known (Berryman, 1982) that if we introduce certain functionals — similar in analytical structure to Hill’s formula for the overall bulk modulus K^* , which is

$$K^* = \left[\sum_{i=1}^J \frac{v_i}{K_i + 4\mu/3} \right]^{-1} - 4\mu/3, \quad (1)$$

valid when the shear modulus μ is a uniform constant throughout the medium. Here K_i is the bulk modulus of the i th constituent out of J constituents, and v_i is the corresponding volume fraction, with the constraint that $\sum_{i=1}^J v_i = 1$. This form is also similar to the form of the Hashin-Shtrikman bounds (Hashin and Shtrikman, 1962; 1963) for both bulk and shear moduli — many of the known formulas for composites can be expressed simply in terms of these functionals. Specifically, for analysis of effective bulk modulus K^* , we introduce

$$\Lambda(\beta) \equiv \left[\sum_{i=1}^J \frac{v_i}{K_i + \beta} \right]^{-1} - \beta, \quad (2)$$

while, for the effective shear modulus μ^* , we have

$$\Gamma(\theta) \equiv \left[\sum_{i=1}^J \frac{v_i}{\mu_i + \theta} \right]^{-1} - \theta. \quad (3)$$

Here μ_i is the shear modulus of the i th constituent out of J isotropic constituents. The arguments β and θ have dimensions of GPa, and are always nonnegative. Both functions increase monotonically as their arguments increase. Furthermore, when the argument of each functional vanishes, the result is the volume weighted *harmonic mean* (or Reuss average) of the corresponding physical property. Similarly, an analysis of the series expansion for each functional at large arguments shows that, in the limit when the arguments go to infinity, the functionals approach the volume weighted *mean* (or Voigt average) of the corresponding physical property. We call these expressions the “canonical functions” for elasticity, as results expressible in these terms appear repeatedly in the literature — although published results are not necessarily manipulated into these canonical forms by all authors. The arguments β and θ are called the “transform parameters.”

TABLE 1. Various bounds on bulk and shear modulus can be expressed in terms of the canonical functions $\Lambda(\beta)$ and $\Gamma(\theta)$. Subscripts \pm for β and θ are for upper/lower (+/-) bounds. Subscripts \pm for the elastic constants imply the highest/lowest (+/-) values of the quantity present in the composite. Θ , X , Ξ , and the averages $\langle \cdot \rangle$ and $\langle \cdot \rangle_\zeta$ are all defined in the text. $K_R = \langle K^{-1} \rangle^{-1}$, $\mu_R = \langle \mu^{-1} \rangle^{-1}$, $K_V = \langle K \rangle$, and $\mu_V = \langle \mu \rangle$ are the Reuss and Voigt averages of the respective moduli.

Bound	β_-	β_+	θ_-	θ_+
HS (HS, 1962; Walpole, 1969)	$\frac{4}{3}\mu_-$	$\frac{4}{3}\mu_+$	$\Theta(K_-, \mu_-)$	$\Theta(K_+, \mu_+)$
BM (Beran and Molyneux, 1966)	$\frac{4}{3}\langle \mu^{-1} \rangle_\zeta^{-1}$	$\frac{4}{3}\langle \mu \rangle_\zeta$		
MS (McCoy, 1970)			$\frac{1}{6}X$	$\frac{1}{6}\Xi^{-1}$
MPT (Milton and Phan-Thien, 1982)			$\frac{1}{6}\hat{X}$	$\frac{1}{6}\hat{\Xi}^{-1}$

Rigorous bounds

Some of the rigorous bounds that are expressible in terms of the canonical functions for $J = 2$ are listed in TABLE 1. Functions and averages required as definitions for some of the more complex terms in TABLE 1 are:

$$\Theta(K, \mu) = \frac{\mu}{6} \left(\frac{9K + 8\mu}{K + 2\mu} \right), \quad (4)$$

and the expressions needed for the McCoy-Silnutzer (MS) bounds (McCoy, 1970; Silnutzer, 1972), which are

$$X = \left[10\mu_V^2 \langle K \rangle_\zeta + 5\mu_V(2K_V + 3\mu_V) \langle \mu \rangle_\zeta + (3K_V + \mu_V)^2 \langle \mu \rangle_\eta \right] / (K_V + 2\mu_V)^2, \quad (5)$$

$$\Xi = \left[10K_V^2 \langle K^{-1} \rangle_\zeta + 5\mu_V(2K_V + 3\mu_V) \langle \mu^{-1} \rangle_\zeta + (3K_V + \mu_V)^2 \langle \mu^{-1} \rangle_\eta \right] / (9K_V + 8\mu_V)^2. \quad (6)$$

The averages $\langle M \rangle = v_1 M_1 + v_2 M_2$, $\langle M \rangle_\eta = \eta_1 M_1 + \eta_2 M_2$, and $\langle M \rangle_\zeta = \zeta_1 M_1 + \zeta_2 M_2$ are defined for any modulus M . The volume fractions are v_1, v_2 , while ζ_1, ζ_2 and η_1, η_2 are the microgeometry parameters or Milton numbers (Milton, 1981; 1982), related to spatial correlation functions of the composite microstructure. The Voigt averages of the moduli are $K_V = \langle K \rangle$ and $\mu_V = \langle \mu \rangle$. For symmetric cell materials: $\zeta_1 = \eta_1 = v_1$ for spherical cells, $\zeta_1 = \eta_1 = v_2$ for disks, while $\zeta_1 = (v_2 + 3v_1)/4$ and $\eta_1 = (v_2 + 5v_1)/6$ for needles.

Alternative bounds that are at least as tight as the McCoy-Silnutzer (MS) bounds for any choice of microstructure were given by Milton and Phan-Thien (1982) as

$$\hat{X} = \frac{\langle 3\mu \rangle_\eta \langle 6K + 7\mu \rangle_\zeta - 5 \langle \mu \rangle_\zeta^2}{\langle 2K - \mu \rangle_\zeta + \langle 5\mu \rangle_\eta} \quad (7)$$

and

$$\hat{\Xi} = \frac{N}{\langle 128/K + 99/\mu \rangle_{\zeta} + \langle 45/\mu \rangle_{\eta}}, \quad (8)$$

where

$$N = \langle 5/\mu \rangle_{\zeta} \langle 6/K - 1/\mu \rangle_{\zeta} + \langle 1/\mu \rangle_{\eta} \langle 2/K + 21/\mu \rangle_{\zeta}. \quad (9)$$

It has been shown numerically that the two sets of bounds (MS and MPT) using the transform parameters X, Ξ and $\hat{X}, \hat{\Xi}$ are nearly indistinguishable for the penetrable sphere model (Berryman, 1985).

Note that “improved bounds” are not necessarily improved for every choice of volume fraction, constituent moduli, and microgeometry. It is possible in some cases that “improved bounds” will actually be less restrictive, than say the Hashin-Shtrikman bounds, for some range of the parameters. In such cases we obviously prefer to use the more restrictive bounds when our parameters happen to fall in this range.

Milton (1987; 2002) has shown that, for the commonly discussed case of two-component composites, the canonical functionals can be viewed as fractional linear transforms with the arguments β and θ of the canonical functionals as the transform variables. In light of the monotonicity properties of the functionals, this point of view is very useful because the problem of determining estimates of the moduli can then be reduced to that of finding estimates of the parameters β and θ . Furthermore, properties of the canonical functions also imply that excellent estimates of the moduli can be obtained from fairly crude estimates of the transformation parameters β and θ . (Recall, for example, that estimates of zero and infinity for these parameters result in Reuss and Voigt bounds on the moduli.) Milton calls this transformation procedure the Y -transform, where Y stands for one of these transform parameters (*i.e.*, β and θ in elasticity, or another combination when electrical conductivity and/or other mathematically analogous properties are being considered).

Estimation schemes based on bounds for elasticity

One very famous approximation scheme for elastic composites is due to Hill (1952). The idea is to take the known Voigt and Reuss averages of the elastic system stiffnesses or compliances, and then make direct use of this information by computing either the arithmetic or geometric mean of these two limiting values. These formulas have been found to be very effective for fitting real data in a wide variety of circumstances (Simmons and Wang, 1971; Thomsen, 1972; Watt and Peselnick 1980). Clearly the same basic idea can be applied to any pairs of bounds for scalars, such as the Hashin-Shtrikman bounds; or, for complex constants, a similar idea based on finding the center-of-mass of a bounded region in the complex plane could be pursued (but to date apparently has not been). The advantage of such approaches is that they can provide the user with just one estimate per choice of volume fraction, while at the same time requiring no additional information over that contained in the bounds themselves.

Hill's concept clearly works just as well, and possibly somewhat better, if we apply it instead — whenever we have an analytical function at our disposal as we do here in the canonical functions — to the transform variables β and θ rather than to the moduli K and μ directly. So one set of estimates we might test in our examples takes the form

$$\beta_H \equiv \frac{1}{2}(\beta_- + \beta_+) \quad \text{and} \quad \theta_H \equiv \frac{1}{2}(\theta_- + \theta_+), \quad (10)$$

where the bounds on β and θ were already given in TABLE 1, and the averages are just the arithmetic means. The subscript H is intended to reference Hill's contribution to this idea.

Another rather different approach (although still expected to give quite similar results) is to examine the forms of the β and θ transform variables in order to determine if some other estimate that lies between the bounds might suggest itself. One useful tool we can introduce here is the weighted geometric mean. For example, if we define

$$\mu_G^\zeta \equiv \mu_1^{\zeta_1} \mu_2^{\zeta_2}, \quad (11)$$

it is well-known (Hardy *et al.*, 1952) that this is a geometric mean and it always lies between (or on) the corresponding mean $\langle \mu \rangle_\zeta$ and harmonic mean $\langle \mu^{-1} \rangle_\zeta^{-1}$:

$$\langle \mu^{-1} \rangle_\zeta^{-1} \leq \mu_1^{\zeta_1} \mu_2^{\zeta_2} \leq \langle \mu \rangle_\zeta. \quad (12)$$

So $\beta_G = \frac{4}{3} \mu_G^\zeta$ is one natural choice we could make for the bulk modulus transform parameter estimate. This approach has one clear advantage over the usual self-consistent estimates in that the microstructural information can easily be incorporated this way, whereas the means of doing so for self-consistent methods usually involves more complicated calculations via scattering theory (Gubernatis and Krumhansl, 1975; Berryman, 1980). This approach also provides a formula, rather than an implicit equation requiring an iteration procedure for its solution, thus eliminating another common criticism of implicit estimators.

Similar results are not as easy to find for the shear modulus bounds. The reason is that there are either two or three averages that come into play for shear, always including $\langle \cdot \rangle_\zeta$ and $\langle \cdot \rangle_\eta$, while the formulas (5) and (6) also depend on the usual volume averages $\langle \cdot \rangle$. Since it is known that the McCoy-Silnutzer bounds are never tighter than those of Milton and Phan-Thien (1982), we will consider only the Milton and Phan-Thien bounds from here on, since they have only two types of averages present.

In general ζ_i and η_i differ. But in some cases (spheres and disks, for example) they are the same. Furthermore, it is easy to show that for any modulus M , we have the result (relevant in particular to needles) that

$$\begin{aligned} \langle M \rangle_\eta - \langle M \rangle_\zeta &= \frac{1}{12} [\langle M \rangle - \langle \tilde{M} \rangle] \\ &= \frac{1}{12} (v_1 - v_2)(M_1 - M_2). \end{aligned} \quad (13)$$

Thus, the differences always vanish for 50 – 50 concentrations, and furthermore the factor of $\frac{1}{12}$ reduces the difference further by an order of magnitude. If we make the approximation that

$\langle \cdot \rangle_\eta \simeq \langle \cdot \rangle_\zeta$, this is often a quite reasonable compromise. When this is so, we can then choose to make the further approximations that

$$\langle M \rangle_\zeta \simeq M_G^\zeta = M_1^{\zeta_1} M_2^{\zeta_2}, \quad (14)$$

and also that

$$\langle M^{-1} \rangle_\zeta \simeq M_G^{-\zeta}. \quad (15)$$

Substituting these approximations into the Milton and Phan-Thien bounds (7) and (8), we find that both transform parameters for the upper and lower bounds are replaced by the same effective transform parameter:

$$\theta_G^\zeta \equiv \Theta(K_G^\zeta, \mu_G^\zeta). \quad (16)$$

This result provides a unique estimate that will always lie between these bounds.

A somewhat better (*i.e.*, more balanced) approximation is achieved for $\zeta_i \neq \eta_i$ by defining $\epsilon_i \equiv \frac{1}{2}(\zeta_i + \eta_i)$. Then, all occurrences of $\langle \mu \rangle_\zeta$, $\langle \mu \rangle_\eta$, $\langle \mu^{-1} \rangle_\zeta^{-1}$, and $\langle \mu^{-1} \rangle_\eta^{-1}$ are replaced by μ_G^ϵ . The errors introduced now through differences $\eta_i - \epsilon_i$ are half those in (13). But new errors are introduced through the differences $\zeta_i - \epsilon_i$. The resulting geometric approximation turns out to be

$$\theta_G^* = \Theta(K_G^\zeta, \mu_G^\epsilon), \quad (17)$$

which still reduces to (16) whenever $\eta_i = \zeta_i$. Also note that, if $\eta_i + \zeta_i = 1$, then $\mu_G^\epsilon = \sqrt{\mu_1 \mu_2}$.

[Note: If ζ_i is known but η_i is not known (either experimentally or theoretically), Berryman and Milton (1988) discuss how to use knowledge of ζ_i to constrain estimates of η_i . However, we will not pursue this option here.]

To maintain internal consistency of the approximation, we can choose to set

$$\beta_G^* = \frac{4}{3} \mu_G^\zeta, \quad (18)$$

or we could choose instead to use β_H from (10). However, we do not expect that these choices will differ by very much for the bulk modulus estimates.

Elasticity for random polycrystals of laminates

In order to have a more precise model for comparison purposes, and to get a better feeling for just how much difference it makes whether we model the microstructure very accurately or not, we will now consider a model material called a “random polycrystal of laminates.” Suppose we construct a random polycrystal by packing small bits of a laminate material (*i.e.*, a composite layered along a symmetry axis) into a large container in a way so that the axis of symmetry of the grains appears randomly over all possible orientations and also such that no misfit of surfaces (and therefore porosity) is left in the resulting composite. If the ratio

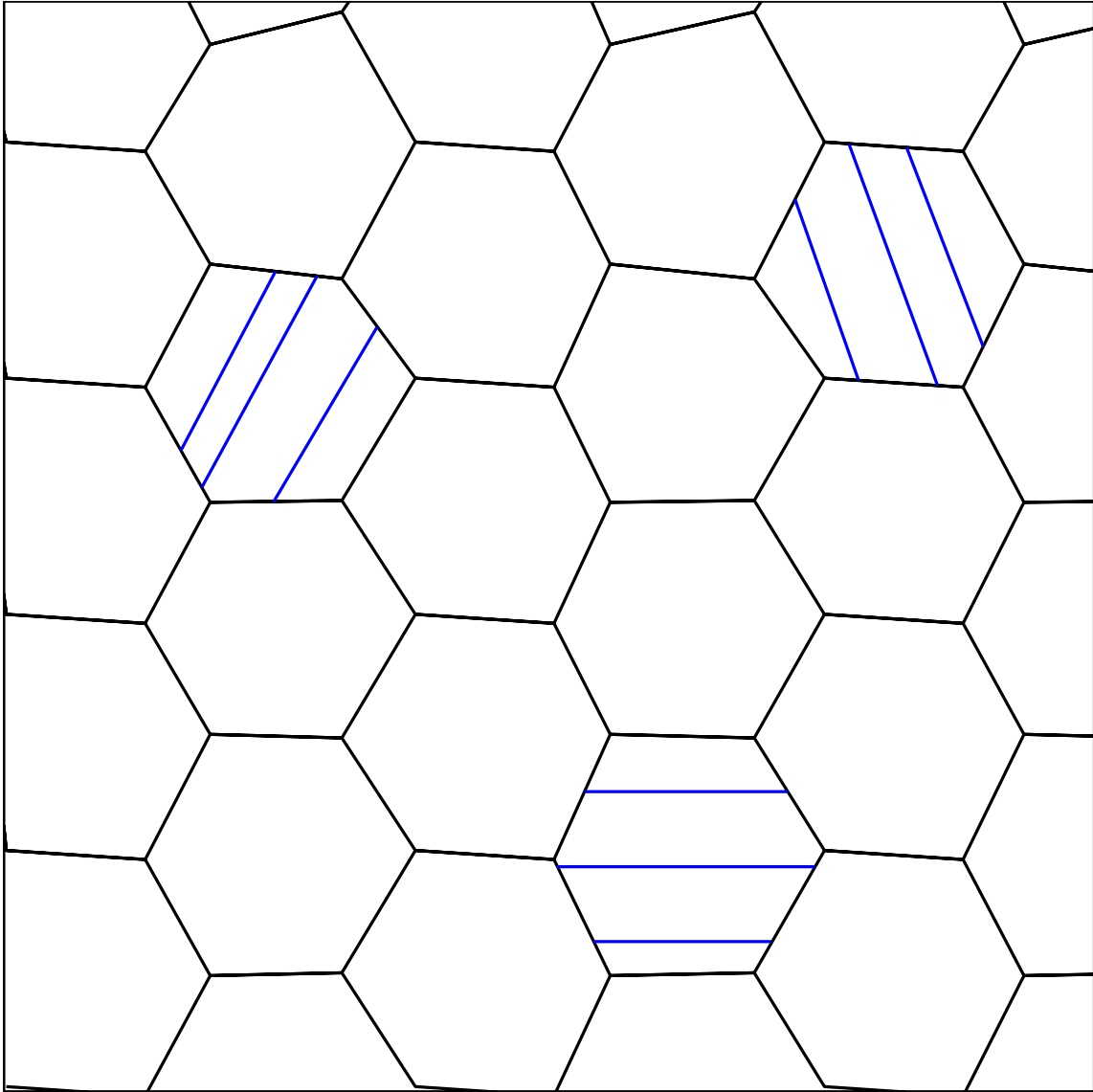


Figure 1: Schematic illustrating the model of random polycrystals of laminates. Grains are assumed to fit tightly so there is no misfit porosity. But the shapes of the grains are not necessarily the same, and the symmetry axes of the grains (three examples are shown here) are randomly oriented so the overall polycrystal is equiaxed (statistically isotropic).

`jim1-laminated_poly_112` [NR]

of laminate grain size to overall composite is small enough so the usual implicit assumption of scale separation applies to the composite — but not so small that we are violating the continuum hypothesis — then we have an example of a random polycrystal of laminates. See schematic in Figure 1.

The analytical advantage of this model is that the layers can be composed of the two elastic constituents in the composites discussed here previously. Furthermore, the elastic behavior of the laminate material itself can be predicted using well-known exact methods (Backus, 1962). We will not dwell on these details here, but just make use of the results to be found in many publications (Berryman, 2004b). The only results needed in the following are the Reuss and Voigt averages for the grains, which are $1/K_R = 2s_{11} + 2s_{12} + 4s_{13} + s_{33}$ for Reuss in terms of compliances, or

$$\frac{1}{K_R - c_{13}} = \frac{1}{c_{11} - c_{66} - c_{13}} + \frac{1}{c_{33} - c_{13}}, \quad (19)$$

in terms of stiffness, and

$$K_V = [2(c_{11} + c_{12}) + 4c_{13} + c_{33}]/9 \quad (20)$$

for the Voigt average of bulk modulus. Similarly, the Voigt average for shear of the stiffness matrix may be written as

$$\mu_V = \frac{1}{5} (G_{\text{eff}}^v + 2c_{44} + 2c_{66}). \quad (21)$$

This expression can be taken as the definition of G_{eff}^v . Eq. (21) implies that $G_{\text{eff}}^v = (c_{11} + c_{33} - 2c_{13} - c_{66})/3$. In fact, G_{eff}^v is the energy per unit volume in a grain when a pure uniaxial shear strain of unit magnitude is applied to the grain along its axis of symmetry (Berryman, 2004a,b). Then, the Reuss average for shear is

$$\mu_R = \left[\frac{1}{5} \left(\frac{1}{G_{\text{eff}}^r} + \frac{2}{c_{44}} + \frac{2}{c_{66}} \right) \right]^{-1}, \quad (22)$$

which is also a rigorous lower bound on the overall shear modulus of the polycrystal (Hill, 1952). Each laminated grain thus has hexagonal symmetry, so the product formulas $3K_R G_{\text{eff}}^v = 3K_V G_{\text{eff}}^r = \omega_+ \omega_- / 2 = c_{33}(c_{11} - c_{66}) - c_{13}^2$ are valid (Berryman, 2004a). The symbols ω_{\pm} stand for the quasi-compressional and quasi-uniaxial shear eigenvalues for all the grains.

Once this notation has been established, then it is straightforward to express the Peselnick-Meister bounds (Peselnick and Meister, 1965) for hexagonal symmetry as

$$K_{PM}^{\pm} = \frac{K_V (G_{\text{eff}}^r + Y_{\pm})}{(G_{\text{eff}}^v + Y_{\pm})}. \quad (23)$$

for effective bulk modulus K^* of the polycrystal, where

$$Y_{\pm} = \frac{G_{\pm}}{6} \left(\frac{9K_{\pm} + 8G_{\pm}}{K_{\pm} + 2G_{\pm}} \right). \quad (24)$$

The precise values of the parameters G_{\pm} and K_{\pm} (being shear and bulk moduli of the HS isotropic comparison material) were given algorithmically by Watt and Peselnick (1980.) Similarly,

$$\frac{1}{\mu_{PM}^{\pm} + Y_{\pm}} = \frac{1}{5} \left[\frac{1 - A_{\pm}(K_V - K_{\pm})}{R_{\pm}(K_V - K_{\pm}) + G_{\text{eff}}^v + Y_{\pm}} + \frac{2}{c_{44} + Y_{\pm}} + \frac{2}{c_{66} + Y_{\pm}} \right], \quad (25)$$

for the effective shear modulus μ^* of the polycrystal. The meaning of Y_{\pm} is the same in (23) and (25). Here $A_{\pm} = \frac{-1}{K_{\pm} + 4G_{\pm}/3}$, $B_{\pm} = \frac{2A_{\pm}}{15} - \frac{1}{5G_{\pm}}$, and $R_{\pm} = A_{\pm}/2B_{\pm}$. These bounds are of Hashin-Shtrikman type, but were first obtained for hexagonal symmetry by Peselnick and Meister (1965) with some corrections supplied later by Watt and Peselnick (1980).

Since we now have analytical forms for the bounds in (23)-(25), it seems it should be possible to arrive at self-consistent formulas (estimates related to the bounds) by making substitutions $K_{\pm} \rightarrow K^*$ and $\mu_{\pm} \rightarrow \mu^*$, as well as $K_{PM}^{\pm} \rightarrow K^*$ and $\mu_{PM}^{\pm} \rightarrow \mu^*$. This procedure can be followed without difficulty for the bulk modulus bounds in (23). However, for the shear modulus estimator, we need to take into account a step in the derivation of (25) that restricted its applicability to a certain curve in the (G_{\pm}, K_{\pm}) -plane. Since the self-consistent estimate will not normally lie on this curve, we need to back up in the analysis presented by Watt and Peselnick (1980) and take into account a correction term that vanishes along the curve in question but not in general. When we do this, and also make use of the self-consistent formula for the bulk modulus K^* , which is

$$K^* = \frac{K_V(G_{\text{eff}}^r + Y^*)}{(G_{\text{eff}}^v + Y^*)}, \quad (26)$$

we find that the self-consistent estimator for the shear modulus μ^* is

$$\frac{1}{\mu^* + Y^*} = \frac{1}{5} \left[\frac{1 - A^*(K_V - K^*)}{G_{\text{eff}}^v + Y^*} + \frac{2}{c_{44} + Y^*} + \frac{2}{c_{66} + Y^*} \right]. \quad (27)$$

The transform variable for these two formulas is just $Y^* = \Theta(K^*, \mu^*)$, with Θ defined as in (4).

From the derivation, it is expected that these self-consistent estimates based on the polycrystal bounds will always lie between the bounds. In fact, this feature is observed in all the results from calculations done using these formulas. It can also be shown that the self-consistent estimator obtained this way is the same as that found by Willis (1981) using different arguments. Furthermore, the results are also in agreement with the self-consistent formulas of Olson and Avellaneda (1992) for polycrystals composed of spherical grains when their results for orthorhombic symmetry are specialized to hexagonal symmetry.

Examples

We will now provide some examples of elastic constant bounds and estimates.

Figures 2 and 3 provide some examples of elastic constant bounds and estimates for a system having two constituents with $K_1 = 20$, $K_2 = 50$, $\mu_1 = 4$, $\mu_2 = 40$, all constants measured in GPa.

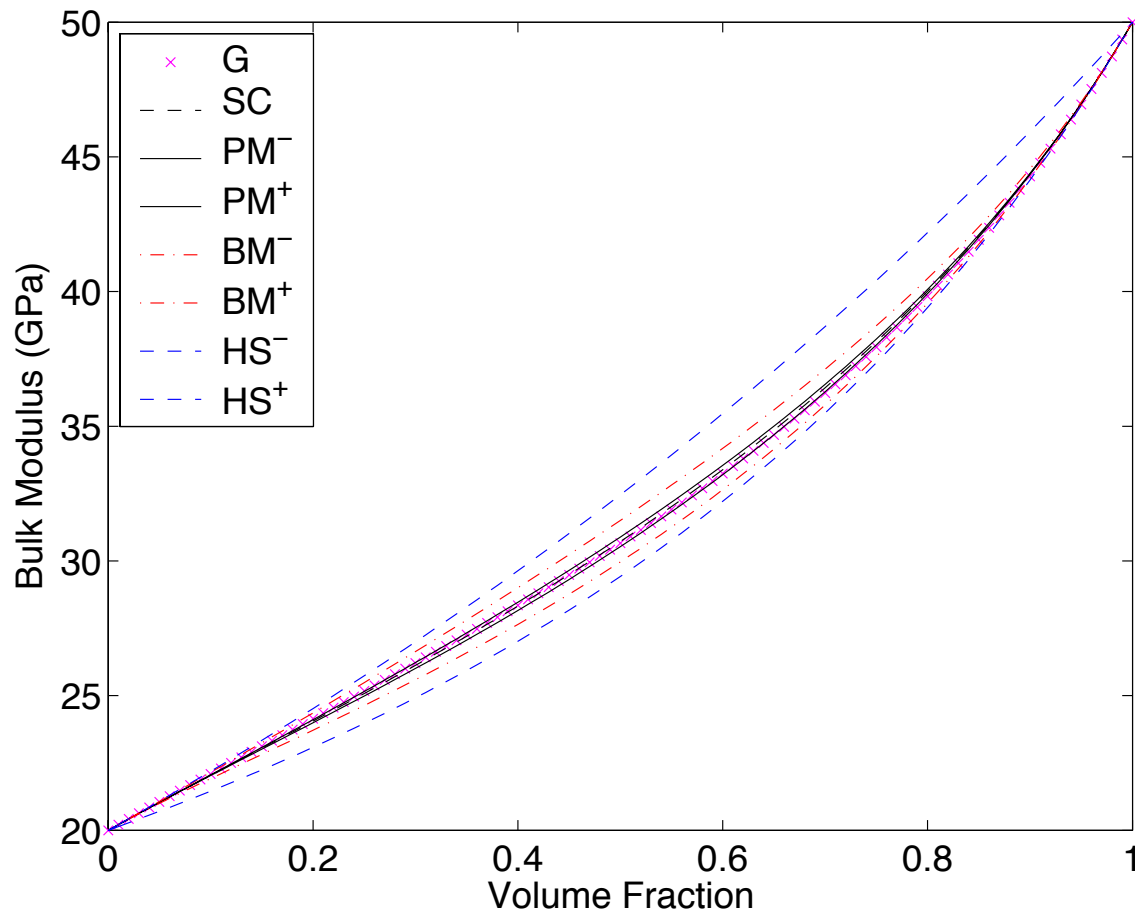


Figure 2: Comparison of (a) the (uncorrelated) bounds of Hashin and Shtrikman (HS^\pm), (b) the microstructure-based bounds (assuming disk inclusions) of Beran and Molyneaux (BM^\pm) for bulk modulus, and (c) the random polycrystal bounds of Peselnick and Meister (PM^\pm) assuming that the composite is an aggregate of randomly oriented laminated (hexagonal symmetry) grains. A self-consistent (SC) estimate based on the Peselnick-Meister bounds lies between the PM^\pm bounds for both bulk and shear moduli. A new estimator (G) is based on the BM and MPT bounds and uses a geometric mean approximation in order to incorporate information contained in the microstructure constants ζ_i and η_i . [jim1-GSCblkmd](#) [NR]

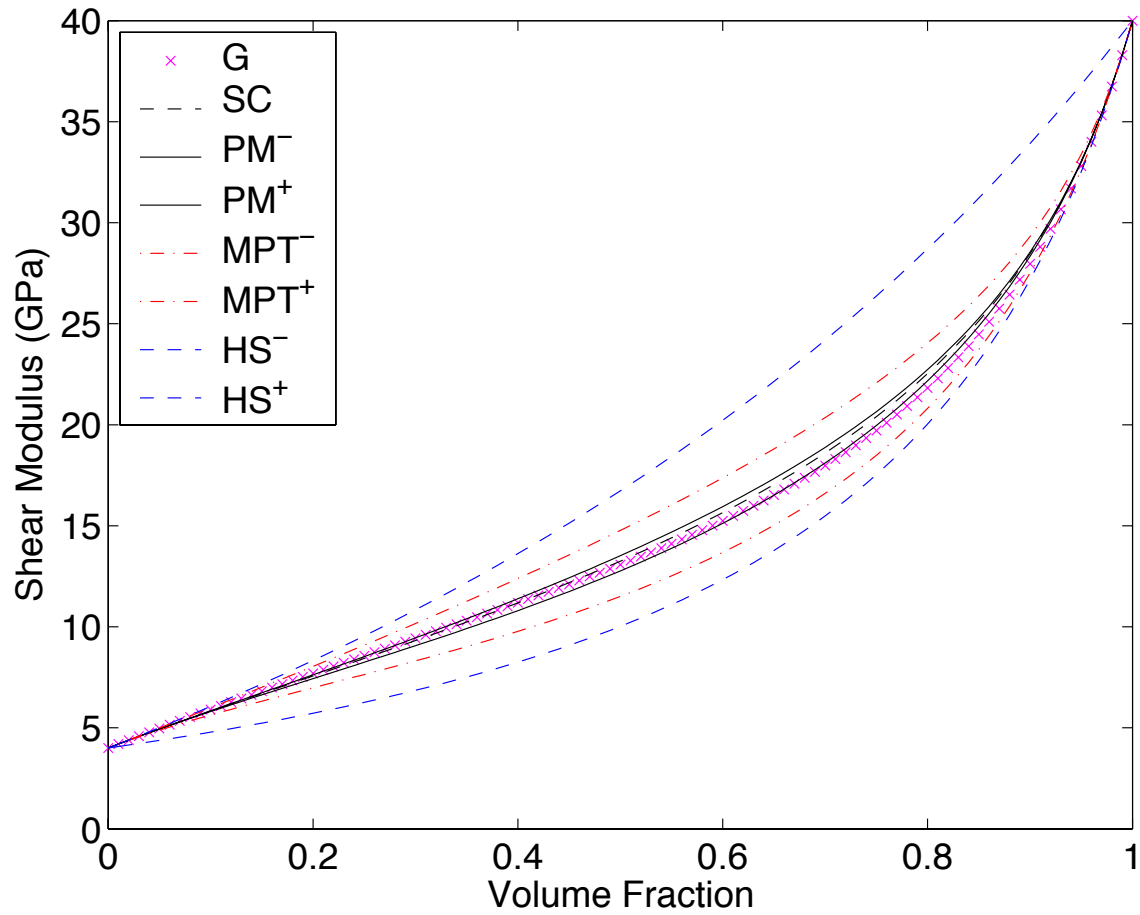


Figure 3: As in Figure 1, but the Milton and Phan-Thien (MPT^\pm) bounds are used instead for shear modulus. [jim1-GSCshrm](#) [NR]

The Hashin-Shtrikman (uncorrelated) bounds (HS^\pm) are the outer most bounds for both bulk and shear modulus. The Beran-Molyneux (BM^\pm) bounds for bulk modulus and the Milton-Phan-Thien (MPT^\pm) bounds for shear modulus — in both cases the shapes of the inclusions are assumed to be disk-like — are the next bounds as we move inward. Then the Peselnick-Meister (PM^\pm) bounds for polycrystals of hexagonal grains are applied to grains laminated so that their volume fractions of type-1 and type-2 are always the same as that of the overall composite being considered here. These PM^\pm bounds lie strictly inside the BM^\pm and MPT^\pm bounds. Then the inner most curve is the SC curve generated as described here by using the analytical forms of the PM^\pm bounds to construct self-consistent estimates for the random polycrystal of laminates model. This SC curve is always inside the PM^\pm bounds and therefore inside all the bounds considered here. Finally, we have the geometric mean estimates G , based on the improved bounds of BM^\pm and MPT^\pm . These estimates always lie between these two bounds, but not always inside the PM^\pm bounds. This result shows that the BM and MPT bounds are allowing for a wider range of microstructures than are the PM bounds, which is entirely reasonable under the circumstances. The main practical observation however is that the PM^\pm , SC , and G curves (both bounds and estimates) are in fact all very close to each other (differing by less than 2% maximum for this high contrast example). This fact suggests that any or all of these curves could be used when designing new composites having preassigned elastic properties, or for analysis of seismic wave data for interpretation purposes. The errors in these predictions would likely be close to the experimental errors in the construction of such composites and therefore negligible for many, though perhaps not all, practical purposes.

CONDUCTIVITY: CANONICAL FUNCTIONS AND ANALYTIC CONTINUATION

Canonical functions

Another topic of broad and continuing interest in the field of composite materials is the study of heterogeneous conductors, dielectrics, and — for porous media — fluid permeability (Beran, 1968; Milton, 2002; Torquato, 2002). Because of the wide range of applications, including both thermal and electrical conduction, and the theoretical interest in analysis of critical phenomena such as percolation thresholds in resistor networks and localization (Kirkpatrick, 1971; 1973), this topic has surely been studied as much or more than any other in the field of heterogeneous media.

Many results in this field of research can also be expressed in terms of canonical functions. First define

$$\Sigma(\sigma) \equiv \left[\sum_{i=1}^J \frac{v_i}{\sigma_i + 2\sigma} \right]^{-1} - 2\sigma, \quad (28)$$

where σ_i is the conductivity in the i th component, and v_i is the corresponding volume fraction, again having the space filling constraint that $\sum_{i=1}^J v_i = 1$. Hashin-Shtrikman bounds (Hashin and Shtirkman, 1962) on conductivity for a multicomponent composite material can then be

expressed as

$$\sigma_{HS}^{\pm} = \Sigma(\sigma_{\pm}), \quad (29)$$

where σ_{\pm} are the largest and smallest values of the J isotropic conductivities present. These bounds are generally improvements on the mean and harmonic mean bounds:

$$\sigma_M = \sum_{i=1}^J v_i \sigma_i \quad \text{and} \quad \sigma_H = \left[\sum_{i=1}^J \frac{v_i}{\sigma_i} \right]^{-1}. \quad (30)$$

Beran (1965; 1968) used variational methods to arrive at improved bounds on conductivity for two-component media, again based on information in spatial correlation functions. His results are also expressible in terms of the canonical functions as

$$\sigma_B^+ = \Sigma(\langle \sigma \rangle_{\zeta}) \quad (31)$$

and

$$\sigma_B^- = \Sigma(\langle 1/\sigma \rangle_{\zeta}^{-1}), \quad (32)$$

where σ_B^+ (σ_B^-) is the upper (lower) bound and the ζ averages are the same ones we introduced here previously [following Eq. (6)]. Since some of the same measures of microstructure (in this case the ζ_i 's) can be used to bound both conductivity and elastic constants, it has been noticed before that this fact and similar relations for other systems can be used to produce various cross-property bounds (Berryman and Milton, 1988; Gibiansky and Torquato, 1995), thereby measuring one physical property in order to bound another.

Estimation schemes based on bounds for conductivity

The fundamental ideas used earlier to obtain estimates of elastic constants by using the analytical structure of the bounds (by making informed approximations for the elastic constants) can again be used for effective conductivity. The ideas are virtually the same, but somewhat easier to apply since we have only one constant to estimate, not two. Since we are now dealing with the Beran bounds on two-component media that depend specifically on the average $\langle \cdot \rangle_{\zeta}$, we want to define again the geometric mean

$$\sigma_G^{\zeta} = \sigma_1^{\zeta_1} \sigma_2^{\zeta_2}. \quad (33)$$

Then we will have an estimator for a new transform variable that lies between the transform variables of the rigorous bounds according to

$$\langle \sigma^{-1} \rangle_{\zeta}^{-1} \leq \sigma_G^{\zeta} \leq \langle \sigma \rangle_{\zeta}. \quad (34)$$

The properties of the canonical function Σ guarantee that

$$\sigma_B^- \leq \sigma_G^* \equiv \Sigma(\sigma_G^{\zeta}) \leq \sigma_B^+. \quad (35)$$

Conductivity for random polycrystals of laminates

For random polycrystals (see the earlier discussion of the basic model in the second section), it is most convenient to define a new canonical function:

$$\Sigma_X(s) = \left[\frac{1}{3} \left(\frac{1}{\sigma_H + 2s} + \frac{2}{\sigma_M + 2s} \right) \right]^{-1} - 2s, \quad (36)$$

where the mean $\sigma_M = \sum_{i=1}^J v_i \sigma_i$ and harmonic mean $\sigma_H = \left[\sum_{i=1}^J \frac{v_i}{\sigma_i} \right]^{-1}$ of the layer constituents are the pertinent conductivities (off-axis and on-axis of symmetry, respectively) in each layered grain. Then, the Hashin-Shtrikman bounds for the conductivity of the random polycrystal are

$$\sigma_{HSX}^{\pm} = \Sigma_X(\sigma_{\pm}), \quad (37)$$

where $\sigma_+ = \sigma_M$ and $\sigma_- = \sigma_H$. These bounds are known not to be the most general ones since they rely on an implicit assumption that the grains are equiaxed. A more general lower bound that is known to be optimal is due to Schulgasser (1983) and Avellaneda *et al.* (1988):

$$\sigma_{ACLMX}^- = \Sigma_X(\sigma_{ACLMX}^-/4). \quad (38)$$

Helsing and Helte (1991) have reviewed the state of the art for conductivity bounds for polycrystals, and in particular have noted that the self-consistent [or CPA (*i.e.*, coherent potential approximation)] for the random polycrystal conductivity is given by

$$\sigma_{CPAX}^* = \Sigma_X(\sigma_{CPAX}^*). \quad (39)$$

It is easy to show (39) always lies between the two rigorous bounds σ_{ACLMX}^- and σ_{HSX}^+ , and also between σ_{HSX}^- and σ_{HSX}^+ . Note that σ_{ACLMX}^- and σ_{HSX}^- cross when $\sigma_m/\sigma_H = 10$, with σ_{ACLMX}^- becoming the superior lower bound for mean/harmonic-mean contrast ratios greater than 10.

Comparisons of conductivity bounds and estimates

We will now provide some comparisons like those presented in the previous section for elastic constant bounds and estimates.

Figure 4 shows a comparison of (a) the correlated bounds of Hashin and Shtrikman (HSX^{\pm}) based on the random polycrystal microgeometry, (b) the microstructure-based bounds (assuming disk inclusions) of Beran (B^{\pm}), (c) the random polycrystal lower bounds of Avellaneda *et al.* (1988) [$ACLMX^-$] laminated (hexagonal symmetry) grains. A self-consistent (CPAX) estimate is based on the random polycrystal microstructure. A new estimator (B^G) is based on the Beran bounds and uses a geometric mean approximation in order to incorporate information contained in the microstructure constants ζ_i .

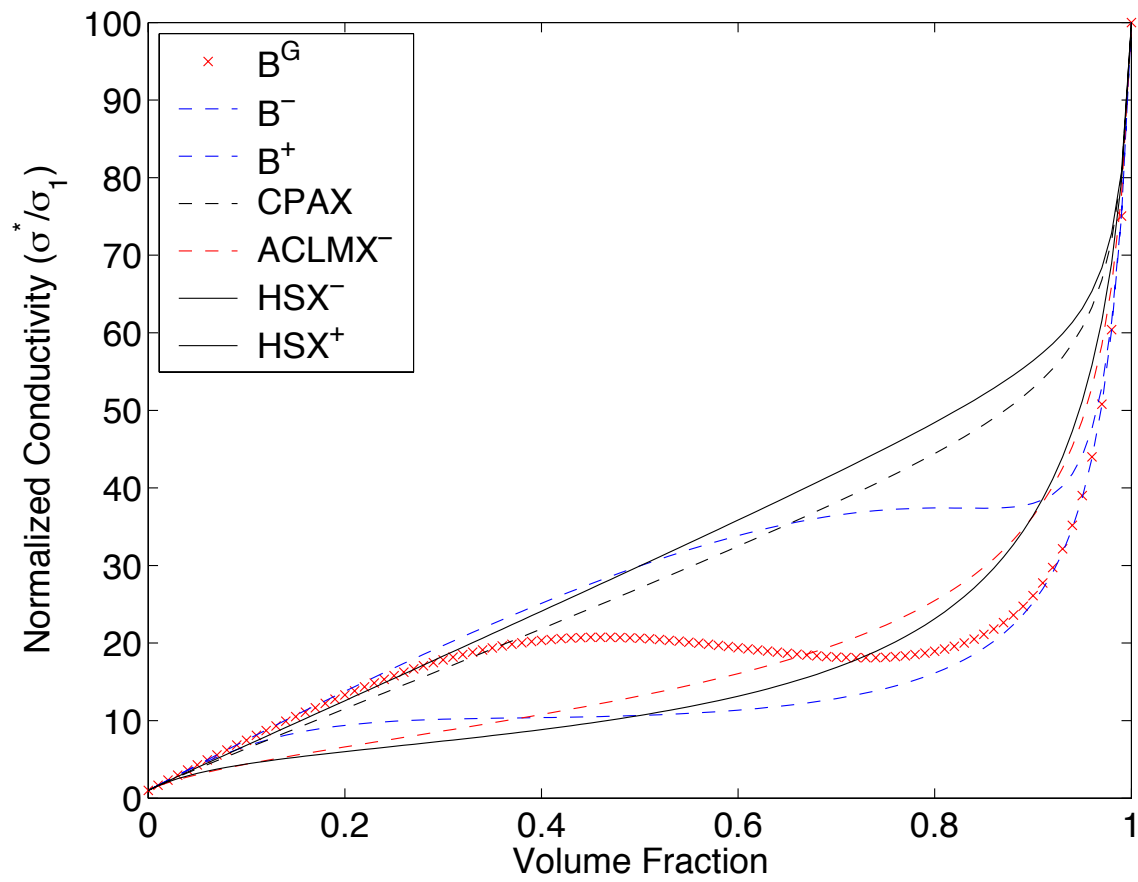


Figure 4: Conductivity comparisons. `jim1-volsigmaall` [NR]

Analytical continuation methods

There are other methods for conductivity/permittivity analysis. The Bergman-Milton (Bergman, 1978; 1980; 1982; Milton, 1980; 1981; Korrington and LaTorraca, 1986; Stroud *et al.*, 1986; Berryman, 1992) analytical approach to understanding some general effective transport coefficient or permittivity — which we take for example to be σ^* — of two-component inhomogeneous media shows that

$$\sigma^* = S(\sigma_1, \sigma_2) = \sigma_1 S(1, 0) + \sigma_2 S(0, 1) + \int_0^\infty \frac{dy \mathfrak{J}(y)}{\frac{1}{\sigma_1} + \frac{y}{\sigma_2}}, \quad (40)$$

where $S(1, 0)$ and $S(0, 1)$ are constants depending only on the geometry and $\mathfrak{J}(y) \geq 0$ is a resonance density functional also depending only on the geometry. The integral in (40) is known as a Stieltjes integral (Baker, 1975). This formula is typically derived and used for the case of complex constants: σ_1 , σ_2 , and σ^* . But we will restrict consideration here — as Bergman (1978) did in his early work — to pure conductors so that σ_1 , σ_2 , and σ^* are all real and nonnegative.

A short derivation of (40) is instructive, so we will present one now.

Following (for example) Korrington and LaTorraca (1986) we consider the defining equation for the function $Z(s)$

$$\sigma^* = \sigma_1 Z(s), \quad (41)$$

where

$$s \equiv \sigma_1 / (\sigma_1 - \sigma_2). \quad (42)$$

Then, Milton (1981) shows [also see Korrington and LaTorraca, 1986] that

$$Z(s) = 1 - \sum_{n=0}^N A_n (1 - s_n) / (s - s_n), \quad (43)$$

where the s_n 's are the locations of the poles, and are enumerated in increasing order. The A_n 's are the residues. These real constants satisfy the following inequalities: $0 < A_n < 1$, $0 \leq s_n < 1$, and $\sum_n A_n \leq 1$. Note that N might be a very large number in practice, so that it may then be more convenient to think of turning this sum into an integral. Define a density functional

$$\mathcal{A}(s) \equiv \sum_{n=1}^N A_n \delta(s - s_n), \quad (44)$$

where δ is the Dirac delta function. Then, (43) can be rewritten as

$$Z(s) = 1 - A_0/s - \int_0^1 dx \mathcal{A}(x) (1 - x) / (s - x), \quad (45)$$

which is so far just a restatement of (43), assuming only that there exists a finite A_0 for which $s_0 \equiv 0$. Substituting (42) into (45) and rearranging, we find

$$Z(s) = 1 - A_0 + A_0 \frac{\sigma_2}{\sigma_1} - \int_0^1 dx \mathcal{A}(x) \frac{(1-x)(\sigma_1 - \sigma_2)}{(1-x)\sigma_1 + x\sigma_2}. \quad (46)$$

We can then symmetrize this expression by adding and subtracting the term $x\sigma_2$ in the numerator of the displayed ratio inside the integral. Then we can pull out another constant and finally have the form we want:

$$Z(s) = [1 - A_0 - \int_0^1 dx \mathcal{A}(x)] + A_0 \frac{\sigma_2}{\sigma_1} + \int_0^1 dx \mathcal{A}(x) \frac{\sigma_2}{(1-x)\sigma_1 + x\sigma_2}. \quad (47)$$

Substituting this back into the original definition (41), we find the symmetrical result

$$\sigma^* = \frac{\sigma_1}{F_1} + \frac{\sigma_2}{F_2} + \int_0^1 dx \mathcal{A}(x) \frac{1}{(1-x)/\sigma_2 + x/\sigma_1}, \quad (48)$$

where $1 \geq 1/F_2 = A_0 > 0$ and $1 > 1/F_1 = 1 - A_0 - \int_0^1 dx \mathcal{A}(x) \geq 0$, since $\sum_{n=0}^{\infty} A_n = A_0 + \int_0^1 dx \mathcal{A}(x) \leq 1$. The F_i 's are known as "formation factors" (Archie, 1942; Avallandea and Torquato, 1991).

This equation is not yet in the same form as (40), but it is nevertheless worthwhile to pause for a moment to consider this form on its own merits. In particular, the first two terms on the right hand side are exactly what is expected when conductors are connected in parallel inside a complex conducting medium. And the remaining integral looks like some sort of weighted average of conductors connected in series. The first physical analogy (conductors in parallel) is entirely appropriate. The second one is no doubt an oversimplification of what is happening in the medium, since the weights in the denominator (*i.e.*, x and $1-x$) are not really volume fractions (even though they do range from 0 to 1), and the density functional \mathcal{A} in the numerator also contributes important numerical weights depending on the local shapes and interconnectedness of the microstructure of the conductors. This dependence on microstructure would correspond approximately to the network connectivity in a resistor network, but usually does not have a perfect analog for most 3D conducting composites.

To complete the derivation of (40), we now need only to make the further substitutions $x = 1/(1+y)$ where y ranges from 0 to ∞ , and define $\mathcal{J}(y) \equiv \mathcal{A}(x)/(1+x)$. Then, we arrive finally at precisely (40), having found that $S(1,0) = 1/F_1$ and $S(0,1) = 1/F_2$. Furthermore, taking the limit $\sigma_1 = \sigma_2 = 1 = \sigma^*$, we find the useful sumrule

$$\frac{1}{F_1} + \frac{1}{F_2} + \int_0^{\infty} dy \frac{\mathcal{J}(y)}{1+y} = 1. \quad (49)$$

Clearly, other choices of the integral transform in (48) may also be useful. In particular, taking instead $x = 1/(1-y)$ is a good choice in preparation for analysis of the resonance density $\mathcal{J}(y)$ itself, as this transform places it most appropriately on the negative real axis. But for present purposes either (40) or (48) is a satisfactory choice for study.

Formation factor bounds

In a porous medium, when $\sigma_2 = \text{const}$ and σ_1 varies [as would be expected in a series of electrical conductivity experiments with different conducting fluids — such as brines (Wildenschild *et al.*, 2000) — in the same pores], then general bounds can be derived from the form of (40). These bounds [see Berryman (2005a) for the full derivation] are given by

$$\min(L_1, L_2) \leq \sigma^*(\sigma_1, \sigma_2) \leq \max(L_1, L_2), \quad (50)$$

where L_1 and L_2 are defined, respectively, by

$$L_1(\sigma_1, \sigma_2) \equiv \sigma_2 + \frac{\sigma_1 - \sigma_2}{F_1}, \quad (51)$$

and

$$L_2(\sigma_1, \sigma_2) \equiv \sigma_1 + \frac{\sigma_2 - \sigma_1}{F_2}. \quad (52)$$

If one of the σ_i 's varies while the other remains constant, L_1 and L_2 are both straight lines, crossing when $\sigma_1 = \sigma_2$. We call (50) the formation factor bounds. One of them (always the lower bound for conductivities) often provides nontrivial improvements over the Hashin-Shtrikman and Beran bounds as we shall demonstrate by example.

The bounds obtained this way are in fact special cases of some earlier bounds by Prager (1969) and Bergman (1976), as discussed recently by Milton (2002, pp. 580–581). The approach as described by Milton is based on Padé approximation methods (Torquato, 1985a; Milton, 2002), although the original papers did not couch the analysis in these terms. Besides the much simpler derivation permitted by direct analysis of the Bergman-Milton analytic formulas (Berryman, 2005a), the main technical difference between the results here and those of Prager and Bergman is that we have implicitly assumed that two distinct (possibly idealized) formation factors have actually been carefully measured. To do so in practice requires either extremely high or extremely low conductivities of one or the other conducting component, or it requires a careful extrapolation process based on multiple measurements (Berryman, 2005b). These assumed direct measurements (or an extrapolation process) are perfectly reasonable when one or the other component is actually (or nearly) an insulator (electrical or thermal) [see Guéguen and Palciauskas (1994) for a discussion]. On the other hand, Prager's approach differs from this by providing bounds directly from any and all measurements on the same system as the constituents or choices of physical constants to be measured are allowed to vary. Bergman's method is very similar in this regard to Prager's. In both cases, these methods were applied to real constants just as we have done, but generalization to complex constants is also possible (Milton, 2002).

In our present notation, Prager's bounds can also be written in terms of the canonical function Σ . Assuming that two measurements have been made of the formation factors, we have four bounds from Prager's results. Two of these are the same as the Wiener (1912) bounds, *i.e.*, the mean and harmonic mean based on volume fractions. The other two bounds are given by

$$\sigma_{P1}^* = \Sigma(x_1\sigma_1) \quad \text{and} \quad \sigma_{P2}^* = \Sigma(x_2\sigma_2), \quad (53)$$

where

$$x_1 = \frac{v_2}{2(v_1 F_1 - 1)} \quad \text{and} \quad x_2 = \frac{v_1}{2(v_2 F_2 - 1)}. \quad (54)$$

Using Hashin-Shtrikman bounds, it is not difficult to show that x_1 and x_2 are both nonnegative and bounded above by unity. Also, since $\sigma_{HS}^\pm = \Sigma(\sigma_\pm)$, one of Prager's bounds is always lower than the lower HS bound, and therefore not an improved bound, so not of interest to us. Furthermore, the other Prager bound is always lower than the upper HS bound. We show in the examples that for the case considered here this bound is in fact a useful lower bound on σ^* that has the right asymptotic behavior — *i.e.*, approaching the formation factor bounds for large ratios of the constituent conductivities.

Similarly, two of the Bergman bounds can be written as

$$\sigma_{B1}^* = \Sigma(x_1 \sigma_1 + (1 - x_1) \sigma_2) \quad \text{and} \quad \sigma_{B2}^* = \Sigma((1 - x_2) \sigma_1 + x_2 \sigma_2), \quad (55)$$

where x_1 and x_2 were defined previously in (54). There are two other Bergman bounds, but these reduce exactly to the HS bounds for the case under consideration here. It is also clear from the monotonicity of the canonical function Σ and the facts $0 \leq x_1, x_2 \leq 1$ that the Bergman bounds given in (55) must always lie between or on the HS bounds. Furthermore, it is easy to see also that $\sigma_{P1}^* \leq \sigma_{B1}^*$ and that $\sigma_{P2}^* \leq \sigma_{B2}^*$, so Bergman's lower bound will always be superior to Prager's lower bound.

Asaad (1955) performed a series of thermal conductivity measurements on three different sandstones. He also measured the electrical formation factor of each sample. This data set is therefore most interesting to us for testing the theory. When the pores are filled with an electrically conducting fluid, current flows (in saturated sandstone) mostly through the pore fluid because sand grains are generally poor electrical conductors (Guéguen and Palciauskas, 1994). When the pores are filled instead with air, heat flows mostly through the sand grains because air is a poor thermal conductor. So the thermal conductivity properties of samples is quite different from those of electrical conductivity. But the microgeometry is still the same and, therefore, the structure of the equations for thermal conductivity is exactly the same as in (40). For Asaad's sandstone sample D, we find that $F_2^D = 3.72$ (from thermal conductivity measurements) and $F_1^D = 33.0$ (from electrical conductivity measurements). The porosity of this sample was $\phi^D = 0.126$, so $x_1 \simeq 0.138$ and $x_2 \simeq 0.028$. With these values known, we can make comparisons between and among the various theoretical results available to us. In particular note that since x_2 is quite small, σ_{B2}^* will clearly be very close to (nearly indistinguishable from) the Hashin-Shtrikman upper bound when $\sigma_1/\sigma_2 > 1$.

The uncorrelated Hashin-Shtrikman bounds (29) apply to this problem, as do the Beran bounds (31) and (32). To apply the Hashin-Shtrikman bounds we need only the volume fractions, but to apply the Beran bounds we also need some estimate of the microstructure parameters (the ζ_i 's). Sandstones having a low porosity like 0.126 might have fairly round grains, but the pores themselves will surely not be well-approximated by spheres. So the common choice $\zeta_i = v_i$ is probably not adequate for this problem. A better choice is available however, since the values of ζ_i and η_i have been computed numerically for the penetrable sphere model (Berryman, 1985b; Torquato, 1985b; 2002). This model microstructure is very much like that

of a sandstone and, therefore, should prove adequate for our present comparisons. For porosity $v_1 = 0.126$, the penetrable sphere model has the value $\zeta_1 \simeq 0.472$. Since both formation factors are known for these experimental data, the formation factor (FF \pm) bounds can also be applied without difficulty. Figure 3 shows the results. (Note that the units of the conductivity have been normalized so all the curves cross at unity on this plot in order to make the Figure universal.)

We will limit this discussion to the region $\sigma_1/\sigma_2 \geq 1$. We find that the formation factor upper bound is well above the Hashin-Shtrikman upper bound, which is above the Beran bound as expected. All the bounds cross at $\sigma_1/\sigma_2 = 1$, as is necessary. The lower bounds have more complicated behavior. The Beran lower bound is always superior to the Hashin-Shtrikman lower bound, but they are both quite close together for all values of the ratio $\sigma_1/\sigma_2 > 1$. Both bounds are also superior to the lower formation factor bound for values of σ_1/σ_2 ratio close to unity. But, for higher values of contrast in the range $\sigma_1/\sigma_2 > 12$, these two bounds become inferior to the formation factor lower bound. This result is expected since it is for the asymptotic regimes (very high or very low ratios of the conductivities) that one of the FF bounds tends to become an exact estimate. Neither the Hashin-Shtrikman lower bounds nor the Beran lower bounds can compete in this regime because they must allow for the possibility that the more poorly conducting component plays host to the more strongly conducting component. Measured formation factor values provide new information that largely determines the status of this important long-range spatial correlation feature (due to the presence or absence of such a host/inclusion arrangement) throughout the microstructure.

Bergman lower bounds are best for moderate to high values of the contrast ratio, and they asymptote to the formation factor lower bounds (as do the Prager lower bounds) in the very high contrast regime. Note that Beran lower bounds can be superior to the Bergman lower bounds for small contrast ratios, since they use different measures of microstructure (ζ_i instead of F_i).

Figure 5 shows comparisons of (a) the uncorrelated bounds of Hashin and Shtrikman (HS $^\pm$), (b) the microstructure-based bounds (assuming penetrable spheres) of Beran (Beran $^\pm$), (c) the Padé approximant bounds of Bergman (B $^\pm$) and Prager (P $^-$), and (d) the new formation factor (FF $^\pm$) bounds. Beran upper bounds are always the best ones shown here. Bergman lower bounds are best for moderate to high values of the contrast ratio, and they asymptote to the formation factor lower bounds (as do the Prager lower bounds) in the very high contrast regime. Beran lower bounds can be superior to the Bergman lower bounds for small contrast ratios. For the sake of universality, units of conductivity have been normalized so the curves all cross at unity.

So at high contrast ($\sigma_1/\sigma_2 \gg 1$), the Beran upper bound and the Bergman lower bound are the best (tightest) bounds for this sample sandstone D. For contrast ratios up to 300, we obtain bounds confining the conductivity to variations less than about a factor of 2, which will often be quite satisfactory for such difficult, but nevertheless fairly typical, estimation problems. The use of the formation factor lower bounds together with some of the earlier bounds like the Hashin-Shtrikman and Beran bounds therefore seems to be one satisfactory solution to some of the problems of high contrast conductivity estimation noted in the previous section.

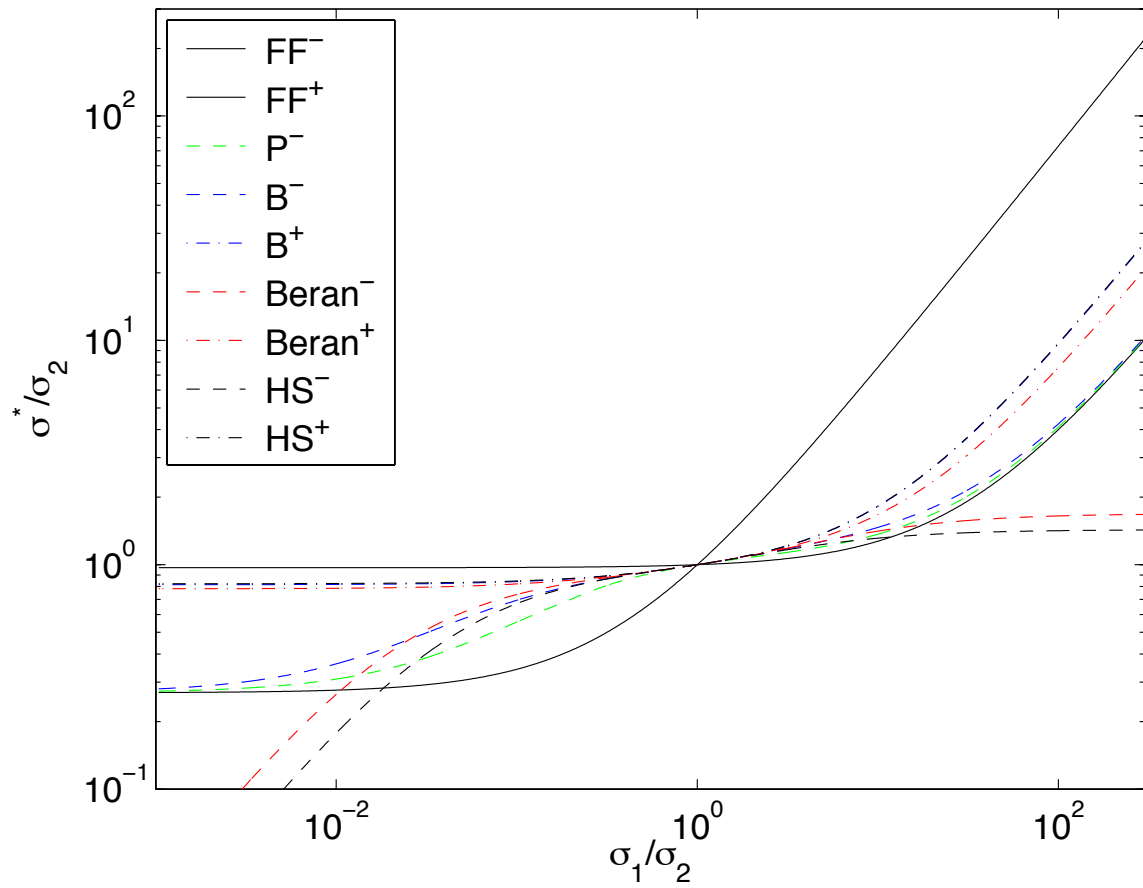


Figure 5: Conductivity comparisons including formation factor bounds. jim1-DNmixed
[NR]

Otherwise, improvements can be made when desired using Prager, Bergman, and also Milton bounds (Milton, 1981b) [not discussed here]. Although the formation factor lower bounds are not the best known bounds, they are nevertheless very easy to use and give remarkably accurate estimates at very high contrasts.

ASSESSMENT AND CONCLUSIONS

The point of the paper has been to study how microstructure, and especially any special knowledge we may have of either quantitative measures or qualitative features of that microstructure, affects estimates of material constants.

For elasticity, we considered various improvements on the Hashin-Shtrikman bounds such as the Beran-Molyneux bounds, the McCoy-Silnutzer bounds, and the Milton-Phan-Thien bounds. We found that knowledge of microstructure can be used very effectively in these improved bounds. New estimates (not themselves rigorous bounds) can also be formulated based on the analytical structure of the bounds, and the microstructure parameters can then be incorporated directly into these estimates in a way so the resulting estimates always satisfy the bounds. When making comparisons between models based on disk-like inclusions in a host medium, and the random polycrystals of laminates model, we found that these models predict very similar results when there is a relatively small volume fraction of disks present. But when the volume fraction of disks is large, the bounds do not constrain the results as well, and so there is still more work to be done relating constants to microstructure in the mid-range of volume fractions, and generally for high contrast problems.

For electrical conductivity and other related physical constants such as thermal conductivity and dielectric constant (and in some cases fluid permeability), the microstructure can be introduced not only through the volume fractions and microstructural parameters as was done in the case of elasticity, but also through the use of more global measures of microstructure such as the formation factors. Global measures like the F_i 's that determine the long-range spatial correlations and connectivity (within our material object of study) — by means of two fairly common and relatively simple measurements — are very advantageous and clearly more information of this type is desirable. The case of high contrast composites is always very important for all types of conductivity estimation and so formation factor bounds and Padé approximant schemes both provide convenient means of addressing this problem. The formation factor bounds are elementary in mathematical structure, but nevertheless provide very useful lower bounds on conductivity and permittivity for high contrast problems.

One general observation is that behavior of high contrast mixtures and composites remains poorly constrained by most of the methods presented, and more work in that direction is therefore still needed. A typical example that always generates high contrast situations is porous and/or granular media, where the pores may be filled with air; then, both the mechanical and the transport properties can have a very wide range of variation depending on the details of the microstructure. Some of the same types of information (such as formation factors) used here for studies of transport properties can also be applied to elasticity estimates in porous media as has been pointed out previously in studies of “cross-property” relationships and bounding

methods (Berryman and Milton, 1988; Gibiansky and Torquato, 1995) – *i.e.*, estimating one physical quantity after measuring another. So, one possibility for future progress that has yet to be explored in very great detail is how the formation factor bounds as well as other improved bounds on electrical or thermal conductivity may provide useful information about microstructure that can then be used to constrain further the elastic behavior of the same system.

REFERENCES

- Archie, G. E., 1942, The electrical resistivity log as an aid in determining some reservoir characteristics: *Trans. AIME*, **146**, 54–62.
- Asaad, Y., 1955, *A Study of the Thermal Conductivity of Fluid-Bearing Porous Rocks*, Ph.D. thesis, University of California – Berkeley, Berkeley, CA.
- Avellaneda, M., A. V. Cherkaev, K. A. Lurie, and G. W. Milton, 1988, On the effective conductivity of polycrystals and a three-dimensional phase-interchange inequality: *J. Appl. Phys.*, **63**, 4989–5003.
- Avellaneda, M., and S. Torquato, 1991, Rigorous link between fluid permeability, electrical conductivity, and relaxation times for transport in porous media: *Phys. Fluids A*, **3**, 2529–2540.
- Backus, G. E., 1962, Long-wave elastic anisotropy produced by horizontal layering: *J. Geophys. Res.*, **67**, 4427–4440.
- Baker, G. A., Jr., 1975, *Essentials of Padé Approximants*, Academic Press, San Diego, CA.
- Benveniste, Y., 1987, A new approach to the application of Mori-Tanaka's theory in composite materials: *Mech. Mat.*, **6**, 147–157.
- Beran, M. J., 1965, Use of the variational approach to determine bounds for the effective permittivity in random media: *Nuovo Cimento*, **38**, 771–782.
- Beran, M. J., 1968, *Statistical Continuum Theories*, Wiley, New York, pp. 181–256.
- Beran, M. J., and J. Molyneux, 1966, Use of classical variational principles to determine bounds for the effective bulk modulus in heterogeneous media: *Quart. Appl. Math.*, **24**, 107–118.
- Berge, P. A., J. G. Berryman, and B. P. Bonner, 1993, Influence of microstructure on rock elastic properties: *Geophys. Res. Lett.*, **20**, 2619–2622.
- Berge, P. A., B. P. Bonner, and J. G. Berryman, 1995, Ultrasonic velocity-porosity relationships for sandstone analogs made from fused glass-beads: *Geophysics*, **60**, 108–119.
- Bergman, D. J., 1976, Calculation of bounds for some average bulk properties of composite materials: *Phys. Rev. B*, **14**, 4304–4312.

- Bergman, D. J., 1978, The dielectric constant of a composite material — A problem of classical physics: *Phys. Repts.*, **43**, 378–407.
- Bergman, D. J., 1980, Exactly solvable microscopic geometries and rigorous bounds for the complex dielectric constant of a two-component composite material: *Phys. Rev. Lett.*, **44**, 1285–1287.
- Bergman, D. J., 1982, Rigorous bounds for the complex dielectric constant of a two-component composite: *Ann. Phys.*, **138**, 78–114.
- Berryman, J. G., 1980a, Long-wavelength propagation in composite elastic media I. Spherical inclusions: *J. Acoust. Soc. Am.*, **68**, 1809–1819.
- Berryman, J. G., 1980b, Long-wavelength propagation in composite elastic media II. Ellipsoidal inclusions: *J. Acoust. Soc. Am.*, **68**, 1820–1831.
- Berryman, J. G., 1982, Effective medium theory for elastic composites: in *Elastic Wave Scattering and Propagation*, edited by V. K. Varadan and V. V. Varadan, Ann Arbor Science, Ann Arbor, Michigan, pp. 111–129.
- Berryman, J. G., 1985a, Measurement of spatial correlations functions using image processing techniques: *J. Appl. Phys.*, **57**, 2374–2384.
- Berryman, J. G., 1985b, Variational bounds on elastic constants for the penetrable sphere model: *J. Phys. D: Appl. Phys.*, **18**, 585–597.
- Berryman, J. G., 1992, Effective stress for transport properties of inhomogeneous porous rock: *J. Geophys. Res.*, **97**, 17409–17424.
- Berryman, J. G., 1995, Mixture theories for rock properties: in *Rock Physics and Phase Relations: American Geophysical Union Handbook of Physical Constants*, edited by T. J. Ahrens, AGU, New York, pp. 205–228.
- Berryman, J. G., 2004a, Poroelastic shear modulus dependence on pore-fluid properties arising in a model of thin isotropic layers: *Geophys. J. Int.*, **157**, 415–425.
- Berryman, J. G., 2004b, Bounds on elastic constants of random polycrystals of laminates: *J. Appl. Phys.*, **96**, 4281–4287.
- Berryman, J. G., 2005a, Thermal conductivity of porous media: *Appl. Phys. Lett.*, **86**, 032905-1–032905-3 (online: January 11, 2005).
- Berryman, J. G., 2005b, Bounds and estimates for transport coefficients of random and porous media with high contrasts: *J. Appl. Phys.*, **97**, 063504-1–063504-11.
- Berryman, J. G., 2005c, Bounds and estimates for elastic constants of random polycrystals of laminates: *Int. J. Solids Structures*, **42**, 3730–3743.
- Berryman, J. G., and P. A. Berge, 1996, Critique of explicit schemes for estimating elastic properties of multiphase composites: *Mech. Materials*, **22**, 149–164.

- Berryman, J. G., and G. W. Milton, 1988, Microgeometry of random composites and porous media: *J. Phys. D: Appl. Phys.*, **21**, 87–94.
- Bruggeman, D. A. G., 1935, Berechnung verschiedener physikalischer Konstanten von heterogenen Substanzen: I. Dielectrizitätskonstanen und Leitfähigkeiten der Mischkörper aus Isotropen Substanzen: *Ann. Phys. (Leipzig)*, **24**, 636–679.
- Budiansky, B., 1965, On the elastic moduli of some heterogeneous materials: *J. Mech. Phys. Solids* **13**, 223–227.
- Cherkaev, A. V., 2000, *Variational Methods for Structural Optimization*, Springer-Verlag, New York, pp. 171–212.
- Christensen, R. M., 1979, *Mechanics of Composite Materials*, Wiley Interscience, New York, pp. 31–72.
- Christensen, R. M., 1990, A critical evaluation for a class of micromechanics models: *J. Mech. Phys. Solids* **38**, 379–404.
- Cleary, M. P., I.-W. Chen, and S.-M. Lee, 1980, Self-consistent techniques for heterogeneous media: *ASCE J. Eng. Mech.*, **106**, 861–887.
- Ferrari, M., and M. Filiponni, 1991, Appraisal of current homogenizing techniques for the elastic response of porous and reinforced glass: *J. Am. Ceramic Soc.*, **74**, 229–231.
- Garboczi, E. J., and J. G. Berryman, 2000, New effective medium theory for the diffusivity or conductivity of a multi-scale concrete microstructure model: *Concrete Science and Engineering* **2**, 88–96.
- Garboczi, E. J., and J. G. Berryman, 2001, New differential effective medium theory for the linear elastic moduli of a material containing composite inclusions: *Mech. Materials* **33**, 455–470.
- Gibiansky, L. V., and G. W. Milton, 1993, On the effective viscoelastic moduli of two-phase media. I. Rigorous bounds on the complex bulk modulus: *Proc. Roy. Soc. London A*, **440**, 163–188.
- Gibiansky, L. V., G. W. Milton, and J. G. Berryman, 1999, On the effective viscoelastic moduli of two-phase media. III. Rigorous bounds on the complex shear modulus in two dimensions: *Proc. Roy. Soc. London A*, **455**, 2117–2149.
- Gibiansky, L. V., and S. Torquato, 1995, Rigorous link between the conductivity and elastic moduli of fibre-reinforced composite materials: *Phil. Trans. R. Soc. A: Physical Sciences and Engineering*, **353**, 243–278.
- Gubernatis, J. E., and J. A. Krumhansl, 1975, Macroscopic engineering properties of polycrystalline materials: Elastic properties: *J. Appl. Phys.*, **46**, 1875–1883.
- Guéguen, Y., and V. Palciaukas, 1994, *Introduction to the Physics of Rocks*, Princeton University Press, Princeton, New Jersey, pp. 193–199.

- Hardy, G. H., J. E. Littlewood, and G. Pólya, 1952, *Inequalities*, Cambridge University Press, Cambridge, UK, p. 78.
- Hashin, Z., 1962, The elastic moduli of heterogeneous materials: *J. Appl. Mech.*, **29**, 143–150.
- Hashin, Z., and S. Shtrikman, 1962, A variational approach to the theory of the effective magnetic permeability of multiphase materials: *J. Appl. Phys.*, **33**, 3125–3131.
- Hashin, Z., and S. Shtrikman, 1963a, A variational approach to the theory of the elastic behavior of multiphase materials: *J. Mech. Phys. Solids*, **11**, 127–140.
- Hashin, Z., and S. Shtrikman, 1963b, Conductivity of polycrystals: *Phys. Rev.*, **130**, 129–133.
- Helsing, J., and A. Helte, 1991, Effective conductivity of aggregates of anisotropic grains: *J. Appl. Phys.*, **69**, 3583–3588.
- Hill, R., 1952, Elastic properties of reinforced solids: Some theoretical principles: *Proc. Phys. Soc. London A*, **65**, 349–354.
- Hill, R., 1965, A self-consistent mechanics of composite materials: *J. Mech. Phys. Solids*, **13**, 213–222.
- Kirkpatrick, S., 1971, Classical transport in disordered media: Scaling and effective medium theories: *Phys. Rev. Lett.*, **27**, 1722–1725.
- Kirkpatrick, S., 1973, Percolation and conduction: *Rev. Mod. Phys.*, **45**, 574–588.
- Korringa, J., R. J. S. Brown, D. D. Thompson, and R. J. Runge, 1979, Self-consistent imbedding and the ellipsoidal model for porous rocks: *J. Geophys. Res.*, **84**, 5591–5598.
- Korringa, J., and G. A. LaTorraca, 1986, Application of the Bergman-Milton theory of bounds to the permittivity of rocks: *J. Appl. Phys.*, **60**, 2966–2976.
- Kuster, G. and M. N. Toksöz, 1974, Velocity and attenuation of seismic waves in two-phase media: Part I. Theoretical formulations: *Geophysics*, **39**, 587–606.
- Landauer, R., 1952, The electrical resistance of binary metallic mixtures: *J. Appl. Phys.*, **23**, 779–784.
- McCoy, J. J., 1970, On the displacement field in an elastic medium with random variations of materials properties: in *Recent Advances in Engineering Science*, Proceedings of the Sixth Annual Meeting of the Society of Engineering Science, Princeton University, Princeton, New Jersey, November 11-13, 1968, edited by A. C. Eringen, Gordon and Breach, New York, pp. 235–254.
- Milton, G. W., 1980, Bounds on the complex dielectric constant of a composite material: *Appl. Phys. Lett.*, **37**, 300–303.
- Milton, G. W., 1981a, Bounds on the complex permittivity of a two-component composite material: *J. Appl. Phys.*, **52**, 5286–5293.

- Milton, G. W., 1981b, Bounds on the transport and optical properties of a two-component composite material: *J. Appl. Phys.*, **52**, 5294–5304.
- Milton, G. W., 1981c, Bounds on the electromagnetic, elastic, and other properties of two-component composites: *Phys. Rev. Lett.*, **46**, 542–545.
- Milton, G. W., 1982, Bounds on the elastic and transport properties of two-component composites: *J. Mech. Phys. Solids*, **30**, 177–191.
- Milton, G. W., 1987, Multicomponent composites, electrical networks, and new types of continued fraction. I.: *Commun. Math. Phys.*, **111**, 281–327.
- Milton, G. W., 2002, *The Theory of Composites*, Cambridge University Press, Cambridge, UK, pp. 77–78, 163, 457–498, 580–581.
- Milton, G. W., and J. G. Berryman, 1997, On the effective viscoelastic moduli of two-phase media. II. Rigorous bounds on the complex shear modulus in three dimensions: *Proc. Roy. Soc. London A*, **453**, 1849–1880.
- Milton, G. W., and N. Phan-Thien, 1982, New bounds on effective elastic moduli of two-component materials: *Proc. Roy. Soc. London A*, **380**, 305–331.
- Mura, T., 1987, *Micromechanics of Defects in Solids*, Kluwer Academic Publishers, Dordrecht, The Netherlands.
- Nemat-Nasser, S., and M. Hori, 1993, *Micromechanics: Overall Properties of Heterogeneous Materials*, North-Holland, Amsterdam, pp. 325–388.
- Norris, A. N., 1985, A differential scheme for the effective moduli of composites: *Mech. Mater.*, **4**, 1–16.
- Norris, A. N., 1989, An examination of the Mori-Tanaka effective medium approximation for multiphase composites: *ASME J. App. Mech.*, **56**, 83–88.
- Olson, T., and M. Avellaneda, 1992, Effective dielectric and elastic constants of piezoelectric polycrystals: *J. Appl. Phys.*, **71**, 4455–4464.
- Peselnick, L., and R. Meister, 1965, Variational method of determining effective moduli of polycrystals: (A) Hexagonal symmetry, (B) trigonal symmetry: *J. Appl. Phys.*, **36**, 2879–2884.
- Prager, S., 1969, Improved variational bounds on some bulk properties of a two-phase random medium: *J. Chem. Phys.*, **50**, 4305–4312.
- Reuss, A., 1929, Berechnung der Fließgrenze von Mischkristallen auf Grund der Plastizitätsbedingung für Einkristalle: *Z. Angew. Math. Mech.*, **9**, 49–58.
- Schulgasser, K., 1983, Sphere assemblage model for polycrystals and symmetric materials: *J. Appl. Phys.*, **54**, 1380–1382.

- Silnutzer, N. R., 1972, *Effective Constants of Statistically Homogeneous Materials*, Ph. D. thesis, University of Pennsylvania.
- Simmons, G., and H. F. Wang, 1971, *Single Crystal Elastic Constants and Calculated Aggregate Properties: A Handbook*, MIT Press, Cambridge, Massachusetts, pp. 1–300.
- Stroud, D., G. W. Milton, and B. R. De, 1986, Analytical model for the dielectric response of brine-saturated rocks: *Phys. Rev. B*, **34**, 5145–5153.
- Thomsen, L., 1972, Elasticity of polycrystals and rocks: *J. Geophys. Res.*, **77**, 315–327.
- Torquato, S., 1980, *Microscopic Approach to Transport in Two-Phase Random Media*, Ph. D. thesis, State University of New York at Stony Brook.
- Torquato, S., 1985a, Effective electrical conductivity of two-phase disordered composite media: *J. Appl. Phys.*, **58**, 3790–3797.
- Torquato, S., 1985b, Bulk properties of two-phase disordered media. V. Effective conductivity of a dilute dispersion of penetrable spheres: *J. Chem. Phys.*, **83**, 4776–4785.
- Torquato, S., 2002, *Random Heterogeneous Materials: Microstructure and Macroscopic Properties*, Springer, New York, pp. 422–423, 598.
- Torquato, S., and G. Stell, 1982, Microstructure of two-phase random media. I. The n -point probability functions: *J. Chem. Phys.*, **77**, 2071–2077.
- Torquato, S., S. Hyun, and A. Donev, 2003, Optimal design of manufacturable three-dimensional composites with multifunctional characteristics: *J. Appl. Phys.*, **94**, 5748–5755.
- Voigt, W., 1928, *Lehrbuch der Kristallphysik*, Teubner, Leipzig.
- Walpole, L. J., 1969, On the overall elastic moduli of composite materials: *J. Mech. Phys. Solids*, **17**, 235–251.
- Watt, J. P., G. F. Davies, and R. J. O’Connell, 1976, The elastic properties of composite materials: *Rev. Geophys. Space Phys.*, **14**, 541–563.
- Watt, J. P., and L. Peselnick, 1980, Clarification of the Hashin-Shtrikman bounds on the effective elastic moduli of polycrystals with hexagonal, trigonal, and tetragonal symmetries: *J. Appl. Phys.*, **51**, 1525–1531.
- Wiener, O., 1912, Die Theorie des Mischkörpers für das Feld des stationären Strömung. Erste Abhandlung die Mittelswertsätze für Kraft, Polarisation und Energie: *Abhandlungen der mathematischphysischen Klasse der Königlich Sächsischen Gesellschaft der Wissenschaften*, **32**, 509–604.
- Wildenschild, D., J. J. Roberts, and E. D. Carlberg, 2000, On the relationship between microstructure and electrical and hydraulic properties of sand-clay mixtures: *Geophys. Res. Lett.*, **27**, 3065–3068.

Willis, J. R., 1981, Variational and related methods for the overall properties of composites: in *Advances in Applied Mechanics*, edited by C.-S. Yih, Academic Press, New York, pp. 1-78.

Geomechanical constants of heterogeneous reservoirs: pore fluid effects on shear modulus

James G. Berryman¹

ABSTRACT

To provide quantitative measures of the importance of fluid effects on shear waves in the heterogeneous reservoirs, a model material called a “random polycrystal of porous laminates” is introduced. This model poroelastic material has constituent grains that are layered (or laminated), and each layer is an isotropic, microhomogeneous porous medium. All grains are composed of exactly the same porous constituents, and have the same relative volume fractions. But the order of lamination is not important because the up-scaling method used to determine the transversely isotropic (hexagonal) properties of the grains is Backus averaging, which — for quasi-static or long-wavelength behavior — depends only on the volume fractions and layer properties. Grains are then jumbled together totally at random, filling the reservoir, and producing an overall isotropic poroelastic medium. The poroelastic behavior of this medium is then analyzed using the Peselnick-Meister-Watt bounds (of Hashin-Shtrikman type). We study the dependence of the shear modulus on pore fluid properties and determine the expected range of behavior. In particular we compare and contrast these results with those anticipated from Gassmann’s fluid substitution formulas, and to the predictions of Mavko and Jizba for very low porosity rocks with flat cracks. This approach also permits the study of arbitrary numbers of constituents, but for simplicity the numerical examples are restricted here to just two constituents. This restriction also permits the use of some special exact results available for computing the overall effective stress coefficient in any two-component porous medium. The bounds making use of polycrystalline microstructure are very tight. Results for shear modulus demonstrate that the ratio of compliance differences R (*i.e.*, shear compliance changes over bulk compliance changes) is usually nonzero and can take a wide range of values, both above and below the value $R = 4/15$ for low porosity, very low aspect ratio flat cracks. Results show the overall shear modulus in this model can depend relatively strongly on mechanical properties of the pore fluids, sometimes (but rarely) more strongly than the dependence of the overall bulk modulus on the fluids.

¹email: berryman@sep.stanford.edu

INTRODUCTION

Heterogeneity of the earth plays a significant role in determining geophysical and geomechanical constants such as the bulk and shear moduli and the elastic and/or poroelastic wave speeds. The heterogeneities of importance may be due to fine layering (Postma, 1955; Backus, 1962) [layers being thin compared to seismic wavelength], due to partial or patchy saturation of pore fluids (White, 1975; Knight and Nolen-Hoeksema, 1990; Dvorkin *et al.*, 1999; Johnson, 2001; Li *et al.*, 2001), due to random positioning of joints and fractures (Berryman and Wang, 1995; Pride and Berryman, 2003; Pride *et al.*, 2004), due to anisotropic stress distribution, etc. There have been many attempts to attack all of these problems, and the up-scaling methods employed have ranged from *ad hoc* to mathematically rigorous, and have had varying degrees of success in modeling field and laboratory data.

One of the main purposes of the present paper is to introduce a semi-analytical model of the earth, and especially of fluid-bearing earth reservoirs, that provides well-controlled estimates of the properties of most interest such as elastic/poroelastic constants, fluid permeability, etc. The concept is based on “random polycrystals of porous laminates.” Locally layered regions are treated as laminates and the poroelastic and other constants can be computed essentially exactly (*i.e.*, within the assumed long wavelength limit and perfect layering of the laminate model) using Backus (1962) averaging for poroelastic constants (and similar methods for other parameters), in the long-wavelength or quasi-static limits. Then, since such layered materials are typically anisotropic (having hexagonal symmetry when the layers are isotropic), I assume that the earth is composed of a statistically isotropic jumble of such layered regions. The locally layered, anisotropic regions may be termed “grains” or “crystals.” Then, the overall behavior of this system can be determined/estimated using another method from the theory of composites: the well-known Hashin-Shtrikman bounds (Hashin and Shtrikman, 1962). In this case the bounds of interest for the types of crystal symmetry that arise are those first obtained by Peselnick and Meister (1965) and later refined by Watt and Peselnick (1980). These bounds have been refined further recently by the author (Berryman, 2004b; 2005). In particular, these recent refinements provide sufficient insight into the resulting equations that self-consistent estimates (lying between the rigorous bounds) of the elastic constants can be formulated and very easily computed. I find that the Peselnick-Meister-Watt upper and lower bounds are already quite close together for this model material, so the resulting self-consistent estimates are very well constrained. The bounds then serve as error bars on the self-consistent model estimates.

The method being introduced can be applied to a wide variety of difficult technical issues concerning geomechanical constants of earth reservoirs. The one issue that will be addressed at length here is the question of how shear moduli in fully saturated, partially saturated, and/or patchy saturated porous earth may or may not depend on mechanical properties of the pore fluids. The well-known fluid substitution formulas of Gassmann (1951) [also see Berryman (1999)] show that — for isotropic, microhomogeneous (single solid constituent) porous media — the undrained bulk modulus depends strongly on a pore-liquid’s bulk modulus, but the undrained shear modulus is not at all affected by changes in the pore-liquid modulus. Since the system we are considering violates Gassmann’s microhomogeneity constraint as well as

the the isotropy constraint in the vicinity of layer interfaces, I expect that the shear modulus will in fact depend on the fluid properties in this model (Mavko and Jizba, 1991; Berryman and Wang, 2001; Berryman *et al.*, 2002b). The semi-analytical model presented here allows me to explore this issue in some detail, to show that overall shear modulus does depend on pore-fluid mechanics, and to quantify these effects.

The next section introduces the basic tools used later in the layer analysis. The third section reviews the Peselnick-Meister-Watt bounds and presents the new formulation of them. The fourth section summarizes the results needed from poroelastic analysis. The fifth section presents the main new results of the paper, including four distinct scenarios that help elucidate the behavior of the overall shear modulus and compare it to that of the bulk modulus. The final section summarizes our conclusions. Appendix A provides a brief proof of one of the results used in the text concerning the behavior of the effective stress coefficient for patchy saturation. Appendix B shows that Hill's equation should be used cautiously in analysis of heterogeneous reservoirs.

ELASTICITY OF LAYERED MATERIALS

We assume that a typical building block of the random system is a small grain of laminate material whose elastic response for such a transversely isotropic (hexagonal) system can be described locally by:

$$\begin{pmatrix} \sigma_{11} \\ \sigma_{22} \\ \sigma_{33} \\ \sigma_{23} \\ \sigma_{31} \\ \sigma_{12} \end{pmatrix} = \begin{pmatrix} c_{11} & c_{12} & c_{13} & & & \\ c_{12} & c_{11} & c_{13} & & & \\ c_{13} & c_{13} & c_{33} & & & \\ & & & 2c_{44} & & \\ & & & & 2c_{44} & \\ & & & & & 2c_{66} \end{pmatrix} \begin{pmatrix} e_{11} \\ e_{22} \\ e_{33} \\ e_{23} \\ e_{31} \\ e_{12} \end{pmatrix}, \quad (1)$$

where σ_{ij} are the usual stress components for $i, j = 1 - 3$ in Cartesian coordinates, with 3 (or z) being the axis of symmetry (the lamination direction for such a layered material). Displacement u_i is then related to strain component e_{ij} by $e_{ij} = (\partial u_i / \partial x_j + \partial u_j / \partial x_i) / 2$. This choice of definition introduces some convenient factors of two into the 44, 55, 66 components of the stiffness matrix shown in (1).

For definiteness we also assume that this stiffness matrix in (1) arises from the lamination of N isotropic constituents having bulk and shear moduli K_n, μ_n , in the $N > 1$ layers present in each building block. It is important that the thicknesses d_n always be in the same proportion in each of these laminated blocks, so that $f_n = d_n / \sum_n d_n$. But the order in which layers were added to the blocks is unimportant, as Backus's formulas (Backus, 1962) for the constants show. For the overall behavior for the quasistatic (long wavelength) behavior of the system we are studying, Backus's results [also see Postma (1955), Berryman (1998, 2004a,b), Milton

(2002)] state that

$$\begin{aligned} c_{33} &= \left\langle \frac{1}{K+4\mu/3} \right\rangle^{-1}, & c_{13} &= c_{33} \left\langle \frac{K-2\mu/3}{K+4\mu/3} \right\rangle, \\ c_{44} &= \left\langle \frac{1}{\mu} \right\rangle^{-1}, & c_{66} &= \langle \mu \rangle, \\ c_{11} &= \frac{c_{13}^2}{c_{33}} + 4c_{66} - 4 \left\langle \frac{\mu^2}{K+4\mu/3} \right\rangle, & c_{12} &= c_{11} - 2c_{66}. \end{aligned} \quad (2)$$

This bracket notation can be correctly viewed: (a) as a volume average, (b) as a line integral along the symmetry axis x_3 , or (c) as a weighted summation $\langle Q \rangle = \sum_n f_n Q_n$ over any relevant physical quantity Q taking a constant value Q_n in the n -th layer.

The bulk modulus for each laminated grain is that given by the compressional Reuss average K_R of the corresponding compliance matrix s_{ij} [the inverse of the usual stiffness matrix c_{ij} , whose nonzero components are shown in (1)]. The well-known result is given by $e = e_{11} + e_{22} + e_{33} = \sigma/K_{\text{eff}}$, where $1/K_{\text{eff}} = 1/K_R = 2s_{11} + 2s_{12} + 4s_{13} + s_{33}$. When $\mu_n = \mu$ is constant in a layered grain, the definition of K_R implies Hill's equation (Hill, 1963, 1964; Milton, 2002), which is given by

$$K^* = \left[\sum_{n=1}^N \frac{f_n}{K_n + 4\mu/3} \right]^{-1} - 4\mu/3. \quad (3)$$

Here the bulk modulus of the n -th constituent is K_n , the shear modulus takes the same value $\mu_n = \mu$ for all $n = 1, \dots, N$, and the overall effective bulk modulus is K^* . The volume fractions f_n are all nonnegative, and sum to unity.

Even though $K_{\text{eff}} = K_R$ is the same for every grain, since the grains themselves are not isotropic, the overall bulk modulus K^* of the random polycrystal does not necessarily have the same value as K_R for the individual grains (Hill, 1952). Hashin-Shtrikman bounds on K^* for random polycrystals whose grains have hexagonal symmetry (Peselnick and Meister, 1965; Watt and Peselnick, 1980) show in fact that the K_R value lies outside the bounds in many situations (Berryman, 2004b).

BOUNDS ON ELASTIC CONSTANTS FOR RANDOM POLYCRYSTALS

Voigt and Reuss Bounds

For hexagonal symmetry, the nonzero stiffness constants are: $c_{11}, c_{12}, c_{13} = c_{23}, c_{33}, c_{44} = c_{55}$, and $c_{66} = (c_{11} - c_{12})/2$.

The Voigt average (Voigt, 1928) for bulk modulus of hexagonal systems is well-known to be

$$K_V = [2(c_{11} + c_{12}) + 4c_{13} + c_{33}]/9. \quad (4)$$

Similarly, for the shear modulus we have

$$\mu_V = \frac{1}{5} (G_{\text{eff}}^v + 2c_{44} + 2c_{66}), \quad (5)$$

where the new term appearing here is essentially defined by (5) and given explicitly by

$$G_{\text{eff}}^v = (c_{11} + c_{33} - 2c_{13} - c_{66})/3. \quad (6)$$

The quantity G_{eff}^v is the energy per unit volume in a grain when a pure uniaxial shear *strain* of unit magnitude [*i.e.*, $(e_{11}, e_{22}, e_{33}) = (1, 1, -2)/\sqrt{6}$], whose main compressive strain is applied to the grain along its axis of symmetry (Berryman, 2004a,b).

The Reuss average (Reuss, 1929) K_R for bulk modulus can also be written in terms of stiffness coefficients as

$$\frac{1}{K_R - c_{13}} = \frac{1}{c_{11} - c_{66} - c_{13}} + \frac{1}{c_{33} - c_{13}}. \quad (7)$$

The Reuss average for shear is

$$\mu_R = \left[\frac{1}{5} \left(\frac{1}{G_{\text{eff}}^r} + \frac{2}{c_{44}} + \frac{2}{c_{66}} \right) \right]^{-1}, \quad (8)$$

which again may be taken as the definition of G_{eff}^r – *i.e.*, the energy per unit volume in a grain when a pure uniaxial shear *stress* of unit magnitude [*i.e.*, $(\sigma_{11}, \sigma_{22}, \sigma_{33}) = (1, 1, -2)/\sqrt{6}$], whose main compressive pressure is applied to a grain along its axis of symmetry.

For each grain having hexagonal symmetry, two product formulas hold (Berryman, 2004a): $3K_R G_{\text{eff}}^v = 3K_V G_{\text{eff}}^r = \omega_+ \omega_- / 2 = c_{33}(c_{11} - c_{66}) - c_{13}^2$. The symbols ω_{\pm} stand for the quasi-compressional and quasi-uniaxial-shear eigenvalues for the crystalline grains. Thus, it follows that

$$G_{\text{eff}}^r = K_R G_{\text{eff}}^v / K_V \quad (9)$$

is a general formula, valid for hexagonal symmetry. We can choose to treat (5) and (8) as the fundamental defining equations for G_{eff}^v and G_{eff}^r , respectively. Equivalently, we can use (9) as the definition of G_{eff}^r .

Hashin-Shtrikman Bounds

It has been shown elsewhere (Berryman, 2004a,b) that the Peselnick-Meister-Watt bounds for bulk modulus of a random polycrystal composed of hexagonal (or transversely isotropic) grains are given by

$$K_{PM}^{\pm} = \frac{K_V(G_{\text{eff}}^r + \zeta_{\pm})}{(G_{\text{eff}}^v + \zeta_{\pm})} = \frac{K_R G_{\text{eff}}^v + K_V \zeta_{\pm}}{G_{\text{eff}}^v + \zeta_{\pm}}, \quad (10)$$

where G_{eff}^v (G_{eff}^v) is the uniaxial shear energy per unit volume for a unit applied shear strain (stress). The second equality follows directly from the product formula (9). Parameters ζ_{\pm} are defined by

$$\zeta_{\pm} = \frac{G_{\pm}}{6} \left(\frac{9K_{\pm} + 8G_{\pm}}{K_{\pm} + 2G_{\pm}} \right). \quad (11)$$

In (11), values of G_{\pm} (shear moduli of isotropic comparison materials) are determined by inequalities

$$0 \leq G_{-} \leq \min(c_{44}, G_{\text{eff}}^r, c_{66}), \quad (12)$$

and

$$\max(c_{44}, G_{\text{eff}}^v, c_{66}) \leq G_{+} \leq \infty. \quad (13)$$

The values of K_{\pm} (bulk moduli of isotropic comparison materials) are then determined by equalities

$$K_{\pm} = \frac{K_V(G_{\text{eff}}^r - G_{\pm})}{(G_{\text{eff}}^v - G_{\pm})}, \quad (14)$$

given by Peselnick and Meister (1965) and Watt and Peselnick (1980). Also see Berryman, 2004b).

Bounds on the shear moduli are then given by

$$\frac{1}{\mu_{\text{hex}}^{\pm} + \zeta_{\pm}} = \frac{1}{5} \left[\frac{1 - \gamma_{\pm}(K_V - K_{\pm})}{G_{\text{eff}}^v + \zeta_{\pm} + \delta_{\pm}(K_V - K_{\pm})} + \frac{2}{c_{44} + \zeta_{\pm}} + \frac{2}{c_{66} + \zeta_{\pm}} \right], \quad (15)$$

where γ_{\pm} and δ_{\pm} are given by

$$\gamma_{\pm} = \frac{-1}{K_{\pm} + 4G_{\pm}/3} \quad \text{and} \quad \delta_{\pm} = \left[\frac{4}{15} - \frac{2}{5G_{\pm}\gamma_{\pm}} \right]^{-1}. \quad (16)$$

K_V is the Voigt average of the bulk modulus as defined previously.

POROELASTICITY ESTIMATES AND BOUNDS

My main focus here will be the extension of earlier work in elasticity to the case of locally layered poroelastic media (Wang, 2000; Coussy, 2004), where the laminated grains (or crystals) are formed by sequential layering of N porous isotropic layers. Although these grains each have the same quasi-static anisotropic elastic behavior, they do not necessarily have the same shapes or the same orientations of their crystal symmetry axes. Specifically, we want to study the case of isotropic random polycrystals, wherein the individuals can and do take on all possible orientations of their symmetry axes (equiaxed, statistically isotropic polycrystals) so that the overall composite polycrystal has isotropic behavior at the macroscopic level. Furthermore, in some applications, the pores of some grain layers may be filled with different fluids (heterogeneous saturation conditions) than those in other layers. This model may or may not be a realistic one for any given fluid-bearing reservoir whose geomechanics we need to model. My first goal is arrive at a model for which many of the available modern tools of elastic and poroelastic analysis apply, including Hashin-Shtrikman bounds for a reservoir having isotropic constituents (Hashin and Shtrikman, 1962a,b,c; 1963a,b), Peselnick-Meister-Watt bounds for

random polycrystals (Peselnick and Meister, 1965; Watt and Peselnick, 1980), certain exact relationships known for two-component poroelastic media (Berryman and Milton, 1991), and — whenever appropriate — self-consistent or other effective medium estimates of both elastic constants and conductivities (electrical, thermal, and hydraulic). By constructing such a model material, we expect to be able to make estimates of the behavior of the system and at the same time be able to predict the range of variation likely to be observed around these estimates, as well as identifying what material and microgeometry properties control those variations. My further goal is to be able to make fairly precise statements about this model that are then useful to our (both mine and the reader's) intuition and to quantify how much is really known about these complex systems. In particular, the hope is to identify assumptions currently and commonly used in the literature without much apparent justification and to provide a means of either verifying or falsifying these assumptions in the context of this model — if that proves to be possible.

Two distinct results that will be required from poroelasticity theory are: (a) Gassmann's equations and (b) certain relationships that determine the overall effective stress coefficient of a composite poroelastic medium when it is composed of two porous materials satisfying Gassmann's assumptions. Gassmann's results (Gassmann, 1951; Berryman, 1999; Wang, 2000) for the undrained bulk (K) and shear (μ) moduli of microhomogeneous (one solid constituent) porous media are:

$$K_u = K_d + \frac{\alpha^2}{(\alpha - \phi)/K_m + \phi/K_f} = \frac{K_d}{1 - \alpha B} \quad (17)$$

and

$$\mu_u = \mu_d. \quad (18)$$

Here, K_u and μ_u are the undrained (pore fluid trapped) constants, while K_d and μ_d are the drained (pore fluid untrapped) constants. Porosity (void volume fraction) is ϕ . Grain bulk and shear moduli of the sole mineral constituent are K_m and μ_m . The bulk modulus of the pore fluid is K_f . The factor α is the Biot-Willis (Biot and Willis, 1957) or volume effective stress coefficient (Nur and Byerlee, 1971; Berryman, 1992; Gurevich, 2004), related to K_m and K_d within each layer by

$$\alpha^{(n)} = 1 - K_d^{(n)}/K_m^{(n)}. \quad (19)$$

Skempton's coefficient (Skempton, 1954) is B in (17).

Although my presentation is based on quasi-static results, my ultimate interest is often applications to seismic wave propagation. In such circumstances a slightly different terminology is used by some authors (Mavko and Jizba, 1991). In particular, for high frequency wave propagation, fluid may be effectively trapped in the pores as it is unable to equilibrate through pore-pressure diffusion on the time scale of wave passage. In this case, the term "unrelaxed" is sometimes used instead of "undrained." We will not make any further issue of this distinction here and stick to the single term "undrained" for both types of applications.

For a porous medium composed of only two constituent porous media, each of which is microhomogeneous and obeys Gassmann's equations, the exact relation (Berryman and

Milton, 1991) that determines the overall effective stress coefficient α^* – assuming only that the constituents are in welded contact (volume fractions and spatial distribution of constituents do not directly affect the result) – is:

$$\frac{\alpha^* - \alpha^{(1)}}{\alpha^{(2)} - \alpha^{(1)}} = \frac{K_d^* - K_d^{(1)}}{K_d^{(2)} - K_d^{(1)}}. \quad (20)$$

Here K_d^* is the overall drained bulk modulus of the composite system, and the superscripts (1) and (2) reference the two distinct components in the composite porous medium.

FOUR SCENARIOS

We now consider four scenarios of progressively greater complexity. For the first pair we assume the mineral K_m and drained K_d bulk moduli of all layers are uniform, and therefore that the effective stress coefficient ($\alpha = 1 - K_d/K_m$) is the same in each layer. Furthermore, the overall volume effective stress coefficient is also the same [a fact that follows from (20)]. Although specific in many respects, this model still permits some flexibility in the choice of pore fluids and their spatial distribution. The other main freedom we have left is to assume that each layer's shear modulus is as sensitive or more sensitive than its bulk modulus to irregularities in the pore space (Makse *et al.*, 1999). So, the shear modulus can vary significantly from layer to layer, which will be important to our main discussion. The second pair of scenarios allow the bulk modulus to vary in the layers, and again study both uniform and patchy pore-fluid saturation.

Constant Drained Bulk Modulus, Uniform Fluid Saturation

For assumed constant isotropic drained bulk modulus, we have $K_d^* = K_d^{(n)} \equiv K_d$ for all N layers as well as the overall medium, and when $N = 2$ we can prove easily using (20) that $\alpha^* = \alpha^{(1)} = \alpha^{(2)}$. When the fluid is uniform throughout the medium, the undrained bulk moduli also satisfy $K_u^* = K_u^{(n)} \equiv K_u$, since Gassmann's equation depends only on constants that are uniform throughout this model material. Now it has been shown previously (Berryman, 2004b) that when the drained bulk modulus is uniform, a general result for $G_{\text{eff}}^v = G_{\text{eff}}^r$ is

$$G_d^v = \left[\sum_{n=1}^N \frac{f_n}{\mu_n + 3K_d/4} \right]^{-1} - 3K_d/4, \quad (21)$$

f_n being the volume fraction of the layers. This result follows easily from the Backus averages presented in (2) and the formula for G_{eff}^v in (6). In the presence of pore fluid and since each layer is a Gassmann material, the shear moduli of the individual porous layers do not change. So, a second result of the same type is available for the undrained uniaxial shear energy per unit volume G_{eff}^v in this medium:

$$G_u^v = \left[\sum_{n=1}^N \frac{f_n}{\mu_n + 3K_u/4} \right]^{-1} - 3K_u/4, \quad (22)$$

f_n again being the volume fraction of the layers.

Neither of these two shear contributions is the overall modulus. They are just contributions of the uniaxial shear component (within each laminated grain) as defined earlier. However, they can be substituted for the term G_{eff}^v in the Peselnick-Meister-Watt bounds defined by (15). Note that it is easy to show from the forms of (21) and (22) that $c_{44} \leq G_d^v \leq c_{66}$, and similarly that $c_{44} \leq G_u^v \leq c_{66}$. [Furthermore, since $K_d \leq K_u$ and the functionals in (21) and (22) vary monotonically with their arguments K_d and K_u , it is easy to see that $G_d^v \leq G_u^v$.] Thus, from (12) and (13), the best choices for shear moduli of the comparison materials are always given by $G_- = c_{44}$ and $G_+ = c_{66}$ for this particular model material. So $\zeta_{\pm} = (G_{\pm}/6)(9K + 8G_{\pm})/(K + 2G_{\pm})$ in (15), where K takes the values $K = K_d$ for the drained case and $K = K_u$ for the undrained case. In both cases, $K_R = K_V = K$ since the drained bulk modulus is uniform, so the form of the shear modulus bounds in (15) also simplifies to

$$\frac{1}{\mu^{\pm} + \zeta_{\pm}} = \frac{1}{5} \left[\frac{1}{G_{\text{eff}}^v + \zeta_{\pm}} + \frac{2}{c_{44} + \zeta_{\pm}} + \frac{2}{c_{66} + \zeta_{\pm}} \right]. \quad (23)$$

We now have upper and lower bounds on the shear modulus in both drained and undrained circumstances by using the appropriate values of G_{eff}^v and ζ_{\pm} for each case. It is also possible to generate self-consistent estimates (Berryman, 2004b) for these moduli directly from the form of these bounds by instead making the substitutions $\mu^{\pm} \rightarrow \mu^*$ and $\zeta_{\pm} \rightarrow \zeta^* \equiv (\mu^*/6)(9K + 8\mu^*)/(K + 2\mu^*)$. The results of all these formulas are illustrated in Figure 1.

Another important concept in these analyses will be the ratio of compliance differences defined by

$$R \equiv \frac{1/\mu_d^* - 1/\mu_u^*}{1/K_d^* - 1/K_u^*}. \quad (24)$$

This quantity has been defined and discussed previously by Berryman *et al.* (2002b). It is most useful for determining the extent to which an identity derived by Mavko and Jizba (1991) for very low porosity media containing randomly oriented fractures is either satisfied or violated by other types of porous media. For the case studied by Mavko and Jizba (1991), $R \equiv 4/15$. However, it has been shown that for penny-shaped cracks at finite porosities R can be either higher or lower than $4/15$, and furthermore that the factor R tends to zero when the pores approach spherical shapes (aspect ratio $\simeq 1$) [see Goertz and Knight (1998) and Berryman *et al.* (2002b)]. So this ratio is a sensitive measure of the dependence of μ_u^* on the fluid content of a porous medium, and also to some extent on the microgeometry of the pores.

Figure 1 shows that, for most choices of volume fractions, the drained and undrained values of shear modulus bounds do not overlap. Clearly, as the volume fractions approach zero or unity, the system approaches a pure Gassmann system; but, away from these limiting cases, the results are both qualitatively and quantitatively different from Gassmann's predictions. Graphically speaking, it appears that the lower bound of the undrained constant is always greater than the upper bound on the drained constants, *i.e.*, $\mu_u^- > \mu_d^+$. But, when this figure is magnified, we find there are small regions of volume fraction where this inequality is violated slightly. So there is still little doubt that shear modulus is affected by pore fluids in these systems, and for some ranges of volume fraction there is no doubt. This result is a clear indication

that Gassmann's results for shear are not generally valid for this model – as expected. Figure 2 shows that the maximum value of R for this case occurs around $f_2 \simeq 0.2$. Furthermore, the magnitude of this value is about 0.32, and therefore greater than $4/15$. This shows again [as was shown previously by Berryman *et al.* (2002b)] that $R = 4/15$ is also *not* in general an upper bound on R .

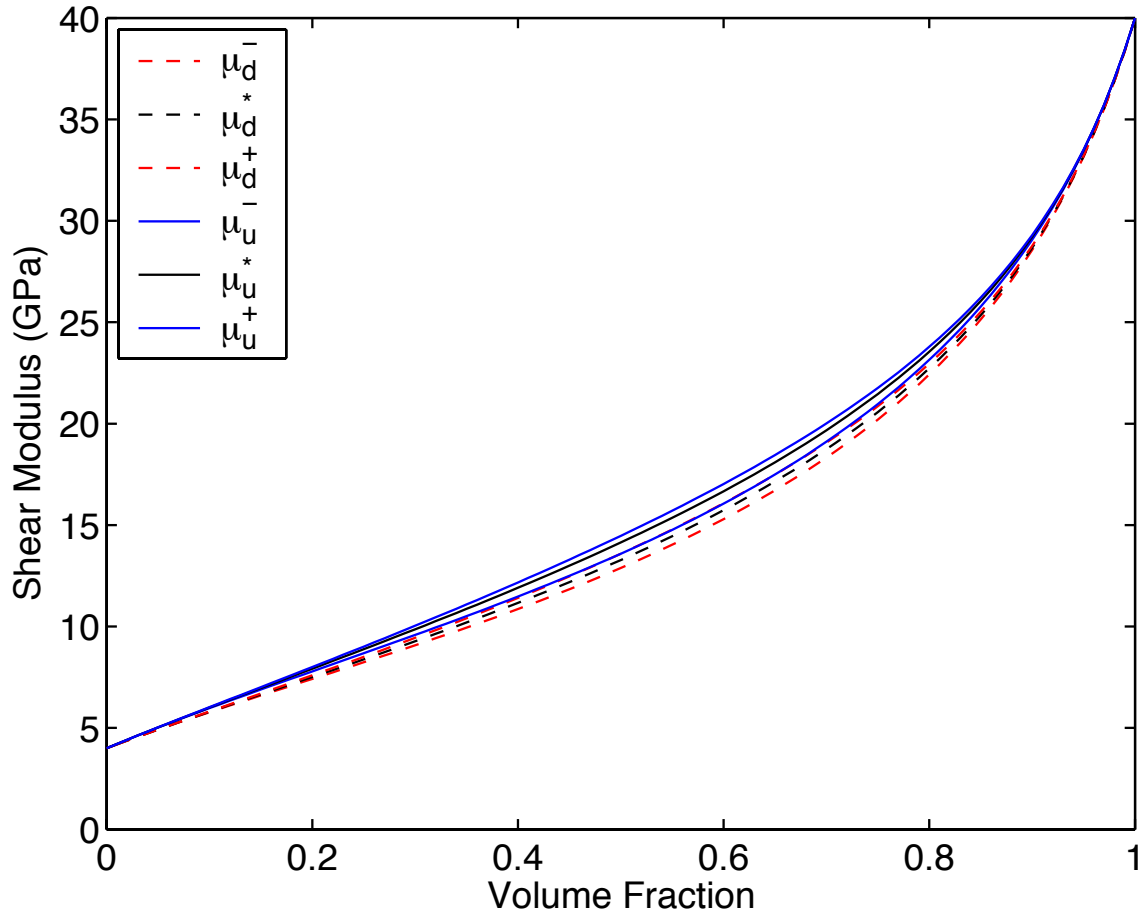


Figure 1: Illustrating the shear modulus results for the random polycrystals of porous laminates model for homogeneous saturation when each grain is composed of two constituents: (1) $K_d^{(1)} = 35.0$ GPa, $\mu_d^{(1)} = 4.0$ GPa and (2) $K_d^{(2)} = 35.0$ GPa, $\mu_d^{(2)} = 40.0$ GPa. Skempton's coefficient is taken to be $B = 0.0$ when the system is gas saturated, and $B = 1.0$ when the system is fully liquid saturated. The effective stress coefficients for the layers are both $\alpha = 0.75$, and $\alpha^* = 0.75$ also. The computed undrained bulk modulus is $K_u = 140$ GPa. Volume fraction of the layers varies from 0 to 100% of constituent number 2. jim2-Fig1 [NR]

Constant Drained Bulk Modulus, Patchy Fluid Saturation

To add one level of complication, consider next the same porous framework as before, but now suppose that the saturation is patchy (White, 1975; Berryman *et al.*, 1998; Norris, 1993;

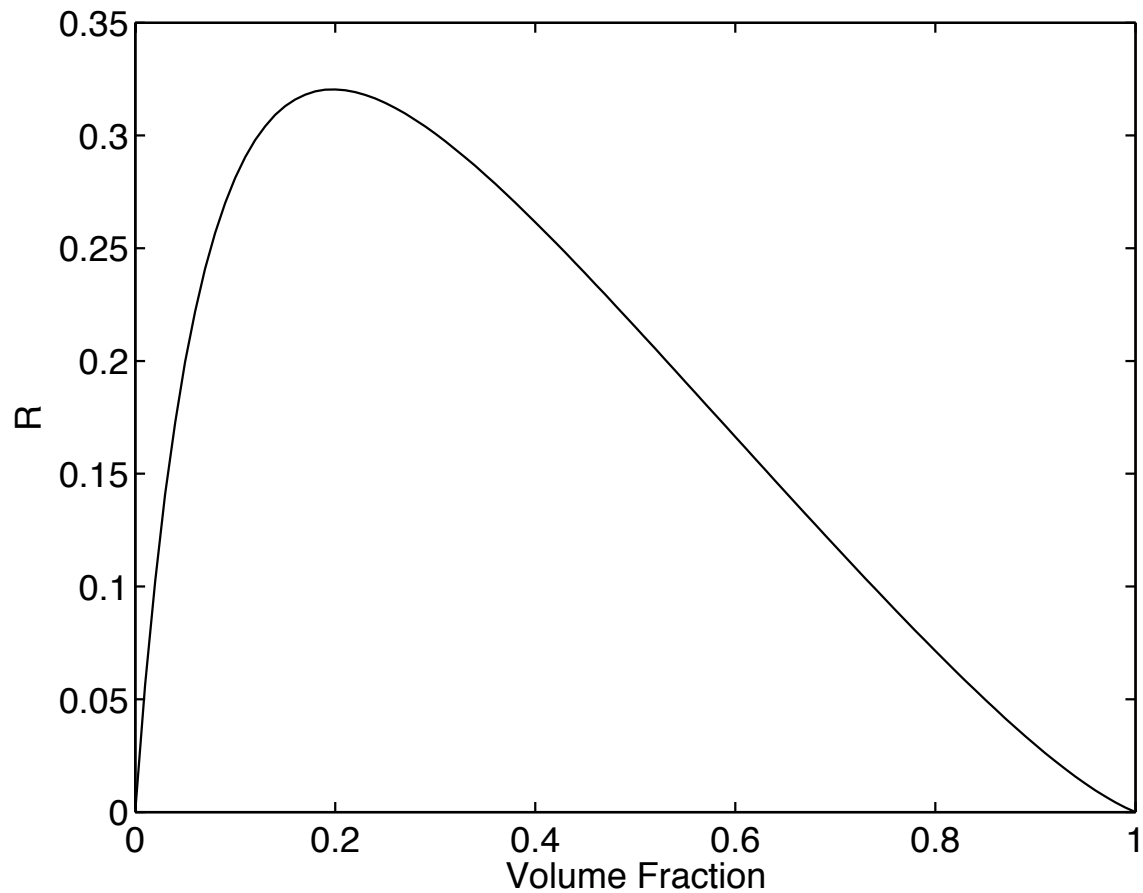


Figure 2: Plot of the ratio R from equation (24), being the ratio of compliance differences due to fluid saturation. These results are for the same model described in Figure 1 for homogeneous saturation. The values of R should be compared to those predicted by Mavko and Jizba (1991) for very low porosity and flat cracks, when $R = 4/15 \simeq 0.267$. We find in contrast that the random polycrystals of porous laminates model for the case considered always has $R \leq 0.32$.

jim2-Fig2 [NR]

Dvorkin *et al.*, 1999; Johnson, 2001; Berryman *et al.*, 2002a), rather than homogeneous. The idea is that some of the layers in the grains will have a liquid saturant having $K_f = K_l$, while others will have a gas saturant having $K_f = K_g$. In general I assume that $K_g \ll K_l$ so that for most purposes the gas saturated parts of the system satisfy $K_u \simeq K_d$, *i.e.*, undrained moduli are to a very good approximation the same as the drained moduli for these layers. If this were not so, then I could treat the second saturant in exactly the same way as I will treat the liquid saturant; but there would be no new ideas required to do this, so I will not stress this approach here.

For this system, the drained constants are all the same as in the preceding example. In particular, the overall volume effective stress coefficient α^* is the same.

The undrained constants differ for this system however because the undrained bulk modulus is not constant in the layers. Gassmann's formula does not provide an answer for this overall bulk modulus because the system is not homogeneous. But Backus averaging determines all the elastic constants in a straightforward way for this system [see Berryman (2004a)]. The correct results are obtained for all the constants related to Voigt and Reuss averages [Eqs. (4)-(9) for both bulk and shear moduli] as long as the K 's shown explicitly in (2) are properly interpreted as the undrained constants K_u from (17) for the fluids having bulk moduli K_l or K_g in the appropriate layers.

One explicit result found useful to quote from some earlier work (Berryman, 2004a) is

$$G_{\text{eff}}^v = c_{66} - \frac{4c_{33}^u}{3} \left[\left\langle \frac{\Delta\mu^2}{K_u + 4\mu/3} \right\rangle \left\langle \frac{1}{K_u + 4\mu/3} \right\rangle - \left\langle \frac{\Delta\mu}{K_u + 4\mu/3} \right\rangle^2 \right], \quad (25)$$

where $c_{33}^u = \langle 1/(K_u + 4\mu/3) \rangle^{-1}$ and the bracket notation has the same meaning as in the Backus formulas (2). The difference $\Delta\mu \equiv \mu - c_{66}$ is the deviation of the layer shear modulus locally from the overall average across all the layers. The term in square brackets in (25) is always non-negative. As K_u in the layers ranges (parametrically) from zero to infinity, the corrections from the square bracket term times the factor $\frac{4c_{33}^u}{3}$ can be shown to decrease from $c_{66} - c_{44}$ to zero. Thus, G_{eff}^v in the layered model ranges for all possible layered poroelastic systems from c_{44} to c_{66} .

Figure 3 shows that the drained bulk modulus does not change with volume fraction, since all the layers have the same drained bulk modulus. The undrained bulk modulus can have some small variations, however, due to variations in the shear modulus, as is shown by the small spread in the bulk modulus bounds. Uncorrelated Hashin-Shtrikman bounds [computed by evaluating (3) at μ 's having the lowest and highest shear modulus values among all those in the layers] are also shown here for comparison purposes. Clearly, the Peselnick-Meister-Watt correlated bounds based on the polycrystals of laminates microstructure are much tighter. Figure 4 shows that the overall shear modulus has only relatively weak dependence (though stronger than that in Figure 3) on patchy saturation when the bulk modulus itself is uniform. Figure 5 shows that shear modulus changes with saturation, while small, are present and not very tightly coupled to the bulk modulus changes (drained to undrained). This observation is seen to be especially significant at the lowest volume fractions of liquid, as the changes in

shear compliance are greater here (by a factor of about 3) than the corresponding changes in the bulk compliance.

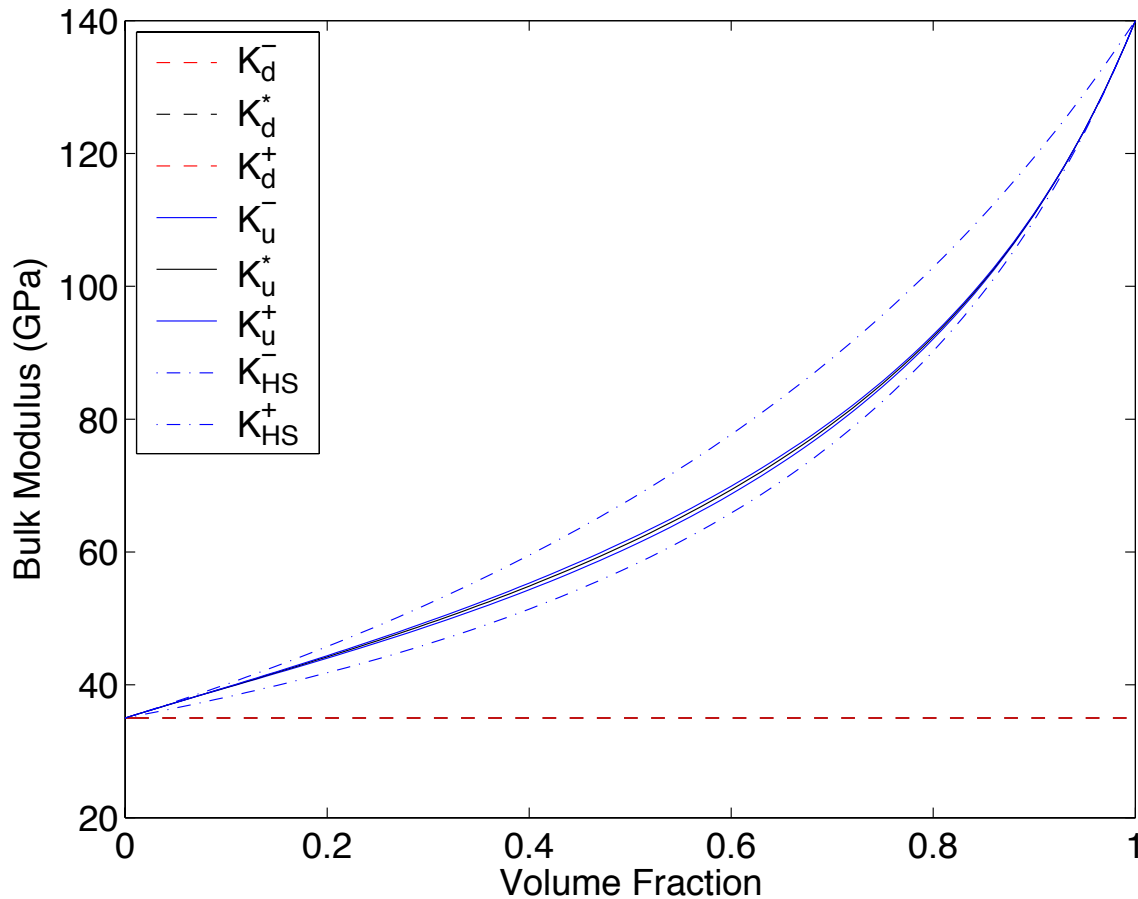


Figure 3: Illustrating the bulk modulus results for the random polycrystals of porous laminates model for patchy saturation when each grain is composed of two constituents: (1) $K_d^{(1)} = 35.0$ GPa, $\mu_d^{(1)} = 4.0$ GPa and (2) $K_d^{(2)} = 35.0$ GPa, $\mu_d^{(2)} = 40.0$ GPa. Skempton's coefficient is taken to be $B = 0.0$ for constituent 1 (gas saturated), and $B = 1.0$ for constituent 2 (liquid saturated). The effective stress coefficients for the layers are both given by $\alpha = 0.75$, so $\alpha^* = 0.75$ also. Porosity does not play a direct role in the calculation when we are using B as the fluid substitution parameter. Volume fraction of the layers varies from 0 to 100% of constituent number 2. To emphasize the tightness of the polycrystal (correlated) bounds, uncorrelated Hashin-Shtrikman bounds K_{HS}^{\pm} on the undrained bulk modulus are also shown. jim2-Fig3
[NR]

Two Distinct Gassmann Materials, Uniform Fluid Saturation

This example and the next one will remove the restriction that the porous frame material is uniform. To have as much control as possible, we limit the heterogeneity to just two types of drained bulk moduli, $K_d^{(1)}$ and $K_d^{(2)}$. These occur with a frequency measured by the volume

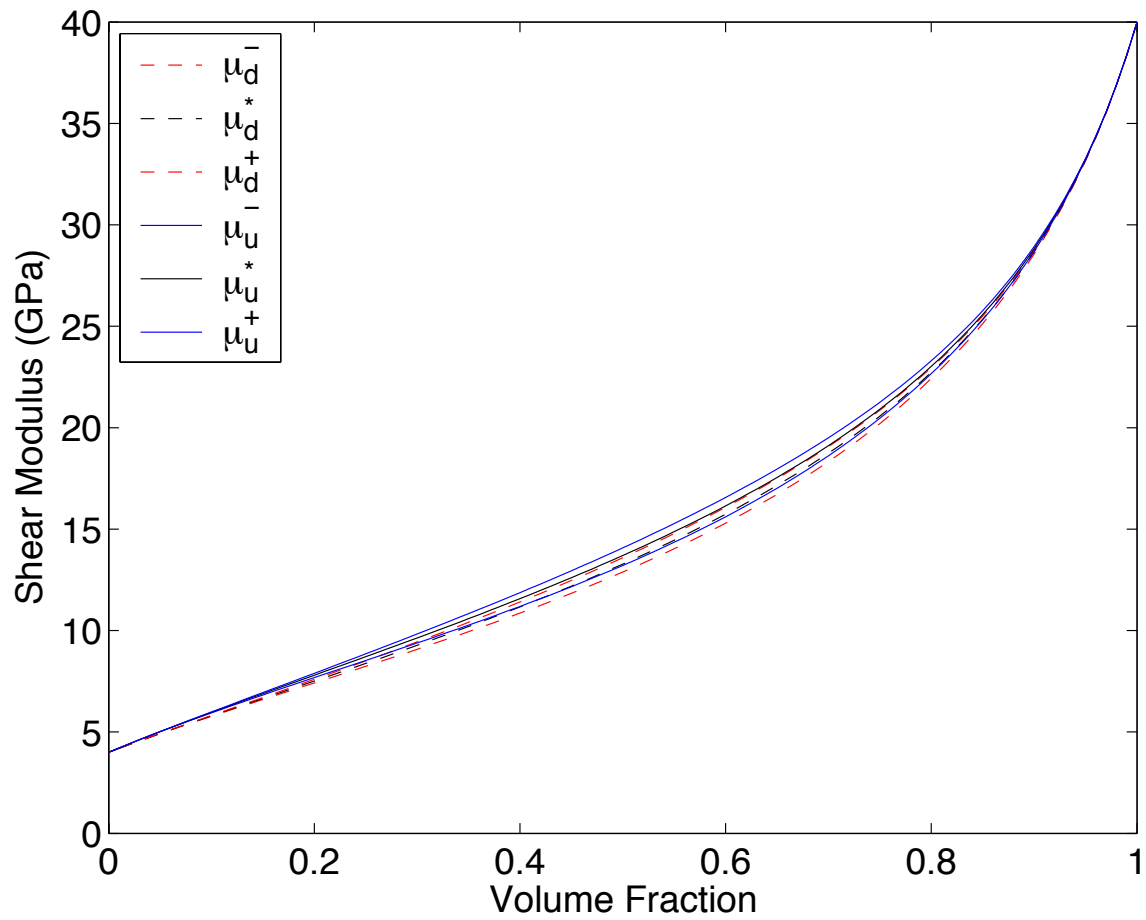


Figure 4: Illustrating the shear modulus results for the random polycrystals of porous laminates model. Model parameters are the same as in Figure 3 for patchy saturation. [jim2-Fig4](#) [NR]

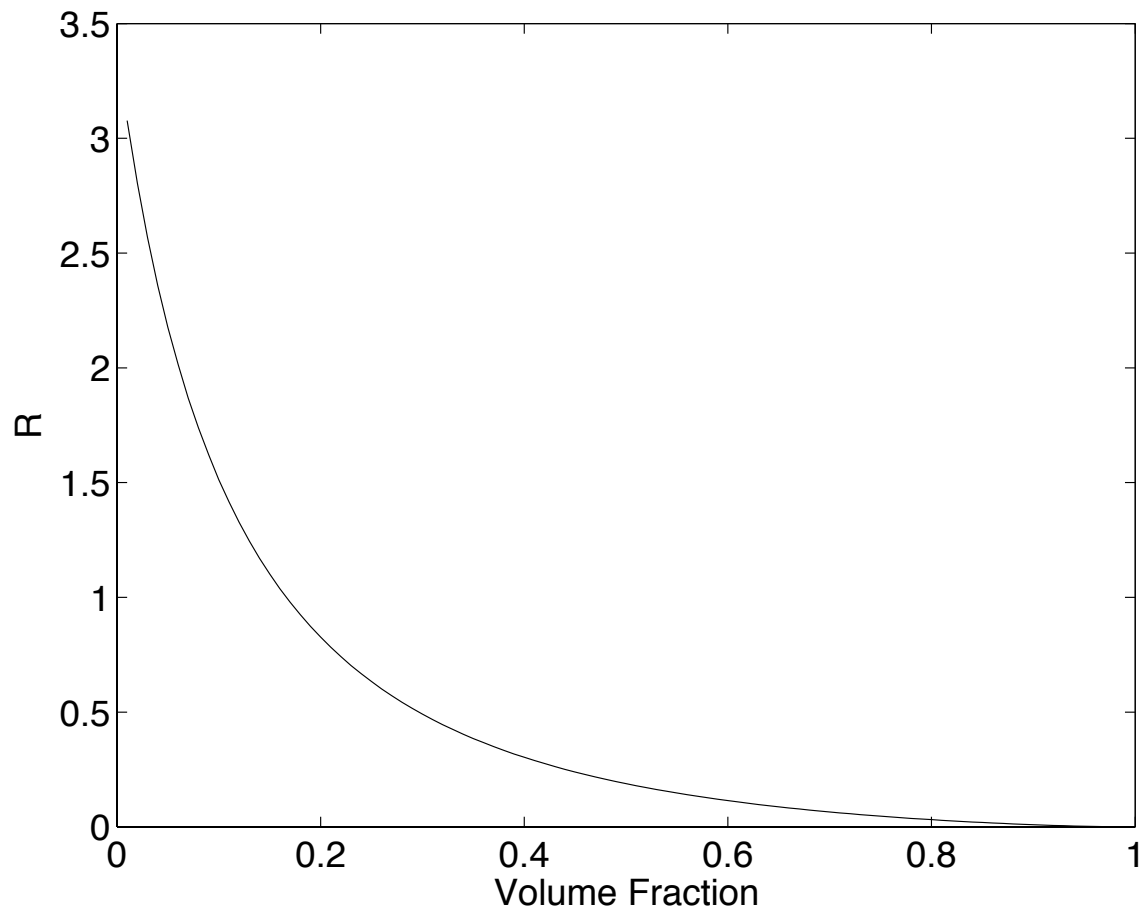


Figure 5: Plot of the ratio R from equation (24), being the ratio of compliance differences due to fluid saturation. These results are for the same model described in Figure 3 for patchy saturation. The values of R should be compared to those predicted by Mavko and Jizba (1991) for very low porosity and flat cracks, when $R = 4/15 \simeq 0.267$. We find in contrast that, for partial and patchy saturation, R can take any positive value, or zero. jim2-Fig5 [NR]

fractions f_1 and f_2 , respectively. These porous materials fill the space, so $f_1 + f_2 = 1$. The effective stress coefficient is known exactly for this model and is given by (20). This result is true both for homogeneously saturated two-component media (Berryman and Milton, 1991) as treated in this example, or for the type of patchy saturation treated in the next example. Proof of this statement is provided in Appendix A. For Gassmann's equations in each material, we also need either the fluid bulk modulus together with the layer porosities $\phi^{(1)}$ and $\phi^{(2)}$, or we just need the Skempton coefficient, B . For simplicity, we take $B = 0.0$ for uniform gas saturation, and $B = 1.0$ for uniform liquid saturation. (Although $B = 1$ may not be exactly correct for real liquid-saturated reservoirs, only the product αB is important for the modeling examples that follow. So desired differences in B can be introduced through differences in α . In this way we hope to capture the essence of this problem using the minimum number of free parameters.) This summarizes the part of the modeling that is the same in this example and the next.

We will now assume that the fluid saturation is uniform throughout the stated model material: $(1l, 2l)$. [Notation indicates first layer is liquid filled (l) and second layer is also liquid filled. The alternative is that some layers are gas filled (g).]

In Figure 6 there appear to be only two curves for bulk modulus, but in fact six curves are plotted here. All three of the drained curves are so close to each other that they cannot be distinguished on the scale of this plot. Similarly, all three of the undrained curves are equally indistinguishable.

Figure 7 appears to be both qualitatively and quantitatively very similar to Figure 1. But this time we find the inequality $\mu_u^- > \mu_d^+$ is never violated. So there is no doubt that shear modulus is affected by pore fluids in this system.

Figure 8 shows that the maximum value of $R \simeq 0.2$ occurs around $f_2 \simeq 0.3$. For this case, $4/15$ is an upper bound on R , but I know this is not a general result.

Two Distinct Gassmann Materials, Patchy Fluid Saturation

This final set of examples will use the same model framework as the preceding example. However, two fluids will be present simultaneously in this case. If the two fluids (g, l) are assumed to saturate only one or the other types of Gassmann materials, then we have a relatively simple two component model: $(1g, 2l)$. On the other hand, the setup is now general enough to permit a variety of other possibilities. For example, porous material 1 might be saturated with either gas or liquid, and the same for porous material 2: $(1g, 1l, 2g, 2l)$. We could also suppose that some of the layers have homogeneously (h) mixed saturation of both liquid and gas, *i.e.*, a partially rather than patchy saturated layer: $(1g, 1h, 1l, 2g, 2h, 2l)$. Although this additional complication is not a problem for the numerical modeling, the large increase in the number of possible cases needing enumeration becomes a bit too burdensome for the short presentation envisioned here. (There is an infinite number of ways these types of materials having homogeneously mixed regions could be incorporated.) So we will instead limit discussion to the two cases mentioned before: (a) just two types of patchy saturated layers $(1g, 2l)$, or (b) four types of patchy saturated layers $(1g, 1l, 2g, 2l)$. Since the case (b) is expected to be more complex

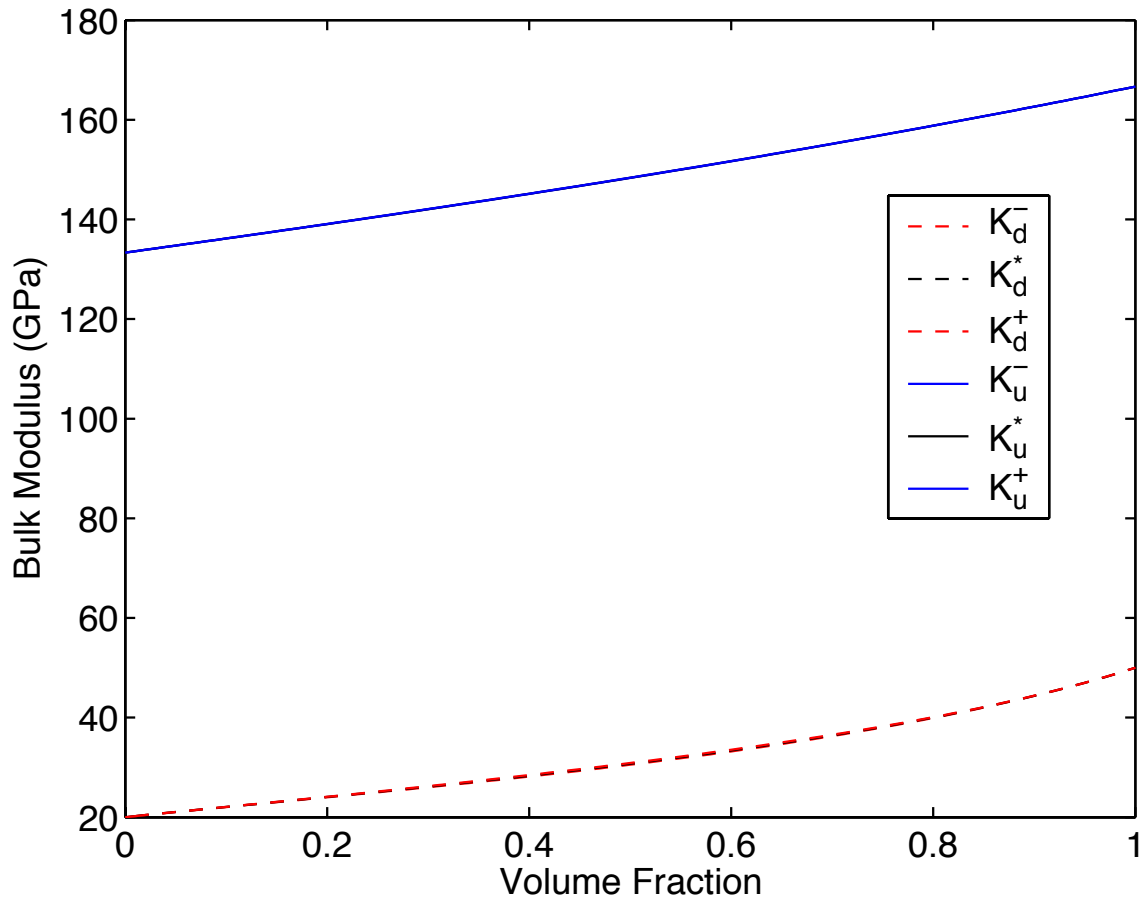


Figure 6: Illustrating the bulk modulus results for the random polycrystals of porous laminates model for homogeneous saturation when each grain is composed of two constituents: (1) $K_d^{(1)} = 20.0$ GPa, $\mu_d^{(1)} = 4.0$ GPa and (2) $K_d^{(2)} = 50.0$ GPa, $\mu_d^{(2)} = 40.0$ GPa. Skempton's coefficient is taken to be $B = 0.0$ when the system is gas saturated, and $B = 1.0$ when the system is fully liquid saturated. The effective stress coefficients for the layers are, respectively, $\alpha^{(1)} = 0.85$ and $\alpha^{(2)} = 0.70$. Porosity does not play a direct role in the calculation when we are using B as the fluid substitution parameter. Volume fraction of the layers varies from 0 to 100% of constituent number 2. [jim2-Fig6](#) [NR]

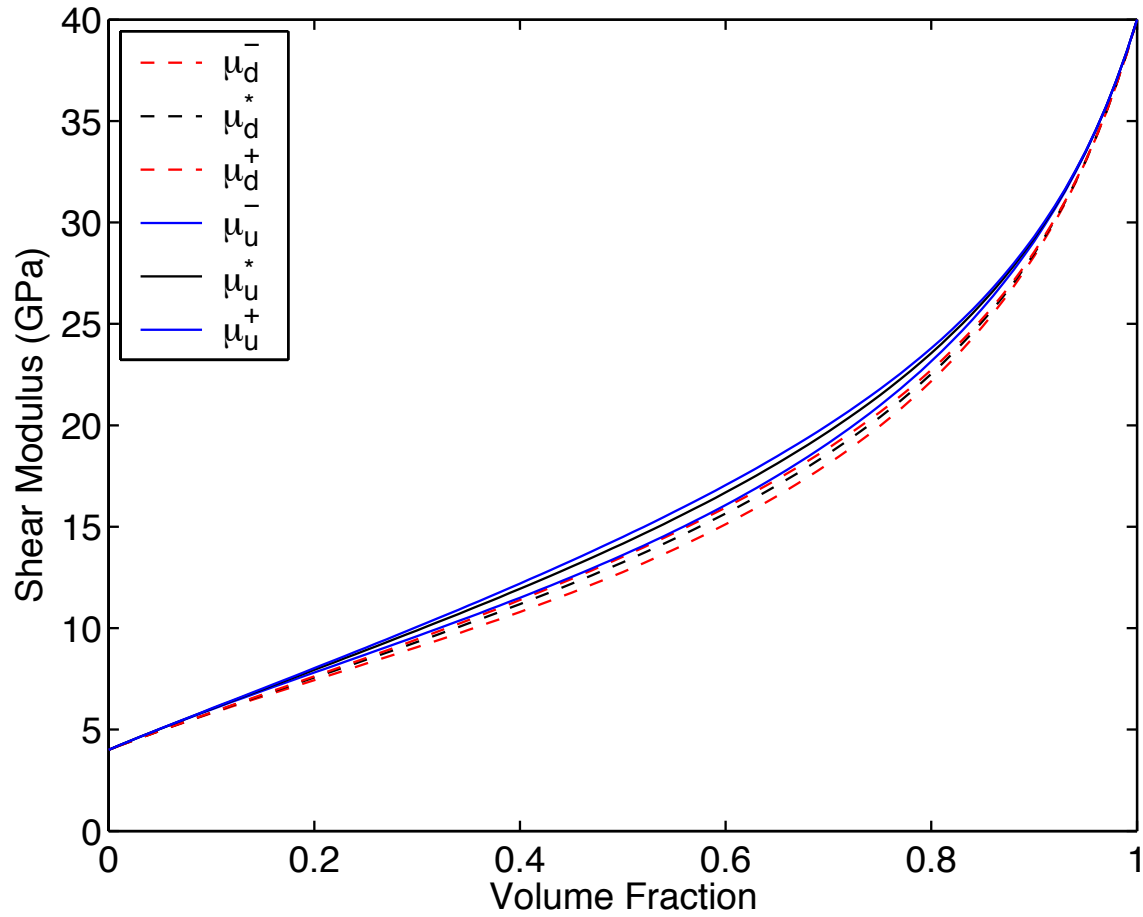


Figure 7: Illustrating the shear modulus results for the random polycrystals of porous laminates model. Model parameters are the same as in Figure 6 for homogeneous saturation. jim2-Fig7
[NR]

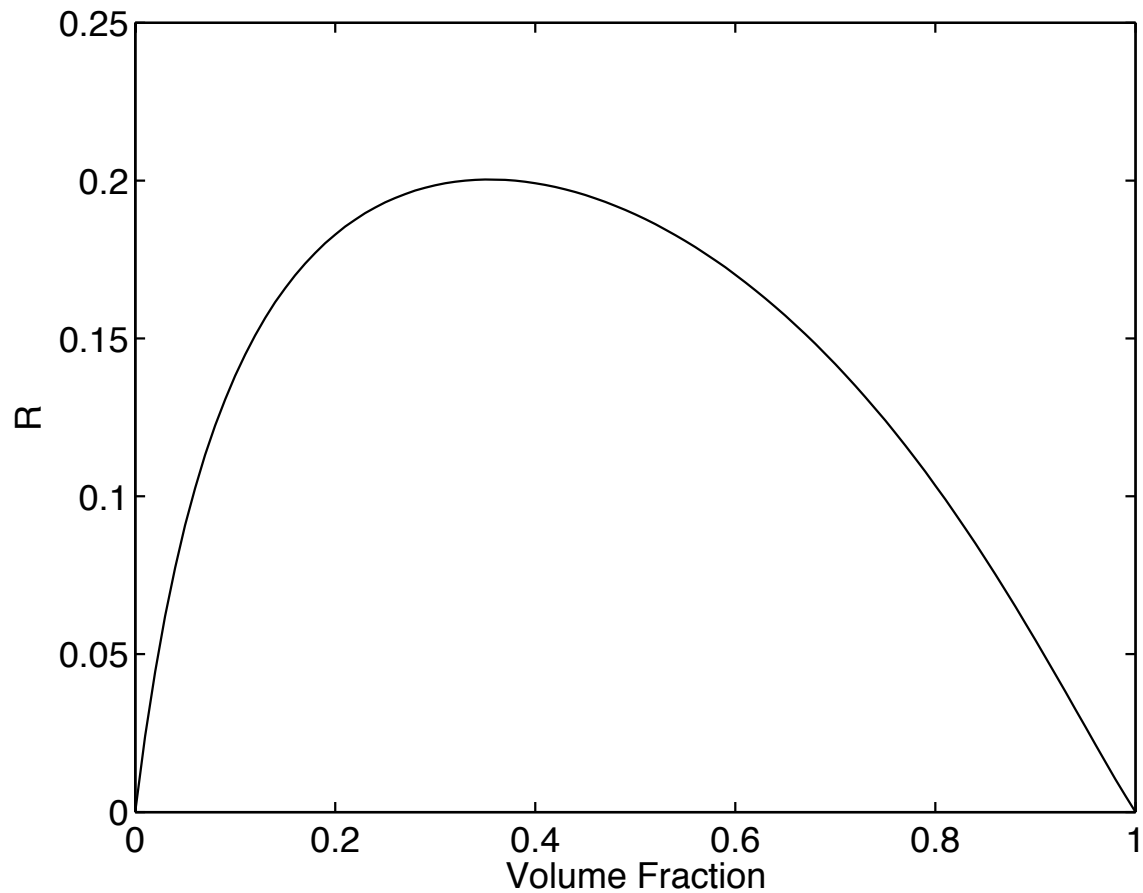


Figure 8: Plot of the ratio R from equation (24), being the ratio of compliance differences due to fluid saturation. These results are for the same model described in Figure 6 for homogeneous saturation. The values of R should be compared to those predicted by Mavko and Jizba (1991) for very low porosity and flat cracks, when $R = 4/15 \simeq 0.267$. We find in contrast that the random polycrystals of porous laminates model for the case considered always has $R \leq 0.20$.

jim2-Fig8 [NR]

but not expected to contain any new ideas, we will limit the discussion further to case (a).

In Figure 9 as in Figure 6, the three drained curves for bulk modulus are so close together that they cannot be distinguished on the scale of this plot (although they can be distinguished if the plot is magnified). In contrast to Figure 6, the three undrained bulk modulus curves can now be distinguished, but they are still quite close together. The undrained curves start out at the same values as the drained curves because at zero volume fraction of constituent 2 the only fluid in the system is air. Then, as the volume fraction of constituent 2 increases, we add liquid up to the point where the final values at full liquid saturation are the same as in Figure 6. Again uncorrelated Hashin-Shtrikman bounds are shown for purposes of comparison, as in Figure 3. The Peselnick-Meister-Watt bounds on undrained bulk modulus — making use of the laminated grain/crystal substructure and the polycrystalline nature of the overall reservoir model — clearly are much tighter. Together Figures 3 and 9 also show that the polycrystalline-based bounding method produces a great improvement over the uncorrelated Hashin-Shtrikman bounds, whose microstructural information is limited to volume fraction data. This result is accomplished without having very detailed knowledge of the spatial correlations, just by using the fact that the local microstructure is layered. Knowledge of local layering is therefore a very important piece of microstructural information that has not been used to greatest advantage in prior applications of bounding methods for up-scaling purposes.

For Figure 10, the results are not so simple, as the six curves are all very close to each other. Undrained curves are always above the corresponding drained curves, but in general there is little separation to be seen here. Figure 11, like Figure 5, shows that the shear modulus changes with saturation are not really tightly coupled to the bulk modulus changes, and especially so at the lowest volume fractions of liquid, as the changes in shear compliance are again greater in magnitude there than the changes in the bulk compliance.

CONCLUSIONS

The “random polycrystals of porous laminates” model introduced and studied here has been shown to be a useful tool for studying some very difficult technical issues concerning how geomechanical constants of reservoirs behave as a function of changes of pore fluid and varying degrees of heterogeneity. This model has the advantage that rigorous bounds [the Hashin-Shtrikman bounds of Peselnick and Meister (1965) and Watt and Peselnick (1980)] on the geomechanical constants (bulk and shear moduli) are available. Furthermore, due to the refined formulation of these bounds presented here, it is also possible to obtain self-consistent estimates directly from these bounds (Berryman, 2004b; 2005). This situation is particularly beneficial as the rigorous bounds then provide immediate theoretical error bars for the self-consistent estimates — a situation that is sometimes but not always true for other effective medium theories (Berryman, 1995). The model should therefore prove useful for a range of applications in geomechanics.

The results obtained for the specific application considered here, *i.e.*, pore fluid effects on shear modulus, show that the pore fluid interaction with overall shear behavior is complicated. The changes from drained to undrained behavior for shear modulus can range from being a

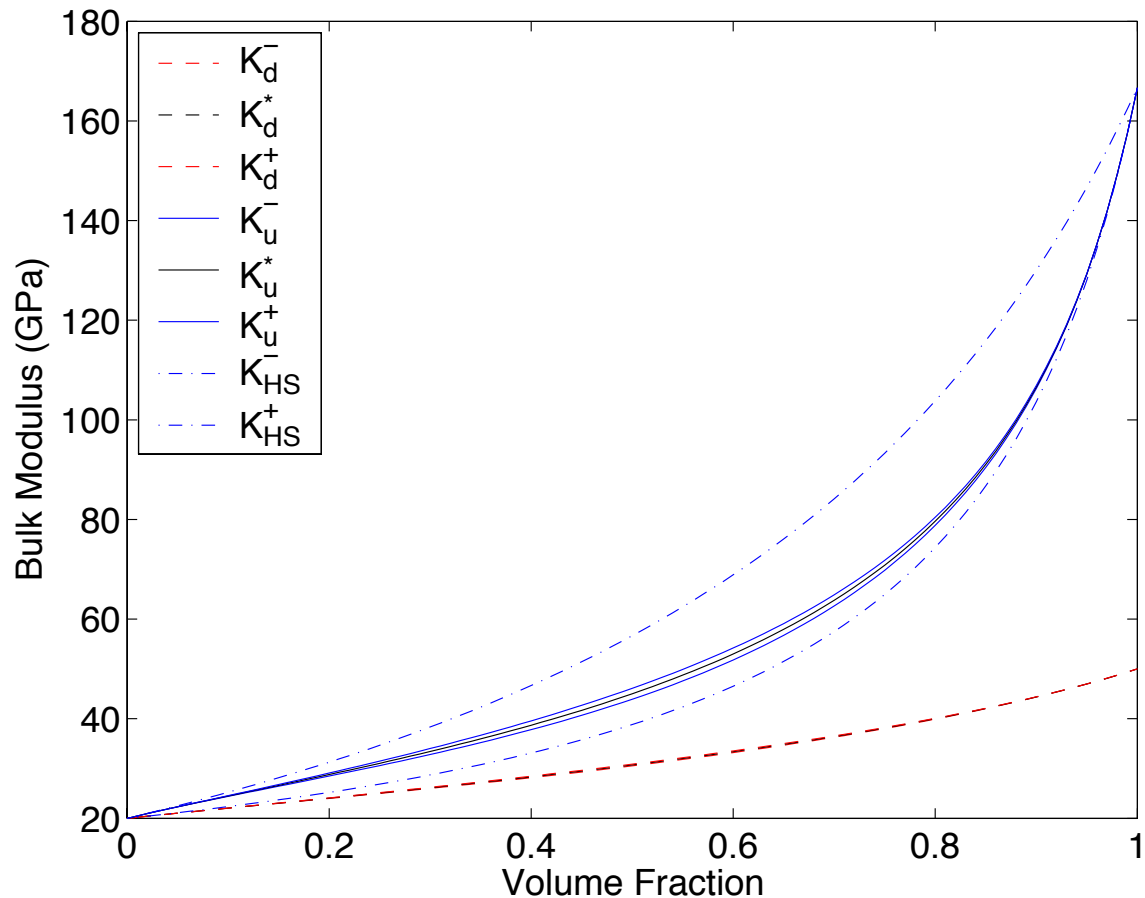


Figure 9: Illustrating the bulk modulus results for the random polycrystals of porous laminates model for patchy saturation when each grain is composed of two constituents: (1) $K_d^{(1)} = 20.0$ GPa, $\mu_d^{(1)} = 4.0$ GPa and (2) $K_d^{(2)} = 50.0$ GPa, $\mu_d^{(2)} = 40.0$ GPa. Skempton's coefficient is taken to be $B = 0.0$ for constituent 1 (gas saturated), and $B = 1.0$ for constituent 2 (liquid saturated). The effective stress coefficients for the layers are, respectively, $\alpha^{(1)} = 0.85$ and $\alpha^{(2)} = 0.70$. Porosity does not play a direct role in the calculation when we are using B as the fluid substitution parameter. Volume fraction of the layers varies from 0 to 100% of constituent number 2. To emphasize the accuracy of the polycrystal bounds and self-consistent estimates, uncorrelated Hashin-Shtrikman bounds K_{HS}^{\pm} on undrained bulk modulus are also shown. jim2-Fig9
[NR]

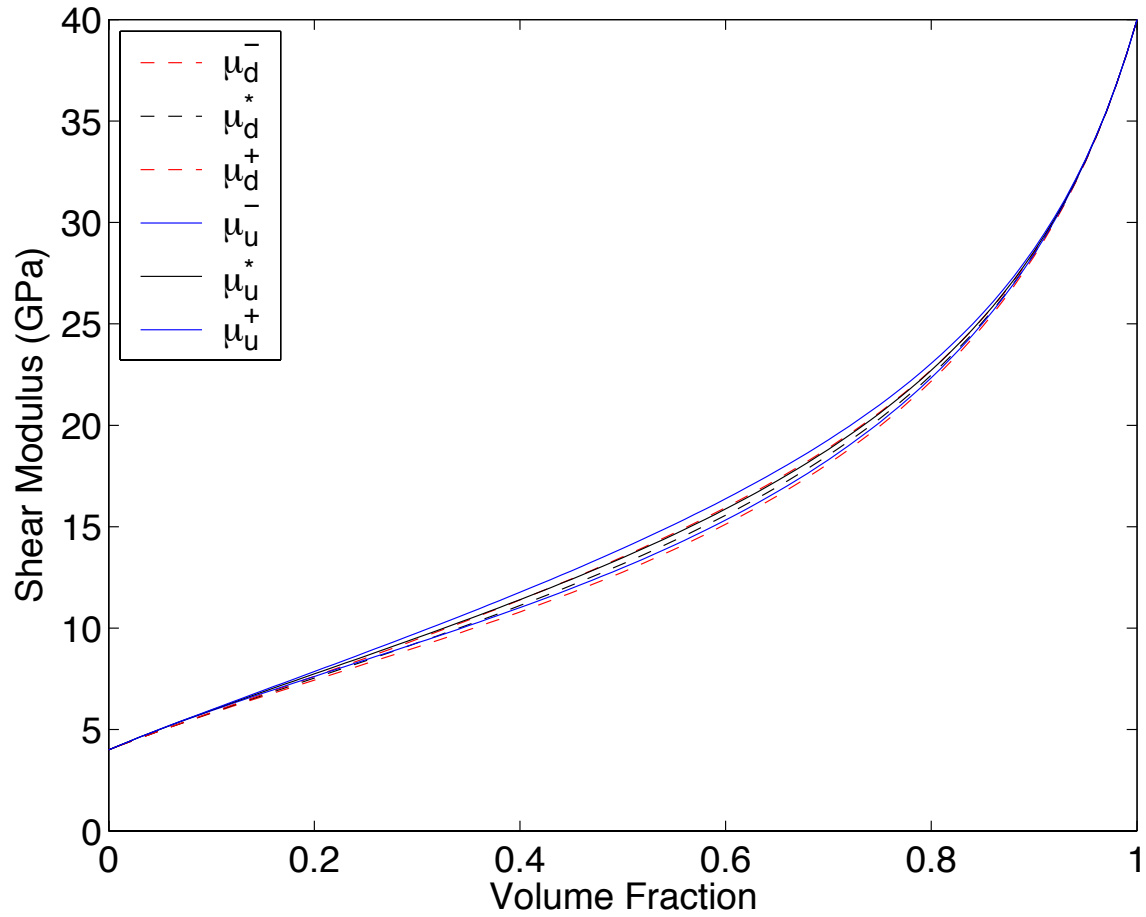


Figure 10: Illustrating the shear modulus results for the random polycrystals of porous laminates model. Model parameters are the same as in Figure 9 for patchy saturation. jim2-Fig10
 [NR]

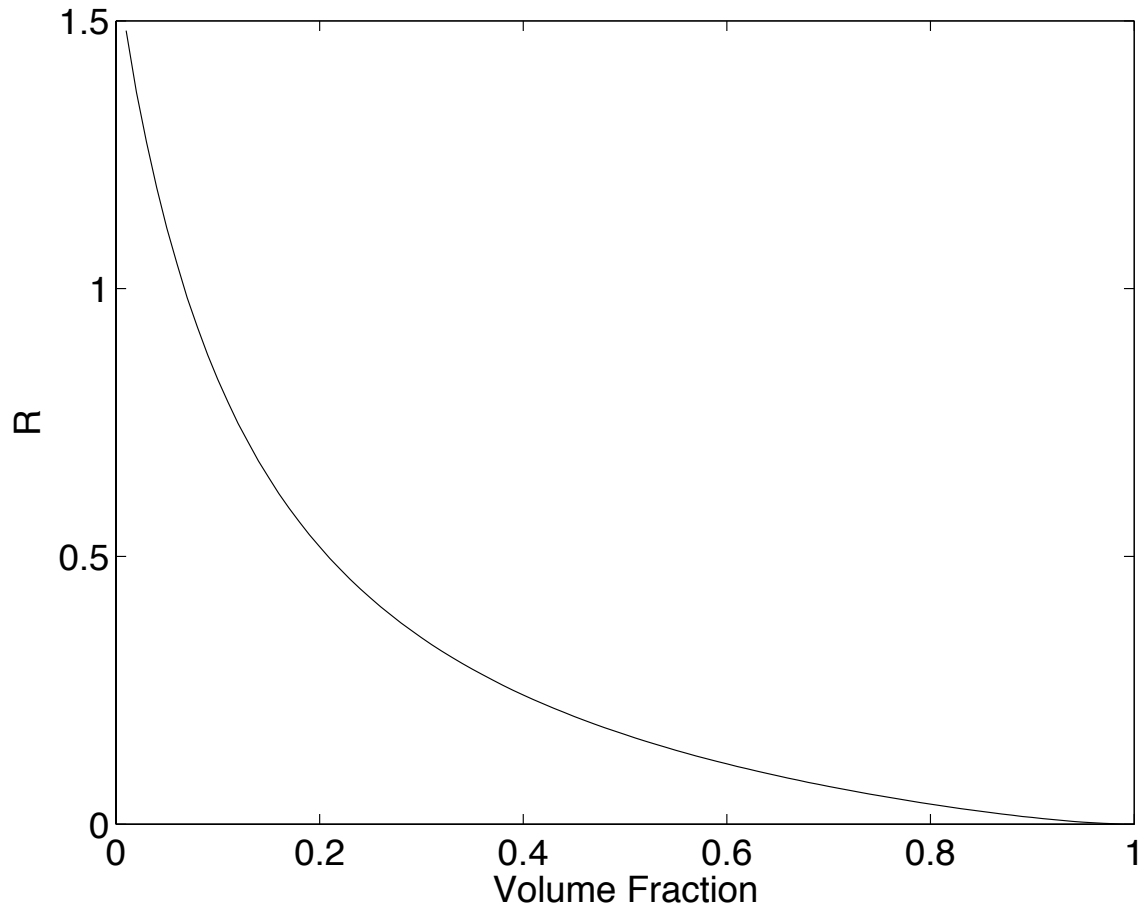


Figure 11: Plot of the ratio R from equation (24), being the ratio of compliance differences due to fluid saturation. These results are for the same model described in Figure 9 for patchy saturation. The values of R should be compared to those predicted by Mavko and Jizba (1991) for very low porosity and flat cracks, when $R = 4/15 \simeq 0.267$. We find in contrast that, for partial and patchy saturation, R can take any positive value, or zero. Note that the magnitude of this effect is smaller than in Figure 5, even though the degree of heterogeneity for bulk modulus is greater here. jim2-Fig11 [NR]

negligible effect (as it is according to Gassmann's results for microhomogeneous and isotropic media) to being a bigger effect than the changes in bulk modulus under some circumstances (see Figures 5 and 11 showing that the ratio of compliance differences $R > 1$ in some cases). Influences of pore geometry can also be studied in this model if desired, but this complication was avoided here by parameterizing the fluid effects through the use of Skempton's coefficient B . All the pore microgeometry effects were thereby hidden in the present analysis, but these could be brought out in future studies of the same and/or many other related systems.

Another related result of some importance to analysis of partially and patchy saturated systems was obtained in Appendix B. The results are illustrated in Figure 12 and show that deviations from a system satisfying Hill's equation (3) need not be small if the shear modulus heterogeneity is large. The analysis does show, however, that if shear modulus variation is small, then the observed deviations from predictions of Hill's equation should also be correspondingly small.

An implicit assumption made throughout the present paper is that the porosity and — most importantly — the fluid permeability of the geomechanical system under consideration is relatively uniform. Then, the pore fluid pressures equilibrate on essentially the same timescale throughout the whole system. If this is not true, as it would not be in a double-porosity dual-permeability system (Berryman and Wang, 1995), then the present analysis needs to be modified to account for the presence of more than one pertinent timescale. One direction for future work along these lines will therefore be focused on this more complex, but nevertheless important, problem commonly encountered in real earth reservoirs. The random polycrystal of porous laminates model is flexible enough to allow this set of problems to be studied within a very similar framework.

APPENDIX A: EFFECTIVE STRESS COEFFICIENT AND PARTIAL SATURATION

Although Eq. (20) for the overall volume effective stress coefficient α^* is known to be true for homogeneous pore saturation, we also need to have a corresponding result here for patchy saturation. It turns out that the same formula applies for arbitrarily patchy saturated media, as long as there are only two types of solid components. To show this, consider

$$\begin{pmatrix} \delta e^{(n)} \\ -\delta \zeta^{(n)} \end{pmatrix} = \frac{1}{K_d^{(n)}} \begin{pmatrix} 1 & -\alpha^{(n)} \\ -\alpha^{(n)} & \alpha^{(n)}/B^{(n)} \end{pmatrix} \begin{pmatrix} -\delta p_c \\ -\delta p_f^{(n)} \end{pmatrix}, \quad (26)$$

where $\delta e^{(n)}$ and $\delta \zeta^{(n)}$ are the change in overall strain and the increment of fluid content in component n , where $n = 1, 2$. [There are also similar formulas for all the overall properties with (n) replaced by $*$ for the corresponding effective properties. See Berryman and Wang (1995) for more discussion.] Similarly, the change in overall confining (external) pressure is δp_c , and the pore pressure change of component n is $\delta p_f^{(n)}$. The porous material coefficients are defined as in the main text, $K_d^{(n)}$ is the drained bulk modulus, $\alpha^{(n)}$ is the volume effective stress coefficient, and $B^{(n)}$ is Skempton's coefficient for the n -th constituent.

Now the rest of the argument follows that given in Berryman and Milton (1991) exactly, since it is not important what fluid is in the pores when trying to determine the overall effective

stress coefficient at long times (when fluid pressure in the system has equilibrated). We simply postulate the existence of any fixed ratio $r = \delta p_f^{(1)}/\delta p_c = \delta p_f^{(2)}/\delta p_c$ such that $\delta e^{(1)} = \delta e^{(2)}$. If there is such a ratio (valid at appropriately long times), then $\delta e^* = \delta e^{(1)} = \delta e^{(2)}$ also follows immediately and we have the condition that must be satisfied:

$$\frac{\delta p_c}{K_d^{(1)}} [1 - \alpha^{(1)} r] = \frac{\delta p_c}{K_d^{(2)}} [1 - \alpha^{(2)} r], \quad (27)$$

which is just a linear relation for ratio r . The result shows that the postulated value of r does exist unless the denominator of the following expression vanishes:

$$r = \frac{1/K_d^{(1)} - 1/K_d^{(2)}}{\alpha^{(1)}/K_d^{(1)} - \alpha^{(2)}/K_d^{(2)}}. \quad (28)$$

If the numerator of (28) vanishes, the results are trivial because Gassmann's microhomogeneity condition is then satisfied. Once the value of r is known, it is easy to see that $\delta e^* = \delta e^{(1)} = \delta e^{(2)}$ implies

$$\frac{\delta p_c}{K_d^*} [1 - \alpha^* r] = \frac{\delta p_c}{K_d^{(1)}} [1 - \alpha^{(1)} r]. \quad (29)$$

This equation can be rearranged into the form (20), as has been shown previously by Berryman and Milton (1991).

Arguments similar to the one just given have also been used, for example, in the context of thermal expansion by Benveniste and Dvorak (1990) and Dvorak and Benveniste (1997), who call this approach "the theory of uniform fields." It turns out this method is not restricted to isotropic constituents as one might infer from the arguments presented here and also in (Berryman and Milton, 1991).

A somewhat more difficult task than the one just accomplished involves deducing the overall effective pore bulk modulus K_ϕ^* as was also done previously by Berryman and Milton (1991). However, this coefficient does not play any direct role in our present analysis, so we will leave this exercise to the interested reader.

APPENDIX B: HILL'S EQUATION AND HETEROGENEOUS POROUS MEDIA

One very common approximation made in studies of partially and patchy saturated porous media (Norris, 1993; Mavko *et al.*, 1998; Johnson, 2001) is based on an assumption that the estimates are being made over a small enough region that it is reasonable to take the shear modulus of the porous frame as constant, even though the bulk modulus over the same small region may vary. Then, when Gassmann's results apply locally, the shear modulus satisfies $\mu_d = \mu_u$, and so remains constant throughout this same region regardless of the distribution of fluids in the pores. When these assumptions are valid, Hill's equation (3) may be used to compute the effective bulk modulus K^* , regardless of anisotropy or of how many constituents might be present. Furthermore, Hill's equation will apply equally to the drained K_d^* and undrained K_u^*

bulk moduli of such a poroelastic system; K_n for the layers must be substituted accordingly for the drained and undrained cases.

This approximation based on Hill's equation is very appealing for applications because of its analytical beauty and overall simplicity, but its use in heterogeneous media has never been given a rigorous justification. In particular, the assumption of variable bulk modulus in a heterogeneous system having constant shear modulus is surely one worthy of careful consideration. It seems more likely (at least to me) that the variations in the bulk modulus in an earth system will be mimicked by the shear modulus and, therefore, that the proposed method is in truth an oversimplification of this complex problem.

The model system presented here (*i.e.*, the random polycrystal of porous laminates) offers one means of checking whether this use of Hill's equation might be justified or not.

It turns out that, when $N = 2$, Hill's equation (3) can be inverted to give μ as a functional of K^* (Milton, 1997). The result is given by

$$\mu = \frac{3K_1K_2}{4K_r} \left(\frac{K^* - K_r}{K_v - K^*} \right), \quad (30)$$

where

$$K_v = \sum_{n=1}^2 f_n K_n \quad \text{and} \quad K_r = \left[\sum_{n=1}^2 \frac{f_n}{K_n} \right]^{-1}. \quad (31)$$

So I can do two calculations based on the results presented here for heterogeneous systems. We can compute effective shear moduli μ_d^{eff} and μ_u^{eff} by taking the self-consistent values to be the true values of the drained and undrained K^* , and layer values of $K_d^{(n)}$ and $K_u^{(n)}$ as the values for K_1 and K_2 . The volume fractions are those already used in these calculations. So everything is known and the computations are straightforward. We want to check whether the resulting values of effective shear moduli μ_d^{eff} and μ_u^{eff} computed this way are approximately constant and/or approximately equal to each other. If they are, then Hill's equation, although not rigorously appropriate in these systems, nevertheless could be capturing some of the observed behavior. If this is not true, then the results would be showing that great care should be exercised in using these formulas for analyzing real data.

My results are illustrated in Figure 12. I find that $\mu_d^{\text{eff}} \simeq \mu_u^{\text{eff}}$. However, except for the volume fractions near 50%, the values of both μ^{eff} 's are very different from the actual shear moduli of the random polycrystals of porous laminates model. The μ^{eff} 's are high when the μ^* 's are low, and vice versa. This observation is a very strong negative result, showing that large errors in analysis can be introduced for systems such as these that are very heterogeneous in shear.

On the positive side, it is also clear from Figure 12 that if the spread of layer μ 's is nonzero but small, then the use of Hill's equation can be well justified. The error in shear estimates will never be greater than the spread in the layer shear modulus values, so if this is a small (though nonzero) number, then the errors will be finite but correspondingly small.

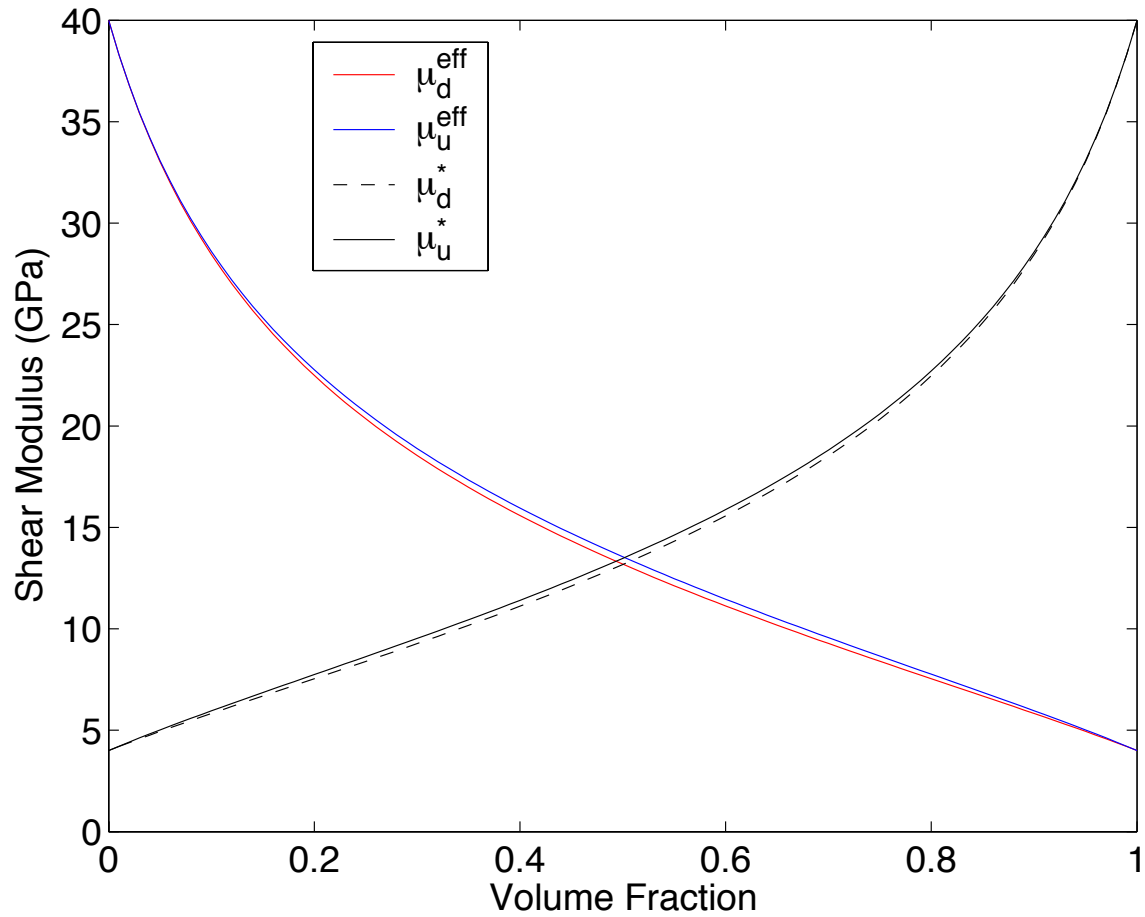


Figure 12: Illustrating computations of an effective shear modulus obtained by inverting Hill's equation for drained (μ_d^{eff}) and for undrained patchy saturation (μ_u^{eff}) conditions. Model parameters are the same as in Figure 9 for patchy saturation. For comparison the curves for self-consistent shear moduli μ_d^* and μ_u^* from Figure 10 are replotted here. jim2-Fig12 [NR]

REFERENCES

- Avellaneda, M., 1987, Iterated homogenization, differential effective medium theory and applications: *Commun. Pure Appl. Math.*, **40**, 527–554.
- Backus, G. E., 1962, Long-wave elastic anisotropy produced by horizontal layering: *J. Geophys. Res.*, **67**, 4427–4440.
- Benveniste, Y., and G. J. Dvorak, 1990, On a correspondence between mechanical and thermal effects in two-phase composites, in *Micromechanics and Inhomogeneity: The Toshio Mura 65th Anniversary Volume*, edited by G. J. Weng, M. Taya, and H. Abé (Springer-Verlag, New York, New York), pp. 65–81.
- Berryman, J. G., 1992, Effective stress for transport properties of inhomogeneous porous rock: *J. Geophys. Res.*, **97**, 17409–17424.
- Berryman, J. G., 1995, Mixture theories for rock properties: in *Rock Physics and Phase Relations: American Geophysical Union Handbook of Physical Constants*, edited by T. J. Ahrens (AGU, New York), pp. 205–228.
- Berryman, J. G., 1998, Transversely isotropic poroelasticity arising from thin isotropic layers: in *Mathematics of Multiscale Materials*, edited by K. M. Golden, G. R. Grimmett, R. D. James, G. W. Milton, and P. N. Sen (Springer-Verlag, New York), pp. 37–50.
- Berryman, J. G., 1999, Origin of Gassmann's equations: *Geophysics*, **64**, 1627–1629.
- Berryman, J. G., 2004a, Poroelastic shear modulus dependence on pore-fluid properties arising in a model of thin isotropic layers: *Geophys. J. Int.*, **157**, 415–425.
- Berryman, J. G., 2004b, Bounds on elastic constants for random polycrystals of laminates: *J. Appl. Phys.*, **96**, 4281–4287.
- Berryman, J. G., 2005, Bounds and estimates on elastic constants for random polycrystals of laminates: *Int. J. Solids Structures* **42**, 3730–3743.
- Berryman, J. G., P. A. Berge, and B. P. Bonner, 2002a, Estimating rock porosity and fluid saturation using only seismic velocities: *Geophysics*, **67**, 391–404.
- Berryman, J. G., and G. W. Milton, 1991, Exact results for generalized Gassmann's equations in composite porous media with two constituents: *Geophysics*, **56**, 1950–1960.
- Berryman, J. G., S. R. Pride, and H. F. Wang, 2002b, A differential scheme for elastic properties of rocks with dry or saturated cracks: *Geophys. J. Int.*, **151**, 597–611.
- Berryman, J. G., L. Thigpen, and R. C. Y. Chin, 1988, Bulk wave propagation for partially saturated porous solids: *J. Acoust. Soc. Am.* **84**, 360–373.
- Berryman, J. G., and H. F. Wang, 1995, The elastic coefficients of double-porosity models for fluid transport in jointed rock: *J. Geophys. Res.*, **100**, 24611–24627.

- Berryman, J. G., and H. F. Wang, 2001, Dispersion in poroelastic systems: *Phys. Rev. E* **64**, 011303.
- Biot, M. A., and D. G. Willis, 1957, The elastic coefficients of the theory of consolidation: *J. Appl. Mech.*, **24**, 594–601.
- Bruggeman, D. A. G., 1937, Berechnung verschiedener physikalischer Konstanten von heterogenen Substanzen: II. Die elastischen Konstanten der quasi-isotropen Mischkörper aus isotropen Substanzen: *Ann. Phys. (Leipzig)*, **29**, 160–178.
- Coussy, O., 2004, *Poromechanics* (John Wiley, Chichester, West Sussex, England).
- Dvorak, G. J., and Y. Benveniste, 1997, On micromechanics of inelastic and piezoelectric composites: in *Theoretical and Applied Mechanics 1996*, edited by T. Tatsumi, E. Watanabe, and T. Kambe (Elsevier Science, Amsterdam), pp. 65–81.
- Dvorkin, J., D. Moos, J. L. Packwood, and A. M. Nur, 1999, Identifying patchy saturation from well logs: *Geophysics*, **64**, 1756–1759.
- Einstein, A., 1906, Eine neue Bestimmung der Moleküldimensionen: *Ann. Phys. (Leipzig)*, **19**, 289–306.
- Gassmann, F., 1951, Über die elastizität poröser medien: *Veierteljahrsschrift der Naturforschenden Gesellschaft in Zürich*, **96**, 1–23.
- Goertz, D., and R. Knight, 1998, Elastic wave velocities during evaporative drying: *Geophysics*, **63**, 171–183.
- Gurevich, B., 2004, A simple derivation of the effective stress coefficient for seismic velocities in porous rocks: *Geophysics*, **69**, 393–397.
- Guéguen, Y., and V. Palciauskas, 1994, *Introduction to the Physics of Rocks*, Princeton University Press, Princeton, NJ, pp. 193–195.
- Hashin, Z., and S. Shtrikman, 1962a, A variational approach to the theory of the effective magnetic permeability of multiphase materials: *J. Appl. Phys.*, **33**, 3125–3131.
- Hashin, Z., and S. Shtrikman, 1962b, On some variational principles in anisotropic and non-homogeneous elasticity: *J. Mech. Phys. Solids*, **10**, 335–342.
- Hashin, Z., and S. Shtrikman, 1962c, A variational approach to the theory of the elastic behaviour of polycrystals, *J. Mech. Phys. Solids*, **10**, 343–352.
- Hashin, Z., and S. Shtrikman, 1963a, A variational approach to the theory of the elastic behavior of multiphase materials: *J. Mech. Phys. Solids*, **11**, 127–140.
- Hashin, Z., and S. Shtrikman, 1963b, Conductivity of polycrystals: *Phys. Rev.* **130**, 129–133.
- Hill, R., 1952, The elastic behaviour of a crystalline aggregate: *Proc. Phys. Soc. London A*, **65**, 349–354.

- Hill, R., 1963, Elastic properties of reinforced solids: Some theoretical principles: *J. Mech. Phys. Solids*, **11**, 357–372.
- Hill, R., 1964, Theory of mechanical properties of fiber-strengthened materials: I. Elastic behavior: *J. Mech. Phys. Solids*, **12**, 199–212.
- Johnson, D. L., 2001, Theory of frequency dependent acoustics in patchy-saturated porous media: *J. Acoust. Soc. Am.*, **110**, 682–694.
- Knight, R., and R. Nolen-Hoeksema (1990), A laboratory study of the dependence of elastic wave velocities on pore scale fluid distribution, *Geophys. Res. Lett.*, **17**, 1529–1532.
- Li, X., L. R. Zhong, and L. J. Pyrak-Nolte, 2001, Physics of partially saturated porous media: Residual saturation and seismic-wave propagation: in *Annual Review of Earth and Planetary Sciences*, Vol. 29 (Annual Reviews, Palo Alto, CA), pp. 419–460.
- Makse, H. A., N. Gland, D. L. Johnson, and L. M. Schwartz, 1999, Why effective medium theory fails in granular materials: *Phys. Rev. Lett.* **83**, 5070–5073.
- Mavko, G., and D. Jizba, 1991, Estimating grain-scale fluid effects on velocity dispersion in rocks: *Geophysics*, **56**, 1940–1949.
- Mavko, G., and T. Mukerji, 1998, Bounds on low-frequency seismic velocities in partially saturated rocks: *Geophysics*, **63**, 918–924.
- Mavko, G., T. Mukerji, and J. Dvorkin, 1998, *The Rock Physics Handbook: Tools for Seismic Analysis in Porous Media* (Cambridge University Press, Cambridge, England).
- Maxwell, J. C., 1873, *Treatise on Electricity and Magnetism*, Clarendon Press, Oxford, England.
- Milton, G. W., 1985, The coherent potential approximation is a realizable effective medium scheme: *Comm. Math. Phys.*, **99**, 463–500.
- Milton, G. W., and J. G. Berryman, 1997, On the effective viscoelastic moduli of two-phase media. II. Rigorous bounds on the complex shear modulus in three dimensions: *Proc. Roy. Soc. London A*, **453**, 1849–1880.
- Milton, G. W., 2002, *The Theory of Composites*. Cambridge, University Press, Cambridge, UK, pp. 77-78, 163, 457–498.
- Norris, A. N., 1985, A differential scheme for the effective moduli of composites: *Mech. Mater.*, **4**, 1–16.
- Norris, A. N., 1993), Low-frequency dispersion and attenuation in partially saturated rocks: *J. Acoust. Soc. Am.*, **94**, 359–370.
- Nur, A., and J. D. Byerlee, 1971, An exact effective stress law for elastic deformation of rocks with fluids: *J. Geophys. Res.* **76**, 6414–6419.

- Peselnick, L., and R. Meister, 1965, Variational method of determining effective moduli of polycrystals: (A) Hexagonal symmetry, (B) trigonal symmetry: *J. Appl. Phys.*, **36**, 2879–2884.
- Postma, G. W., 1955, Wave propagation in a stratified medium: *Geophysics*, **20**, 780–806.
- Pride, S. R., and J. G. Berryman, 2003, Linear dynamics of double-porosity dual-permeability materials: I. Governing equations and acoustic attenuation, *Phys. Rev. E*, **68**, 036603.
- Pride, S. R., J. G. Berryman, and J. M. Harris, 2004, Seismic attenuation due to wave induced flow: *J. Geophys. Res.*, **109**, B01201.
- Reuss, A., 1929, Berechnung der Fließgrenze von Mischkristallen auf Grund der Plastizitätsbedingung für Einkristalle: *Z. Angew. Math. Mech.*, **9**, 49–58.
- Skempton, A. W., 1954, The pore-pressure coefficients *A* and *B*: *Geotechnique*, **4**, 143–147.
- Voigt, W., 1928, *Lehrbuch der Kristallphysik*, Teubner, Leipzig.
- Wang, H. F., 2000, *Theory of Linear Poroelasticity with Applications to Geomechanics and Hydrogeology*, Princeton University Press, Princeton, NJ.
- Watt, J. P., and L. Peselnick, 1980, Clarification of the Hashin-Shtrikman bounds on the effective elastic moduli of polycrystals with hexagonal, trigonal, and tetragonal symmetries: *J. Appl. Phys.*, **51**, 1525–1531.
- White J. E., 1983, Computed seismic speeds and attenuation in rocks with partial gas saturation: *Geophysics* **40**, 224–232.
- Zimmerman, R. W., 2000, Coupling in poroelasticity and thermoelasticity: *Int. J. Rock Mech.*, **37**, 79–87.

SEP ARTICLES PUBLISHED OR IN PRESS

- Alkhalifah, T., and Biondi, B., 2004, Numerical analysis of the azimuth moveout operator for vertically inhomogeneous media: *Geophysics*, **69**, 554–561.
- Alvarez, G., and Larner, K., 2004, Relative performance of moveout-based multiple-suppression methods for amplitude variation with offset (AVO) analysis and common midpoint (CMP) stacking: *Geophysics*, **69**, no. 1, 275–285.
- Alvarez, G., Biondi, B., and Guitton, A., 2004a, Attenuation of diffracted multiples in angle domain common image gathers: 74th Ann. Internat. Mtg., Soc. of Expl. Geophys., Expanded Abstracts, 1[301]–1304.
- Alvarez, G., Pereyra, V., and Carcione, L., 2004b, Model-based 3-D seismic survey design as an optimization problem: 74th Ann. Internat. Mtg., Soc. of Expl. Geophys., Expanded Abstracts, 63–66.
- Biondi, B., and Bevc, D., 2004, Seismic imaging of complex structures by reflection seismic data *in* Levander, A., and Nolet, G., Eds., *Data Analysis and Imaging with Global and Local Arrays*: American Geophysical Union, in press.
- Biondi, B., and Symes, W., 2004, Angle-domain common-image gathers for migration velocity analysis by wavefield-continuation imaging: *Geophysics*, **69**, 1283–1298.
- Biondi, B., and Tisserant, T., 2004, 3-D angle-domain common-image gathers for migration velocity analysis: *Geophysical Prospecting*, **52**, 575–591.
- Brown, M., and Guitton, A., 2004a, Efficient prestack modeling and imaging of pegleg multiples: 74th Ann. Internat. Mtg., Soc. of Expl. Geophys., Expanded Abstracts, 2148–2151.
- Brown, M., and Guitton, A., 2004b, Least-squares joint imaging of multiples and primaries: 74th Ann. Internat. Mtg., Soc. of Expl. Geophys., Expanded Abstracts, 1277–1280.
- Clapp, R. G., Biondi, B., and Claerbout, J. F., 2004, Geologically constrained migration velocity analysis: *Geophysics*, **69**, 533–546.
- Clapp, R. G., 2004, Reference velocity selection by a generalized Lloyd method: 74th Ann. Internat. Mtg., Soc. of Expl. Geophys., Expanded Abstracts, 981–984.
- Draganov, D., Wapenaar, K., Artman, B., and Biondi, B., 2004, Migration methods for passive seismic data: 74th Ann. Internat. Mtg., Soc. of Expl. Geophys., Expanded Abstracts, 1123–1126.
- Guitton, A., and Claerbout, J., 2004, Interpolation of bathymetry data from the Sea of Galilee: a noise attenuation problem: *Geophysics*, **69**, 608–616.
- Guitton, A., and Verschuur, D. J., 2004, Adaptive subtraction of multiples with the ℓ^1 norm: *Geophysical Prospecting*, **52**, 27–38.

- Guitton, A., Claerbout, J., and Lomask, J., 2004, First order lateral interval velocity estimates without picking: 74th Ann. Internat. Mtg., Soc. of Expl. Geophys., Expanded Abstracts, 2339–2342.
- Guitton, A., 2004, Amplitude and kinematic corrections of migrated images for non-unitary imaging operators: *Geophysics*, **69**, 1017–1024.
- Guitton, A., 2005a, Multiple attenuation in complex geology with a pattern-based approach: accepted for publication in *Geophysics*.
- Guitton, A., 2005b, A pattern-based approach for multiple removal applied to a 3D Gulf of Mexico dataset: accepted for publication in *Geophysical Prospecting*.
- Haines, S., Pride, S., Klemperer, S., and Biondi, B., 2004, Development of electroseismic experimental methods: Symposium on the Application of Geophysics to Engineering and Environmental Problems, Environmental and Engineering Geophysical Society, Proceedings, 1490–1503.
- Liner, C. L., and Clapp, R. G., 2004a, Nonlinear pairwise alignment of seismic traces: 74th Ann. Internat. Mtg., Soc. of Expl. Geophys., Expanded Abstracts, 2072–2075.
- Liner, C. L., and Clapp, R. G., 2004b, Nonlinear pairwise alignment of seismic traces: *Geophysics*, in press.
- Lomask, J., Biondi, B., and Shragge, J., 2004, Image segmentation for tracking salt boundaries: 74th Ann. Internat. Mtg., Soc. of Expl. Geophys., Expanded Abstracts, 2443–2446.
- Rosales, D., and Biondi, B., 2004a, Multicomponent azimuth moveout: submitted for publication in *Geophysics*.
- Rosales, D. A., and Biondi, B., 2004b, Acquisition geometry regularization for multicomponent data: Soc. of Expl. Geophys., Expanded Abstracts, 2052–2055.
- Sava, P., and Biondi, B., 2004a, Wave-equation migration velocity analysis - I: Theory: *Geophysical Prospecting*, **52**, 593–606.
- Sava, P., and Biondi, B., 2004b, Wave-equation migration velocity analysis - II: Subsalt imaging examples: *Geophysical Prospecting*, **52**, 607–623.
- Sava, P., and Fomel, S., 2004a, Seismic imaging using Riemannian wavefield extrapolation: submitted for publication in *Geophysics*.
- Sava, P., and Fomel, S., 2004b, Seismic modeling with Riemannian wavefield extrapolation: 66th Mtg., Eur. Assoc. Geosc. Eng., Abstracts.
- Sava, P., and Fomel, S., 2004c, Wavefield extrapolation in Riemannian coordinates: 74th Ann. Internat. Mtg., Soc. of Expl. Geophys., Expanded Abstracts, 1049–1052.
- Sava, P., and Guitton, A., 2004, Multiple attenuation in the image space: *Geophysics*, in press.

- Sava, P., Biondi, B., and Etgen, J., 2004a, Diffraction-focusing migration velocity analysis: 74th Ann. Internat. Mtg., Soc. of Expl. Geophys., Expanded Abstracts, 2395–2398.
- Sava, P., Biondi, B., and Etgen, J., 2004b, Diffraction-focusing migration velocity analysis with application to seismic and GPR data: Geophysics, in press.
- Shan, G., and Biondi, B., 2004, Imaging overturned waves by plane-wave migration in tilted coordinates: 74th Ann. Internat. Mtg., Soc. of Expl. Geophys., Expanded Abstracts, 969–972.
- Shan, G., and Guitton, A., 2004, Migration of surface-related multiples: tests on the Sigsbee2B dataset: 74th Ann. Internat. Mtg., Soc. of Expl. Geophys., Expanded Abstracts, 1285–1288.
- Shragge, J., and Sava, P., 2004, Adaptive phase-rays wavefield extrapolation: 74th Ann. Internat. Mtg., Soc. of Expl. Geophys., Expanded Abstracts, 2044–2047.
- Tisserant, T., and Biondi, B., 2004, Residual move-out analysis with 3-D angle-domain common-image gathers: 74th Ann. Internat. Mtg., Soc. of Expl. Geophys., Expanded Abstracts, 2391–2394.
- Valenciano, A. A., Brown, M., Guitton, A., and Sacchi, M. D., 2004, Interval velocity estimation using edge-preserving regularization: 74th Ann. Internat. Mtg., Soc. of Expl. Geophys., Expanded Abstracts, 2431–2434.
- Vlad, I., and Biondi, B., 2004, Velocity estimation for seismic data exhibiting focusing-effect AVO: Soc. of Expl. Geophys., Expanded Abstracts, 2427–2430.
- Wolf, K., Rosales, D., Guitton, A., and Claerbout, J., 2004, Robust moveout without velocity picking: Soc. of Expl. Geophys., Expanded Abstracts, 2423–2426.

SEP PHONE DIRECTORY

Name	Phone	Login Name
Alvarez, Gabriel	724-0461	gabriel
Artman, Brad	723-6007	brad
Berryman, James	724-0461	berryman
Biondi, Biondo	723-1319	biondo
Claerbout, Jon	723-3717	jon
Clapp, Bob	725-1334	bob
Clapp, Marie	725-1334	marie
Curry, Bill	723-5911	bill
Guitton, Antoine	723-6007	antoine
Lau, Diane	723-1703	diane
Lomask, Jesse	723-6006	lomask
Rosales, Daniel	723-1250	daniel
Sen, Satyakee	723-3187	ssen
Shan, Guojian	723-0463	shan
Shragge, Jeff	724-0461	jeff
Valenciano, Alejandro	723-6006	valencia
Vlad, Ioan	723-1250	nick

SEP fax number: (650) 723-0683

E-MAIL

Our Internet address is "sep.stanford.edu"; i.e., send Jon electronic mail with the address "jon@sep.stanford.edu".

WORLD-WIDE WEB SERVER INFORMATION

Sponsors who have provided us with their domain names are not prompted for a password when they access from work. If you are a sponsor, and would like to access our restricted area away from work, visit our website and attempt to download the material. You will then fill out a form, and we will send the username/password to your e-mail address at a sponsor company.

STEERING COMMITTEE MEMBERS, 2004-2005

Name	Company	Telephone	E-Mail
Raymond Abma	BP	(281) 366-4604	abmar1@bp.com
Francois Audebert	CGG	(281) 646-2524	faudebert@cgg.com
Dimitri Bevc	3DGeo	(650) 969-3886	dimitri@3dgeo.com
Biondo Biondi	SEP	(650) 723-1319	biondo@sep.stanford.edu
Luis Canales	WesternGeco	(713) 806-5271	lcanales@houston.westerngeco.slb.com
Jon Claerbout	SEP	(650) 723-3717	jon@sep.stanford.edu
Richard Cook (Co-chair, 2nd year)	Shell	(713) 245-7195	richard.cook@shell.com
Helmut Jakubowicz (Co-chair, 1st year)	Veritas DGC	(44) 1293 443219	helmut_jakubowicz@veritasdgc.com
Stewart Levin	Landmark Graphics	(303) 779-8080	salevin@lgc.com
Simon Spitz	CGG	(281) 646-2502	sspitz@cgg.com

Research Personnel

Gabriel Alvarez received a B.S. degree in Physics from the National University of Colombia in 1985 and an M.Sc. in Geophysics from the Colorado School of Mines in 1995, where he was a member of the Center for Wave Phenomena. From 1989 to 2000, he worked at the Instituto Colombiano del Petroleo (ICP), the Research and Development Division of Ecopetrol, the National Oil Company of Colombia. Joined SEP in 2000, and is currently working towards a Ph.D. in geophysics at Stanford University.



Brad Artman received his B.Sc. in Geophysical Engineering from the Colorado School of Mines in December 1996. He worked at Shell Deepwater Development Company in New Orleans in petrophysical and geophysical capacities until joining SEP in the fall of 2000 to work toward a Ph.D. Brad is a member of SEG and SPWLA.



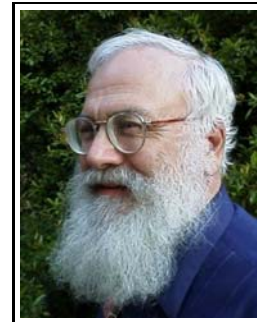
James G. Berryman received a B.S. degree in physics from Kansas University (Lawrence) in 1969 and a Ph.D. degree in physics from the University of Wisconsin (Madison) in 1975. He subsequently worked on seismic prospecting at Conoco. His later research concentrated on seismic waves in rocks and sediments – at AT&T Bell Laboratories (1978-81) and at Lawrence Livermore National Laboratory (1981-), where he is currently a physicist in the Earth Sciences Division. Continuing research interests include acoustic, seismic, and electrical methods of geophysical imaging and waves in porous media containing fluids. He is a member of ASA, AGU, APS, and SEG.



Biondo L. Biondi graduated from Politecnico di Milano in 1984 and received an M.S. (1988) and a Ph.D. (1990) in geophysics from Stanford. SEG Outstanding Paper award 1994. During 1987, he worked as a Research Geophysicist for TOTAL, Compagnie Francaise des Petroles in Paris. After his Ph.D. at Stanford, Biondo worked for three years with Thinking Machines Co. on the applications of massively parallel computers to seismic processing. After leaving Thinking Machines, Biondo started 3DGeo Development, a software and service company devoted to high-end seismic imaging. Biondo is now Associate Professor (Research) of Geophysics and leads SEP efforts in 3-D imaging. He is a member of SEG and EAGE.



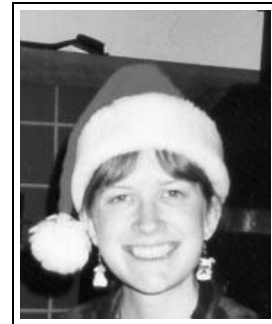
Jon F. Claerbout (M.I.T., B.S. physics, 1960; M.S. 1963; Ph.D. geophysics, 1967), professor at Stanford University, 1967. Best Presentation Award from the Society of Exploration Geophysicists (SEG) for his paper, *Extrapolation of Wave Fields*. Honorary member and SEG Fessenden Award “in recognition of his outstanding and original pioneering work in seismic wave analysis.” Founded the Stanford Exploration Project (SEP) in 1973. Elected Fellow of the American Geophysical Union. Authored three published books and five internet books. Elected to the National Academy of Engineering. Maurice Ewing Medal, SEG’s highest award. Honorary Member of the European Assn. of Geoscientists & Engineers (EAGE). EAGE’s highest recognition, the Erasmus Award.



Robert Clapp received his B.Sc. (Hons.) in Geophysical Engineering from Colorado School of Mines in May 1993. He joined SEP in September 1993, received his Masters in June 1995, and his Ph.D. in December 2000. He is a member of the SEG and AGU.



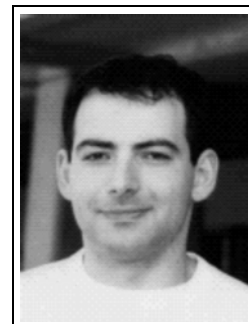
Marie Clapp, formerly Marie Prucha, received her B.Sc. in Geophysical Engineering from Colorado School of Mines in May 1997. She joined SEP in September 1997 and received her M.S. in June 1999. She married one of her fellow SEPers in 2001 and finally changed her last name in the summer of 2002. She is currently edging towards a Ph.D. in geophysics. She is a member of SEG.



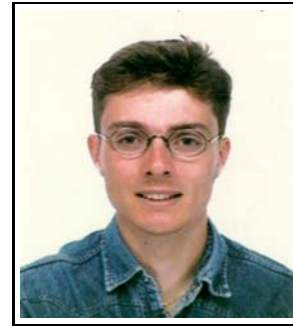
William Curry has been with SEP since 2000. He graduated in 2000 from the University of Alberta with a B.Sc. (Hons.) in Geophysics, and received his M.S. from SEP in 2002. From 1998-1999, he worked as a seismic interpreter with Jet Energy Corporation in Calgary, Canada, and during the summer of 2002 with Marathon Oil in Houston. Bill is a student member of the AGU, CGU, CSEG, EAGE, IEEE, SEG, and SIAM.



Sergey Fomel is a Research Scientist at the Bureau of Economic Geology, University of Texas at Austin. Before joining the Stanford Exploration Project, he worked at the Institute of Geophysics in Novosibirsk, Russia. Received a Ph.D. in Geophysics from Stanford in 2001. Honored with J. Clarence Karcher award by SEG in 2001 for "numerous contributions to seismology." Postdoctoral fellow at the Lawrence Berkeley National Laboratory and visiting assistant professor at the University of California at Berkeley in 2001-2002.



Antoine Guitton received a M.Sc. in geophysics from Universite de Strasbourg, France in 1996 and from Stanford University in 2000. Received a "Diplome d'ingenieur de L'Ecole de Physique du Globe de Strasbourg" in 1996. He received the Best Student Paper Award from the SEG in 1999. Assistant research geophysicist at the Institut Francais du Petrole (Paris-1996/97) working on well seismic imaging. Assistant research geophysicist at CGG Houston (1997-98) working on multiples attenuation. He joined SEP in September 1998. Current research topics are nonlinear inversion and noise attenuation. He is a member of the SEG.



Jesse Lomask graduated in 1993 with a B.S. in Geology from Temple University in Philadelphia. He then worked as a field engineer for Anadrill-Schlumberger in the Gulf of Mexico for two years. In 1998, he completed a Masters in Exploration and Development at Stanford which included a summer internship at Mobil Exploration and Producing in Houston. He then worked as a staff geophysicist for Occidental Oil and Gas at Elk Hills, California, where he interpreted recently acquired 3D seismic survey. In the fall of 2001, he returned to Stanford to join SEP.



Daniel A. Rosales received his B.S. in Geophysics from Universidad Simon Bolivar, Venezuela, in 1997. From 1996 to 1998, he worked at PDVSA-INTEVEP S.A. in seismic modeling, 2-D prestack depth migration, and velocity estimation by wave-field downward continuation. In 1998, he joined Simon Bolivar University as an instructor in geophysics. He obtained his M.Sc in geophysics from Stanford University in June 2001, and is currently working towards his Ph.D. in geophysics with the Stanford Exploration Project. He is a member of SEG and AAPG.



Satyakee Sen received his B.Tech. in Mining Engineering from Institute of Technology, BHU, India in June, 2002. From 2002 to 2004, he was a Masters student in Geosciences at Pennsylvania State University. He joined SEP in 2004. He is a member of the SEG and AGU.



Guojian Shan received his B.Sc. in Mathematics School of Peking University in July, 1998. From 1998 to 2001, he studied in Institute of Computational Mathematics and Scientific/Engineering Computing, Chinese Academy of Sciences (CAS), and received his M.S. in Applied Mathematics in July, 2001. He joined SEP in 2001 and is currently working towards a Ph.D. in geophysics. He is a member of the SEG.



Jeff Shragge graduated in 1998 with a BScH in Honours Physics from Queen's University in Kingston, Canada. After completing a MSc degree in 2001 in teleseismic imaging at the UBC in Vancouver, Canada, he spent 2001 and 2002 working for a small geophysical consulting company based out of Woburn, MA. He joined SEP in 2002, and is working towards a Ph.D. in Geophysics. His main research interest is migration and wavefield inversion. He is a member of SEG and AGU.



Alejandro A. Valenciano received a B.Sc. degree in Physics from Havana University (Cuba) in 1994, and a M.Sc. in Physics from Simon Bolivar University (Venezuela) in 1998. He worked in the Earth Science Department of PDVSA-INTEVEP from 1995 to 2001. He joined SEP to work towards a Ph.D in geophysics in the Fall of 2001.



Ioan Vlad graduated in June 2000 with an Engineer Diploma (5-year degree) in Geophysics from the University of Bucharest, with a thesis on gravity and geodynamical modeling of the lithosphere. He joined SEP in 2000 and is currently working towards a Ph.D. in geophysics at Stanford. He is a member of SEG.



Huazhong Wang graduated in April 1991 with M.S in Geophysics and in June 1997 with a Ph.D in Geophysics from School of Ocean and Earth Sciences, Tongji University, Shanghai, China. We worked with BGP for three years as a research engineer and he became a faculty member in Tongji University after receiving his Ph.D. He is a visitng scholar now at SEP. He is a member of SEG.



Charlie Wilson received his B.Sc. degree in geology from the University of Arizona in 1998 and a Ph.D. in Geophysics from the University of Colorado, Boulder in 2003. His thesis was on imaging the continental lithosphere using teleseismic earthquakes to solve tectonic problems. He joined the Stanford Geophysics Department as a Post-Doc in December 2003 and is currently working on several projects related to tectonics and earthquake imaging. He is a member of AGU.



SPONSORS OF THE STANFORD EXPLORATION PROJECT, 2004-2005

Amerada Hess Corporation
One Allen Center
500 Dallas St.
Houston, TX 77002
USA
tel: (713) 609-5829
fax: (713) 609-5666
contact: Scott A. Morton
email: morton@hess.com

ChevronTexaco Corporation
6001 Bollinger Canyon Rd.
Rm D1084
San Ramon, CA 94583
USA
tel: (925) 842-0257
fax: (925)
contact: Yue Wang
email: yue.wang@chevrontexaco.com

Aramco Services Company
Saudi Aramco
Geophysics Technology
P.O. Box 750, EXPEC Bldg., X-1370
Dhahran 31311
Saudi Arabia
tel: 966 (3) 874 7262
fax: 966 (3) 874 1020
contact: Mohammed N. Alfaraj
email: mohammed.faraj@aramco.com

ConocoPhillips Inc.
P.O. Box 2197
Lobo 3000
Houston, TX 77252
USA
tel: (281) 293-5696
fax: (281)
contact: Robert M. Habiger
email: rob.m.habiger@conocophillips.com

BP America Inc.
200 Westlake Park Blvd., #1018
Houston, TX 77079
USA
tel: (281) 366-3611
fax: (281) 366-5856
contact: John T. Etgen
email: john.etgen@bp.com

ENI - E & P Division
Dept. RIGE
via Unione Europea 3
20097 S. Donato Milanese
Italy
tel: 39 (02) 520 55308
fax: 39 (02) 520 45694
contact: Vittorio De Tomasi
email: vittorio.detomasi@agip.it

CGG Americas Inc.
16430 Park Ten Place
Houston, TX 77079
USA
tel: (281) 646-2525
fax: (281) 646-2620
contact: Francois S. Audebert
email: faudebert@cgg.com

ExxonMobil Upstream Research Company
Seismic Processing Research
URC-GW3-834A
P.O. Box 2189, 3319 Mercer St.
Houston, TX 77081-2189
USA
tel: (713) 431-6011
fax: (713) 431-6161
contact: Thomas A. Dickens
email: tom.a.dickens@exxonmobil.com

SPONSORS OF THE STANFORD EXPLORATION PROJECT, 2004-2005

Fairfield Industries Inc.
14100 Southwest Fwy.
Suite 100
Sugar Land, TX 77478
USA
tel: (281) 275-7597
fax: (281) 275-7660
contact: Bill Schneider, Jr.
email: bschneiderjr@fairfield.com

Paradigm Geophysical Corporation
Two Memorial Plaza
820 Gessner, Suite 400
Houston, TX 77024
USA
tel: (713) 393-4979
fax: (713) 393-4801
contact: Orhan Yilmaz
email: yilmaz@paradigmgeo.com

GX Technology Corporation
5847 San Felipe
Suite 3500
Houston, TX 77057-3010
USA
tel: (713) 789-7250
fax: (713) 789-7201
contact: Nick Bernitsas
email: nxb@gxt.com

Paulsson Geophysical Services, Inc.
1215 W. Lambert Rd.
Brea, CA 92821
USA
tel: (562) 697-9711
fax: (562) 697-9773
contact: Martin Karrenbach
email: martin.karrenbach@paulsson.com

Landmark Graphics Corporation
1805 Shea Center Dr.
Suite 400
Highlands Ranch, CO 80129-2258
USA
tel: (303) 779-8080
fax: (303) 796-0807
contact: Stewart A. Levin
email: salevin@lgc.com

Petrobras S.A.
Avenida Chile 65, s/1302
Rio de Janeiro
20031-912 RJ
Brazil
tel: 55 (21) 2534-2706
fax: 55 (21) 2534-1076
contact: Carlos A. Cunha Filho
email: ccunha@petrobras.com.br

Norsk Hydro Produksjon as
PB 7190
Sandsliveien 90
Bergen, N-5020
Norway
tel: (47) 5599 6861
fax: (47) 5599 6970
contact: Arnfinn Sagehaug
email: arnfinn.sagehaug@nho.hydro.com

PGS Technology Division
10550 Richmond Ave.
Suite 250
Houston, TX 77042
USA
tel: (713) 735-6322
fax: (713) 532-6774
contact: Ruben D. Martinez
email: ruben.martinez@pgs.com

SPONSORS OF THE STANFORD EXPLORATION PROJECT, 2004-2005

Shell International E&P Inc.
 3737 Bellaire Blvd.
 P.O. Box 481
 Houston, TX 77001-0481
 USA
 tel: (713) 245-7195
 fax: (713) 245-7339
 contact: Richard W. Cook
 email: richard.cook@shell.com

TOTAL E&P USA, Inc.
 800 Gessner
 Suite 700
 Houston, TX 77024
 USA
 tel: (713) 647-3940
 fax: (713) 647-3875
 contact: Henri Calandra
 email: henri.calandra@total.com

Statoil ASA
 Arkitekt Ebbellsvei 10
 Rotvoll
 Trondheim, N-7005
 Norway
 tel: (47) 73584917
 fax: (47) 73584665
 contact: Constantin Gereaa
 email: geco@statoil.com

Deepwater USA, UNOCAL
 14141 Southwest Fwy.
 Sugar Land, TX 77478
 USA
 tel: (281) 287-7481
 fax: (281) 287-5360
 contact: Philip S. Schultz
 email: phil.schultz@unocal.com

TGS-NOPEC Geophysical Company
 4434 Bluebonnet Dr.
 Stafford, TX 77477
 USA
 tel: (713) 860-2273
 fax: (713) 334-3308
 contact: Young Kim
 email: ykim@tgsnopec.com

Veritas DGC Ltd.
 Crompton Way
 Manor Royal Estate
 Crawley, West Sussex RH10 2QR
 England
 tel: 44 (1293) 443219
 fax: 44 (1293) 443010
 contact: Helmut Jakubowicz
 email: helmut_jakubowicz@veritasdgc.com

3DGeo Development Inc.
 4633 Old Ironsides Dr.
 Suite 401
 Santa Clara, CA 95054
 USA
 tel: (408) 450 7840, x102
 fax: (408) 450 7809
 contact: Dimitri Bevc
 email: dimitri@3dgeo.com

Weinman GeoScience
 17103 Preston Rd.
 Suite 200 N.
 Dallas, TX 75248
 USA
 tel: (972) 818-2550
 fax: (972) 818-2553
 contact: Barry L. Weinman
 email: barryw@weinmangeoscience.com

SPONSORS OF THE STANFORD EXPLORATION PROJECT, 2004-2005

WesternGeco
Houston Technology Center
10001 Richmond Ave.
Houston, TX 77042-4299
USA
tel: (713) 806-5271
fax: (713) 689-5757
contact: Luis L. Canales
email: lcanales@houston.westerngeco.slb.com